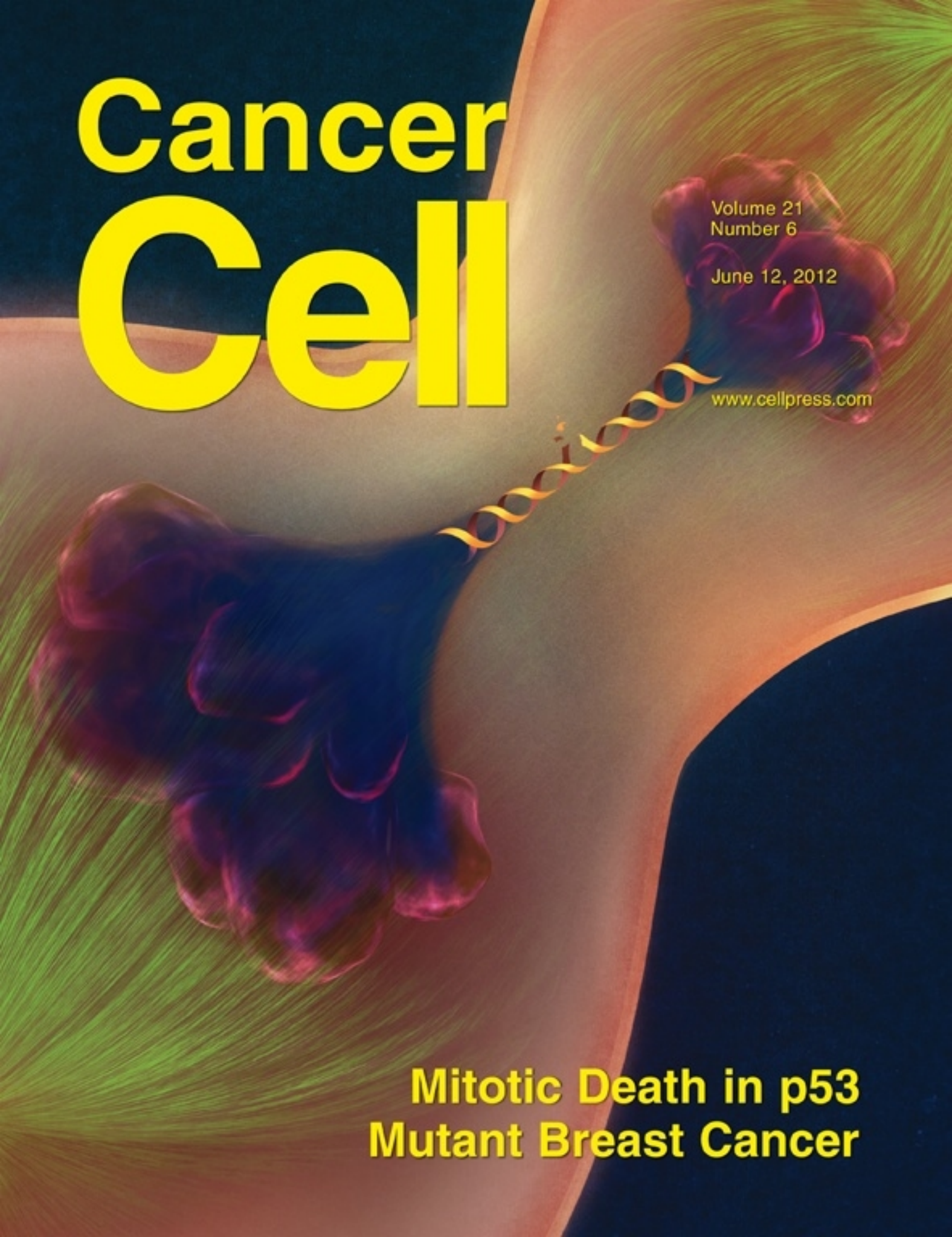
Cancer
Cell
Volume 21
Number 6
June 12, 2012
www.cellpress.com
Mitotic Death in p53
Mutant Breast Cancer

CYLD and HCC: When Being Too Sensitive to Your Dirty Neighbors Results in Self-Destruction

Joan Font-Burgada,[1] Ekihiro Seki,[2] and Michael Karin[1,*]
[1]Laboratory of Gene Regulation and Signal Transduction, Departments of Pharmacology and Pathology
[2]Department of Medicine
School of Medicine, University of California, San Diego, 9500 Gilman Drive, La Jolla, CA 92093, USA
*Correspondence: karinoffice@ucsd.edu
DOI 10.1016/j.ccr.2012.05.034

Hepatocellular carcinoma is the outcome of ongoing cycles of cell death and regeneration in chronic liver disease. In this issue of *Cancer Cell*, Nikolaou et al. show that the deubiquitinating enzyme CYLD is critical for controlling the balance between hepatocyte loss, regeneration, and malignant progression.

The liver is the quintessential regenerative organ in mammals as first documented in the Greek mythology. It has been molded through evolution to endure extreme challenges by environmental pollutants, toxic metabolites, infections, and all kinds of cellular stress. The liver is equipped with an astonishing capacity for cellular repopulation even after massive cell death. Despite the obvious benefits of these regenerative properties, they come at a high cost. Chronic liver injury and the sustained regeneration it induces provide the perfect breeding grounds for one of the deadliest cancers, hepatocellular carcinoma (HCC). Chronic liver disease is supported and sustained by unresolved fibrotic and inflammatory responses. It is in this context where NF-κB signaling has acquired a title role in the liver cancer field despite its Janus-like character.

NF-κB signaling in Kupffer cells and other immune cell types is critical in propagation of liver inflammation. However, hepatocyte-specific NF-κB deficiency caused by ablation of either IκB kinase β (IKKβ) or its regulatory subunit IKKγ/NEMO can either augment chemically induced liver carcinogenesis (Maeda et al., 2005) or lead to spontaneous liver damage, inflammation, and tumorigenesis (Luedde et al., 2007). Inactivation of hepatocyte NF-κB results in critical overactivation of JNK and ablation of *Jnk1* in $Ikk\beta^{\Delta hep}$ mice prevents enhanced susceptibility to hepatic carcinogens (Sakurai et al., 2006). In addition, defective expression of IKKγ/NEMO and TAK1 also results in spontaneous tumorigenesis with persistent JNK activation (Luedde et al., 2007; Inokuchi et al., 2010; Bettermann et al., 2010). Treatment of $Ikk\beta^{\Delta hep}$ and $Ikk\gamma/Nemo^{\Delta hep}$ mice with an antioxidant or ablation of *Tnfrl* in $Tak1^{\Delta hep}$ mice suppressed JNK over-activation and HCC formation. These results underscore that HCC formation in these mice is caused mainly by compensatory hepatocyte proliferation following massive hepatocyte death with enhanced reactive oxygen species production and JNK activation due to TNF over-production combined with loss of protective NF-κB activity and expression of antioxidant proteins. Paradoxically, however, NF-κB is a key driver of spontaneous HCC development in $Mdr2^{-/-}$ mice. Indeed, inhibition of NF-κB or titration of TNF in these mice inhibited HCC development (Pikarsky et al., 2004). In this issue of *Cancer Cell*, Nikolaou et al. (2012) show that specific deletion of the cylindromatosis tumor suppressor gene (*Cyld*) in hepatocytes results in HCC formation. Surprisingly, the authors found a procarcinogenic effect for TAK1, NF-κB, and JNK in $Cyld^{\Delta hep}$ mice.

Nikolaou et al. (2012) deleted *Cyld* specifically in hepatocytes to analyze its effects on the liver. CYLD is a negative regulator of NF-κB signaling, being a key deubiquitinase that removes K63-linked ubiquitin chains from several key effectors of the pathway, including TAK1 and IKKγ/NEMO. Since some of these effectors control the activation of MAP kinases (MAPK), the absence of CYLD also results in upregulation of MAPKs, including JNK. When $Cyld^{\Delta hep}$ mice are born, their liver appears normal. However after 25 days of age, periportal hepatocytes start dying. The authors demonstrate that this spontaneous cell death is due to prolonged JNK activation. This finding prompted Nikolaou and colleagues (2012) to identify the upstream effector responsible for JNK activation. Because TAK1 activation requires K63-linked ubiquitination and CYLD counteracts this modification in CYLD-deficient livers, TAK1 is spontaneously activated. Although previous reports showed that deletion of TAK1 in hepatocytes also results in spontaneous cell death, chronic TAK1 activation leads to sustained JNK activation which eventually promotes cell death even in the presence of NF-κB. To better investigate this point, the authors generated *Cyld* and *Tak1* double knockout mice. These animals exhibit a complete reversion of periportal hepatocyte death accompanied by a reduction in fibrosis and JNK activity, similar to those found in $Tak1^{\Delta hep}$ single mutants. Remarkably, periportal cell death and fibrosis in $Cyld^{\Delta hep}$ mice, with time, are extended toward the central vein region. This is accompanied by increased infiltration of inflammatory cells and TNF production on postnatal day 45 when hepatic NF-κB activation becomes detectable. This result prompted the authors to hypothesize that there are two different phases in the life of the CYLD-deficient liver. Initially, CYLD-devoid periportal hepatocytes suffer spontaneous cell death, provoking a second phase of injury expansion mediated by immune cells through TNF-mediated death receptor signaling. Ablation of the *Tnfr1* gene in $Cyld^{\Delta hep}$ mice demonstrated that expansion of the damage is TNF-dependent, but the persistent periportal damage pinpoints the TNF-independent nature of the initial defect. Progressive and sustained liver injury and fibrosis eventually lead to development of HCC after 12 months of age.

The work of Nikolaou et al. (2012) offers novel insights into the role of NF-κB signaling in liver homeostasis and

disease. So far, most of our knowledge of NF-κB signaling in liver pathophysiology is derived from studies in which NF-κB activation or activity is inhibited. The authors used the opposite approach trying to activate NF-κB by removing CYLD. Surprisingly, only hepatocytes in close vicinity to the portal triad suffer spontaneous apoptosis but only after postnatal day 10, arguing against a cell autonomous promotion of cell death in the absence of CYLD. If this is the case, what triggers the periportal cell death from postnatal day 10 onward? Pertinently, the authors point to commensal bacteria in the gut. During embryogenesis and shortly after birth, the gut is sterile and thus, the portal circulation to the liver is free of bacteria or microbial products. However, after the first postnatal days, the microflora start colonizing the gut, and an influx of microbial components, such as lipopolysaccharide (LPS) reaches the liver. At this point, if the hepatocytes are devoid of CYLD, an important attenuator of NF-κB signaling, they misinterpret the amount of LPS and other TLR agonists to which they are exposed. Invariably, this would lead to programmed cell death in hepatocytes that overreact to TLR agonists. Of note, CYLD is expressed in a gradient, being higher in the periportal region and lower close to the central vein, supporting an important role for CYLD in signal fine-tuning in the area where TLR agonist concentration can fluctuate the most. New investigations using germ-free *Cyld*$^{\Delta hep}$ mice would provide an important test of this hypothesis. After this initial trigger, the CYLD-deficient liver starts on a self-destruction spiral. The initial death of periportal hepatocytes triggers an inflammatory response mediated by Kupffer cells. These cells produce TNF and other death cytokines that act on hyper-responsive hepatocytes, causing more cell death and more inflammation, eventually enhancing compensatory proliferation. Interestingly, Dapito et al. (2012) recently reported that HCC promotion is affected by intestinal microbiota through TLR4 signaling in the liver. Considering that in several human liver diseases there is an increase in intestinal permeability and consequently an increase of microbial components in the portal circulation, the studies of Nikolaou et al. (2012) and Dapito et al. (2012) establish a new paradigm in liver disease in which intestinal microbiota can determine hepatocyte cellular survival and death. Thus, the intestinal barrier and commensal microflora further influence the NF-κB-JNK interplay that is already known to play a central role in the control of liver pathophysiology.

REFERENCES

Bettermann, K., Vucur, M., Haybaeck, J., Koppe, C., Janssen, J., Heymann, F., Weber, A., Weiskirchen, R., Liedtke, C., Gassler, N., et al. (2010). Cancer Cell *17*, 481–496.

Dapito, D.H., Mencin, A., Gwak, G.Y., Pradere, J.P., Jang, M.K., Mederacke, I., Caviglia, J.M., Khiabanian, H., Adeyemi, A., Bataller, R., et al. (2012). Cancer Cell *21*, 504–516.

Inokuchi, S., Aoyama, T., Miura, K., Osterreicher, C.H., Kodama, Y., Miyai, K., Akira, S., Brenner, D.A., and Seki, E. (2010). Proc. Natl. Acad. Sci. USA *107*, 844–849.

Luedde, T., Beraza, N., Kotsikoris, V., van Loo, G., Nenci, A., De Vos, R., Roskams, T., Trautwein, C., and Pasparakis, M. (2007). Cancer Cell *11*, 119–132.

Maeda, S., Kamata, H., Luo, J.L., Leffert, H., and Karin, M. (2005). Cell *121*, 977–990.

Nikolaou, K., Tsagaratou, A., Eftychi, C., Kollias, G., Mosialos, G., and Taliandis, I. (2012). Cancer Cell *21*, this issue, 738–750.

Pikarsky, E., Porat, R.M., Stein, I., Abramovitch, R., Amit, S., Kasem, S., Gutkovich-Pyest, E., Urieli-Shoval, S., Galun, E., and Ben-Neriah, Y. (2004). Nature *431*, 461–466.

Sakurai, T., Maeda, S., Chang, L., and Karin, M. (2006). Proc. Natl. Acad. Sci. USA *103*, 10544–10551.

"Two" Much of a Good Thing: Telomere Damage-Induced Genome Doubling Drives Tumorigenesis

Gianluca Varetti[1,2] **and David Pellman**[1,2,3,*]
[1]Department of Pediatric Oncology, Dana-Farber Cancer Institute, 450 Brookline Avenue, Boston, MA 02115, USA
[2]Department of Cell Biology, Harvard Medical School, 240 Longwood Avenue, Boston, MA 02115, USA
[3]Howard Hughes Medical Institute, Chevy Chase, MD 20815-6789, USA
*Correspondence: david_pellman@dfci.harvard.edu
DOI 10.1016/j.ccr.2012.05.033

Data from human tumors and mouse models suggest that tetraploidy, one example of polyploidy, can promote tumorigenesis. In this issue of *Cancer Cell*, Davoli and De Lange make important connections between tetraploidy, tumorigenesis, and telomere crisis—a common event during the development of human cancers.

Organism-level polyploidy-increased complete sets of chromosomes are very frequent in plants and are often found in insects, fish, and amphibians. Genome doublings are less common in metazoans, but at least two tetraploidization events are thought to have occurred during the evolution of vertebrates. Although still debated, it has been proposed that during

evolution, the extra chromosomes coming from a genome doubling could provide fodder for evolutionary experimentation, with the extra chromosomes being mutated, broken, and rearranged while viability is maintained by the set of intact chromosomes (Otto, 2007). This is an appealing idea that could be relevant to tumorigenesis. Indeed, tetraploid cells lacking the p53 tumor suppressor, generated by cytokinesis failure, are tumorigenic, and the resulting tumors display markedly altered genomes (Fujiwara et al., 2005).

The role of polyploidy in certain cell lineages during development is interesting but even more poorly understood. Polyploidy occurs in many metabolically active cells—hepatocytes, cardiomyocytes, trophoblast giant cells, and retinal pigment epithelial cells, to name a few (Davoli and de Lange, 2011). The correlation between polyploidy and metabolic activity has led to the speculation that polyploidy might confer a metabolic benefit, but the nature of this postulated benefit is entirely mysterious. Perhaps these poorly understood benefits drive polyploidization during the development of some cancers.

Although in special circumstances polyploidy may confer some benefits, it is not always a good deal. Newly-generated tetraploid cells, in organisms as diverse as yeasts and humans, exhibit mitotic defects and very high rates of whole chromosome aneuploidy (Davoli and de Lange, 2011). In mammals, most if not all of the chromosomal instability that accompanies tetraploidy is due to the presence of extra centrosomes. For example, it has been possible to isolate tetraploid cells in vitro that have spontaneously lost their extra centrosomes, and these cells exhibit normal genetic stability (Ganem et al., 2009). Indeed, most polyploid cells in mammalian tissues do not divide or only rarely divide, presumably because of the genetic instability that results from cell division of polyploid cells. When dividing cells do accidentally become tetraploid, a stress response is triggered that, with variable penetrance, can activates p53 and limit cell proliferation (Margolis et al., 2003).

Even though most mammalian cells are not programmed to become tetraploid, tetraploidy can occur as a consequence of a variety of pathological events. Errors in DNA replication or mitosis can lead to chromatin trapped in the cleavage furrow, eventually causing cytokinesis failure and tetraploidization. After a prolonged mitotic arrest, due to the activation of the spindle checkpoint, cells can undergo "mitotic slippage" and become tetraploid. Tetraploidization may also occur by cell fusion, for example, induced by viruses (Davoli and de Lange, 2011).

More recently, a surprising new mechanism to induce tetraploidy was uncovered: the endoreduplication of chromosomes (the absence of mitosis between two rounds of DNA replication) in the face of a persistent DNA damage signal, either from unprotected telomeres or from DNA damaging agents (Davoli et al., 2010). Deprotected telomeres are of particular interest because telomeres have been found to shorten during the early stages of many epithelial cancers. When p53-deficient cells suffer persistent DNA damage, DNA damage response kinases are activated. Among other substrates, these kinases phosphorylate and inactivate the Cdc25 phosphatases, thus blocking CyclinB/Cdk1 activity and preventing mitotic entry. However, Davoli and de Lange (2012), in this issue of *Cancer Cell*, found unexpectedly that the cell cycle does not halt, but rather flips between the G2 and the G1 phase without nuclear envelope breakdown or mitosis. During these endocycles, the origins of DNA replication are first licensed in G1, cells then enter S phase and complete DNA synthesis, but after a period of time in G2, geminin, a key inhibitor of DNA re-replication, is eventually degraded, allowing the entire cycle noted above to be repeated if the cells lack p53 (Davoli et al., 2010).

The new paper from Davoli and de Lange (2012) goes more deeply into the underlying mechanism and directly establishes that these events can promote tumorigenesis. In their previous work, Davoli and de Lange had induced telomere crisis in mouse cells somewhat artificially by genetic ablation of *Pot1*, which encodes a key protein required for telomere protection (Davoli et al., 2010). Here, they show that endoreduplication occurs in cells undergoing a more "physiological" telomere crisis, using late passage telomerase-negative cells. In a variety of human cell types, tetraploidization occurs either by endoreduplication, as described above, or by cytokinesis failure, with different proportions of these events observed in different cell types (Figure 1). The development of large numbers of tetraploid cells not only requires loss of p53, but also loss of the Rb tumor suppressor. Loss of Rb prevents a G1 arrest that would otherwise be imposed by activation of the CDK inhibitor p16. Finally, after transiently inactivating telomere protection in p53-deficient mouse embryo fibroblasts, diploid and tetraplopid cells were separated by FACS-sorting and tested for their transforming potential. Satisfyingly, the tetraploid cells exhibited significantly greater tumorigenic activity than the diploid cells carried through the same isolation procedure. Analysis of tumor karyotypes showed that the tumor genomes had evolved a subtetraploid chromosome content. The generation of unstable tetraploid cells, followed by evolution to a subtetraploid genome may occur in human tumors, as was recently inferred from genomic analysis of metastases from a renal carcinoma (Gerlinger et al., 2012).

Altogether, these findings show that telomere attrition is a double whammy. It is already known that critical telomere shortening can lead to chromosome breaks and rearrangements via breakage-fusion-bridge cycles. The new findings reveal that tetraploidy adds further fuel to the fire. Importantly, both sources of instability are potentially reversible. After telomere crisis, breakage-fusion-bridge cycles are short-circuited by reexpression of telomerase. Likewise, the transformed tetraploid cells generated by Davoli and de Lange (2012) evolved to presumably more stable subtetraploid genomes (Figure 1). Transient genetic instability may be beneficial to a developing cancer cell; it increases the chances of obtaining transforming mutations but obviates the need to pay the fitness cost of ongoing instability.

This work raises a host of interesting biological and mechanistic questions. First: if nascent tumor cells go through a genome doubling, at what point in tumor development does that occur? Recent work by Carter et al. (2012) took a computational approach to analyze DNA copy number data from a huge number of tumors. This study confirms that genome doublings and near-tetraploid genomes are remarkably common.

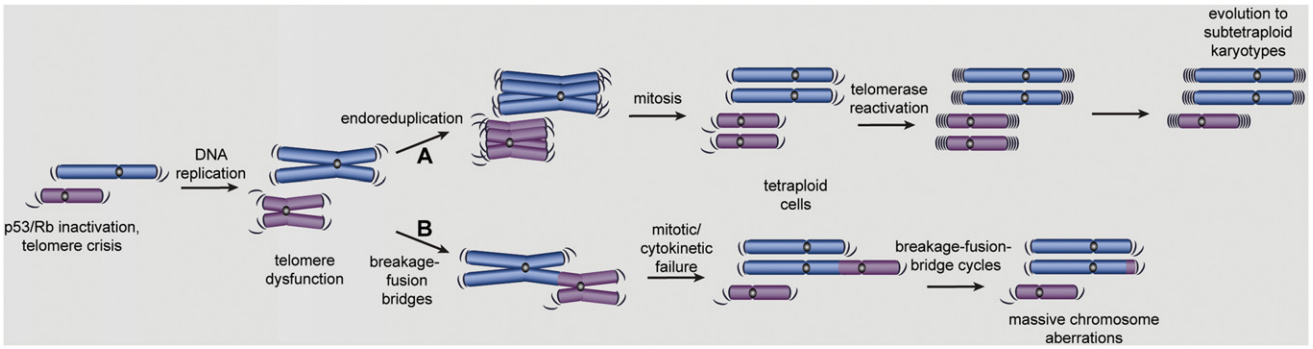

Figure 1. Telomere Dysfunction Promotes Tetraploidy

(A) Endoreduplication after prolonged DNA damage of p53 deficient cells. Telomere dysfunction, or other persistent DNA damage, generates a DNA damage response that arrests p53 deficient cells in the G2 phase of the cell cycle. After a prolonged arrest, diploid (2N) cells degrade the DNA replication inhibitor geminin, license DNA replication origins, and start a new round of DNA synthesis without entering mitosis. The resultant tetraploid cells survive and proliferate if telomerase is re-expressed. This tetraploid clone can promote tumorigenesis and often evolves to a subtetraploid karyotype.

(B) Tetraploidization after cytokinesis failure. In the setting of deprotected telomeres, cells can develop telomere end-to-end fusions. This generates dicentric chromosomes and initiates chromosome breakage-fusion-bridge cycles. The dicentric chromosomes generated by this mechanism can result in chromatin trapped at the cleavage furrow and subsequent failure of cytokinesis. Both mechanisms of tetraploidization result in centrosome amplification and additional chromosomal instability.

However, their data suggest that genome doublings often occur relatively late, after the acquisition of other chromosome aneuploidies. This is perhaps not that surprising given the need for p53 loss to enable the proliferation of polyploid cells. Also, polyploidy need not always be integral to tumor development; in some circumstances, it may be consequence rather than cause. Second: what is the mechanism by which polyploidy accelerates oncogenesis? Recent work has revealed that errors in mitotis can cause DNA damage and thus potentially produce cancer-causing mutations (Crasta et al., 2012; Janssen et al., 2011). Given that centrosome amplification is instrumental in driving the instability of tetraploid cells (Ganem et al., 2009), a parsimonious hypothesis is that genome doublings may drive tumor development in the old-fashioned way—by generating mutations that activate oncogenes and inactivate tumor suppressors.

REFERENCES

Carter, S.L., Cibulskis, K., Helman, E., McKenna, A., Shen, H., Zack, T., Laird, P.W., Onofrio, R.C., Winckler, W., Weir, B.A., et al. (2012). Nat. Biotechnol. Published online April 29, 2012. 10.1038/nbt.2203.

Crasta, K., Ganem, N.J., Dagher, R., Lantermann, A.B., Ivanova, E.V., Pan, Y., Nezi, L., Protopopov, A., Chowdhury, D., and Pellman, D. (2012). Nature *482*, 53–58.

Davoli, T., and de Lange, T. (2011). Annu. Rev. Cell Dev. Biol. *27*, 585–610.

Davoli, T., and de Lange, T. (2012). Cancer Cell *21*, this issue, 765–776.

Davoli, T., Denchi, E.L., and de Lange, T. (2010). Cell *141*, 81–93.

Fujiwara, T., Bandi, M., Nitta, M., Ivanova, E.V., Bronson, R.T., and Pellman, D. (2005). Nature *437*, 1043–1047.

Ganem, N.J., Godinho, S.A., and Pellman, D. (2009). Nature *460*, 278–282.

Gerlinger, M., Rowan, A.J., Horswell, S., Larkin, J., Endesfelder, D., Gronroos, E., Martinez, P., Matthews, N., Stewart, A., Tarpey, P., et al. (2012). N. Engl. J. Med. *366*, 883–892.

Janssen, A., van der Burg, M., Szuhai, K., Kops, G.J., and Medema, R.H. (2011). Science *333*, 1895–1898.

Margolis, R.L., Lohez, O.D., and Andreassen, P.R. (2003). J. Cell. Biochem. *88*, 673–683.

Otto, S.P. (2007). Cell *131*, 452–462.

Silencing the Killers: Paracrine Immune Suppression in Pancreatic Cancer

Adrienne D. Cox[1,*] and Kenneth P. Olive[2]
[1]Departments of Radiation Oncology and Pharmacology, Lineberger Comprehensive Cancer Center, University of North Carolina at Chapel Hill, Chapel Hill, NC 27599, USA
[2]Departments of Medicine and Pathology, Herbert Irving Comprehensive Cancer Center, Columbia University Medical Center, New York, NY 10032, USA
*Correspondence: adrienne_cox@med.unc.edu
DOI 10.1016/j.ccr.2012.05.029

Pancreatic cancers are characterized by high levels of inflammatory cells and profound immune suppression. In this issue of *Cancer Cell*, Bayne et al. and Pylayeva-Gupta et al. show that KRAS-driven, tumor cell-secreted GM-CSF recruits myeloid-derived suppressor cells to the stroma to abrogate tumor cell immune clearance by killer T lymphocytes.

Soldiers in the army of immune surveillance may fight on the side of the host or may be be co-opted to fight on the side of the tumor. Host immune surveillance is thought to be important to limit both cancer development and cancer progression (Schreiber et al., 2011), whereas failure may be due to a countervailing local immunosuppression mediated by the tumor.

Pancreatic ductal adenocarcinomas (PDA or PDAC) are among the deadliest cancers, notable for their aggressiveness, profound immunosuppression, and remarkable degree of desmoplasia surrounding the nests of ductal epithelial cells (Clark et al., 2007). Tumor cells are encased in a high-pressure, fibrous stromal mass composed of a dense extracellular matrix and of fibroblasts, pancreatic stellate cells, endothelial cells, nerve cells, and large numbers of inflammatory cells, especially of immature myeloid lineages. This intricate stromal remodeling in PDAC is also distinguished by the conspicuous absence of T lymphocytes.

Inflammation leading to PDAC desmoplasia depends on paracrine signals produced by neoplastic epithelial cells, a process largely driven by oncogenic *KRAS*, which is mutated in essentially all human PDAC (Jones et al., 2008). Indeed, acute loss of mutant *KRAS* in established pancreatic tumors results in rapid quiescence and involution of pancreatic tumor stroma (Collins et al., 2012). Hedgehog signaling is known to promote fibroblast proliferation in pancreatic tumors, but the signals for other cell types have not been well established. Two new studies provide some answers to this critical question.

In this issue of *Cancer Cell*, Bayne et al. (2012) sought to determine which signals lead to the accumulation in PDAC of myeloid-derived suppressor cells (MDSCs), the immature myeloid cells that are characterized by $Gr1^{+}CD11b^{+}$ markers and are thought to play a key immunosuppressive role in this tumor type (Ostrand-Rosenberg and Sinha, 2009). Pylayeva-Gupta et al. (2012), also in this issue of *Cancer Cell*, asked which early changes in pancreata harboring oncogenically mutated *KRAS* drive initiation of the desmoplastic stromal response. Both groups of researchers have applied neutralizing antibodies and short hairpin (sh) RNAs to systematically test the requirements for candidates in PDAC stromal responses, using cell culture, mouse models, and human PDAC samples. Their investigations led to the identification of a paracrine circuit in PDAC, based on the pro-inflammatory cytokine GM-CSF secreted by tumor cells, that engages stromal myeloid cells to exert an immunosuppressive effect on local killer T cells (Figure 1) (Bayne et al., 2012; Pylayeva-Gupta et al., 2012). Several themes emerged from these investigations: (1) a key role for KRAS in driving the inflammatory tumor microenvironment, beginning early in pancreatic intraepithelial neoplasia (PanIN) development and continuing through frank carcinoma; (2) the critical and surprisingly specific importance of GM-CSF; (3) the dependence of both emerging and established PDAC on GM-CSF-responsive MDSCs recruited to the pancreatic stroma; and (4) the failure of CD8 cytotoxic T cell immunity unless either GM-CSF or MDSCs was disrupted.

An important strength of these complementary reports is their use of genetically engineered mouse strains that express the oncogenic $KRAS^{G12D}$ from the endogenous *KRAS* locus specifically in the pancreas (Hingorani et al., 2005). Pylayeva-Gupta et al. (2012) isolated primary pancreatic ductal epithelial cells (PDECs) from such mice and compared the secretion of cytokines before and after the expression of $KRAS^{G12D}$ in vitro. They also generated orthotopic allografts by injecting $KRAS^{G12D}$ or wild-type PDECs into the pancreata of syngeneic hosts. This model is particularly suitable for studying the early pancreatic lesions known as PanINs, and this group used it to interrogate how initial immune responses to *KRAS* activation enable nascent tumors to proliferate and survive. In contrast, Bayne et al. (2012) allowed tumor formation to occur spontaneously in the "KPC" mouse model, in which both $KRAS^{G12D}$ and the *p53* mutant $Tp53^{R172H}$ were expressed (Hingorani et al., 2005). This model faithfully recapitulates the pathophysiological characteristics of different stages of human PDAC. Bayne et al. (2012) used this model to identify inflammatory cytokines upregulated during tumor progression and to determine the origin of MDSCs and their importance in negative regulation of local T cell immunity in established PDAC tumors. Crucially,

both approaches maintain an intact immune system, without which these studies would not have been possible.

Which inflammatory cytokines are secreted in KRAS-driven PDAC? Surprisingly, only GM-CSF was consistently upregulated in tumor cells and tumors from both *KRAS*-driven models, but not in PDEC that lacked $KRAS^{G12D}$ or in normal pancreatic duct cells. GM-CSF was also upregulated in conditioned medium from KPC-derived PDAC and in human tumor samples, where its expression was detected by immunohistochemistry in the vast majority of PanINs and PDAC. Lineage marking of the pancreatic epithelial compartment in KPC mice demonstrated conclusively that cells of epithelial but not stromal origin elaborated GM-CSF (Bayne et al., 2012). Near-complete abrogation of GM-CSF mRNA upon pharmacological inhibition of MEK or PI3K in KRAS-PDEC demonstrated that the Ras/MAPK and PI3K effector pathways regulate GM-CSF in these cells at the level of transcription (Pylayeva-Gupta et al., 2012).

How do we know that KRAS-mediated escape from T cell immunity is important? First, no CD8 T cells were present in nascent orthotopic tumors established from $KRAS^{G12D}$-PDECs, whereas tumors established from $shKRAS^{G12D}$-PDECs displayed a CD8 cell infiltrate and underwent apoptosis at 2 weeks after implant (Pylayeva-Gupta et al., 2012). These results suggest that CD8 cytotoxic T cells can recognize and clear incipient PDAC tumors, but that KRAS signaling is able to overcome that clearance. The extensive secretion of GM-CSF suggested that this cytokine plays a central role: disrupting GM-CSF secretion or neutralizing its activity inhibited tumor growth and maintenance. Conversely, depleting CD8 could rescue tumor growth impaired by loss of GM-CSF.

What are the origins of myeloid-derived immune suppressor cells in PDAC? The growth of KPC-derived PDAC was dependent upon $Gr1^+CD11b^+$ cells, which showed hallmarks of MDSCs, namely increased levels of arginase and iNOS (Bayne et al., 2012). iNOS played an important role in suppressing antigen-specific proliferation of T cells. The MDSCs were derived from c-kit^+ splenic precursors (Bayne et al., 2012), which proliferated and differentiated in response to conditioned medium from PDAC cells or to GM-CSF. Their maturation from bone marrow-derived $Gr1^-CD11b^-$ cells, recruitment, and immune-suppressing ability required GM-CSF. Collectively, these results support the existence and importance of a GM-CSF-driven paracrine immune suppression circuit in PDAC.

Many complexities remain to be unraveled. Which subcategory of $Gr1^+CD11b^+$ MDSCs are these? How do MDSCs block CD8+ cell activity? What antigen(s) do the successful CD8+ killer cells recognize on pancreatic precursor lesions and carcinomas? What dictates the selective upregulation and importance of GM-CSF seen here? GM-CSF is sufficient to elicit CD8 suppression by $Gr1^+CD11b^+$ MDSCs in a non-PDAC context (Bronte et al., 1999), yet KRAS induction of other important growth factors and inflammatory cytokines such as VEGF, IL-6, and IL-1beta also can regulate these cells. In what context does the GM-CSF axis interact with other KRAS-driven inflammatory pathways such as STAT3/MMP7 or PI3K/STAT3/SOCS? Should GM-CSF be used for KRAS vaccines in PDAC (Abou-Alfa et al., 2011)? How can KRAS-driven GM-CSF be downregulated? Are transplant recipients with chronic pancreatitis or cancer patients on chemotherapy at greater risk for PDAC if they also receive GM-CSF?

The great Yogi Berra famously said, "When you come to a fork in the road, take it." The winning side of the war on pancreatic cancer may be determined in part by fork control: whether CD8 soldiers are battling for the host or are run off the battlefield by the tumor.

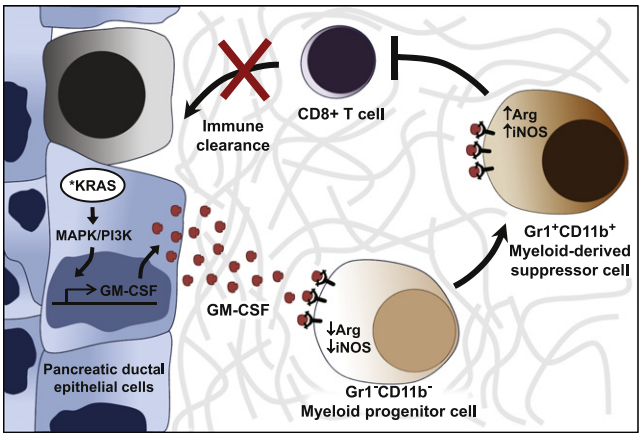

Figure 1. Tumor Cell-Derived GM-CSF Drives Immune Suppression in Pancreatic Cancer

Oncogenically activated KRAS (*KRAS) expressed in pancreatic ductal epithelial cells (PDECs) reprograms the tumor microenvironment by directing transcription of the inflammatory cytokine GM-CSF. Tumor-derived GM-CSF promotes recruitment of myeloid progenitor cells to the surrounding stroma and subsequent differentiation into myeloid-derived suppressor cells (MDSCs). MDSCs suppress the immune surveillance function of CD8+ killer T cells, preventing them from recognizing and clearing transformed PDECs. Arg, arginase; iNOS, inducible nitric oxide synthase. Both Arg and iNOS have been linked with immunosuppressive capabilities of MDSCs.

REFERENCES

Abou-Alfa, G.K., Chapman, P.B., Feilchenfeldt, J., Brennan, M.F., Capanu, M., Gansukh, B., Jacobs, G., Levin, A., Neville, D., Kelsen, D.P., and O'Reilly, E.M. (2011). Am. J. Clin. Oncol. *34*, 321–325.

Bayne, L.J., Beatty, G.L., Jhala, N., Clark, C.E., Rhim, A.D., Stanger, B.Z., and Vonderheide, R.H. (2012). Cancer Cell *21*, this issue, 822–835.

Bronte, V., Chappell, D.B., Apolloni, E., Cabrelle, A., Wang, M., Hwu, P., and Restifo, N.P. (1999). J. Immunol. *162*, 5728–5737.

Clark, C.E., Hingorani, S.R., Mick, R., Combs, C., Tuveson, D.A., and Vonderheide, R.H. (2007). Cancer Res. *67*, 9518–9527.

Collins, M.A., Bednar, F., Zhang, Y., Brisset, J.C., Galbán, S., Galbán, C.J., Rakshit, S., Flannagan, K.S., Adsay, N.V., and Pasca di Magliano, M. (2012). J. Clin. Invest. *122*, 639–653.

Hingorani, S.R., Wang, L., Multani, A.S., Combs, C., Deramaudt, T.B., Hruban, R.H., Rustgi, A.K., Chang, S., and Tuveson, D.A. (2005). Cancer Cell *7*, 469–483.

Jones, S., Zhang, X., Parsons, D.W., Lin, J.C., Leary, R.J., Angenendt, P., Mankoo, P., Carter, H., Kamiyama, H., Jimeno, A., et al. (2008). Science *321*, 1801–1806.

Ostrand-Rosenberg, S., and Sinha, P. (2009). J. Immunol. *182*, 4499–4506.

Pylayeva-Gupta, Y., Lee, K.E., Hajdu, C.H., Miller, G., and Bar-Sagi, D. (2012). Cancer Cell *21*, this issue, 836–847.

Schreiber, R.D., Old, L.J., and Smyth, M.J. (2011). Science *331*, 1565–1570.

Rolling the Dice to Discover the Role of DICER in Tumorigenesis

Veronica Davalos[1] and Manel Esteller[1,2,3,*]
[1]Cancer Epigenetics and Biology Program (PEBC), Bellvitge Biomedical Research Institute (IDIBELL), Barcelona, 08908 Catalonia, Spain
[2]Departament de Ciencies Fisiologiques II, School of Medicine, University of Barcelona, Barcelona, 08007 Catalonia, Spain
[3]Institucio Catalana de Recerca i Estudis Avançats (ICREA), Barcelona, 08010 Catalonia, Spain
*Correspondence: mesteller@idibell.cat
DOI 10.1016/j.ccr.2012.05.030

In an effort to identify the consequences of complete DICER1 loss in tumorigenesis, in this issue of *Cancer Cell*, Ravi et al. characterize the effects of homozygous deletion of *Dicer1*. Using an in vivo mouse model, they show that genetic deletion of *Dicer1* does not preclude tumor formation.

MicroRNAs (miRNAs) are small noncoding RNAs that inhibit gene expression at the posttranscriptional level. miRNAs are synthesized in the nucleus by RNA polymerase II as long primary transcripts, termed primary miRNAs (pri-miRNAs). They are subsequently cleaved by DROSHA to release hairpin-shaped precursors of 70–90 nucleotides (nt) in length (pre-miRNAs). These are transported by Ran-GTP/EXPORTIN-5 (XPO5) to the cytoplasm, where DICER1 processes them to yield a 19–22 nt-long duplex. One strand of the duplex is loaded into the RNA-induced silencing complex (RISC), which delivers mature miRNAs to their mRNA targets. TARBP2, an RNA-binding protein that forms a complex with DICER, acts as a biosensor selecting the miRNA to be loaded into the RISC complex. It has been predicted that miRNAs regulate the translation rate of about half of all protein-coding genes, so their role in most biological processes, including development, metabolism, cell proliferation, differentiation, and apoptosis, is now well-recognized. For this reason, it is not surprising that deregulation of miRNA levels has been associated with tumorigenesis.

Although both tumor suppressor and oncogenic miRNAs have been described, the global downregulation of miRNAs is emerging as a common hallmark of cancer. Recent studies have highlighted possible mechanisms, including epigenetic and genetic events, which could explain this decrease in miRNAs in tumors. In the same way as previously described for protein-coding genes, several studies have identified CpG island promoter hypermethylation-associated epigenetic silencing as a common mechanism for miRNA repression in cancer (Saito et al., 2006; Lujambio et al., 2007; Davalos et al., 2012).

On the other hand, tumor-specific genetic defects in genes encoding members of the miRNA-processing machinery, such as TARBP2, XPO5, and DICER1, have been described. Truncating mutations in TARBP2, associated with destabilization of the DICER1 protein and consequent impairment of miRNA processing, have been identified in sporadic and hereditary carcinomas with microsatellite instability (MSI) (Melo et al., 2009). Also, in a subset of human tumors with MSI, XPO5-inactivating mutations that cause trapping of pre-miRNAs in the nucleus and impair the production of mature miRNAs have been detected in cancer cells (Melo et al., 2010). In the case of DICER1, heterozygous germline truncating mutations have been identified in families with the pleuropulmonary blastoma-inherited cancer syndrome (Hill et al., 2009) and hypomorphic somatic missense mutations have been detected in non-epithelial ovarian tumors (Heravi-Moussavi et al., 2012). However, the complete loss of DICER1 has not been reported. This fact and evidence from mouse models have led to the suggestion that total DICER1 depletion could be deleterious to tumor development.

In an effort to identify the consequences of complete DICER1 loss in tumorigenesis, Ravi et al. (2012 [in this issue of *Cancer Cell*]) characterize the effects of homozygous deletion of *Dicer1* using two cellular models: *Dicer1* null cells derived from a mouse sarcoma and those established from murine mesenchymal stem cells (MSCs) (Figure 1). To ensure accurate assessment, while preventing competition from cells that retain *Dicer1*, clonal isolation of $Dicer1^{-/-}$ cells was compulsory in both cases, since preferential outgrowth of heterozygous DICER1-expressing cells was detected after multiple passages. In comparison with parental heterozygous $Dicer^{f/-}$ cells, monoclonal homozygous $Dicer1^{-/-}$ cells derived from both models exhibited a global loss of mature miRNAs, a concomitant accumulation of precursors, derepression of miRNA luciferase reporters, proliferative lag, delayed exit from G1 phase of the cell cycle, and higher levels of basal apoptosis.

Having confirmed the tolerance of *Dicer1* depletion in vitro, to address the main issue at hand—the role of DICER1 in tumorigenesis—Ravi and coworkers developed an in vivo mouse model. $Dicer1^{-/-}$ sarcoma cells were injected into both immune-compromised and immunocompetent mice. In view of the growth disadvantage of *Dicer1* null cells relative to those retaining *Dicer1* expression detected in vitro, the authors accurately confirmed that the tumors were composed predominantly of $Dicer1^{-/-}$ cells. Strikingly, the experiments revealed that genetic ablation of DICER1 impaired but did not preclude tumor formation. $Dicer1^{-/-}$ sarcoma cells did retain their in vivo tumorigenicity, albeit at lower rates than $Dicer1^{f/-}$.

Considering previous publications and the apparently contrasting results obtained from other mouse models, one of the main findings of this study is the detection of the selective growth advantage of *Dicer1*-expressing cells over

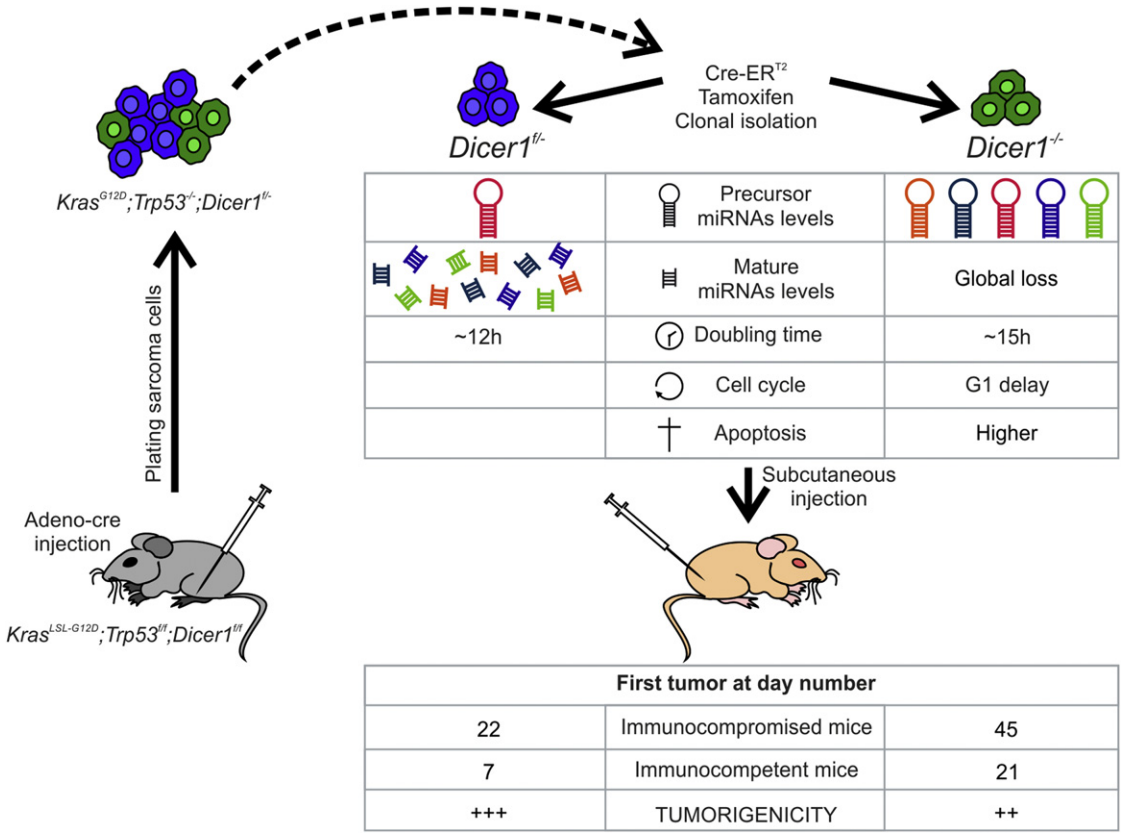

Figure 1. Characterization of the Effects of Homozygous Deletion of *Dicer1* Using a Murine Sarcoma Model

Dicer1-heterozygous sarcoma tumors were generated after hindlimb injection of Adeno-cre virus in Kras$^{LSL-G12D/+}$;Trp53$^{f/f}$;Dicer1$^{f/f}$ mice. Sarcoma cell lines were established and clones were isolated following Cre-ER integration and tamoxifen treatment. In comparison with parental heterozygous *Dicer*$^{f/-}$ cells, monoclonal homozygous *Dicer1*$^{-/-}$ cells exhibited a global loss of mature miRNAs with concomitant accumulation of precursors, proliferative lag, delayed exit from G1 phase of the cell cycle, and higher levels of basal apoptosis. Next, *Dicer*$^{f/-}$ or *Dicer1*$^{-/-}$ sarcoma cells were injected in the flanks of immunocompromised and immunocompetent mice. Although at slower rates relative to *Dicer1*$^{f/-}$, *Dicer1*$^{-/-}$ sarcoma cells retained their tumorigenicity in vivo.

Dicer1 null cells. A significant advance in our knowledge about DICER1's role in cancer has been achieved through the use of clonally isolated *Dicer1*$^{-/-}$ cells in the experiments described in this study. Thus, the interpretations of previous results, including those involving analyses of tumor samples, should be reconsidered since it is possible that subpopulations exist with different proliferative rates and because of the preferential outgrowth of cells expressing *Dicer1*. Ravi et al. (2012) present convincing evidence that *Dicer1*$^{-/-}$ cells are able to survive, proliferate without recovery of miRNA processing, and form tumors in mice. However, the occurrence of homozygous mutations in nature remains to be demonstrated, so the conclusions drawn from *Dicer1*$^{-/-}$ models must be considered cautiously. In addition, the experiments of Ravi et al. (2012) are limited to mesenchymal settings (sarcoma and MSCs), so their confirmation in other cell models is imperative, especially given the epithelial origin of most human tumors.

Certainly, however, the experimental models developed by Ravi et al. (2012) are a valuable tool for expanding our knowledge about the function of the miRNA processing pathway in the context of cancer. Consistent with previous findings from other genes of the miRNA pathway that show cancer-related loss-of-function mutations (Melo et al., 2009, 2010), as well as the well-recognized global downregulation of miRNAs in tumors, this study firmly supports the tumor suppressor role of the miRNA machinery. In this scenario, restoration of normal miRNA levels represents an attractive approach in cancer therapy. A new "miRNAome-based" strategy has been suggested, involving the use of the small molecule enoxacin. Proof-of-principle studies in human cancer cell lines and xenografted primary tumors have shown the powerful cancer-specific growth-inhibitory effect of this drug, mediated by the TARBP2-dependent restoration of the expression of tumor suppressor miRNAs (Melo et al., 2011). The global activation of miRNA processing by DICER1 stabilization with enoxacin has also been confirmed in neurons (Huang et al., 2012). The tumor suppressor role of miRNAs themselves and genes encoding members of the miRNA processing machinery warrants intensive research addressing the pharmacological approaches required to restore the global miRNAome in cancer.

REFERENCES

Davalos, V., Moutinho, C., Villanueva, A., Boque, R., Silva, P., Carneiro, F., and Esteller, M. (2012). Oncogene *31*, 2062–2074.

Heravi-Moussavi, A., Anglesio, M.S., Cheng, S.W., Senz, J., Yang, W., Prentice, L., Fejes, A.P., Chow,

C., Tone, A., Kalloger, S.E., et al. (2012). N. Engl. J. Med. *366*, 234–242.

Hill, D.A., Ivanovich, J., Priest, J.R., Gurnett, C.A., Dehner, L.P., Desruisseau, D., Jarzembowski, J.A., Wikenheiser-Brokamp, K.A., Suarez, B.K., Whelan, A.J., et al. (2009). Science *325*, 965.

Huang, Y.W., Ruiz, C.R., Eyler, E.C., Lin, K., and Meffert, M.K. (2012). Cell *148*, 933–946.

Lujambio, A., Ropero, S., Ballestar, E., Fraga, M.F., Cerrato, C., Setién, F., Casado, S., Suarez-Gauthier, A., Sanchez-Cespedes, M., Git, A., et al. (2007). Cancer Res. *67*, 1424–1429.

Melo, S., Villanueva, A., Moutinho, C., Davalos, V., Spizzo, R., Ivan, C., Rossi, S., Setien, F., Casanovas, O., Simo-Riudalbas, L., et al. (2011). Proc. Natl. Acad. Sci. USA *108*, 4394–4399.

Melo, S.A., Moutinho, C., Ropero, S., Calin, G.A., Rossi, S., Spizzo, R., Fernandez, A.F., Davalos, V., Villanueva, A., Montoya, G., et al. (2010). Cancer Cell *18*, 303–315.

Melo, S.A., Ropero, S., Moutinho, C., Aaltonen, L.A., Yamamoto, H., Calin, G.A., Rossi, S., Fernandez, A.F., Carneiro, F., Oliveira, C., et al. (2009). Nat. Genet. *41*, 365–370.

Ravi, A., Gurtan, A., Kumar, M., Bhutkar, A., Chin, C., Lu, V., Lees, J., Jacks, T., and Sharp, P. (2012). Cancer Cell *21*, this issue, 848–855.

Saito, Y., Liang, G., Egger, G., Friedman, J.M., Chuang, J.C., Coetzee, G.A., and Jones, P.A. (2006). Cancer Cell *9*, 435–443.

A Big Step for SIRT7, One Giant Leap for Sirtuins… in Cancer

Paloma Martínez-Redondo,[1] Irene Santos-Barriopedro,[1] and Alejandro Vaquero[1,*]
[1]Chromatin Biology Laboratory, Cancer Epigenetics and Biology Program (PEBC), Bellvitge Biomedical Research Institute (IDIBELL), Avinguda Gran Via de l'Hospitalet, 199-203, 08908 L'Hospitalet de Llobregat, Barcelona, Spain
*Correspondence: avaquero@idibell.cat
DOI 10.1016/j.ccr.2012.05.028

Recently reporting in *Nature*, Barber et al. demonstrated that SIRT7 maintains critical features that define cancer cells by removing the acetylation mark on lysine 18 of histone H3. Interestingly, hypoacetylation of H3K18 has been described as a general marker of tumor prognosis and oncoviral transformation.

Sirtuins are NAD^+-dependent deacetylases that target histone and non-histone proteins and are major factors in the response to oxidative, metabolic, and genotoxic stresses. Their responses are global and occur at many different levels; consequently, Sirtuins are at the crossroads among the foremost pathways that control cellular fate, including those for survival, genomic stability, apoptosis, and energy or metabolic adaptation. The importance of Sirtuins is reflected by their implication in several major human pathologies, including cancer, diabetes, cardiovascular diseases and neurodegenerative diseases (Bosch-Presegué and Vaquero, 2011).

Mammals have seven Sirtuins (denoted SIRT1–7) that have considerably different functions and catalytic activities. SIRT7 has been one of the most puzzling Sirtuins. Although researchers had clearly identified SIRT7 in chromatin, they had not found any clear catalytic activity or target specificity for it. The only target that had been proposed for SIRT7 was p53, but this is currently under debate. Evidence has supported a crucial role for SIRT7 in oxidative and genotoxic stress response. Homozygous knockout of *Sirt7* in mice causes diminished lifespan and leads to heart hypertrophy and inflammatory cardiopathy. Cardiomyocytes derived from these mice show increased apoptosis as well as hypersensitivity to oxidative and genotoxic stress. However, other than an ill-defined functional relationship between SIRT7 and p53 activity, no clear molecular explanation has been determined for these phenomena (Vakhrusheva et al., 2008b).

Another reported role for SIRT7 is in the control of ribosomal RNA (rRNA) expression. SIRT7 localizes mainly in the nucleolus, where it binds to the rRNA genes (rDNA) and participates in activation of RNA-polymerase I (pol-I) transcription (Figure 1A). Although this function apparently depends on SIRT7 having an intact "catalytic domain" (defined by homology to other Sirtuins), no mechanism has been described (Ford et al., 2006). However, some evidence suggests that this SIRT7 function may be specific to certain cell types (Vakhrusheva et al., 2008b; Barber et al., 2012). Interestingly, SIRT7 is relevant for the reactivation of rDNA transcription at the end of mitosis. Although the exact mechanism of SIRT7 action here is unknown, its interactions with the pol-I cofactors UBF and chromatin remodeling complex B-WICH have been described (Grob et al., 2009). Based on these findings and that SIRT7 is more abundant in highly proliferative tissues than in lowly proliferative tissues, a role for SIRT7 as a principal activator of proliferation has been proposed. On the contrary, other findings have suggested that SIRT7 may inhibit proliferation (Ford et al., 2006; Vakhrusheva et al., 2008a). This discrepancy has been a subject of controversy until now.

A recent report in *Nature* by Barber et al. (2012) represents a major breakthrough in SIRT7 research and redefines our view on the role of Sirtuins in cancer. The authors discovered a specific target of SIRT7 and identified a crucial role for SIRT7 in the maintenance of cancer phenotype and transformation. They found that SIRT7 is specific for a single histone mark, acetylated lysine 18 in histone H3 (H3K18Ac), directly linked to

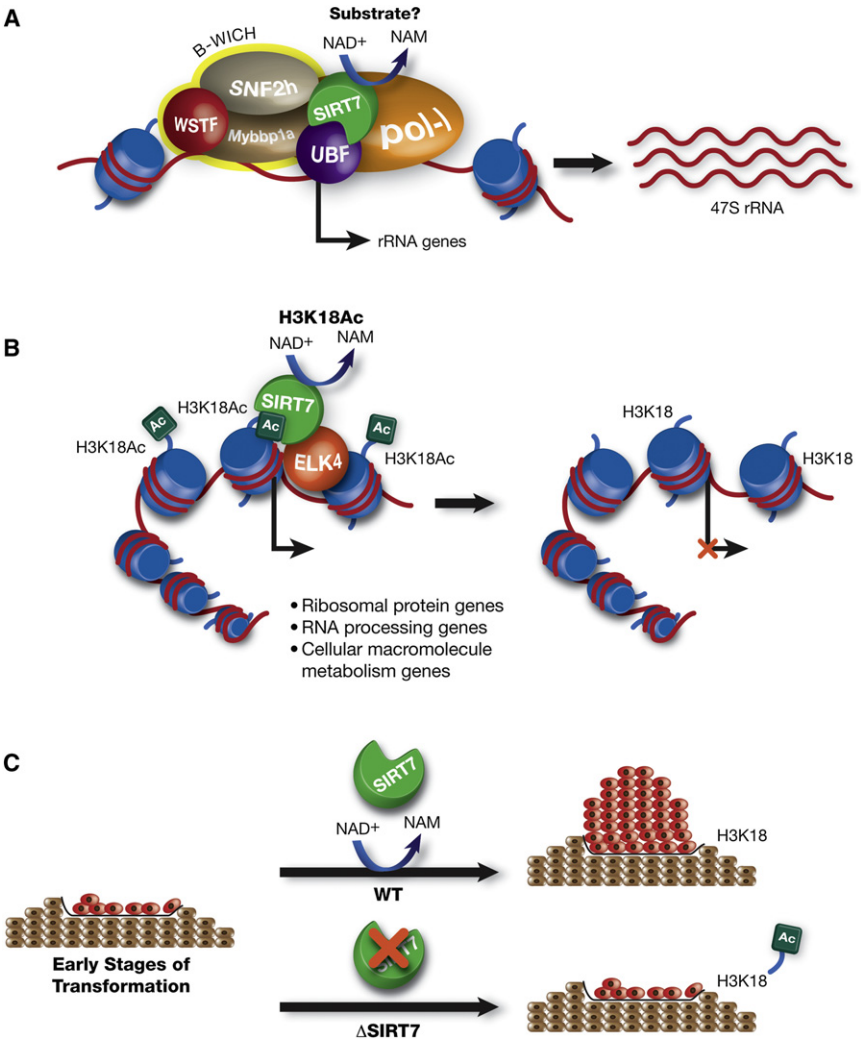

Figure 1. SIRT7 Modulates Protein Biosynthesis and Maintains Tumor Phenotype through H3K18Ac Deacetylation

(A) SIRT7 is involved in the transcription of rDNA by RNA-polymerase I (pol-I) through its catalytical activity of an undescribed substrate. For this function, SIRT7 has been shown to interact with the pol-I cofactor UBF and the UBF-binding chromatin remodeling complex B-WICH.

(B) SIRT7 represses the transcription of 241 genes, many of which are involved in protein synthesis, through deacetylation of H3K18Ac in these promoters.

(C) SIRT7 is responsible for tumor phenotype maintenance and proliferation through deacetylation of H3K18Ac. Depletion of SIRT7 inhibits tumor growth in vivo.

control of gene expression. Interestingly, H3K18Ac is mainly present in a sharp peak around the transcription start site of genes and has been linked to activation of nuclear hormone receptors (Wang et al., 2008). Moreover, H3K18 hypoacetylation has been reported as a marker of malignancy in various human cancers (Seligson et al., 2009) and has been linked to the ability of the adenovirus small early region 1a (e1a) protein to trigger oncogenic transformation (Ferrari et al., 2008; Horwitz et al., 2008).

Barber et al. (2012) performed ChIP sequencing experiments and identified 276 binding sites for SIRT7 in the genome, corresponding to 241 protein-coding genes. In 74% of these genes, SIRT7 was mainly present in the promoter proximal regions where it directly regulated the H3K18Ac level. Among the most represented genes regulated by SIRT7 through H3K18 deacetylation were those involved in different stages of regulation of protein biosynthesis, including RNA processing and protein translation (Figure 1B). Interestingly, the expression of many of these genes is deregulated in various cancers. A limitation of this study is that binding of SIRT7 to rDNA sites was not determined in this approach, as repetitive DNA sequences are not easily processed in ChIP-seq analysis. Sequence analysis of SIRT7-occupied promoters led to identification of ELK4, a MAPK-signaling dependent ETS transcription factor, as a partner of SIRT7. Almost 60% of the SIRT7-binding sites contain ELK4-binding motifs, and ELK4 depletion decreases the binding of SIRT7 at these promoters.

How this repressive regulatory function of SIRT7 in protein biosynthesis reconciles with a proactive role in rDNA transcription activation should be determined in the future; the mechanism involved in rDNA transcription is likely distinct to that of H3K18Ac deacetylation. Whether both events occur simultaneously or under different physiological conditions (e.g., stress or tumorigenesis) also remains to be addressed.

The ChIP-seq results of Barber et al. (2012) and the previously known link between H3K18Ac and cancer together corroborate an important role for SIRT7 in tumorigenesis. Consistent with this premise, SIRT7 has been reported to be upregulated in breast and thyroid cancers (Bosch-Presegué and Vaquero, 2011). Based on these findings, Barber et al. (2012) show that SIRT7 enzymatic activity is responsible for maintaining some of the most important features of human cancer cells, such as anchorage-independent growth, growth in low serum, and loss of contact inhibition. Importantly, depletion of SIRT7 inhibited the growth of human cancer cells as tumor xenografts in mice (Figure 1C). Interestingly, SIRT7 is also required for transformation by e1a and is responsible for the H3K18 hypoacetylation observed upon transformation. Given the limited number of SIRT7-regulated genes, it is possible that a small pool of genes is involved in the pro-tumorigenic function of SIRT7. In the case of e1a transformation, SIRT7 may undergo specific relocalization. Future studies should be able to clarify this issue and identify these genes.

The work of Barber et al. (2012) is a significant advance toward

understanding the implication of Sirtuins in cancer, a rather complicated subject. To date, Sirtuins have only been linked to cancer as collateral factors, rather than as direct effectors. They may help modulate various pathways that could favor or disfavor tumor development according to physiological context. Interestingly, SIRT7 is not actively involved in establishing cancer phenotype, but it is fundamental for maintaining this phenotype (Barber et al., 2012). Thus, it would be interesting to determine whether *Sirt7* knockout mice are more resistant to tumorigenesis. Whether this function stems from a specific role of SIRT7 in promoting tumor proliferation or is related to the functions of other Sirtuins, remains an open question. The relationship of this SIRT7 function to stress response and the context of this relationship are also unknown. The answer probably lies in the control of protein biosynthesis, as metabolic and energetic stress induce blockage of ribosome production and alterations in these processes are linked to tumorigenesis and aging.

In the light of the report by Barber et al. (2012), we speculate that development of specific modulators of SIRT7 may be crucial for helping control tumor progression or even for reversing cancer phenotype. Answering these questions should prove to be an exciting challenge in the future. Regardless, this work has made it clear that when it comes to cancer, Sirtuins are here to stay.

REFERENCES

Barber, M.F., Michishita-Kioi, E., Xi, Y., Tasselli, L., Kioi, M., Moqtaderi, Z., Tennen, R.I., Paredes, S., Young, N.L., Chen, K., et al. (2012). Nature. Published online May 6, 2012. 10.1038/nature11043.

Bosch-Presegué, L., and Vaquero, A. (2011). Genes Cancer *2*, 648–662.

Ferrari, R., Pellegrini, M., Horwitz, G.A., Xie, W., Berk, A.J., and Kurdistani, S.K. (2008). Science *321*, 1086–1088.

Ford, E., Voit, R., Liszt, G., Magin, C., Grummt, I., and Guarente, L. (2006). Genes Dev. *20*, 1075–1080.

Grob, A., Roussel, P., Wright, J.E., McStay, B., Hernandez-Verdun, D., and Sirri, V. (2009). J. Cell Sci. *122*, 489–498.

Horwitz, G.A., Zhang, K., McBrian, M.A., Grunstein, M., Kurdistani, S.K., and Berk, A.J. (2008). Science *321*, 1084–1085.

Seligson, D.B., Horvath, S., McBrian, M.A., Mah, V., Yu, H., Tze, S., Wang, Q., Chia, D., Goodglick, L., and Kurdistani, S.K. (2009). Am. J. Pathol. *174*, 1619–1628.

Vakhrusheva, O., Braeuer, D., Liu, Z., Braun, T., and Bober, E. (2008a). J. Physiol. Pharmacol. *59*, 201–212.

Vakhrusheva, O., Smolka, C., Gajawada, P., Kostin, S., Boettger, T., Kubin, T., Braun, T., and Bober, E. (2008b). Circ. Res. *102*, 703–710.

Wang, Z., Zang, C., Rosenfeld, J.A., Schones, D.E., Barski, A., Cuddapah, S., Cui, K., Roh, T.Y., Peng, W., Zhang, M.Q., and Zhao, K. (2008). Nat. Genet. *40*, 897–903.

Cancer Cell
Article

Exploiting Synthetic Lethality for the Therapy of ABC Diffuse Large B Cell Lymphoma

Yibin Yang,[1,7] Arthur L. Shaffer III,[1,7] N.C. Tolga Emre,[1,7,8] Michele Ceribelli,[1] Meili Zhang,[1] George Wright,[4] Wenming Xiao,[2] John Powell,[2] John Platig,[1,5] Holger Kohlhammer,[1] Ryan M. Young,[1] Hong Zhao,[1] Yandan Yang,[1] Weihong Xu,[1] Joseph J. Buggy,[6] Sriram Balasubramanian,[6] Lesley A. Mathews,[3] Paul Shinn,[3] Rajarshi Guha,[3] Marc Ferrer,[3] Craig Thomas,[3] Thomas A. Waldmann,[1] and Louis M. Staudt[1,*]
[1]Metabolism Branch, Center for Cancer Research, National Cancer Institute
[2]Bioinformatics and Molecular Analysis Section, Division of Computational Bioscience, Center for Information Technology
[3]National Center for Advancing Translational Sciences
National Institutes of Health, Bethesda, MD 20892, USA
[4]Biometric Research Branch, National Cancer Institute, National Institutes of Health, Rockville, MD 20852, USA
[5]Institute for Research in Electronics and Applied Physics, University of Maryland, College Park, MD 20742, USA
[6]Pharmacyclics, Sunnyvale, CA 94085, USA
[7]These authors contributed equally to this work
[8]Present address: Boğaziçi University, Department of Molecular Biology and Genetics, Laboratory of Genome Regulation, Kuzey Park Binasi, 3.Kat, Bebek 34342, Istanbul, Turkey
*Correspondence: lstaudt@mail.nih.gov
DOI 10.1016/j.ccr.2012.05.024

SUMMARY

Knowledge of oncogenic mutations can inspire therapeutic strategies that are synthetically lethal, affecting cancer cells while sparing normal cells. Lenalidomide is an active agent in the activated B cell-like (ABC) subtype of diffuse large B cell lymphoma (DLBCL), but its mechanism of action is unknown. Lenalidomide kills ABC DLBCL cells by augmenting interferon β (IFNβ) production, owing to the oncogenic *MYD88* mutations in these lymphomas. In a cereblon-dependent fashion, lenalidomide downregulates IRF4 and SPIB, transcription factors that together prevent IFNβ production by repressing *IRF7* and amplify prosurvival NF-κB signaling by transactivating *CARD11*. Blockade of B cell receptor signaling using the BTK inhibitor ibrutinib also downregulates IRF4 and consequently synergizes with lenalidomide in killing ABC DLBCLs, suggesting attractive therapeutic strategies.

INTRODUCTION

The activated B cell-like (ABC) subtype of diffuse large B cell lymphoma (DLBCL) is much less curable than the other common DLBCL subtypes—germinal center B cell-like (GCB DLBCL) and primary mediastinal B cell lymphoma (PMBL)—necessitating new therapeutic strategies (Alizadeh et al., 2000; Lenz et al., 2008b; Rosenwald et al., 2002, 2003). ABC DLBCL tumors have constitutive NF-κB activity, which maintains their viability (Davis et al., 2001). Additionally, NF-κB induces expression of IRF4 (Davis et al., 2001; Saito et al., 2007), a key transcription factor in B cell differentiation and activation (Shaffer et al., 2009). IRF4 binds to a 10-base-pair motif, termed the ETS/IRF composite element (EICE) (Kanno et al., 2005; Marecki and Fenton, 2000), in conjunction with one of two highly homologous ETS-family transcription factors, PU.1 and SPIB (Brass et al., 1996; Eisenbeis et al., 1995; Shaffer et al., 1997). SPIB is required for the survival of ABC DLBCL lines and is recurrently amplified and occasionally translocated in ABC DLBCL, suggesting an oncogenic function (Lenz et al., 2007, 2008c). IRF4 is required for the survival of multiple myeloma cells, but its role in ABC DLBCL has not been addressed (Shaffer et al., 2008).

The molecular basis for constitutive NF-κB activation in ABC DLBCL was elucidated using functional and structural genomics.

Significance

New therapies are needed for the activated B cell-like (ABC) subtype of diffuse large B cell lymphoma (DLBCL), the most refractory subtype of this lymphoma. Oncogenic mutations activate the BCR and MYD88 pathways in ABC DLBCL, engaging NF-κB and IFNβ signaling. Lenalidomide, a drug showing clinical activity against DLBCL, kills ABC DLBCLs by inducing IFNβ and blocking NF-κB. Lenalidomide antagonizes a central regulatory hub in ABC DLBCL governed by transcription factors IRF4 and SPIB, which together suppress IFNβ while augmenting NF-κB. Oncogenic BCR signaling to NF-κB induces IRF4 expression in ABC DLBCL. Inhibition of BCR signaling with the drug ibrutinib synergizes with lenalidomide to block IRF4 and kill ABC DLBCL cells, supporting clinical trials of this synthetically lethal drug combination.

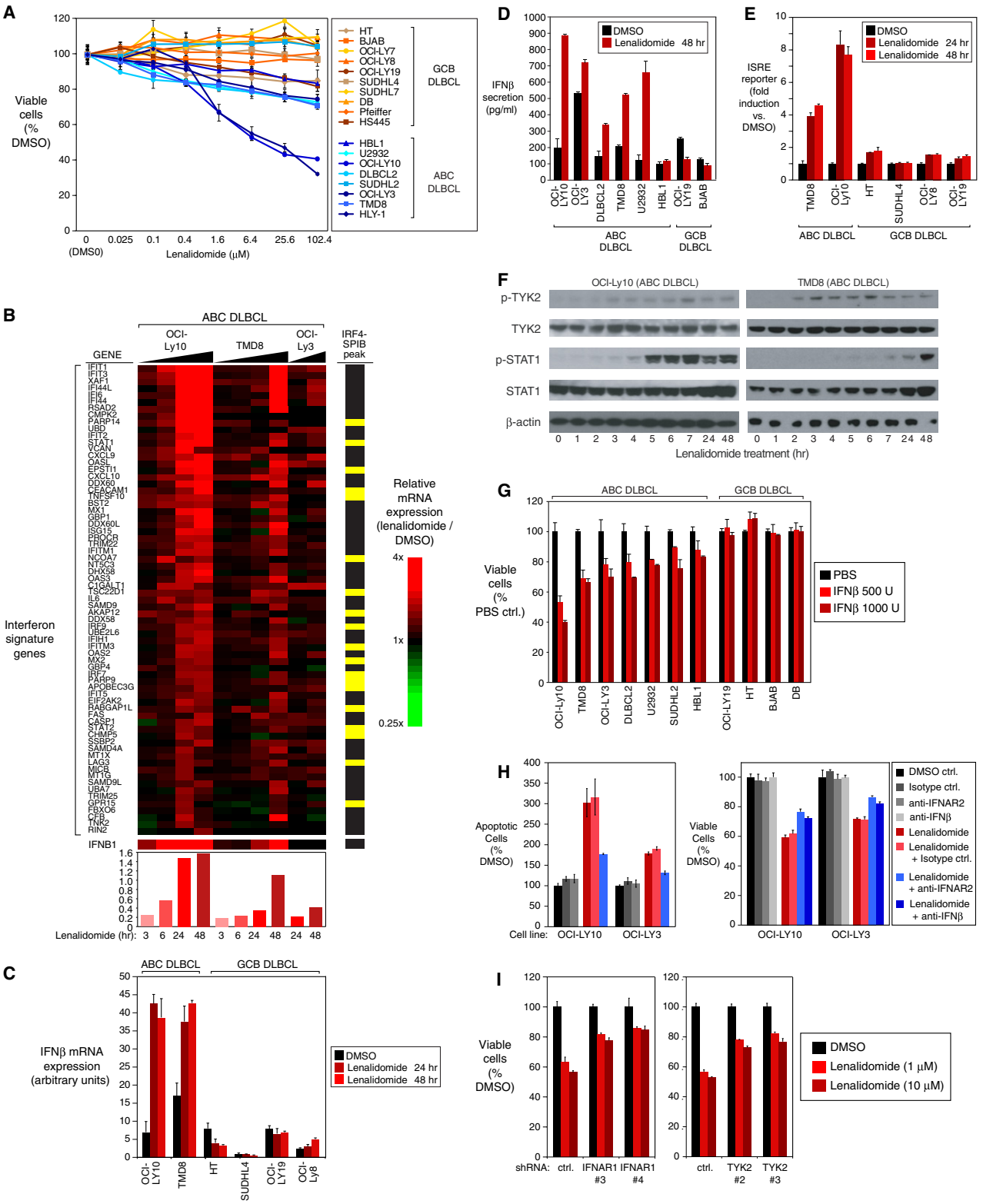

Figure 1. Lenalidomide Induces a Toxic Type I Interferon Response in ABC DLBCL

(A) Viability (MTS assay) of ABC and GCB DLBCL cell lines treated with lenalidomide for 4 days. Error bars show the SEM of triplicates.

(B) Relative expression of interferon signature genes over a time course of lenalidomide (10 μM) treatment. Gene-expression changes induced by lenalidomide are depicted according to the color scale shown. Average relative expression of interferon signature genes is at the bottom. Yellow bars, genes with overlapping IRF4/SPIB ChIP-seq peaks.

Following BCR engagement, the signaling adaptor CARD11 coordinates the activation of IκB kinase (IKK), a key regulator of NF-κB signaling (Thome et al., 2010). CARD11 is required for NF-κB activity and viability of ABC DLBCL lines (Ngo et al., 2006), and in ~10% of ABC DLBCLs, CARD11 acquires oncogenic mutations leading to spontaneous IKK and NF-κB activity (Lenz et al., 2008a). In other DLBCLs, BCR signaling engages wild-type CARD11 to activate NF-κB, a phenomenon termed chronic active BCR signaling (Davis et al., 2010). More than 20% of ABC DLBCL tumors have mutant forms of the CD79B and CD79A subunits of the BCR that augment receptor signaling, establishing the pathogenetic importance of the BCR pathway in ABC DLBCL (Davis et al., 2010).

The survival of ABC DLBCL lines also depends upon MYD88, a key adaptor in Toll-like receptor signaling (Ngo et al., 2011). Oncogenic gain-of-function mutations in *MYD88* are among the most recurrent genetic aberrations in ABC DLBCL (Ngo et al., 2011). MYD88 promotes NF-κB and JAK/STAT3 signaling, thereby sustaining ABC DLBCL viability. Additionally, MYD88 mutants induce interferon β (IFNβ) production and autocrine type I interferon signaling, which paradoxically promotes cell-cycle arrest and apoptosis (Stark et al., 1998).

New therapeutic strategies are being devised to exploit the separate oncogenic mechanisms in the DLBCL subtypes. A recent phase 2 clinical trial revealed that lenalidomide is an active agent in relapsed/refractory DLBCL (Hernandez-Ilizaliturri et al., 2011). Retrospective analysis showed a 55% response rate in non-GCB DLBCL (including ABC DLBCL cases) compared with a 9% response rate in GCB DLBCL. More than half of the responses in non-GCB DLBCL were complete, extending the progression-free survival of this cohort, although overall survival remained unchanged. In the present study, we investigated the molecular mechanisms underlying the toxicity of lenalidomide for ABC DLBCL cells in order to design rational strategies to optimize its therapeutic effect.

RESULTS

Lenalidomide Induces a Lethal Type I Interferon Response in ABC DLBCL

To understand the molecular basis for the efficacy and specificity of lenalidomide in treating lymphoma, we assessed its effect on the viability of cell line models of DLBCL. Lenalidomide treatment was toxic to most ABC DLBCL cell lines, whereas most GCB DLBCL lines were unaffected (Figure 1A). To investigate the mechanisms of this toxicity, we profiled gene-expression changes in ABC DLBCL lines upon exposure to lenalidomide (Figure 1B). Lenalidomide increased the expression of 476 genes and reduced the expression of 272 genes (Tables S1F and S1G, available online). To gain biological insight into these lenalidomide-responsive genes, we used a database of gene-expression signatures that reflect signaling and regulatory processes in normal and malignant cells (Shaffer et al., 2006). The most consistent signatures upregulated by lenalidomide were those associated with the type I interferon response (Table S1A; Figure 1B). Conversely, signatures of NF-κB, JAK, and MYD88 signaling were downregulated by lenalidomide (Table S1B), suggesting that blockade of these prosurvival pathways contributes to lenalidomide toxicity (see below).

Lenalidomide increased interferon β (IFNβ) mRNA expression and protein secretion in the majority of ABC DLBCL lines, but not in most other DLBCL lines (Figures 1B–1D). In ABC DLBCL lines, lenalidomide activated a reporter gene driven by an interferon-stimulated response element (ISRE), which did not occur in GCB DLBCL lines, even though they respond to exogenously added interferon (Figures 1E and S1B). Moreover, the drug induced phosphorylation of TYK2, a JAK-family kinase associated with the type I interferon receptor, and STAT1, a transcription factor that is phosphorylated by TYK2 (Figure 1F).

Addition of IFNβ to cultures of ABC DLBCL lines induced cell death, with a potency that paralleled the effect of lenalidomide, suggesting that IFNβ might contribute to lenalidomide toxicity (Figures 1G and S1A). Indeed, antibodies against the interferon α/β receptor chain 2 (anti-IFNAR2) or IFNβ inhibited lenalidomide-induced death (Figure 1H). Likewise, silencing of the interferon α/β receptor chain 1 (IFNAR1) or TYK2 by RNA interference reduced lenalidomide toxicity (Figures 1I, S1C, and S1I). Moreover, lenalidomide-induced STAT1 phosphorylation was blunted by anti-IFNAR2 antibodies or by IFNAR1 knockdown (Figure S1D).

Apoptosis induced by interferon is associated with induction of TRAIL (Oshima et al., 2001; Ucur et al., 2003). TRAIL (*TNFSF10*) mRNA and protein levels were increased by lenalidomide in ABC DLBCL cells and anti-IFNAR2 antibodies blocked this induction (Figures 1B and S1E–S1G). Anti-TRAIL antibodies partially rescued ABC DLBCL cells from lenalidomide-induced death (Figure S1H), suggesting that TRAIL induction contributes to lenalidomide toxicity but is not the only cell-death mechanism involved (see below).

The IRF4 and SPIB Regulatory Network in ABC DLBCL

In a separate initiative, we defined the gene network controlled by the transcription factor IRF4, allowing us to appreciate an unexpected regulatory connection between IRF4 and lenalidomide. IRF4 expression is a hallmark of ABC DLBCL, secondary to the constitutive NF-κB activation and plasmacytic

(C and D) IFNβ mRNA expression and secretion in lenalidomide-treated (10 μM) cells. Error bars show the SEM of triplicates.
(E) Activity of an ISRE-driven luciferase reporter in cells treated with lenalidomide (10 μM) or vehicle control (DMSO) at the indicated times. Error bars show the SEM of triplicates.
(F) Western blot analysis of the indicated proteins in lenalidomide-treated (10 μM) ABC DLBCL cells.
(G) Viability (MTS assay) of DLBCL cells treated with the indicated amount of human recombinant IFNβ for 4 days. Error bars show the SEM of triplicates.
(H) Measurement of viability (MTS assay; right) and apoptosis (PARP cleavage and caspase-3 activation by FACS; left) in ABC DLBCL cells treated with control compounds (DMSO or isotype-matched antibody), lenalidomide (1 μM), or lenalidomide plus the indicated blocking antibodies (2.5 μg/ml) for 4 days. Error bars show the SEM of triplicates.
(I) Viability (MTS assay) of OCI-Ly10 ABC DLBCL cells in which the indicated shRNAs were induced for 2 days before treatment with DMSO or lenalidomide, as indicated, for 4 days. Error bars show the SEM of triplicates.
See also Figure S1 and Table S1.

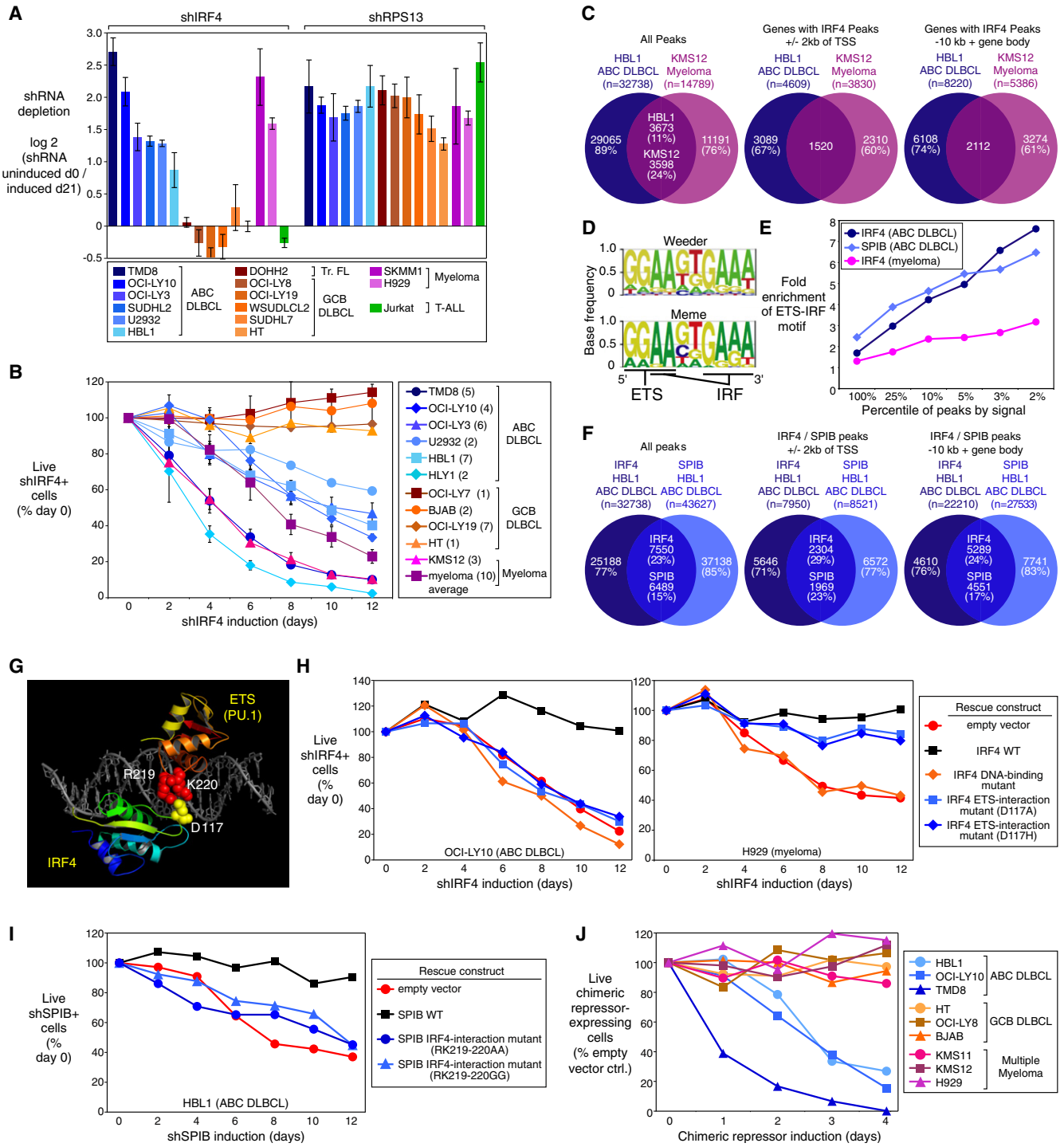

Figure 2. IRF4 and SPIB Are Required for ABC DLBCL Viability

(A) Toxicity of an IRF4 shRNA in a loss-of-function RNA interference screen of the indicated cell lines. Shown are the log2 ratios of shRNA abundance before induction (uninduced d0) versus abundance after 21 days in culture (induced d21). shRPS13 targets ribosomal protein S13, an essential gene in all cell types. Error bars show the SEM for quadriplicates.

(B) Viability of shIRF4+ (GFP+) cells over time after induction as a percentage of live shIRF4+ cells following shIRF4 induction relative to day 0. The number of replicate infections is shown in parentheses. Error bars represent the SEM of replicates.

(C) Overlap of IRF4 ChIP-Seq peaks in ABC DLBCL and multiple myeloma, based on all peaks (left), genes with an IRF4 peak within ±2 kb of the TSS (middle), and genes with an IRF4 peak in a region encompassing the gene body and 10 kb upstream of the TSS (right).

(D) Motif discovery using the Weeder and MEME algorithms based on the top 1,000 ABC DLBCL IRF4 ChIP-Seq peaks by sequence tag abundance. The highest scoring motif is shown with core recognition motifs indicated.

differentiation that characterizes this subtype (Alizadeh et al., 2000; Lam et al., 2005; Saito et al., 2007; Wright et al., 2003). Previously, we demonstrated that all multiple myeloma cell lines depend on IRF4 for survival (Shaffer et al., 2008). In a focused RNA interference screen, we observed that IRF4 knockdown was toxic to both ABC DLBCL and multiple myeloma lines, but not to a variety of other lymphoma and leukemia lines (Figure 2A; Table S2A). However, all cell lines were killed comparably when ribosomal or proteasomal proteins were knocked down. In confirmatory experiments, induction of an IRF4 shRNA killed ABC DLBCL and multiple myeloma cells in a time-dependent fashion, but GCB DLBCL lines were not affected (Figure 2B; Figure S2H). The toxicity of the IRF4 shRNA was reversed by ectopic expression of an IRF4 cDNA, confirming its specificity (Figure S2A). IRF4 mRNA and protein levels were reduced by ~40%–60% by this shRNA, indicating that the ABC DLBCL lines are sensitive to partial IRF4 knockdown (Figure S2B). The cell cycle was not affected by IRF4 knockdown, but an increase in cells with sub-G1 DNA content was evident, indicating cell death (Figure S2C). IRF4 knockdown activated caspase-3, suggesting that apoptosis was initiated (Figures S2D and S2E), but a caspase inhibitor did not alter the kinetics of ABC DLBCL cell death (Figures S2F and S2G), suggesting that nonapoptotic cell-death mechanisms are also invoked (Shaffer et al., 2008).

To identify genes directly regulated by IRF4, we performed chromatin immunoprecipitation (ChIP) followed by high throughput DNA sequencing (ChIP-seq) in cell line models of ABC DLBCL (HBL1) and multiple myeloma (KMS12), as well as in a GCB DLBCL line that does not express IRF4 (OCI-Ly19). We identified significant binding events (''peaks''; see Supplemental Experimental Procedures) in HBL1 and KMS12 that were not present in OCI-Ly19 (Figure 2C), and observed that IRF4 peaks were enriched near transcription start sites (TSSs) of protein-coding genes (Figure S2I). We confirmed the presence of 10 IRF4 binding sites in ABC DLBCL by conventional ChIP (Figure S2J).

Among IRF4 peaks in the ABC DLBCL line, 3,673 (11%) coincided with IRF4 peaks in the multiple myeloma line (Figure 2C). We defined a ''whole gene'' window from −10kb relative to the TSS and extending through the body of the gene, and observed that 2,112 genes had IRF4 peaks within this window in both ABC DLBCL and multiple myeloma (Figure 2C; Tables S2B and S2C). However, a substantial fraction (>60%) of the IRF4 target genes in these ABC DLBCL and multiple myeloma cell lines were unique to each tumor. For example, we previously identified a positive feedback loop between IRF4 and MYC in multiple myeloma cells whereby each factor binds the other's promoter and drives expression (Shaffer et al., 2008). The IRF4 ChIP-Seq data confirmed IRF4 binding to the *MYC* locus in multiple myeloma but not ABC DLBCL (Figure S2K), despite high MYC expression in ABC DLBCL (Shaffer et al., 2006). *IRF4* was itself an IRF4 target gene in multiple myeloma, suggesting positive autoregulation, but not in ABC DLBCL (Figure S2K). Conversely, many genes, such as *CD44* and *CD40*, were bound by IRF4 in ABC DLBCL but not in multiple myeloma (Figure S2K). These data suggest distinct IRF4 regulatory networks in these two malignancies, but analysis of more cell lines will be needed to fully elucidate these differences.

Using de novo DNA motif discovery algorithms, the most common sequence in ABC DLBCL IRF4 peaks was an exact match to the EICE motif (Figure 2D; Table S2D). IRF4 peaks in multiple myeloma were enriched not for this motif but rather for a direct repeat of an IRF binding site (GAAT(G/C)GAAT; Table S2D). Among promoter-proximal peaks, EICE enrichment steadily increased as a function of IRF4 peak intensity in ABC DLBCL ($p = 1.81E-24$) and was located near the point of highest ChIP-seq intensity within each peak (Figures 2E and S2L). These data imply that IRF4 binds with an ETS family member to the EICE motif in ABC DLBCL but relies on other mechanisms to interact with its target genes in multiple myeloma.

IRF4 binds to the EICE motif with either PU.1 or SPIB, neither of which is expressed in myeloma cells. SPIB is characteristically expressed in ABC DLBCL and can be further upregulated by amplification or translocation of its genomic locus (Lenz et al., 2007, 2008c). Given that ABC DLBCL lines require SPIB for survival (Lenz et al., 2008c), we suspected that SPIB was the relevant IRF4 binding partner in these cells. To perform ChIP-seq for SPIB, we engineered the HBL1 ABC DLBCL line to express biotinylated SPIB (SPIB biotag; see Experimental Procedures). SPIB peaks were found preferentially near TSSs in ABC DLBCL (Figure S2M), and were enriched for the ETS-family DNA-binding motif (GGAA; Table S2D). SPIB and IRF4 peaks in ABC DLBCL overlapped 4.3-fold more often than expected by chance ($p < 10E-300$) (Figure 2F, Tables S2E and S2F). EICE motifs within IRF4 and SPIB binding peaks were enriched near TSSs ($p = 1.91E-135$) and their frequency increased as a function of peak intensity (Figures 2E, S2L, and S2M). Overlapping IRF4-SPIB peaks were present at 3610 genes in ABC DLBCL, with 33% of those peaks containing at least one EICE (Table S2F).

The dependence of ABC DLBCLs on IRF4 and SPIB predicted that disruption of the IRF4-SPIB interaction would be deleterious to ABC DLBCL viability. A crystal structure of the mouse IRF4 and PU.1 DNA binding domains bound to an EICE motif allowed us to model the human IRF4-SPIB interaction (Escalante et al., 2002a, 2002b). IRF4 contacts PU.1 across the DNA minor

(E) Enrichment for the EICE motif in promoter-proximal peaks (±2 kb from the TSS) based on IRF4 and SPIB ChIP-Seq data in ABC DLBCL or multiple myeloma, as a function of peak percentile, ranked by sequencing tag abundance.
(F) Overlap of IRF4 and SPIB ChIP-seq peaks in ABC DLBCL, as in (C).
(G) Crystal structure of the mouse IRF4 and PU.1 DNA binding domains interacting with an EICE, showing the interacting charged residues conserved in human IRF4 and SPIB.
(H) Rescue experiment showing the viability of the indicated cell lines bearing empty vector, wild-type IRF4, or mutant IRF4 expression vectors, plotted as the fraction of shIRF4+ (GFP+) cells at times following shIRF4 induction relative to day 0.
(I) Rescue experiment as in (H) with cells bearing the indicated SPIB expression vectors and an inducible SPIB-3′UTR-targeted shRNA.
(J) Viability (FACS for live cells) of the indicated cell lines expressing an inducible IRF4-SPIB chimeric repressor, plotted as a percentage of live chimeric repressor+ cells relative to empty vector-bearing control cells, at various times following chimeric repressor induction.
See also Figure S2 and Table S2.

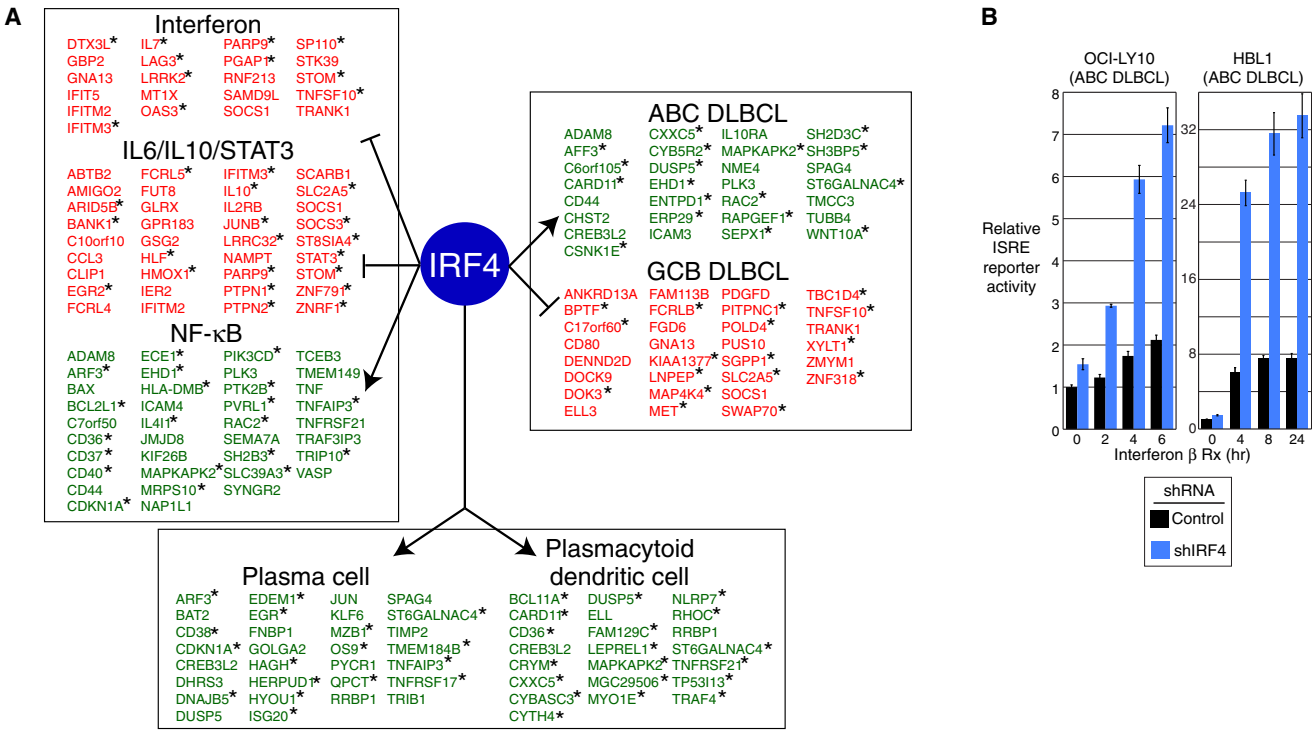

Figure 3. IRF4 Controls Essential Gene-Expression Programs in ABC DLBCL

(A) IRF4 direct target genes grouped according to gene-expression signatures (Shaffer et al., 2006). Signatures with significant enrichment for IRF4 targets were grouped by function (Table S3A). Genes that are induced or repressed by IRF4 are indicated in green and red, respectively. Asterisks indicate genes with an overlapping IRF4-SPIB ChIP-seq peak.

(B) ISRE-driven luciferase reporter activity in ABC DLBCL lines with control or IRF4 shRNAs after 2 days of induction and subsequent addition of IFNβ (1,000 U). Error bars show the SEM of triplicates.

See also Figure S3 and Table S3.

groove via charged residues that are conserved in human IRF4 (aspartic acid 117) and human SPIB (arginine 219 and lysine 220) (Figure 2G). We generated IRF4 and SPIB mutants to test whether this protein-protein interface is essential for ABC DLBCL survival. As expected, ectopic expression of the wild-type IRF4 coding region rescued ABC DLBCL and multiple myeloma lines from the toxicity of a 3′UTR-directed IRF4 shRNA, whereas an IRF4 DNA-binding mutant was inactive (Figure 2H). IRF4 interaction mutants with histidine or alanine at position 117 were expressed as efficiently as wild-type IRF4 and were not toxic (data not shown), but did not sustain ABC DLBCL viability (Figure 2H). By contrast, these mutants did rescue multiple myeloma cells from IRF4 shRNA toxicity, demonstrating that they are functional in this context. Wild-type SPIB was able to rescue ABC DLBCL cells from SPIB knockdown, but SPIB interaction mutants with alanine or glycine substitutions at positions 219 and 220 were ineffective, while being equivalently expressed and nontoxic (Figure 2I; data not shown).

This mutational analysis indicated that the IRF4-SPIB interaction is critical for ABC DLBCL viability. To test this further, we created a fusion protein between the DNA binding domains of IRF4 and SPIB based on previous work showing that an IRF4-PU.1 fusion functions as a sequence-specific transcriptional repressor (Brass et al., 1999). The IRF4-SPIB chimeric protein was acutely toxic to ABC DLBCL but not to GCB DLBCL lines (Figure 2J, and see below). This chimeric repressor was not toxic to IRF4-dependent multiple myeloma lines, suggesting that it specifically represses genes that require both IRF4 and SPIB for expression.

Pathways Regulated by IRF4-SPIB in ABC DLBCL

To determine the nature of the genes and pathways controlled by IRF4 and SPIB in ABC DLBCL, we profiled gene-expression changes upon IRF4 knockdown, allowing us to define a set of genes that were consistently downregulated (n = 435) or upregulated (n = 410) (Tables S3G and S3H; Figure S3A). Many of these genes were similarly regulated by SPIB and the chimeric IRF4-SPIB repressor (Tables S3I, S3J, and S3K). For example, among the downregulated genes, 46% and 42% also decreased in expression following SPIB knockdown and IRF4-SPIB chimeric repressor induction, respectively. Among IRF4-regulated genes, we defined "direct targets" as those that had an IRF4 binding peak within the whole-gene window specified above (Figure 2C). Many IRF4 direct targets had overlapping IRF4-SPIB peaks (Figure 3A).

Gene-expression signatures that were enriched among IRF4 targets were those that distinguish the DLBCL subtypes, characterize hematopoietic differentiation states, or are regulated by signaling pathways active in ABC DLBCL (Figure 3A; Table S3).

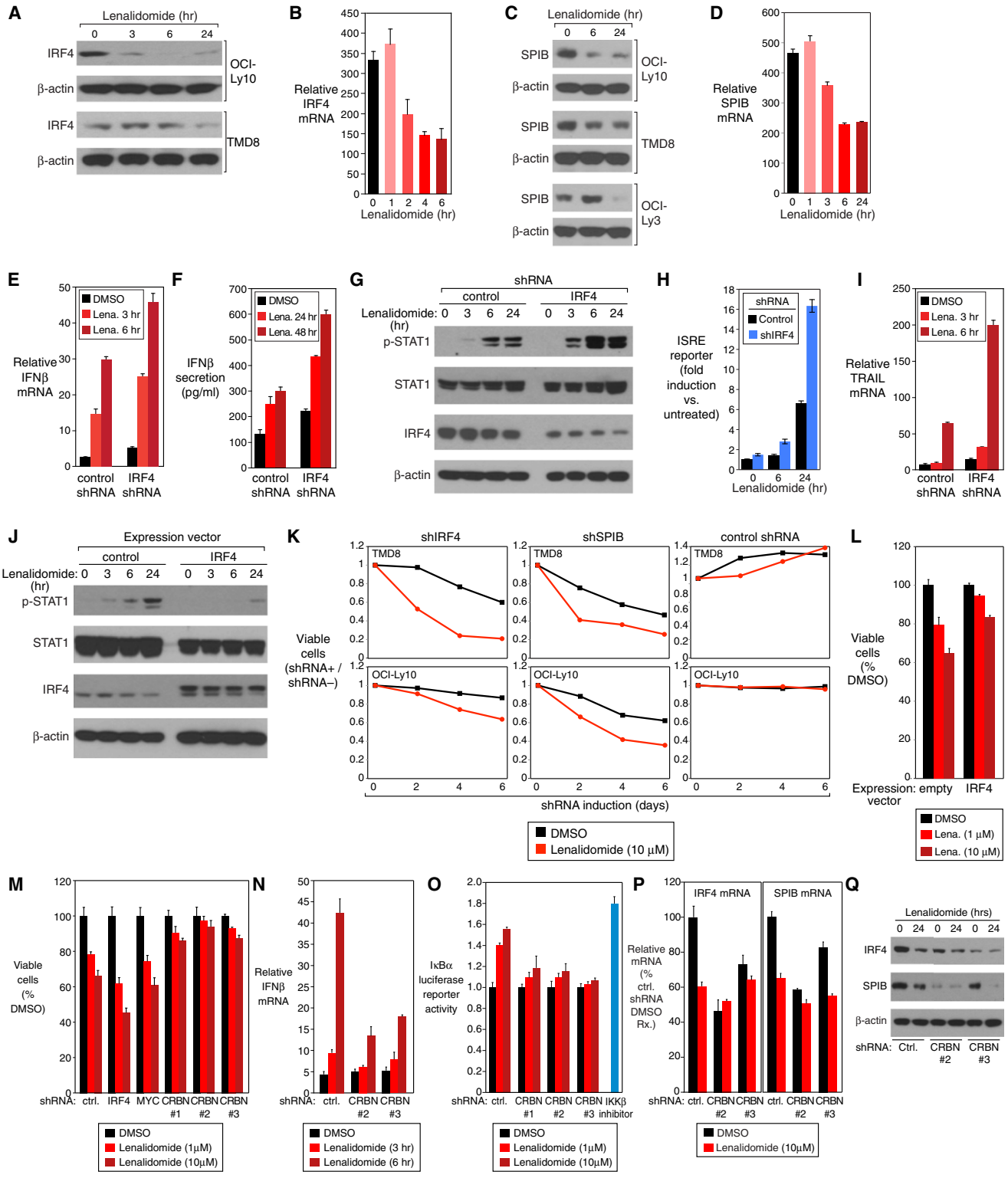

Figure 4. Lenalidomide Toxicity in ABC DLBCL is Opposed by IRF4 and SPIB

(A and C) Western blot of IRF4, SPIB, and β-actin proteins in ABC DLBCL cell lines treated with lenalidomide (10 μM) over time.

(B and D) IRF4 and SPIB mRNA expression quantified by Q-PCR, normalized to β2-microglobulin (B2M) expression, in the ABC DLBCL line OCI-Ly10 treated with lenalidomide (10 μM). Error bars show the SEM of triplicates.

(E and F) IFNβ mRNA expression and protein secretion in the OCI-Ly10 ABC DLBCL line induced for IRF4 or control shRNA expression for 2 days and treated with lenalidomide (10 μM). Error bars represent the SEM of triplicates.

Among IRF4 upregulated genes, a signature of genes more highly expressed in ABC DLBCL than GCB DLBCL was the most enriched (ABCDLBCL-4, p = 1.18E-18). Represented are genes that specify the cell-surface phenotype of ABC DLBCL (*CD44*, *ENTPD1*, *IL10RA*), as well as genes encoding important regulatory proteins, notably *CARD11* (see below). Conversely, among IRF4 downregulated genes, a signature of genes more highly expressed in GCB DLBCL than ABC DLBCL was enriched (GCBDLBCL-3, p = 3.84E-5). IRF4 upregulated genes also included genes more highly expressed in plasma cells than in mature B cells (PC-2, p = 2.33E-08), in keeping with the essential role of IRF4 in plasmacytic differentiation (Klein et al., 2006; Sciammas et al., 2006). A signature of plasmacytoid dendritic cells was also enriched among IRF4 upregulated genes (DC-4, p = 1.53E-08), consonant with the role of IRF4 in the differentiation of this lineage (Lehtonen et al., 2005; Schotte et al., 2003; Tamura et al., 2005).

Prominent among IRF4 direct targets were genes regulated by key ABC DLBCL signaling pathways. A signature of NF-κB activation was enriched among genes that were upregulated by IRF4 (NFKB-10, p = 1.38E-17; Figure 3A). As discussed above, this NF-κB signature was downregulated by the treatment of ABC DLBCLs with lenalidomide (Table S1). Signatures that reflect autocrine IL-10 and/or IL-6 signaling in ABC DLBCL cells were enriched among genes that were repressed by IRF4, suggesting that IRF4 dampens JAK/STAT3 signaling in ABC DLBCL (IL10Up-1, p = 1.83E-15; IL6Up-4, p = 2.23E-11; Figure 3A; Table S3) (Lam et al., 2008). Finally, a signature of type I interferon signaling was significantly represented among IRF4-repressed target genes (IFN-3, p = 5.80E-06; Figure 3A, Table S3). These interferon signature genes were induced by lenalidomide treatment of ABC DLBCL cells, and many of these induced genes had IRF4-SPIB intersection peaks (Figure 1B). Accordingly, IRF4 knockdown in ABC DLBCL lines increased their response to exogenous IFNβ, as measured by an ISRE reporter (Figures 3B and S3B).

Lenalidomide Toxicity in ABC DLBCL Is Opposed by IRF4 and SPIB

This signature analysis suggested that IRF4 and SPIB cooperate to modulate type I interferon and NF-κB signaling in ABC DLBCL in a manner opposite to their regulation by lenalidomide. We therefore wondered if lenalidomide might have a direct effect on IRF4 or SPIB expression in ABC DLBCL. Indeed, IRF4 and SPIB mRNA and protein levels dropped rapidly upon lenalidomide treatment of ABC DLBCL cells (Figures 4A–4D), suggesting that lenalidomide affects the expression of IRF4 and SPIB target genes by decreasing the levels of both factors.

Given that lenalidomide only reduced IRF4 expression partially, we tested whether further silencing of IRF4 by RNA interference would enhance the interferon response in ABC DLBCL cells. Induction of IFNβ mRNA expression and secretion by lenalidomide was augmented by IRF4 knockdown (Figures 4E and 4F). IRF4 knockdown also increased lenalidomide-induced STAT1 phosphorylation, ISRE promoter activity, and TRAIL upregulation (Figures 4G–4I). Conversely, ectopic expression of IRF4 suppressed lenalidomide-induced STAT1 phosphorylation (Figure 4J).

We next tested whether expression of IRF4 and SPIB in ABC DLBCL interferes with the toxicity of lenalidomide. We infected cells with vectors that expressed IRF4 or SPIB shRNAs along with green fluorescent protein (GFP), allowing us to visualize the subpopulation of cells that had been transduced with the shRNA. By comparing the viability of shRNA-transduced (GFP+) and shRNA-nontransduced (GFP–) cells, which were equally exposed to lenalidomide, we could discern how IRF4 or SPIB knockdown influenced lenalidomide toxicity. In the absence of lenalidomide, knockdown of IRF4 or SPIB alone was toxic for ABC DLBCLs, as expected (Figure 4K). The addition of lenalidomide accelerated the loss of cells bearing IRF4 and SPIB shRNAs relative to those bearing a control shRNA (Figure 4K). Conversely, ectopic expression of IRF4 counteracted lenalidomide toxicity in ABC DLBCL (Figure 4L). Also,

(G) Western blot of the indicated proteins in OCI-Ly10 following induction of IRF4 or control shRNAs for 2 days and treatment with lenalidomide (10 μM) for the indicated times.
(H) ISRE-driven luciferase reporter activity in OCI-Ly10 with control or IRF4 shRNAs after lenalidomide (10 μM) treatment. Error bars represent the SEM of triplicates.
(I) TRAIL mRNA quantified by Q-PCR, normalized to B2M, in OCI-Ly10 cells with shRNA induction for 2 days and lenalidomide (10 μM) treatment for the indicated times. Error bars show the SEM of triplicates.
(J) Western blot analysis of the indicated proteins in OCI-Ly10 cells transduced with a flag epitope-tagged IRF4 expression vector or an empty vector, induced for 48 hr, then treated with lenalidomide (10 μM) for the indicated times. The lower IRF4 band is endogenous IRF4; the upper band is FLAG-tagged exogenous IRF4.
(K) Viability of ABC DLBCL lines induced to express control, IRF4, or SPIB shRNAs and treated with DMSO or lenalidomide (10 μM) over a time course of induction. See text for details.
(L) Viability of OCI-Ly10 cells transduced with an IRF4 expression or empty vector, induced for 24 hr, and then treated with DMSO or lenalidomide for 4 days. Error bars represent the SEM of triplicates.
(M) Viability (MTS assay) of OCI-Ly10 cells induced to express the indicated shRNAs for 2 days and treated with lenalidomide at the indicated concentrations for 4 days. ctrl.,control. Error bars show the SEM of triplicates.
(N) IFNβ mRNA expression, measured by Q-PCR, in OCI-Ly10 cells induced to express CRBN shRNAs for 2 days and treated with lenalidomide (10 μM) for the indicated times. Error bars show the SEM of triplicates.
(O) TMD8 ABC DLBCL cells expressing an IκBα-luciferase fusion protein were induced to express control or CRBN shRNAs for 2 days, then treated with lenalidomide at the indicated concentrations or DMSO for 2 days. Luciferase activity was normalized to the DMSO control. As a positive control, cells were treated with the IKKβ inhibitor MLN120B (10 μM) for 2 days. Error bars show the SEM of triplicates.
(P) IRF4 and SPIB mRNA expression, quantified by Q-PCR, in TMD8 cells transduced with the indicated shRNAs. shRNA expression was induced for 2 days followed by lenalidomide treatment (10 μM) for 24 hr. Error bars show the SEM of triplicates.
(Q) Western blot for the indicated proteins in TMD8 cells induced to express CRBN or control shRNAs for 2 days, followed by treatment with lenalidomide (10 μM) for 24 hr.
See also Figure S4.

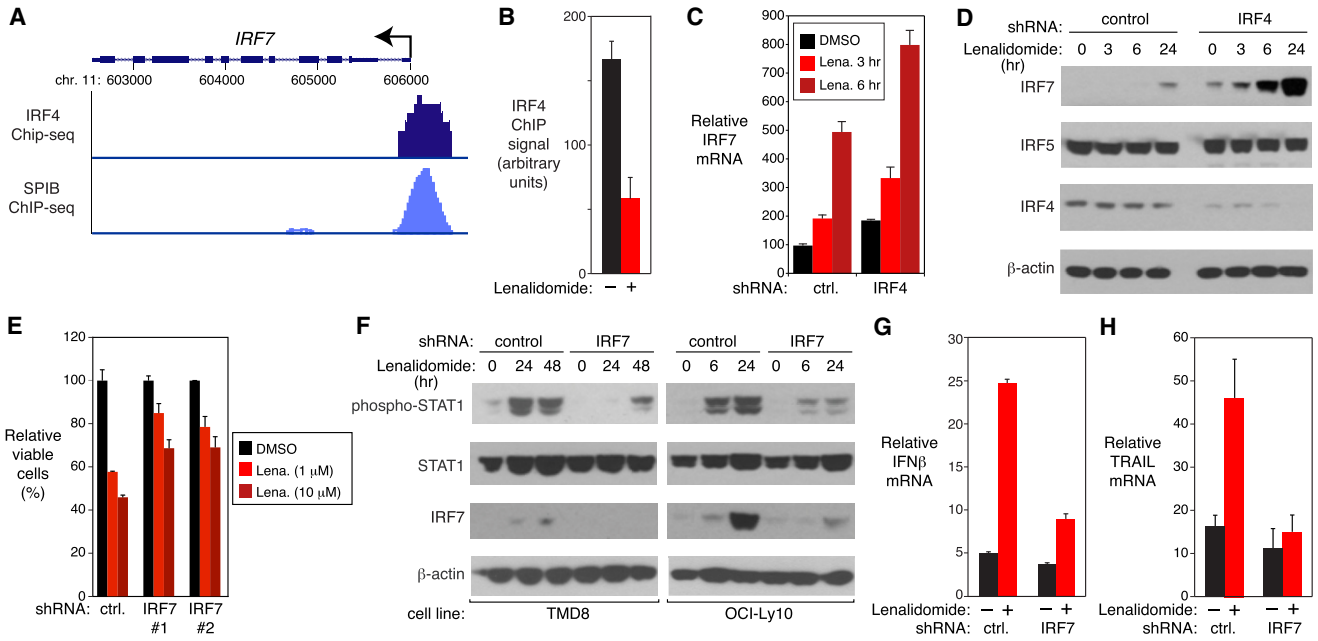

Figure 5. IRF4-SPIB Block Interferon Signaling by Repressing IRF7

(A) UCSC browser depiction of ChIP-seq data from HBL1 ABC DLBCL cells showing IRF4 and SPIB-biotag binding at the IRF7 promoter. Arrow indicates the TSS.

(B) IRF4 binding at the IRF7 locus by ChIP in OCI-Ly10 ABC DLBCL cells treated with DMSO (–) or lenalidomide (10 μM) for 24 hr. Error bars show SEM of triplicates.

(C) Q-PCR quantification of IRF7 mRNA levels, normalized to B2M, in OCI-Ly10 cells with control (ctrl.) or IRF4 shRNAs, treated with lenalidomide (10 μM) or DMSO. Error bars show SEM of triplicates.

(D) Western blot of the indicated proteins in cells from (C).

(E) Viability (MTS assay) of OCI-Ly10 cells induced to express the indicated shRNAs for 2 days and then treated with DMSO or lenalidomide (10 μM) for 4 days. Error bars show SEM of triplicates.

(F) Western blot of the indicated proteins in ABC DLBCL lines induced to express control or IRF7 shRNAs for 2 days and then treated with DMSO or lenalidomide (10 μM) for the indicated times.

(G and H) Q-PCR analysis, normalized to B2M, of IFNβ (G) or TRAIL (H) mRNA levels in OCI-Ly10 cells induced to express control or IRF7 shRNAs for 2 days and treated with DMSO (–) or lenalidomide (10 μM; +) for 24 hr. Error bars show SEM of triplicates.

the IRF4-SPIB chimeric repressor potentiated lenalidomide-induced IFNβ expression and increased lenalidomide toxicity (Figures S5F and S5G). Hence, IRF4 and SPIB regulate lenalidomide-induced interferon responses and toxicity in ABC DLBCL.

Cereblon Mediates the Toxic Effect of Lenalidomide in ABC DLBCL

Recent studies have demonstrated that the activity of thalidomide and lenalidomide is mediated by cereblon (CRBN), a component of a ubiquitin-ligase complex (Ito et al., 2010; Zhu et al., 2011). To address whether CRBN is required for the toxic effects of lenalidomide in ABC DLBCL, we identified three shRNAs that reduced CRBN mRNA expression by ~50% (Figure S4A). CRBN knockdown was moderately toxic for ABC DLBCL cells (Figure S4C), an effect that was reversed by ectopic expression of CRBN. CRBN depletion substantially reduced the toxicity of lenalidomide for ABC DLBCL cells (Figures 4M, S4B, and S4C) and interfered with the ability of lenalidomide to induce an interferon response and block NF-κB signaling (Figures 4N, 4O, S4D, and S4E). CRBN depletion lowered IRF4 mRNA and protein levels in ABC DLBCL cells and reduced the effect of lenalidomide on IRF4 levels (Figures 4P, 4Q, and S4F). Similarly, SPIB mRNA and protein levels were also diminished upon CRBN knockdown (Figures 4P and 4Q). Thus, CRBN is required to maintain IRF4 and SPIB levels in ABC DLBCL, accounting for the toxicity of CRBN depletion. Moreover, these findings suggest that CRBN mediates most of the effects of lenalidomide in ABC DLBCL.

IRF4 Represses the Interferon Pathway by Inhibiting IRF7 Expression

We noted that three IRF family member genes that regulate the type I interferon responses—*IRF2*, *IRF7*, and *IRF9*—were bound by IRF4 and SPIB (Table S3F). We focused on a strong IRF4-SPIB peak in the promoter of the *IRF7* gene (Figure 5A), since it is a master regulator of interferon responses that is strongly induced by IFNβ as part of a positive-feedback loop (Honda et al., 2005; Marié et al., 1998; Sato et al., 1998). Binding of IRF4 to the *IRF7* promoter was confirmed by an independent ChIP assay, and lenalidomide reduced this binding (Figure 5B). IRF7 mRNA and protein were specifically induced in ABC DLBCL by lenalidomide and were further induced by knocking down IRF4 (Figures 5C and 5D). Together, these results suggest that IRF7 is negatively regulated by IRF4 and SPIB, and that lenalidomide can blunt this negative regulation.

We next examined whether IRF7 expression is important for the toxicity of lenalidomide in ABC DLBCL cells. IRF7

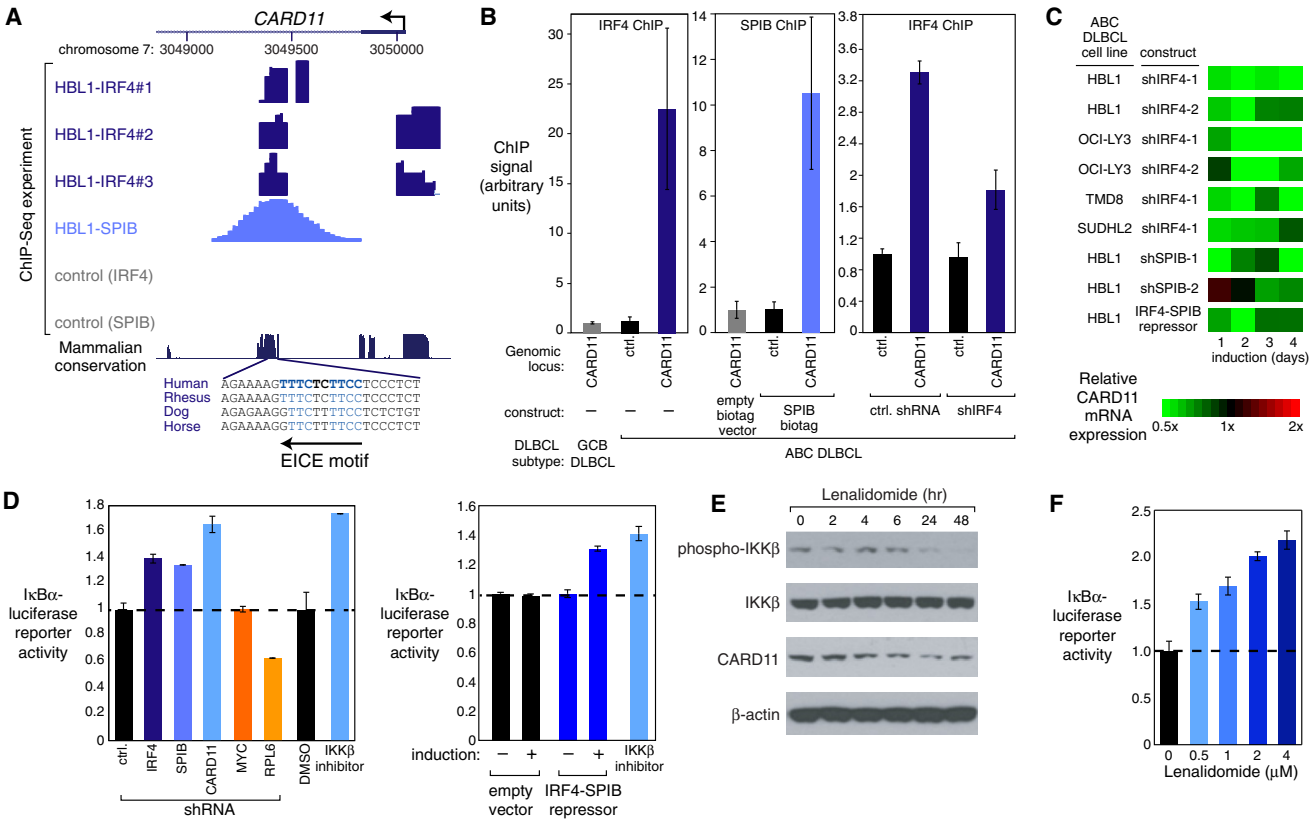

Figure 6. IRF4-SPIB and CARD11 Form an Essential Oncogenic Loop in ABC DLBCL

(A) UCSC browser depiction of ChIP-seq data from the HBL1 ABC DLBCL line showing IRF4 (in triplicate) and SPIB-biotag binding at the *CARD11* locus, with an evolutionarily conserved EICE binding motif indicated. Control (IRF4): OCI-Ly19 (IRF4-). Control (SPIB): HBL1 with empty biotag vector. Arrow indicates the TSS.

(B) ChIP analysis in HBL1 cells for IRF4 and SPIB binding at the *CARD11* peak identified in (A) or at a negative control (ctrl.) locus. IRF4 or control shRNAs were induced for 4 days. GCB DLBCL line: OCI-Ly19 (IRF4-) is IRF4-negative. Error bars show SEM of triplicates.

(C) Relative *CARD11* mRNA expression, depicted according to the color scale shown, from gene-expression profiling of ABC DLBCL lines after induction of shIRF4 or the IRF4-SPIB chimeric repressor for 4 days.

(D) IKK activity measured by an IκBα-luciferase reporter in TMD8 (ABC DLBCL) after induction of various shRNAs for 3 days (left) or the IRF4-SPIB chimeric repressor for 1 day (right). Also shown is the effect of 1 day exposure to an IKKβ inhibitor (MLN120B) or DMSO. Error bars show SD of triplicates.

(E) Western blot analysis of the indicated proteins following treatment of OCI-Ly10 cells with lenalidomide (10 μM) for the indicated times.

(F) IKK activity measured by an IκBα-luciferase reporter after treatment of TMD8 cells with lenalidomide at the indicated concentrations for 48 hr. Error bars show the SEM of triplicates.

See also Figure S5.

knockdown attenuated the toxicity of lenalidomide in ABC DLBCL cells (Figure 5E). IRF7 depletion additionally impaired lenalidomide-induced STAT1 phosphorylation, IFNβ expression, and *TRAIL* mRNA induction (Figures 5F–5H). Hence, IRF7 promotes lenalidomide toxicity by facillitating lenalidomide-induced IFNβ secretion and signaling.

IRF4-SPIB and CARD11 Form an Essential Oncogenic Loop in ABC DLBCL

While treatment with lenalidomide induces a toxic interferon response in ABC DLBCLs, blocking interferon signaling did not fully rescue the cells. We therefore wondered if there might be other mechanisms by which lenalidomide kills these lymphoma cells. Given that ABC DLBCL cells depend upon the NF-κB pathway for survival (Davis et al., 2001; Lam et al., 2005) and that lenalidomide suppressed the NF-κB gene-expression signature (Table S1), we hypothesized that decreased NF-κB signaling contributes to the toxicity of lenalidomide in ABC DLBCL cells.

Since lenalidomide downregulates IRF4 and SPIB (Figures 4A and 4B), we were intrigued that *CARD11* was a direct IRF4 and SPIB target (Figure 3A, Tables S2B, S2E, and S2F). CARD11 plays an essential role in the constitutive NF-κB activity that maintains ABC DLBCL viability (Davis et al., 2001; Lam et al., 2005; Ngo et al., 2006). The *CARD11* locus had prominent, overlapping IRF4 and SPIB binding peaks located +705 bp relative to the TSS, coinciding with an evolutionarily conserved EICE motif (Figure 6A). IRF4 and SPIB binding was confirmed by independent ChIP assays, and IRF4 knockdown diminished this binding (Figure 6B). Gene-expression profiling and quantitative PCR analysis showed that CARD11 mRNA levels are diminished by knockdown of IRF4 or SPIB, as well as by expression of the IRF4-SPIB chimeric repressor (Figures 6C and S5A). CARD11 protein levels were also reduced after

IRF4 knockdown or chimeric repressor induction (Figure S5B and S5C).

Since CARD11 coordinates the activation of IKK (Thome, 2004), the key regulatory kinase in the classical NF-κB pathway, we assessed IKK function using an ABC DLBCL reporter line engineered to express a fusion protein between luciferase and the IKK substrate IκBα (Lam et al., 2005). Phosphorylation of this fusion protein by IKK promotes its degradation, and thus IKK inhibition increases luciferase activity. Knockdown of either IRF4 or SPIB reduced IKK activity in the ABC DLBCL line TMD8, as did CARD11 knockdown or treatment with a small molecule IKK inhibitor, but two other toxic shRNAs targeting MYC and RPL6 did not (Lam et al., 2005) (Figure 6D). Moreover, induction of the chimeric IRF4-SPIB repressor also inhibited IKK activity (Figure 6D). Similar results were observed in an ABC DLBCL line, OCI-Ly3, that relies on an oncogenically active CARD11 mutant for survival (Lenz et al., 2008a), in keeping with an effect of IRF4 and SPIB on *CARD11* transcription (Figure S5H). In accord with these functional experiments, knockdown of IRF4 decreased IKKβ phosphorylation, a modification associated with IKK activation downstream of CARD11 (Figure S5E). The effect of IRF4 on the NF-κB pathway was confirmed using an independent ABC DLBCL reporter system in which luciferase is driven by an NF-κB-dependent promoter (Figure S5D).

Lenalidomide treatment of an ABC DLBCL line reduced CARD11 expression and IKKβ phosphorylation, and inhibited IKK activity (Figures 6E and 6F). Together, these data suggest that IRF4 and SPIB act together to amplify NF-κB signaling in ABC DLBCL by transactivating *CARD11* and that lenalidomide inhibits NF-κB by downregulating IRF4 and SPIB, breaking this positive feed-forward loop.

Synergism between Lenalidomide and NF-κB Pathway Inhibitors

Since lenalidomide only partially inhibits IRF4 and SPIB expression (Figures 4A–4D), we speculated that we could achieve greater toxicity by additionally blocking IKK, thereby further reducing NF-κB-dependent IRF4 expression. The IKKβ inhibitor MLN120B selectively kills ABC DLBCL cells, as does ibrutinib, a BTK kinase inhibitor that blocks signaling from the BCR to IKK (Davis et al., 2010; Lam et al., 2005). Treatment of ABC DLBCL cells with either MLN120B or ibrutinib alone decreased IRF4 protein levels, but when these agents were combined with lenalidomide, IRF4 became undetectable (Figure 7A). The combination of ibrutinib and lenalidomide induced a stronger interferon response than lenalidomide alone, as measured by ISRE reporter activity and STAT1 phosphorylation (Figures 7A and 7B). These two drugs also cooperated in blocking IKK activity (Figure 7C).

To test for synergistic toxicity, an ABC DLBCL line was treated with the MLN120B at a range of doses that were only modestly toxic, in the presence or absence of low dose lenalidomide. The ABC DLBCL cells were killed more efficiently with the combination of these drugs than with either drug alone (Figure 7D). Similarly, synergistic toxicity was observed in ABC DLBCL lines when lenalidomide and ibrutinib were combined, but no toxicity was observed in GCB DLBCL lines that lack oncogenic activation of the BCR and MYD88 pathways (Figures 7E and S6A). A formal mathematical algorithm (Greco et al., 1990) confirmed the strong synergism between ibrutinib and lenalidomide in killing three ABC DLBCL lines (Figure S6B). Finally, we tested this drug combination in a xenograft mouse model created using the OCI-Ly10 ABC DLBCL cell line (Figures 7F and S6C). At the concentrations of lenalidomide and ibrutinib chosen, both drugs had little effect on the growth of the xenografts as single agents (Figures 7F and S6C) but were quite effective in combination in arresting the growth of established tumors.

DISCUSSION

New treatments for ABC DLBCL should ideally exploit emerging insights into oncogenic pathways, which create opportunities for synthetic lethal interactions with drugs that target these pathways (Figure 8). The BCR and MYD88 signaling pathways promote ABC DLBCL viability by inducing NF-κB, and both pathways are affected by recurrent oncogenic mutations in ABC DLBCL. However, the penalty that ABC DLBCLs pay by acquiring oncogenic MYD88 mutations is the production of IFNβ (Ngo et al., 2011), which is toxic to these tumors. The present study revealed that IRF4 places a brake on IFNβ expression by repressing IRF7, allowing ABC DLBCLs with MYD88 mutations to survive and proliferate. Additionally, IRF4 sustains ABC DLBCL survival by transactivating CARD11 and potentiating NF-κB signaling. IRF4 emerges from these studies as a central regulatory hub in ABC DLBCL, making it an attractive therapeutic target. IRF4 and its regulatory partner SPIB were downregulated by treatment of ABC DLBCL lines with lenalidomide, a drug that has shown preferential activity against this lymphoma subtype in early-phase clinical trials (Hernandez-Ilizaliturri et al., 2011). Lenalidomide toxicity for ABC DLBCL was associated with heightened IFNβ production and diminished NF-κB activity. Hence, lenalidomide toxicity in ABC DLBCL relies upon its modulation of oncogenically activated signaling pathways, and therefore is an instance of "synthetic lethality" (Kaelin, 2005).

This study highlights the central role of IRF4-SPIB heterodimers in ABC DLBCL biology, particularly in amplifying NF-κB signaling while blocking type I interferon signaling. In addition, IRF4 directly upregulates a large number of genes that distinguish ABC DLBCL from other lymphoma subtypes, many of which may contribute to viability or other attributes of these lymphoma cells. Remarkably, survival of ABC DLBCL cells depended on a single amino acid in IRF4 that mediates its interaction with SPIB on composite EICE motifs. IRF4 is clearly central to the action of lenalidomide in ABC DLBCL, since enforced overexpression of IRF4 blocked the toxic effect of this drug, presumably by driving IRF4-SPIB interactions by mass action. IRF4 is similarly downregulated by lenalidomide in multiple myeloma (Li et al., 2011; Lopez-Girona et al., 2011; Zhu et al., 2011). In both ABC DLBCL and multiple myeloma, IRF4 levels are maintained by CRBN, a subunit of a ubiquitin ligase complex. We discovered that CRBN also controls SPIB levels in ABC DLBCL, which is not relevant to multiple myeloma, as these cells do not express SPIB. Thalidomide, a chemically related cousin of lenalidomide, physically interacts with CRBN and blocks the ability of this ubiquitin ligase complex to autoubiquitinate (Ito et al., 2010). Further investigation is needed to discern how this ubiquitin ligase might control IRF4 and SPIB expression, apparently at the level of transcription.

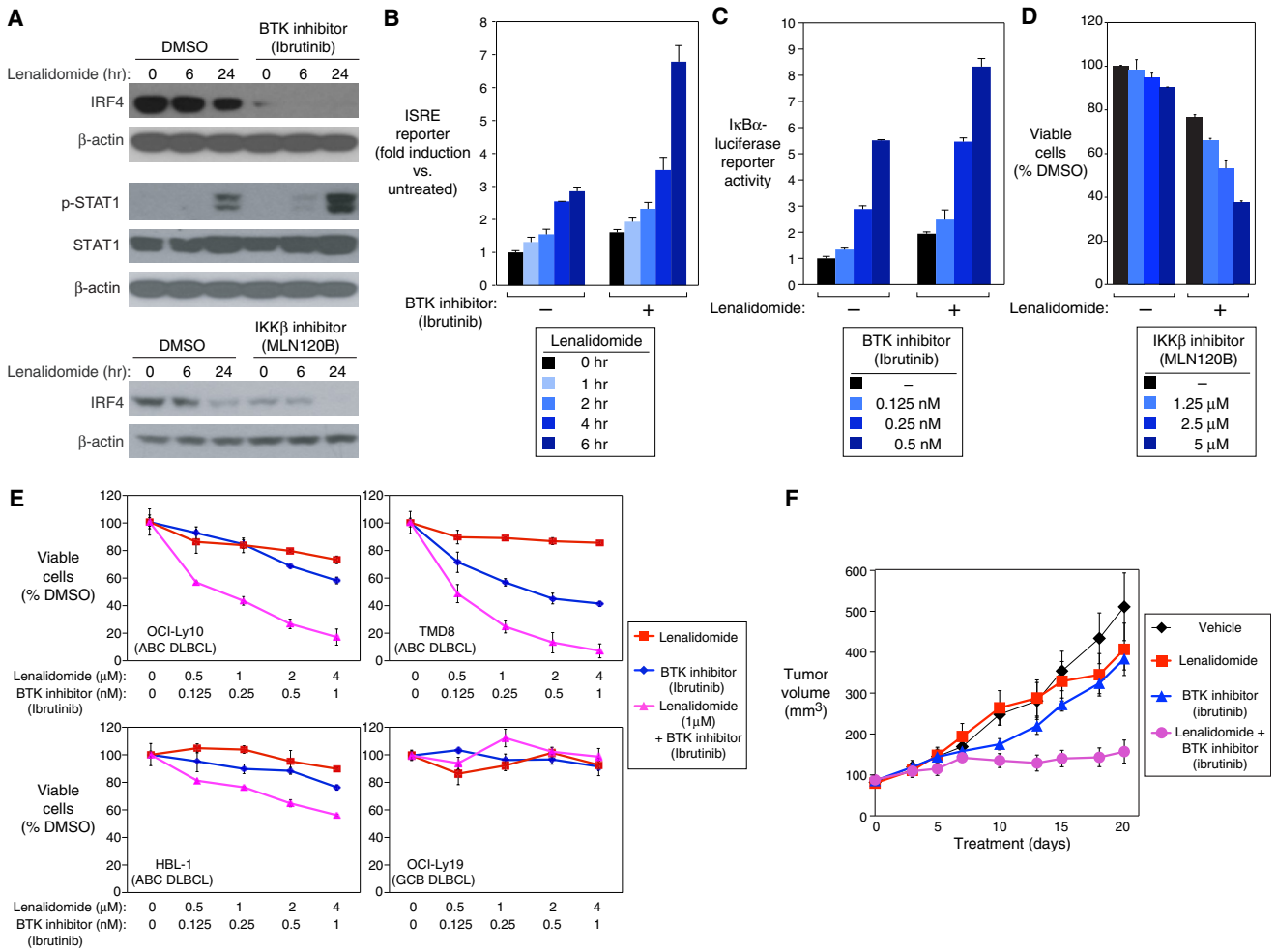

Figure 7. Synergy between Lenalidomide and NF-κB Pathway Inhibitors in ABC DLBCL

(A) Western blot of the indicated proteins in OCI-Ly10 cells treated with lenalidomide (5 μM) alone or with MLN120B (10 μM), ibrutinib (5nM), or DMSO for the indicated times.

(B) ISRE-driven luciferase activity in OCI-Ly10 cells treated with lenalidomide (5 μM) ± ibrutinib (5 nM) for the indicated times. Error bars show the SEM of triplicates.

(C) IKK activity measured by an IκBα-luciferase reporter in TMD8 cells treated with ibrutinib at the indicated concentrations ± lenalidomide (1 μM) for 48 hr. Error bars show the SEM of triplicates.

(D) Viability (MTS assay) of OCI-Ly10 treated with MLN120B at the indicated concentrations ± lenalidomide (1 μM) for 4 days relative to DMSO-treated cells. Error bars show the SEM of triplicates.

(E) Viability (MTS assay) of DLBCL lines treated with ibrutinib, lenalidomide, or both for 4 days at the concentrations indicated. Error bars show the SEM of triplicates.

(F) OCI-Ly10 ABC DLBCL cells were established as a subcutaneous tumor (average 80 mm^3) in immunodeficient mice, and then treated daily for 20 days with DMSO, lenalidomide (10 mg/kg), ibrutinib (3 mg/kg), or lenalidomide plus ibrutinib by intraperitoneal injection. Tumor progression was monitored as a function of tumor volume. Error bars show the SEM of 5 mice per group.

See also Figure S6.

Our findings provide a sound mechanistic basis for clinical trials in ABC DLBCL that rationally combine lenalidomide with other drugs that modulate NF-κB signaling. Drugs targeting NF-κB hold promise in cancer therapy, despite some concerns about long-term suppression of this pathway (Baud and Karin, 2009; Gupta et al., 2010). In ABC DLBCL, NF-κB activity relies upon chronic active BCR signaling, which can be blocked by several drugs that are currently in clinical trials, including ibrutinib (targeting BTK) (Davis et al., 2010), fostamatinib (targeting SYK) (Friedberg et al., 2009), and CAL-101 [targeting PI(3) kinase δ] (Herman et al., 2010; Hoellenriegel et al., 2011). Additionally, NF-κB signaling can be inhibited by interfering with IκBα degradation, which can be achieved with the proteasome inhibitor bortezomib (Dunleavy et al., 2009) or the neddylation inhibitor MLN4924 (Milhollen et al., 2010). As a single agent, the BTK inhibitor ibrutinib is highly active against ABC DLBCL cells in vitro (Davis et al., 2010), and is showing clinical activity in a subset of patients with relapsed/refractory ABC DLBCL (L.M.S., unpublished data). We observed striking synergy between ibrutinib and lenalidomide in blocking IRF4 expression, increasing

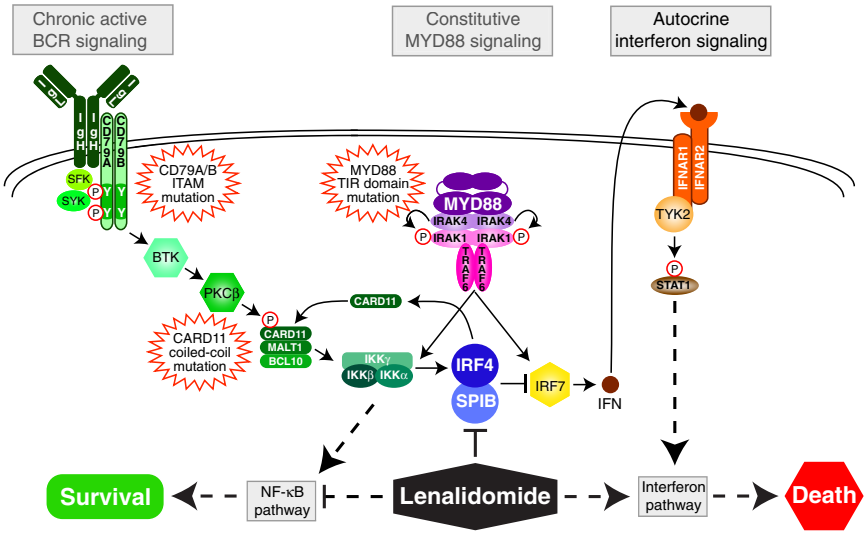

Figure 8. Exploiting Synthetic Lethality for the Therapy of ABC DLBCL

Recurrent oncogenic mutations in ABC DLBCL activate both the BCR and MYD88 pathways to drive prosurvival NF-κB signaling. However, MYD88 signaling also induces IFNβ, which is detrimental to ABC DLBCL survival. IRF4 and SPIB lie at the nexus of both pathways, promoting ABC DLBCL survival by repressing IRF7, thereby blocking IFNβ, and transactivating *CARD11*, thereby increasing NF-κB signaling. NF-κB factors transactivate *IRF4*, creating a positive feedback oncogenic loop. Lenalidomide targets this circuitry by downmodulating IRF4 and SPIB, thereby increasing toxic IFNβ secretion and decreasing NF-κB activity.

IFNβ production, and killing ABC DLBCL cells in vitro and in vivo, supporting clinical evaluation of this treatment regimen.

The effectiveness of this drug combination in ABC DLBCL capitalizes on recurrent genetic alterations in ABC DLBCL in two ways. First, the MYD88 L265P mutant promotes the abnormal synthesis and secretion of IFNβ. Second, mutations in the BCR subunits CD79A and CD79B promote chronic active BCR signaling, which activates NF-κB and induces IRF4, thereby dampening the toxic type I interferon response while augmenting the prosurvival NF-κB response. Hence, these recurrent oncogenic mutations in ABC DLBCL and the constitutive signaling pathways that they engage place IRF4 in a central regulatory position (Figure 8). Indeed, one reason that CD79B mutations often coexist with the MYD88 L265P mutation in ABC DLBCL tumors (Ngo et al., 2011) may be that the production of IRF4 in response to chronic active BCR signaling is necessary for the tumor to dampen the interferon response caused by the MYD88 L265P mutation. The rational therapeutic combinations proposed herein act in a synthetic lethal fashion to exploit this IRF4 addiction.

EXPERIMENTAL PROCEDURES

(See Supplemental Experimental Procedures for details.)

Cell Culture and Constructs

Methods for cell culture, plasmid transfection, retroviral transduction, and plasmid constructs were described previously (Lenz et al., 2008c; Ngo et al., 2006; Shaffer et al., 2008).

Chromatin Immunoprecipitation

Chromatin immunoprecipitations (ChIP) were performed as described (Shaffer et al., 2008). Such ChIP-enriched DNA was either used in region-specific assessment of antibody binding by real-time PCR, or made into libraries for ChIP sequencing on a Genome Analyzer II (GAII, Illumina, Inc.) according to manufacturer's recommendations. See Supplemental Experimental Procedures for details.

Gene Expression: Q-RTPCR and Profiling

Unless otherwise described, Q-RTPCR was performed on cDNA as previously described in Sciammas et al. (2006) and Shaffer et al. (2004, 2008), using pre-tested Assay-on-demand probe/primer sets from Applied Biosystems or primers designed for use with SYBR green using an ABI 7700 Taqman machine for 40 cycles with an annealing temperature of 60°C. Gene expression was normalized to the expression of beta-2-microglobulin for all samples. Gene-expression profiling was performed using two-color human Agilent 4x44K gene-expression arrays, exactly as described by the manufacturer, comparing signal from control cells (Cy3) and experimentally manipulated cells (Cy5). Array elements were filtered for those meeting confidence thresholds for spot size, architecture, and level above local background. These criteria are a feature of the Agilent gene-expression software package for Agilent 4x44k arrays.

Cell Viability—MTS—Assay

Cells were plated in triplicate at a density of 15,000 cells per well in 96-well plates. Cell viability after indicated treatments was assayed by adding 3-(4,5-dimethylthiazol-2-yl)-5-(3-carboxymethoxyphenyl)-2-(4-sulphophenyl)-2H tetrazolium and an electron coupling reagent (phenazine methosulphate; Promega), incubated for 3 hr and measured by the amount of 490 nm absorbance using a 96-well plate reader. The background was subtracted using a media-only control.

NF-κB Reporter Assays

The assay for IκB kinase activity using the IκBalpha-photinus luciferase reporter has been described (Lenz et al., 2008a), as has use of the IκB kinase inhibitor (Lam et al., 2005). In addition, cell lines were created with an NF-κB transcriptional reporter by transduction with lentiviral particles containing an inducible NF-κB -responsive luciferase reporter construct (SA Biosciences) and selected with puromycin. Luciferase activity was measured using the Dual-Luciferase Reporter Assay System (Promega) on a Microtiter Plate Luminometer (Dyn-Ex Technologies).

ISRE Reporter Assay

Cell lines were transduced with lentiviral particles containing an inducible ISRE-responsive luciferase reporter construct (SA Biosciences) and selected with puromycin. Luciferase activity was measured using the Dual-Luciferase Reporter Assay System (Promega) on a Microtiter Plate Luminometer (Dyn-Ex Technologies).

IFNβ ELISA

Human IFNβ was measured using ELISA kits from PBL InterferonSource. The results were normalized to live cell numbers.

Tumor Model and Therapy Study

The xenograft tumor model of human ABC DLBCL lymphoma was established by subcutaneous (s.c.) injection of cells into nonobese diabetic/severe combined immunodeficient (NOD/SCID) mice (NCI-Frederick, Frederick, MD). Tumor growth was monitored by measuring tumor size in two

orthogonal dimensions. See Supplemental Experimental Procedures for details. All animal experiments were approved by the National Cancer Institute Animal Care and Use Committee (NCI ACUC) and were performed in accordance with NCI ACUC guidelines.

ACCESSION NUMBERS

Gene-expression data has been deposited under accession numbers GSE32456 and GSE33012. All ChIP-Seq data can be found under accession SRA025850.

SUPPLEMENTAL INFORMATION

Supplemental Information includes six figures, three tables, and Supplemental Experimental Procedures and can be found with this article online at doi:10.1016/j.ccr.2012.05.024.

ACKNOWLEDGMENTS

This research was supported by the Intramural Research Program of the NIH, National Cancer Institute, Center for Cancer Research. We also thank Carla Heise and Celgene for support. J.P. was supported by the UMD-NCI Partnership for Cancer Technology. We thank M. Celeste Simon for the anti-SPIB antibody. We wish to thank Kathleen Meyer for her assistance with GEO submissions, and the members of the Staudt lab for their assistance and helpful discussions. J.J.B. and S.B. are employees and shareholders of Pharmacyclics, Inc.

Received: October 26, 2011
Revised: March 13, 2012
Accepted: May 22, 2012
Published: June 11, 2012

REFERENCES

Alizadeh, A.A., Eisen, M.B., Davis, R.E., Ma, C., Lossos, I.S., Rosenwald, A., Boldrick, J.C., Sabet, H., Tran, T., Yu, X., et al. (2000). Distinct types of diffuse large B-cell lymphoma identified by gene expression profiling. Nature *403*, 503–511.

Baud, V., and Karin, M. (2009). Is NF-kappaB a good target for cancer therapy? Hopes and pitfalls. Nat. Rev. Drug Discov. *8*, 33–40.

Brass, A.L., Kehrli, E., Eisenbeis, C.F., Storb, U., and Singh, H. (1996). Pip, a lymphoid-restricted IRF, contains a regulatory domain that is important for autoinhibition and ternary complex formation with the Ets factor PU.1. Genes Dev. *10*, 2335–2347.

Brass, A.L., Zhu, A.Q., and Singh, H. (1999). Assembly requirements of PU.1-Pip (IRF-4) activator complexes: inhibiting function in vivo using fused dimers. EMBO J. *18*, 977–991.

Davis, R.E., Brown, K.D., Siebenlist, U., and Staudt, L.M. (2001). Constitutive nuclear factor κB activity is required for survival of activated B cell-like diffuse large B cell lymphoma cells. J. Exp. Med. *194*, 1861–1874.

Davis, R.E., Ngo, V.N., Lenz, G., Tolar, P., Young, R.M., Romesser, P.B., Kohlhammer, H., Lamy, L., Zhao, H., Yang, Y., et al. (2010). Chronic active B-cell-receptor signalling in diffuse large B-cell lymphoma. Nature *463*, 88–92.

Dunleavy, K., Pittaluga, S., Czuczman, M.S., Dave, S.S., Wright, G., Grant, N., Shovlin, M., Jaffe, E.S., Janik, J.E., Staudt, L.M., and Wilson, W.H. (2009). Differential efficacy of bortezomib plus chemotherapy within molecular subtypes of diffuse large B-cell lymphoma. Blood *113*, 6069–6076.

Eisenbeis, C.F., Singh, H., and Storb, U. (1995). Pip, a novel IRF family member, is a lymphoid-specific, PU.1-dependent transcriptional activator. Genes Dev. *9*, 1377–1387.

Escalante, C.R., Brass, A.L., Pongubala, J.M., Shatova, E., Shen, L., Singh, H., and Aggarwal, A.K. (2002a). Crystal structure of PU.1/IRF-4/DNA ternary complex. Mol. Cell *10*, 1097–1105.

Escalante, C.R., Shen, L., Escalante, M.C., Brass, A.L., Edwards, T.A., Singh, H., and Aggarwal, A.K. (2002b). Crystallization and characterization of PU.1/IRF-4/DNA ternary complex. J. Struct. Biol. *139*, 55–59.

Friedberg, J.W., Sharman, J., Sweetenham, J., Johnston, P.B., Vose, J.M., Lacasce, A., Schaefer-Cutillo, J., De Vos, S., Sinha, R., Leonard, J.P., et al. (2009). Inhibition of Syk with fostamatinib disodium has significant clinical activity in non-Hodgkin lymphoma and chronic lymphocytic leukemia. Blood *115*, 2578–2585.

Greco, W.R., Park, H.S., and Rustum, Y.M. (1990). Application of a new approach for the quantitation of drug synergism to the combination of cis-diamminedichloroplatinum and 1-beta-D-arabinofuranosylcytosine. Cancer Res. *50*, 5318–5327.

Gupta, S.C., Sundaram, C., Reuter, S., and Aggarwal, B.B. (2010). Inhibiting NF-κB activation by small molecules as a therapeutic strategy. Biochim. Biophys. Acta *1799*, 775–787.

Herman, S.E., Gordon, A.L., Wagner, A.J., Heerema, N.A., Zhao, W., Flynn, J.M., Jones, J., Andritsos, L., Puri, K.D., Lannutti, B.J., et al. (2010). Phosphatidylinositol 3-kinase-δ inhibitor CAL-101 shows promising preclinical activity in chronic lymphocytic leukemia by antagonizing intrinsic and extrinsic cellular survival signals. Blood *116*, 2078–2088.

Hernandez-Ilizaliturri, F.J., Deeb, G., Zinzani, P.L., Pileri, S.A., Malik, F., Macon, W.R., Goy, A., Witzig, T.E., and Czuczman, M.S. (2011). Higher response to lenalidomide in relapsed/refractory diffuse large B-cell lymphoma in nongerminal center B-cell-like than in germinal center B-cell-like phenotype. Cancer *117*, 5058–5066.

Hoellenriegel, J., Meadows, S.A., Sivina, M., Wierda, W.G., Kantarjian, H., Keating, M.J., Giese, N., O'Brien, S., Yu, A., Miller, L.L., et al. (2011). The phosphoinositide 3′-kinase delta inhibitor, CAL-101, inhibits B-cell receptor signaling and chemokine networks in chronic lymphocytic leukemia. Blood *118*, 3603–3612.

Honda, K., Yanai, H., Negishi, H., Asagiri, M., Sato, M., Mizutani, T., Shimada, N., Ohba, Y., Takaoka, A., Yoshida, N., and Taniguchi, T. (2005). IRF-7 is the master regulator of type-I interferon-dependent immune responses. Nature *434*, 772–777.

Ito, T., Ando, H., Suzuki, T., Ogura, T., Hotta, K., Imamura, Y., Yamaguchi, Y., and Handa, H. (2010). Identification of a primary target of thalidomide teratogenicity. Science *327*, 1345–1350.

Kaelin, W.G., Jr. (2005). The concept of synthetic lethality in the context of anticancer therapy. Nat. Rev. Cancer *5*, 689–698.

Kanno, Y., Levi, B.Z., Tamura, T., and Ozato, K. (2005). Immune cell-specific amplification of interferon signaling by the IRF-4/8-PU.1 complex. J. Interferon Cytokine Res. *25*, 770–779.

Klein, U., Casola, S., Cattoretti, G., Shen, Q., Lia, M., Mo, T., Ludwig, T., Rajewsky, K., and Dalla-Favera, R. (2006). Transcription factor IRF4 controls plasma cell differentiation and class-switch recombination. Nat. Immunol. *7*, 773–782.

Lam, L.T., Davis, R.E., Pierce, J., Hepperle, M., Xu, Y., Hottelet, M., Nong, Y., Wen, D., Adams, J., Dang, L., and Staudt, L.M. (2005). Small molecule inhibitors of IκB kinase are selectively toxic for subgroups of diffuse large B-cell lymphoma defined by gene expression profiling. Clin. Cancer Res. *11*, 28–40.

Lam, L.T., Wright, G., Davis, R.E., Lenz, G., Farinha, P., Dang, L., Chan, J.W., Rosenwald, A., Gascoyne, R.D., and Staudt, L.M. (2008). Cooperative signaling through the signal transducer and activator of transcription 3 and nuclear factor-κB pathways in subtypes of diffuse large B-cell lymphoma. Blood *111*, 3701–3713.

Lehtonen, A., Veckman, V., Nikula, T., Lahesmaa, R., Kinnunen, L., Matikainen, S., and Julkunen, I. (2005). Differential expression of IFN regulatory factor 4 gene in human monocyte-derived dendritic cells and macrophages. J. Immunol. *175*, 6570–6579.

Lenz, G., Nagel, I., Siebert, R., Roschke, A.V., Sanger, W., Wright, G.W., Dave, S.S., Tan, B., Zhao, H., Rosenwald, A., et al. (2007). Aberrant immunoglobulin class switch recombination and switch translocations in activated B cell-like diffuse large B cell lymphoma. J. Exp. Med. *204*, 633–643.

Lenz, G., Davis, R.E., Ngo, V.N., Lam, L., George, T.C., Wright, G.W., Dave, S.S., Zhao, H., Xu, W., Rosenwald, A., et al. (2008a). Oncogenic CARD11 mutations in human diffuse large B cell lymphoma. Science *319*, 1676–1679.

Lenz, G., Wright, G., Dave, S.S., Xiao, W., Powell, J., Zhao, H., Xu, W., Tan, B., Goldschmidt, N., Iqbal, J., et al; Lymphoma/Leukemia Molecular Profiling Project. (2008b). Stromal gene signatures in large-B-cell lymphomas. N. Engl. J. Med. *359*, 2313–2323.

Lenz, G., Wright, G.W., Emre, N.C., Kohlhammer, H., Dave, S.S., Davis, R.E., Carty, S., Lam, L.T., Shaffer, A.L., Xiao, W., et al. (2008c). Molecular subtypes of diffuse large B-cell lymphoma arise by distinct genetic pathways. Proc. Natl. Acad. Sci. USA *105*, 13520–13525.

Li, S., Pal, R., Monaghan, S.A., Schafer, P., Ouyang, H., Mapara, M., Galson, D.L., and Lentzsch, S. (2011). IMiD immunomodulatory compounds block C/EBPβ translation through eIF4E down-regulation resulting in inhibition of MM. Blood *117*, 5157–5165.

Lopez-Girona, A., Heintel, D., Zhang, L.H., Mendy, D., Gaidarova, S., Brady, H., Bartlett, J.B., Schafer, P.H., Schreder, M., Bolomsky, A., et al. (2011). Lenalidomide downregulates the cell survival factor, interferon regulatory factor-4, providing a potential mechanistic link for predicting response. Br. J. Haematol. *154*, 325–336.

Marecki, S., and Fenton, M.J. (2000). PU.1/Interferon Regulatory Factor interactions: mechanisms of transcriptional regulation. Cell Biochem. Biophys. *33*, 127–148.

Marié, I., Durbin, J.E., and Levy, D.E. (1998). Differential viral induction of distinct interferon-alpha genes by positive feedback through interferon regulatory factor-7. EMBO J. *17*, 6660–6669.

Milhollen, M.A., Traore, T., Adams-Duffy, J., Thomas, M.P., Berger, A.J., Dang, L., Dick, L.R., Garnsey, J.J., Koenig, E., Langston, S.P., et al. (2010). MLN4924, a NEDD8-activating enzyme inhibitor, is active in diffuse large B-cell lymphoma models: rationale for treatment of NF-κB-dependent lymphoma. Blood *116*, 1515–1523.

Ngo, V.N., Davis, R.E., Lamy, L., Yu, X., Zhao, H., Lenz, G., Lam, L.T., Dave, S., Yang, L., Powell, J., and Staudt, L.M. (2006). A loss-of-function RNA interference screen for molecular targets in cancer. Nature *441*, 106–110.

Ngo, V.N., Young, R.M., Schmitz, R., Jhavar, S., Xiao, W., Lim, K.H., Kohlhammer, H., Xu, W., Yang, Y., Zhao, H., et al. (2011). Oncogenically active MYD88 mutations in human lymphoma. Nature *470*, 115–119.

Oshima, K., Yanase, N., Ibukiyama, C., Yamashina, A., Kayagaki, N., Yagita, H., and Mizuguchi, J. (2001). Involvement of TRAIL/TRAIL-R interaction in IFN-alpha-induced apoptosis of Daudi B lymphoma cells. Cytokine *14*, 193–201.

Rosenwald, A., Wright, G., Chan, W.C., Connors, J.M., Campo, E., Fisher, R.I., Gascoyne, R.D., Muller-Hermelink, H.K., Smeland, E.B., Giltnane, J.M., et al; Lymphoma/Leukemia Molecular Profiling Project. (2002). The use of molecular profiling to predict survival after chemotherapy for diffuse large-B-cell lymphoma. N. Engl. J. Med. *346*, 1937–1947.

Rosenwald, A., Wright, G., Leroy, K., Yu, X., Gaulard, P., Gascoyne, R.D., Chan, W.C., Zhao, T., Haioun, C., Greiner, T.C., et al. (2003). Molecular diagnosis of primary mediastinal B cell lymphoma identifies a clinically favorable subgroup of diffuse large B cell lymphoma related to Hodgkin lymphoma. J. Exp. Med. *198*, 851–862.

Saito, M., Gao, J., Basso, K., Kitagawa, Y., Smith, P.M., Bhagat, G., Pernis, A., Pasqualucci, L., and Dalla-Favera, R. (2007). A signaling pathway mediating downregulation of BCL6 in germinal center B cells is blocked by BCL6 gene alterations in B cell lymphoma. Cancer Cell *12*, 280–292.

Sato, M., Hata, N., Asagiri, M., Nakaya, T., Taniguchi, T., and Tanaka, N. (1998). Positive feedback regulation of type I IFN genes by the IFN-inducible transcription factor IRF-7. FEBS Lett. *441*, 106–110.

Schotte, R., Rissoan, M.C., Bendriss-Vermare, N., Bridon, J.M., Duhen, T., Weijer, K., Brière, F., and Spits, H. (2003). The transcription factor Spi-B is expressed in plasmacytoid DC precursors and inhibits T-, B-, and NK-cell development. Blood *101*, 1015–1023.

Sciammas, R., Shaffer, A.L., Schatz, J.H., Zhao, H., Staudt, L.M., and Singh, H. (2006). Graded expression of interferon regulatory factor-4 coordinates isotype switching with plasma cell differentiation. Immunity *25*, 225–236.

Shaffer, A.L., Peng, A., and Schlissel, M.S. (1997). In vivo occupancy of the kappa light chain enhancers in primary pro- and pre-B cells: a model for kappa locus activation. Immunity *6*, 131–143.

Shaffer, A.L., Shapiro-Shelef, M., Iwakoshi, N.N., Lee, A.-H., Qian, S.-B., Zhao, H., Yu, X., Yang, L., Tan, B.K., Rosenwald, A., et al. (2004). XBP1, downstream of Blimp-1, expands the secretory apparatus and other organelles, and increases protein synthesis in plasma cell differentiation. Immunity *21*, 81–93.

Shaffer, A.L., Wright, G., Yang, L., Powell, J., Ngo, V., Lamy, L., Lam, L.T., Davis, R.E., and Staudt, L.M. (2006). A library of gene expression signatures to illuminate normal and pathological lymphoid biology. Immunol. Rev. *210*, 67–85.

Shaffer, A.L., Emre, N.C., Lamy, L., Ngo, V.N., Wright, G., Xiao, W., Powell, J., Dave, S., Yu, X., Zhao, H., et al. (2008). IRF4 addiction in multiple myeloma. Nature *454*, 226–231.

Shaffer, A.L., Emre, N.C., Romesser, P.B., and Staudt, L.M. (2009). IRF4: Immunity. Malignancy! Therapy? Clin. Cancer Res. *15*, 2954–2961.

Stark, G.R., Kerr, I.M., Williams, B.R., Silverman, R.H., and Schreiber, R.D. (1998). How cells respond to interferons. Annu. Rev. Biochem. *67*, 227–264.

Tamura, T., Tailor, P., Yamaoka, K., Kong, H.J., Tsujimura, H., O'Shea, J.J., Singh, H., and Ozato, K. (2005). IFN regulatory factor-4 and -8 govern dendritic cell subset development and their functional diversity. J. Immunol. *174*, 2573–2581.

Thome, M. (2004). CARMA1, BCL-10 and MALT1 in lymphocyte development and activation. Nat. Rev. Immunol. *4*, 348–359.

Thome, M., Charton, J.E., Pelzer, C., and Hailfinger, S. (2010). Antigen receptor signaling to NF-κB via CARMA1, BCL10, and MALT1. Cold Spring Harb. Perspect. Biol. *2*, a003004.

Ucur, E., Mattern, J., Wenger, T., Okouoyo, S., Schroth, A., Debatin, K.M., and Herr, I. (2003). Induction of apoptosis in experimental human B cell lymphomas by conditional TRAIL-expressing T cells. Br. J. Cancer *89*, 2155–2162.

Wright, G., Tan, B., Rosenwald, A., Hurt, E.H., Wiestner, A., and Staudt, L.M. (2003). A gene expression-based method to diagnose clinically distinct subgroups of diffuse large B cell lymphoma. Proc. Natl. Acad. Sci. USA *100*, 9991–9996.

Zhu, Y.X., Braggio, E., Shi, C.X., Bruins, L.A., Schmidt, J.E., Van Wier, S., Chang, X.B., Bjorklund, C.C., Fonseca, R., Bergsagel, P.L., et al. (2011). Cereblon expression is required for the antimyeloma activity of lenalidomide and pomalidomide. Blood *118*, 4771–4779.

Cancer Cell
Article

Inactivation of the Deubiquitinase CYLD in Hepatocytes Causes Apoptosis, Inflammation, Fibrosis, and Cancer

Kostas Nikolaou,[1] Ageliki Tsagaratou,[1,2] Christina Eftychi,[1] George Kollias,[1] George Mosialos,[2] and Iannis Talianidis[1,*]
[1]Biomedical Sciences Research Center Alexander Fleming, 16672 Vari, Greece
[2]School of Biology, Aristotle University of Thessaloniki, 54124 Thessaloniki, Greece
*Correspondence: talianidis@fleming.gr
DOI 10.1016/j.ccr.2012.04.026

SUMMARY

The tumor suppressor cylindromatosis (CYLD) inhibits the NFκB and mitogen-activated protein kinase (MAPK) activation pathways by deubiquitinating upstream regulatory factors. Here we show that liver-specific disruption of CYLD triggers hepatocyte cell death in the periportal area via spontaneous and chronic activation of TGF-β activated kinase 1 (TAK1) and c-Jun N-terminal kinase (JNK). This is followed by hepatic stellate cell and Kupffer cell activation, which promotes progressive fibrosis, inflammation, tumor necrosis factor (TNF) production, and expansion of hepatocyte apoptosis toward the central veins. At later stages, compensatory proliferation results in the development of cancer foci featuring re-expression of oncofetal hepatic and stem cell-specific genes. The results demonstrate that, in the liver, CYLD acts as an important regulator of hepatocyte homeostasis, protecting cells from spontaneous apoptosis by preventing uncontrolled TAK1 and JNK activation.

INTRODUCTION

The nuclear factor (NF)-κB signaling pathway regulates multiple physiological and pathological processes, including immune responses and carcinogenesis (Vallabhapurapu and Karin, 2009). The principal regulatory step of NFκB-mediated signal transduction is the activation of IκB kinase (IKK), which phosphorylates members of the IκB family of inhibitory proteins that keep NFκB transcription factors inactive in the cytoplasm. The IKK complex consists of two catalytic subunits (IKK1 and IKK2) and the regulatory subunit (NEMO/IKKγ). It is interesting and pertinent to function that IKK activation by different receptor signals involves conjugation of K63-linked ubiquitin chains to several upstream regulatory components of the signaling cascade. These include the TNF receptor associated factors TRAF2 and TRAF6, the TGFβ-activated kinase TAK1, the receptor interacting protein RIP1 and NEMO (Sun, 2008; Chen, 2005). K63-linked poly-ubiquitin chains serve as interaction surfaces to facilitate the formation of stable TNFR1 core signaling complexes and/or act as modulators of the enzymatic activities of the modified factors (Chen, 2005; Sun, 2010). For example, poly-ubiquitination of TAK1 is required for its activity to phosphorylate IKK1 and IKK2 in their activation loops and trigger IκBα phosphorylation (Rincón and Davis, 2009; Sun, 2010).

The recent finding that K63-linked ubiquitination is a reversible reaction provides a strong indication that this modification represents an important layer of regulation in the process. The major enzyme that removes K63-linked polyubiquitin chains from NFκB pathway effectors is the cylindromatosis tumor suppressor CYLD (Trompouki et al., 2003; Brummelkamp et al., 2003; Kovalenko et al., 2003; Wright et al., 2007). Overexpression of CYLD in mammalian cells results in deubiquitination of NEMO and several upstream regulators like TRAF2, TRAF6, or TAK1 (Trompouki et al., 2003; Brummelkamp et al., 2003; Kovalenko et al., 2003; Yoshida et al., 2005). In addition, knockdown

Significance

Previous studies have revealed protumorigenic effects of genetic ablation of TAK1, NFκB essential modulator (NEMO), and IKKβ, suggesting that the NFκB signaling pathway plays a central role in the pathogenesis of hepatocellular carcinoma (HCC). The results presented here provide further insights into the mechanisms that link inflammation to cancer. In contrast to expectations, we found that liver-specific inactivation of CYLD leads to the development of HCC. CYLD deficiency triggers a multistep mechanism that mimics the major hallmarks of human HCC: hepatocyte death, inflammation, and fibrosis. The data suggest that controlling TAK1-induced downstream signaling cascades by the enzymatic activity of CYLD is critical for the maintenance of physiological liver homeostasis, as the final outcome of either inactivation or activation of the pathway is cancer.

or knockout of CYLD in different cell types leads to increased ubiquitination of these factors (Reiley et al., 2005; Zhang et al., 2006; Reiley et al., 2007). Together, these findings have established the view that CYLD is primarily a negative regulator of NFκB signaling.

CYLD was initially identified as a gene mutated in familial cylindromatosis that predisposes patients to the development of skin appendage tumors (Bignell et al., 2000). The broad role of CYLD in the regulation of cell survival and proliferation is highlighted by the downregulation of CYLD expression in several other types of human cancer, including colon cancer, lung cancer, multiple myeloma, and hepatocellular carcinoma (Zhong et al., 2007; Annunziata et al., 2007; Keats et al., 2007; Hellerbrand et al., 2007). Hepatocellular carcinoma (HCC) is the most common type of liver cancer, which in most cases develops in conjunction with chronic hepatitis or cirrhosis. Previous studies have revealed a major role of the NFκB signaling pathway in the mechanisms that link chronic inflammation to the pathogenesis of HCC (Maeda et al., 2005; Luedde et al., 2007; Bettermann et al., 2010; Luedde and Schwabe, 2011). Impediment of NFκB activation by disruption of *IKKβ* in the liver sensitized mice to diethylnitrosamine-induced hepatocarcinogenesis, while its deletion in both hepatocytes and Kupffer cells had the opposite effect (Maeda et al., 2005). Similarly, hepatocyte specific deletion of *NEMO* or *TAK1* in mice resulted in spontaneous development of hepatocellular carcinoma (Luedde et al., 2007; Inokuchi et al., 2010; Bettermann et al., 2010). As NFκB in most cancer types is activated to provide important survival signals that prevent apoptosis, the above, unexpected findings pointed to the operation of a more complex process in inflammation-mediated hepatocarcinogenesis, in which mediators of the NFκB activation pathway have tumor suppressor roles (Luedde and Schwabe, 2011).

Because TAK1 and NEMO are subject to regulation by CYLD-mediated deubiquitination, we investigated the potential role of CYLD in liver cancer.

RESULTS

Spontaneous Hepatocyte Apoptosis and Liver Fibrosis in $CYLD^{L\Delta/\Delta}$ Mice

To study the role of CYLD in the liver, we generated mice carrying liver-specific homozygous deletion of *CYLD* exon 9 (designated $CYLD^{L\Delta/\Delta}$), by crossing mice carrying *CYLD* with floxed exon 9 (Trompouki et al., 2009) with *ALFP-Cre* transgenic mice (Kellendonk et al., 2000). Exon 9 deletion results in the expression of a deubiquitinase-deficient form of CYLD that mimics oncogenic mutations described in humans (Trompouki et al., 2009). Polymerase chain reaction (PCR) analysis of hepatocytes from newborn mice confirmed that excision of exon 9 was complete during embryonic life (data not shown). In adult stages, $CYLD^{L\Delta/\Delta}$ mice display hepatomegaly and perceptible stiffness (Figure 1A; Table S1 available online). Western blot analyses and immunostainings using an antibody recognizing the C-terminal epitope of CYLD revealed loss of detectable signals in all hepatocytes, but not in biliary epithelial cells and other smaller non-hepatocyte cells (Figures 1A and 1B), suggesting that *ALFP-Cre*-driven excision of *CYLD* exon 9 in embryonic life is hepatocyte-specific and occurs after hepatoblasts have differentiated into hepatocytes. Interestingly, CYLD exhibits a partially zonal expression pattern in wild-type livers, with higher levels of expression in periportal hepatocytes and reduced levels in hepatocytes surrounding the central veins (Figure 1B). Hematoxylin eosin staining of $CYLD^{L\Delta/\Delta}$ liver sections revealed disorganized regions around the portal veins containing cells with smaller nuclei as early as postnatal day 35 (P35). At later stages of postnatal development (P45 to P120), the number of these cells was dramatically increased, resulting in a staining pattern that highly resembles fibrotic livers (Figure 1C). Indeed, we could detect fibrillar collagen deposition by Sirius red staining initially around portal veins, which was gradually enhanced at later time points, resulting in a massively fibrotic liver at postnatal day 60 (P60) and postnatal day 120 (P120) (Figures 1D and 1E). This correlated with the appearance and expansion of activated hepatic stellate cells (HSCs) visualized by α smooth muscle actin (αSMA) staining (Figure S1A).

Liver damage and associated hepatocyte death is a prerequisite for stellate cell activation. In line with this, TUNEL assays detected substantial cell death around the portal veins of $CYLD^{L\Delta/\Delta}$ livers, as early as P25 (Figures 2A and 2B). The number of TUNEL positive apoptotic cells was greatly increased during the period between P25 and P120, which correlated with increasing levels of cleaved caspase 3 and parallel elevation of serum ALT levels (Figures 2A–2D). These results also indicate that apoptosis is the main pathway of cell death in $CYLD^{L\Delta/\Delta}$ livers. Supporting this notion, only a negligible increase in the levels of the necrosis marker RIP3 protein was detected in $CYLD^{L\Delta/\Delta}$ livers (Figure S1B).

To understand the mechanism by which CYLD inactivation leads to cell death, we first analyzed the activation of Jun N-terminal kinase (JNK), which is known to trigger apoptosis in several cell types when its activity is sustained for long periods of time (Kamata et al., 2005; Schwabe and Brenner, 2006). Spontaneous activation of JNK was observed in $CYLD^{L\Delta/\Delta}$ livers from P25 day onward (Figure 2E). The enhanced intensity of the phospho-JNK signal in western blots of extracts from P35, P45, and P60 $CYLD^{L\Delta/\Delta}$ livers correlated with an increased number of phospho-JNK positive hepatocytes detected by immunohistochemistry (Figure 2F). Double staining with HNF4 antibody revealed that more than 90% of p-JNK positive cells were hepatocytes at P25 and P35 days, while at later time points hepatocytes corresponded to about two-thirds of the pJNK positive cell population (Figure 2G). Importantly, phospho-JNK positive hepatocytes were initially observed only around portal veins, while at later time points, cells in the surrounding area toward the central veins also stained positively (Figure 2F). Activation of JNK was confirmed by a similar time-dependent induction of c-JUN phosphorylation (Figure 2H) and by the induction of expression of downstream target genes *DR5* and *PUMA* (Figure S2A).

Further evidence for the role of sustained JNK activation in hepatocyte death in $CYLD^{L\Delta/\Delta}$ livers was provided by experiments using the JNK inhibitor compound SP600125. Apoptosis and fibrosis were dramatically reduced in mice that were treated twice daily with SP600125 between P30 and P60 compared to those treated with vehicle only (Figures S2B–S2F). In addition, we could detect phosphorylated JNK in primary hepatocytes from $CYLD^{L\Delta/\Delta}$ livers, whose levels increased after treatment

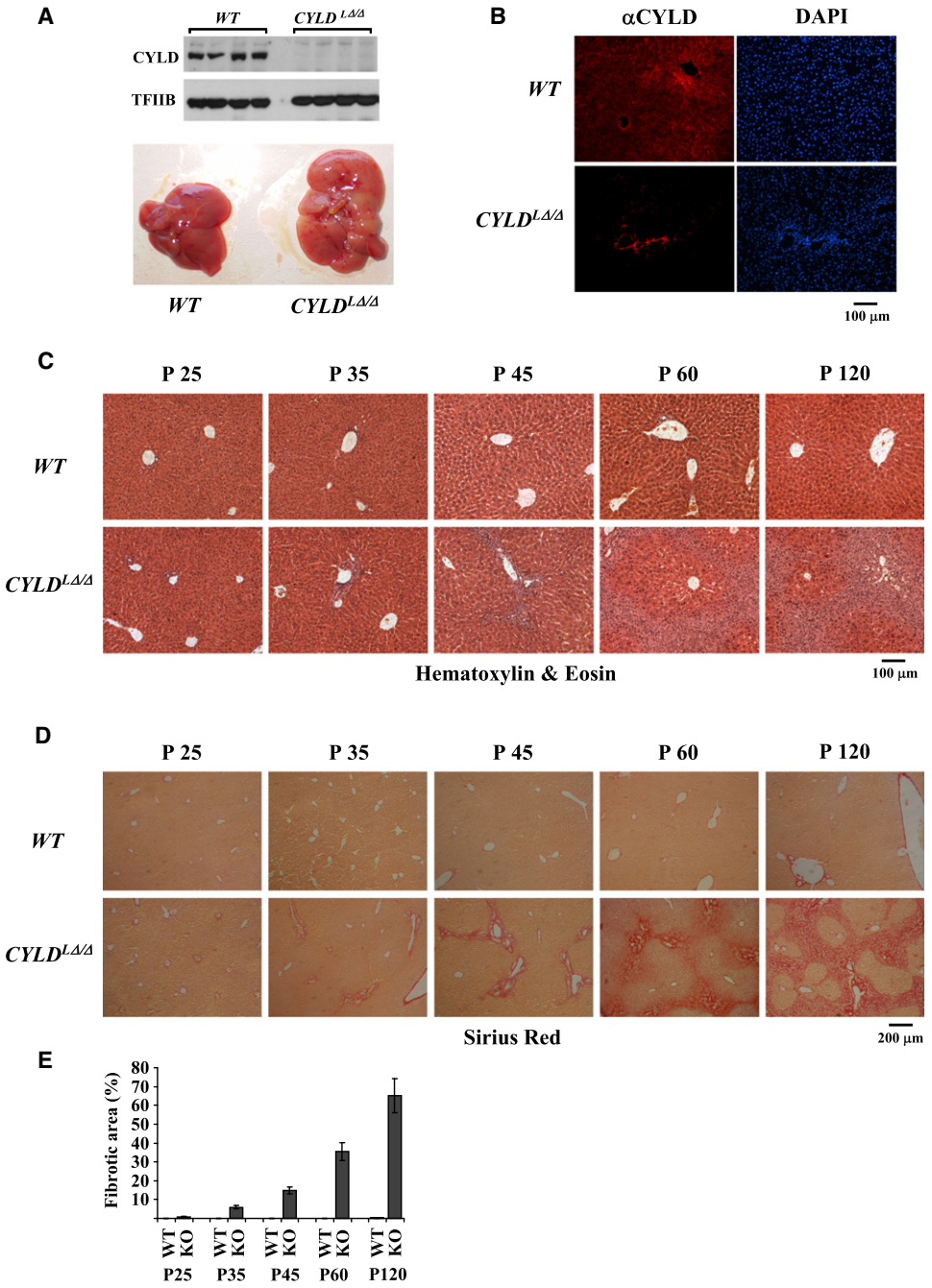

Figure 1. Loss of CYLD Causes Hepatomegaly, Histological Alterations, and Progressive Fibrosis in the Liver

(A) Western blot analysis of whole liver protein extracts from 45-day-old (P45) *CYLD*$^{lox/lox}$/*ALFP-Cre* (*CYLD*$^{L\Delta/\Delta}$) mice and control littermates (WT) using antibodies recognizing the C-terminal part of CYLD or TFIIB. Lower panel: Macroscopic appearance of P60 *CYLD*$^{L\Delta/\Delta}$ and WT livers.

(B) Representative immunohistological staining of liver sections from 45-day-old *CYLD*$^{L\Delta/\Delta}$ mice and control littermates (WT) with αCYLD antibody.

(C) Hematoxylin and Eosin staining of liver sections from postnatal 25-day-old (P25), 35-day-old (P35), 45-day-old (P45), 60-day-old (P60), and 120-day-old (P120) *CYLD*$^{L\Delta/\Delta}$ mice and control littermates (WT).

(D) Sirius Red staining of liver sections from mice indicated as in (C).

(E) Quantitation of Sirius red positive areas. Bars represent percentages of Sirius red positive areas compared to total areas and standard errors of the mean (SEM) from data obtained by examination of nine whole sections from three different animals.

See also Figure S1 and Table S1.

with TNFα (Figure S2G). In wild-type hepatocytes, TNFα-mediated JNK activation was transient but could be prolonged by priming with cycloheximide (CHX). In contrast, prolonged JNK activation without CHX was readily detected in *CYLD*$^{L\Delta/\Delta}$ hepatocytes (Figure S2I). The length of JNK activation correlated with the extent of cell death mediated by TNFα: significant

TNFα-induced cell death could be observed in $CYLD^{L\Delta/\Delta}$ hepatocytes, without concomitant CHX treatment, while in the case of wild-type cells, it was detected only after CHX priming (Figure S2H). Importantly, inhibition of JNK activation by SP600125 greatly prevented death in both cases (Figure S2H).

Collectively, the above results indicate that CYLD inactivation causes spontaneous hepatocyte death via prolonged activation of JNK. In turn, hepatocyte damage triggers the activation and proliferation of hepatic stellate cells, which produce ECM proteins generating progressively expanding fibrotic lesions.

Constitutive Hyperactivation of TAK1 in $CYLD^{L\Delta/\Delta}$ Mice

The mechanism of prolonged JNK activation-mediated apoptosis in our mouse model is likely to involve upstream signaling enzymes, which are direct enzymatic targets of CYLD. In agreement with this, western blot analysis using phospho-specific TAK1 antibodies detected spontaneous activation of TAK1 in $CYLD^{L\Delta/\Delta}$ livers and in primary hepatocyte extracts (Figures 3A and S3A). Phospho-TAK1 induction in $CYLD^{L\Delta/\Delta}$ livers positively correlated with increased K63-linked ubiquitination of endogenous TAK1 (Figure 3C). The amount of phosphorylated TAK1 was further elevated upon LPS treatment (Figure 3B). Importantly, high phospho-TAK1 levels were sustained for at least 2 hr following LPS treatment in $CYLD^{L\Delta/\Delta}$ livers, as opposed to wild-type livers in which TAK1 phosphorylation declined after 1 hr (Figure 3B).

To obtain direct evidence into the role of TAK1 hyperactivation in the phenotype of $CYLD^{L\Delta/\Delta}$ mice, we generated liver-specific $CYLD^{L\Delta/\Delta}/TAK1^{L\Delta/\Delta}$ double knockout mice. In agreement with previous reports (Bettermann et al., 2010; Inokuchi et al., 2010), $TAK1^{L\Delta/\Delta}$ mice developed early liver tumors as evidenced by macroscopically visible nodules in the liver, and, by the observation of cellular dysplasia, lost portal tracts and the appearance of cells with enlarged and hyperchromatic nuclei (Figures 3D and 3E). Serum ALT levels were dramatically induced, reaching levels that were four times higher than those detected in $CYLD^{L\Delta/\Delta}$ mice (Figure 3K). TAK1-deficient mice also displayed liver fibrosis and apoptosis, albeit at much lower levels compared to those observed in $CYLD^{L\Delta/\Delta}$ mice (Figures 3E–3I).

The phenotype of 2-month-old $CYLD^{L\Delta/\Delta}/TAK1^{L\Delta/\Delta}$ double knockout mice greatly differed from that observed in $CYLD^{L\Delta/\Delta}$ mice and very much resembled that of $TAK1^{L\Delta/\Delta}$ mice. Double knockout mice did not develop hepatomegaly, as was seen in $CYLD^{L\Delta/\Delta}$ mice. Instead, cancerous nodules were observed, as was seen in $TAK1^{L\Delta/\Delta}$ mice. Hepatic fibrosis and apoptosis and pJNK levels were dramatically reduced in double knockout mice while serum ALT levels were increased, reaching a level comparable to $TAK1^{L\Delta/\Delta}$ mice (Figures 3D–3K and Table S1). Importantly, the few apoptotic cells observed in different fields were scattered throughout the liver parenchyma in the $CYLD^{L\Delta/\Delta}/TAK1^{L\Delta/\Delta}$ double knockout mice as opposed to their periportal zonation in $CYLD^{L\Delta/\Delta}$ mice (Figures 3G and 2A). Likewise, the relatively minor fibrotic lesions in the $CYLD^{L\Delta/\Delta}/TAK1^{L\Delta/\Delta}$ double knockout mice appeared around both central and portal areas, a distribution that clearly differed from the strict periportal pattern observed in $CYLD^{L\Delta/\Delta}$ mice (Figure 3E). These quantitative and qualitative differences suggest that induction of cell death is achieved via different mechanisms in TAK1 and CYLD-deficient mice. Nevertheless, we can conclude that TAK1 activation is required for the initiation of periportal cell death and fibrosis in $CYLD^{L\Delta/\Delta}$ mice, as these early phenotypic changes were not observed in $CYLD^{L\Delta/\Delta}/TAK1^{L\Delta/\Delta}$ double knockout mice.

Constitutively active TAK1 can fully explain the observed long-term activation of JNK in $CYLD^{L\Delta/\Delta}$ hepatocytes, as it acts upstream of JNK. However, other mechanisms, including reactive oxygen species (ROS) accumulation, may also contribute to it (Kamata et al., 2005; He et al., 2010). To explore this possibility, ROS production was evaluated by staining liver sections with the H_2O_2-sensitive fluorescent dye CM-H_2DCFDA. As shown in Figure S3B, a few positive signals can be specifically detected in $CYLD^{L\Delta/\Delta}$ liver sections as early as P35, which greatly expand at P60 and 1 year of age. Similar to previous findings in IKKβ-deficient mice (He et al., 2010), ROS production resulted in the activation of STAT3 in $CYLD^{L\Delta/\Delta}$ mice (Figure S4A). No significant differences were detected in activated p38 levels, which also acts downstream of TAK1 (Figure S4B). Thus, we conclude that, apart from constitutively active TAK1, the accumulation of ROS, especially at later stages, can play a significant role in sustaining JNK activation and the consequent hepatocyte death.

Expansion of Cell Death in $CYLD^{L\Delta/\Delta}$ Livers Requires TNF Receptor Signaling

As described above, initially (at P25) only few apoptotic cells could be detected in the periportal region of $CYLD^{L\Delta/\Delta}$ livers, whose number gradually increased over time and expanded toward central veins. A possible explanation for this phenomenon could be that the initial, periportally restricted spontaneous hepatocyte injury could trigger inflammation and the consequent inflammation-mediated death receptor signaling may induce more widespread hepatocyte apoptosis. To explore this hypothesis, we first analyzed Kupffer cell activation using the F4/80 and CD68 macrophage markers. As shown in Figure 4A and Figure S4C, we could detect an increasing number of F4/80 and CD68 positive cells in $CYLD^{L\Delta/\Delta}$ livers from day P35 and onward. Using the CD45 marker, we also observed the appearance and expansion of other inflammatory cells in a similar time-dependent manner (Figure 4B). A parallel increase in hepatic *TNFα* mRNA levels was detected (Figure 4C). NFκB activation was evaluated by electrophoretic mobility shift assays and immunostaining. After LPS treatment, activated NFκB signal in $CYLD^{L\Delta/\Delta}$ livers occurred earlier than in wild-type livers, suggesting that loss of CYLD sensitizes hepatocytes to LPS-mediated NFκB activation (Figure 4D). TNFα-mediated activation of NFκB was more pronounced in $CYLD^{L\Delta/\Delta}$ primary hepatocytes, but unlike JNK activation, the induction of NFκB was transient, displaying a similar time-dependent decline in wild-type and CYLD-deficient cells (Figure S4D).

Unexpectedly, the earliest time point when activation of NFκB could be detected in vivo was only at P45 (Figure 4D). This coincides with the timing of first detection of elevated levels of hepatic *TNFα* mRNA (Figure 4C). Potential technical concerns in the sensitivity of the assay were eliminated by examining the expression of NFκB target cellular FLICE-like inhibitory protein

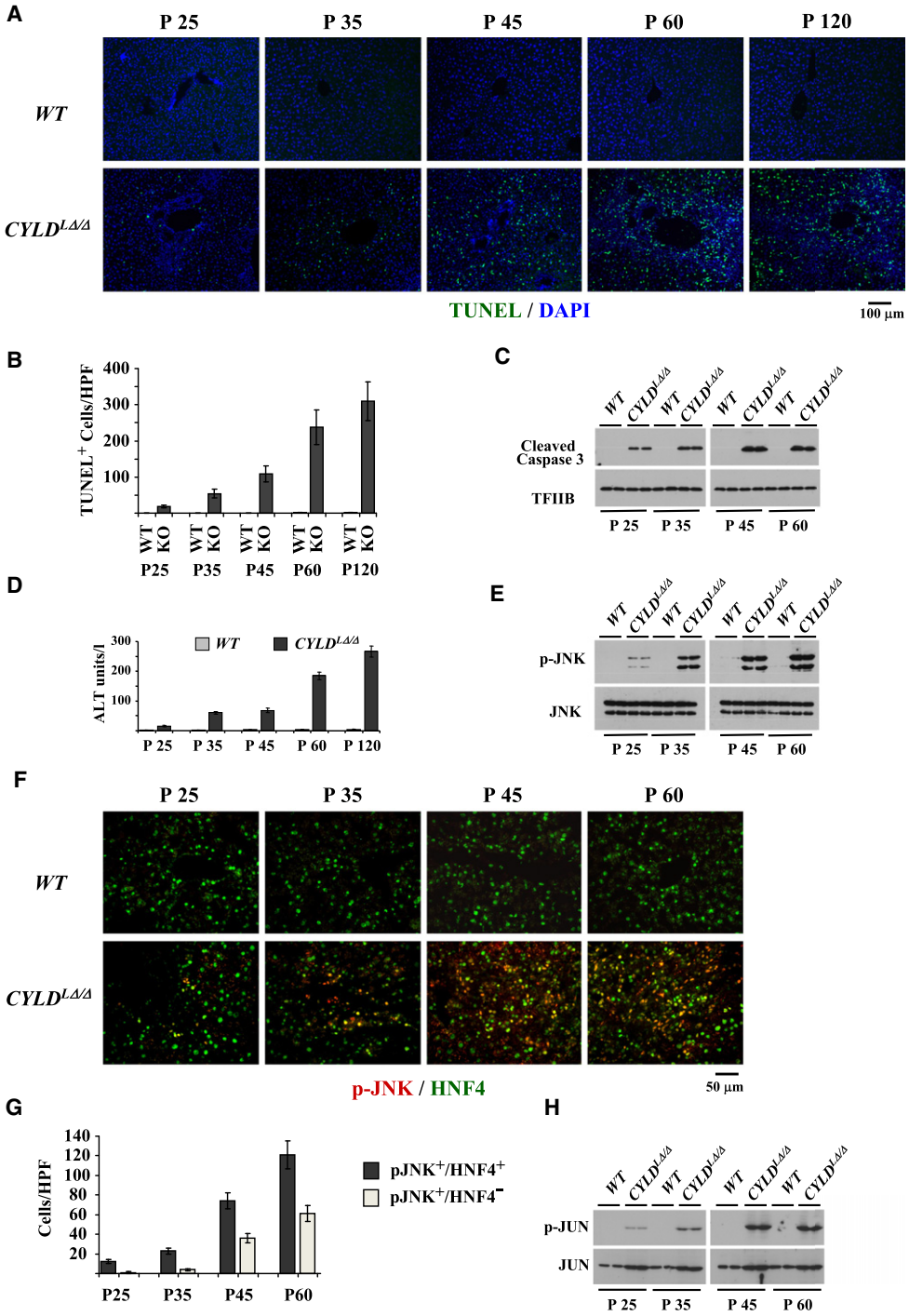

Figure 2. Liver-Specific Ablation of CYLD Leads to Spontaneous and Persistent Activation of JNK and Hepatocyte Apoptosis

(A) TUNEL staining of apoptotic cells in sections from livers of *CYLD*$^{L\Delta/\Delta}$ mice and control littermates (WT) between 25 and 120 days.

(B) Quantitation of TUNEL positive cells. Bars represent mean numbers of TUNEL positive cells per high power field (HPF) and SEM in 10 HPFs of three different animals.

(C) Western blot analysis of extracts from individual livers of 25- to 60-day-old *CYLD*$^{L\Delta/\Delta}$ mice and control littermates (WT) using an antibody specifically detecting cleaved caspase 3 (upper panel) or TFIIB (lower panel).

(D) Serum alanine aminotransferase levels (ALT) in 25- to 120-day-old *CYLD*$^{L\Delta/\Delta}$ mice and control littermates (WT). Bars represent mean values and SEM from samples of five individual mice.

(E) Western blot analysis of extracts from individual livers using antibody recognizing the Thr183/Tyr185-phosphorylated form of JNK (p-JNK) or total JNK (JNK).

(F) Immunohistological staining of liver sections from mice indicated as in (B) using phospho-JNK and HNF4 antibody.

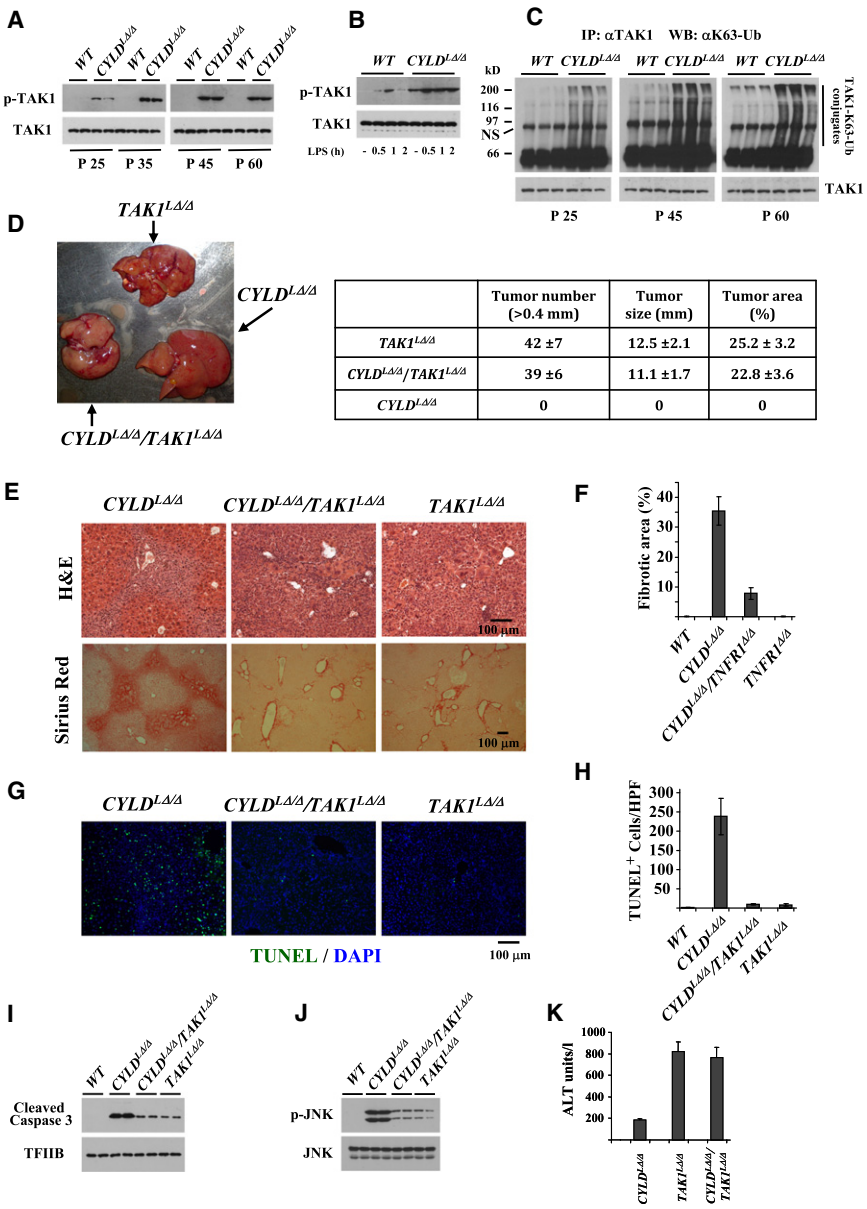

	Tumor number (>0.4 mm)	Tumor size (mm)	Tumor area (%)
$TAK1^{L\Delta/\Delta}$	42 ±7	12.5 ±2.1	25.2 ± 3.2
$CYLD^{L\Delta/\Delta}/TAK1^{L\Delta/\Delta}$	39 ±6	11.1 ±1.7	22.8 ±3.6
$CYLD^{L\Delta/\Delta}$	0	0	0

Figure 3. Spontaneous Activation of TAK1 Is Required for Apoptosis and Fibrosis in Liver-Specific CYLD-Deficient Mice

(A) Western blot analysis of extracts from individual livers of P25 to P60 $CYLD^{L\Delta/\Delta}$ mice and control littermates (WT) using an antibody specifically detecting the Thr184/187-phosphorylated form of TAK1 (p-TAK1) and total TAK1 (TAK1).

(B) Western blot analysis of extracts from the livers P60 $CYLD^{L\Delta/\Delta}$ mice and control littermates (WT) prepared at the indicated time points after intraperitoneal injection with 5 mg/kg LPS.

(C) Detection of K63-linked polyubiquitination of TAK1 in liver extracts from animals indicated as in (A) by immunoprecipitation with αTAK1 antibody followed by western blot analysis using αK63-Ub antibody. The amounts of total TAK1 in the immunoprecipitates were detected by western blot using αTAK1 antibody (bottom panel).

(D) Macroscopic appearance of 60-day-old $TAK1^{lox/lox}$/*ALFP-Cre* ($TAK1^{L\Delta/\Delta}$), $CYLD^{L\Delta/\Delta}$, and $CYLD^{lox/lox}/TAK1^{lox/lox}$/*ALFP-Cre* ($CYLD^{L\Delta/\Delta}$ / $TAK1^{L\Delta/\Delta}$) livers. The number of tumor foci, tumor sizes, and areas were evaluated in five mice at 2 months of age.

(E) Hematoxylin-eosin and Sirius red staining of liver sections from P60 $CYLD^{L\Delta/\Delta}$, $CYLD^{L\Delta/\Delta}$/$TAK1^{L\Delta/\Delta}$, and $TAK1^{L\Delta/\Delta}$ mice.

(F) Quantitation of Sirius red positive areas.

(G and H) TUNEL assays in liver sections and quantitations in P60 mice indicated as in (E).

(I) Western blot assay detecting cleaved caspase 3 in P60 mice indicated as in (E).

(J) Western blot assay detecting p-JNK in P60 mice indicated as in (E).

(K) Serum ALT levels in mice indicated as in (E). Bars represent mean values and SEM from samples of five individual mice.

See also Figure S3.

(cFLIP) and by immunohistochemical assays detecting the distribution of NFκB between the nucleus and the cytoplasm. Increased cFLIP protein levels were detected in P45 and P60 $CYLD^{L\Delta/\Delta}$ livers, but not at earlier time points (Figure S4E). Despite examining a large number of fields, we could not identify cells with nuclear NFκB staining at P25 and P35 (Figure 4E and data not shown). In contrast, our immunohistochemical assays indicate that the source of the observed NFκB DNA binding signal at P60 must be, at least in part, hepatocytes, as we detected nuclear localization of NFκB-p65 in several hepatocytes of P60 $CYLD^{L\Delta/\Delta}$ livers (Figure 4E).

Compelling evidence for the requirement of TNF receptor signaling in the expansion of hepatocyte apoptosis was provided by the data obtained with $CYLD^{L\Delta/\Delta}/TNFR1^{-/-}$ double knockout mice. Genetic ablation of *p55-TNFR1* in CYLD-deficient mice prevented the development of hepatomegaly (Figure 5A and Table S1). Sirius red and TUNEL staining was limited to the periportal area in 2-month-old mice, without expansion to the neighboring areas (Figures 5B–5E). In agreement with the reduced number of TUNEL positive cells, we detected smaller amounts of cleaved caspase 3 and serum alanine transaminase (ALT) levels in

(G) Quantitation of pJNK positive hepatocytes. Bars represent mean numbers per HPF and SEM of JNK positive hepatocytes (JNK+/HNF4+) and JNK positive non-hepatic cells (JNK+/HNF4-) in 10 HPFs of three different mice.

(H) Western blot analysis of extracts from individual livers using antibody recognizing Ser63-phosphorylated form of c-JUN (p-JUN) or total JUN (JUN).

See also Figure S2.

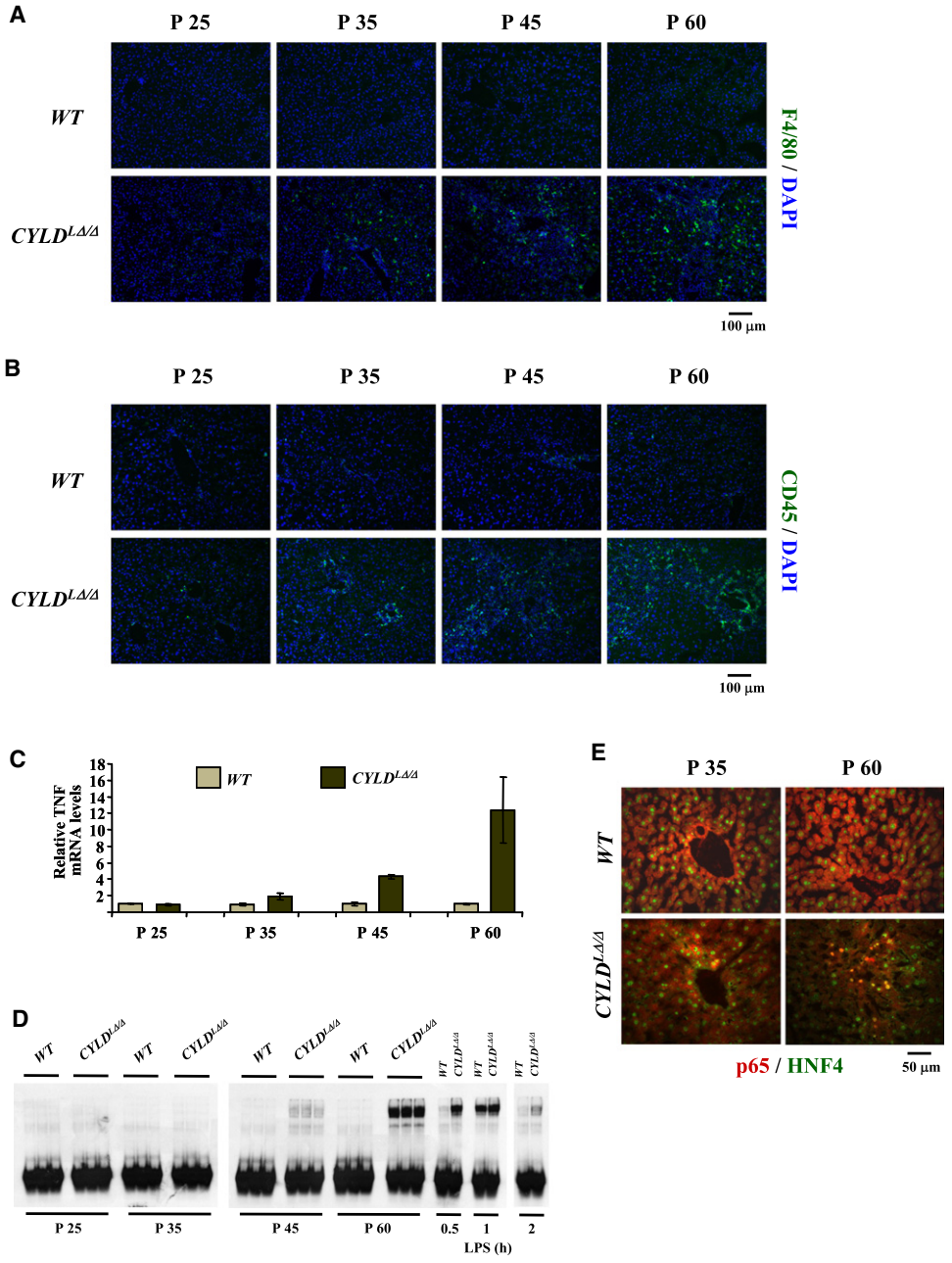

Figure 4. Spontaneous and Progressive Kupffer Cell Activation, Inflammatory Cell Infiltration, TNF Production, and NFκB Activation in the Livers of CYLD-Deficient Mice

(A and B) Immunohistological staining of liver sections from P25 to P60 $CYLD^{L\Delta/\Delta}$ mice and control littermates (WT) with F4/80 and CD45 antibody.

(C) *TNFα* mRNA levels from RT-qPCR assays in the livers of mice as indicated in (A). Bars represent mean values of TNFα mRNA levels normalized to glyceraldehyde-3-phosphate dehydrogenase (*GAPDH*) mRNA and SEM from samples of four individual mice.

(D) Electrophoretic mobility shift assays were performed using radioactive double stranded oligonucleotide containing NFκB binding site sequence and extracts from the livers of indicated mice. Where indicated, mice were injected intraperitoneally with 5 mg/kg LPS.

(E) Representative immunohistological staining detects cytoplasmic and nuclear NFκB-p65 in P35 and P60 $CYLD^{L\Delta/\Delta}$ mice and control littermate (WT).

See also Figure S4.

$CYLD^{L\Delta/\Delta}/TNFR1^{-/-}$ mice compared to $CYLD^{L\Delta/\Delta}$ mice (Figures 5F and 5G).

These data suggest that after the initial spontaneous apoptosis of periportal hepatocytes, inflammatory cells are recruited to the liver, in parallel with proliferation and activation of resident Kupffer cells. They produce inflammatory cytokines, such as TNFα, which, in turn, induce apoptosis in neighboring cells via the TNFR1-dependent signaling cascade.

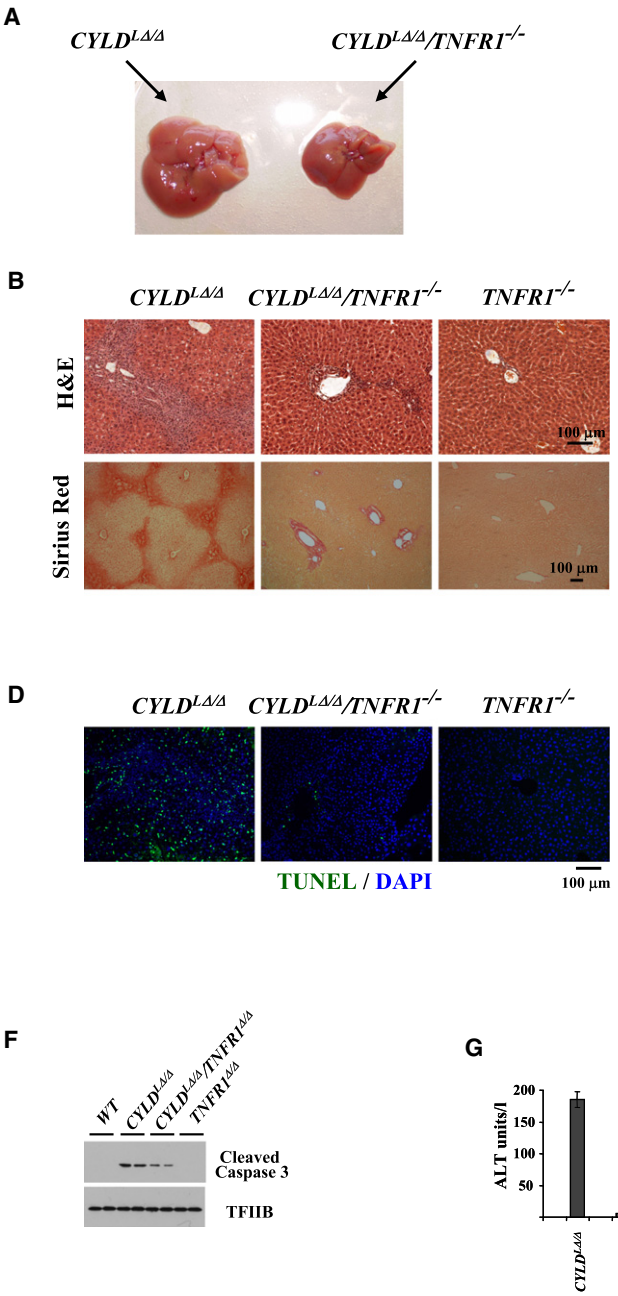

Figure 5. TNF Receptor 1 Is Required for the Expansion of Apoptosis and Fibrosis in Liver-Specific CYLD-Deficient Mice

(A) Macroscopic appearance of P60 $CYLD^{L\Delta/\Delta}$ and $CYLD^{L\Delta/\Delta}$ /$TNFR1^{-/-}$ livers.

(B) Hematoxylin-eosin and Sirius red staining of liver sections from P60 $CYLD^{L\Delta/\Delta}$, $CYLD^{L\Delta/\Delta}$/$TNFR1^{-/-}$, and $TNFR1^{-/-}$ livers mice.

(C) Quantitation of Sirius red positive areas.

(D and E) TUNEL assays and quantitation of P60 livers indicated as in (B).

(F) Western blot analysis of extracts from individual livers of P60 mice indicated as in (B) using an antibody specifically detecting cleaved caspase 3 (upper panel) or TFIIB (lower panel).

(G) Serum ALT levels in mice indicated as in (B). Bars represent mean values and SEM from samples of 5 individual mice.

Late Onset Development of Hepatocellular Carcinoma in $CYLD^{L\Delta/\Delta}$ Mice

Examination of 12-month-old $CYLD^{L\Delta/\Delta}$ livers revealed the presence of numerous cancerous foci of different sizes (Figure 6A). Microscopically, we could detect several histopathological features of hepatocellular carcinoma, including nuclear atypia, frequent pleomorphism, irregular trabeculae, obliteration of portal tracts, mitotic figures, and the presence of cells with increased eosinophilic inclusions or cytoplasmic clearance (Figure 6B).

Genome-wide comparative genomic hybridization (CGH) analysis revealed a large number of amplifications and deletions ranging from 0.62 MB to 14.8 MB in all chromosomes (Figure S5). Notably, several of the amplifications or deletions were detected in foci derived from different animals, pointing to the existence of common signatures generated by CYLD-dependent signals that affect chromosomal integrity. In addition, the expression of several known oncogenes and tumor suppressor genes was upregulated (38 genes) or downregulated (9 genes) in 1-year-old $CYLD^{L\Delta/\Delta}$ livers (Table S2).

Malignant tumor formation was further confirmed by the detection of proliferating cells using BrdU and Ki67 staining and by the detection of increased *Cyclin D1* expression in $CYLD^{L\Delta/\Delta}$ livers (Figures 6D and 7A). Excessive inflammation and liver damage in $CYLD^{L\Delta/\Delta}$ mice was also evident from the massive infiltration of CD45 positive cells and the highly elevated serum ALT levels (Figures 6C and 6D). Importantly, we observed positive staining and/or increased RNA levels of several oncofetal HCC marker genes, such as alpha-fetoprotein (*AFP*), *H19*, insulin-like growth factor 2 (*IGF2*), as well as hepatic stem cell marker genes like glypican 3 (*GPC-3*), *CD133*, or the oval cell-specific *A6* (Figures 6D, 7A, and 7B). Interestingly, we could detect activation of *NANOG*, *SOX2*, and *KLF4*, which are involved in the maintenance of pluripotency of embryonic stem cells (Figure 7C). Within the tumor area, about 25% of HNF4 positive cells stained positively for SOX2 and all SOX2 positive cells co-stained for HNF4 (Figure 7D).

The mRNA and protein levels of *β-catenin* were significantly increased in $CYLD^{L\Delta/\Delta}$ livers. However, the observed increase was due to the accumulation of non-hepatic cells with elevated *β-catenin* expression (Figure S6). Of note, in both wild-type and $CYLD^{L\Delta/\Delta}$ livers, we could detect only the membrane-associated form of the protein, which argues

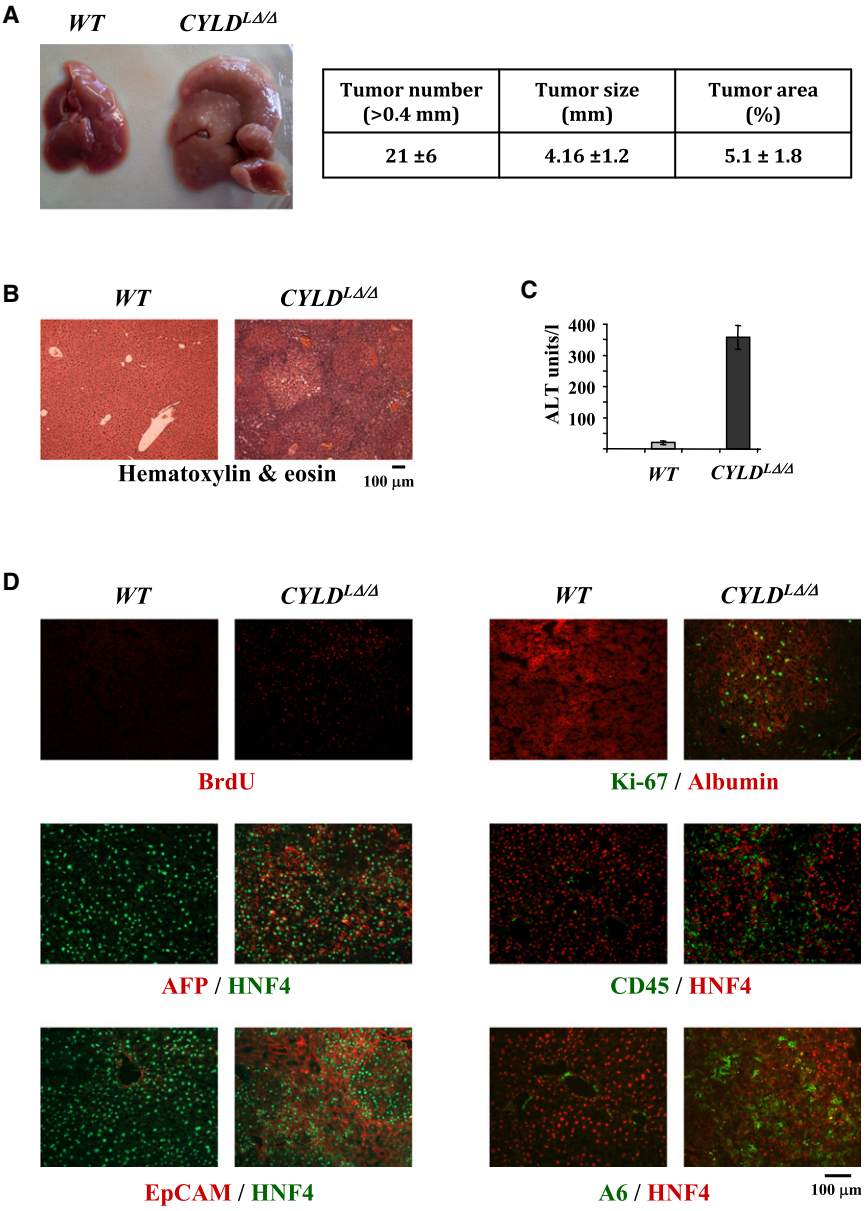

Figure 6. Spontaneous, Late-Onset Development of Hepatocellular Carcinoma in Liver-Specific CYLD-Deficient Mice

(A) Macroscopic appearance of 1-year-old *CYLD*$^{L\Delta/\Delta}$ mice and their control littermate (WT). The numbers of tumor foci, tumor sizes, and areas were evaluated in 11 mice at 1 year of age.

(B) Representative hematoxylin-eosin staining of liver sections of 1-year-old *CYLD*$^{L\Delta/\Delta}$ mice and their control littermate (WT).

(C) Serum ALT levels in 1-year-old mice. Bars represent mean values and SEM from samples of five individual mice.

(D) Representative immunohistochemical staining of liver sections of 1-year-old *CYLD*$^{L\Delta/\Delta}$ mice and control littermates (WT) with combinations of antibodies indicated at the bottom of the images. See also Figure S5.

against the involvement of Wnt signaling in the process of tumorigenesis.

The expression of other cancer marker genes, including connective tissue growth factor (*CTGF*) and *EpCAM*, was also increased in *CYLD*$^{L\Delta/\Delta}$ livers (Figures 6D and 7A). Counterstaining of the sections with the hepatocyte markers HNF4 or albumin showed that all of the AFP positive cells and a large number of Ki-67, EpCAM, or A6 positive cells are hepatocytes. Positive staining for EpCAM and A6, which besides cancerous hepatocytes also mark biliary epithelial cells in normal liver, was observed in a significant number of non-hepatic cells. These cells may correspond to proliferating cholangiocytes (Figure 6D). The observed mixed pattern of *EpCAM* and *A6* expression, together with the expression of oncofetal and stem cell marker genes, suggests that the tumors developing in *CYLD*$^{L\Delta/\Delta}$ livers resemble highly aggressive hepatocellular carcinoma, possibly combined with cholangiocarcinoma.

DISCUSSION

Previous studies have established that CYLD is a negative regulator of NFκB activation (Trompouki et al., 2003; Brummelkamp et al., 2003; Kovalenko et al., 2003). Because NFκB is a key regulator of cell survival and plays a protective role against programmed hepatocyte death (Ghosh and Karin, 2002; Pikarsky et al., 2004; Schwabe and Brenner, 2006), its inhibition was assumed to contribute to the known tumor suppressor function of CYLD, at least in some malignancies (Espinosa et al., 2010; Sun, 2010). Contrasting this view, the results of the present study demonstrate that loss of CYLD in hepatocytes causes spontaneous apoptosis. Initial hepatocyte death triggers inflammation, fibrosis, and late onset carcinogenesis, pointing to the crucial role of CYLD in the control of hepatocyte homeostasis. Phenotypic and molecular-level analyses of liver-specific CYLD-deficient mice revealed at least three temporally distinct events schematically presented in Figure 7E.

The first observable phenotypic change in *CYLD*$^{L\Delta/\Delta}$ livers is spontaneous apoptosis of periportal hepatocytes (Figure 7E, left panel). This coincides with spontaneous activation of TAK1 and JNK. The well-known proapototic function of sustained JNK activation (Kamata et al., 2005; Sakurai et al., 2006; Schwabe and Brenner, 2006; Hui et al., 2008) provides a mechanistic explanation for the observed occurrence of cell death. JNK is a downstream substrate of the TAK1-induced kinase cascade, suggesting that the initial triggering event of cell death must be the spontaneous hyperactivation of TAK1. In agreement with this, periportally restricted apoptosis was not observed in *CYLD*$^{L\Delta/\Delta}$/*TAK1*$^{L\Delta/\Delta}$ double knockout mice.

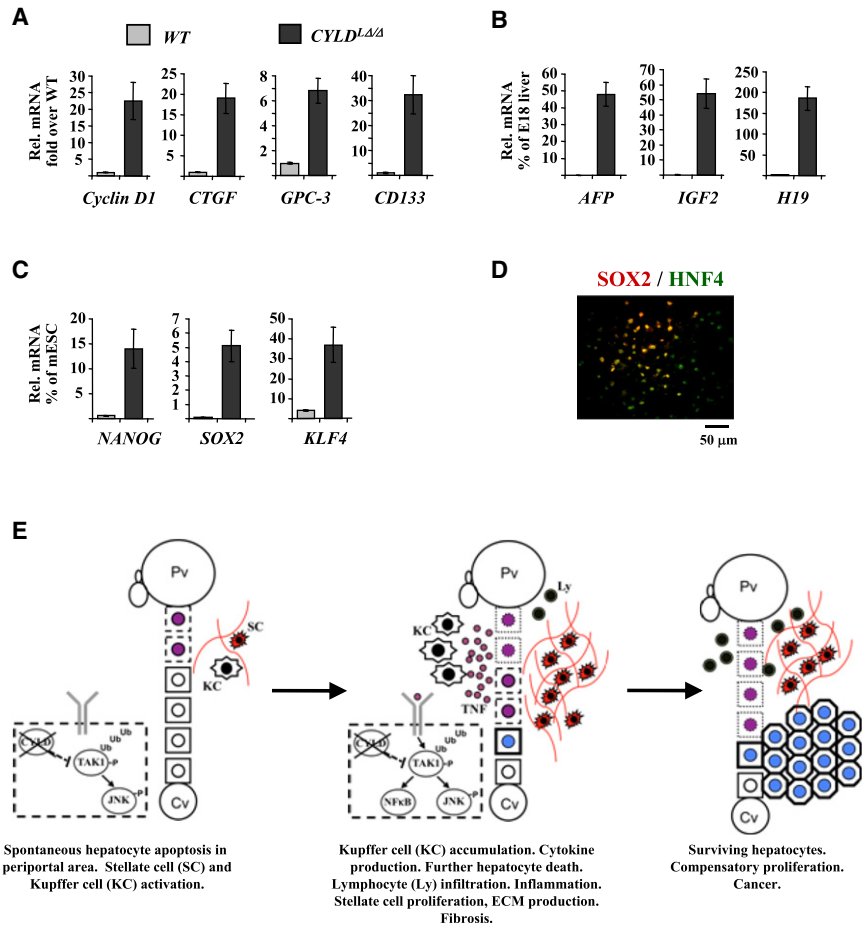

Figure 7. Hepatic Tumors Developed in $CYLD^{L\Delta/\Delta}$ Mice Express Oncofetal and Stem Cell-Specific Genes

(A–C) RT-qPCR assays in total liver RNA from 1-year-old $CYLD^{L\Delta/\Delta}$ mice and control littermates (WT) with primers amplifying the mRNAs of cancer and stem cell markers indicated at the bottom of the graphs. Bars represent mean mRNA levels normalized to GAPDH mRNA and SEM from samples of four individual mice. The data are presented either as a fold over wild-type values (A) for *Cyclin D1*, *CTGF*, *GPC-3*, and *CD133* mRNAs, or as percent of the values obtained with embryonic day 18.5 (E18) mouse livers (B) for *AFP*, *IGF2*, and *H19* mRNAs or as a percent of the values obtained with RNAs prepared from pluripotent mouse embryonic stem cells (C) *NANOG*, *SOX2*, and *KLF4* mRNAs.

(D) Representative immunohistochemical staining of liver sections of 1-year-old $CYLD^{L\Delta/\Delta}$ mice with SOX2 and HNF4 antibodies.

(E) Schematic presentation of the temporal order of molecular and phenotypic changes in liver-specific CYLD-deficient mice.

See also Table S2 and Figure S6.

How is TAK1 activated in the periportal hepatocytes of $CYLD^{L\Delta/\Delta}$ mice without external administration of signaling molecules? The most straightforward and simplest explanation is that the lack of CYLD-mediated cleavage of polyubiquitin chains increases K63-linked ubiquitination of TAK1, which stimulates TAK1 enzymatic activity independently of receptor signaling. An alternative, but conceptually related, mechanism is also suggested by our finding that CYLD-deficient hepatocytes, due to lack of deubiquitination-mediated control, are more sensitive to activate TAK1 in response to low amounts of LPS. Mice that are not kept under germ-free conditions are constantly challenged with small doses of lipopolysaccharide (LPS) produced by the intestinal bacterial flora, which can reach the liver via the portal tract and induce cytokine production by resident Kupffer cells (Enomoto et al., 2002). Thus, due to sensitization, hepatocytes in the periportal area of $CYLD^{L\Delta/\Delta}$ mice may respond to the locally available low amounts of LPS by activating TAK1 via death receptor signaling. Supporting this scenario is the time frame of apoptotic cell appearance: although CYLD is lost from hepatocytes before birth, apoptotic cells are first detected about 10 days after weaning (at P25), when the physiological bacterial flora of the gut is fully formed. Interestingly, CYLD is expressed at higher levels in periportal hepatocytes, compared to those in the pericentral area. We speculate that this partial zonal expression pattern may reflect an increased demand for CYLD-mediated control in the periportal area to protect hepatocytes from apoptosis induced by locally accumulating death-signaling molecules.

Following the initial apoptosis of periportal hepatocytes in $CYLD^{L\Delta/\Delta}$ mice, hepatic stellate cells and Kupffer cells are activated, leading to progressive fibrosis, inflammation, and TNFR1 signaling-dependent propagation of cell death into an expanded area of the liver (Figure 7E, middle panel). Dying hepatocytes release various mediators that induce transdifferentiation of hepatic stellate cells into myofibroblasts, which proliferate and produce a network of extracellular matrix, the hallmark of a fibrotic scar (Bataller and Brenner, 2005; Friedman, 2008). The resulting fibrosis acts as a precursor of cirrhosis during chronic liver damage-induced inflammation, in which excessive extracellular matrix deposition disrupts liver cytoarchitecture (Bataller and Brenner, 2005).

Similar to human fibrotic livers, hepatocyte death in $CYLD^{L\Delta/\Delta}$ mice is also associated with Kupffer cell activation and invasion of inflammatory cells parallel to stellate cell activation. Kupffer cells are resident macrophages in the liver and produce various inflammatory cytokines (Gao et al., 2008). In $CYLD^{L\Delta/\Delta}$ livers, the proliferation of Kupffer cells and the infiltration of other CD45 positive inflammatory cells correlated with the gradual increase of TNFα mRNA and phospho-JNK levels. This provides a mechanistic clue for the observed expansion of hepatocyte death toward the central vein areas, as locally elevated levels of TNFα could induce apoptosis in neighboring cells via the TNFR1-dependent signaling cascade. Evidence for this was provided by experiments in mice lacking both CYLD and p55-TNFR1. Apoptotic hepatocytes and fibrotic lesions in the double knockout mice were limited to the periportal areas even after

P60, suggesting that TNFR1 is required for the propagation of liver damage in $CYLD^{L\Delta/\Delta}$ mice.

We also noted that the expression of DR5 was highly increased in $CYLD^{L\Delta/\Delta}$ mice at P60, suggesting that signaling through DR5 may also contribute to the observed phenotype. However, such an effect should involve cooperation with TNFR-1, as the latter was absolutely required for the propagation and expansion of cell death in CYLD-deficient mice.

Of particular interest is the timing of NFκB activation in $CYLD^{L\Delta/\Delta}$ mice. As CYLD is known to act as a negative regulator of NFκB activation, it was surprising that we could not detect NFκB-p65 stimulation up until P45. The levels of activated NFκB-p65 peaked at P60, when massive cell death and inflammation was evident, but long after complete CYLD inactivation (embryonic life) or the first detection of apoptotic hepatocytes and TAK1 hyperactivation (P25). Although the mechanism behind this phenomenon is not understood, it is possible that the TAK1-NFκB activation cascade requires more robust signals that are available only at P45–P60 in $CYLD^{L\Delta/\Delta}$ livers. Thus, TAK1 activation does not always lead to NFκB induction. A similar lack of correlation between TAK1 and NFκB activation has also been observed in LPS-stimulated bone marrow-derived macrophages (Tseng et al., 2010). The observed preferential induction and chronic persistence of TAK1-JNK phosphorylation cascade over NFκB activation are in agreement with the observed cell death phenotype at the "early" stage. Induction of NFκB-p65 at later stages (at P60) cannot reverse cell death progression, suggesting that the dominance of the TAK1-JNK cascade, which persists for a long period of time, disrupts the balance between death signaling and compensatory survival pathways.

Loss of CYLD has been described in human hepatocellular carcinomas (Hellerbrand et al., 2007). The large majority of hepatocellular carcinomas are detected in patients with hepatic fibrosis or cirrhosis (Okuda, 2000). They develop in a setting of chronic hepatocyte injury and inflammation, similar to that observed in $CYLD^{L\Delta/\Delta}$ mice. In accordance with the above, we found that $CYLD^{L\Delta/\Delta}$ mice spontaneously developed hepatocellular carcinoma at the age of 12 months, pointing to a potential causative and mechanistic relationship between CYLD expression and the development of HCC. The preceding massive cell death and the late appearance of carcinoma in $CYLD^{L\Delta/\Delta}$ mice suggests that, similar to other HCC models generated by genetic ablation of NFκB regulators (Maeda et al., 2005; Luedde et al., 2007; Inokuchi et al., 2010; Bettermann et al., 2010), the mechanism of carcinogenesis involves compensatory cell proliferation (Figure 7E, right panel). Of interest is that the hepatocellular carcinoma in $CYLD^{L\Delta/\Delta}$ mice associates with the reactivation of oncofetal hepatic genes (*AFP*, *H19*, *IGF2*), with the expression of cancer stem cell (CSC) related genes (*GPC-3*, *CD133*), and with genes involved in maintenance of embryonic stem cells (*NANOG*, *SOX2*, *KLF4*). Activation of these latter genes has been implicated in highly aggressive epithelial tumors, with very poor prognosis (Ben-Porath et al., 2008). The above features demonstrate that tumors developing in $CYLD^{L\Delta/\Delta}$ livers highly resemble human hepatocellular carcinomas, whose expression profiles are enriched in stem cell traits (Marquardt et al., 2011). The activation of the oncofetal and "stem cell signature" genes may arise from the high degree of dedifferentiation of hepatocytes that enter the cell cycle via G0-G1 transition or from the proliferation of resident hepatic "stem cells," or both. The available data do not allow discrimination between these possibilities.

Compensatory cell growth could be initiated by ROS accumulation-mediated activation of the oncogenic transcription factor STAT3 (He et al., 2010). The high levels of STAT3 activation in $CYLD^{L\Delta/\Delta}$ mice from P60 and onward and the correlation of STAT3 activation with the levels of ROS accumulation provide a strong indication for its involvement in the process.

Both NEMO and TAK1 are subject to negative regulation by CYLD-mediated deubiquitination (Kovalenko et al., 2003; Reiley et al., 2007). Thus, it was surprising to see that several of the phenotypic characteristics $CYLD^{L\Delta/\Delta}$ mice resemble those reported in liver-specific NEMO and TAK1-deficient mice (Luedde et al., 2007; Inokuchi et al., 2010; Bettermann et al., 2010). The similar phenotypic features include: hepatocyte death, fibrosis, inflammation and cancer. The similarities between $CYLD^{L\Delta/\Delta}$ and $TAK1^{L\Delta/\Delta}$ mice are of particular concern, since TAK1 hyperactivation represents the earliest triggering event in the pathogenesis of liver damage observed in the $CYLD^{L\Delta/\Delta}$ mice. While our analysis of $TAK1^{L\Delta/\Delta}$ mice confirmed the findings of previous reports, it also revealed significant differences between $CYLD^{L\Delta/\Delta}$ and $TAK1^{L\Delta/\Delta}$ mice in terms of timing, localization, and the severity of cell death, fibrosis, and cancer phenotypes. $TAK1^{L\Delta/\Delta}$ mice, generated by crossing $TAK1^{lox}$ with *ALFP-Cre* (this study and Bettermann et al., 2010), developed full-blown HCC at 1.5 months of age, as opposed to $CYLD^{L\Delta/\Delta}$ mice, which develop cancer at 10–12 months of age. In contrast to the massive hepatocyte death and liver fibrosis of $CYLD^{L\Delta/\Delta}$ mice, TAK1-deficient livers display only a few TUNEL positive cells and much milder fibrotic lesions. An additional significant difference between $CYLD^{L\Delta/\Delta}$ and $TAK1^{L\Delta/\Delta}$ mice is the different local distribution of apoptotic hepatocytes and fibrotic lesions. Hepatocyte death and fibrosis are initially limited and later expand to an extended periportal zone in $CYLD^{L\Delta/\Delta}$ mice, while in TAK1-deficient mice, the small number of apoptotic cells and milder fibrotic lesions are uniformly distributed between central vein and portal vein areas.

Despite these qualitative and quantitative differences, the end result of both constitutive activation or inactivation of TAK1 is spontaneously developing inflammation and cancer. Thus, either aberrant increase or decrease of TAK1 activity is detrimental to hepatocyte function. Our results highlight the role of CYLD in keeping TAK1 activity in equilibrium, protecting the liver from spontaneous damage. Therefore, we propose that CYLD acts as a master regulator of TAK1-induced signaling cascades and plays a critical role in the maintenance of physiological liver homeostasis.

EXPERIMENTAL PROCEDURES

Animal Models

$CYLD^{lox}$ mice carrying floxed exon 9 alleles of *CYLD* have been described previously (Trompouki et al., 2009). To obtain liver-specific inactivation of *CYLD,* we crossed $CYLD^{lox}$ mice with *ALFP-Cre* transgenic mice (Kellendonk et al., 2000). $CYLD^{lox}$ littermates without *Cre* transgene were used as wild-type controls. For the generation of conditional TAK1-deficient mice, we crossed mice containing floxed TAK1 exon 2 allele (Eftychi et al.,

2012) with *ALFP-Cre* transgenic mice. *TNFR1*$^{-/-}$ mice have been described previously (Rothe et al., 1993). All animals were in C57Bl6 background. Mice were maintained in grouped cages in a temperature-controlled, specific-pathogen-free facility on a 12-hr light/dark cycle and fed by a standard chow diet (Altromin 1324; 19% protein, 5% fat) and water ad libitum. All animal experiments were approved by the Prefecture of Attica and were performed in accordance with the respective national and European Union regulations.

Histological Analysis

Histological assays were performed in paraffin-embedded or frozen tissue sections as described previously (Boulias et al., 2005; Kyrmizi et al., 2006). Briefly, livers were dissected, fixed in 4% paraformaldehyde, and embedded in paraffin. Liver sections (5–6 μm thick) were boiled in 10 mM Na-citrate for 20 min and, after washings with PBS, were blocked with normal goat serum in PBS and used for staining with αSMA antibody. For immunohistochemistry with all of the other antibodies, cryosections were used. Freshly isolated liver tissues were embedded in optimal cutting temperature (OCT) embedding medium without fixation and samples were frozen in liquid nitrogen. Frozen sections were air-dried before fixation in 4% formaldehyde for 15 min at room temperature. Blocking was performed in 1% BSA/0,1% Triton X-100 for 1 hr and then incubated with primary antibodies at room temperature for 2 hr or at 4°C overnight. After incubation with AlexaFluor 568, 555, or 488 (Molecular Probes) secondary antibodies for 1 hr at room temperature and counterstaining with DAPI, fluorescence images were observed using a Zeiss Axioscope 2 Plus microscope. Paraffin-embedded tissue sections were used for staining with 0.1% Sirius red dissolved in saturated picric acid or with hematoxylin and eosin (H&E). Sirius-red positive areas were quantitated using NIH Image-J software. TUNEL assays were performed using the Fluorescein cell death detection kit (Roche). To detect proliferating cells, mice were injected intraperitonelly with 1 mg/kg 5′-Bromo-2′-deoxyuridine (Sigma) twice, in 12-hr intervals. Incorporated BrdU was detected in cryosections using mouse monoclonal αBrdU antibody (Sigma).

Accumulation of reactive oxygen species (ROS) was measured by staining frozen liver sections with 2 μM of 5-(and-6)-chloromethyl-2′,7′-dichlorodihydrofluorescein diacetate, acetyl ester (CM-H_2DCFDA) for 30 min at 37°C. Cell survival in primary hepatocyte cultures was evaluated by MTT assays using 3-(4,5-dimethylthiazol-2-yl)-2,5-diphenyltetrazolium bromide, as described previously (Kontaki and Talianidis, 2010).

Biochemical Analysis

Blood was collected and centrifuged at 1000 g for 10 min. Freshly isolated supernatant plasma fractions were used for measuring alanine aminotransferase (ALT) activity with the Dyasis assay kit.

Preparation of nuclear and whole cell extracts, immunoprecipitations, and western blot assays were performed as described (Tatarakis et al., 2008; Martinez-Jimenez et al., 2010; Kontaki and Talianidis, 2010). For electrophoretic mobility shift assays, double-stranded oligonucleotide was radiolabeled by filling in with Klenow enzyme in the presence of α^{32}P-dCTP. The oligonucleotide used represents an NFκB consensus sequence: sense: 5′-GGG TTG AGG GGA CTT TCC CAG G; antisense: 5′-GGG CCT GGG AAA CTC CCC TCA A. Binding reactions were performed in 15 μl volume containing 20 mM HEPES pH 7.9, 50 mM KCl, 2 mM $MgCl_2$, 4 mM spermidine, 0.02 mM Zn-acetate, 0.1 μg/ml bovine serum albumin, 10% glycerol, 0.5 mM dithiotreitol, 2 μg poly (dI-dC), and 5 μg nuclear extracts. After incubation in ice for 30 min, the protein/DNA complexes were resolved in 5% native polyacrylamide gels and visualized by autoradiography.

RNA Analysis

Total RNA was prepared by the Trizol extraction. After digestion with DNase I, 1 μg of total RNA was used for first strand cDNA synthesis using MMLV reverse transcriptase. Quantitative PCR analyses were carried out in CHROMO4 Real time PCR detection system by using SYBR Green reagent, as described before (Kyrmizi et al., 2006). The nucleotide sequences of primer sets are shown in Supplementary Information. For global gene expression, profiling total RNAs from the whole livers of 1-year-old *CYLD*$^{L\Delta/\Delta}$ mice were analyzed using Affimetrix GeneChIP Exon 1.0 ST Arrays, as described previously (Tatarakis et al., 2008).

ACCESSION NUMBERS

Expression profiling and αCGH data were deposited to ArrayExpress under accession numbers E-MEXP-3478 and E-MTAB-905, respectively.

SUPPLEMENTAL INFORMATION

Supplemental Information includes six figures, two tables, and Supplemental Experimental Procedures and can be found with this article online at doi:10.1016/j.ccr.2012.04.026.

ACKNOWLEDGMENTS

We thank V. Harokopos, S. Kotschote, V. Factor, P. Hatzis, and the Graduate Program MBHD at the University of Crete, Medical School. This work was supported by grants from EU (HEALTH-F5-2009-241783), AICR (09-0586), and GSRT (09SYN-13-901, Thalis656).

Received: June 27, 2011
Revised: January 12, 2012
Accepted: April 2, 2012
Published: June 11, 2012

REFERENCES

Annunziata, C.M., Davis, R.E., Demchenko, Y., Bellamy, W., Gabrea, A., Zhan, F., Lenz, G., Hanamura, I., Wright, G., Xiao, W., et al. (2007). Frequent engagement of the classical and alternative NF-kappaB pathways by diverse genetic abnormalities in multiple myeloma. Cancer Cell *12*, 115–130.

Bataller, R., and Brenner, D.A. (2005). Liver fibrosis. J. Clin. Invest. *115*, 209–218.

Ben-Porath, I., Thomson, M.W., Carey, V.J., Ge, R., Bell, G.W., Regev, A., and Weinberg, R.A. (2008). An embryonic stem cell-like gene expression signature in poorly differentiated aggressive human tumors. Nat. Genet. *40*, 499–507.

Bettermann, K., Vucur, M., Haybaeck, J., Koppe, C., Janssen, J., Heymann, F., Weber, A., Weiskirchen, R., Liedtke, C., Gassler, N., et al. (2010). TAK1 suppresses a NEMO-dependent but NF-kappaB-independent pathway to liver cancer. Cancer Cell *17*, 481–496.

Bignell, G.R., Warren, W., Seal, S., Takahashi, M., Rapley, E., Barfoot, R., Green, H., Brown, C., Biggs, P.J., Lakhani, S.R., et al. (2000). Identification of the familial cylindromatosis tumour-suppressor gene. Nat. Genet. *25*, 160–165.

Boulias, K., Katrakili, N., Bamberg, K., Underhill, P., Greenfield, A., and Talianidis, I. (2005). Regulation of hepatic metabolic pathways by the orphan nuclear receptor SHP. EMBO J. *24*, 2624–2633.

Brummelkamp, T.R., Nijman, S.M., Dirac, A.M., and Bernards, R. (2003). Loss of the cylindromatosis tumour suppressor inhibits apoptosis by activating NF-kappaB. Nature *424*, 797–801.

Chen, Z.J. (2005). Ubiquitin signalling in the NF-kappaB pathway. Nat. Cell Biol. *7*, 758–765.

Eftychi, C., Karagianni, N., Alexiou, M., Apostolaki, M., and Kollias, G. (2012). Myeloid TAKL acts as a negative regulator of the LPS response and mediates resistance to endotoxemia. PLoS ONE *7*, e31550.

Enomoto, N., Takei, Y., Hirose, M., Ikejima, K., Miwa, H., Kitamura, T., and Sato, N. (2002). Thalidomide prevents alcoholic liver injury in rats through suppression of Kupffer cell sensitization and TNF-alpha production. Gastroenterology *123*, 291–300.

Espinosa, L., Cathelin, S., D'Altri, T., Trimarchi, T., Statnikov, A., Guiu, J., Rodilla, V., Inglés-Esteve, J., Nomdedeu, J., Bellosillo, B., et al. (2010). The Notch/Hes1 pathway sustains NF-κB activation through CYLD repression in T cell leukemia. Cancer Cell *18*, 268–281.

Friedman, S.L. (2008). Mechanisms of hepatic fibrogenesis. Gastroenterology *134*, 1655–1669.

Gao, B., Jeong, W.I., and Tian, Z. (2008). Liver: An organ with predominant innate immunity. Hepatology *47*, 729–736.

Ghosh, S., and Karin, M. (2002). Missing pieces in the NF-kappaB puzzle. Cell Suppl. *109*, S81–S96.

He, G., Yu, G.Y., Temkin, V., Ogata, H., Kuntzen, C., Sakurai, T., Sieghart, W., Peck-Radosavljevic, M., Leffert, H.L., and Karin, M. (2010). Hepatocyte IKKbeta/NF-kappaB inhibits tumor promotion and progression by preventing oxidative stress-driven STAT3 activation. Cancer Cell *17*, 286–297.

Hellerbrand, C., Bumes, E., Bataille, F., Dietmaier, W., Massoumi, R., and Bosserhoff, A.K. (2007). Reduced expression of CYLD in human colon and hepatocellular carcinomas. Carcinogenesis *28*, 21–27.

Hui, L., Zatloukal, K., Scheuch, H., Stepniak, E., and Wagner, E.F. (2008). Proliferation of human HCC cells and chemically induced mouse liver cancers requires JNK1-dependent p21 downregulation. J. Clin. Invest. *118*, 3943–3953.

Inokuchi, S., Aoyama, T., Miura, K., Osterreicher, C.H., Kodama, Y., Miyai, K., Akira, S., Brenner, D.A., and Seki, E. (2010). Disruption of TAK1 in hepatocytes causes hepatic injury, inflammation, fibrosis, and carcinogenesis. Proc. Natl. Acad. Sci. USA *107*, 844–849.

Kamata, H., Honda, S., Maeda, S., Chang, L., Hirata, H., and Karin, M. (2005). Reactive oxygen species promote TNFalpha-induced death and sustained JNK activation by inhibiting MAP kinase phosphatases. Cell *120*, 649–661.

Keats, J.J., Fonseca, R., Chesi, M., Schop, R., Baker, A., Chng, W.J., Van Wier, S., Tiedemann, R., Shi, C.X., Sebag, M., et al. (2007). Promiscuous mutations activate the noncanonical NF-kappaB pathway in multiple myeloma. Cancer Cell *12*, 131–144.

Kellendonk, C., Opherk, C., Anlag, K., Schütz, G., and Tronche, F. (2000). Hepatocyte-specific expression of Cre recombinase. Genesis *26*, 151–153.

Kontaki, H., and Talianidis, I. (2010). Lysine methylation regulates E2F1-induced cell death. Mol. Cell *39*, 152–160.

Kovalenko, A., Chable-Bessia, C., Cantarella, G., Israël, A., Wallach, D., and Courtois, G. (2003). The tumour suppressor CYLD negatively regulates NF-kappaB signalling by deubiquitination. Nature *424*, 801–805.

Kyrmizi, I., Hatzis, P., Katrakili, N., Tronche, F., Gonzalez, F.J., and Talianidis, I. (2006). Plasticity and expanding complexity of the hepatic transcription factor network during liver development. Genes Dev. *20*, 2293–2305.

Luedde, T., Beraza, N., Kotsikoris, V., van Loo, G., Nenci, A., De Vos, R., Roskams, T., Trautwein, C., and Pasparakis, M. (2007). Deletion of NEMO/IKKgamma in liver parenchymal cells causes steatohepatitis and hepatocellular carcinoma. Cancer Cell *11*, 119–132.

Luedde, T., and Schwabe, R.F. (2011). NF-κB in the liver—linking injury, fibrosis and hepatocellular carcinoma. Nat Rev Gastroenterol Hepatol *8*, 108–118.

Maeda, S., Kamata, H., Luo, J.L., Leffert, H., and Karin, M. (2005). IKKbeta couples hepatocyte death to cytokine-driven compensatory proliferation that promotes chemical hepatocarcinogenesis. Cell *121*, 977–990.

Marquardt, J.U., Raggi, C., Andersen, J.B., Seo, D., Avital, I., Geller, D., Lee, Y.H., Kitade, M., Holczbauer, A., Gillen, M.C., et al. (2011). Human hepatic cancer stem cells are characterized by common stemness traits and diverse oncogenic pathways. Hepatology *54*, 1031–1042. 10.1002/hep.24454.

Martinez-Jimenez, C.P., Kyrmizi, I., Cardot, P., Gonzalez, F.J., and Talianidis, I. (2010). Hepatocyte nuclear factor 4alpha coordinates a transcription factor network regulating hepatic fatty acid metabolism. Mol. Cell. Biol. *30*, 565–577.

Okuda, K. (2000). Hepatocellular carcinoma. J. Hepatol. *32* (1, Suppl), 225–237.

Pikarsky, E., Porat, R.M., Stein, I., Abramovitch, R., Amit, S., Kasem, S., Gutkovich-Pyest, E., Urieli-Shoval, S., Galun, E., and Ben-Neriah, Y. (2004). NF-kappaB functions as a tumour promoter in inflammation-associated cancer. Nature *431*, 461–466.

Reiley, W., Zhang, M., Wu, X., Granger, E., and Sun, S.C. (2005). Regulation of the deubiquitinating enzyme CYLD by IkappaB kinase gamma-dependent phosphorylation. Mol. Cell. Biol. *25*, 3886–3895.

Reiley, W.W., Jin, W., Lee, A.J., Wright, A., Wu, X., Tewalt, E.F., Leonard, T.O., Norbury, C.C., Fitzpatrick, L., Zhang, M., and Sun, S.C. (2007). Deubiquitinating enzyme CYLD negatively regulates the ubiquitin-dependent kinase Tak1 and prevents abnormal T cell responses. J. Exp. Med. *204*, 1475–1485.

Rincón, M., and Davis, R.J. (2009). Regulation of the immune response by stress-activated protein kinases. Immunol. Rev. *228*, 212–224.

Rothe, J., Lesslauer, W., Lötscher, H., Lang, Y., Koebel, P., Köntgen, F., Althage, A., Zinkernagel, R., Steinmetz, M., and Bluethmann, H. (1993). Mice lacking the tumour necrosis factor receptor 1 are resistant to TNF-mediated toxicity but highly susceptible to infection by Listeria monocytogenes. Nature *364*, 798–802.

Sakurai, T., Maeda, S., Chang, L., and Karin, M. (2006). Loss of hepatic NF-kappa B activity enhances chemical hepatocarcinogenesis through sustained c-Jun N-terminal kinase 1 activation. Proc. Natl. Acad. Sci. USA *103*, 10544–10551.

Schwabe, R.F., and Brenner, D.A. (2006). Mechanisms of Liver Injury. I. TNF-alpha-induced liver injury: role of IKK, JNK, and ROS pathways. Am. J. Physiol. Gastrointest. Liver Physiol. *290*, G583–G589.

Sun, S.C. (2008). Deubiquitylation and regulation of the immune response. Nat. Rev. Immunol. *8*, 501–511.

Sun, S.C. (2010). CYLD: a tumor suppressor deubiquitinase regulating NF-kappaB activation and diverse biological processes. Cell Death Differ. *17*, 25–34.

Tatarakis, A., Margaritis, T., Martinez-Jimenez, C.P., Kouskouti, A., Mohan, W.S., 2nd, Haroniti, A., Kafetzopoulos, D., Tora, L., and Talianidis, I. (2008). Dominant and redundant functions of TFIID involved in the regulation of hepatic genes. Mol. Cell *31*, 531–543.

Trompouki, E., Hatzivassiliou, E., Tsichritzis, T., Farmer, H., Ashworth, A., and Mosialos, G. (2003). CYLD is a deubiquitinating enzyme that negatively regulates NF-kappaB activation by TNFR family members. Nature *424*, 793–796.

Trompouki, E., Tsagaratou, A., Kosmidis, S.K., Dollé, P., Qian, J., Kontoyiannis, D.L., Cardoso, W.V., and Mosialos, G. (2009). Truncation of the catalytic domain of the cylindromatosis tumor suppressor impairs lung maturation. Neoplasia *11*, 469–476.

Tseng, P.H., Matsuzawa, A., Zhang, W., Mino, T., Vignali, D.A., and Karin, M. (2010). Different modes of ubiquitination of the adaptor TRAF3 selectively activate the expression of type I interferons and proinflammatory cytokines. Nat. Immunol. *11*, 70–75.

Vallabhapurapu, S., and Karin, M. (2009). Regulation and function of NF-kappaB transcription factors in the immune system. Annu. Rev. Immunol. *27*, 693–733.

Wright, A., Reiley, W.W., Chang, M., Jin, W., Lee, A.J., Zhang, M., and Sun, S.C. (2007). Regulation of early wave of germ cell apoptosis and spermatogenesis by deubiquitinating enzyme CYLD. Dev. Cell *13*, 705–716.

Yoshida, H., Jono, H., Kai, H., and Li, J.D. (2005). The tumor suppressor cylindromatosis (CYLD) acts as a negative regulator for toll-like receptor 2 signaling via negative cross-talk with TRAF6 AND TRAF7. J. Biol. Chem. *280*, 41111–41121.

Zhang, J., Stirling, B., Temmerman, S.T., Ma, C.A., Fuss, I.J., Derry, J.M., and Jain, A. (2006). Impaired regulation of NF-kappaB and increased susceptibility to colitis-associated tumorigenesis in CYLD-deficient mice. J. Clin. Invest. *116*, 3042–3049.

Zhong, S., Fields, C.R., Su, N., Pan, Y.X., and Robertson, K.D. (2007). Pharmacologic inhibition of epigenetic modifications, coupled with gene expression profiling, reveals novel targets of aberrant DNA methylation and histone deacetylation in lung cancer. Oncogene *26*, 2621–2634.

Cancer Cell
Article

LKB1/STK11 Inactivation Leads to Expansion of a Prometastatic Tumor Subpopulation in Melanoma

Wenjin Liu,[1] Kimberly B. Monahan,[1] Adam D. Pfefferle,[2] Takeshi Shimamura,[9] Jessica Sorrentino,[1] Keefe T. Chan,[3,4] David W. Roadcap,[3] David W. Ollila,[7] Nancy E. Thomas,[6] Diego H. Castrillon,[10] C. Ryan Miller,[2] Charles M. Perou,[1,2,8] Kwok-Kin Wong,[11] James E. Bear,[3,4] and Norman E. Sharpless[1,5,*]

[1]Department of Genetics
[2]Department of Pathology and Laboratory Medicine
[3]Department of Cell and Developmental Biology
[4]Howard Hughes Medical Institute
[5]Department of Medicine
[6]Department of Dermatology
The Lineberger Comprehensive Cancer Center, University of North Carolina School of Medicine, Chapel Hill, NC 27599-7295, USA
[7]Division of Surgical Oncology and Endocrine Surgery, University of North Carolina at Chapel Hill School of Medicine, Chapel Hill, NC 27599-7213, USA
[8]The Carolina Genome Sciences Center, University of North Carolina at Chapel Hill, Chapel Hill, NC 27599-3175, USA
[9]Department of Molecular Pharmacology and Therapeutics, Loyola University Chicago Stritch School of Medicine, Maywood, IL 60153, USA
[10]Department of Pathology, University of Texas Southwestern Medical Center, Dallas, TX 75390-9073, USA
[11]Department of Medicine, The Dana Farber Cancer Institute and Harvard Medical School, Boston, MA 02115, USA
*Correspondence: nes@med.unc.edu
DOI 10.1016/j.ccr.2012.03.048

SUMMARY

Germline mutations in *LKB1* (*STK11*) are associated with the Peutz-Jeghers syndrome (PJS), which includes aberrant mucocutaneous pigmentation, and somatic *LKB1* mutations occur in 10% of cutaneous melanoma. By somatically inactivating *Lkb1* with *K-Ras* activation (±*p53* loss) in murine melanocytes, we observed variably pigmented and highly metastatic melanoma with 100% penetrance. LKB1 deficiency resulted in increased phosphorylation of the SRC family kinase (SFK) YES, increased expression of WNT target genes, and expansion of a CD24$^+$ cell population, which showed increased metastatic behavior in vitro and in vivo relative to isogenic CD24$^-$ cells. These results suggest that *LKB1* inactivation in the context of RAS activation facilitates metastasis by inducing an SFK-dependent expansion of a prometastatic, CD24$^+$ tumor subpopulation.

INTRODUCTION

The *LKB1* (or *STK11*) gene encodes a serine/threonine kinase that phosphorylates and activates several targets, including AMPK and the AMPK-related kinases (Alessi et al., 2006). LKB1 regulates cancer-relevant cell biologic phenotypes, including migration, invasion, metabolism, and polarity (Alessi et al., 2006; Shah et al., 2008). Germline mutations in *LKB1* cause the Peutz-Jeghers syndrome (PJS; OMIM 175200), an autosomal, dominant disorder characterized by hamartomatous polyps of the gastrointestinal tract and increased mucocutaneous pigmentation (Jeghers et al., 1949). Patients with PJS are tumor prone, demonstrating a significantly increased risk for several cancers (e.g., of colon, pancreas, breast, ovary, and testis) (Giardiello et al., 2000; Lim et al., 2004; Sanchez-Cespedes, 2007). Somatic *LKB1* mutations also are common in sporadic cancers: most notably lung adenocarcinoma (~30%; Ji et al., 2007; Weir et al., 2007), cervical carcinoma (~15%; Forbes

Significance

Although LKB1 loss has been linked to metastasis in epithelial cancers, and *LKB1* compromise occurs frequently in melanoma, the role of *LKB1* inactivation in melanoma progression and metastasis is unknown. Here, we show that mice with *Lkb1* loss and *K-Ras* activation develop highly penetrant melanomas that are extraordinarily metastatic. Further investigation revealed that *LKB1* loss leads to expansion of a highly invasive and tumor-clonogenic subpopulation of cells expressing high levels of CD24, a modulator of metastasis and marker of stem-progenitor cells. The expansion of the CD24$^+$ subpopulation in response to *LKB1* inactivation requires the activity of the YES SRC family kinase. These data suggest a mechanism whereby LKB1 regulates metastasis and identify a promising therapeutic target, YES, in LKB1-deficient melanoma.

et al., 2011; Wingo et al., 2009), and melanoma (~10%; Forbes et al., 2011; Guldberg et al., 1999; Rowan et al., 1999).

In addition to the finding of frequent somatic inactivation in melanoma, several lines of evidence suggest that LKB1 plays an important role in melanocyte biology and limits melanocyte transformation. Patients with PJS demonstrate hyperpigmentation of the lips, oral mucosa, hands, and feet, which are comprised of atypical epidermal melanocytes. Although pathognomonic for PJS, the pathologic basis for these macular lesions is unknown. Moreover, recent reports have suggested that *LKB1* is functionally inactivated by activating mutations of *B-RAF* (Esteve-Puig et al., 2009; Zheng et al., 2009), which are found in approximately 50% of human melanoma, suggesting that functional compromise of *LKB1* is common in melanoma.

A role for LKB1 in regulating tumor differentiation and metastasis has been suggested in epithelial cancers. For example somatic inactivation of *Lkb1* combined with activation of *K-Ras* in genetically engineered murine models (GEMMs) of lung cancer results in tumors with an expanded spectrum of differentiation and considerably augmented metastasis compared to K-Ras-driven tumors lacking *p53* or *Ink4a/Arf* (Ji et al., 2007). LKB1 mutation is associated with advanced stage and metastasis in human patients with aerodigestive carcinomas (Guervos et al., 2007; Matsumoto et al., 2007). Loss of LKB1 has been reported to promote metastatic behaviors (e.g., resistance to anoikis, increased invasiveness) in a variety of epithelial cell types in vitro through diverse mechanisms including inhibition of SIK1 (Cheng et al., 2009) or AMPK (Taliaferro-Smith et al., 2009) as well as activation of EMT, focal adhesion, and SRC family kinases (SFKs) (Carretero et al., 2010). Given these observations suggesting a role for LKB1 in melanocyte biology and transformation, we sought to determine the effects of LKB1 inactivation in human cell lines and GEMMs of melanoma.

RESULTS

Lkb1 Deletion in Melanocytes In Vitro and In Vivo

We intercrossed an established 4-hydroxytamoxifen (4-OHT)-inducible melanocyte-specific CRE allele (*Tyr-CRE-ER^{T2}*, abbreviated "T"; Bosenberg et al., 2006) and three conditional alleles: *Lox-Stop-Lox-(LSL)-Kras^{G12D}* (abbreviated "K"; Johnson et al., 2001); *Lkb1$^{L/L}$* (Bardeesy et al., 2002); and *p53$^{L/L}$* (Jonkers et al., 2001). To investigate the effect of Lkb1 on melanocyte growth and proliferation, we isolated murine melanocytes from neonatal mice of these defined genotypes. Melanocytic origin of the cells was confirmed by immunofluorescence staining for the expression of tyrosinase and tyrosinase-related protein 1 (see Figure S1A available online). Cells were treated with 4-OHT in vitro to allow CRE activation and induce allelic recombination, which was confirmed by PCR (data not shown). Although wild-type (WT), *TK*, *TLkb1$^{L/L}$*, and 4-OHT-untreated control melanocytes grew poorly in vitro, 4-OHT-treated, primary melanocytes from *TKLkb1$^{L/L}$* and *TKp53$^{L/L}$; Lkb1$^{L/L}$* mice demonstrated robust in vitro proliferation without growth arrest over 2 months (Figure 1A; data not shown). Given that *Ink4a/Arf*-deficient melanocytes are immortal in culture (Sviderskaya et al., 2002), we assessed *Ink4a/Arf* expression in cultured melanocytes with and without Lkb1. In accord with prior studies by Bardeesy et al. (2002) and Ji et al. (2007), *Ink4a/Arf* expression was significantly attenuated in *TKLkb1$^{L/L}$* versus *TK* melanocytes (Figure S1B). These findings suggest that Lkb1 loss leads to melanocyte immortalization by compromising Ras-mediated *Ink4a/Arf* activation.

To examine the role of Lkb1 in melanocytes in vivo, neonatal mice were topically treated with 4-OHT to activate CRE and induce recombination as previously described by Bosenberg et al. (2006) and Monahan et al. (2010). Within 4 weeks of 4-OHT treatment, mice from K-Ras-expressing cohorts (*TK*, *TKLkb1$^{L/L}$*, *TKp53$^{L/L}$*, and *TKp53$^{L/L}$; Lkb1$^{L/L}$*) developed melanocytic hyperproliferation and exhibited pigmented cutaneous macules not seen in WT or 4-OHT-untreated littermates (Figure 1B; data not shown). These effects were stronger in *TKLkb1$^{L/L}$* and *TKp53$^{L/L}$* cohorts than in the *TK* cohort, and the most pronounced effects were observed in *TKp53$^{L/L}$; Lkb1$^{L/L}$* mice. Accompanying the obvious melanocytic hyperproliferation in the tails and paws, coat color was more heterogeneous and darker when K-Ras activation was combined with Lkb1 loss (Figure 1C; data not shown). Interestingly, the skin and coat color from K-Ras WT cohorts (*TLkb1$^{L/L}$*, *Tp53$^{L/L}$*, and *Tp53$^{L/L}$; Lkb1$^{L/L}$*) appeared normal (Figure 1B). In aggregate these in vitro and in vivo data show that homozygous Lkb1 inactivation is not sufficient to induce melanocytic hyperproliferation in isolation but potently cooperates with somatic K-Ras activation in this regard.

Lkb1 Loss Promotes Melanoma Formation and Metastasis

We next followed these cohorts for melanoma formation. In accord with our prior results, tumors were not observed in *TK* mice, or in animals of any genotype without K-Ras activation (*TLkb1$^{L/L}$*, *Tp53$^{L/L}$*, or *Tp53$^{L/L}$; Lkb1$^{L/L}$*) when followed to 70 weeks (Figure 2A). Combined somatic Lkb1 loss and K-Ras activation, however, led to melanoma formation with 100% penetrance and latencies ranging from 24 to 56 weeks (median of 38.5). As previously reported by Monahan et al. (2010), concomitant somatic p53 deletion combined with K-Ras activation also potently facilitated tumorigenesis, with a penetrance and latency similar to that seen in the *TKLkb1$^{L/L}$* mice. Despite suggestions that Lkb1 loss compromises p53 function (Jones et al., 2005; Karuman et al., 2001), we nonetheless noted strong cooperation between deletion of Lkb1 and p53 in the context of K-Ras activation (*TKp53$^{L/L}$; Lkb1$^{L/L}$*), with a sharp reduction of median tumor latency to 11 weeks. Therefore, Lkb1 and p53 independently restrain Ras-mediated melanomagenesis.

Although metastasis is seen with multicopy *N-Ras* and *c-Met* transgenic alleles (Ackermann et al., 2005; Scott et al., 2011), metastasis is not a feature of melanoma models driven by a multicopy *H-Ras* transgenic allele (Chin et al., 1997; Scott et al., 2011) or endogenous expression of mutant K-Ras (Monahan et al., 2010). Likewise, we have not observed hematogenous or lymph node metastases in K-Ras-driven melanoma models with intact Lkb1 function, including *TKp16$^{L/L}$*, *TKp53$^{L/L}$*, and *TKp53$^{L/L}$; p16$^{L/L}$* mice (Table S1; see also Monahan et al., 2010). Against this prior experience, we were surprised to note high-volume metastasis in 100% of tumor-bearing mice with somatic K-Ras activation and Lkb1 loss (*TKLkb1$^{L/L}$* and *TKp53$^{L/L}$; Lkb1$^{L/L}$*). In these mice, metastases were found in lymph node, lung, liver, and spleen, but not in kidney or brain (Figures 2B and 2C; Table S1). Because we do not observe metastasis in Lkb1-intact

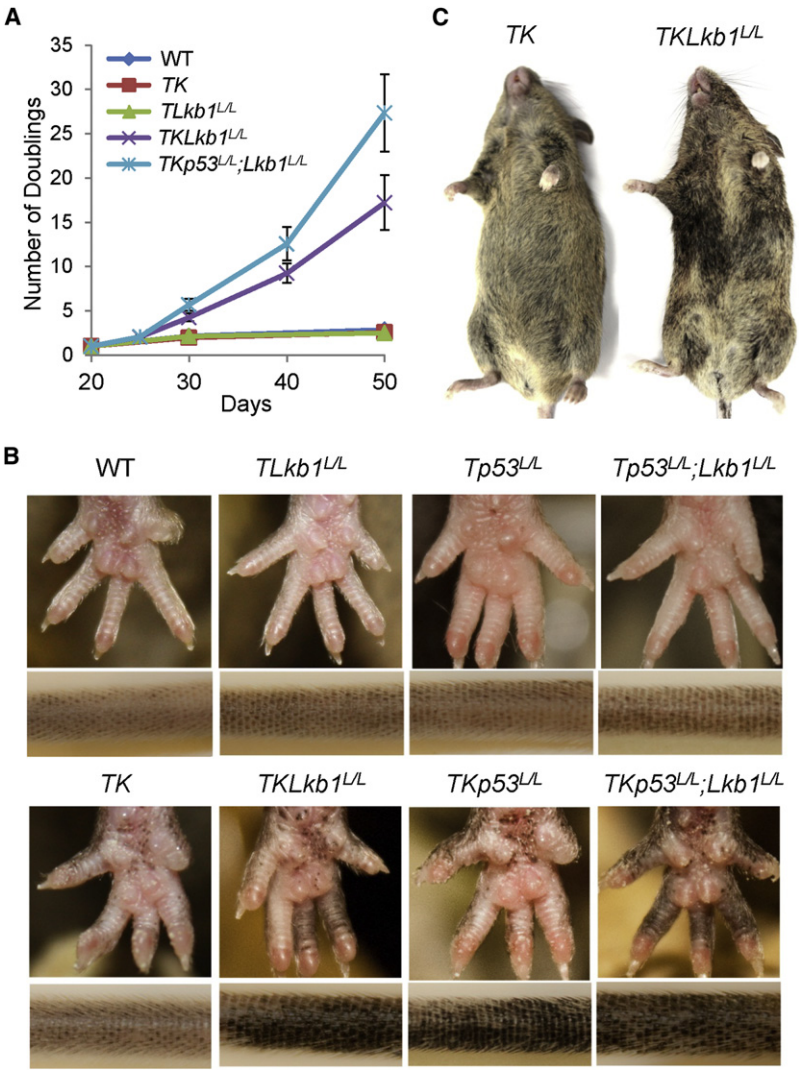

Figure 1. Lkb1 Restrains Melanocytic Hyperproliferation Induced by K-Ras Activation

(A) Growth curves of primary melanocyte cultures from mice of indicated genotypes are illustrated. Cells were treated with or without 4-OHT at 20 days postisolation to activate CRE recombinase, and cell numbers were counted during serial passage. At least three primary lines were generated for each group, and representative results are shown. Error bars show SD.

(B) Changes in pigmentation of representative 8-week-old adult mice of the indicated melanocyte-specific genotypes are shown. Mice without K-Ras activation exhibit normal pigmentation, whereas K-Ras-expressing cohorts showed pigmented macules on the paws and tails, with increasing hyperpigmentation noted with concomitant Lkb1 and/or p53 loss.

(C) Representative mice with melanocyte-specific loss of Lkb1 and K-Ras activation show increased and heterogeneous coat color pigmentation compared to Lkb1-intact mice.

See also Figure S1.

tumors induced by activated H- or K-Ras (e.g., with combined *Ink4a/Arf* or *p53* loss), we concluded that the strong enhancement of metastasis in this model resulted from Lkb1 inactivation.

Although the primary melanomas in both *TKLkb1*$^{L/L}$ and *TKp53*$^{L/L}$*; Lkb1*$^{L/L}$ mice were unpigmented or hypopigmented, metastases found in lymph node, lung, liver, and spleen contained both unpigmented and deeply pigmented lesions (Figures 2B and 2C). These results are reminiscent of prior findings in lung cancer by Ji et al. (2007), where Lkb1 loss both promoted metastasis as well as an extended spectrum of tumor differentiation (e.g., adenocarcinoma versus squamous carcinoma). Therefore, loss of Lkb1 appears to promote melanoma metastasis in the context of increased differentiation potential, consistent with an effect of Lkb1 on a tumor-initiating compartment with augmented multipotency.

The YES SRC Family Kinase Is Activated by LKB1 Loss and Results in Enhanced Metastatic Properties

In order to understand the mechanism whereby Lkb1 regulates metastasis, we studied the effects of Lkb1 on cell migration and invasion in vitro. Toward that end, we generated tumor cell lines from mice of defined genotypes with and without Lkb1. We observed a strong effect of Lkb1 loss on the in vitro wound healing or scratch assay. Compared to melanoma cells with WT Lkb1, including *TKp53*$^{L/L}$*; p16*$^{L/L}$ and *Tyr-Ras; Ink4a/Arf*$^{-/-}$ ("TRIA"; Chin et al., 1997) cells, Lkb1-deficient melanoma cells migrated more rapidly to fill an in vitro wound (Figure 3A; Movies S1 and S2). Likewise, loss of Lkb1 increased tumor invasiveness as quantified using the Matrigel invasion assay (Figure 3B), whereas proliferation in 2D culture or soft agar was not influenced by Lkb1 status (Figure S3). To confirm that these effects reflected Lkb1 function, Lkb1 null melanoma cells were transduced with WT Lkb1 or kinase-dead Lkb1 (Lkb1-KD), and Lkb1 expression was knocked down in Lkb1 intact melanoma cell lines by transducing a small hairpin RNA (shRNA) targeting *Lkb1* (Figure 3C). In scratch assays and Matrigel invasion, Lkb1 restoration in Lkb1 null tumor cells inhibited cell migration and invasion, which was dependent on the kinase activity of Lkb1. Likewise, partial knockdown of Lkb1 in *TKp53*$^{L/L}$*; p16*$^{L/L}$ cell lines significantly promoted cell migration and invasion (Figures 3D and 3E). These data demonstrate that loss of Lkb1 promotes melanoma cell migration and invasion in vitro.

Unbiased proteomic analysis has revealed that Lkb1 loss activates SFKs in lung tumors (Carretero et al., 2010), and therefore, we examined the effect of Lkb1 function on SFK phosphorylation, which correlates with SFK activation, in melanoma cells. Lkb1 knockdown led to increased phosphorylation of SFKs in murine *TKp53*$^{L/L}$*; p16*$^{L/L}$ melanoma cells using a pan-SFK phospho-specific antibody (Figure 4A). We further examined the phosphorylation states of individual SFK members that are abundantly expressed in melanoma, including Src, Fyn, and Yes, by immunoprecipitation of each protein with an

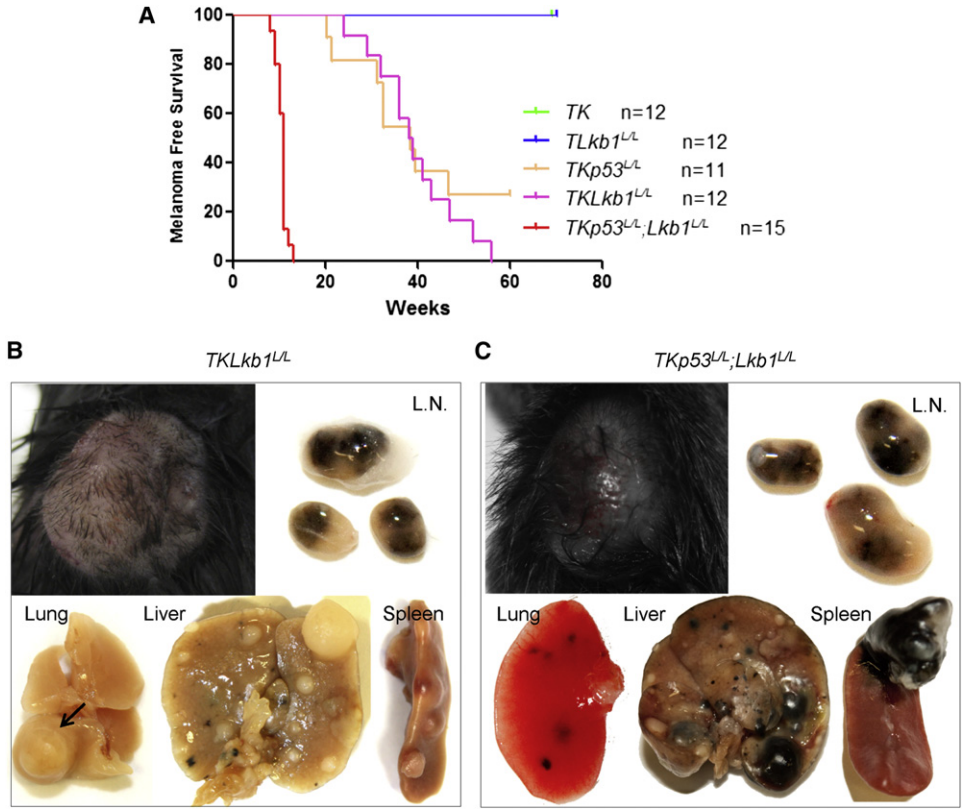

Figure 2. Lkb1 Inactivation Promotes Melanoma Formation and Metastasis

(A) Kaplan-Meier analysis of melanoma-free survival of cohorts of indicated genotypes is presented.

(B and C) Representative primary tumors and metastases exhibiting variable pigmentation from *TKLkb1*$^{L/L}$ (B) and *TKp53*$^{L/L}$*; Lkb1*$^{L/L}$ (C) mice are shown. L.N., lymph node. Arrow in (B) indicates a hypopigmented lung metastasis.

See also Table S1 and Figure S2.

SFK-specific antibody followed by immunoblotting with an antibody to a shared phospho-tyrosine site (Y416). Although Src and Fyn phosphorylation was not significantly changed by Lkb1 knockdown, Yes phosphorylation was significantly increased by Lkb1 knockdown (Figure 4A). These results suggest that Yes activity, at least in part, reflects Lkb1 function in melanoma.

To test whether increased SFK activity is involved in the effect of Lkb1 loss on melanoma cells, we treated the *TKp53*$^{L/L}$*; p16*$^{L/L}$ melanoma cells with or without Lkb1 knockdown with the pan-SFK inhibitor dasatinib. Dasatinib treatment inhibited melanoma cell proliferation (Figure S4A); however, this effect was independent of Lkb1 knockdown. In contrast whereas treatment with dasatinib resulted in a modest decrease (14%) in cell migration in Lkb1-intact cells, the effect was enhanced (27%) in melanoma cells with Lkb1 knockdown (Figure 4B). A similar Lkb1-dependent effect of dasatinib on cell invasion was noted in Matrigel invasion (Figure 4C). These observations suggest that the activation of SFKs due to Lkb1 loss contributes to melanoma cell migration and invasion, but not proliferation.

To confirm the effects of LKB1 loss and SFK activity across species, we turned to the study of human melanoma cell lines. We examined LKB1 expression in a panel of human melanoma cell lines by western analysis and immunohistochemistry on a cell line tissue microarray (TMA). LKB1 expression was heterogeneous in these human melanoma cell lines, with an ~30-fold range of expression observed (Figures 4D and S4B). Two lines with heterozygous LKB1 mutations (A2058 and PMWK) demonstrated lowest expression of functional protein. No correlation between LKB1 expression and RAS/RAF status was observed (Figures 4D and S4B). Further examination revealed that phospho-YES level anticorrelated with LKB1 expression in these human melanoma cell lines (Figures 4E and 4F). To investigate cell motility, invasion, and dasatinib sensitivity in these cells, we focused on lines SKMel23, SKMel63, and A2058 with high, medium, and low LKB1 expression, respectively. As shown in Figures 4G and 4H, LKB1 expression anticorrelated with cell motility, invasion, and sensitivity to dasatinib treatment. In accord with prior studies showing a potent effect of Lkb1 haploinsufficiency on tumorigenesis (Ji et al., 2007), these data show that complete loss of LKB1 is not required to promote malignant growth because even reduced levels of functional LKB1 protein promote phospho-YES expression and invasive behavior in vitro.

To study the relationship of LKB1 and SFK activity in isogenic lines, we knocked down LKB1 expression in A2058 cells (Figure S5A) and analyzed the phosphorylation status of all SFKs using an 8-plex Luminex assay. In accord with the murine results (Figure 4A), LKB1 knockdown in human A2058 cells resulted in

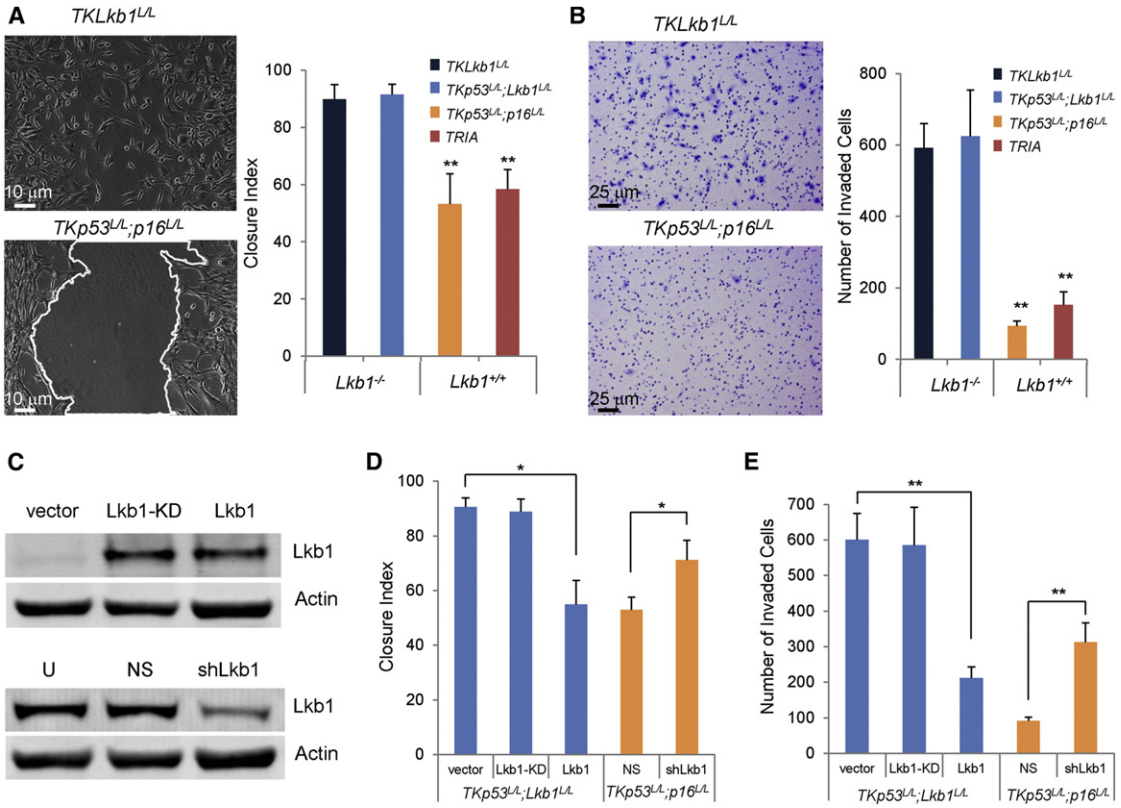

Figure 3. Loss of Lkb1 Promotes Melanoma Cell Migration and Invasion In Vitro

(A) Cells of indicated genotypes were subjected to in vitro wound healing or scratch assay. Representative photomicrographs of *TKLkb1*$^{L/L}$ cells and *TKp53*$^{L/L}$; *p16*$^{L/L}$ are shown on the left. Mean closure index, determined as described in the Supplemental Experimental Procedures, is graphed by genotype on the right (n = 3 replicates per genotype).

(B) Cells of indicated genotypes were subjected to Matrigel invasion assay. Representative photomicrographs of cells that have invaded through Matrigel are shown on the left and mean values graphed for cells of indicated genotypes on the right (n = 3 replicates per genotype).

(C) Western analysis of *TKp53*$^{L/L}$; *Lkb1*$^{L/L}$ cells transduced with nonfunctional Lkb1-KD ("kinase dead") or Lkb1, and *TKp53*$^{L/L}$; *p16*$^{L/L}$ cells transduced with nonspecific shRNA (NS) or shRNA targeting Lkb1 (shLkb1) is presented. U, untreated.

(D and E) Isogenic cells with and without Lkb1 as indicated were subjected to in vitro scratch assay (D) and Matrigel invasion assay (E) as in (A) and (B), respectively. Error bars show SD. *$p < 0.05$; **$p < 0.01$.

See also Movies S1 and S2, and Figure S3.

an increase in YES phosphorylation as well as a more modest but significant effect on FYN phosphorylation (Figure 5A). The activity of all the other SFK members was not changed by LKB1 knockdown (Figure 5A). To assess the role of individual SFKs in mediating the effects of LKB1 loss, we knocked down the expression of individual SFK members by transfecting A2058 cells with siRNAs specifically targeting SRC, FYN, or YES (Figure 5B). We noted that LKB1 knockdown in A2058 cells had a similar effect on wound healing and Matrigel invasion to that seen in murine melanoma (Figures 5C and 5D). This effect of LKB1 inactivation was reverted by knockdown of YES, but not FYN or SRC (Figures 5C and 5D). Of note the proliferation of these cells was not affected by knockdown of YES (Figure S5B). The effect of LKB1 inactivation on YES phosphorylation, cell motility, and invasion was also observed in a second human melanoma cell line, SKMel28, with relatively high expression of LKB1 (Figures S5C–S5F). Therefore, as opposed to lung cancer where greater effect of LKB1 loss is on SRC (Carretero et al., 2010), the effects of increased SFK activity on cell migration and invasion associated with LKB1 loss in melanoma cells are predominantly mediated by YES.

To determine the role of Yes activity in metastasis of Lkb1-deficient melanoma in vivo, we employed the tail vein metastasis assay. Targeting of *Yes* by shRNA was used to knock down expression in *TKp53*$^{L/L}$; *Lkb1*$^{L/L}$ melanoma cells (Figure S5G), which did not affect cellular proliferation (Figure S5H). Cells with or without *Yes* knockdown were injected into nude mice via the tail vein, and lung metastases were examined 3 weeks later. As shown in Figures 5E and 5F, *TKp53*$^{L/L}$; *Lkb1*$^{L/L}$ melanoma cells were highly metastatic in vivo, whereas knockdown of Yes resulted in a 7-fold decrease of tumor metastasis. In contrast, dasatinib treatment (50 mg/kg/day orally) did not significantly inhibit tumor metastasis in vivo (Figures S5I and S5J). This result is in contrast to the in vitro effects of dasatinib treatment (Figures 4B and 4C) as well as previous studies in lung cancer models by Carretero et al. (2010). Given this discrepancy, we investigated the potency of dasatinib in cell-based assays against SFKs. In accord with previous in vitro kinase

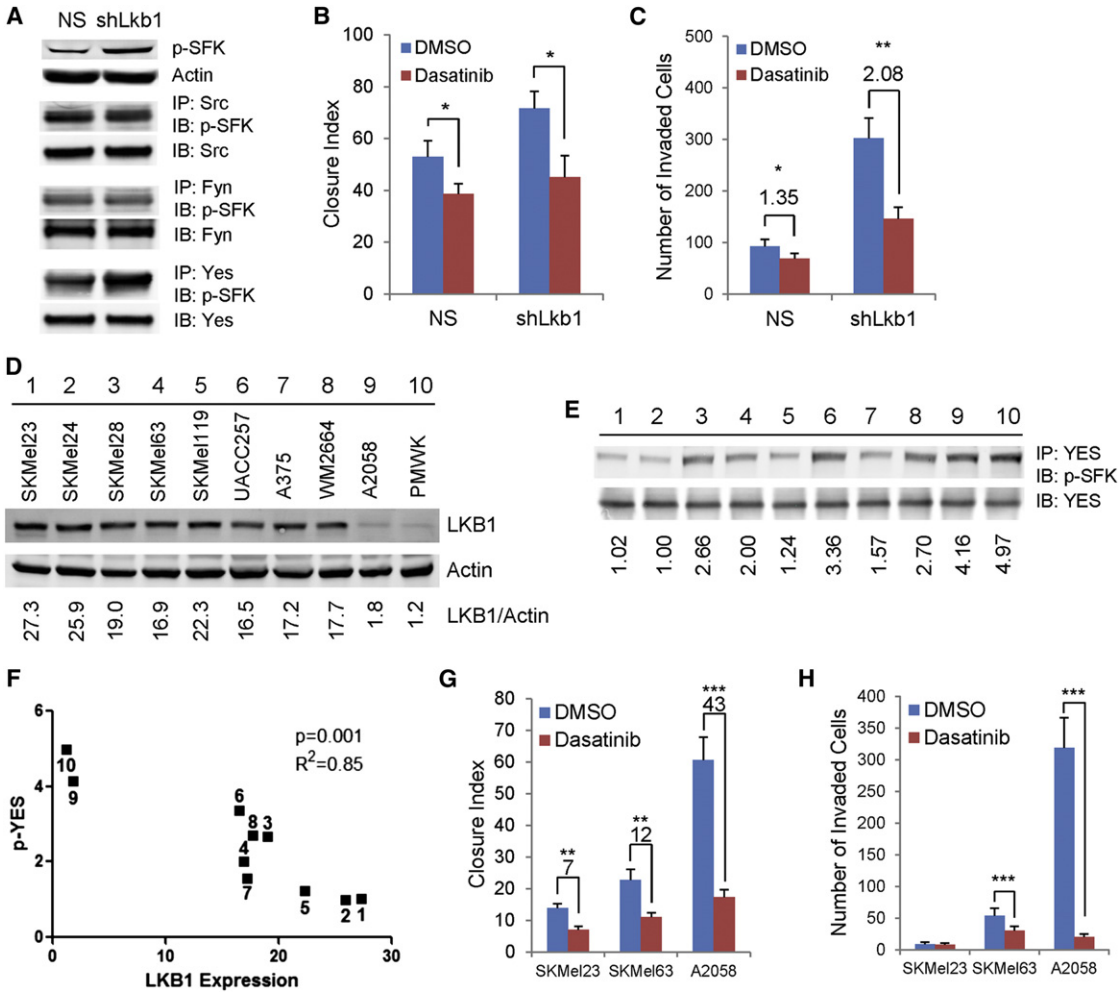

Figure 4. Lkb1 Loss Results in SFK Activation

(A) Representative western analysis of *TKp53$^{L/L}$; p16$^{L/L}$* cells with or without Lkb1 knockdown is shown. Cell lysates were either directly immunoblotted (IB) with antibody against p-SFKs (Y416) or immunoprecipitated (IP) first with indicated antibodies against Src, Fyn, or Yes. NS, nonspecific shRNA.

(B) *TKp53$^{L/L}$; p16$^{L/L}$* melanoma cells with or without LKB1 knockdown were grown in media containing vehicle (DMSO) or dasatinib (30 nM). Closure index was measured 12 hr after wounding.

(C) *TKp53$^{L/L}$; p16$^{L/L}$* melanoma cells with or without LKB1 knockdown were subjected to Matrigel invasion assay with and without treatment with pan-SFK inhibitor, dasatinib (30 nM).

(D) Representative western analysis of indicated human melanoma cells with LKB1 quantification by LICOR analysis is shown.

(E) YES phosphorylation in indicated human melanoma cells with phospho-YES level quantification by LICOR analysis is presented. Cells were labeled with the same number as in (D).

(F) Correlation analysis of LKB1 and phospho-YES expression in human melanoma cells is illustrated. Cells were labeled with the same number as in (D).

(G and H) SKMel23, SKMel63, and A2058 cells were treated with DMSO or 30 nM dasatinib and subjected to in vitro scratch assay (G) or Matrigel invasion assay (H).

Error bars show SD. *p < 0.05; **p < 0.01; ***p < 0.001.

See also Figure S4.

and cell-based assays by Deguchi et al. (2008) and Konecny et al. (2009), Src and Fyn were inhibited by lower doses of dasatinib than those needed to inhibit Yes (Figure S5K, ~10-fold difference in the EC_{50} for Src versus Yes). Therefore, whereas dasatinib is adequately potent for in vitro studies (Figures 4B, 4C, 4G, and 4H), in vivo inhibition of Yes activity appears to require greater doses of dasatinib than those needed to inhibit SRC, the more important SFK in LKB1-deficient lung cancer. These data suggest that an SFK inhibitor with greater potency against YES may exhibit better antimelanoma efficacy in humans.

Microarray Analysis of Lkb1-Regulated Transcript

To provide a mechanistic understanding of how LKB1 loss promotes melanoma metastasis, we performed RNA expression profiling on 20 melanoma cell lines and 9 primary tumors with or without functional Lkb1. The transcriptional effects of Lkb1 inactivation were large: a total of 2,767 and 15,795 genes were

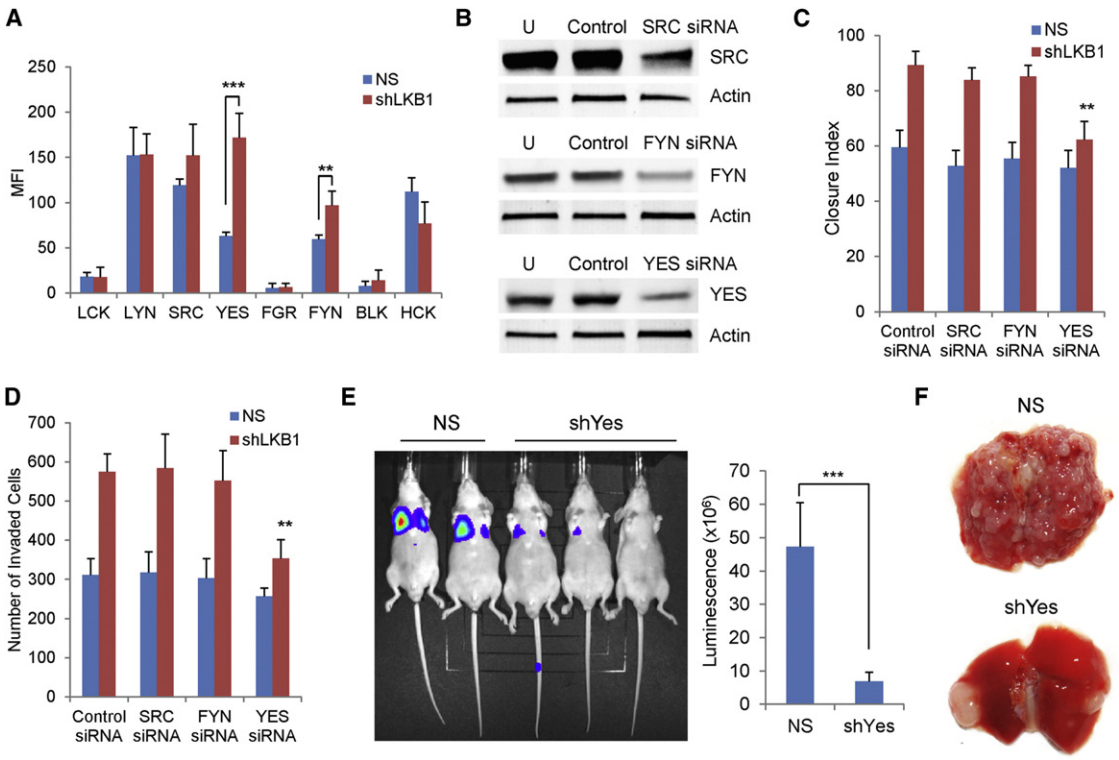

Figure 5. The Effects of LKB1 Loss on Melanoma Cells Are Mediated by the YES Kinase

(A) Tyrosine phosphorylation status of SFK members in A2058 cells with or without LKB1 knockdown is illustrated. Mean values of three replicates per kinase are graphed. MFI, median fluorescence intensity. NS, nonspecific shRNA.

(B) A2058 cells expressing shLKB1 were transfected with scrambled control siRNAs or siRNAs targeting SRC, FYN, or YES. Cell lysates were immunoblotted with indicated antibodies 48 hr after transfection. U, untreated.

(C and D) A2058 cells with or without LKB1 knockdown were transfected with indicated SFK siRNAs. Cells were subjected to in vitro scratch assay (C) or Matrigel invasion assay (D) 48 hr after siRNA transfection.

(E and F) Luciferase-expressing *TKp53$^{L/L}$; Lkb1$^{L/L}$* melanoma cells with or without Yes knockdown were injected into nude mice via tail vein. Mice were examined by luciferase imaging (E) and dissection (F). Luminescence was quantified (E).

Error bars show SD. $^{**}p < 0.01$; $^{***}p < 0.001$.

See also Figure S5.

differentially associated with Lkb1 competence in cell lines and primary tumors, respectively (false discovery rate [FDR] <5%) (Table S2). To better understand pathways regulated by Lkb1 in melanoma cells, we constructed an "overlap" list of transcripts that were differentially regulated by Lkb1 inactivation in both melanoma cell lines and primary tumors. Toward that end, we picked the top 1,000 upregulated and downregulated transcripts associated with Lkb1 loss in cell lines and primary tumors and identified all transcripts appearing on both lists. This winnowed overlap list contained 55 upregulated genes, and 55 downregulated genes (Figures S6A and S6B). Gene Set Enrichment Analysis (GSEA) of this overlap list indicated a significant enrichment for several pathways (Table S3), with targets of mir27 and Lef1 being particularly highly represented (Figures S6A and S6B). Lef1 is a critical transcriptional activator responsive to WNT/β-catenin, and this observation is consistent with recent work suggesting that mir27 expression promotes metastasis via activation of β-catenin signaling (Zhang et al., 2011). Moreover, we noted a more than 2-fold increased expression of other validated WNT targets (*Axin2*, *Nkd1*, *Lgr5*, and *Bmp4*, FDR <1%) in Lkb1-deficient tumors. Therefore, these transcriptional analyses suggest that increased expression of targets of mir27 and Wnt/β-catenin is associated with melanoma metastasis.

LKB1 Inactivation Induces an SFK-Dependent Expansion of a Prometastatic, CD24+ Tumor Subpopulation

The association of Lkb1 loss with increased *Lef1* expression has been previously noted in lung cancer by Ji et al. (2007), and therefore, we looked for other transcripts associated with Lkb1 loss in both tissues. Although we also noted increased expression of *Nedd9* and *Vegf-c* in both tumor types (data not shown), the most reliably upregulated gene associated with LKB1 loss in cell lines and primary tumors from both tumor types was CD24 ("CD24a" in the mouse, Figure S6A; Ji et al., 2007). We considered this protein of interest for further study given its role as a known modulator of advanced disease and metastasis (Baumann et al., 2005; Kristiansen et al., 2003; Lee et al., 2011; Senner et al., 1999) and marker of stem-progenitor cells in several tumor types (Al-Hajj et al., 2003; Gao et al., 2010; Lee et al., 2011). Prior work has demonstrated heterogeneous

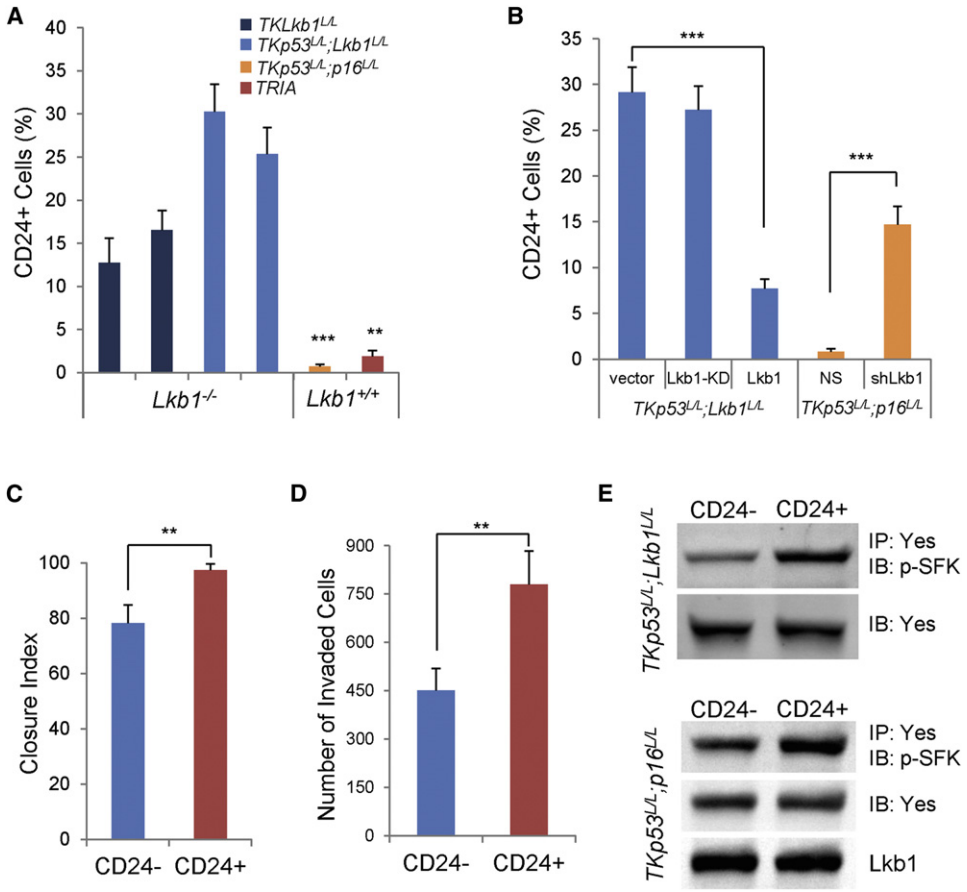

Figure 6. Lkb1 Loss Expands a Prometastatic CD24$^+$ Cell Population

(A) CD24 expression of melanoma cells of indicated genotypes was examined by flow cytometry.

(B) *TKp53$^{L/L}$; Lkb1$^{L/L}$* cells were transduced with Lkb1-KD or Lkb1. *TKp53$^{L/L}$; p16$^{L/L}$* cells were transduced with NS or shLkb1. Cells with and without Lkb1 function as indicated were examined for CD24 expression by flow cytometry.

(C and D) CD24$^+$ cells and CD24$^-$ cells were isolated from *TKp53$^{L/L}$; Lkb1$^{L/L}$* cells by FACS. Sorted cells were subjected to scratch assay (C) and Matrigel invasion assay (D).

(E) CD24$^+$ and CD24$^-$ cells were isolated from *TKp53$^{L/L}$; Lkb1$^{L/L}$* and *TKp53$^{L/L}$; p16$^{L/L}$* cells. Cell lysates were subjected to direct immunoblotting or immunoblotting following immunoprecipitation as indicated.

Error bars show SD. **p < 0.01; ***p < 0.001.

See also Figure S6 and Tables S2 and S3.

expression of CD24 in human melanoma (Shields et al., 2007; Stuelten et al., 2010), and expression is not uniform on all cells within a given cell line. Instead, consistent with its ability to mark tumor-initiating fractions, CD24 expression is noted on a tumor subfraction, with expression ranging from <1% to 13% of cells in melanoma lines.

We therefore investigated the relationship of Lkb1 status and CD24 expression. Cell lines derived from murine melanomas with intact Lkb1 function exhibited a low fraction (<3%) of CD24$^+$ cells. Remarkably, inactivation of Lkb1 was associated with a marked expansion of the CD24$^+$ population ranging from 10% to more than 30% of cells (Figures 6A, 6B, S6C, and S6D). Correspondingly, restored expression of Lkb1 in Lkb1 null melanoma cells suppressed CD24 expression within 6 days of transduction, which was dependent on the kinase activity of Lkb1 (Figures 6B and S6E). Likewise, *Lkb1* null (*TKLkb1$^{L/L}$*) tumors contained an increased CD24$^+$ subpopulation compared to *Lkb1*-competent (*TRIA*) tumors in vivo (Figure S6F). These data demonstrate a highly dynamic, 3- to 10-fold effect of Lkb1-kinase activity on expression of cell surface CD24, a known facilitator of metastasis.

Given that CD24 expression (both increased and decreased) has been associated with functional heterogeneity and tumor-initiating cells in other cancer types, we examined the in vitro properties of CD24$^+$ versus CD24$^-$ cells in melanoma cell lines. CD24$^+$ and CD24$^-$ cells were isolated from *TKp53$^{L/L}$; Lkb1$^{L/L}$* cells by fluorescence-activated cell sorting (FACS) (Figure S6G), and the separated populations were assessed for proliferation, migration, and invasion. Although no difference was observed in the proliferation of CD24$^+$ versus CD24$^-$ cells (Figure S6H), CD24$^+$ cells showed significantly increased cell migration and invasion (Figures 6C and 6D). Correspondingly, Yes phosphorylation was higher in CD24$^+$ cells than in CD24$^-$ cells from both Lkb1-competent and -deficient cell lines (Figure 6E). These

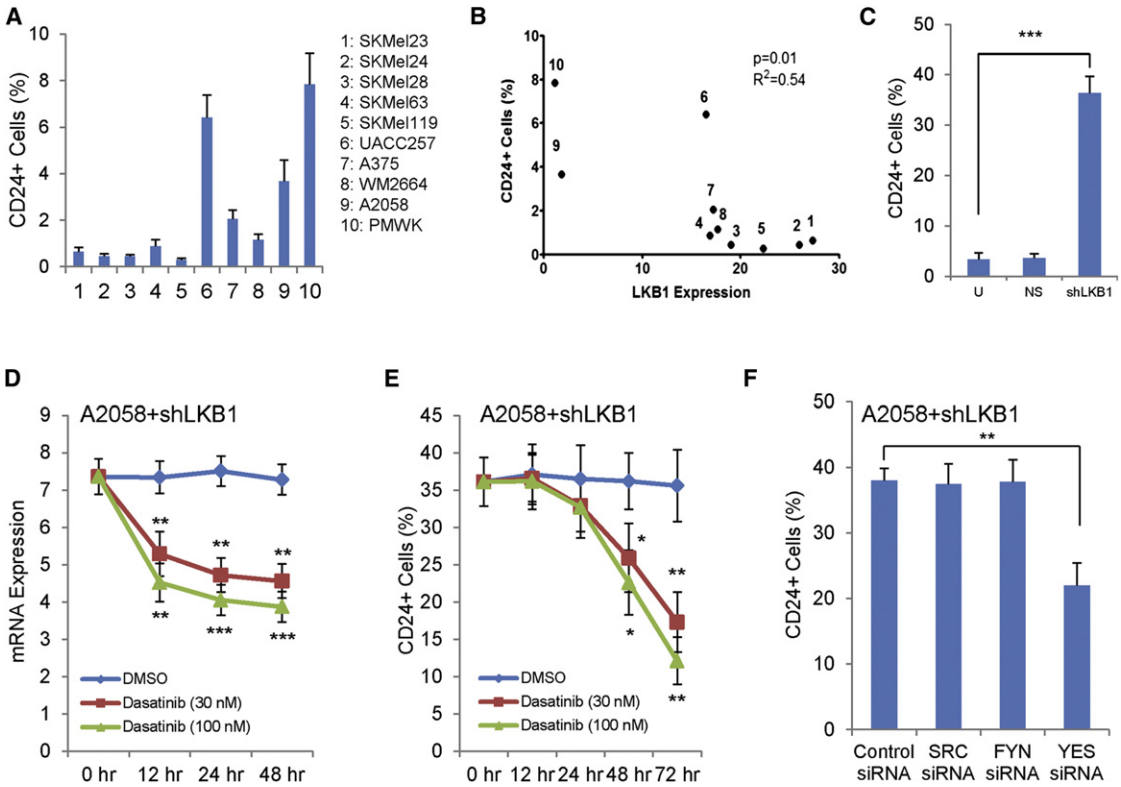

Figure 7. Expansion of the CD24$^+$ Fraction in Response to LKB1 Inactivation Requires YES Kinase

(A) Percentage of CD24$^+$ cells in indicated human melanoma cells determined by flow cytometry is illustrated.

(B) Correlation analysis of LKB1 and CD24 expression in human melanoma cells is presented. LKB1 expression was quantified in Figure 4D. Cells were labeled with the same number as in (A) and Figure 4D.

(C) CD24 expression in A2058 human melanoma cells increases with LKB1 knockdown (shLKB1). U, untreated. NS, nonspecific shRNA.

(D and E) A2058 cells with LKB1 knockdown were treated with the indicated concentrations of dasatinib and harvested for analysis at the indicated times. The expression of *CD24* mRNA (D) was measured by quantitative RT-PCR and calculated as relative expression to A2058 cells with NS-shRNA. The expression of CD24 protein (E) was measured by flow cytometry (n = 3 replicates).

(F) A2058 cells with LKB1 knockdown were transfected with indicated SFK siRNAs. CD24 expression was measured by flow cytometry 72 hr after the transfection (n = 3 replicates).

Error bars show SD. *p < 0.05; **p < 0.01; ***p < 0.001.

See also Figure S7.

results suggest that CD24 expression is associated with increased metastatic behavior in vitro as well as Yes phosphorylation and that increased Yes activation is a common feature of the CD24$^+$ subpopulation regardless of Lkb1 status in melanoma.

To confirm the effects of LKB1 loss on CD24 expression in human cells, we examined CD24 expression in a large panel of human melanoma cell lines. CD24 expression varied over a 28-fold range and anticorrelated with LKB1 expression (Figures 7A and 7B). In A2058 cells, shRNA targeting of *LKB1* led to a marked and rapid increase in CD24 expression (from 4% to 36% with LKB1 knockdown) (Figure 7C), and a similar effect was also observed in SKMel28 cells (Figure S7A). Expression of CD44, another commonly used "tumor stem cell" marker, was not modulated by LKB1 knockdown within this time frame (Figure S7B). As in murine cells, the activity of YES and total SFKs was predominantly observed in CD24$^+$ compared to CD24$^-$ cells (Figures S7C and S7D). Moreover, the level of phospho-ERK was also increased by LKB1 knockdown, with a greater effect in CD24$^+$ versus CD24$^-$ cells, whereas no effect of LKB1 knockdown was noted on phospho-AKT levels (Figure S7E). The increase in CD24 mRNA and protein expression due to LKB1 loss was suppressed in a dose-dependent fashion by transiently treating cells with dasatinib in both human and murine melanoma cells (Figures 7D, 7E, and S7F), with *CD24* mRNA sharply decreasing with as little as 12 hr of dasatinib treatment. In accord with the in vitro motility and invasion results (Figures 5C and 5D), the effect of LKB1 loss on CD24 expression was rescued by siRNA to YES, but not SRC or FYN (Figure 7F). These data show that the ability of LKB1 loss to induce expansion of the prometastatic CD24$^+$ compartment requires the activity of YES kinase.

We next performed an analysis of the relationship between CD24 expression and tumor formation. More colony-forming cells (CFCs) were noted in the CD24$^+$ fraction from both Lkb1-deficient (*TKp53$^{L/L}$; Lkb1$^{L/L}$*) and Lkb1-competent (*TKp53$^{L/L}$; p16$^{L/L}$*) cell lines (Figure S8A). We investigated the in vivo tumor growth of isolated CD24$^+$ and CD24$^-$ cells (Figure S8B) by

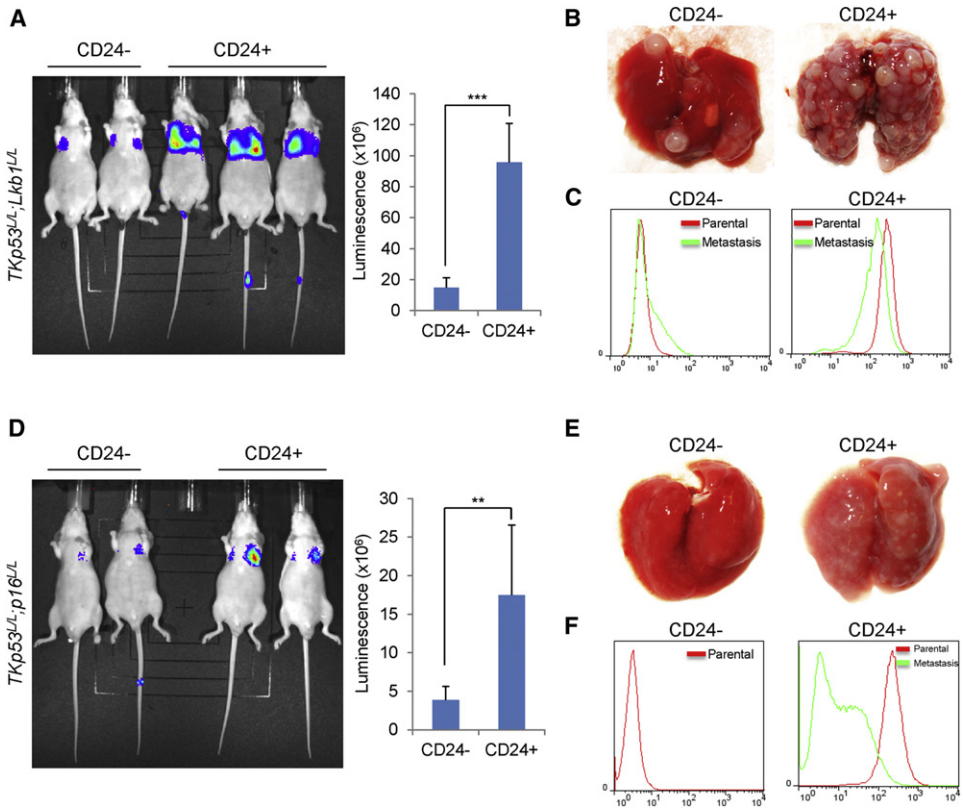

Figure 8. CD24⁺ Cells Exhibit Higher Metastatic Potential than CD24⁻ Cells In Vivo

(A–F) CD24⁺ and CD24⁻ cells were isolated from luciferase-expressing Lkb1-deficient (*TKp53$^{L/L}$; Lkb1$^{L/L}$*, A–C) and Lkb1-competent (*TKp53$^{L/L}$; p16$^{L/L}$*, D–F) melanoma cells and injected into nude mice via tail vein (n = 6 mice for each group). Three weeks after tail vein injection, mice were examined by luciferase imaging (A and D) and dissection (B and E). Luminescence was quantified, and statistical analysis was performed. Error bars show SD. $^{**}p < 0.01$; $^{***}p < 0.001$. Tumor cells were examined by flow cytometry for CD24 expression (C and F) prior to tail vein injection (parental) or 3 weeks later after metastatic growth in the lung (metastasis). No metastasis sample was retrievable from the CD24⁻ fraction of *TKp53$^{L/L}$; p16$^{L/L}$* cells. See also Figure S8.

xenograft transplantation. Although all mice developed tumors, CD24⁺ cells grew more rapidly whether they were derived from Lkb1-defective or -competent melanomas (Figure S8C). FACS-sorted CD24⁺ and CD24⁻ cells were injected into nude mice via tail vein, with in vivo metastases examined 3 weeks later. CD24⁺ cells from both *Lkb1*-deficient and *Lkb1*-competent melanomas exhibited greater metastatic ability than CD24⁻ cells (Figure 8). Examination of CD24 expression detected both CD24⁺ and CD24⁻ cells in tumor metastases formed by either CD24⁺ or CD24⁻ cells (Figures 8C and 8F). Yes knockdown significantly attenuated the size of the CD24⁺ subpopulation in metastases formed after tail vein injection of *TKp53$^{L/L}$; Lkb1$^{L/L}$* (Figure S8D). These data indicate that CD24⁺ melanoma cells exhibit a qualitative increase in metastatic propensity regardless of Lkb1 status and suggest that Lkb1 inactivation predominantly promotes tumor progression by leading to a marked expansion of this CD24⁺ fraction.

DISCUSSION

In this work we show that mice with melanocyte-specific *Lkb1* loss and *K-Ras* activation develop highly metastatic melanomas. *Lkb1*-deficient melanoma cells increased invasive behavior in vitro compared to isogenic *Lkb1*-competent melanoma cells. Further investigation revealed that LKB1 deficiency resulted in activation of SFKs, particularly YES, and expansion of a CD24⁺ cell population that showed increased invasive behavior in vitro and in vivo. Inhibition of YES activity suppressed CD24 expression and decreased metastatic behavior. Collectively, these results demonstrate that *LKB1* functions as a strong suppressor of melanoma metastasis by regulating YES activity, which determines the size of a prometastatic CD24⁺ tumor subpopulation.

Of interest with regard to the phenotypic expression of PJS, we showed that combined melanocyte-specific Lkb1 loss and K-Ras activation results in increased melanocyte proliferation and in vivo hyperpigmentation. The excess melanocytic proliferation in *TKLkb1$^{L/L}$* (and *TKLkb1$^{L/+}$*), but not in *TLkb1$^{L/L}$*, mice, suggests that melanocytic hyperproliferation seen in patients with PJS may reflect sporadic secondary events that activate regulators of proliferation (e.g., RAS) rather than loss of the second copy of LKB1. Therefore, *TKLkb1$^{L/L}$* mice serve as a model to study this poorly understood feature of PJS. A weakness of this model is the reliance on K-RAS mutation, which is ~10-fold less common than that of N-RAS in human melanoma. To date, we have not been able to generate tumors with an *N-Ras^{LSL}* allele featuring a codon 12 mutation (Haigis et al.,

2008), even when combined with inactivation of several different tumor suppressor genes. The explanation for this difference in the melanoma-promoting effects of the various RAS isoforms is an area of active ongoing investigation.

In addition to altered pigmentation, *TKLkb1*$^{L/L}$ and *TKp53*$^{L/L}$*; Lkb1*$^{L/L}$ mice exhibited highly metastatic melanoma. Although metastasis has been reported in a small number of autochthonous murine tumor models (Ackermann et al., 2005; Guy et al., 1992; Scott et al., 2011), these models feature lower volumes of metastatic disease with variable penetrance and rely on supraphysiologic expression of oncogenes. In contrast the present model couples melanocyte-specific, somatic single-copy *K-Ras* activation under the control of its endogenous promoter with homozygous *Lkb1* deletion to produce 100% penetrance of metastasis with a high burden of metastatic disease. For example several tumor-bearing *TKLkb1*$^{L/L}$ and *TKp53*$^{L/L}$*; Lkb1*$^{L/L}$ mice exhibited >50% involvement of the liver, lung, and/or spleen with multifocal metastasis (Figures 2B, 2C, and S2). We believe that the high burden and penetrance of metastases in this model address a significant unmet need in cancer research for experimentally tractable, highly metastatic, autochthonous tumor models. Moreover, in murine models of both lung cancer (Carretero et al., 2010; Ji et al., 2007) and melanoma, *Lkb1*-deficient tumors demonstrate increased histomorphometric heterogeneity and more frequent metastasis compared to tumors lacking *p53* or *Ink4a/Arf*. Because metastasis is not noted in *TKp53*$^{L/L}$, *TKp16*$^{L/L}$, or *TRIA* mice (Table S1; Monahan et al., 2010), the effects of Lkb1 loss on metastasis are not explained by the effects of Lkb1 on expression of p16^{INK4a}, Arf, or p53.

Of interest, Dankort et al. have recently reported melanoma metastasis, albeit with lower tumor burdens, in 4-OHT-treated *Tyr-CRE-ER*^{T2}*B-Raf*$^{LSL/+}$*Pten*$^{L/L}$ mice (Dankort et al., 2009). This result is consistent with the notion that *B-Raf* mutation (Esteve-Puig et al., 2009; Zheng et al., 2009) induces a partial compromise of Lkb1 function. More recently, this group has shown that WNT/β-catenin activation strongly enhances metastasis in this model (Damsky et al., 2011), which matches our findings of increased expression of β-catenin/Lef1 targets in Lkb1-deficient tumors (Figures S6A and S6B). It is not clear from our data if the YES-dependent expansion of the prometastatic, CD24$^+$ melanoma subfraction requires expression of β-catenin/LEF1 targets, but both events appear to result from LKB1 inactivation.

SFK activity has been shown to closely associate with melanoma metastasis (Homsi et al., 2009; Putnam et al., 2009), and prior work in particular has suggested a prominent role for YES among the SFKs in melanoma pathogenesis. For example the kinase activity of YES, but not SRC, is significantly higher in most melanoma cell lines than in melanocytes (Loganzo et al., 1993). Likewise, activation of YES, but not FYN or SRC, appears essential to mediate the increased invasiveness of human melanoma cells in response to stimulation with gangliosides or neurotrophins (Hamamura et al., 2011; Marchetti et al., 1998). Although the mechanism whereby loss of LKB1 kinase activity induces YES activation is not clear, the present data suggest YES as a promising therapeutic target in melanoma lacking LKB1 function. Dasatinib exhibits modest antimelanoma activity in human patients (Kluger et al., 2011). Because we and others (Deguchi et al., 2008; Konecny et al., 2009) have noted an ~10-fold decrease in the potency of dasatinib for YES compared to SRC and other SFKs, these results suggest that an SFK inhibitor with greater potency against YES inhibitor would exhibit greater in vivo antimelanoma efficacy.

Increased YES activity in turn leads to an expansion of a tumor subpopulation that is characterized by increased cell motility and invasion, as well as CD24$^+$ expression. Surprisingly, although LKB1 function is inhibited in most or all of the cells, the activation of YES and expression of CD24 in response to LKB1 inactivation is limited to a minority (~10%–30%) of cells, which exhibit enhanced metastatic properties. A CD24$^+$ population of cells is present, albeit at lower frequency, in LKB1-competent melanoma cells, and loss of LKB1 kinase activity appears to induce an expansion of this prometastatic fraction. The prometastatic properties of CD24$^+$ cells were increased relative to isogenic CD24$^-$ cells regardless of whether the CD24$^+$ cells were derived from *LKB1*-deficient or -competent cell lines. This observation is consistent with evidence that CD24 expression is associated with advanced disease and increased metastasis in glioma and epithelial cancers (Baumann et al., 2005; Kristiansen et al., 2003; Lee et al., 2011; Senner et al., 1999). Therefore, our data are most consistent with the model that the principal effect of LKB1 inactivation with regard to metastasis is to markedly increase the frequency of this prometastatic subpopulation.

Importantly, whereas CD24 expression appears to play a direct role in facilitating tumor metastasis, it has also been observed to mark heterogeneous subpopulations (e.g., "tumor stem cells") of a variety of cancers (Al-Hajj et al., 2003; Gao et al., 2010; Lee et al., 2011). Therefore, our data are consistent with the model that CD24 expression directly facilitates melanoma metastasis but also that CD24 expression merely serves as a marker of a tumor subpopulation with increased metastatic properties. With regard to the latter possibility, LKB1 loss led to an increase in a tumor subfraction with increased colony-forming activity and expanded tumor differentiation potential in vivo (as reflected by the variable degree of tumor pigmentation), which are properties of "tumor stem cells." Although the concept of a tumor stem cell in melanoma is controversial, our results are compatible with the possibility that the increased tumor heterogeneity noted in the setting of LKB1 inactivation reflects an augmented tumor stem cell fraction.

In summary this work shows a prominent role for LKB1 in melanocyte biology and the suppression of melanoma metastasis. We observed that a principal effect of LKB1 loss on metastasis required expansion of a CD24$^+$ prometastatic tumor subfraction that exhibited some properties of a tumor stem cell. Expansion of this compartment required the activity of YES kinase. These data suggest that a determination of LKB1 mutational status in patients with advanced melanoma will contribute to prognosis prediction and identify promising therapeutic targets (YES and CD24) in melanoma with compromised LKB1 function.

EXPERIMENTAL PROCEDURES

Mouse Colony

Mice were housed and treated in accordance with protocols approved by the institutional care and use committee for animal research at the University of

North Carolina. Animals were generated and genotyped as previously described: T (Bosenberg et al., 2006); *K-Ras*$^{L/L}$ (or "K"; Johnson et al., 2001); *Lkb1*$^{L/L}$ (Bardeesy et al., 2002); *p53*$^{L/L}$ (Jonkers et al., 2001); and *TRIA* (Chin et al., 1997). All cohorts reported in Figures 1 and 2 (*TK*, *TLkb1*$^{L/L}$, *Tp53*$^{L/L}$, *Tp53*$^{L/L}$*; Lkb1*$^{L/L}$, *TKLkb1*$^{L/L}$, *TKp53*$^{L/L}$, *TKp53*$^{L/L}$*; Lkb1*$^{L/L}$) were newly generated and contemporaneously housed for this work. Data from the *TKp16*$^{L/L}$ and *TKp53*$^{L/L}$*; p16*$^{L/L}$ cohorts shown in Table S1 are a historical comparison from a prior study by Monahan et al. (2010). All cohorts were N1 in C57BL/6 and, where possible, compared to littermate controls. To induce CRE recombinase in vivo, pups were treated with 4-OHT as described by Dankort et al. (2009) and Monahan et al. (2010). In tumor survival cohorts, mice were monitored for tumors three times per week and sacrificed for tumor size (>1.3 cm) or morbidity (ulceration, weight loss). All sacrificed animals were analyzed for metastasis by necropsy. H&E of tumors after formalin fixation and paraffin embedding was performed, with analysis showing spindle-shaped melanoma with variable pigmentation (Figure S2). Melanocytic lineage was further confirmed by staining for melanocytic markers (Figure S2). Kaplan-Meier analysis of melanoma-free survival was determined using GraphPad Prism software.

Cell Lines and Cell Culture

Primary melanocyte cultures and murine tumor cell lines were generated as described by Bennett et al. (1989) and Sharpless et al. (2002). Human melanoma cells studied were immortalized cell lines and were IRB exempt. To induce CRE recombinase in vitro, primary melanocyte cultures were treated with 4-OHT at 20 days postisolation for 48 hr. Melanoma cells were maintained in DMEM containing 10% FBS. Dasatinib was from LC Laboratories (D-3307). Immunoprecipitation, immunoblotting, immunofluorescence, SFK 8-Plex, and quantitative RT-PCR assays are described in the Supplemental Experimental Procedures.

Cell Migration and Invasion Assays

The in vitro scratch (wound healing) assay was performed as described previously by Carretero et al. (2010). Matrigel invasion was determined using invasion chambers obtained from BD Biosciences, with assays performed according to the manufacturer's instructions. See Supplemental Experimental Procedures.

Flow Cytometric Analysis and FACS

Cells were labeled with indicated antibodies, washed, resuspended, and strained (40 μm). Data were recorded with a CyAn ADP flow cytometer (Dako Cytomation) and analyzed by FlowJo software. Antibodies used were Anti-Human APC-CD24 (eBioscience), Anti-Mouse FITC-CD24 (eBioscience), Anti-Mouse PE-Cy5-CD24 (eBioscience), and Anti-Human FITC-CD44 (BD Biosciences). For CFC assay, single cells were FACS-sorted into individual wells of 96-well plates. CFCs were counted after culturing the cells for 3 weeks.

Tail Vein Metastasis Assay

Five to 6-week-old female *nu/nu* mice were maintained under pathogen-free conditions. Cells were transduced with a luciferase reporter gene prior to injection. $CD24^+$ cells and $CD24^-$ cells were separated by FACS. A total of 0.5×10^5 cells were injected into *nu/nu* mice via tail vein (n = 6 per experimental group). Three weeks after the injection, mice were subjected to luciferase imaging and necropsy to determine lung metastasis. Luminescence was quantified using Living Image software (Caliper Life Sciences).

shRNA, siRNA, and Lentiviruses

shRNA constructs used for knocking down *LKB1* expression in A2058 cells were described previously by Carretero et al. (2010). shRNA targeting Yes was from Thermo Scientific. For suppression of Src, Fyn, and Yes expression, cells were transfected with the appropriate antisense oligonucleotides using Lipofectamine RNAiMAX (Invitrogen). Src siRNA (sc-29228), Fyn siRNA (sc-29321), Yes siRNA (sc-29860), and scrambled control siRNA (sc-37007) were from Santa Cruz Biotechnology.

ACCESSION NUMBERS

Microarray data have been deposited at GEO with the accession number GSE34866.

SUPPLEMENTAL INFORMATION

Supplemental Information includes eight figures, three tables, two movies, and Supplemental Experimental Procedures and can be found with this article online at doi:10.1016/j.ccr.2012.03.048.

ACKNOWLEDGMENTS

The authors wish to thank the UNC Lineberger Comprehensive Cancer Center Mouse Phase 1 Unit for assistance with animal handling and tumor assessment. We thank the UNC gastrointestinal histology and flow cytometry core facilities for assistance. This work was supported by the UNC University Cancer Research Fund, and grants from the NCI.

Received: July 29, 2011
Revised: January 20, 2012
Accepted: March 28, 2012
Published: June 11, 2012

REFERENCES

Ackermann, J., Frutschi, M., Kaloulis, K., McKee, T., Trumpp, A., and Beermann, F. (2005). Metastasizing melanoma formation caused by expression of activated N-RasQ61K on an INK4a-deficient background. Cancer Res. *65*, 4005–4011.

Alessi, D.R., Sakamoto, K., and Bayascas, J.R. (2006). LKB1-dependent signaling pathways. Annu. Rev. Biochem. *75*, 137–163.

Al-Hajj, M., Wicha, M.S., Benito-Hernandez, A., Morrison, S.J., and Clarke, M.F. (2003). Prospective identification of tumorigenic breast cancer cells. Proc. Natl. Acad. Sci. USA *100*, 3983–3988.

Bardeesy, N., Sinha, M., Hezel, A.F., Signoretti, S., Hathaway, N.A., Sharpless, N.E., Loda, M., Carrasco, D.R., and DePinho, R.A. (2002). Loss of the Lkb1 tumour suppressor provokes intestinal polyposis but resistance to transformation. Nature *419*, 162–167.

Baumann, P., Cremers, N., Kroese, F., Orend, G., Chiquet-Ehrismann, R., Uede, T., Yagita, H., and Sleeman, J.P. (2005). CD24 expression causes the acquisition of multiple cellular properties associated with tumor growth and metastasis. Cancer Res. *65*, 10783–10793.

Bennett, D.C., Cooper, P.J., Dexter, T.J., Devlin, L.M., Heasman, J., and Nester, B. (1989). Cloned mouse melanocyte lines carrying the germline mutations albino and brown: complementation in culture. Development *105*, 379–385.

Bosenberg, M., Muthusamy, V., Curley, D.P., Wang, Z., Hobbs, C., Nelson, B., Nogueira, C., Horner, J.W., 2nd, Depinho, R., and Chin, L. (2006). Characterization of melanocyte-specific inducible Cre recombinase transgenic mice. Genesis *44*, 262–267.

Carretero, J., Shimamura, T., Rikova, K., Jackson, A.L., Wilkerson, M.D., Borgman, C.L., Buttarazzi, M.S., Sanofsky, B.A., McNamara, K.L., Brandstetter, K.A., et al. (2010). Integrative genomic and proteomic analyses identify targets for Lkb1-deficient metastatic lung tumors. Cancer Cell *17*, 547–559.

Cheng, H., Liu, P., Wang, Z.C., Zou, L., Santiago, S., Garbitt, V., Gjoerup, O.V., Iglehart, J.D., Miron, A., Richardson, A.L., et al. (2009). SIK1 couples LKB1 to p53-dependent anoikis and suppresses metastasis. Sci. Signal. *2*, ra35.

Chin, L., Pomerantz, J., Polsky, D., Jacobson, M., Cohen, C., Cordon-Cardo, C., Horner, J.W., 2nd, and DePinho, R.A. (1997). Cooperative effects of INK4a and ras in melanoma susceptibility in vivo. Genes Dev. *11*, 2822–2834.

Damsky, W.E., Curley, D.P., Santhanakrishnan, M., Rosenbaum, L.E., Platt, J.T., Gould Rothberg, B.E., Taketo, M.M., Dankort, D., Rimm, D.L., McMahon, M., and Bosenberg, M. (2011). beta-Catenin signaling controls metastasis in Braf-activated Pten-deficient melanomas. Cancer Cell *20*, 741–754.

Dankort, D., Curley, D.P., Cartlidge, R.A., Nelson, B., Karnezis, A.N., Damsky, W.E., Jr., You, M.J., DePinho, R.A., McMahon, M., and Bosenberg, M. (2009). Braf(V600E) cooperates with Pten loss to induce metastatic melanoma. Nat. Genet. *41*, 544–552.

Deguchi, Y., Kimura, S., Ashihara, E., Niwa, T., Hodohara, K., Fujiyama, Y., and Maekawa, T. (2008). Comparison of imatinib, dasatinib, nilotinib and INNO-406 in imatinib-resistant cell lines. Leuk. Res. *32*, 980–983.

Esteve-Puig, R., Canals, F., Colome, N., Merlino, G., and Recio, J.A. (2009). Uncoupling of the LKB1-AMPKalpha energy sensor pathway by growth factors and oncogenic BRAF. PLoS One *4*, e4771.

Forbes, S.A., Bindal, N., Bamford, S., Cole, C., Kok, C.Y., Beare, D., Jia, M., Shepherd, R., Leung, K., Menzies, A., et al. (2011). COSMIC: mining complete cancer genomes in the Catalogue of Somatic Mutations in Cancer. Nucleic Acids Res. *39*, D945–D950.

Gao, M.Q., Choi, Y.P., Kang, S., Youn, J.H., and Cho, N.H. (2010). CD24+ cells from hierarchically organized ovarian cancer are enriched in cancer stem cells. Oncogene *29*, 2672–2680.

Giardiello, F.M., Brensinger, J.D., Tersmette, A.C., Goodman, S.N., Petersen, G.M., Booker, S.V., Cruz-Correa, M., and Offerhaus, J.A. (2000). Very high risk of cancer in familial Peutz-Jeghers syndrome. Gastroenterology *119*, 1447–1453.

Guervos, M.A., Marcos, C.A., Hermsen, M., Nuno, A.S., Suarez, C., and Llorente, J.L. (2007). Deletions of N33, STK11 and TP53 are involved in the development of lymph node metastasis in larynx and pharynx carcinomas. Cell. Oncol. *29*, 327–334.

Guldberg, P., thor Straten, P., Ahrenkiel, V., Seremet, T., Kirkin, A.F., and Zeuthen, J. (1999). Somatic mutation of the Peutz-Jeghers syndrome gene, LKB1/STK11, in malignant melanoma. Oncogene *18*, 1777–1780.

Guy, C.T., Cardiff, R.D., and Muller, W.J. (1992). Induction of mammary tumors by expression of polyomavirus middle T oncogene: a transgenic mouse model for metastatic disease. Mol. Cell. Biol. *12*, 954–961.

Haigis, K.M., Kendall, K.R., Wang, Y., Cheung, A., Haigis, M.C., Glickman, J.N., Niwa-Kawakita, M., Sweet-Cordero, A., Sebolt-Leopold, J., Shannon, K.M., et al. (2008). Differential effects of oncogenic K-Ras and N-Ras on proliferation, differentiation and tumor progression in the colon. Nat. Genet. *40*, 600–608.

Hamamura, K., Tsuji, M., Hotta, H., Ohkawa, Y., Takahashi, M., Shibuya, H., Nakashima, H., Yamauchi, Y., Hashimoto, N., Hattori, H., et al. (2011). Functional Activation of Src Family Kinase Yes Protein Is Essential for the Enhanced Malignant Properties of Human Melanoma Cells Expressing Ganglioside GD3. J. Biol. Chem. *286*, 18526–18537.

Homsi, J., Cubitt, C.L., Zhang, S., Munster, P.N., Yu, H., Sullivan, D.M., Jove, R., Messina, J.L., and Daud, A.I. (2009). Src activation in melanoma and Src inhibitors as therapeutic agents in melanoma. Melanoma Res. *19*, 167–175.

Jeghers, H., Mc, K.V., and Katz, K.H. (1949). Generalized intestinal polyposis and melanin spots of the oral mucosa, lips and digits; a syndrome of diagnostic significance. N. Engl. J. Med. *241*, 1031–1036.

Ji, H., Ramsey, M.R., Hayes, D.N., Fan, C., McNamara, K., Kozlowski, P., Torrice, C., Wu, M.C., Shimamura, T., Perera, S.A., et al. (2007). LKB1 modulates lung cancer differentiation and metastasis. Nature *448*, 807–810.

Johnson, L., Mercer, K., Greenbaum, D., Bronson, R.T., Crowley, D., Tuveson, D.A., and Jacks, T. (2001). Somatic activation of the K-ras oncogene causes early onset lung cancer in mice. Nature *410*, 1111–1116.

Jones, R.G., Plas, D.R., Kubek, S., Buzzai, M., Mu, J., Xu, Y., Birnbaum, M.J., and Thompson, C.B. (2005). AMP-activated protein kinase induces a p53-dependent metabolic checkpoint. Mol. Cell *18*, 283–293.

Jonkers, J., Meuwissen, R., van der Gulden, H., Peterse, H., van der Valk, M., and Berns, A. (2001). Synergistic tumor suppressor activity of BRCA2 and p53 in a conditional mouse model for breast cancer. Nat. Genet. *29*, 418–425.

Karuman, P., Gozani, O., Odze, R.D., Zhou, X.C., Zhu, H., Shaw, R., Brien, T.P., Bozzuto, C.D., Ooi, D., Cantley, L.C., and Yuan, J. (2001). The Peutz-Jegher gene product LKB1 is a mediator of p53-dependent cell death. Mol. Cell *7*, 1307–1319.

Kluger, H.M., Dudek, A.Z., McCann, C., Ritacco, J., Southard, N., Jilaveanu, L.B., Molinaro, A., and Sznol, M. (2011). A phase 2 trial of dasatinib in advanced melanoma. Cancer *117*, 2202–2208.

Konecny, G.E., Glas, R., Dering, J., Manivong, K., Qi, J., Finn, R.S., Yang, G.R., Hong, K.L., Ginther, C., Winterhoff, B., et al. (2009). Activity of the multikinase inhibitor dasatinib against ovarian cancer cells. Br. J. Cancer *101*, 1699–1708.

Kristiansen, G., Schluns, K., Yongwei, Y., Denkert, C., Dietel, M., and Petersen, I. (2003). CD24 is an independent prognostic marker of survival in nonsmall cell lung cancer patients. Br. J. Cancer *88*, 231–236.

Lee, T.K., Castilho, A., Cheung, V.C., Tang, K.H., Ma, S., and Ng, I.O. (2011). CD24(+) liver tumor-initiating cells drive self-renewal and tumor initiation through STAT3-mediated NANOG regulation. Cell Stem Cell *9*, 50–63.

Lim, W., Olschwang, S., Keller, J.J., Westerman, A.M., Menko, F.H., Boardman, L.A., Scott, R.J., Trimbath, J., Giardiello, F.M., Gruber, S.B., et al. (2004). Relative frequency and morphology of cancers in STK11 mutation carriers. Gastroenterology *126*, 1788–1794.

Loganzo, F., Jr., Dosik, J.S., Zhao, Y., Vidal, M.J., Nanus, D.M., Sudol, M., and Albino, A.P. (1993). Elevated expression of protein tyrosine kinase c-Yes, but not c-Src, in human malignant melanoma. Oncogene *8*, 2637–2644.

Marchetti, D., Parikh, N., Sudol, M., and Gallick, G.E. (1998). Stimulation of the protein tyrosine kinase c-Yes but not c-Src by neurotrophins in human brain-metastatic melanoma cells. Oncogene *16*, 3253–3260.

Matsumoto, S., Iwakawa, R., Takahashi, K., Kohno, T., Nakanishi, Y., Matsuno, Y., Suzuki, K., Nakamoto, M., Shimizu, E., Minna, J.D., and Yokota, J. (2007). Prevalence and specificity of LKB1 genetic alterations in lung cancers. Oncogene *26*, 5911–5918.

Monahan, K.B., Rozenberg, G.I., Krishnamurthy, J., Johnson, S.M., Liu, W., Bradford, M.K., Horner, J., Depinho, R.A., and Sharpless, N.E. (2010). Somatic p16(INK4a) loss accelerates melanomagenesis. Oncogene *29*, 5809–5817.

Putnam, A.J., Schulz, V.V., Freiter, E.M., Bill, H.M., and Miranti, C.K. (2009). Src, PKCalpha, and PKCdelta are required for alphavbeta3 integrin-mediated metastatic melanoma invasion. Cell Commun. Signal. *7*, 10.

Rowan, A., Bataille, V., MacKie, R., Healy, E., Bicknell, D., Bodmer, W., and Tomlinson, I. (1999). Somatic mutations in the Peutz-Jeghers (LKB1/STKII) gene in sporadic malignant melanomas. J. Invest. Dermatol. *112*, 509–511.

Sanchez-Cespedes, M. (2007). A role for LKB1 gene in human cancer beyond the Peutz-Jeghers syndrome. Oncogene *26*, 7825–7832.

Scott, K.L., Nogueira, C., Heffernan, T.P., van Doorn, R., Dhakal, S., Hanna, J.A., Min, C., Jaskelioff, M., Xiao, Y., Wu, C.J., et al. (2011). Proinvasion metastasis drivers in early-stage melanoma are oncogenes. Cancer Cell *20*, 92–103.

Senner, V., Sturm, A., Baur, I., Schrell, U.H., Distel, L., and Paulus, W. (1999). CD24 promotes invasion of glioma cells in vivo. J. Neuropathol. Exp. Neurol. *58*, 795–802.

Shah, U., Sharpless, N.E., and Hayes, D.N. (2008). LKB1 and lung cancer: more than the usual suspects. Cancer Res. *68*, 3562–3565.

Sharpless, N.E., Alson, S., Chan, S., Silver, D.P., Castrillon, D.H., and DePinho, R.A. (2002). p16(INK4a) and p53 deficiency cooperate in tumorigenesis. Cancer Res. *62*, 2761–2765.

Shields, J.M., Thomas, N.E., Cregger, M., Berger, A.J., Leslie, M., Torrice, C., Hao, H., Penland, S., Arbiser, J., Scott, G., et al. (2007). Lack of extracellular signal-regulated kinase mitogen-activated protein kinase signaling shows a new type of melanoma. Cancer Res. *67*, 1502–1512.

Stuelten, C.H., Mertins, S.D., Busch, J.I., Gowens, M., Scudiero, D.A., Burkett, M.W., Hite, K.M., Alley, M., Hollingshead, M., Shoemaker, R.H., and Niederhuber, J.E. (2010). Complex display of putative tumor stem cell markers in the NCI60 tumor cell line panel. Stem Cells *28*, 649–660.

Sviderskaya, E.V., Hill, S.P., Evans-Whipp, T.J., Chin, L., Orlow, S.J., Easty, D.J., Cheong, S.C., Beach, D., DePinho, R.A., and Bennett, D.C. (2002). p16(Ink4a) in melanocyte senescence and differentiation. J. Natl. Cancer Inst. *94*, 446–454.

Taliaferro-Smith, L., Nagalingam, A., Zhong, D., Zhou, W., Saxena, N.K., and Sharma, D. (2009). LKB1 is required for adiponectin-mediated modulation of AMPK-S6K axis and inhibition of migration and invasion of breast cancer cells. Oncogene *28*, 2621–2633.

Weir, B.A., Woo, M.S., Getz, G., Perner, S., Ding, L., Beroukhim, R., Lin, W.M., Province, M.A., Kraja, A., Johnson, L.A., et al. (2007). Characterizing the cancer genome in lung adenocarcinoma. Nature *450*, 893–898.

Wingo, S.N., Gallardo, T.D., Akbay, E.A., Liang, M.C., Contreras, C.M., Boren, T., Shimamura, T., Miller, D.S., Sharpless, N.E., Bardeesy, N., et al. (2009). Somatic LKB1 mutations promote cervical cancer progression. PLoS One *4*, e5137.

Zhang, Z., Liu, S., Shi, R., and Zhao, G. (2011). miR-27 promotes human gastric cancer cell metastasis by inducing epithelial-to-mesenchymal transition. Cancer Genet. *204*, 486–491.

Zheng, B., Jeong, J.H., Asara, J.M., Yuan, Y.Y., Granter, S.R., Chin, L., and Cantley, L.C. (2009). Oncogenic B-RAF negatively regulates the tumor suppressor LKB1 to promote melanoma cell proliferation. Mol. Cell *33*, 237–247.

Cancer Cell
Article

Telomere-Driven Tetraploidization Occurs in Human Cells Undergoing Crisis and Promotes Transformation of Mouse Cells

Teresa Davoli[1] and Titia de Lange[1,*]
[1]Laboratory for Genetics and Cell Biology, The Rockefeller University, 1230 York Avenue, New York, NY 10065, USA
*Correspondence: delange@mail.rockefeller.edu
DOI 10.1016/j.ccr.2012.03.044

SUMMARY

Human cancers with a subtetraploid karyotype are thought to originate from tetraploid precursors, but the cause of tetraploidization is unknown. We previously documented endoreduplication in mouse cells with persistent telomere dysfunction or genome-wide DNA damage. We now report that endoreduplication and mitotic failure occur during telomere crisis in human fibroblasts and mammary epithelial cells and document the role of p53 and Rb in repressing tetraploidization. Using an inducible system to generate transient telomere damage, we show that telomere-driven tetraploidization enhances the tumorigenic transformation of mouse cells. Similar to human solid cancers, the resulting tumors evolved subtetraploid karyotypes. These data establish that telomere-driven tetraploidization is induced by critically short telomeres and has the potential to promote tumorigenesis in early cancerous lesions.

INTRODUCTION

Aneuploidy is a general feature of human solid tumors. An important source of aneuploidy is an elevated rate of chromosome mis-segregation (Lengauer et al., 1997). However, a substantial fraction of tumors have very high chromosome numbers, ranging from hypertriploid to subtetraploid, making it unlikely that nondisjunction of individual chromosomes is the sole mechanism responsible for their abnormal karyotypes (reviewed in Ganem et al., 2007; Storchova and Kuffer, 2008; Davoli and de Lange, 2011). More likely, these tumors arise from an initial tetraploidization event that is followed by frequent chromosome loss (Shackney et al., 1989). Indeed, tetraploid nuclei and supernumerary centrosomes have been noted in the early stages of some solid tumors (Reid et al., 1996; Kirkland et al., 1967). Importantly, tetraploidization after chemically induced cytokinesis failure has been shown to promote tumorigenesis in p53-deficient mouse mammary epithelial cells (Fujiwara et al., 2005).

Potential sources of tetraploidization in cancer are mutations in the tumor suppressor Adenomatous Polyposis Coli or deregulation of mitotic factors such as Mad2, Emi1, LATS1, and AuroraA (Davoli and de Lange, 2011). An additional mechanism for the duplication of cancer genomes was suggested by the frequent tetraploidization in mouse cells experiencing telomere dysfunction (de Lange, 2005; Hockemeyer et al., 2006; Davoli et al., 2010; Kibe et al., 2010). In these experiments, telomere dysfunction was induced by removing the shelterin proteins POT1a and POT1b from the telomeres of p53-deficient mouse embryo fibrobloasts (MEFs). The resulting ataxia telangiectasia- and Rad3-related (ATR) signaling forestalls the activation of Cdk1/CyclinB, blocking entry into mitosis. However, after a prolonged period in G2, the replication inhibitor geminin is degraded and the licensing factor Cdt1 is re-expressed allowing the cells to re-enter S phase, resulting in endoreduplication. Endoreduplication and tetraploidy are also induced by continuous treatment of p53-deficient MEFs with genotoxic drugs, indicating that the endocycles are due to the persistence of the DNA damage signal rather than its origin.

We have proposed that the telomere-dependent pathway for tetraploidization is relevant to human cancer because telomere attrition is widespread during tumorigenesis (de Lange et al., 1990; Hastie et al., 1990; Meeker et al., 2002, 2004; van Heek et al., 2002; Meeker and Argani, 2004). Due to the absence of telomerase (Kim et al., 1994), telomeres shorten with cell

Significance

Tetraploidization can occur early in tumorigenesis and is thought to be responsible for the emergence of aneuploid cancer karyotypes with high chromosome numbers. Here, we show that tetraploidy is induced when human p53/Rb-deficient fibroblasts and mammary epithelial cells enter telomere crisis. Mouse cells that have become tetraploid after telomere dysfunction have an increased transformation potential. These findings can explain how tetraploidization occurs in human cancer and point to the importance of telomere dysfunction in shaping cancer genomes.

divisions in most human somatic cells, including cells undergoing the first stages of tumorigenic transformation. After extensive proliferation, dysfunctional short telomeres are recognized as sites of DNA damage by the ATM and ATR kinases and induce p53/Rb-mediated senescence or apoptosis (d'Adda di Fagagna et al., 2003; Herbig et al., 2004). In the absence of p53 and Rb function, cells continue to proliferate despite the presence of dysfunctional telomeres (Wright and Shay, 1992; Shay and Wright, 2005). Eventually, the cells enter telomere crisis, a stage in which the rampant genome instability associated with lack of telomere function curbs cell proliferation and survival (Wright and Shay, 1992; Shay et al., 1993; Shay and Wright, 2005; Counter et al., 1992).

There is mounting evidence that prior to the activation of telomerase, developing cancers can experience a period of telomere crisis (Meeker et al., 2004; de Lange, 2005). Molecular analysis of chronic lymphocytic leukemia has revealed evidence for telomere fusions, a product of telomere crisis (Lin et al., 2010). Furthermore, telomere crisis was inferred to occur in the ductal carcinoma in situ (DCIS) stage of breast cancer based on the presence of short telomeres and an abrupt rise in genome instability before telomerase is activated (Chin et al., 2004). Modeling in the mouse has provided evidence that the genome instability arising in telomere crisis can promote tumorigenesis in a permissive setting (Artandi and DePinho, 2010; Artandi et al., 2000).

Here, we investigate the frequency and mechanism of tetraploidization in human fibroblasts and epithelial cells undergoing telomere crisis. FUCCI imaging for geminin and Cdt1 revealed that tetraploidization was due to both mitotic failure and endoreduplication. Moreover, using mouse cells we show that tetraploidization-induced by telomere dysfunction can promote tumorigenesis, as is the case for tetraploidization induced by cytokinesis inhibitors (Fujiwara et al., 2005). The resulting tumors have a chromosome complement reminiscent of the subtetraploid karyotypes of human solid tumors. These data are consistent with a role for telomere dysfunction in the induction of tetraploidy in the early stages of human tumor development.

RESULTS

Tetraploidization in Telomere Crisis

To generate cells in telomere crisis, telomerase-negative human IMR90 and BJ fibroblasts were rendered p53- and Rb-deficient through expression of SV40 large T antigen (SV40-LT). As expected, the telomeres shortened progressively in these cultures (Figure 1A), resulting in telomere crisis at population doubling (PD) 80–90 for IMR90-SV40LT and at PD 105–110 for BJ-SV40LT. Telomere crisis was evident from the plateau in the growth curve (Figure 1B), the increased number of 53BP1 DNA damage foci (Figure 1C), and the phosphorylation of Chk1 and Chk2 (Figure 1D). Fluorescence-activated cell sorting (FACS) analysis showed that the fraction of tetraploid cells (estimated based on the fraction of cells with a DNA content >4N) progressively increased from 2%–3% at early PDs to 30%–35% at the time of telomere crisis (Figure 1E). Similarly, BJ fibroblasts transformed by HPV E6 and E7 displayed hallmarks of telomere crisis and accompanying tetraploidization at PD 90–100 (Figures S1A–S1D available online).

Telomere crisis was also induced in two telomerase-negative human mammary epithelial cell strains (hMECs), 184B-GSE22 and 48RS-GSE22, which lack a functional Rb pathway and express the p53 inhibitory peptide GSE22 (Romanov et al., 2001; Garbe et al., 2007). When these cells divide beyond senescence, they continue to erode their telomeres and enter a telomere crisis that is accompanied by genome instability (Romanov et al., 2001). The p53-proficient 184B and 48RS precursors were used as controls. The 184B-GSE22 and 48RS-GSE22 cultures entered telomere crisis at passage 18-20 and passage 28-32, respectively, showing shortened telomeres, an increase in the frequency of 53BP1 foci, and phosphorylation of Chk1 and Chk2 (Figures 2A and 2B; Figures S2A and S2B). FACS analysis showed an increase in the fraction of cells with >4N DNA content upon entry into telomere crisis in the two p53/Rb-negative hMEC cultures, whereas the parallel p53-proficient counterparts showed a G1/S arrest without tetraploidization (Figures 2C and 2D). Tetraploidization in telomere crisis was confirmed by analyzing the chromosome numbers of metaphase spreads (Figure S2C). The GSE-22 expressing hMECs, but not their p53-proficient counterparts, showed evidence for tetraploidization when precrisis cultures were treated with zeocin for 96 hr (Figures 2E and 2F).

Thus, in epithelial cells as well as in fibroblasts, telomere crisis and prolonged genome-wide DNA damage is accompanied by polyploidization resulting in tetraploid cells. While the formation of tetraploid cells is readily demonstrable, we note that the 8N peak in the FACS profiles of cells in crisis could represent octoploid cells in G1 as well as tetraploid cells in G2. As two successive aberrant cell cycles are required to generate octoploid cells, octoploidization might be too infrequent to result in a clear 16N peak in the FACS profiles.

Endoreduplication and Mitotic Failure in Telomere Crisis

The increased ploidy of cells in telomere crisis could be due to either endoreduplication or a failure in the late stages of mitosis, since dicentrics formed by telomere fusions (Figure S2D) hinder the completion of cytokinesis. To distinguish between these events, we performed live-cell imaging using the FUCCI system (Sakaue-Sawano et al., 2008), which previously demonstrated endoreduplication in POT1a/b DKO cells (Davoli et al., 2010). FUCCI is based on the cell cycle dependent expression of fluorescently tagged fragments of Cdt1 and geminin. The licensing factor Cdt1, which mediates the formation of prereplication complexes, is expressed in G1 and degraded upon entry into S phase in a process that is coupled to DNA replication (Arias and Walter, 2005; Remus and Diffley, 2009). Cdt1 is further inhibited by geminin, which is expressed in S/G2. In a normal mitotic cycle, geminin is degraded during mitosis, thereby re-establishing a state that is permissive to origin licensing in the daughter cells. However, in cells undergoing telomere-driven endoreduplication, geminin degradation takes place in the absence of mitosis, allowing cells to enter a G1-like state in which Cdt1 can mediate a second round of DNA replication. Thus, mitosis-independent geminin degradation is an indicator for endoreduplication (Figures 3A and 3B; Movie S1). In addition, FUCCI imaging can be used to detect mitotic failure based on the breakdown of the nuclear envelope that signifies entry into mitosis and

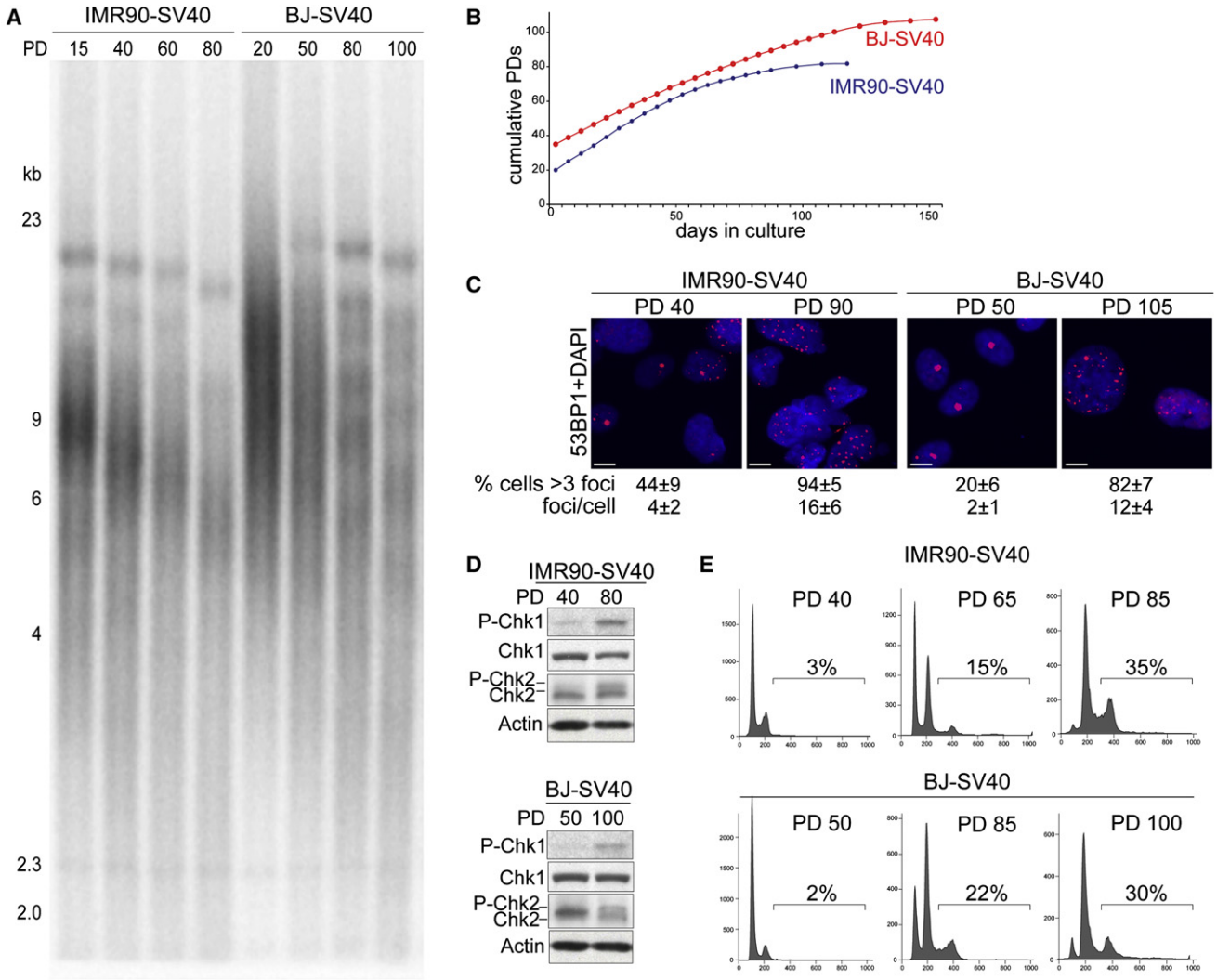

Figure 1. Tetraploidization of BJ-SV40 and IMR90-SV40 in Telomere Crisis

(A) Genomic blot for telomere restriction fragments of SV40-LT transformed IMR90 and BJ human fibroblasts at the indicated PD.

(B) Growth curve of IMR90-SV40 and BJ-SV40 from PD 20 or 38, respectively, until crisis (105–110 PDs for BJ-SV40 cells and at 80–90 for IMR90-SV40).

(C) IF analysis of 53BP1 foci in the cells at the indicated PDs. The average number of 53BP1 foci per cell and the percentage of cells with more than three foci are shown with SD. Scale bar = 5 μm.

(D) Immunoblots for P-Chk1 and P-Chk2 in the BJ-SV40 and IMR90-SV40 cells at the indicated PD.

(E) FACS profiles (PI staining) of IMR90-SV40 and BJ-SV40 cells indicated PD. The percentage of cells with >4N DNA content is indicated.

See also Figure S1.

the binucleated or multinucleated cells that result from a failure in cytokinesis (Figures 3A and 3B; Movie S1).

As expected, FUCCI imaging at early PDs (PD < 50) of BJ-SV40 and BJ-E6/E7 fibroblasts showed that in most cells geminin degradation coincided with mitosis, whereas endocycles and mitotic failure were rare (<5%) (Figures 3A–3C; Movie S1). However, at the late PDs when the cells entered telomere crisis, the fraction of BJ-SV40, BJ-E6E7 and IMR90-SV40 cells undergoing geminin degradation in the absence of mitosis increased to 12%–17% (Figures 3A–3C; Figure S3; Movies S1 and S2). After loss of geminin, most of these cells expressed Cdt1 and entered a second S phase as deduced from the degradation of Cdt1 and reappearance of geminin. During these endocycles there was no evidence of nuclear envelope breakdown. The BJ-SV40 fibroblasts in telomere crisis also displayed a prolonged S/G2 phase whereas G1 was only minimally affected (Figure 3D; Movie S1). In addition, the cells showed occasional metaphase spreads with diplochromosomes, a characteristic consequence of endoreduplication representing duplicated sister chromatids that are held together by the centromeric cohesin (Figure S2D).

In addition to endoreduplication, fibroblasts in telomere crisis showed a considerable level of mitotic failure (Figures 3A–3C; Figure S3; Movies S1 and S2). Their aberrant mitosis was presumably due to the dicentric chromosomes resulting from telomere fusions (Figure S2D). The cells attempted mitosis as

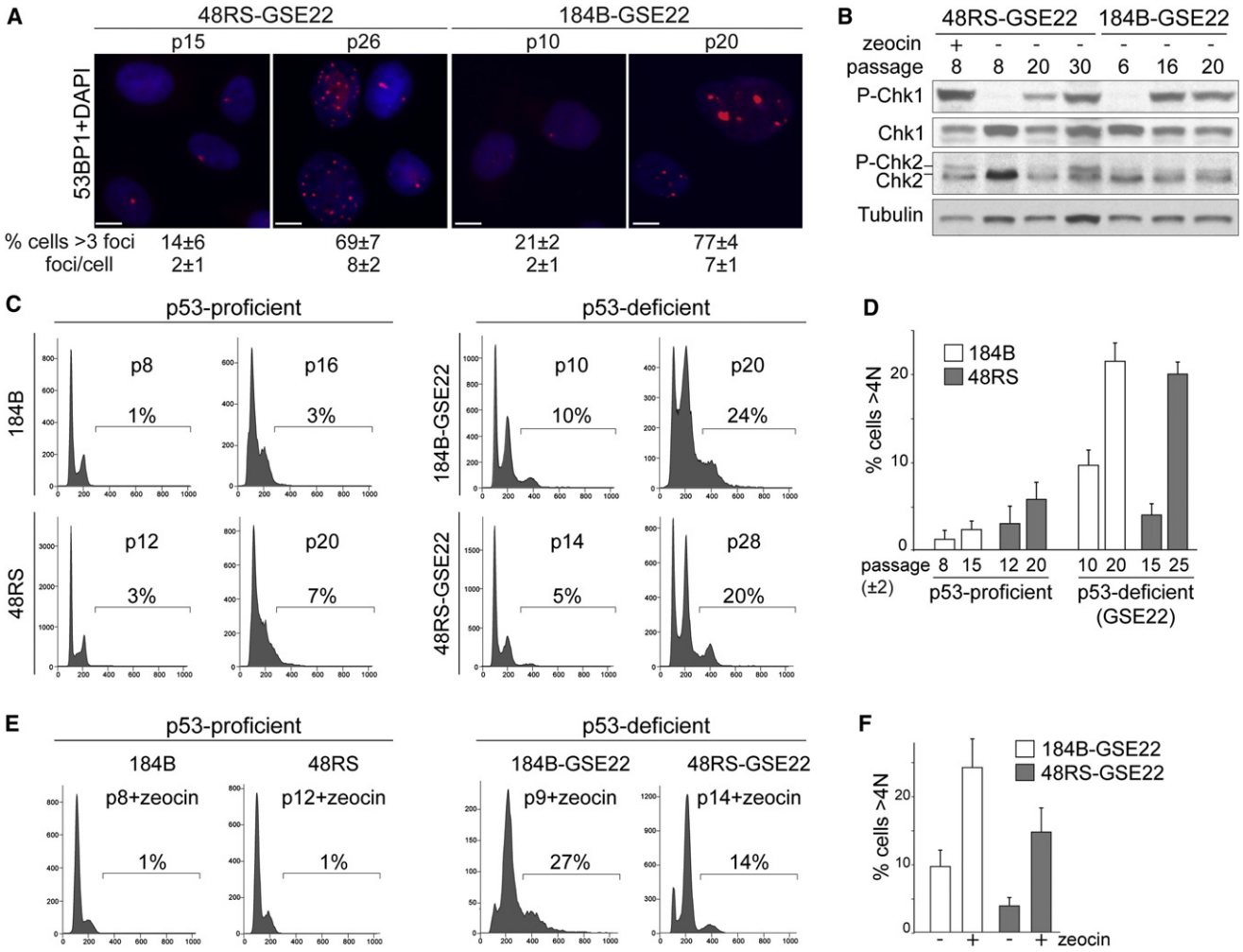

Figure 2. Tetraploidization of hMECs in Telomere Crisis

(A) IF for 53BP1 foci in 184B-GSE22 and 48RS-GSE22 hMECs at the indicated passage. The average number of 53BP1 foci per nucleus and the percentage of cells with more than three foci are given with standard deviation. Scale bar = 5 μm.

(B) Immunoblots for Chk1 and Chk2 phosphorylation in 48RS-GSE22 and 184B-GSE22 at the indicated passage and after zeocin treatment.

(C and D) FACS analysis of the indicated hMECs at the indicated passage. The percentage of cells with DNA content >4N is indicated. Quantification of averages of two or three independent experiments is shown in (D).

(E and F) FACS analysis of 184B-GSE22 and 48RS-GSE22 at the indicated (early) passage treated with zeocin. The percentage of cells with a DNA content >4N is indicated. Quantification of three independent experiments is shown in (F).

See also Figure S2.

evidenced by their rounding up and breakdown of the nuclear envelope leading to the presence of geminin throughout the cells. However, the execution of cytokinesis appeared to fail, resulting in binucleated or multinucleated cells (Movies S1 and S2).

Endoreduplication and mitotic failure was also observed in the hMEC lines 48RS-GSE22 and 184B-GSE22 in telomere crisis and upon continuous treatment with zeocin (Figures 4A and 4B; Movie S3). Mitotic failure appeared to be more frequent in the hMECs compared to the BJ and IMR90 fibroblasts. For instance, in the presence of zeocin, BJ-SV40 fibroblasts predominantly show endoreduplication, whereas hMECs also show mitotic failure events (Figures 4A and 4B; Movie S3; Davoli et al., 2010; data not shown).

Role of Rb in Blocking Telomere-Driven Tetraploidization

In human cells, activation of the Rb pathway contributes to the cell cycle arrest in response to a genome-wide or telomere-derived DNA damage signal (Jacobs and de Lange, 2004; Shay et al., 1991; Smogorzewska and de Lange, 2002; Shay and Wright, 2005). In order to determine whether the Rb pathway can block tetraploidization, we analyzed telomerase-negative BJ fibroblasts with an unaltered Rb pathway. The p53 dominant-negative allele (p53 dn, p53175H) was used to abrogate the p53 response to DNA damage (p53 dn, Baker et al., 1990; Jacobs and de Lange, 2004).

To measure their propensity for tetraploidization, the BJ-p53 dn cells were either subjected to continuous zeocin treatment

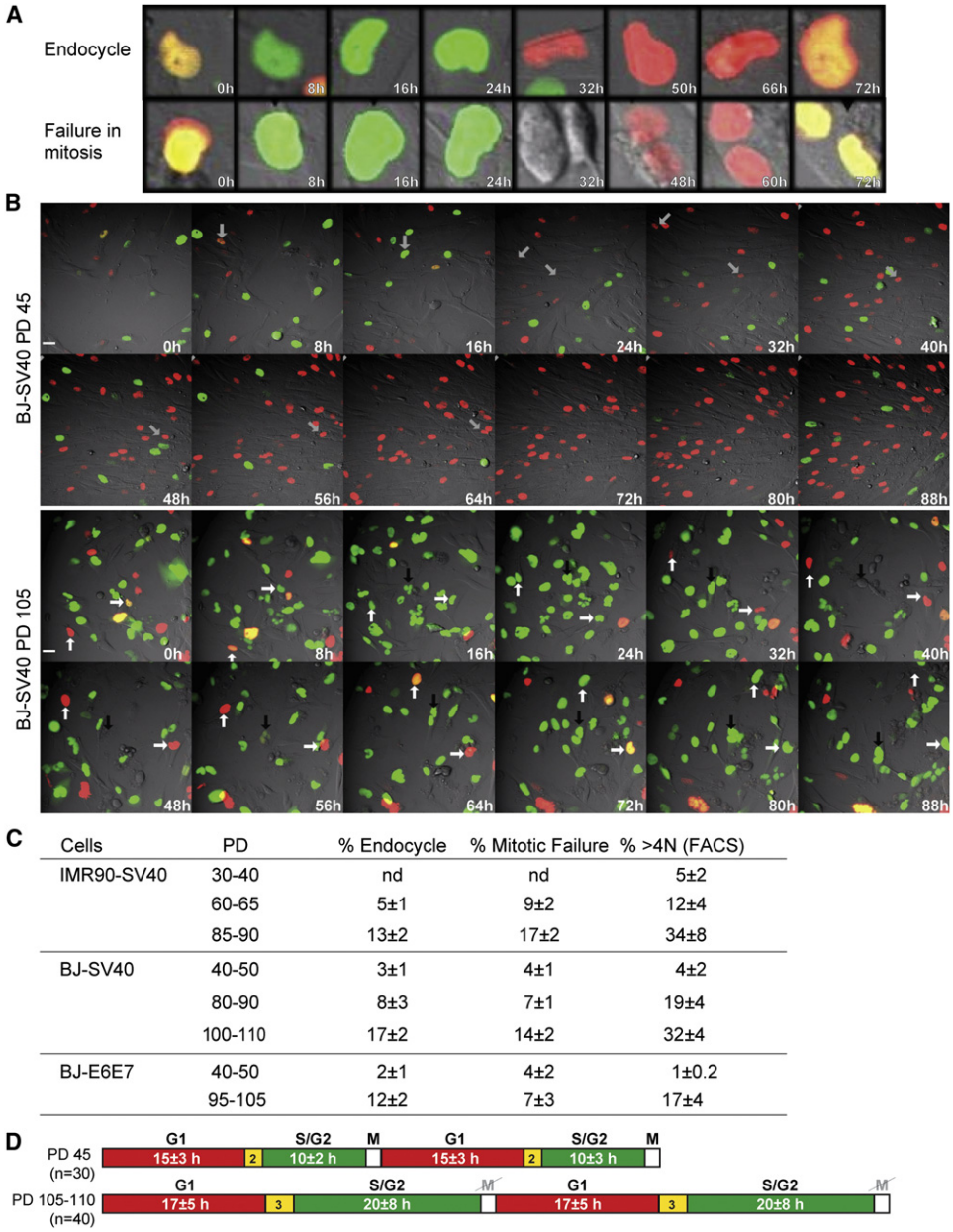

Figure 3. Endoreduplication and Mitotic Failure in Telomere Crisis

(A and B) FUCCI live-cell imaging of BJ-SV40 cells at PD45 and PD105 analyzed by time-lapse every 20 min for 96 hr. (A) Enlarged images exemplifying endoreduplication and mitotic failure. (B) Selected time points from Movie S1. Arrows with the same orientation highlight the same cell over time. In BJ-SV40 PD 45, the arrow highlights one cell progressing through a normal cell cycle. In BJ-SV40 cells PD 105, the white arrows highlight two cells undergoing endoreduplication; the black arrow highlights mitotic failure. Scale bar = 20 μm.

(C) Table summarizing the data derived from FUCCI imaging as in (B) (Movies S1 and S2) and FACS of BJ-SV40, IMR90-SV40, and BJ-E6E7. The average and SD obtained from three independent experiments is given (n is the total number of cells analyzed in each case).

(D) BJ-SV40 cells at the indicated PDs were imaged as in (A). The indicated number of cells was followed during the imaging session and the duration (hours) of the presence of geminin and Cdt1 was analyzed (average values are indicated).

See also Figure S3 and Movies S1 and S2.

or extensive replicative telomere shortening (PD 70–80; Figures 5A–5C; Figures S4A–S4C). As compared to PD 30, at PD 70–80 the BJ-p53 dn cells showed a small increase in the fraction of tetraploid cells (<1% to ~7%) (Figures 5A and 5B). The DNA damage response was active in BJ-p53 dn cells at PD 70–80, as shown by Chk1 phosphorylation and an increased number of 53BP1 foci compared to earlier PDs (Figure 5C; Figure S4C). FACS analysis indicated that BJ-p53dn showed fewer tetraploid cells and a lower fraction of cells in G2 compared to BJ-SV40 at the same PD (Figures 1E, 5A, and 5B). Furthermore, after 96 hr of zeocin treatment, only ~9% of BJ-p53dn cells had a DNA content >4N (Figures 5A and 5B), whereas 20%–25% of

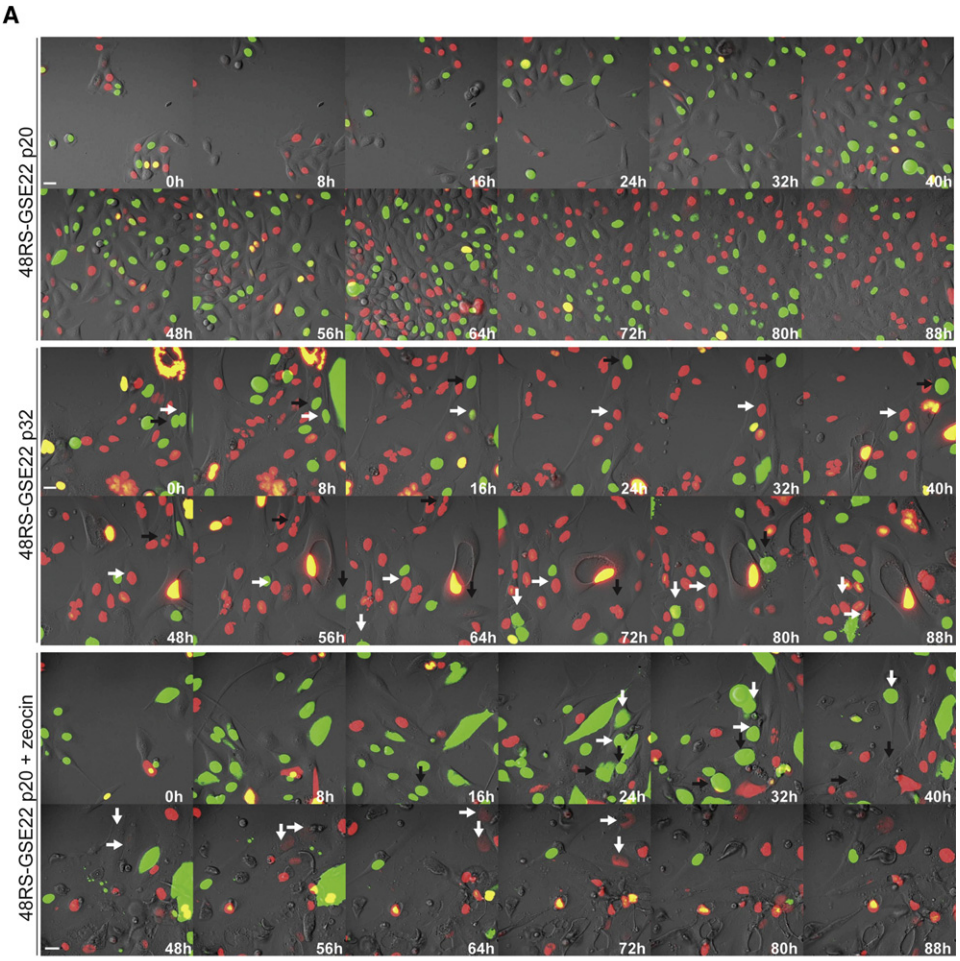

B

			FUCCI data	
Cells	passage	% >4N (FACS)	% Endocycle	% Mitotic Failure
48RS-GSE22	15-20	3±2	1±0.5	2±1
	28-35	20±3	7±1	13±2
	18-20 + zeocin	16±5	18±5	14±3
184B-GSE22	10-12	9±2	3±1	7±1
	18-20	25±5	9±2	18±5

Figure 4. Endoreduplication and Mitotic Failure in hMECs in Telomere Crisis

(A) FUCCI imaging (as in Figures 3A and 3B) of 48RS-GSE22 at the indicated passages with or without zeocin treatment. Indicated time points are from Movie S3. Arrows with the same orientation highlight the same cell over time. In 48RS-GSE22 p32 and p20+zeocin, the white arrows highlight cells showing endoreduplication and the black arrows highlight cells undergoing mitotic failure. Scale bar = 20 μm.

(B) Table summarizing data derived from FUCCI imaging (Movie S3) and FACS (as in Figure 3C).

See also Figure S2 and Movie S3.

BJ-SV40 became tetraploid after zeocin treatment (Figures 5A and 5B; Davoli et al., 2010). Similar data were obtained using IMR90 and RPE (retinal pigment epithelial) cells lacking p53 function (Figures S4D and S4E and data not shown), whereas tetraploidy was not induced in primary RPE and BJ cells, which arrested in G1/S (Figures S4D and S4E and data not shown). Consistent with a role of the Rb pathway in mediating a G1/S arrest in response to telomere and genome-wide DNA damage, the level of p16 increased at increasing PDs and after zeocin treatment (Figure 5C). These data suggest that the activation of the Rb/p16 pathway contributes to the repression of tetraploidization in cells experiencing a persistent DNA damage response.

The low level of residual tetraploidization in the Rb-proficient cells could be explained if the Rb pathway led to a block in G1 but not in G2. We therefore isolated FACS-sorted G1 and S/G2 cells, subjected them to zeocin treatment soon after plating, and then used FUCCI imaging to determine their tendency to undergo cell cycle progression and/or tetraploidization. Approximately 60% of the G1-sorted BJ-p53dn cells treated with

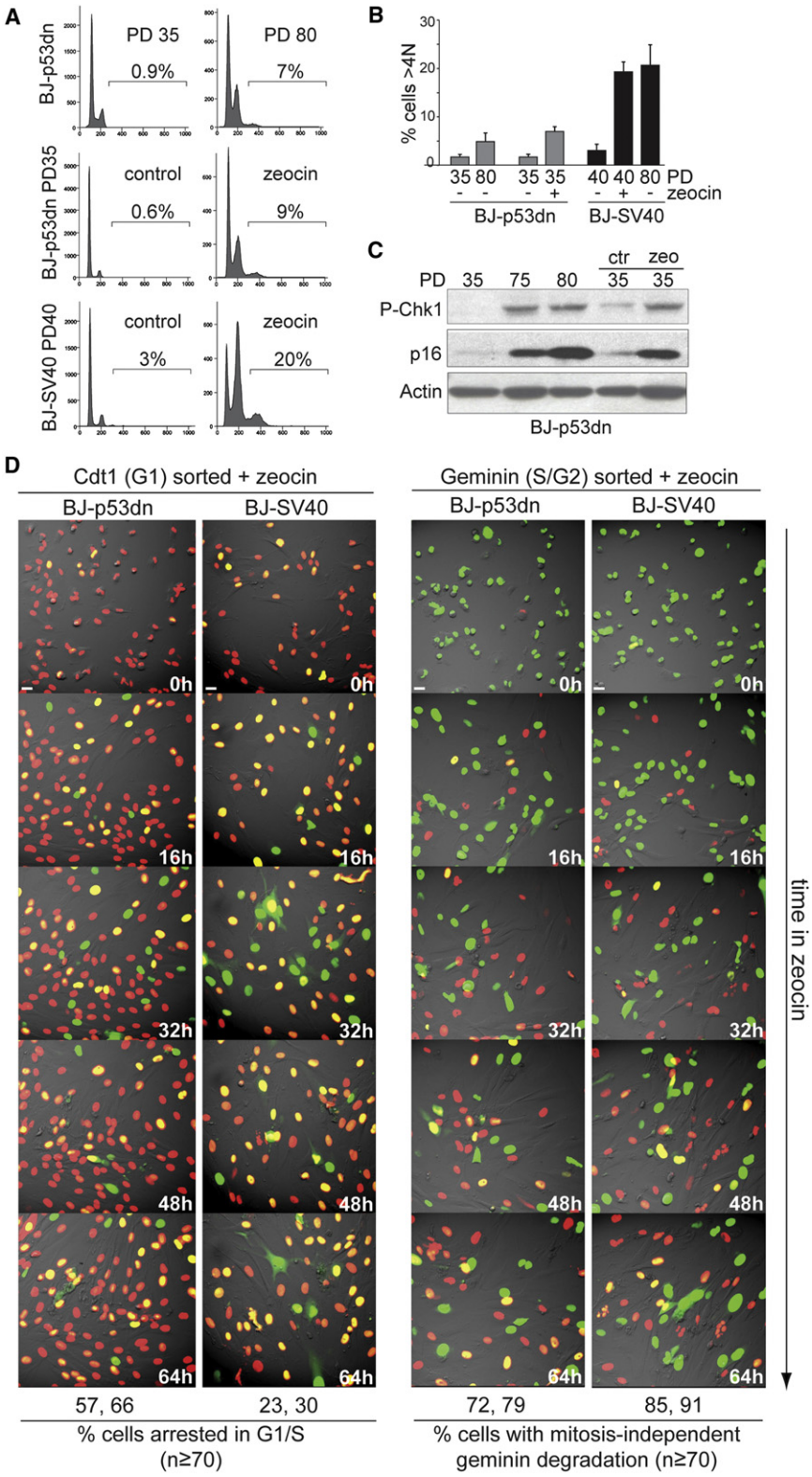

Figure 5. Rb-Mediated G1 Arrest Represses Tetraploidization

(A) FACS analysis of BJ cells expressing p53175H (p53 dn) or SV40-LT at the indicated PD with or without treatment with zeocin.

(B) Quantification of the FACS data in (A) (as in Figure 2D).

(C) Immunoblot for Chk1 phosphorylation and p16 expression in BJ-p53 dn at the indicated PD or after treatment with zeocin.

(D) FUCCI imaging of BJ-p53 dnPD 35 and BJ-SV40 PD 40 cells that were first FACS sorted for G1 (Cdt1, red) or S/G2 (geminin, green) and then imaged in the presence of zeocin (Movies S4 and S5). Selected time points are shown. Quantification of the movies is shown below the images. The number of cells that remain arrested in G1/S (red/yellow color) throughout the imaging session and the cells showing geminin degradation in the absence of mitosis were scored in the indicated cases. Average numbers obtained in two experiments are shown.

See also Figure S4 and Movies S4 and S5. Scale bar = 20 μm.

zeocin remained in G1/S phase of the cell cycle (red or yellow) throughout the 96 hr imaging session (Figure 5D; Movie S4) whereas only 25%–30% of G1-sorted BJ-SV40 cells arrested in G1/S after zeocin treatment (Figure 5D; Movie S4). In contrast, approximately 75% of the BJ-p53dn S/G2 cells underwent endoreduplication, showing mitosis-independent geminin degradation and re-entry into G1 and S-phase (Figure 5D; Movie S5). BJ-SV40 cells in S/G2 showed the same percentage of endoreduplication, indicating that Rb status does not affect tetraploidization of cells experiencing prolonged DNA damage in S/G2. Although we cannot exclude other aspects of SV40 large T antigen expression, these data suggest that activation of the Rb/p16 pathway blocks entry into S phase in cells that experience a DNA damage signal in G1, thereby limiting the occurrence of tetraploidization. In contrast, the Rb/p16 pathway alone is not capable of preventing endoreduplication when the DNA damage takes place in G2.

Telomere-Driven Tetraploidization Promotes Transformation in Mouse Cells

To address the tumorigenic potential of tetraploidization, we used an inducible system to elicit transient telomere dysfunction, mimicking the temporary loss of telomere protection that is thought to occur early in tumorigenesis before telomerase activation. We employed the previously established tet-OFF inducible system for POT1a expression in MEFs expressing SV40-LT (Davoli et al., 2010). Two POT1a-tetOFF cell

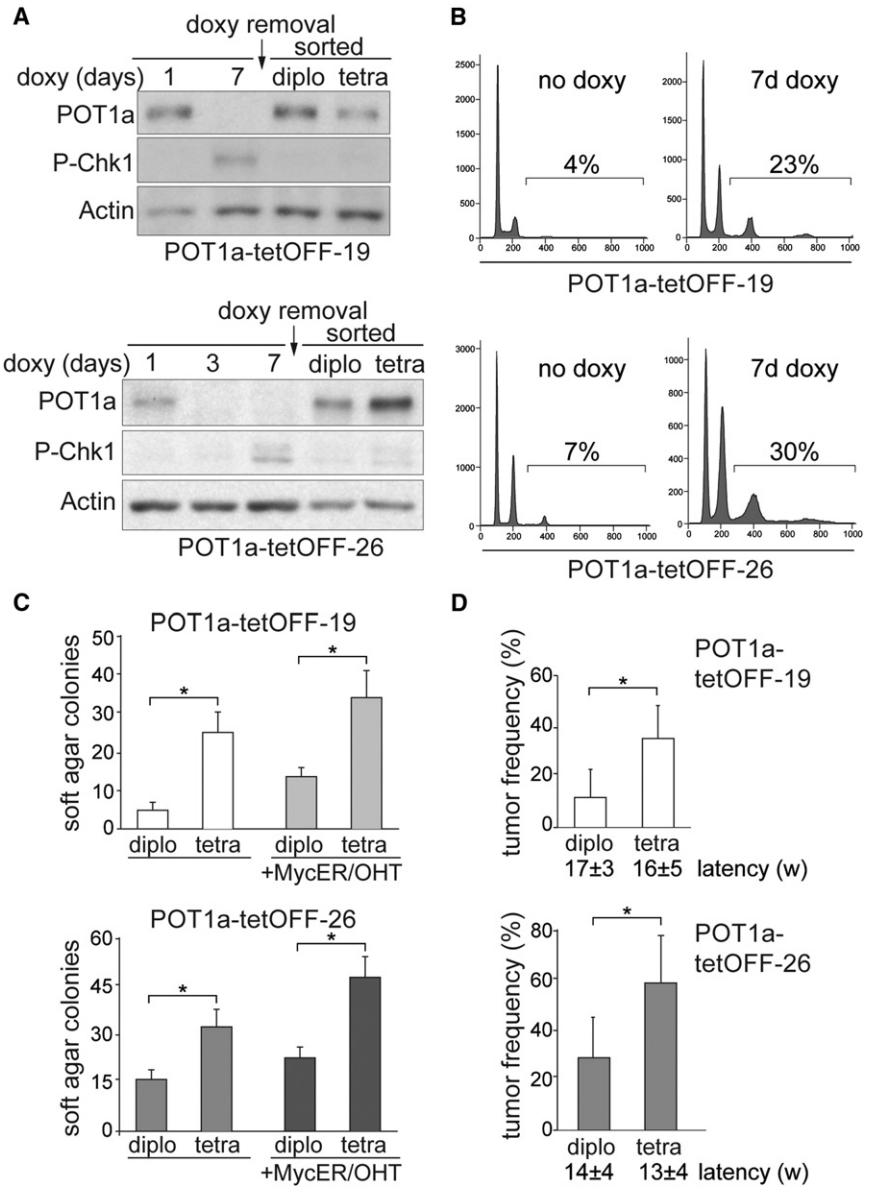

Figure 6. Telomere-Driven Tetraploidy Promotes Cellular Transformation in Mouse Cells

(A) Immunoblot for Chk1 phosphorylation and POT1a in POT1a-tetOFF-19 and -26 cells (SV40-LT expressing MEFs) at the indicated time after treatment with doxycycline and after release of the FACS-sorted diploid and tetraploid cells. POT1a-tetOFF clones 19 and 26 (Davoli et al., 2010) were treated with doxycycline for 10 days, FACS sorted after Hoechst 33342 staining, and cultured in the absence of doxycycline.

(B) FACS analysis of POT1a-tetOFF-19 and -26 treated as in (A). The percentage of cells with >4N DNA content is indicated.

(C) POT1a-tetOFF-19 and -26 with or without pBabe-Myc-ER were treated as in (A). FACS sorted diploid and tetraploid cells were expanded for 2 weeks or for 6–8 weeks and plated in soft-agar. The colonies were counted after 4–6 weeks. Myc-ER was induced with 0.5 μM OHT. The average number of colonies per well and SD obtained after 3 or 4 independent experiments is shown. Stars indicate statistically significant difference ($p < 0.05$ after paired Student's t test, Prism 5 software).

(D) Tumorigenicity assay in nude mice. Diploid and tetraploid descendants of POT1a-tetOFF-19 and-26 were expanded for 2 weeks or for 5–6 weeks in culture in the absence of doxycycline subcutaneously injected in nude mice (2.5 or 5 10^5 cells injected on each side; the number of injected mice is shown). The average frequencies of tumor formation and latencies are indicated with standard deviation (three or four experiments, five or ten mice per experiment). Stars indicate a statistically significant difference ($p < 0.05$ after paired Student's t test).

See also Figure S5.

lines were derived (POT1atetOFF-19 and -26) in which treatment with doxycycline transiently depletes POT1a. As expected from previous data, the loss of POT1a was accompanied by the accumulation of 53BP1 at telomeres, phosphorylation of Chk1 (Figures 6A and 6B; Figure S5A) and tetraploidization as measured by FACS (Figure 6B). Tetraploidization was also evident in these cells from the supernumerary centrosomes and telomere clustering in interphase which are consistent with chromosome reduplication without chromosome segregation (Hockemeyer et al., 2006; Figures S5A and S5B). After doxycycline treatment, POT1a-tetOFF-19 and -26 cells were FACS-sorted based on Hoechst-staining for DNA content to derive tetraploid and diploid cells (Figure S5C). The diploid and tetraploid cells were cultured for either 2 or 5–6 weeks in the absence of doxycycline, allowing POT1a re-expression (Figure 6A). The results at these two time points were essentially the same.

The resulting diploid and tetraploid cultures were then tested for their ability to form colonies in soft-agar and tumors in nude mice (Figures 6C and 6D). For both POT1a-tetOFF-19 and -26, the tetraploid descendants were more transformed based on both assays. The transformation efficiency after long-term culture (5–6 weeks) was slightly higher than the one after short-term culture (2 weeks). Overexpression of c-Myc further enhanced the transformation of diploid and tetraploid POT1a-tetOFF cells but even without this oncogene, the greater tumorigenic potential of the tetraploid population was significant (Figures 6C and 6D). POT1atetOFF control cells not treated with doxycycline transformed at a rate similar to the sorted diploid cells (not shown). The increased transformation potential in the tetraploid cells was not due to increased proliferation rate, since the tetraploid cells grew slower than their diploid counterparts (Figure S5D).

Evolution of Subtetraploid Karyotypes

In order to monitor the karyotypic changes during tumor outgrowth, we established cell lines from tumors formed upon injection of diploid and tetraploid mouse cells. Prior to injection

into nude mice, the cells were infected with the histone H2B-GFP construct allowing separation of tumor cells from host-derived cells present in the tumor mass. GFP-positive cells of tumors derived from injected tetraploid cells showed a tetraploid-like profile, consistent with their cells of origin (Figures S5E and S5F). As expected, the host-derived GFP-negative cells showed a diploid-like profile. A total of eight GFP-positive cell lines were derived from tumors formed by the POT1a-tetOFF-19 and -26 tetraploid cells. Their chromosome numbers, determined after propagation of the cells for 7–10 days in culture revealed subtetraploid karyotypes, with the exception of one line which was hyper-tetraploid (chromosome number ~120, Figures 7A and 7B). Evolution of subtetraploid karyotypes had also occurred in three of four cell lines derived from soft-agar colonies formed by tetraploid POT1a-tetOFF-26 cells (Figure 7C). As a control, cell lines established from a soft-agar colony and a tumor formed by diploid cells had a near-diploid karyotype (Figures 7B and 7C). These results indicate that tetraploid cells generated through telomere dysfunction have a high rate of chromosome loss.

DISCUSSION

Here, we show that telomere crisis induces tetraploidization in human fibroblasts and mammary epithelial cells, lending further credence to the role of telomeres in shaping cancer genomes. Telomere dysfunction has long been held responsible for the initiation of breakage-fusion-bridge cycles and their accompanying rearrangements, including nonreciprocal translocations, regional amplifications, and segmental deletions. The finding that tetraploidization is an additional corollary of unmitigated telomere attrition adds to this inventory of telomere-related genome instability and provides a framework for the genesis of human tumors carrying heavily rearranged subtetraploid genomes. Among the potentially pervasive sources of genome instability in cancer, which include rearrangements originating from common fragile sites, chromothrypsis, and deficiencies in double-strand break repair (Durkin and Glover, 2007; Harper and Elledge, 2007; Negrini et al., 2010; Stephens et al., 2011), an episode of telomere dysfunction stands out, however, due its potential aggregate effect. Upon activation of telomerase, the cells emerging from telomere crisis could potentially combine the mutator phenotype of breakage-fusion-bridge cycles, the mutational robustness of a tetraploid genome, and the high chromosome missegregation rate associated with supernumary centrosomes.

Although we had previously used mouse embryo fibroblasts to document endoreduplication after removal of POT1a from mouse telomeres, it was unclear whether the resulting telomere dysfunction resembles the molecular events at telomeres that have become too short after prolonged attrition. For instance, removal of POT1a from mouse telomeres exposes the single-stranded DNA and permanently activates the ATR kinase pathway whereas critically shortened telomeres may be expected to lose several (or all) shelterin proteins rather than POT1 alone and are known to activate both ATM and ATR signaling (d'Adda di Fagagna et al., 2003). It is also unlikely that all telomeres in crisis cells become dysfunctional at the same time so that the overall level of the DNA damage signal elicited by telomere crisis might be less than in the POT1a knockout cells.

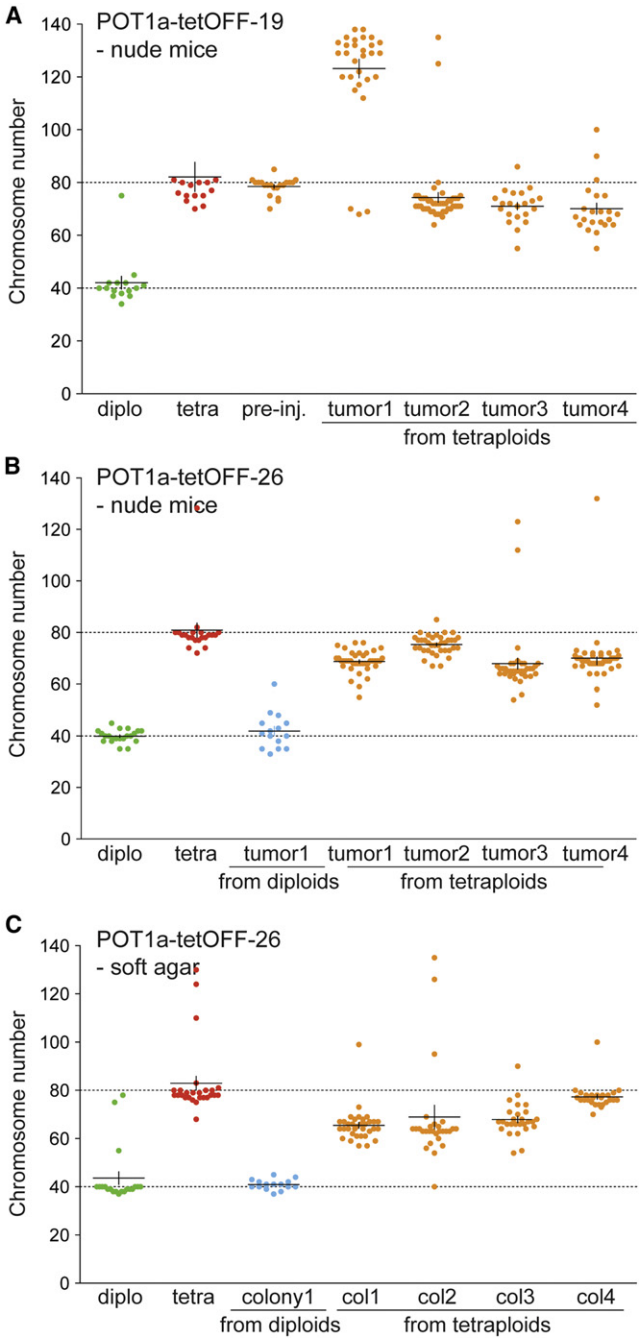

Figure 7. Evolution of Subtetraploid Karyotypes

(A and B) Graphs indicating the number of chromosomes/metaphase in cells derived from tumors formed by diploid and tetraploid POT1a-tetOFF-19 and -26 cells (as in Figure 6D). Cell lines were derived from tumors and metaphase spreads were analyzed after 7–10 days. The distribution of the chromosome number of POT1a-tetOFF diploid and tetraploid cells before injection and of cell lines derived from the indicated tumors derived from injected diploid or tetraploid cells is shown.

(C) Graphs indicating the number of chromosomes/metaphase in cells derived from soft-agar colonies formed POT1a-tetOFF-26 (as in Figure 6D).

Furthermore, rather than the irreparable damage at all telomeres generated by POT1a deletion, critically shortened telomeres are repaired by NHEJ and the resulting damage signal at each telomere is therefore transient. The current data now clarify these issues and demonstrate that endoreduplication can be induced by the DNA damage response to shortened telomeres as they occur in cells in crisis. Furthermore, the data argue that this pathway is similar in human and mouse cells, despite the distinctions in their telomere damage response pathways (Smogorzewska and de Lange, 2002; Jacobs and de Lange, 2004), and demonstrate the relevance of telomere-driven tetraploidization in epithelial cells, which are a cancer relevant cell type.

The data indicate that tetraploid mouse cells generated telomere-driven tetraploidization are more tumorigenic than their diploid counterparts. This result is consistent with prior work showing a higher tumorigenic potential of tetraploid cells generated through the use of a cytokinesis inhibitor (Fujiwara et al., 2005). In the case of telomere-driven tetraploidization there is no prolonged arrest in mitosis, no binucleate intermediate is formed, and there is no reorganization of the two chromosome sets into a tetraploid genome in the next mitosis. Our findings therefore indicate that the tetraploidization per se is the most likely source of the greater tumorigenic potential of the cells.

Order of Events

Telomere-dependent tetraploidization requires a precise sequence of events during tumorigenesis. Specifically, both the p53 and Rb pathways have to be inactivated and the telomeres have to become sufficiently short to induce telomere crisis before telomerase is activated. Loss of p53 is required for the by-pass of telomere-driven senescence and is well-established as a prerequisite for the proliferation of tetraploid cells (Margolis et al., 2003; Ganem et al., 2007). The Rb pathway also blocks cell cycle progression in response to telomere dysfunction and thereby curbs the emergence and proliferation of tetraploid descendants (Jacobs and de Lange, 2004). For most human tumors, there is limited information of the exact order of events relevant to telomere-driven tetraploidization. In particular, no prior study has examined indices of tetraploidization, changes in the status of p53/Rb, and telomerase expression in the same set of pathological specimen representing different stages in tumorigenesis. However, for a number of tumor types, it is known that tetraploidization arises at a stage when both p53 and Rb become inactivated and telomerase is not yet active (Davoli and de Lange, 2011). Examples include HPV induced cervical carcinoma, bladder cancer, lung cancer, breast cancer, and colon cancer. Breast cancer represents a particularly interesting case because there is good evidence for loss of Rb and p53, telomere crisis, and tetraploidization in DCIS before telomerase is activated (Shay and Bacchetti, 1997; Chin et al., 2004; Ottesen, 2003; Shackney and Silverman, 2003). On the other hand, there are also several tumor types that express high levels of telomerase at an early stage (e.g., certain leukemias and lymphomas) and are therefore unlikely to experience telomere crisis. Perhaps not surprisingly, these tumors lack the frequent rearrangements that scar the genomes of solid human tumors and are mostly near diploid.

Collectively, these data suggest a general mechanism for tetraploidization in the early stages of human tumorigenesis. When the p53 and Rb pathway are inactive, extreme telomere shortening can induce tetraploidization through endoreduplication or mitotic failure in precancerous lesions. Reactivation of telomerase (or other mechanisms of telomere maintenance) will allow the tetraploid clone to expand and evolve into a fully transformed cancerous state. The chromosome instability due to prior telomere dysfunction and the inherent high rate of chromosome mis-segregation of tetraploid cells may then foster the evolution of a profoundly rearranged subtetraploid cancer karyotype.

EXPERIMENTAL PROCEDURES

Cell Culture Procedure and Viral Gene Delivery

BJ (ATCC#: CRL2522) and IMR90 (ATCC#: CCl186) human fibroblasts were transduced with retroviral vectors expressing SV40-LT, HPV-E6/E7, or p53175H (p53 dn) as described in (Karlseder et al., 2002; Jacobs and de Lange, 2004). RPE human retinal pigment epithelial cells were purchased from ATCC (ATCC#: 2302) and retrovirally infected with pLPC-Puro-SV40-LT or pRetro-Super-Hygro-p53sh vectors. Human mammary epithelial cell lines 184B and 48RS (Romanov et al., 2001), expressing or not the GSE22 peptide (GSE), acting as a p53 dominant negative (Garbe et al., 2007) were kindly provided by Dr. Martha Stampfer. POT1a-tetOFF MEFs cell lines 19 and 26 were derived as described elsewhere (Davoli et al., 2010). POT1a-tetOFF MEFs, IMR90, BJ, and RPE cells were grown in DMEM (containing 10% of Medium 199 in the case of BJ cells) supplemented with 10% FBS, 100 U penicillin, 0.1 mg/ml streptomycin, 2 mM L-glutamine. hMEC cells were grown in MEMG (Lonza) supplemented with isoproterenol (10 μM) and transferrin (5 μg/ml). Human cells were transduced with FUCCI lentiviral vectors expressing mKO2-hCdt1 (red) and mAG-hGeminin (green) (Sakaue-Sawano et al., 2008), generously provided by Dr. Atsushi Miyawaki. Dr. Pier Giuseppe Pelicci provided pBabe-Puro-MycER. For retroviral and lentiviral infections, phoenix cells (retro) or 293T (lenti) cells were transfected with 10–20 μg of the transgene-expressing plasmid (in addition to lentiviral packaging vectors in the case of 293T). Supernatants were used for two to four infections of 4–6 hr were performed starting 36 hr after transfection with addition of 2–4 μg/ml of polybrene. Cells were selected for 4–6 days in the presence of 500 ng/ml of puromycin or 200 μg/ml of hygromycin. Zeocin (Invitrogen, 100 μg/ml final concentration) and doxycycline (1–2 μg/ml) were added to the cell culture medium every 2–3 days.

FACS Analysis and FACS Sorting

DNA content was analyzed by FACS in ethanol-fixed after staining with propidium iodide (PI), using standard procedures. Flow cytometry was performed using the FACScalibur (Becton Dickinson) and data were analyzed using FlowJo 8.7.1 software. To calculate the percentage of polyploid cells (DNA content >4N), cell doublets and sub-G1 apoptotic cells were excluded. Diploid and tetraploid cells were isolated by sorting for a G1 diploid DNA content or a G2 tetraploid DNA content using an BD FACSAria-2 cell sorter (BD Biosciences) after incubation with Hoechst 33342 (10 μM, AnaSpec, Inc.) for 30 min. GFP-positive cells expressing H2B-GFP were sorted using the same instrument.

In Vitro and In Vivo Transformation Assay

For in vitro soft-agar colony forming assay, a bottom layer of 2 ml 0.9% agar in medium was prepared and allow to solidify and cells were seeded in a top layer of 0.45% agar in medium at a density of 10^4 cells per well in 6-well dishes (triplicates were made for each cell line in each experiment). Cells were incubated at 37°C (medium was added periodically) and colonies formed after 4–6 weeks were scored. In the indicated cases, 0.5 nM 4-hydroxytamoxifen (4-OHT, Sigma) was added to the top layer. In vivo tumorigenic assay was performed by subcutaneous injection in nude mice. Diploid or tetraploid POT1a-tetOFF-19 or -26 cells (5×10^5) were resuspended in PBS and injected into the contralateral sides of NCR-*Foxn1*$^{nu/nu}$ female mice (Taconic). The recipient mice were

checked once or twice a week for tumor formation and euthanized when tumors reached 1 cm diameter, in accordance with institutional procedures. Tumors were dissociated into single cells by treatment with collagenase A at 250 units/ml in DMEM for 3 hr at 37°C. Cells were then washed repeatedly and plated in 10 cm dishes. All experiments involving mice were performed in accordance with institutional regulations and ethical guidelines, and have been authorized by the Institutional Animal Care and Use Committee at Rockefeller University.

Immunofluorescence, Fluorescence In Situ Hybridization-Immunofluorescence, and Immunoblotting

Immunofluorescence (IF) and fluorescence in situ hybridization (FISH)-IF on coverslips and telomeric FISH on metaphase spreads were performed as described previously (Celli and de Lange, 2005). Briefly, after fixation, cells on coverslips were blocked in for 30 min in blocking solution (PBS with 0.1% Triton X-100, 1 mM EDTA, 3% goat serum, and 1 mg/ml BSA). Cells were then incubated for 1 hr with primary antibody diluted in blocking solution (anti-53BP1, 100-304-A, Novus Biologicals; anti-centrin2, sc-27793-R, Santa Cruz), washed three times in PBS and incubated with Rhodamine Red-X or Alexa Fluor 488 conjugated secondary antibody. Finally cells were washed in PBS and the DNA was counterstained with DAPI. In the case of IF-FISH or FISH on metaphase spreads, cells or slides with metaphases were dehydrated in ethanol and hybridized with PNA-probe FITC-OO-(AATCCC)3 (Applied Biosystems) in hybridizing solution (70% formamide, 10 mM Tris-HCl [pH 7.2], 1 mg/ml blocking reagent [Roche]). After denaturation (10 min at 80°C), hybridization was performed at room temperature for 2 hr, followed by two washes for 15 min with washing solution (70% formamide, 10 mM Tris-HCl [pH 7.2]). Finally cells or metaphase spreads were washed in PBS and DNA was then counterstained with DAPI. Digital images were captured with a Zeiss Axioplan II microscope using Improvision OpenLab software. Immunoblotting was performed as described in (Celli and de Lange, 2005) with the following antibodies were used: Chk2 (611570, BD Biosciences); Chk1, P-S317 (A300-163A, Bethyl) for human cells; Chk1 pS345 (#2348, Cell Signaling Technology) for mouse cells; β-actin (I-19) (sc-1616, Santa Cruz); p16 (C-20) (Santa Cruz); POT1a (1221).

Telomere Length Analysis

For genomic blotting, cells were harvested at the indicated PD, DNA was isolated as described (de Lange et al., 1990), digested with AluI and MboI, size-fractionated on a 0.7% agarose gel and transferred to a Hybond membrane for hybridization using an 800 bp telomeric DNA probe from pSP73Sty11 labeled with [CCCTAA]3-primed Klenow polymerase and ^{32}P-alpha-dCTP. Blots were exposed to a phosphorimaging screen and analyzed using ImageQuant software.

SUPPLEMENTAL INFORMATION

Supplemental Information includes five figures and five movies and can be found with this article online at doi:10.1016/j.ccr.2012.03.044.

ACKNOWLEDGMENTS

We thank Martha Stampfer for generously providing hMECs and her expert advice and Nazario Bosco for help with cytogenetic analysis. Devon White is thanked for his expert assistance in the work with mice. We thank Atsushi Miyawaki for providing the FUCCI vectors and Pier Giuseppe Pelicci for providing the Myc-ER vector. We are very thankful to the Bioimaging and Flow Cytometry Facilities at Rockefeller University. Members of the de Lange lab are thanked for discussion and comments on this manuscript. This work was supported by the a grants from the Breast Cancer Research Foundation and the NIH (CA160924) to T.d.L. T.d.L. is a Research Professor of the American Cancer Society.

Received: July 21, 2011
Revised: October 20, 2011
Accepted: March 23, 2012
Published: June 11, 2012

REFERENCES

Arias, E.E., and Walter, J.C. (2005). Replication-dependent destruction of Cdt1 limits DNA replication to a single round per cell cycle in Xenopus egg extracts. Genes Dev. *19*, 114–126.

Artandi, S.E., and DePinho, R.A. (2010). Telomeres and telomerase in cancer. Carcinogenesis *31*, 9–18.

Artandi, S.E., Chang, S., Lee, S.L., Alson, S., Gottlieb, G.J., Chin, L., and DePinho, R.A. (2000). Telomere dysfunction promotes non-reciprocal translocations and epithelial cancers in mice. Nature *406*, 641–645.

Baker, S.J., Preisinger, A.C., Jessup, J.M., Paraskeva, C., Markowitz, S., Willson, J.K., Hamilton, S., and Vogelstein, B. (1990). p53 gene mutations occur in combination with 17p allelic deletions as late events in colorectal tumorigenesis. Cancer Res. *50*, 7717–7722.

Celli, G.B., and de Lange, T. (2005). DNA processing is not required for ATM-mediated telomere damage response after TRF2 deletion. Nat. Cell Biol. *7*, 712–718.

Chin, K., de Solorzano, C.O., Knowles, D., Jones, A., Chou, W., Rodriguez, E.G., Kuo, W.L., Ljung, B.M., Chew, K., Myambo, K., et al. (2004). In situ analyses of genome instability in breast cancer. Nat. Genet. *36*, 984–988.

Counter, C.M., Avilion, A.A., LeFeuvre, C.E., Stewart, N.G., Greider, C.W., Harley, C.B., and Bacchetti, S. (1992). Telomere shortening associated with chromosome instability is arrested in immortal cells which express telomerase activity. EMBO J. *11*, 1921–1929.

d'Adda di Fagagna, F., Reaper, P.M., Clay-Farrace, L., Fiegler, H., Carr, P., Von Zglinicki, T., Saretzki, G., Carter, N.P., and Jackson, S.P. (2003). A DNA damage checkpoint response in telomere-initiated senescence. Nature *426*, 194–198.

Davoli, T., and de Lange, T. (2011). The causes and consequences of polyploidy in normal development and cancer. Annu. Rev. Cell Dev. Biol. *27*, 22.1–22.26.

Davoli, T., Denchi, E.L., and de Lange, T. (2010). Persistent telomere damage induces bypass of mitosis and tetraploidy. Cell *141*, 81–93.

de Lange, T. (2005). Telomere-related genome instability in cancer. Cold Spring Harb. Symp. Quant. Biol. *70*, 197–204.

de Lange, T., Shiue, L., Myers, R.M., Cox, D.R., Naylor, S.L., Killery, A.M., and Varmus, H.E. (1990). Structure and variability of human chromosome ends. Mol. Cell. Biol. *10*, 518–527.

Durkin, S.G., and Glover, T.W. (2007). Chromosome fragile sites. Annu. Rev. Genet. *41*, 169–192.

Fujiwara, T., Bandi, M., Nitta, M., Ivanova, E.V., Bronson, R.T., and Pellman, D. (2005). Cytokinesis failure generating tetraploids promotes tumorigenesis in p53-null cells. Nature *437*, 1043–1047.

Ganem, N.J., Storchova, Z., and Pellman, D. (2007). Tetraploidy, aneuploidy and cancer. Curr. Opin. Genet. Dev. *17*, 157–162.

Garbe, J.C., Holst, C.R., Bassett, E., Tlsty, T., and Stampfer, M.R. (2007). Inactivation of p53 function in cultured human mammary epithelial cells turns the telomere-length dependent senescence barrier from agonescence into crisis. Cell Cycle *6*, 1927–1936.

Harper, J.W., and Elledge, S.J. (2007). The DNA damage response: ten years after. Mol. Cell *28*, 739–745.

Hastie, N.D., Dempster, M., Dunlop, M.G., Thompson, A.M., Green, D.K., and Allshire, R.C. (1990). Telomere reduction in human colorectal carcinoma and with ageing. Nature *346*, 866–868.

Herbig, U., Jobling, W.A., Chen, B.P., Chen, D.J., and Sedivy, J.M. (2004). Telomere shortening triggers senescence of human cells through a pathway involving ATM, p53, and p21(CIP1), but not p16(INK4a). Mol. Cell *14*, 501–513.

Hockemeyer, D., Daniels, J.P., Takai, H., and de Lange, T. (2006). Recent expansion of the telomeric complex in rodents: Two distinct POT1 proteins protect mouse telomeres. Cell *126*, 63–77.

Jacobs, J.J., and de Lange, T. (2004). Significant role for p16INK4a in p53-independent telomere-directed senescence. Curr. Biol. *14*, 2302–2308.

Karlseder, J., Smogorzewska, A., and de Lange, T. (2002). Senescence induced by altered telomere state, not telomere loss. Science *295*, 2446–2449.

Kibe, T., Osawa, G.A., Keegan, C.E., and de Lange, T. (2010). Telomere protection by TPP1 is mediated by POT1a and POT1b. Mol. Cell. Biol. *30*, 1059–1066.

Kim, N.W., Piatyszek, M.A., Prowse, K.R., Harley, C.B., West, M.D., Ho, P.L., Coviello, G.M., Wright, W.E., Weinrich, S.L., and Shay, J.W. (1994). Specific association of human telomerase activity with immortal cells and cancer. Science *266*, 2011–2015.

Kirkland, J.A., Stanley, M.A., and Cellier, K.M. (1967). Comparative study of histologic and chromosomal abnormalities in cervical neoplasia. Cancer *20*, 1934–1952.

Lengauer, C., Kinzler, K.W., and Vogelstein, B. (1997). Genetic instability in colorectal cancers. Nature *386*, 623–627.

Lin, T.T., Letsolo, B.T., Jones, R.E., Rowson, J., Pratt, G., Hewamana, S., Fegan, C., Pepper, C., and Baird, D.M. (2010). Telomere dysfunction and fusion during the progression of chronic lymphocytic leukemia: evidence for a telomere crisis. Blood *116*, 1899–1907.

Margolis, R.L., Lohez, O.D., and Andreassen, P.R. (2003). G1 tetraploidy checkpoint and the suppression of tumorigenesis. J. Cell. Biochem. *88*, 673–683.

Meeker, A.K., and Argani, P. (2004). Telomere shortening occurs early during breast tumorigenesis: a cause of chromosome destabilization underlying malignant transformation? J. Mammary Gland Biol. Neoplasia *9*, 285–296.

Meeker, A.K., Hicks, J.L., Platz, E.A., March, G.E., Bennett, C.J., Delannoy, M.J., and De Marzo, A.M. (2002). Telomere shortening is an early somatic DNA alteration in human prostate tumorigenesis. Cancer Res. *62*, 6405–6409.

Meeker, A.K., Hicks, J.L., Iacobuzio-Donahue, C.A., Montgomery, E.A., Westra, W.H., Chan, T.Y., Ronnett, B.M., and De Marzo, A.M. (2004). Telomere length abnormalities occur early in the initiation of epithelial carcinogenesis. Clin. Cancer Res. *10*, 3317–3326.

Negrini, S., Gorgoulis, V.G., and Halazonetis, T.D. (2010). Genomic instability—an evolving hallmark of cancer. Nat. Rev. Mol. Cell Biol. *11*, 220–228.

Ottesen, G.L. (2003). Carcinoma in situ of the female breast. A clinico-pathological, immunohistological, and DNA ploidy study. APMIS Suppl. *108*, 1–67.

Reid, B.J., Barrett, M.T., Galipeau, P.C., Sanchez, C.A., Neshat, K., Cowan, D.S., and Levine, D.S. (1996). Barrett's esophagus: ordering the events that lead to cancer. Eur. J. Cancer Prev. *5* (*Suppl 2*), 57–65.

Remus, D., and Diffley, J.F. (2009). Eukaryotic DNA replication control: lock and load, then fire. Curr. Opin. Cell Biol. *21*, 771–777.

Romanov, S.R., Kozakiewicz, B.K., Holst, C.R., Stampfer, M.R., Haupt, L.M., and Tlsty, T.D. (2001). Normal human mammary epithelial cells spontaneously escape senescence and acquire genomic changes. Nature *409*, 633–637.

Sakaue-Sawano, A., Kurokawa, H., Morimura, T., Hanyu, A., Hama, H., Osawa, H., Kashiwagi, S., Fukami, K., Miyata, T., Miyoshi, H., et al. (2008). Visualizing spatiotemporal dynamics of multicellular cell-cycle progression. Cell *132*, 487–498.

Shackney, S.E., and Silverman, J.F. (2003). Molecular evolutionary patterns in breast cancer. Adv. Anat. Pathol. *10*, 278–290.

Shackney, S.E., Smith, C.A., Miller, B.W., Burholt, D.R., Murtha, K., Giles, H.R., Ketterer, D.M., and Pollice, A.A. (1989). Model for the genetic evolution of human solid tumors. Cancer Res. *49*, 3344–3354.

Shay, J.W., and Bacchetti, S. (1997). A survey of telomerase activity in human cancer. Eur. J. Cancer *33*, 787–791.

Shay, J.W., and Wright, W.E. (2005). Senescence and immortalization: role of telomeres and telomerase. Carcinogenesis *26*, 867–874.

Shay, J.W., Pereira-Smith, O.M., and Wright, W.E. (1991). A role for both RB and p53 in the regulation of human cellular senescence. Exp. Cell Res. *196*, 33–39.

Shay, J.W., Van Der Haegen, B.A., Ying, Y., and Wright, W.E. (1993). The frequency of immortalization of human fibroblasts and mammary epithelial cells transfected with SV40 large T-antigen. Exp. Cell Res. *209*, 45–52.

Smogorzewska, A., and de Lange, T. (2002). Different telomere damage signaling pathways in human and mouse cells. EMBO J. *21*, 4338–4348.

Stephens, P.J., Greenman, C.D., Fu, B., Yang, F., Bignell, G.R., Mudie, L.J., Pleasance, E.D., Lau, K.W., Beare, D., Stebbings, L.A., et al. (2011). Massive genomic rearrangement acquired in a single catastrophic event during cancer development. Cell *144*, 27–40.

Storchova, Z., and Kuffer, C. (2008). The consequences of tetraploidy and aneuploidy. J. Cell Sci. *121*, 3859–3866.

van Heek, N.T., Meeker, A.K., Kern, S.E., Yeo, C.J., Lillemoe, K.D., Cameron, J.L., Offerhaus, G.J., Hicks, J.L., Wilentz, R.E., Goggins, M.G., et al. (2002). Telomere shortening is nearly universal in pancreatic intraepithelial neoplasia. Am. J. Pathol. *161*, 1541–1547.

Wright, W.E., and Shay, J.W. (1992). The two-stage mechanism controlling cellular senescence and immortalization. Exp. Gerontol. *27*, 383–389.

Cancer Cell
Article

ID1 and ID3 Regulate the Self-Renewal Capacity of Human Colon Cancer-Initiating Cells through p21

Catherine A. O'Brien,[1,2,3,7,*] Antonija Kreso,[1,4,7] Paul Ryan,[5] Karin G. Hermans,[1] Lianne Gibson,[1] Yadong Wang,[1] Andrew Tsatsanis,[1] Steven Gallinger,[2,6] and John E. Dick[1,4,*]
[1]Campbell Family Institute, Ontario Cancer Institute, Princess Margaret Hospital
[2]Department of Surgery
University Health Network, Toronto, Ontario M5G 1L7, Canada
[3]Department of Laboratory Medicine and Pathobiology and Department of Surgery, University of Toronto, Toronto, Ontario M5L 1F4, Canada
[4]Department of Molecular Genetics, University of Toronto, Toronto, Ontario M5G 1L7, Canada
[5]Department of Pathology, Bon Secours Hospital, Cork, Ireland
[6]Fred Litwin Centre for Cancer Genetics Samuel Lunenfeld Research Institute, Mount Sinai Hospital, Toronto, Ontario M7H 2B9, Canada
[7]These authors contributed equally to this work
*Correspondence: cobrien@uhnres.utoronto.ca (C.A.O.), jdick@uhnres.utoronto.ca (J.E.D.)
DOI 10.1016/j.ccr.2012.04.036

SUMMARY

There is increasing evidence that some cancers are hierarchically organized, sustained by a relatively rare population of cancer-initiating cells (C-ICs). Although the capacity to initiate tumors upon serial transplantation is a hallmark of all C-ICs, little is known about the genes that control this process. Here, we establish that ID1 and ID3 function together to govern colon cancer-initiating cell (CC-IC) self-renewal through cell-cycle restriction driven by the cell-cycle inhibitor p21. Regulation of p21 by ID1 and ID3 is a central mechanism preventing the accumulation of excess DNA damage and subsequent functional exhaustion of CC-ICs. Additionally, silencing of ID1 and ID3 increases sensitivity of CC-ICs to the chemotherapeutic agent oxaliplatin, linking tumor initiation function with chemotherapy resistance.

INTRODUCTION

There is increasing experimental evidence from cell fractionation experiments that many, but perhaps not all, tumors are organized as a cellular hierarchy sustained by a so-called cancer-initiating cell (C-IC) or cancer stem cell (CSC) (Al-Hajj and Clarke, 2004; Dick, 2008; O'Brien et al., 2009). Several attributes distinguish C-ICs from the remaining cells of a tumor, including ability to initiate cancer growth in xenotransplantation assays, restoration of the tumor hierarchy by generating non-C-ICs, and capacity for long-term self-renewal (Dick, 2003). It is becoming evident that the acquisition of dysregulated self-renewal mechanisms represents a key step in the generation of C-ICs (Morrison and Kimble, 2006; He et al., 2009). The strongest evidence for C-ICs has come from clonal serial xenotransplantation assays and lentiviral-tracking studies carried out in leukemia by Bonnet and Dick (1997) and Hope et al. (2004). Experimental data are now accumulating that several solid tumors, including breast (Al-Hajj et al., 2003), brain (Singh et al., 2004), and colon (O'Brien et al., 2007; Ricci-Vitiani et al., 2007), adhere to the hierarchical model and contain C-ICs. The focus of our study is on colon C-ICs (CC-ICs), which typically represent a small subset of the total colon cancer cell population and can be prospectively isolated based on the expression of specific cell surface (i.e., CD133 [O'Brien et al., 2007; Ricci-Vitiani et al., 2007], CD44 [Dalerba et al., 2007], CD166 [Dalerba et al., 2007]) or functional (aldehyde dehydrogenase-1; Dylla et al., 2008; Huang et al., 2009) markers. Evidence is also emerging that the C-ICs from several cancers possess properties that make them resistant to chemotherapy and radiation, including expression of drug efflux pumps, altered DNA damage response, or cellular quiescence (Bao et al., 2006; Todaro et al., 2008; Hermann et al., 2007; Schatton et al., 2008; Viale et al., 2009). Collectively, little is known of the molecular regulation of solid tumor C-ICs and whether intrinsic stem cell properties are directly linked to survival mechanisms and therapeutic resistance.

Significance

There is emerging evidence that the capacity for self-renewal is dysregulated in cancer-initiating cells (C-ICs) and that C-ICs also possess properties that make them resistant to chemotherapy and radiation. We found that ID1, ID3, and p21 function together to govern self-renewal of colon cancer-initiating cells (CC-ICs) through cell-cycle restriction and protection from DNA damage accumulation. These components of the tumor-initiating machinery of human CC-ICs are also linked to chemotherapy resistance at the stem cell level, opening the way for stem cell-based therapeutic strategies to manipulate self-renewal as a means to potentiate chemotherapeutic drug combinations.

As a first step to uncover specific factors that govern the maintenance of CC-ICs, we focused on genes that have been implicated in self-renewal properties of somatic or embryonic stem cells, narrowed the list to those that were dysregulated in cancer, and finally to those implicated in human colon cancer specifically. One family of proteins that satisfies these criteria are the inhibitor of DNA binding proteins (IDs), a family of homologous helix-loop-helix (HLH) transcriptional regulatory factors (Gray et al., 2008) (ID1–ID4) with recognized roles in development, senescence, differentiation, angiogenesis, and migration (Fong et al., 2004). The ability of ID proteins to drive self-renewal is well established in embryonic stem cells, where the upregulation of IDs by bone morphogenic protein 4 (BMP4) is required to maintain self-renewal and pluripotency (Hollnagel et al., 1999; Ruzinova and Benezra, 2003). Studies in a murine model of hematopoiesis revealed that *Id1*$^{-/-}$ whole-bone marrow displayed impaired self-renewal capacity relative to wild-type controls (Perry et al., 2007). Similar results were observed in murine cortical neural stem cells where overexpression of Id1 increased self-renewal capacity (Nam and Benezra, 2009). Evidence suggesting that IDs play a role in cancer comes from studies demonstrating increased expression in a variety of solid tumors, including pancreatic (Kleeff et al., 1998), cervical (Schindl et al., 2001), ovarian (Schindl et al., 2003) prostate (Ouyang et al., 2002), breast (Lin et al., 2000; Fong et al., 2003), and colon (Meteoglu et al., 2008; Gray et al., 2008). ID upregulation correlates with both poor prognosis and chemoresistance (Cheung et al., 2004; Hu et al., 2009; Li et al., 2007). Furthermore, studies from Gupta et al. using murine models of breast cancer demonstrated a role for Id1/Id3 in the initiation of metastases, a process that may be closely related to the concept of C-ICs (Gupta et al., 2007). Considering the overall importance of IDs in cancer biology and their role in embryonic and somatic stem cell self-renewal, they represent prime candidates to evaluate in CC-ICs.

In some systems, ID1 functions to maintain self-renewal through repressive effects on expression of the cell-cycle inhibitor, p21/cip1/waf1 (p21) (Ciarrocchi et al., 2007; Jankovic et al., 2007). However, p21 has also been linked to maintenance of self-renewal capacity in leukemic and normal hematopoietic stem cells, indicating that cellular context can impact on functional properties of these regulators (Cheng et al., 2000; Viale et al., 2009). Although, to our knowledge, there are no reports on a role for p21 in CC-IC self-renewal, p21 has a well-established role in protecting colon cancer cells against a variety of stress stimuli, including exposure to radiation and chemotherapy (Mahyar-Roemer and Roemer, 2001; Bene and Chambers, 2009; Gorospe et al., 1996; Sharma et al., 2005; Tian et al., 2000). These studies point to the plausibility that therapy resistance may be linked to tumor initiation and maintenance mechanisms and that pathways driving self-renewal may also function to protect CC-ICs when exposed to environmental stress.

Mechanistic studies on properties governing tumor initiation require large numbers of CC-ICs to carry out functional genomic experiments aimed at identifying the key players in CC-IC function. However, this has proved difficult because CC-ICs are typically rare in primary human cancers, and culture systems that permit genetic studies as well as the production of large numbers of CC-ICs are not well established. Here, we developed a robust culture system that enabled the expansion and genetic manipulation of CC-ICs. Utilizing this system, we interrogated the role of ID1 and ID3 in driving CC-IC self-renewal capacity, as well as their role in determining response to oxaliplatin, a commonly used chemotherapeutic agent in colon cancer (Alberts and Wagman, 2008).

RESULTS

Enrichment of CC-ICs in Primary Human Colon Cancer Cultures

In colon cancer the C-IC fraction is typically small, rendering these cells difficult to identify and making molecular studies aimed at manipulating tumor initiation programs very challenging (O'Brien et al., 2007). We characterized a commercially available cell line, LS174T, and determined that xenografts from this cell line can be initiated with a high frequency (Figure 1A; see Table S2 available online). Furthermore, xenografts derived from LS174T injections were hierarchically organized based on CD44 expression (Figure 1D; Table S3). To determine if the culture conditions could be applied to primary samples, three colon cancers were obtained at the time of surgical resection and established as sphere cultures in serum-free media (Kreso and O'Brien, 2008). There was approximately a 200-fold increase in CC-IC activity in the sphere-cultured cells as compared to in vivo-limiting dilution assay (LDA) results using xenograft cells derived from the same tumor (Figure 1A; Tables S1 and S2).

To establish that the primary cultures retained their ability to reestablish a cellular hierarchy, they were transplanted into mice, and expression of known CC-IC surface markers, CD133 and CD44, was assessed. Sample 3 did not express either marker but contained CC-ICs based on in vivo serial passage LDA (Figures 1A–1C). For sample 2, CD44 and CD133 expression during in vitro culture closely resembled the expression from xenograft-derived cells (Figures 1B and 1C). Sample 1 displayed yet a different pattern where CD133 was expressed on a subset of cells in vitro, whereas CD44 was expressed on most cells. However, when sample 1 cells were obtained from xenografts, no CD44 expression was identified, and the CD133 subset remained relatively stable (Figures 1B and 1C). Similar results were observed with LS174T where in vitro culture resulted in expression of CD44 on the majority of cells (Figure 1B), whereas only approximately 50% of xenograft-derived cells expressed CD44 (Figure 1C). To ensure that there was no contamination, each colon cancer sample was checked for nonmalignant cells, including endothelial, hematopoietic, and murine cells (Figure S1).

To determine whether the cell surface phenotype correlated with CC-IC function, CD133^{+} and CD44^{+} subsets were tested using both in vitro and in vivo LDAs and found to be enriched for CC-IC activity (Figure 1D; Table S3), with two exceptions. CD44 expression in LS174T and sample 1 did not enrich from in vitro culture, indicating that CD44 is an unreliable marker of CC-IC activity for these samples under in vitro conditions (Figures 1B and 1D). In contrast, serial transplantation of CD44^{+} and CD44^{-} LS174T xenograft-derived cells demonstrated that CD44^{+} cells possessed increased CC-IC capacity as compared to the CD44^{-} fraction (Figure 1D; Table S3).

A

Sample	CC-IC frequency of xenograft cells in vivo	CC-IC frequency of sphere cells in vivo	SFU frequency in vitro	CFU frequncy in vitro
1	1 in 11498 (18301-7224)	1 in 54 (93-31)	1 in 20 (26-16)	1 in 1.6 (2.1-1.3)
2	1 in 32162 (46614-22191)	1 in 118 (218-64)	1 in 22 (28-17)	1 in 2.4 (2.8-1.9)
3	1 in 57636 (83861-39612)	1 in 580 (1067-317)	1 in 39 (49-31)	1 in 2.7 (3.3-2.1)
LS174T		1 in 111 (156-76)	1 in 40 (72-26)	1 in 2 (2.6-1.6)

B

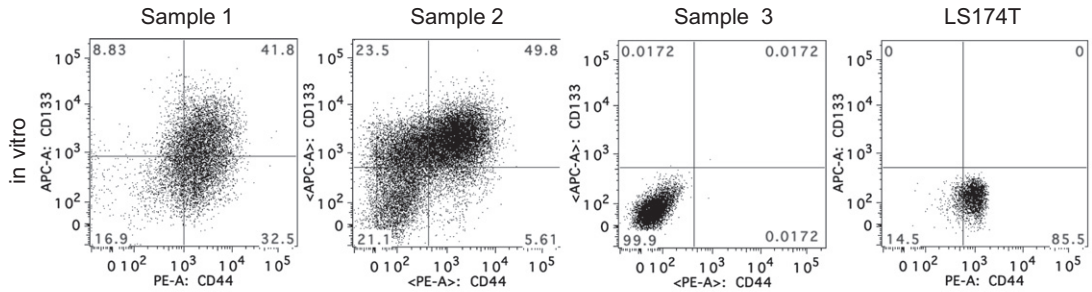

C

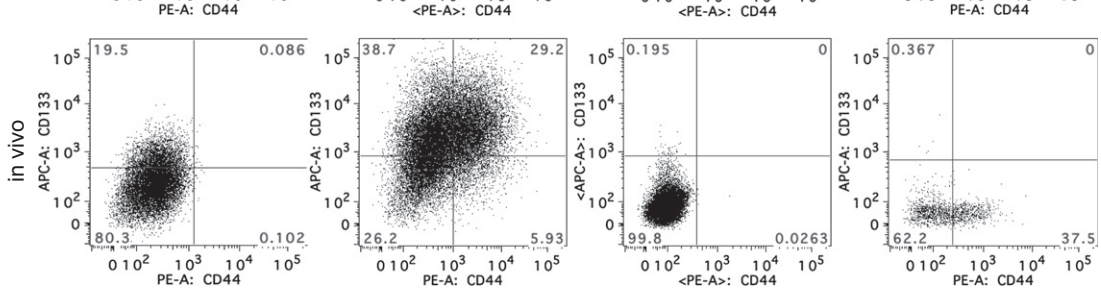

D

Colon cancer sample	Cell subset injected	Sphere LDA			Xenograft LDA		
		CC-IC frequency 1 in x			CC-IC frequency 1 in x		
		Lower	Estimate	Upper	Lower	Estimate	Upper
Sample 2	CD133+	97	62	39	247	121	60
	CD133-	22,439	13,295	7,878	119,974	38,826	12,565
Sample 2	CD44+	173	86	43	674	355	187
	CD44-	7,448	3959	2,105	128,409	40,764	12,941
LS174T	CD44+				358	190	100
	CD44-				14,866	8,748	5,148

Figure 1. In Vitro Expansion and Xenograft Generation of Human Colon Cancer Cells

(A) Comparison of in vivo xenograft formation with in vitro sphere and colony formation at limiting dilution is shown. All data are represented as the frequency of CC-IC, SFU, or CFU; 95% CI is shown in parentheses.

(B) Representative flow cytometric profiles of CD44 and CD133 expression in vitro (n = 5).

(C) Flow cytometric profiles of xenograft-derived cells (n = 5).

(D) Fractionation of CC-IC activity based on CC-IC marker expression. All data are represented as the CC-IC (95% CI). CC-IC frequency 1 in x (x, number of colon cancer cells).

See also Figure S1 and Tables S1, S2, S3, S4, and S5.

Collectively, these findings demonstrate the importance of functionally validating each sample in the context of the system being studied because a change in phenotypic expression does not necessarily correlate to function. Thus, by robust functional criteria we can conclude that the culture conditions we developed resulted in highly enriched CC-ICs that retain their capacity to generate a tumor hierarchy. Recently, a more immune-deficient mouse strain has become available, NOD/SCID γ (NSG), that results in a dramatic enhancement in the detection of C-ICs in some tumors, such as melanoma (Quintana et al., 2008). We observed similar CC-IC frequencies in NOD/SCID versus NSG recipients (Table S4), suggesting that the wide variation observed in melanoma does not necessarily apply to all types of cancer, including the colon cancer samples employed in this study.

Comparison of the Frequency of Cells Capable of In Vitro Sphere and Colony Formation with CC-IC Activity

The gold standard test for enumerating the frequency of C-ICs is in vivo serial transplantation of single C-ICs. However, recently, many groups have commenced utilizing sphere (serum-free media) or colony-forming (10% serum media) assays as attractive surrogates (Todaro et al., 2008; Korkaya et al., 2009). To determine whether these in vitro assays constitute valid surrogates for the measurement of C-IC capacity, each culture was subjected to a detailed quantitative analysis to determine the frequency of colony-forming cells, sphere-forming cells, and in vivo C-ICs. The frequency of sphere and colony-forming cells was 6- and 88-fold greater than in vivo CC-IC frequencies, respectively (Figure 1A). Therefore, it was evident that the number of colon cancer cells capable of forming colonies in vitro was significantly greater than those capable of forming spheres. To determine if colony-forming cells and sphere-forming cells still possessed CC-IC activity, cells from each assay were injected into NOD/SCID mice using LDA. Interestingly, the exact opposite was seen when these cells were injected in vivo: the tumor-initiating capacity was significantly less in the cells cultured in the colony-forming media versus the same cells cultured under sphere conditions. For example when injected in vivo, the LS174T CC-IC frequencies were 1 in 111 in sphere media (Figure 1A) versus 1 in 15,166 in the colony-forming media containing serum (Table S5). This experiment was repeated with a tumor sample taken at the time of surgical resection, and similar results were obtained (Table S5). These results indicate that the sphere assay more closely reflects the in vivo CC-IC frequencies.

Knockdown of ID1/ID3 Expression Reduces Tumor Growth In Vivo

Protein expression of ID1 and ID3 was determined for each of the samples (Figure S2A). To investigate a possible role for ID1 and ID3 in maintaining the CC-IC fraction, the level of expression in CC-IC-enriched and non-enriched fractions was determined by qPCR. There was a trend for *ID1* mRNA expression levels to be higher in the $CD133^+$ and $CD44^+$ fractions, as compared to the negative counterparts (Figure 2A). *ID3* expression levels were similar in both fractions (Figure 2B). To determine the functional significance of ID1 and ID3 expression, we utilized retrovirus-mediated silencing in CC-IC cultures using control (PRS), ID1 knockdown (ID1KD), ID3KD, or combined ID1 and ID3 KD (ID1/ID3KD). To account for potential off-target effects, two independently designed hairpins for ID1 and ID3 were tested (Figure S2B). The two sets of hairpins yielded very similar in vitro results, and the set of hairpins we utilized was previously validated by Gupta et al. (2007). Western blot analysis demonstrated >50% reduction of ID1 and ID3 protein in ID1/ID3KD cells as compared to control cells, indicating efficient KD. However, both ID1 and ID3 are not completely eliminated at the protein level; nevertheless, we will continue to use the nomenclature of ID1/ID3KD to denote this partial KD situation (Figure 2C). Following transduction and selection, colon cancer cells were injected subcutaneously (s.c.) into NOD/SCID mice. The KD of ID1 or ID3 protein expression individually resulted in partial inhibition of tumor growth. However, ID1/ID3KD resulted in a profound decrease in the ability of these cells to form colon cancer xenografts in the LS174T cells (Figures 2D and 2H). There was a complete loss of tumor formation in the ID1/ID3KD group for samples 1, 2, and 3 (Figures 2E–2G).

Because the role of ID1 in vasculogenesis is well established by Lyden et al. (1999), we investigated whether the drastic difference in tumor size was due to poor vascularization at the site of injection. Control and ID1/ID3KD-transduced LS174T cells were injected into the spleen, a well-vascularized site. A significant reduction in tumor growth and metastatic burden was observed (Figures S2E–2H), suggesting that the effect of ID1/ID3KD was not solely due to effects on vasculogenesis.

ID1/ID3KD Affects Proliferation and Xenograft Microvessel Formation

To elucidate the mechanism of action of ID1/ID3KD, the xenografts generated from each experimental group were examined for microvessel density (MVD), apoptosis, necrosis, and proliferation. MVD was significantly decreased by 50% in the ID1/ID3KD group as compared to control (Figure 3A). This result was anticipated because previous studies have recognized the importance of ID1 expression in vasculogenesis both in endothelial and cancer cells (Lyden et al., 1999; Ling et al., 2005; Swarbrick et al., 2008). There was no significant difference between the experimental and control groups with respect to apoptosis, proliferative index, or percent necrosis (Figures 3B–3E). In contrast to the xenograft results, the in vitro proliferative capacity was 2-fold lower in all three KD groups as compared to control (Figure 3F). Another measure of proliferative capacity is sphere diameter, which showed no significant difference among the three KD groups (Figure S3A). The modest decrease in proliferation observed in vitro could partially explain the significantly smaller xenografts in the ID1KD and ID3KD groups as compared to controls but could not explain the profound decrease in xenograft growth observed in the ID1/ID3KD group. Another mechanism known to be affected by ID proteins is senescence (Swarbrick et al., 2008); however, no differences in the β-galactosidase senescence marker were seen between KD and control groups (data not shown).

The IDs have a well-established role in the inhibition of differentiation in a variety of cell types (Fong et al., 2004). To determine whether ID1/ID3KD was inducing differentiation, the LS174T control and KD xenografts were stained for known colon cancer

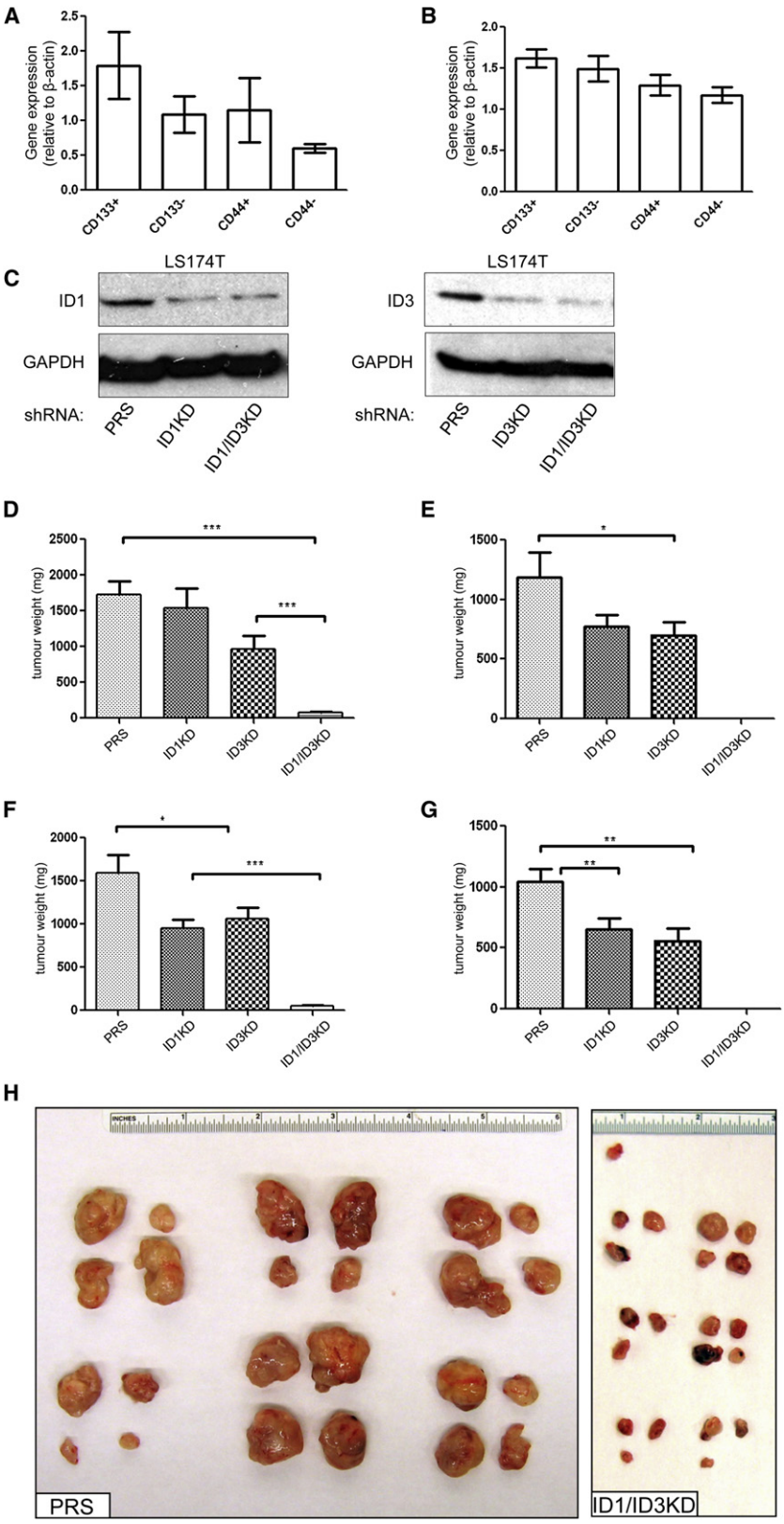

Figure 2. ID1/ID3KD Reduces Tumor Growth In Vivo

(A and B) qPCR for *ID1* (A) and *ID3* (B) expression in the CD133 and CD44 subsets is presented.

(C) Western blot of ID1 and ID3 is illustrated.

(D) Mean tumor weights for LS174T following s.c. injection of PRS, ID1KD, ID3KD, or ID1/ID3KD cells (n = 32 tumors per group) are shown.

(E) Mean tumor weights for sample 1 are presented; no tumors were observed in the ID1/ID3KD group.

(F) Mean tumor weights for sample 2 are shown.

(G) Mean tumor weights for sample 3 are presented; no tumors were observed in the ID1/ID3KD group.

(H) Photographs of excised tumors from mice injected with either ID1/ID3KD or PRS cells are shown.

For (E)–(G) n = 20 tumors/group. Error bars represent ± SD. ***$p < 0.0001$, **$p < 0.001$, *$p < 0.01$.

See also Figure S2.

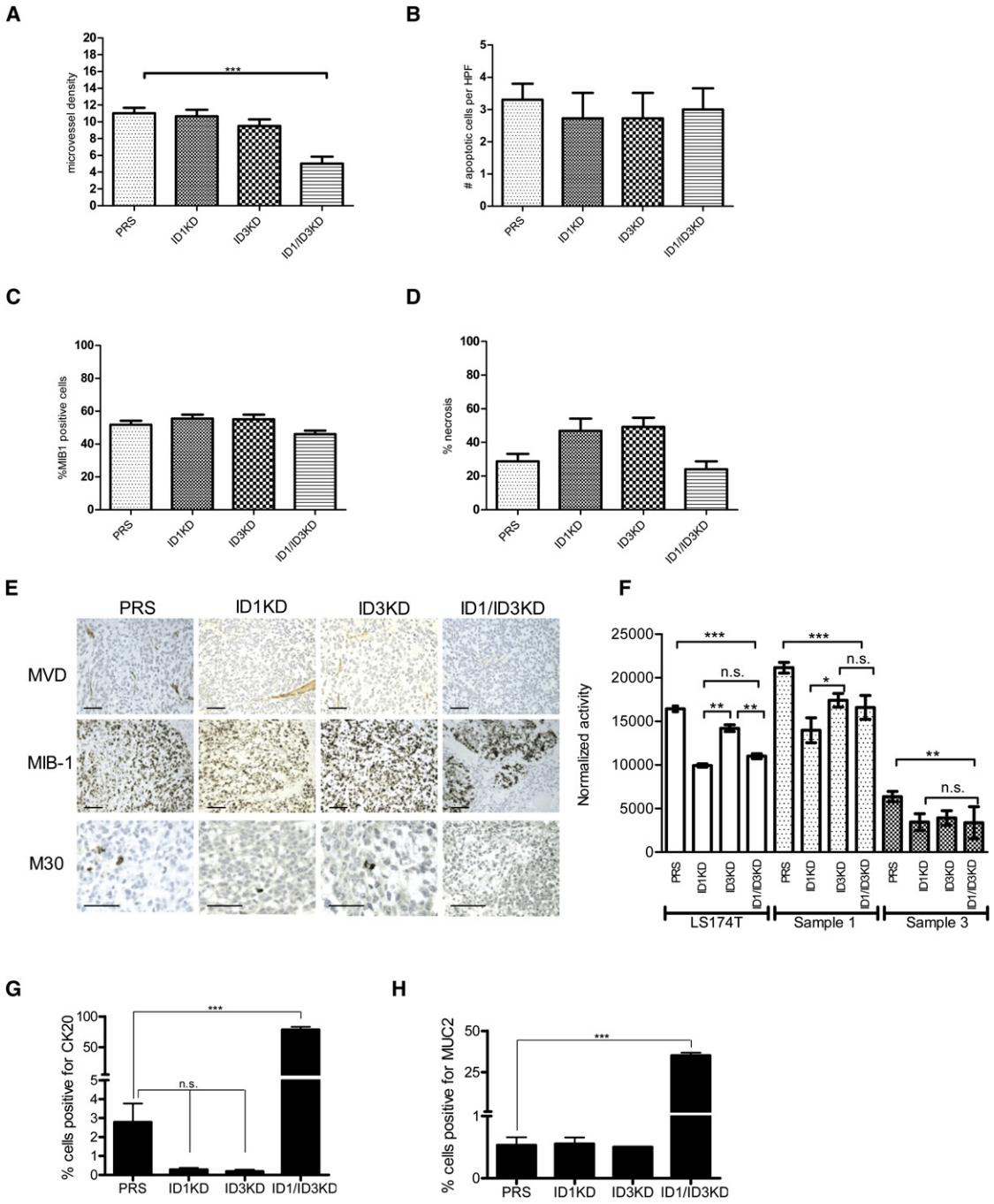

Figure 3. Effect of ID1/ID3KD on Xenograft Histology

(A–D) Quantification of MVD by CD31 staining (A), apoptosis by M30 staining (B), proliferation index by MIB1 staining (C), and percent necrosis (D) are shown.

(E) Histological depiction of the staining (magnification 200×) is illustrated; scale bars represent 50 μm.

(F) Proliferative activity of the PRS and ID1/ID3KD cells for LS174T, sample 1 and 3, is presented.

(G and H) Quantification of CK20 (G) and MUC2 (H) staining is shown.

The histological data are displayed as the mean per high-power field, with ten high-power fields counted per slide, and all error bars represent ± SEM. ***$p < 0.0001$, **$p < 0.001$, *$p < 0.01$. n.s., not significant.

See also Figure S3.

differentiation markers: Muc2 (van de Wetering et al., 2002), and cytokeratin 20 (CK20) (Vermeulen et al., 2008). There was increased expression of differentiation markers in the ID1/ID3KD xenografts, which was not seen in the individual KD or control groups (Figures 3G, 3H, and S3B). This implies that the induction of differentiation is a potential mechanism through

A

CC-IC enriched cultures	Control PRS SRF In Vitro LDA	ID1KD SRF In Vitro LDA	ID3KD SRF In Vitro LDA	ID1/ID3KD SRF In Vitro LDA
Sample 1	1 in 15 (7-33)	1 in 24 (13-45)	1 in 19 (5-58)	1 in 10349 (7923-18209)
Sample 2	1 in 29 (13-51)	1 in 46 (31-75)	1 in 22 (11-43)	1 in 20107 (12497-35280)
Sample 3	1 in 429 (231-657)			1 in 44290 (36518-59173)
LS174T	1 in 39 (24-70)	1 in 62 (34-89)	1 in 25 (11-67)	1 in 3139 (1906-5188)

B

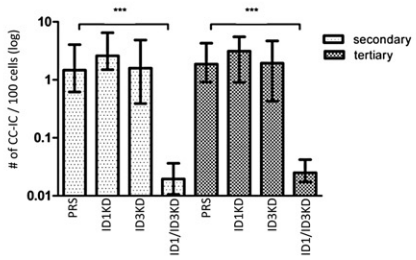

C

CC-IC enriched cultures	Control PRS PKH26$^+$ SRF In Vitro LDA	Control PRS PKH26$^-$ SRF In Vitro LDA	ID1/ID3KD PKH26$^+$ SRF In Vitro LDA	ID1/ID3KD PKH26$^-$ SRF In Vitro LDA
Sample 1	1 in 1.2 (1.1-1.4)	1 in 417 (281-619)	1 in 3.9 (2.7-5.6)	0
LS174T	1 in 1.4 (1.2-1.9)	1 in 265 (172-408)	1 in 2.4 (1.6-3.4)	1 in 75876 (34197-168352)

D

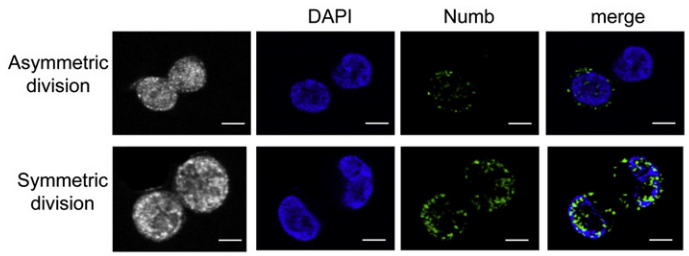

E

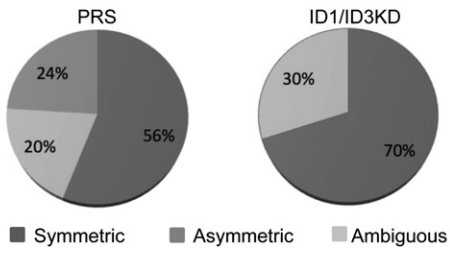

Figure 4. ID1/ID3KD Impairs CC-IC Self-Renewal

(A) Comparison of the sphere-replating frequency (SRF) for PRS, ID1KD, ID3KD, and ID1/ID3KD, as determined by in vitro LDAs, is shown; 95% CI is shown in parentheses.

(B) In vivo serial transplantation assays of LS174T cells derived from PRS, ID1KD, ID3KD, or ID1/ID3KD xenografts are presented.

(C) Comparison of the sphere-replating frequency (SRF) for the PKH26$^+$ and PKH26$^-$ subsets of PRS and ID1/ID3KD cells is shown; in parentheses is the 95% CI.

(D) Confocal images of symmetric and asymmetric division in PKH26$^+$ cells derived from sample 1 are presented: gray scale overlay, DAPI, Numb, and merge (magnification 60×); scale bars represent 10 μm.

(E) Determination of percent asymmetric, symmetric, and ambiguous cell divisions in the PRS and ID1/ID3KD groups (n = 100 cells counted: 50 cells per sample with 2 samples analyzed) is illustrated.

Error bars represent 95% CI. See also Figure S4.

which ID1/ID3KD is exerting its effect (Nam and Benezra, 2009; Anido et al., 2010).

ID1/ID3KD Impairs CC-IC Tumor-Initiating Capacity

To determine whether ID1/ID3KD was affecting the capacity of serial sphere formation, experiments were undertaken where clonally derived primary cells were replated at limiting dilution into secondary sphere-forming assays. The mean sphere-forming capacity decreased on average 300-fold in the ID1/ID3KD versus the other groups (Figures 4A and S4A). These results suggested that ID1 and ID3 together play an essential role in the ability of CC-ICs to sustain propagation through a self-renewal-like mechanism. Despite showing a functional loss of serial sphere formation in the ID1/ID3KD group, we did not identify a significant change in the CD133 or CD44 expression status either in vitro or in vivo (data not shown). Thus, serial sphere formation remains a functional definition, which may or may not be reflected in the phenotypic profile.

To conclusively establish that ID1 and ID3 were affecting the capacity for serial tumor initiation of CC-ICs at the clonal level, in vivo secondary and tertiary transplantation studies were carried out (Figures 4B and S4B). This work could only be carried out using LS174T because the remaining samples did not yield primary tumors in the ID1/ID3KD group (Figures 2E–2G). There was a 200-fold decrease in tumor reinitiation capacity in the ID1/ID3KD group, a difference that was maintained upon multiple passages (Figure 4B). To ensure that KD was maintained, westerns were carried out on the ID1/ID3KD xenograft cells prior to passage (Figure S2C). The decreased capacity for serial tumor initiation was only observed in the ID1/ID3KD group (Figure 4B). Because the in vitro proliferative capacity was equally reduced in all three experimental groups (Figure 3F), our results suggest that the major effect of ID1/ID3KD is not through impaired proliferation but rather through inhibition of the serial tumor initiation capacity of CC-ICs.

ID1/ID3KD Influences Asymmetric Cell Division

The profound loss of CC-ICs and the direct effects we observed on tumor initiation prompted us to determine whether ID1 and ID3 were influencing the asymmetric versus symmetric fates of

the daughter cells derived when CC-ICs divided. However, the ability to address this question was dependent on finding a method to purify the CC-IC fraction. The CC-IC-enriched cultures were labeled with PKH26, a lipophilic fluorescent dye, which labels relatively quiescent cells within a bulk population (Cicalese et al., 2009; Pece et al., 2010). We found that human colon cancer contains a small population of slowly dividing cells that retain the PKH26 dye and are enriched for CC-ICs, whereas the majority of the cells that progressively lose the dye through proliferation are depleted of CC-IC function. The $PKH26^+$ population was significantly higher in the control (4.5% ± 1.7%) versus ID1/ID3KD (0.5% ± 0.3%) group, suggesting that there were fewer label-retaining cells in the ID1/ID3KD group (Figure S4C). To determine if this correlated with the frequency of sphere-forming cells, in vitro serial-replating LDAs were carried out using flow-sorted $PKH26^+$ and $PKH26^-$ cell subsets for both control and ID1/ID3KD cells. For the control group the sphere-initiating frequency was 1 in 1.2–1.4 in the $PKH26^+$ cells, representing a significant enrichment over bulk cultures, much better than established cell surface markers (CD133 and CD44). The frequency of sphere-initiating cells in the $PKH26^-$ fraction was significantly lower (1 in 265–417) than the $PKH26^+$ fraction. In the ID1/ID3KD group, sphere-initiating cells were only detected in the $PKH26^+$ subset with a frequency of approximately 1 in 2.4–3.9 (Figure 4C). There were no sphere-initiating cells detected in the ID1/ID3KD $PKH26^-$ subset for sample 1; however, in LS174T there were very rare (1 in 75,876) sphere-initiating cells at (Figure 4C).

We hypothesized that the difference in the initiating capacity and PKH26 labeling in the ID1/ID3KD versus control group was related to a shift in the proportion of symmetric versus asymmetric cell divisions. To further investigate this possibility, Numb was utilized as a marker of asymmetric cell division (Cicalese et al., 2009; Pece et al., 2010; Kharas et al., 2010). $PKH26^+$ cells from each group were stained for Numb expression to determine the dominant mode of cell division (Figure 4D). The control cells underwent both asymmetric and symmetric divisions at a frequency of 24% and 56%, respectively. In contrast in the ID1/ID3KD group approximately 70% of dividing cells displayed equal distribution of Numb, with 30% of the cell divisions being ambiguous (Figure 4E). In the cells undergoing symmetric division, approximately 90% of the daughter cells expressed CK20 (Figure S4D), a marker of colon cancer differentiation; in the remaining 10% approximately half was weakly positive, and the remainder was negative. This result suggests that the majority of cell divisions that the ID1/ID3KD cells undergo are symmetric giving rise to two differentiated progeny. Collectively, this work along with our functional serial tumor initiation experiments provide strong support that ID1/ID3 is governing CC-IC stem cell functions.

ID1/ID3KD Increases Sensitivity to Oxaliplatin

The chemoresistance of C-ICs has emerged as an important cellular property that enables tumors to regrow following initial cytoreductive therapy. Prior literature has identified a potential role for ID1 in maintaining the chemoresistance of cancer cells in a variety of solid tumors; however, to our knowledge, no such data exist for colon cancer (Cheung et al., 2004). Oxaliplatin is a chemotherapeutic agent commonly used in colon cancer therapy. In LS174T the IC_{50} for the control cells was approximately 200 μM oxaliplatin versus 50 μM in the ID1/ID3KD group; similar results were obtained with sample 2 (Figures 5A and 5B). The enhanced chemosensitivity was also reflected in the approximate 2-fold increase in apoptotic cells following oxaliplatin exposure (IC_{50}), as determined by both annexinV and cleaved caspase-3 staining (Figures 5C–5E). To determine whether oxaliplatin had any effect on in vitro propagation of CC-ICs, sphere-replating assays were carried out in the presence of oxaliplatin. In vitro treatment of the control transduced cells with oxaliplatin (IC_{50}) did not significantly change sphere-replating capacity. In contrast the ID1/ID3KD cells displayed a further 5-fold decrease in sphere-replating capacity following treatment (Table 1; Figure 5F). To determine if this result could be translated to an in vivo model, xenograft studies were carried out with ongoing oxaliplatin treatment to transplanted mice (LS174T). Despite a highly significant decrease in tumor growth in the ID1/ID3KD versus control groups, the addition of oxaliplatin led to a further significant decrease in mean tumor weight (Figure 5G). There was no significant difference in the tumor weights in the oxaliplatin versus vehicle-treated control groups. This was likely related to the dose of oxaliplatin; however, due to toxicity in immune-deficient mice. we were unable to increase the dose. Nevertheless, even in the absence of an objective tumor response in the control group, our results demonstrated a further decrease in xenograft formation in the ID1/ID3KD oxaliplatin-treated group as compared to the vehicle-treated ID1/ID3KD group, indicating that ID1/ID3KD was potentiating tumor cell killing.

ID1/ID3KD Decreases Tumor-Initiating Capacity through Downregulation of p21

To further delineate the molecular machinery by which ID1/ID3 affects tumor-initiating capacity, we investigated a known target, p21. ID1-mediated repression of p21 represents a mechanism to preserve self-renewal capacity in endothelial progenitor cells (Ciarrocchi et al., 2007). Our interest was to determine whether p21, a cell-cycle inhibitor, was playing a similar role in CC-ICs. Interestingly, western blot analysis in the CC-IC lines revealed that p21 expression levels in vitro were high in the parental and control transduced cells but undetectable in the ID1/ID3KD cells (Figure 6A); the exact opposite of the pattern reported in endothelial progenitor cells (Ciarrocchi et al., 2007). Examination of *p21* expression by qPCR revealed a trend toward increased expression in the $CD133^+$ versus $CD133^-$ subsets; however, this did not reach statistical significance. No difference was detected in the level of *p21* mRNA expression in the $CD44^+$ and $CD44^-$ fractions (Figure 6B). Evaluation of p21 protein expression using immunohistochemistry revealed clearly higher levels in both the $CD133^+$ and $CD44^+$ fractions, as compared to their negative counterparts (Figure 6C). From these results we can infer that the effect of ID1/ID3 on p21 is likely through stabilization of the protein as opposed to regulation at a transcriptional level.

In contrast to endothelial progenitor cells, silencing of p21 in leukemic and normal hematopoietic cells impairs stem cell self-renewal (Cheng et al., 2000; Viale et al., 2009), although, to our knowledge, no studies have explored lowered p21 expression in the context of ID1/ID3KD. To determine whether the

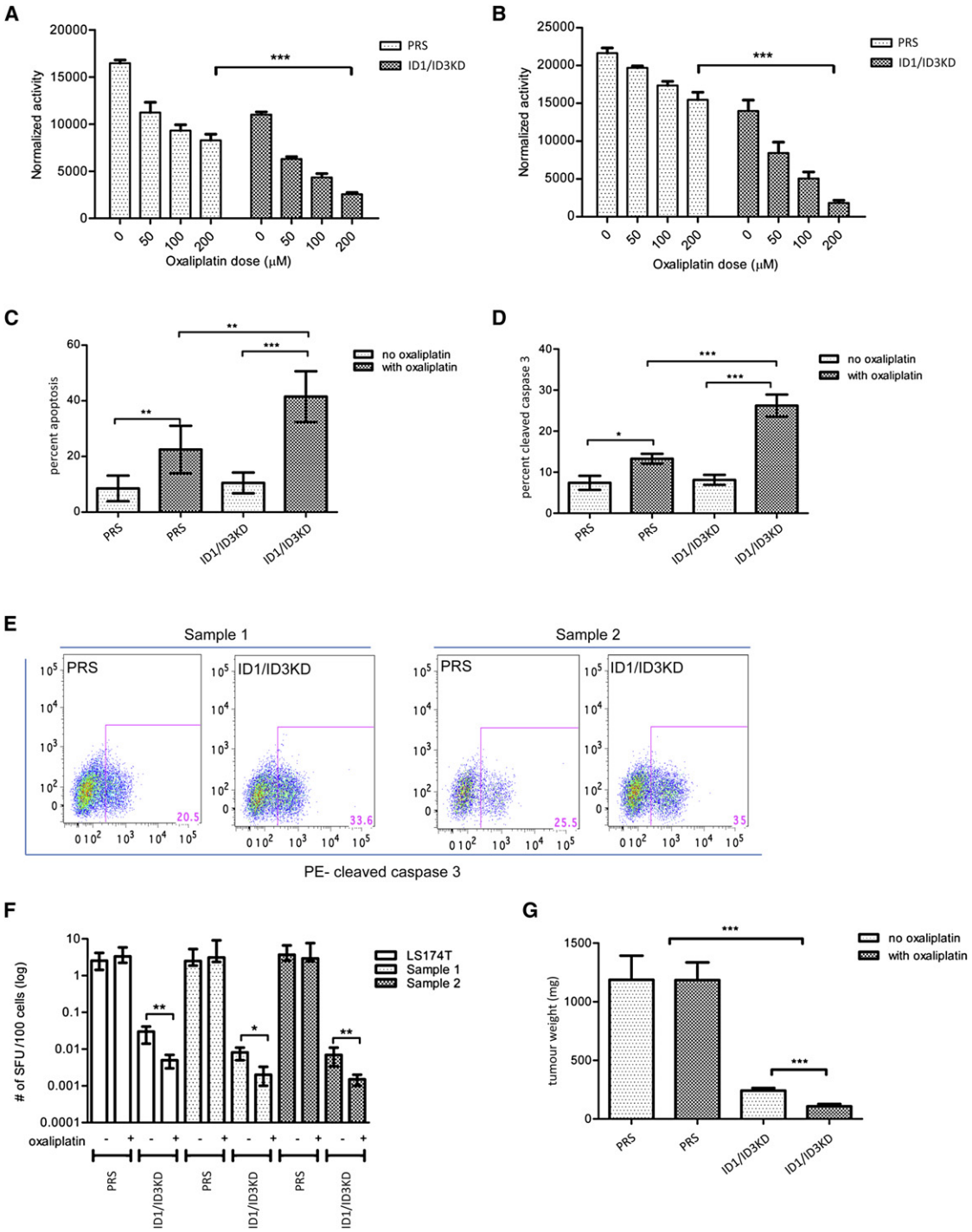

Figure 5. ID1/ID3KD Increases the Sensitivity of CC-ICs to Oxaliplatin

(A and B) Proliferation analysis following a 48 hr oxaliplatin exposure for LS174T and sample 2 (mean ± SEM) is illustrated.

(C) Percent apoptotic cells as measured by annexin V analysis (mean ± SEM) is shown.

(D) Cleaved caspase-3 staining (mean ± SEM) is presented.

(E) Cleaved caspase-3 FACS plots of oxaliplatin-treated ID1/ID3KD and PRS cells from sample 1 and 2 (C–E n = 10 per group) is illustrated.

(F) LDA analysis of SFUs after exposing ID1/ID3KD cells to oxaliplatin (IC_{50}) is shown; error bars represent 95% CI.

(G) Tumor weight following oxaliplatin treatment is presented. PRS or ID1/ID3KD LS174T cells were injected s.c. and the tumors allowed to grow until 0.5 cm^3; mice were then treated with oxaliplatin (mean ± SD).

***$p < 0.0001$, **$p < 0.001$, *$p < 0.01$.

Table 1. Comparison of the SRF for the Control versus ID1/ID3KD Cells in the Presence and Absence of Oxaliplatin

CC-IC-Enriched Cultures	PRS SRF In Vitro LDA	PRS with Oxaliplatin SRF In Vitro LDA	ID1/ID3KD SRF In Vitro LDA	ID1/ID3KD with Oxaliplatin SRF In Vitro LDA
Sample 1	1 in 40 (19–53)	1 in 32 (11–43)	1 in 12,392 (9,048–20,810)	1 in 52,379 (30,007–75,228)
Sample 2	1 in 27 (15–39)	1 in 34 (13–41)	1 in 14,740 (8,660–29,105)	1 in 64,399 (49,583–79,332)
LS174T	1 in 39 (24–70)	1 in 30 (17–45)	1 in 3,493 (2,400–6,930)	1 in 19,215 (13,901–28,985)

All data are represented as the SRF for each group; the 95% CI is shown in parentheses.

decreased expression of p21 observed in the ID1/ID3KD group was playing a functional role in maintaining tumor-initiating capacity, a genetic rescue experiment was designed to reintroduce p21 into the ID1/ID3KD cells. Sample 2 and LS174T were tested by in vivo xenograft formation; ID1/ID3KD/p21 overexpressing (OE) xenografts were significantly larger than those generated by injection of ID1/ID3KD cells alone, although they remained significantly smaller than controls (Figures 6D and 6E). This partial rescue of tumor formation indicated that the decreased expression of p21 in the ID1/ID3KD cells was functionally important for tumor initiation and maintenance. Secondary LDA experiments revealed a sustained increase in CC-IC frequency in the ID1/ID3KD/p21OE cells as compared to ID1/ID3KD alone (Figure 6F), establishing that CC-IC sustainability is affected by p21. Our preliminary data suggest that one possible mechanism by which ID1/ID3 may influence p21 protein stability is through inhibitory effects on phosphatase and tensin homolog (PTEN). Genetic KD of ID1/ID3 in our model system results in the re-expression of PTEN at the protein level (Figure S2D). Our results lend additional support to the notion that the ID/p21 regulatory axis is important in tumor initiation and warrants further investigation, including confirmation of the role of PTEN.

Effect of ID1/ID3KD on Cell Cycle and Accumulation of DNA Damage-Induced Foci

It is well established that p21 inhibits cell-cycle progression by binding to G1 cyclin/CDK complexes (Abbas and Dutta, 2009). Because p21 protein expression was decreased following ID1/ID3KD, it was important to determine whether this reflected a change in cell-cycle distribution. The mean proportion of cells in G0/G1 was significantly higher in the control versus ID1/ID3KD cells, whereas the opposite was observed for cells in S phase. There was no significant difference between the two groups in the proportion of cells in G2/M; however, there was a trend toward ID1/ID3KD having more cells in G2/M (Figure 7A). In support of the cell-cycle results, BrdU incorporation experiments demonstrated that the ID1/ID3KD group exhibited a 2- to 3-fold increase in BrdU incorporation, as compared to the control cells (Figures 7B and 7C). p21 has previously been shown to play a critical role in leukemia stem cell (LSC) maintenance, where it imposes a cell-cycle restriction that in turn acts to limit the accumulation of DNA damage in LSCs (Viale et al., 2009). In our samples there was an approximate 2-fold increase in γH2AX foci in the ID1/ID3KD versus control cells (Figures 7D and 7E). These results suggest that the reduced levels of p21 and the subsequent lack of cell-cycle restriction resulted in an accumulation of DNA damage leading to CC-IC exhaustion.

DISCUSSION

Our findings establish that ID1 and ID3 govern self-renewal of CC-ICs derived from primary colon cancer samples. Silencing both genes together resulted in a dramatic loss of tumor-initiating potential. Second, we found that ID1/ID3 orchestrate their regulation of CC-ICs via p21, providing a linkage of the ID1/ID3-p21 regulatory axis with maintenance of tumor initiation capacity in any solid tumor C-IC. Finally, we show that in the presence of oxaliplatin, a commonly used chemotherapeutic agent, ID1/ID3 functions to protect the tumor-initiating capacity of CC-ICs. Following ID1/ID3KD, exposure to oxaliplatin resulted in a further decrease in tumor-initiating capacity. Thus, our study connects the capacity for serial propagation of tumor-initiating cells with CC-IC chemoresistance, knowledge that could be exploited in future therapeutic strategies.

ID1/ID3 Govern Self-Renewal

As expected from studies of ID family proteins in other model systems, we observed effects on proliferation and angiogenesis upon silencing of ID1 and ID3 individually or together. However, these effects alone could not explain the drastic decrease in xenograft growth observed in the ID1/ID3KD group. The ID proteins have a central role in maintaining cells in an immature state; in keeping with this the ID1/ID3KD group displayed increased expression of markers of intestinal cell differentiation, a finding that correlates with a decrease in self-renewal potential. Emerging data indicate that the *ID* genes play an important role in maintaining C-ICs in a variety of solid tumors (Hollnagel et al., 1999; Nam and Benezra, 2009; Perry et al., 2007). Most recently, Andio et al. reported that TGF-β-induced inhibition of $CD44^+$ glioblastoma-initiating cells was due to repression of ID1 and ID3, pointing to a potential link between ID genes and C-IC self-renewal (Anido et al., 2010). Our data support this prior work by providing direct evidence that ID1/ID3 govern CC-IC maintenance.

Moreover, we demonstrate that ID1/ID3KD dramatically alters the ratio of asymmetric and symmetric cell divisions in the CC-IC fraction. This provides another line of evidence linking ID1/ID3 with canonical stem cell properties. Numb staining of $PKH26^+$ control cells suggested that these cells normally undergo both asymmetric and symmetric cell divisions. In contrast following ID1/ID3KD the majority of divisions became symmetric, giving rise to two daughter cells both displaying evidence of differentiation, as demonstrated by increased CK20 staining. These results are in keeping with prior studies in normal neural stem cells where high ID1 expression drove self-renewal by promoting asymmetric cell division (Nam and Benezra, 2009). They found that ID1 was expressed as a gradient with the highest levels in

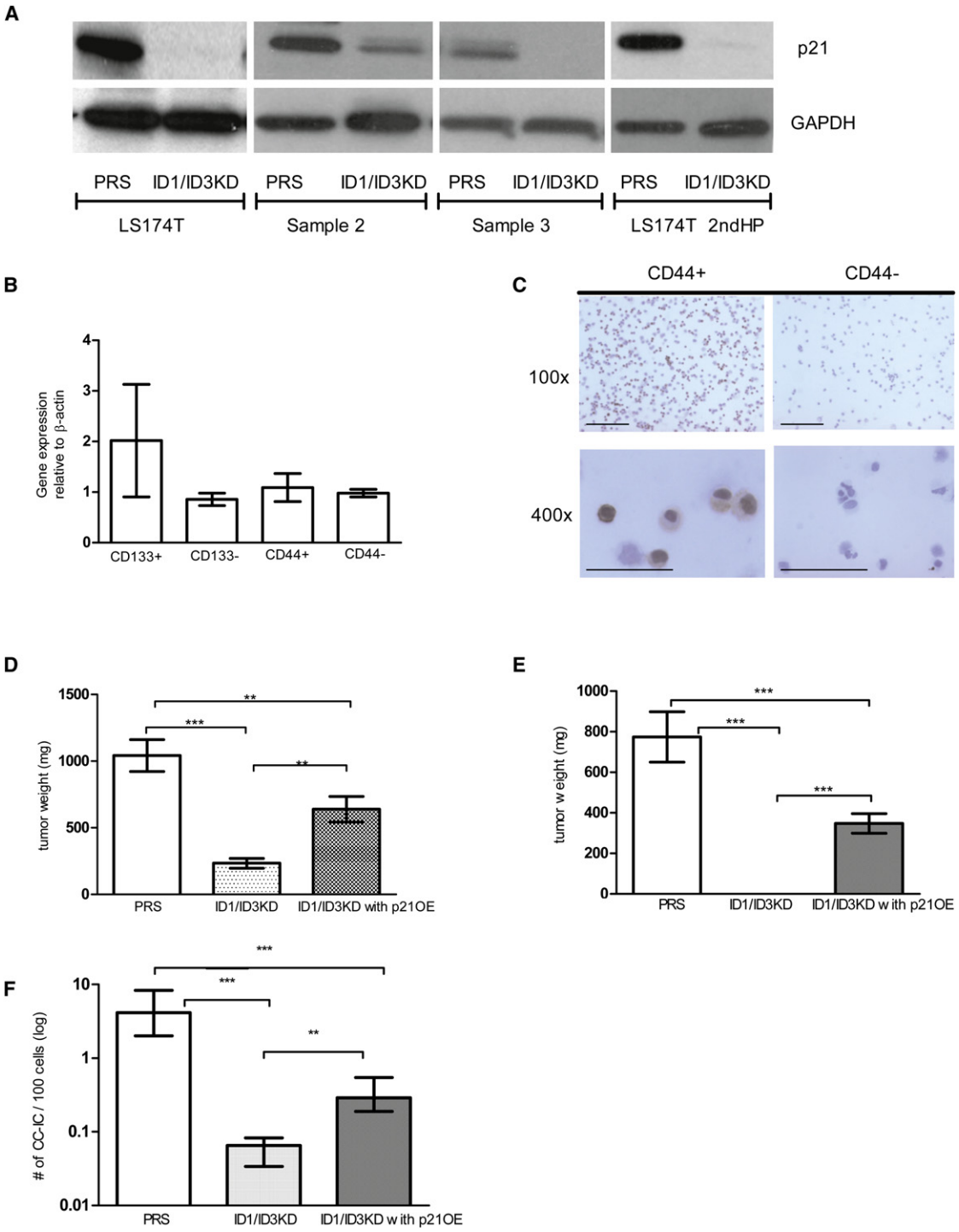

Figure 6. ID1/ID3KD Decreased the Self-Renewal Capacity of CC-IC through p21 Downregulation

(A) Western blot analysis of p21 protein levels in PRS versus ID1/ID3KD cells is presented. Displayed are LS174T, samples 1 and 2, and LS174T transduced with second set of ID1/ID3KD hairpins. GAPDH was utilized as the housekeeping gene.

(B) p21 mRNA expression in CC-IC-enriched and nonenriched fractions (n = 3 replicates) is shown; error bars indicate ± SEM.

(C) Immunohistochemical staining for p21 on $CD44^{+}$ and $CD44^{-}$ cell subsets is illustrated. Top scale bars (100×) represent 100 μm; bottom scale bars (400×) represent 50 μm.

(D and E) Tumor weights for LS174T and sample 2, and three groups, PRS, ID1/ID3KD, and ID1/ID3KD with p21 overexpression (ID1/ID3KDp21OE), are presented. In both samples expression of p21 partially rescued the effect of ID1/ID3KD on xenograft growth; mean ± SD is shown (n = 20 injections per group).

(F) In vivo secondary transplantation LDA with LS174T.

Error bars represent 95% CI. ***$p < 0.0001$, **$p < 0.001$.

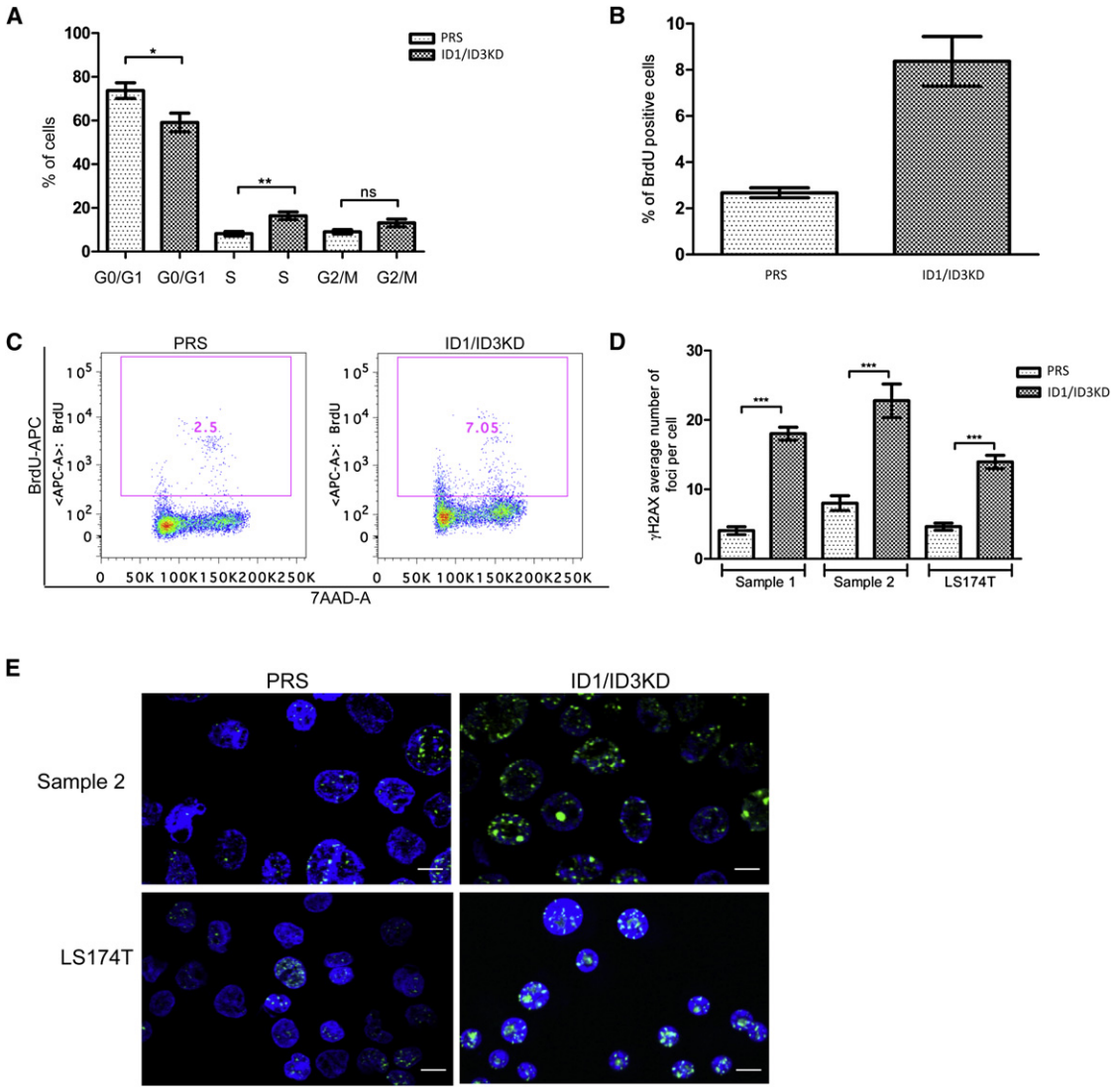

Figure 7. Effect of ID1/ID3KD on Cell Cycle and DNA Damage

(A) Cell-cycle distribution was determined by flow cytometry (n = 3 replicates).

(B and C) BrdU incorporation analysis (n = 3 replicates) is illustrated.

(D) Quantification of γH2AX staining (n = 100 cells counted) is shown.

(E) Confocal images of γH2AX staining (×60) are presented; scale bars represent 10 μm.

For bar graphs, mean ± SEM is shown; ***p < 0.0001, **p < 0.001, *p < 0.01. ns, not significant.

self-renewing neural stem cells and the lower levels in non-stem cells correlating with increased expression of markers of neural cell differentiation (Nam and Benezra, 2009). Similarly, CC-IC confocal imaging of ID1 and ID3 in our PKH26$^+$ and PKH26$^-$ colon cancer cells demonstrated ID1/ID3 staining in both subsets; however, the expression level appeared higher in the PKH26$^+$ cells, as compared to the PKH26$^-$ cells (data not shown). It is possible that, similar to neural stem cells (Nam and Benezra, 2009), ID expression may be on a continuum where colon cancer cells expressing the highest combined levels have the capacity to initiate tumors. Our work, as well as that of others, clearly indicates that ID1/ID3 play a central role in both normal stem cell and C-IC maintenance, making it essential that the molecular mechanisms driving this process are better understood.

ID1/ID3 Function through Effects on p21

We initially hypothesized that the mechanism by which ID1/ID3KD was decreasing tumor-initiating capacity may be similar to the effect observed in endothelial progenitor cells where ID1KD resulted in increased p21 levels and a subsequent decrease in self-renewal capacity (Ciarrocchi et al., 2007). Unexpectedly, we observed the exact opposite: p21 was highly expressed in the parental and control transduced cells, whereas the ID1/ID3KD cells displayed an almost complete loss of p21 expression in all samples tested. Moreover, CD133$^+$ and

$CD44^+$ CC-IC-enriched fractions expressed significantly higher p21 protein levels as compared to their negative counterparts. This result suggests that in the context of CC-ICs, p21 may function to maintain ID1/ID3-dependent tumor-initiating potential.

Interestingly, an association between ID1 overexpression and high levels of p21 was initially identified in a mouse mammary carcinoma model that showed ID1 overexpression resulted in tumors that continued to proliferate despite high levels of p21 (Swarbrick et al., 2008). These authors hypothesized that ID1 must act downstream of p21, rendering cells refractory to p21-dependent cell-cycle arrest. However, this was not the case in our colon cancer samples because the reintroduction of p21 resulted in a partial rescue of the ID1/ID3KD-induced tumor-initiating defect, providing strong genetic evidence that p21 plays a functional role in maintaining CC-ICs. One possible explanation for the rescue only being partial is that the effect of ID1/ID3 on proliferation is independent of their combined effects on p21 and self-renewal. Each of the ID1KD, ID3KD, and ID1/ID3KD groups exhibited an approximate 2-fold decrease in proliferative capacity, yet the effect on self-renewal was only seen in the ID1/ID3KD cells. Alternatively, ID1/ID3KD may have influenced other downstream pathways in addition to p21 that are involved in the maintenance of CC-ICs. Studies of a variety of normal and neoplastic stem cell systems are pointing to the integrated functioning of multiple genetic and epigenetic components working together to maintain self-renewal potential (Morrison and Spradling, 2008; Shackleton et al., 2009; He et al., 2009).

One possible mechanism by which ID1/ID3 may regulate p21 is through inhibition of PTEN. Lee et al. have previously shown that ID1 can negatively regulate PTEN at a transcriptional level in MCF7 human breast cancer cells (Lee et al., 2009). Furthermore, attenuation of PTEN has been shown to increase p21 levels through stabilization of the protein (Lin et al., 2007). Our preliminary data also show that ID1/ID3KD results in the re-expression of PTEN. In renal cell carcinoma, p21 stabilization is one of the key mechanisms by which PTEN-deficient tumors escape chemotherapy-induced cell death (Lin et al., 2007). The notion that p21, a cell-cycle inhibitor, is maintaining self-renewal seems counterintuitive. However, there is strong evidence from murine models of normal hematopoietic and leukemic stem cells that p21 is an important regulator of self-renewal. In the absence of p21, hematopoietic and leukemic stem cells underwent functional exhaustion and were unable to maintain the clone (Cheng et al., 2000; Viale et al., 2009).

Our results support a role for p21 in the prevention of CC-IC exhaustion through cell-cycle restriction and the resulting accumulation of DNA damage as shown by increased γH2AX foci. These results are consistent with a number of publications over the past 20 years that have recognized a role for p21 in the protection of cancer cells from stress and DNA damage (Mahyar-Roemer and Roemer, 2001; Bene and Chambers, 2009; Gorospe et al., 1996; Sharma et al., 2005; Tian et al., 2000). Bunz et al. (1998) were the first to demonstrate that $p21^{-/-}$ colon cancer cells treated with a DNA-damaging agent undergo aberrant progression through S and M phases of the cell-cycle-triggering apoptosis. Also in support of our findings, there are numerous reports linking p21 expression with protection of colon cancer cells from apoptosis induced by a wide range of insults, including exposure to radiation (Tian et al., 2000), chemotherapeutic agents (Mahyar-Roemer and Roemer, 2001; Bene and Chambers, 2009), and cryotherapy (Sharma et al., 2005). Finally, clinical trial data from patients with rectal tumors undergoing neoadjuvant chemoradiation show association between increased p21 expression and the development of resistance resulting in decreased disease-specific survival (Kuremsky et al., 2009; Rau et al., 2003). Taken together, these observations support the clinical relevance of our findings and extend the functional roles of p21 to include preservation of CC-IC self-renewal.

Role of ID1/ID3 in Chemoresistance

Our studies also provide a direct link between the capacity of CC-ICs for serial tumor initiation and chemoresistance. Although existing literature supports a role for ID1 and p21 in maintaining chemoresistance in some solid tumors (Cheung et al., 2004; Hu et al., 2009; Li et al., 2007), to our knowledge, the effect of ID1/ID3KD on colon cancer cells and their response to treatment with oxaliplatin has not been investigated. We found that the dose of oxaliplatin that reduced overall cell proliferation did not inhibit the sphere-replating capacity of control transduced cells. This finding may in part explain clinical observations related to oxaliplatin treatment. When oxaliplatin is used in the adjuvant setting with 5-fluorouracil (5-FU), the tumor response rates are in the range of 40%–50%, whereas the actual survival advantage conferred is on average less than 10% (Alberts and Wagman, 2008; Chau and Cunningham, 2009). This suggests that the response rates may actually be monitoring decreased proliferative capacity of the bulk cancer cells; however, if there are CC-ICs surviving despite oxaliplatin treatment, the drug may not affect their function. In contrast, oxaliplatin treatment of ID1/ID3KD cells decreased tumor initiation capacity, which warrants further investigation of the linkage between CC-ICs and chemoresistance. If this linkage is universally important, then understanding the mechanisms that drive C-IC self-renewal will lead to the development of therapeutic agents that target this essential aspect of tumor maintenance and may potentiate the efficacy of chemotherapies.

In conclusion our study demonstrates the feasibility of utilizing primary human cancer cells to enrich for CC-IC activity thereby providing a powerful tool to carry out genetic approaches to unravel the molecular pathways sustaining tumor growth. Our findings point to the central role that ID1/ID3 and p21 play in regulating the tumor-initiating program of CC-ICs and in governing their response to chemotherapy. Collectively, our findings put forth self-renewal pathways as potential targets for the development of effective therapies to eradicate CC-ICs.

EXPERIMENTAL PROCEDURES

Culture and Xenografting of Colon Cancer Cells

Human colon cancer specimens were obtained with informed patient consent as approved by the Research Ethics Board (University Health Network, Toronto). Cells were isolated and cultured in DMEM/F-12 with EGF and bFGF as previously described by Kreso and O'Brien (2008). Unless otherwise noted, tumor cells were injected s.c. into NOD/SCID mice using procedures that conform to the standards approved by the Animal Care Committee (Ontario Cancer Institute, Toronto).

Viral Vectors

Short hairpins to ID1 and ID3 were obtained from Dr. J. Massague (Memorial Sloan-Kettering Cancer Center) (Gupta et al., 2007). Dr. J. Moffat (University of Toronto) provided a second set of hairpins to ensure that the effects were not off target. For combined KD, cells were sequentially infected and puromycin selected. For p21 overexpression a pBabe construct (Dr. G. Peters) was utilized for both overexpression and control viruses.

LDAs

Viable cells were diluted, and defined cell doses were (i) injected into mice to assess CC-IC frequency in vivo and (ii) plated in 96-well plates to assess the number of sphere-forming units (SFUs) in vitro. The ELDA website was used to determine the estimated cell frequency (http://bioinf.wehi.edu.au/software/elda/index.html). For in vitro LDAs a number of cell doses were tested, and the lowest cell dose was one cell per well, all plated in a fixed volume of 200 μl per well. Any well with one or more spheres was considered positive for ELDA. To assess the number of colony-forming units (CFUs), similar methods were used, but cells were plated in medium containing 10% serum.

Statistical Analysis

PRISM software was used to analyze results; values are reported as mean ± SD unless otherwise indicated. The limiting dilution function (http://bioinf.wehi.edu.au/software/elda/index.html) was used to calculate the estimated cell frequencies for LDAs; 95% confidence intervals (CIs) are reported for each frequency.

SUPPLEMENTAL INFORMATION

Supplemental Information includes four figures, five tables, and Supplemental Experimental Procedures and can be found with this article online at doi:10.1016/j.ccr.2012.04.036.

ACKNOWLEDGMENTS

We would like to thank Eric Lechman, Faiyaz Notta, Elisa Laurenti, and Michael Milyavsky for their critical review of this manuscript; Fanong Meng, Mayleen Sukhram, and Viktor Son for providing colon cancer samples; PRP for assistance with immunohistochemistry; and Shane Harding, Peter Dirks, and Ian Clarke for their assistance with planning experiments. This work was supported by funds from the Krandel Fund at Princess Margaret Hospital, Genome Canada through the Ontario Genomics Institute, Ontario Institute for Cancer Research and a Summit Award with funds from the province of Ontario, the Canadian Institutes for Health Research, and a Canada Research Chair. This research was funded in part by the Ontario Ministry of Health and Long Term Care (OMOHLTC). The views expressed do not necessarily reflect those of the OMOHLTC.

Received: March 4, 2010
Revised: September 14, 2011
Accepted: April 23, 2012
Published: June 11, 2012

REFERENCES

Abbas, T., and Dutta, A. (2009). p21 in cancer: intricate networks and multiple activities. Nat. Rev. Cancer *9*, 400–414.

Alberts, S.R., and Wagman, L.D. (2008). Chemotherapy for colorectal cancer liver metastases. Oncologist *13*, 1063–1073.

Al-Hajj, M., and Clarke, M.F. (2004). Self-renewal and solid tumor stem cells. Oncogene *23*, 7274–7282.

Al-Hajj, M., Wicha, M.S., Benito-Hernandez, A., Morrison, S.J., and Clarke, M.F. (2003). Prospective identification of tumorigenic breast cancer cells. Proc. Natl. Acad. Sci. USA *100*, 3983–3988.

Anido, J., Sáez-Borderías, A., Gonzàlez-Juncà, A., Rodón, L., Folch, G., Carmona, M.A., Prieto-Sánchez, R.M., Barba, I., Martínez-Sáez, E., Prudkin, L., et al. (2010). TGF-β receptor inhibitors target the CD44(high)/Id1(high) glioma-initiating cell population in human glioblastoma. Cancer Cell *18*, 655–668.

Bao, S., Wu, Q., McLendon, R.E., Hao, Y., Shi, Q., Hjelmeland, A.B., Dewhirst, M.W., Bigner, D.D., and Rich, J.N. (2006). Glioma stem cells promote radioresistance by preferential activation of the DNA damage response. Nature *444*, 756–760.

Bene, A., and Chambers, T.C. (2009). p21 functions in a post-mitotic block checkpoint in the apoptotic response to vinblastine. Biochem. Biophys. Res. Commun. *380*, 211–217.

Bonnet, D., and Dick, J.E. (1997). Human acute myeloid leukemia is organized as a hierarchy that originates from a primitive hematopoietic cell. Nat. Med. *3*, 730–737.

Bunz, F., Dutriaux, A., Lengauer, C., Waldman, T., Zhou, S., Brown, J.P., Sedivy, J.M., Kinzler, K.W., and Vogelstein, B. (1998). Requirement for p53 and p21 to sustain G2 arrest after DNA damage. Science *282*, 1497–1501.

Chau, I., and Cunningham, D. (2009). Treatment in advanced colorectal cancer: what, when and how? Br. J. Cancer *100*, 1704–1719.

Cheng, T., Rodrigues, N., Shen, H., Yang, Y., Dombkowski, D., Sykes, M., and Scadden, D.T. (2000). Hematopoietic stem cell quiescence maintained by p21cip1/waf1. Science *287*, 1804–1808.

Cheung, H.W., Ling, M.T., Tsao, S.W., Wong, Y.C., and Wang, X. (2004). Id-1-induced Raf/MEK pathway activation is essential for its protective role against taxol-induced apoptosis in nasopharyngeal carcinoma cells. Carcinogenesis *25*, 881–887.

Ciarrocchi, A., Jankovic, V., Shaked, Y., Nolan, D.J., Mittal, V., Kerbel, R.S., Nimer, S.D., and Benezra, R. (2007). Id1 restrains p21 expression to control endothelial progenitor cell formation. PLoS One *2*, e1338.

Cicalese, A., Bonizzi, G., Pasi, C.E., Faretta, M., Ronzoni, S., Giulini, B., Brisken, C., Minucci, S., Di Fiore, P.P., and Pelicci, P.G. (2009). The tumor suppressor p53 regulates polarity of self-renewing divisions in mammary stem cells. Cell *138*, 1083–1095.

Dalerba, P., Dylla, S.J., Park, I.K., Liu, R., Wang, X., Cho, R.W., Hoey, T., Gurney, A., Huang, E.H., Simeone, D.M., et al. (2007). Phenotypic characterization of human colorectal cancer stem cells. Proc. Natl. Acad. Sci. USA *104*, 10158–10163.

Dick, J.E. (2003). Stem cells: self-renewal writ in blood. Nature *423*, 231–233.

Dick, J.E. (2008). Stem cell concepts renew cancer research. Blood *112*, 4793–4807.

Dylla, S.J., Beviglia, L., Park, I.K., Chartier, C., Raval, J., Ngan, L., Pickell, K., Aguilar, J., Lazetic, S., Smith-Berdan, S., et al. (2008). Colorectal cancer stem cells are enriched in xenogeneic tumors following chemotherapy. PLoS One *3*, e2428.

Fong, S., Itahana, Y., Sumida, T., Singh, J., Coppe, J.P., Liu, Y., Richards, P.C., Bennington, J.L., Lee, N.M., Debs, R.J., and Desprez, P.Y. (2003). Id-1 as a molecular target in therapy for breast cancer cell invasion and metastasis. Proc. Natl. Acad. Sci. USA *100*, 13543–13548.

Fong, S., Debs, R.J., and Desprez, P.Y. (2004). Id genes and proteins as promising targets in cancer therapy. Trends Mol. Med. *10*, 387–392.

Gorospe, M., Wang, X., Guyton, K.Z., and Holbrook, N.J. (1996). Protective role of p21(Waf1/Cip1) against prostaglandin A2-mediated apoptosis of human colorectal carcinoma cells. Mol. Cell. Biol. *16*, 6654–6660.

Gray, M.J., Dallas, N.A., Van Buren, G., Xia, L., Yang, A.D., Somcio, R.J., Gaur, P., Mangala, L.S., Vivas-Mejia, P.E., Fan, F., et al. (2008). Therapeutic targeting of Id2 reduces growth of human colorectal carcinoma in the murine liver. Oncogene *27*, 7192–7200.

Gupta, G.P., Perk, J., Acharyya, S., de Candia, P., Mittal, V., Todorova-Manova, K., Gerald, W.L., Brogi, E., Benezra, R., and Massagué, J. (2007). ID genes mediate tumor reinitiation during breast cancer lung metastasis. Proc. Natl. Acad. Sci. USA *104*, 19506–19511.

He, S., Nakada, D., and Morrison, S.J. (2009). Mechanisms of stem cell self-renewal. Annu. Rev. Cell Dev. Biol. *25*, 377–406.

Hermann, P.C., Huber, S.L., Herrler, T., Aicher, A., Ellwart, J.W., Guba, M., Bruns, C.J., and Heeschen, C. (2007). Distinct populations of cancer stem cells

determine tumor growth and metastatic activity in human pancreatic cancer. Cell Stem Cell *1*, 313–323.

Hollnagel, A., Oehlmann, V., Heymer, J., Rüther, U., and Nordheim, A. (1999). Id genes are direct targets of bone morphogenetic protein induction in embryonic stem cells. J. Biol. Chem. *274*, 19838–19845.

Hope, K.J., Jin, L., and Dick, J.E. (2004). Acute myeloid leukemia originates from a hierarchy of leukemic stem cell classes that differ in self-renewal capacity. Nat. Immunol. *5*, 738–743.

Hu, H., Han, H.Y., Wang, Y.L., Zhang, X.P., Chua, C.W., Wong, Y.C., Wang, X.F., Ling, M.T., and Xu, K.X. (2009). The role of Id-1 in chemosensitivity and epirubicin-induced apoptosis in bladder cancer cells. Oncol. Rep. *21*, 1053–1059.

Huang, E.H., Hynes, M.J., Zhang, T., Ginestier, C., Dontu, G., Appelman, H., Fields, J.Z., Wicha, M.S., and Boman, B.M. (2009). Aldehyde dehydrogenase 1 is a marker for normal and malignant human colonic stem cells (SC) and tracks SC overpopulation during colon tumorigenesis. Cancer Res. *69*, 3382–3389.

Jankovic, V., Ciarrocchi, A., Boccuni, P., DeBlasio, T., Benezra, R., and Nimer, S.D. (2007). Id1 restrains myeloid commitment, maintaining the self-renewal capacity of hematopoietic stem cells. Proc. Natl. Acad. Sci. USA *104*, 1260–1265.

Kharas, M.G., Lengner, C.J., Al-Shahrour, F., Bullinger, L., Ball, B., Zaidi, S., Morgan, K., Tam, W., Paktinat, M., Okabe, R., et al. (2010). Musashi-2 regulates normal hematopoiesis and promotes aggressive myeloid leukemia. Nat. Med. *16*, 903–908.

Kleeff, J., Ishiwata, T., Friess, H., Büchler, M.W., Israel, M.A., and Korc, M. (1998). The helix-loop-helix protein Id2 is overexpressed in human pancreatic cancer. Cancer Res. *58*, 3769–3772.

Korkaya, H., Paulson, A., Charafe-Jauffret, E., Ginestier, C., Brown, M., Dutcher, J., Clouthier, S.G., and Wicha, M.S. (2009). Regulation of mammary stem/progenitor cells by PTEN/Akt/beta-catenin signaling. PLoS Biol. *7*, e1000121.

Kreso, A., and O'Brien, C.A. (2008). Colon cancer stem cells. Curr. Protoc. Stem Cell Biol. *7*, 3.1.1–3.1.12.

Kuremsky, J.G., Tepper, J.E., and McLeod, H.L. (2009). Biomarkers for response to neoadjuvant chemoradiation for rectal cancer. Int. J. Radiat. Oncol. Biol. Phys. *74*, 673–688.

Lee, J.Y., Kang, M.B., Jang, S.H., Qian, T., Kim, H.J., Kim, C.H., Kim, Y., and Kong, G. (2009). Id-1 activates Akt-mediated Wnt signaling and p27(Kip1) phosphorylation through PTEN inhibition. Oncogene *28*, 824–831.

Li, B., Cheung, P.Y., Wang, X., Tsao, S.W., Ling, M.T., Wong, Y.C., and Cheung, A.L. (2007). Id-1 activation of PI3K/Akt/NFkappaB signaling pathway and its significance in promoting survival of esophageal cancer cells. Carcinogenesis *28*, 2313–2320.

Lin, C.Q., Singh, J., Murata, K., Itahana, Y., Parrinello, S., Liang, S.H., Gillett, C.E., Campisi, J., and Desprez, P.Y. (2000). A role for Id-1 in the aggressive phenotype and steroid hormone response of human breast cancer cells. Cancer Res. *60*, 1332–1340.

Lin, P.Y., Fosmire, S.P., Park, S.H., Park, J.Y., Baksh, S., Modiano, J.F., and Weiss, R.H. (2007). Attenuation of PTEN increases p21 stability and cytosolic localization in kidney cancer cells: a potential mechanism of apoptosis resistance. Mol. Cancer *6*, 16.

Ling, M.T., Lau, T.C., Zhou, C., Chua, C.W., Kwok, W.K., Wang, Q., Wang, X., and Wong, Y.C. (2005). Overexpression of Id-1 in prostate cancer cells promotes angiogenesis through the activation of vascular endothelial growth factor (VEGF). Carcinogenesis *26*, 1668–1676.

Lyden, D., Young, A.Z., Zagzag, D., Yan, W., Gerald, W., O'Reilly, R., Bader, B.L., Hynes, R.O., Zhuang, Y., Manova, K., and Benezra, R. (1999). Id1 and Id3 are required for neurogenesis, angiogenesis and vascularization of tumour xenografts. Nature *401*, 670–677.

Mahyar-Roemer, M., and Roemer, K. (2001). p21 Waf1/Cip1 can protect human colon carcinoma cells against p53-dependent and p53-independent apoptosis induced by natural chemopreventive and therapeutic agents. Oncogene *20*, 3387–3398.

Meteoglu, I., Meydan, N., and Erkus, M. (2008). Id-1: regulator of EGFR and VEGF and potential target for colorectal cancer therapy. J. Exp. Clin. Cancer Res. *27*, 69.

Morrison, S.J., and Kimble, J. (2006). Asymmetric and symmetric stem-cell divisions in development and cancer. Nature *441*, 1068–1074.

Morrison, S.J., and Spradling, A.C. (2008). Stem cells and niches: mechanisms that promote stem cell maintenance throughout life. Cell *132*, 598–611.

Nam, H.S., and Benezra, R. (2009). High levels of Id1 expression define B1 type adult neural stem cells. Cell Stem Cell *5*, 515–526.

O'Brien, C.A., Pollett, A., Gallinger, S., and Dick, J.E. (2007). A human colon cancer cell capable of initiating tumour growth in immunodeficient mice. Nature *445*, 106–110.

O'Brien, C.A., Kreso, A., and Dick, J.E. (2009). Cancer stem cells in solid tumors: an overview. Semin. Radiat. Oncol. *19*, 71–77.

Ouyang, X.S., Wang, X., Lee, D.T., Tsao, S.W., and Wong, Y.C. (2002). Over expression of ID-1 in prostate cancer. J. Urol. *167*, 2598–2602.

Pece, S., Tosoni, D., Confalonieri, S., Mazzarol, G., Vecchi, M., Ronzoni, S., Bernard, L., Viale, G., Pelicci, P.G., and Di Fiore, P.P. (2010). Biological and molecular heterogeneity of breast cancers correlates with their cancer stem cell content. Cell *140*, 62–73.

Perry, S.S., Zhao, Y., Nie, L., Cochrane, S.W., Huang, Z., and Sun, X.H. (2007). Id1, but not Id3, directs long-term repopulating hematopoietic stem-cell maintenance. Blood *110*, 2351–2360.

Quintana, E., Shackleton, M., Sabel, M.S., Fullen, D.R., Johnson, T.M., and Morrison, S.J. (2008). Efficient tumour formation by single human melanoma cells. Nature *456*, 593–598.

Rau, B., Sturm, I., Lage, H., Berger, S., Schneider, U., Hauptmann, S., Wust, P., Riess, H., Schlag, P.M., Dörken, B., and Daniel, P.T. (2003). Dynamic expression profile of p21WAF1/CIP1 and Ki-67 predicts survival in rectal carcinoma treated with preoperative radiochemotherapy. J. Clin. Oncol. *21*, 3391–3401.

Ricci-Vitiani, L., Lombardi, D.G., Pilozzi, E., Biffoni, M., Todaro, M., Peschle, C., and De Maria, R. (2007). Identification and expansion of human colon-cancer-initiating cells. Nature *445*, 111–115.

Ruzinova, M.B., and Benezra, R. (2003). Id proteins in development, cell cycle and cancer. Trends Cell Biol. *13*, 410–418.

Schatton, T., Murphy, G.F., Frank, N.Y., Yamaura, K., Waaga-Gasser, A.M., Gasser, M., Zhan, Q., Jordan, S., Duncan, L.M., Weishaupt, C., et al. (2008). Identification of cells initiating human melanomas. Nature *451*, 345–349.

Schindl, M., Oberhuber, G., Obermair, A., Schoppmann, S.F., Karner, B., and Birner, P. (2001). Overexpression of Id-1 protein is a marker for unfavorable prognosis in early-stage cervical cancer. Cancer Res. *61*, 5703–5706.

Schindl, M., Schoppmann, S.F., Ströbel, T., Heinzl, H., Leisser, C., Horvat, R., and Birner, P. (2003). Level of Id-1 protein expression correlates with poor differentiation, enhanced malignant potential, and more aggressive clinical behavior of epithelial ovarian tumors. Clin. Cancer Res. *9*, 779–785.

Shackleton, M., Quintana, E., Fearon, E.R., and Morrison, S.J. (2009). Heterogeneity in cancer: cancer stem cells versus clonal evolution. Cell *138*, 822–829.

Sharma, R.R., Ravikumar, T.S., Raimo, D., and Yang, W.L. (2005). Induction of p21WAF1 expression protects HT29 colon cancer cells from apoptosis induced by cryoinjury. Ann. Surg. Oncol. *12*, 743–752.

Singh, S.K., Hawkins, C., Clarke, I.D., Squire, J.A., Bayani, J., Hide, T., Henkelman, R.M., Cusimano, M.D., and Dirks, P.B. (2004). Identification of human brain tumour initiating cells. Nature *432*, 396–401.

Swarbrick, A., Roy, E., Allen, T., and Bishop, J.M. (2008). Id1 cooperates with oncogenic Ras to induce metastatic mammary carcinoma by subversion of the cellular senescence response. Proc. Natl. Acad. Sci. USA *105*, 5402–5407.

Tian, H., Wittmack, E.K., and Jorgensen, T.J. (2000). p21WAF1/CIP1 antisense therapy radiosensitizes human colon cancer by converting growth arrest to apoptosis. Cancer Res. *60*, 679–684.

Todaro, M., Perez Alea, M., Scopelliti, A., Medema, J.P., and Stassi, G. (2008). IL-4-mediated drug resistance in colon cancer stem cells. Cell Cycle *7*, 309–313.

van de Wetering, M., Sancho, E., Verweij, C., de Lau, W., Oving, I., Hurlstone, A., van der Horn, K., Batlle, E., Coudreuse, D., Haramis, A.P., et al. (2002). The beta-catenin/TCF-4 complex imposes a crypt progenitor phenotype on colorectal cancer cells. Cell *111*, 241–250.

Vermeulen, L., Todaro, M., de Sousa Mello, F., Sprick, M.R., Kemper, K., Perez Alea, M., Richel, D.J., Stassi, G., and Medema, J.P. (2008). Single-cell cloning of colon cancer stem cells reveals a multi-lineage differentiation capacity. Proc. Natl. Acad. Sci. USA *105*, 13427–13432.

Viale, A., De Franco, F., Orleth, A., Cambiaghi, V., Giuliani, V., Bossi, D., Ronchini, C., Ronzoni, S., Muradore, I., Monestiroli, S., et al. (2009). Cell-cycle restriction limits DNA damage and maintains self-renewal of leukaemia stem cells. Nature *457*, 51–56.

Cancer Cell
Article

p53-Mediated Senescence Impairs the Apoptotic Response to Chemotherapy and Clinical Outcome in Breast Cancer

James G. Jackson,[1] Vinod Pant,[1] Qin Li,[1,5] Leslie L. Chang,[1] Alfonso Quintás-Cardama,[2] Daniel Garza,[1] Omid Tavana,[3] Peirong Yang,[1] Taghi Manshouri,[2] Yi Li,[6] Adel K. El-Naggar,[4] and Guillermina Lozano[1,*]
[1]Department of Genetics
[2]Department of Leukemia
[3]Department of Immunology
[4]Department of Pathology
The University of Texas MD Anderson Cancer Center, Houston, TX 77030, USA
[5]The University of Texas Graduate School of Biomedical Sciences Program in Genes and Development, Houston, TX 77030, USA
[6]Lester & Sue Smith Breast Center and Department of Molecular and Cell Biology, Baylor College of Medicine, Houston, TX 77030, USA
*Correspondence: gglozano@mdanderson.org
DOI 10.1016/j.ccr.2012.04.027

SUMMARY

Studies on the role of *TP53* mutation in breast cancer response to chemotherapy are conflicting. Here, we show that, contrary to dogma, MMTV-*Wnt1* mammary tumors with *mutant* p53 exhibited a superior clinical response compared to tumors with wild-type p53. Doxorubicin-treated *p53* mutant tumors failed to arrest proliferation, leading to abnormal mitoses and cell death, whereas *p53* wild-type tumors arrested, avoiding mitotic catastrophe. Senescent tumor cells persisted, secreting senescence-associated cytokines exhibiting autocrine/paracrine activity and mitogenic potential. Wild-type p53 still mediated arrest and inhibited drug response even in the context of heterozygous *p53* point mutations or absence of p21. Thus, we show that wild-type *p53* activity hinders chemotherapy response and demonstrate the need to reassess the paradigm for *p53* in cancer therapy.

INTRODUCTION

The tumor suppressor *TP53* is mutated or inactivated in the majority of cancers (Soussi and Lozano, 2005). *p53* exerts its effects by binding specific promoter sequences following cellular stress and activating transcription of genes involved in cell-cycle arrest, senescence, and apoptosis (Riley et al., 2008). DNA damage, such as that induced by radiation or chemotherapy drugs, is a potent activator of p53.

Classic studies using mouse models have demonstrated an in vivo role for *p53* in the induction of apoptosis following DNA damage (Jackson et al., 2011). Thymocytes from *p53* null mice do not undergo apoptosis after radiation (Clarke et al., 1993; Lowe et al., 1993b), and the embryonic neural tube in *p53* null mice is similarly resistant (Lang et al., 2004; Liu et al., 2004). *p53* also contributes to response after exposure to DNA-damaging drugs by inducing apoptosis in E1A/Ras-transformed mouse embryo fibroblasts (Lowe et al., 1993a, 1994).

Interestingly, studies examining the paradigm that wild-type *p53* activity improves drug response are lacking in tumors arising from epithelial tissues (Brown and Attardi, 2005). This deficiency is exemplified in breast cancer. Some reports on the response of breast cancer with or without *TP53* mutation to chemotherapy drugs have been inconclusive (Bonnefoi et al., 2011; Makris et al., 1995; Mathieu et al., 1995), whereas others show that wild-type *TP53* activity is beneficial to response (Aas et al., 1996; Berns et al., 2000; Kröger et al., 2006; Rahko et al., 2003). Intriguingly, still other reports have shown that *TP53*

Significance

Approximately one-third of human breast cancers harbor mutations in the tumor suppressor gene *TP53*. The long-held paradigm that wild-type p53 mediates apoptosis resulting in a favorable chemotherapy response is less clear in breast cancer because many reports conflict, including some suggesting that tumors harboring *TP53* mutations respond more favorably. Here, we show that wild-type p53 activity is paradoxically detrimental to chemotherapy response because, unlike mutant *p53* tumors, *p53* wild-type tumors can avoid aberrant mitoses by undergoing arrest, which is followed by expression of cytokines in senescent cells that can stimulate cell proliferation and tumor relapse. Furthermore, our data demonstrate that in order to accurately predict clinical response of *TP53*-mutated tumors, the status of the second allele must be determined.

mutant tumors respond better (Bertheau et al., 2002, 2007; Mathieu et al., 1995). It is unclear why these reports reached different conclusions, and importantly, the notion that wild-type *TP53* activity would hinder response, given its known apoptotic and tumor suppressive functions, is controversial and lacks a mechanistic explanation. Thus, it is desirable to have a controlled setting to examine if wild-type p53 activity is beneficial in breast cancer response, and if not, as some have suggested (Bertheau et al., 2008), then why?

RESULTS

Superior Response of *p53* Mutant Mammary Tumors to Doxorubicin Treatment

In order to address the role of the *p53* response in breast cancer, we bred MMTV-*Wnt1* (Tsukamoto et al., 1988) mice into *p53* wild-type as well as $p53^{-/-}$ (Jacks et al., 1994) and $p53^{R172H}$ (Lang et al., 2004) ("*p53* mutant" herein) backgrounds. p53R172H is a structurally defective mutant that cannot bind DNA, and mice that are homozygous or heterozygous for this mutation are identical to $p53^{-/-}$ or $p53^{+/-}$ mice, respectively, in survival (Lang et al., 2004) and for results presented here. After mammary tumors formed, mice were treated with doxorubicin and monitored. We found that, despite heterogeneity of responses (see Figure S1A available online), tumors from mice in the wild-type *p53* background generally underwent minimal tumor regression, stabilized for several days, and quickly relapsed (Figures 1A and 1E).

We next examined *p53* mutant MMTV-*Wnt1* mammary tumors. In most human tumors, biallelic point mutations or deletions of *p53* are relatively rare. More typically, a *p53* point mutation is acquired in a single allele, and the other allele is subsequently retained or lost. Thus, we treated MMTV-*Wnt1* *p53* heterozygous mutant mice ($p53^{R172H/+}$ genotype) bearing tumors, of which approximately 40% undergo loss of heterozygosity (LOH) for the wild-type *p53* allele (Donehower et al., 1995). Surprisingly, we found that tumors in $p53^{R172H/+}$ MMTV-*Wnt1* mice that lost the wild-type allele (rendering the tumor $p53^{R172H/0}$ and functionally null) showed greater tumor regression and longer time to relapse (Figures 1B, 1E, and S1B).

Also to our surprise, we found that as long as tumors from $p53^{R172H/+}$ mice retained the wild-type *p53* allele, they exhibited a response typical of *p53* wild-type tumors (Figures 1C and S1C), despite the presence of a mutant allele with reported dominant-negative activity (Lang et al., 2004; Willis et al., 2004). We also observed dramatic tumor volume reductions in MMTV-*Wnt1* mammary tumors from treated *p53* homozygous mutant mice (Figures 1D and S1D), although these mice were typically harvested within 1 week following the final doxorubicin treatment (Figure 1D) due to gastrointestinal syndrome (Komarova et al., 2004). Use of the *p53* homozygous mutant mice was also limited by the difficulty of acquiring females in the cohort (Sah et al., 1995). In sum although tumors of all genotypes eventually relapsed, treated tumors lacking all p53 activity, whether homozygous null or heterozygous mutant with LOH, had significantly greater decrease in tumor volume and significantly longer time to relapse compared to tumors retaining p53 activity (Figure 1E).

To assess the acute biochemical response to treatment, we examined *p53* function in MMTV-*Wnt1* tumors 24 hr after the final doxorubicin dose. *p53* target genes *p21*, *Puma*, and *Ccng1* were induced 4- to 6-fold compared to untreated tumors (Figure 1F), demonstrating retention of wild-type *p53* in MMTV-*Wnt1* tumors from $p53^{+/+}$ mice, as others have shown (Donehower et al., 1995). Predictably, *p53* homozygous mutant tumors did not induce target genes (Figure 1F). *Noxa* levels, however, were elevated in some tumors in a *p53*-independent fashion. *p53* heterozygous mutant MMTV-*Wnt1* tumors that retained the wild-type allele also induced *p53* target genes, in contrast to tumors with *p53* LOH (Figure 1G).

To address the mechanism of response in *p53* wild-type versus mutant tumors, we examined growth arrest and apoptosis in tumors 24 hr after doxorubicin treatment. Examining proliferation, we found that untreated tumors of all genotypes were highly positive for Ki67, a marker of cells outside G0 of the cell cycle. Following treatment, only *p53* wild-type MMTV-*Wnt1* tumors had large areas that were Ki67 negative or sparsely positive, demonstrating cell-cycle exit, whereas *p53* mutant tumors remained positive for Ki67 (Figure 2A). Furthermore, tumors from parallel orthotopic transplants of a *p53* wild-type MMTV-*Wnt1* tumor ceased incorporating bromodeoxyuridine (BrdU) following treatment, whereas transplanted *p53* mutant tumors continued to enter S phase (Figure 2B). This failure to arrest in the presence of DNA damage resulted in aberrant mitoses, as evidenced by anaphase bridges, in treated *p53* mutant tumors, whereas *p53* wild-type tumors arrested and, thus, were not mitotic (Figures 2C–2E). The *p53* mutant MMTV-*Wnt1* tumors also showed a significant increase in both cleaved caspase-3 and terminal deoxynucleotidyl transferase dUTP nick end labeling (TUNEL)-positive cells after doxorubicin treatment (Figure 2F). *p53* wild-type tumors, however, did not undergo apoptosis following treatment (Figure 2F). Taken together, our data show that despite induction of apoptotic genes such as *Puma* and *Noxa*, growth arrest, not apoptosis, was acutely induced in *p53* wild-type tumors following doxorubicin treatment, and lack of arrest in mutant tumors resulted in aberrant mitoses, cell death, and ultimately, a superior clinical response.

Doxorubicin Induces a Senescent-like Phenotype in *p53* Wild-type Mammary Tumors

To further address the mechanism responsible for the suboptimal response in *p53* wild-type tumors, we harvested *p53* wild-type or heterozygous MMTV-*Wnt1* tumors 5–7 days post-treatment (Figures S2A–S2C) and examined them for markers of senescence. We quantitatively determined that many markers of senescence (*p21*, *Dcr2*, *p16*, *p15*, *Dec1*, and *Pml*) (Collado et al., 2005; te Poele et al., 2002) were elevated in many stably arrested MMTV-*Wnt1* tumors that were *p53* wild-type or heterozygous with retention of the wild-type allele, when compared to untreated tumors (Figures 3A, 3B, and 3D). Treated and harvested *p53* mutant tumors (Figure S2C) exhibited heterogeneity in expression levels of several senescence markers, although only *Pml* was consistently elevated to a degree similar to that observed in *p53* wild-type tumors 5 days following treatment (Figure 3C). *Dcr2* was induced slightly following treatment in $p53^{R172H/0}$ tumors, possibly attributable to stromal cells within the tumor that still have the *p53* wild-type allele. We used orthotopic transplants of *p53* wild-type and mutant MMTV-*Wnt1*

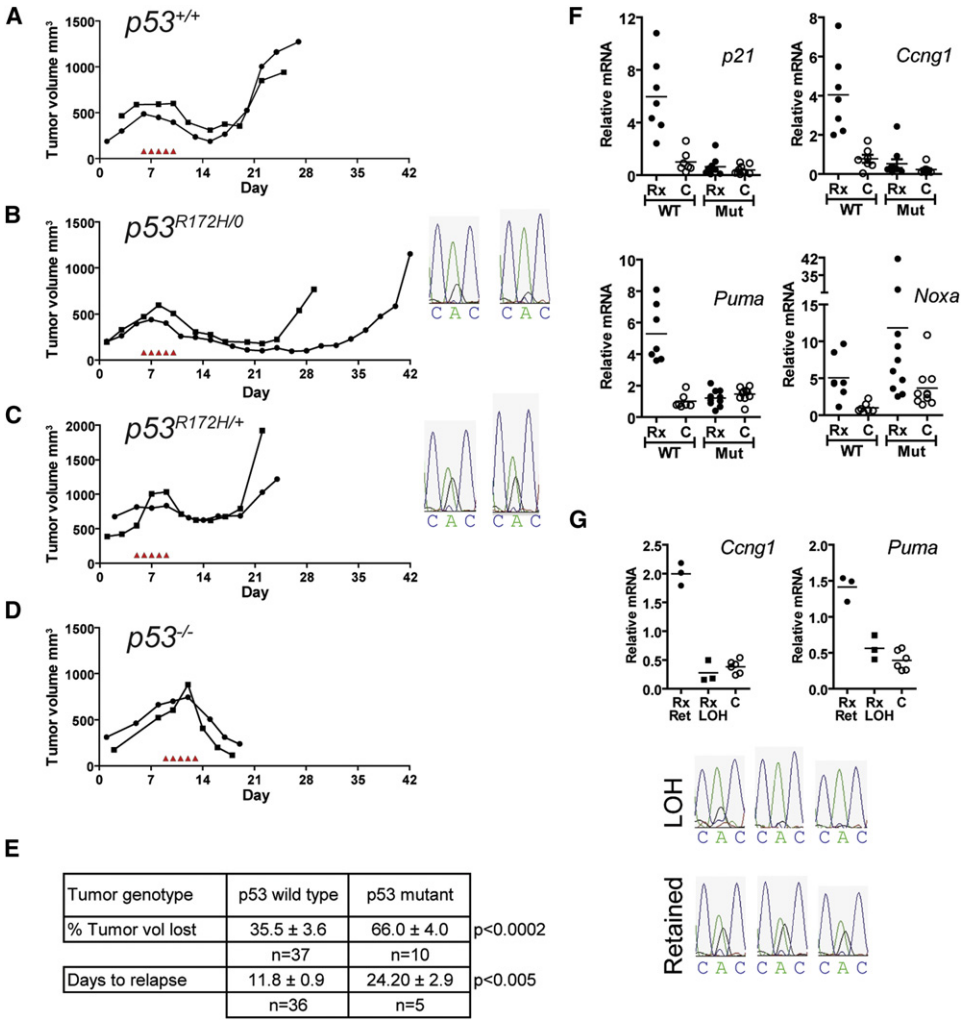

Tumor genotype	p53 wild type	p53 mutant	
% Tumor vol lost	35.5 ± 3.6	66.0 ± 4.0	p<0.0002
	n=37	n=10	
Days to relapse	11.8 ± 0.9	24.20 ± 2.9	p<0.005
	n=36	n=5	

Figure 1. Superior Response of *p53* Mutant MMTV-*Wnt1* Mammary Tumors to Doxorubicin Treatment

(A–D) MMTV-*Wnt1* mice bearing spontaneous, measurable, growing mammary tumors of approximately 500 mm^3 were injected once daily with 4 mg/kg doxorubicin for 5 consecutive days as indicated by arrowheads in graphs. Tumors with *p53* wild-type ($p53^{+/+}$) (A), heterozygous mutant that lost the wild-type allele ($p53^{R172H/0}$) (B), or retained the wild-type allele ($p53^{R172H/+}$) (C), and homozygous mutant ($p53^{-/-}$) (D) were measured regularly, and tumor volume was calculated. Shown are two representative mice for each genotype. LOH was determined by sequencing DNA from tumors across the region of the knockin point mutation. The double peak observed in (C) shows *p53* heterozygous status, whereas the single peak observed in (B) indicates LOH.

(E) Summary of responses for MMTV-*Wnt1* tumors with wild-type *p53* or $p53^{R172H/+}$ that retained the wild-type allele (n = 22 and n = 15, respectively, for tumor volume, total = 37; and n = 21 and n = 15, respectively, for relapse, total = 36) ("p53 wild-type") versus tumors homozygous mutant or $p53^{R172H/+}$ that underwent LOH (n = 2 and n = 8, respectively, for tumor volume, total = 10; and n = 1 and n = 4, respectively, for relapse, total = 5) ("p53 mutant"). Tumors showing primary resistance (~20%) were not included in analysis of response. Time to relapse is the number of days posttreatment by which tumor exceeded maximum tumor volume. Values shown are ± SEM.

(F) To measure *p53* activity, tumors were harvested 24 hr after the fifth and final doxorubicin injection ("Rx"), or from untreated control mice ("C") in *p53* wild-type (WT) or homozygous mutant (Mut) backgrounds. Relative mRNA levels determined by real-time RT-PCR are shown for indicated genes, with mean of WT C set to 1. Horizontal line is the mean.

(G) Tumors from $p53^{R172H/+}$ mice either retaining (Ret) or having lost (LOH) the wild-type allele were harvested 24 hr after the final doxorubicin treatment ("Rx") or from untreated control mice ("C"), and mRNA levels for indicated genes were determined as in (F). Horizontal line is the mean.

See also Figure S1.

tumors to further validate these findings. Parallel transplants of a *p53* wild-type tumor showed increased expression of senescence genes *p21* and *Dcr2* in cohorts that were treated and harvested 2 or 5 days following the final treatment compared to untreated or relapsed tumors, whereas induction of *Dec1* and *Pml* showed more variation among individual tumors (Figure 3E). A transplanted *p53* mutant tumor did not express markers of senescence following treatment at levels near the *p53* wild-type tumor, although a low-level induction of *p21* was observed, possibly attributable to *p53* wild-type stromal cells from the recipient (Figure 3F). We next examined senescence-associated β-galactosidase (SAβGal) staining in untreated versus treated MMTV-*Wnt1* tumor transplants. We found clearly positive SAβGal staining in gross tumor specimens from treated *p53*

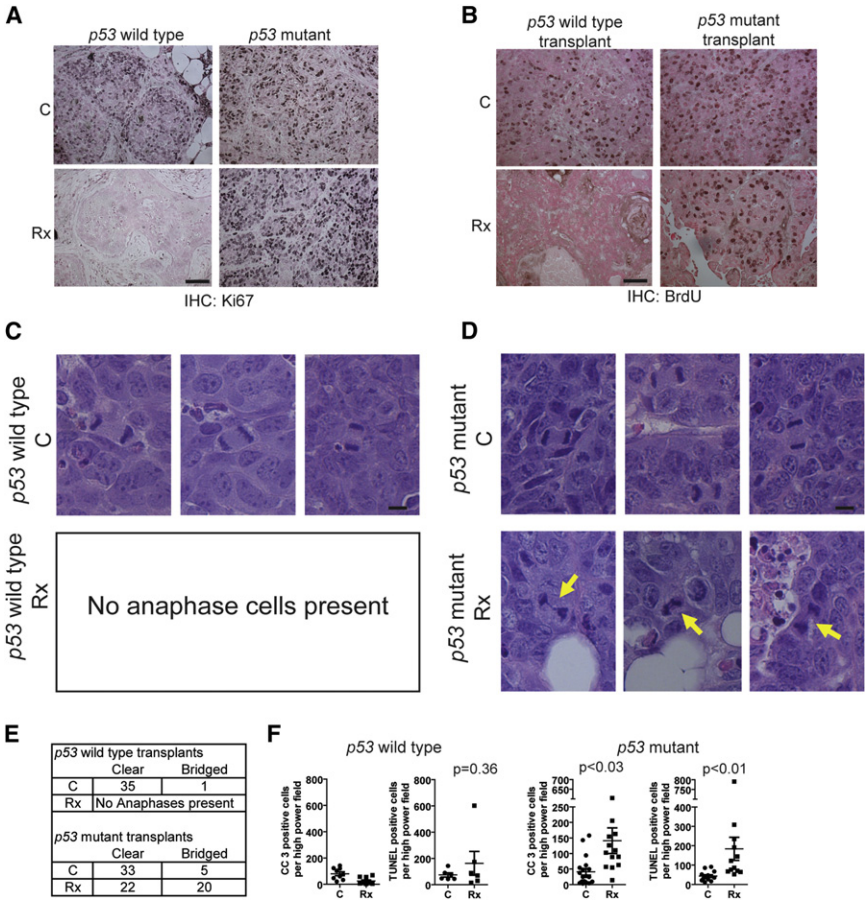

Figure 2. Failure to Arrest Leads to Aberrant Mitoses and Cell Death in Doxorubicin-Treated *p53* Mutant MMTV-*Wnt1* Tumors

(A) *p53* homozygous mutant and *p53* wild-type MMTV-*Wnt1* spontaneous tumors were harvested 24 hr following final treatment as in Figure 1F, and formalin-fixed, paraffin-embedded sections were stained for Ki67. Shown are representative images of five tumors from each group. Scale bar, 50 μM.

(B) An MMTV-*Wnt1* *p53* wild-type tumor and mutant ($p53^{R172H/0}$) tumor were harvested and processed to single-cell suspension by mincing and trypsinizing, and then 4 × 10^6 cells were injected into the abdominal mammary fat pads of recipient female C57BL6 mice. Tumors that formed were left untreated or given the usual five treatments of doxorubicin, followed by 2 BrdU injections 24 and 44 hr later, and then harvest 4 hr later (48 hr after final doxorubicin treatment). Formalin-fixed, paraffin-embedded sections were stained for BrdU. Scale bar, 50 μM.

(C and D) H&E sections from transplanted tumors in (B) were examined for anaphases and scored for bridges. Shown are three representative images from the *p53* wild-type tumor (C) and mutant ($p53^{R172H/0}$) tumor (D). Scale bars, 10 μM. Bridges are indicated by yellow arrows.

(E) Quantitation of anaphase bridges. "Clear" indicates no bridge observed.

(F) *p53* wild-type and *p53* homozygous mutant MMTV-*Wnt1* spontaneous tumors were harvested 24 hr following final treatment as in (A), and formalin-fixed, paraffin-embedded sections were stained for cleaved caspase-3 antibody or TUNEL as indicated in the figure. At least four random 200× high-powered fields per tumor were counted, averaged, and plotted, with mean ± SEM shown as line with error bars. The one *p53* wild-type tumor with a very high number of TUNEL-positive cells was also the only *p53* wild-type tumor that regressed during the treatment period (data not shown).

wild-type or $p53^{R172H/+}$ tumors, but not untreated tumors or transplanted $p53^{R172H/0}$ tumors that were treated (Figure S2D). Likewise, histological sections of only the treated *p53* wild-type or $p53^{R172H/+}$ tumors, but not $p53^{R172H/0}$ tumors, were positive for SAβGal (Figure 3G; data not shown). In sum we found that three out of three different *p53* wild-type tumors and three out of three different $p53^{R172H/+}$ tumor transplants were positive for SAβGal only after doxorubicin treatment, whereas histological sections of transplants from two different $p53^{R172H/0}$ tumors were negative, and gross specimens showed only faint staining in <10% of the tumor surface area. Together with the analysis of mRNA markers in Figures 3A–3C, our data show that transplanted and spontaneous tumors that retain a wild-type *p53* allele undergo cellular senescence following doxorubicin treatment.

The Role of *p21* in the Wild-type p53-Mediated Arrest Response to Doxorubicin

p21 is a major mediator of *p53*-dependent cell-cycle arrest and senescence and was strongly induced in the arrested *p53* wild-type tumors. Previous studies show that cells deficient for *p21* fail to arrest following DNA damage and fail to undergo senescence (Brown et al., 1997; Brugarolas et al., 1995; Bunz et al., 1998; Chang et al., 1999; Deng et al., 1995; Waldman et al., 1995), similar to the treated *p53* mutant MMTV-*Wnt1* tumors in this study. Thus, we hypothesized that *p21* null MMTV-*Wnt1* tumors would respond similarly to *p53* mutant tumors. To our surprise, we found that the *p21* null MMTV-*Wnt1* tumors exhibited on average a response intermediate between *p53* wild-type and mutant tumors (Figures 4A and S3A), with a significant subset showing a muted response similar to wild-type tumors (Figure 4A, upper chart) in addition to tumors that responded like *p53* mutant tumors (Figure 4A, lower chart). However, all *p21* null tumors examined were Ki67 positive (Figure 4B), suggesting that these tumors failed to arrest in G0. To further examine the *p21* null phenotypes, we used the amenable system of parallel orthotopic transplants of *p21* null MMTV-*Wnt1* tumors. We found examples of *p21* null MMTV-*Wnt1* tumors that arrested following treatment, ceased incorporating BrdU, and halted mitotic activity (transplant #1, Figure 4C), as well as *p21* null tumor transplants that failed to arrest, continued to incorporate BrdU, and underwent aberrant mitoses following treatment (Figures 4D, S3B, and S3C). In order to expand our examination of the arrest phenotype in *p21* null MMTV-*Wnt1*

tumors beyond these parallel transplants, we quantitated mitotic activity in ten spontaneous *p21* null MMTV-*Wnt1* tumors 24 hr following treatment to assess the fraction of these tumors that undergo arrest following treatment, compared to *p53* wild-type and mutant tumors. We found that six of ten tumors were essentially in mitotic arrest 24 hr following treatment, similar to five out of five *p53* wild-type-treated tumors (Figure 4E). However, mitotic activity persisted in four of ten treated tumors at a level similar to untreated tumors (Figure 4E). *p53* mutant MMTV-*Wnt1* tumors failed to arrest in all cases examined because mitotic figures were abundant in all eight treated spontaneous tumors. These data show that *p53* can mediate arrest in the absence of *p21* in a subset of tumors, providing a plausible explanation for the observation that some *p21* null tumors respond like *p53* wild-type tumors that arrest, and some like mutant tumors that fail to arrest.

The aforementioned results show that some *p21* null MMTV-*Wnt1* tumors arrested mitotic activity and cease incorporating BrdU after treatment, but all treated tumors examined were Ki67 positive (Figure 4B). This suggests that tumor cells were arrested somewhere in the cell cycle other than in G0. Indeed, FACS analysis revealed that orthotopic transplants of the BrdU-negative *p21* null tumor in Figure 4C arrested with 4n DNA content after treatment, consistent with a G2 arrest (Figure 5B), whereas the *p21/p53* wild-type transplanted MMTV-*Wnt1* tumor responded to treatment by a predominantly G1 arrest (Figure 5A). DNA content histograms of proliferating, relapsed tumors resembled those of proliferating untreated tumors (Figures 5A and 5B).

To address the mechanism of the G2 arrest in the two types of *p21* null responses, we examined G2 regulators. The *p21* null transplanted tumor that ceased DNA synthesis and mitosis (Figure 4C) had reduced levels of G2 regulators such as Cyclin B, Cdc2, and Stathmin1 (Figure 5C, upper chart, transplant #1). In contrast, *p21* null tumors that were BrdU positive after treatment and had aberrant mitoses (Figure 4D) failed to downregulate genes that promote transition through mitosis (Figure 5C, middle chart, transplant #2; Figure S4), similar to a transplanted *p53* mutant tumor (Figure 5C, lower chart). Thus, *p53*, in the absence of the cyclin-dependent kinase inhibitor *p21*, can still direct a G2 cell-cycle arrest in treated tumors, preventing the mitotic catastrophes associated with the superior response of *p53* mutant tumors. Although we were able to perform the extensive analysis using parallel orthotopic transplants of *p21* null tumors in only a limited number of tumors, our finding that even the *p21* null spontaneous tumors that lacked mitotic figures remained Ki67 positive suggests that these tumors likewise arrested outside of G0.

Senescence-Associated Cytokines Are Expressed in Doxorubicin-Treated Mammary Tumors

To further address the reason for early relapse in the arrested, senescent, *p53* wild-type MMTV-*Wnt1* tumors, we examined an array of cytokines and their receptors and cofactors that others have shown to be produced by normal cells made senescent after oncogenic stress (Acosta et al., 2008; Coppé et al., 2008; Kuilman et al., 2008; Wajapeyee et al., 2008). We found that our stably arrested, senescent MMTV-*Wnt1* tumors, either *p53* wild-type or heterozygous with retention of the wild-type allele (from Figures 3A and 3B), expressed elevated levels of a cytokine signaling network that included ligands and receptors (Figures 6A and 6B). Most tumors with mutant *p53* did not have significantly elevated levels of cytokines following treatment, with the exception of Rantes and Tnfα, although some approached significance (Figure 6C).

The senescent, cytokine-producing cells of the treated *p53* wild-type tumors did not undergo apoptosis, and the tumors did not lose significant volume as did *p53* mutant tumors (Figures 1 and 2). Therefore, we next tested whether the cytokines produced by the persistent senescent tumor cells could be detected in the sera of treated mice. Interestingly, we found no changes in serum levels of cytokines in treated *p53* wild-type mice with and without MMTV-*Wnt1* tumors at various stages before and following treatment (Figures S5A–S5D). This led us to test whether the expressed cytokines in treated tumors might be acting in a paracrine/autocrine manner. Stat transcription factors are activated by many of the cytokines elevated in treated, senescent, *p53* wild-type tumors and are important mediators of cytokine signaling (Clevenger, 2004; Novakova et al., 2010). Staining serial tumor sections, we found that untreated tumors were largely phospho-Stat3 negative, or showed only light nuclear staining, but were highly positive for the proliferation marker Ki67 (Figures S5E and S5F). Treated tumors, however, had regions of intense nuclear phospho-Stat3 staining that were Ki67 negative (Figures 6D, S5G, and S5H). Conversely, some regions in treated tumors were phospho-Stat3 negative, and Ki67 positive (Figure 6E). In fact many tumors had adjacent regions in the same field of view with this inverse phospho-Stat3/Ki67 staining (Figures 6F, 6G, S5I, and S5J). Interestingly, we also observed small areas within treated tumors that contained a mixed population of phospho-Stat3 and Ki67-positive cells along the borders of the inversely staining areas (Figure 6F, red outline; Figures S5K and S5L). This suggested the possibility that cytokines secreted by senescent cells could induce proliferation in neighboring, nonsenescent cells. Indeed, we found that Eotaxin and, to a lesser extent, Cxcl5 and Rantes could induce proliferation in cultured MMTV-*Wnt1* mammary tumor cells (Figure 6H, stimulation by known mitogens epidermal growth factor plus insulin is shown for comparison), suggesting a functional role for the cytokines produced by senescent cells in promoting tumor cell proliferation leading to clinical relapse.

To determine the role of *p21* in the induction of the senescence-associated cytokines, we examined treated, *p21* null MMTV-*Wnt1* tumors for expression of these genes. Treated spontaneous tumors did not show a clear induction of senescence markers, including cytokines and chemokines, when compared to untreated tumors (Figures S5M and S5N). It is possible that combining *p21* null MMTV-*Wnt1* tumors that arrest with those that continue proliferation following treatment could confound the interpretation of results in the spontaneous tumors. Therefore, we examined three parallel orthotopic transplants. We found that the *p21* null tumor that arrested following treatment (transplant #1) induced some senescent markers and cytokines following treatment (Figures S5O and S5P). Of the two tumors that failed to arrest following treatment, we found that one failed to induce any senescent markers or cytokines (Figures S5S and S5T), whereas the other strongly induced several

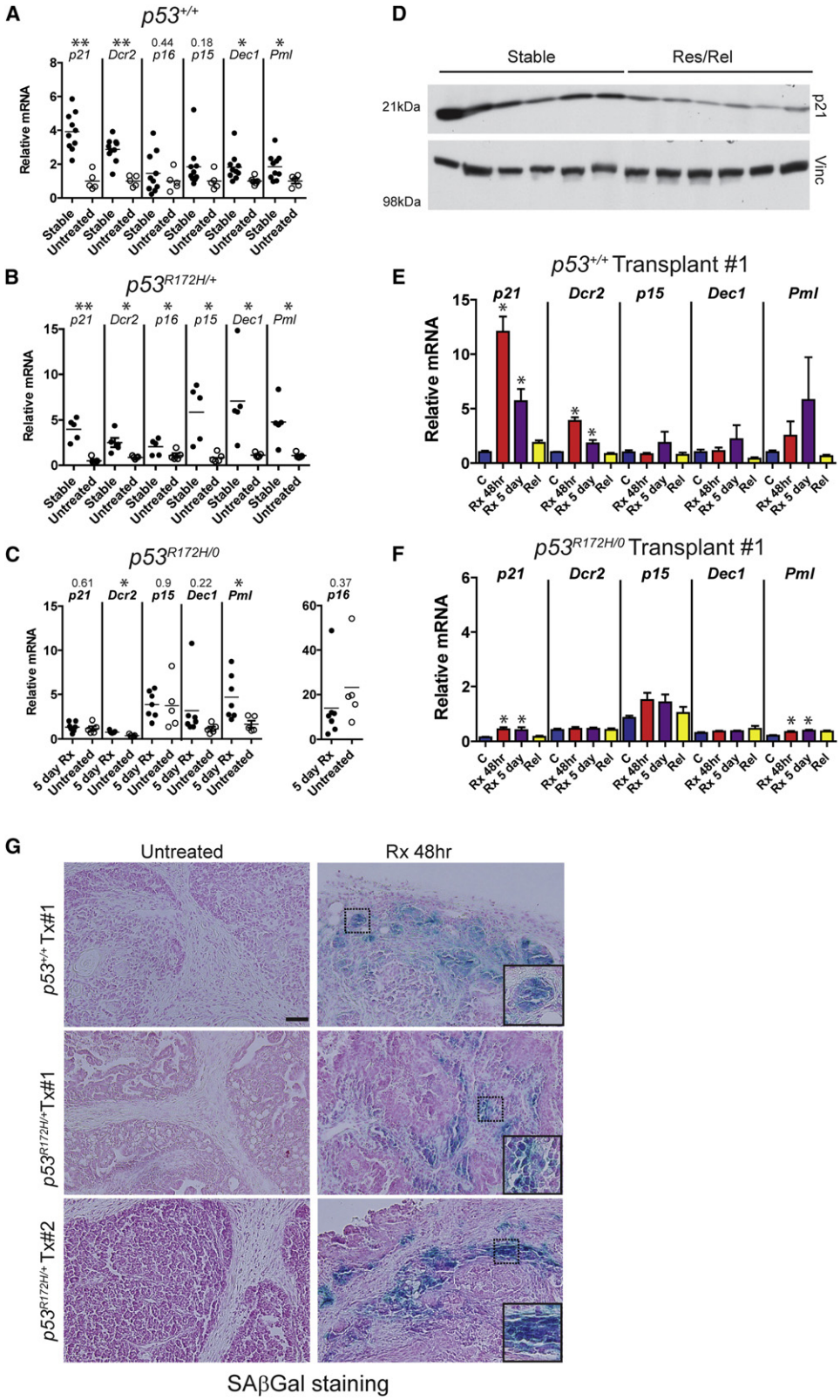

Figure 3. Wild-type *p53* Mediates Senescence following Doxorubicin Treatment of MMTV-*Wnt1* Tumors

(A–C) Spontaneous tumors were harvested from untreated mice or from mice 5–7 days following final doxorubicin treatment ("Stable"), and mRNA levels for senescence genes indicated in the figure were determined for *p53* wild-type MMTV-*Wnt1* tumors ($p53^{+/+}$) (A), *p53* heterozygous mutant tumors that retained the

senescence-associated cytokines (Figures S5Q and S5R). The fact that some treated *p21* null MMTV-*Wnt1* tumors retain the ability to induce senescence-associated cytokines following treatment could be a contributing factor in their early relapse.

Wild-type p53-Mediated Arrest Impairs Doxorubicin Response in Human Breast Cancer Cell Lines

We next investigated *p53-p21*-mediated response to doxorubicin in human breast cancer cells in culture. We found that MCF-7 and ZR-75.1 cells (*TP53* wild-type) treated with doxorubicin were positive for SAβGal activity, and induced cytokines following treatment that led to phosphorylation of STAT3 (Figures 7A–7C and S6A–S6C). Both cell lines also induced p53 and p21, ceased incorporating BrdU, and adopted a flattened morphology following doxorubicin treatment (Figures 7D–7F, S6D, and S6E), as previously described by Jackson and Pereira-Smith (2006). However, similar to the treated MMTV-*Wnt1* tumors lacking functional *p53*, MCF-7 and ZR-75.1 cells with *TP53* knockdown failed to arrest, adopted a rounded morphology consistent with cell death, and had fewer viable cells present following treatment than Si control-transfected, treated cells that adopted a senescent-like phenotype (Figures 7D–7G and S6D–S6F). Also consistent with our results in p53 wild-type and mutant MMTV-*Wnt1* tumors, both cell lines exhibited numerous aberrant mitoses, including anaphase bridges, and stark evidence of cell death such as micronuclei and condensed nuclei when treated after *TP53* or *p21* knockdown (Figures 7H and S6G). The response of MCF-7 and ZR-75.1 cells with *p21* knockdown was consistent with the subset of *p21* null MMTV-*Wnt1* tumors that continued to proliferate and enter mitosis following treatment. These data in breast cancer cell lines are similar to observations in other cell lines, such as the isogenic variants of the HCT-116 colon cancer cell line that lack *p53* or *p21* (Bunz et al., 1999; Waldman et al., 1997).

DISCUSSION

In this study we show that a robust response of breast cancer to chemotherapy is highly dependent on the absence of *p53*-mediated arrest. Functional *p53* activated a cell-cycle arrest/senescence program, preventing mitosis in the presence of DNA strand breaks. Treated tumors with mutant *p53* proceeded through the cell cycle and into aberrant mitoses. Another recent study observed that a *p53* mutant xenografted cell line showed an increase in aberrant mitotic figures after chemotherapy treatment, whereas a *p53* wild-type xenograft had increased SAβGal staining; however, outcome was not examined in this study (Varna et al., 2009).

Our data are consistent with retrospective human breast cancer studies showing that tumors with functional *p53* respond worse to dose-dense doxorubicin-based chemotherapy than tumors with nonfunctional *p53* (Bertheau et al., 2002, 2007). The delivery of a high dose of DNA-damaging agent is critical for this effect (Lehmann-Che et al., 2010). In addition to differing dose regimens used in conflicting studies, none of these reports stratified responses by LOH status of *TP53*. Our data presented here show that determining LOH status is critical for predicting response. We found that MMTV-*Wnt1* $p53^{R172H/+}$ tumors that retained the wild-type allele, despite the presence of the "dominant negative" point mutant (Lang et al., 2004; Willis et al., 2004), exhibited minimal tumor regression and had a transcriptional profile very similar to *p53* wild-type MMTV-*Wnt1* tumors, with acute expression of p53 targets and long-term expression of senescence markers. This finding has important clinical implications for using *TP53* status to risk stratify patients with breast cancer, where the wild-type allele is often retained (Mazars et al., 1992). Thus, identifying a *TP53* mutation without assessing LOH is a confounding factor likely responsible for the contradictory results observed in multiple studies analyzing the role of *TP53* mutational status in breast cancer response (Aas et al., 1996; Berns et al., 2000; Bertheau et al., 2002, 2007, 2008; Kröger et al., 2006; Makris et al., 1995; Mathieu et al., 1995). Furthermore, our results suggest that *TP53* mutations that occur in basal-like breast cancers contribute to the relatively high rate of complete responses observed in this subset (Carey et al., 2007; Straver et al., 2010) and also imply that these tumors are likely to undergo LOH. Conversely, in the luminal subtypes of breast cancer, which are mostly *TP53* wild-type, p53 activity could contribute to the lower frequency of complete remissions (Carey et al., 2007; Straver et al., 2010), and in instances where a *TP53* mutation is present in this subtype, the wild-type allele is likely to be retained. It will also be interesting to determine if the p53-mediated arrest phenotype we describe here is also predictive of poor chemotherapy response in other cancers.

Cells induced by doxorubicin to undergo senescence evidently persisted and likely contributed to the relapse. Our immunohistochemical analysis suggests that the cytokines secreted by senescent tumors operate in an autocrine or

wild-type allele ($p53^{R172H/+}$) (B), or lost the wild-type allele ($p53^{R172H/0}$) (C). p16 is shown on a separate axis due to the aberrantly high values in some tumors. All graphs in (A)–(C) are relative to the mean of untreated *p53* wild-type tumors set to a value of 1. For *p53* mutant tumors, responding tumors harvested 5 days after treatment (5 day Rx) (the time point when *p53* wild-type tumors express senescence markers) were used. $^{**}p < 0.005$; $^{*}p < 0.05$ by Student's t test; p values of nonsignificant comparisons are shown above the gene symbol. Horizontal line is the mean.

(D) *p21* protein levels in six of the tumors from (A) compared to growing, relapsed tumors as determined by western blot, with Vinculin (Vinc) used as a control. Student's t test of densitometric analysis of the two groups, $p = 0.0045$.

(E and F) Parallel transplanted tumors as in Figure 2B were untreated ("C") or doxorubicin treated ("Rx") and harvested 48 hr or 5 days after the final treatment, or followed until relapse ("Rel"). mRNA levels for senescence genes indicated in the figure were determined for *p53* wild-type (E) and mutant (F) transplanted tumors, in at least four tumors for each treatment group. Values in mutant tumors in (F) are relative to untreated tumors in (E) and shown on a smaller scale so differences can be discerned. $^{*}p < 0.05$ by ANOVA and Newman-Keuls posttest for comparison to untreated. Error bars are ± SEM.

(G) SAβGal staining in histological sections of untreated and treated orthotopic tumor transplants. Shown are representative sections from one *p53* wild-type donor and two different $p53^{R172H/+}$ donors, with and without doxorubicin treatment. Similar results were observed in a total of three out of three wild-type and three out of three $p53^{R172H/+}$-transplanted tumors. Insets shown in bottom-right corner are higher-magnification images of the area shown outlined in black within the image. Scale bar, 50 μM.

See also Figure S2.

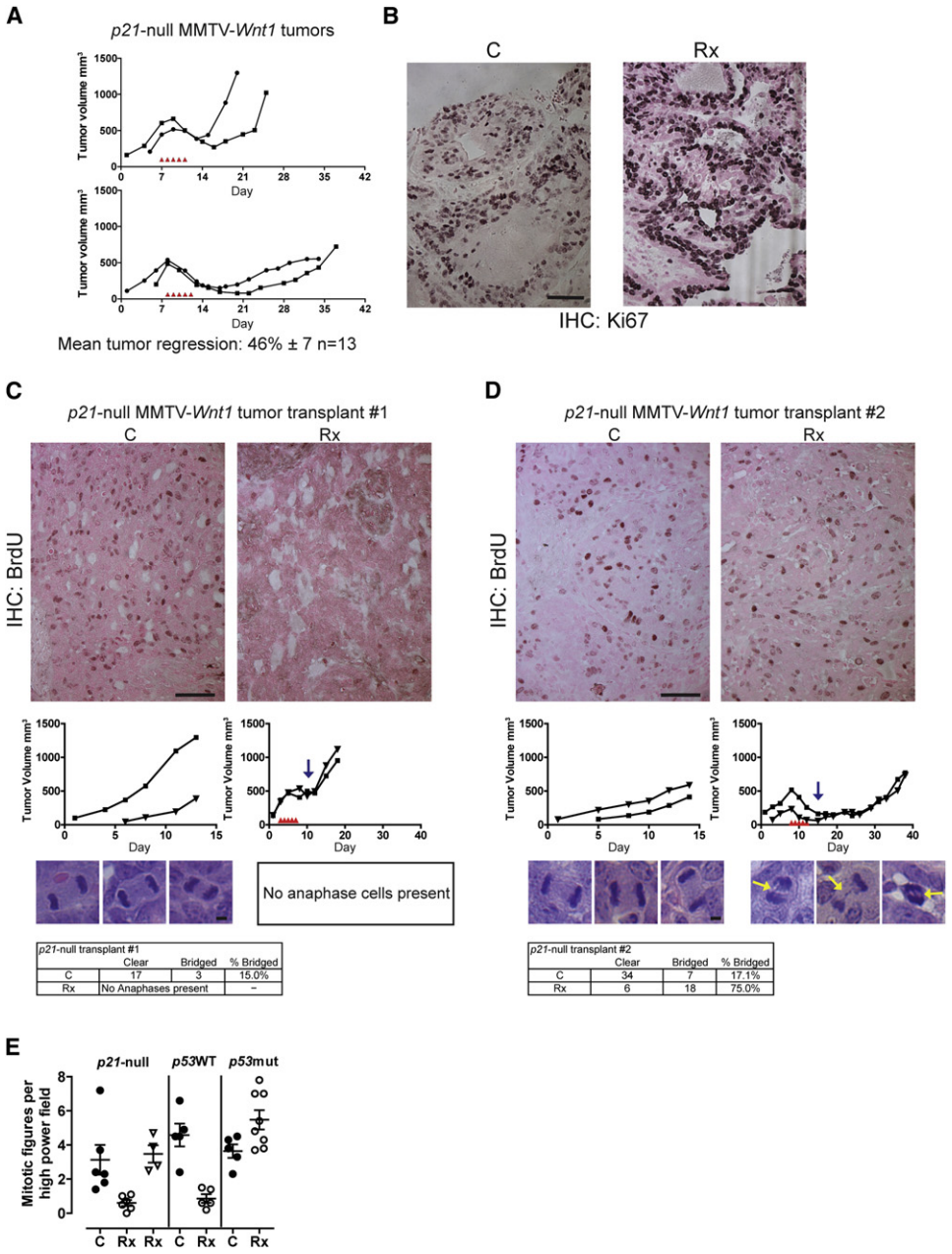

Figure 4. Dichotomous Responses in Doxorubicin-Treated *p21* null MMTV-*Wnt1* Mice: Subsets of Tumors Retain Arrest Capability, whereas Others Continue Proliferation

(A) *p21* null MMTV-*Wnt1* mice bearing spontaneous, measurable, growing mammary tumors of approximately 500 mm^3 were injected once daily with 4 mg/kg doxorubicin for 5 consecutive days as indicated by red arrowheads in graphs. Shown are representative charts from mice with poor (top) and favorable (bottom) responses, and mean tumor regression ± SEM.

(B) Ki67 IHC staining of untreated ("C") and treated ("Rx") *p21* null MMTV-*Wnt1* tumors harvested 24 hr following the final treatment is presented. Shown are representative images from seven treated and six untreated or relapsed tumors. Scale bar, 50 μM.

(C and D) Two different *p21* null MMTV-*Wnt1* tumors were transplanted, treated in parallel, and BrdU incorporation was determined as in Figure 2B. Shown are representative images of BrdU staining (scale bar, 50 μM), the corresponding tumor volume charts for parallel transplanted tumors that were followed (blue arrow indicates the 48 hr time point when parallel transplants were harvested for analysis), representative anaphases (scale bar, 5 μM), and a table quantitating the anaphase data.

(E) H&E sections from untreated ("C") and treated ("Rx") tumors of the indicated genotypes were quantitated for mitotic figures. Each data point represents the average count of mitotic figures in ten 400× high-power field views. *p21* null MMTV-*Wnt1*-treated tumors were separated into arrested (open circles) and mitotic (open triangles) groups. Mean (horizontal line) with error bars (SEM) is shown.

See also Figure S3.

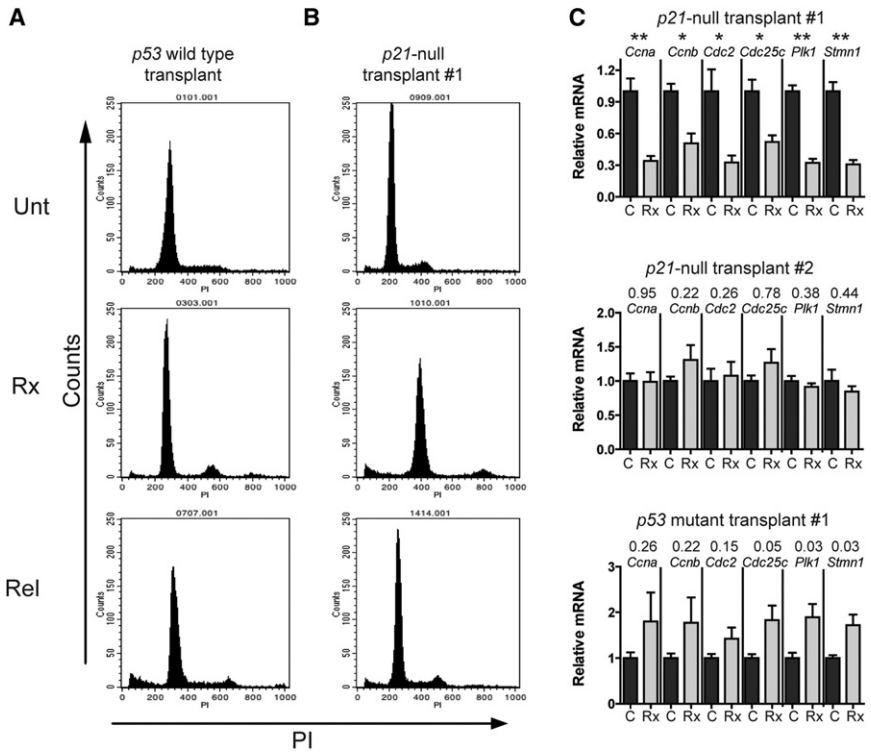

Figure 5. G2 Arrest with Downregulated G2-M Regulators in Nonproliferating *p21* Null MMTV-*Wnt1*-Treated Tumors

(A and B) *p53* wild-type and *p21* null MMTV-*Wnt1* tumors were transplanted and treated in parallel as in Figure 2B and harvested. Tumors as indicated in the figure were processed to single-cell suspension by mincing and trypsinizing, followed by fixation and staining for DNA content with propidium iodide (PI). Unt, untreated; Rx, doxorubicin treated; Rel, relapsed.

(C) mRNA levels for G2-M regulatory genes as indicated in the figure were determined for untreated tumors ("C") or tumors harvested 48 hr after final treatment ("Rx"); at least three tumors were analyzed per treatment group. Error bars are ± SEM. $^{**}p < 0.005$, $^{*}p < 0.05$ by Student's t test. p Values of nonsignificant comparisons and comparisons where treated tumors were higher are shown above the gene symbol.

See also Figure S4.

paracrine fashion, reinforcing the dormant state (Kuilman et al., 2008). However, we also found Ki67 and phospho-Stat3 double-positive regions in treated tumors that were nearing the time at which they typically relapse. Because cytokines promote the proliferation of nonsenescent mammary tumor cells, this suggests that neighboring, nonsenescent cells within the tumor could be stimulated to proliferate by cytokines produced by senescent cells. Of note the cytokines we tested for growth stimulation represent just three of many potentially mitogenic cytokines expressed in the senescent tumor cells. Also, it is not known what additive or synergistic growth effects the array of cytokines expressed by tumor cells would have within the natural environment of the tumor. Indeed, others have shown various cytokines elevated in our tumors to have protumorigenic properties in different cellular contexts (Begley et al., 2008; Dhawan and Richmond, 2002; Pirianov and Colston, 2001; Takamori et al., 2000; Yang et al., 2006). Furthermore, it is also possible that the cytokines promote other phenotypes such as metastasis and cell survival (Clevenger, 2004; Karnoub and Weinberg, 2006-2007; Krtolica et al., 2001). The finding that some *p53* mutant tumors also expressed selected cytokines following treatment underscores the importance of apoptosis in these tumors. Apoptosis likely eliminated the damaged *p53* mutant tumor cells that expressed mitogenic cytokines, whereas cytokine producing cells in a *p53* wild-type tumor persisted in a senescent state.

Our work also suggests that pharmacological inhibition of arrest and/or senescence, by inactivating *p53*, could improve chemotherapy response by redirecting cells toward apoptosis. However, it is important to note that complete loss of *p21* in the MMTV-*Wnt1* tumors was insufficient to bypass the *p53*-mediated arrest phenotype in a subset of tumors. *p21* null MMTV-*Wnt1* tumors showed a dichotomy of responses, resulting in an intermediate mean tumor regression following treatment. This is consistent with these tumors having both a "*p53* wild-type like" response, where treated tumors do not enter S phase or mitosis, arresting in G2, and a "*p53* mutant-like" response, where treated tumors continued through S phase and mitosis. This effect has not been observed in several in vitro studies of a *p21* null cell line. Using isogenic variants of the colon cancer cell line HCT-116, Waldman et al. observed a superior response to radiation in *p21* null xenografts, as compared to the parental cell line (Waldman et al., 1997). These data, from a single xenografted cell line, are consistent with the fraction of tumors in our study that failed to arrest following treatment (Waldman et al., 1997).

In summary we have modeled chemotherapy response in mice, showing that p53 activity induces *p21*-dependent and -independent growth arrest and cellular senescence instead of cell death, resulting in minimal tumor regression and early relapse. Bypassing senescence, via *p53* deletion/mutation, initiated *p53*-independent cell death and improved tumor response. These results provide a compelling explanation for previous studies that showed improved patient response to anthracycline-based chemotherapy in *TP53* mutant human breast tumors (Bertheau et al., 2002, 2007).

EXPERIMENTAL PROCEDURES

Mice

All experiments were approved by the MD Anderson Cancer Center Institutional Animal Care and Use Committee, Protocol ID# 079906634, and conformed to the guidelines of the United States Animal Welfare Act and the National Institutes of Health. MMTV-*Wnt1*, $p53^{R172H/R172H}$, $p53^{-/-}$, and $p21^{-/-}$ mice have been described by Brugarolas et al. (1995), Jacks et al. (1994), Lang et al. (2004), and Tsukamoto et al. (1988). Breeders were backcrossed into C57Bl6J background (The Jackson Laboratory, Bar Harbor, ME, USA) until >90% C57Bl6J as determined by polymorphic allele analysis

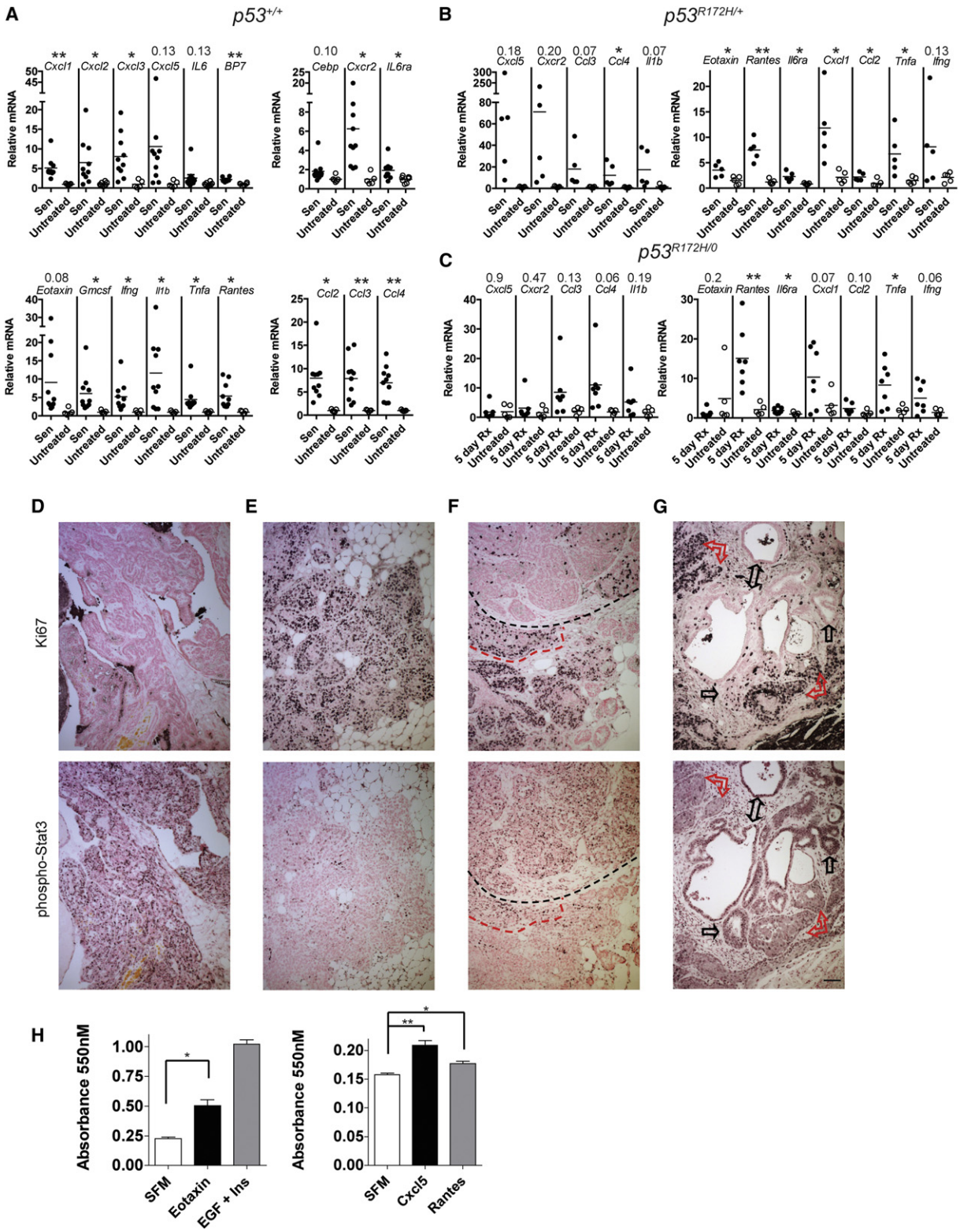

Figure 6. Senescence-Associated Cytokines Are Expressed in Treated MMTV-*Wnt1* Mammary Tumors

(A–C) *p53* wild-type tumors (A), *p53* heterozygous mutant tumors that retained the wild-type allele (B), or lost the wild-type allele (C), corresponding to spontaneous tumors from Figures 3A–3C, were harvested, and mRNA levels for genes indicated in the figure were determined. All graphs in (A)–(C) are relative to the mean of untreated *p53* wild-type tumors set to a value of 1. $^{**}p < 0.005$, $^{*}p < 0.05$ by Student's t test. p Values of nonsignificant comparisons are shown above the gene symbol. Horizontal line is the mean.

by the Research Animal Support Facility-Smithville, Genetic Services. Subsequent breedings produced MMTV-*Wnt1* mice in *p53* wild-type, $p53^{R172H/R172H}$, $p53^{-/-}$, $p53^{R172H/+}$, and $p21^{-/-}$ backgrounds. Homozygous *p53* mutant mice, particularly females, were not born at Mendelian ratio, consistent with other reports by Sah et al. (1995), and were thus difficult to acquire in the cohort. Mammary tumors formed in MMTV-*Wnt1* mice in our study with median latency of 185 days. $p53^{R172H/R172H}$, $p53^{-/-}$ and $p53^{R172H/+}$ mice had median latencies of 108, 111, and 173 days, respectively. Mice were monitored frequently for tumor formation and tumors measured regularly using digital calipers: tumor volume in mm^3 = (width^2 × length)/2 (Bearss et al., 2000). Histologically, all of the MMTV-*Wnt1* tumors were ductal carcinomas, generally of solid, cystic, or mixed subtypes. *p53* wild-type, $p53^{R172H/+}$, $p21^{-/-}$ were all 68%–79% mixed, whereas $p53^{R172H/R172H}$ and $p53^{R172H/0}$ were 61% solid. When tumors reached a volume of ~500 mm^3 and were growing, 4 mg/kg doxorubicin (Sigma-Aldrich, St. Louis) in PBS was injected intraperitoneally once daily for 5 consecutive days. Treatments were well tolerated in *p53* wild-type and heterozygous mutant mice as well as $p21^{-/-}$ mice, with minimal (less than 10%) or no weight loss during or after treatment. *p53* homozygous mutant mice, however, did show signs of toxicity, primarily weight loss ~4 days after treatment, likely due to GI syndrome, as previously described in *p53* mutant mice by Komarova et al. (2004). This toxicity did not appear to contribute to tumor regression because *p53* heterozygous mutant mice with LOH in the tumor had no toxicity and had similar tumor regression as the homozygous mutant mice. At the defined endpoint for each mouse, tumors were harvested, and portions were fixed in formalin for 48 hr and paraffin embedded (FFPE), and also flash frozen for biochemical analysis. LOH analysis was performed exactly as previously described by Post et al. (2010).

Real-Time RT-PCR

RNA was extracted from frozen, pulverized tumors using TRIzol reagent (Invitrogen, Carlsbad, CA, USA), subjected to DNase treatment (Roche, Indianapolis, IN, USA), and then reverse transcribed using a kit (GE Healthcare, Piscataway, NJ, USA). Real-time PCR using Sybr green (BioRad, Valencia, CA, USA) was performed as previously described by Jackson and Pereira-Smith (2006). Expression was normalized to Gapdh and verified with Rplp0. Primer sequences are available on request.

Immunohistochemistry

Cleaved caspase staining was performed as previously described by Post et al. (2010), and staining for phospho-Stat3 polyclonal antibody (1:100; Cell Signaling, Danvers, MA, USA) and Ki67 (1:100; Leica, Newcastle Upon Tyne, UK, Ki67-MM1) were performed similarly. For phospho-Stat3 monoclonal, antigen retrieval was in Tris EDTA buffer (pH 9). For detecting incorporation of BrdU, tumor-bearing mice were injected with BrdU (Invitrogen) according to manufacturer's instructions, 24 and 4 hr before harvest, followed by standard fixation and processing. Denaturation was in 2 N HCl for 90 min, followed by neutralization in 0.1 M $Na_2B_4O_7$, standard processing, and then incubation with anti-BrdU (BD Immunocytometry Systems, San Jose, CA, USA) at 1:40 for 1 hr (McGinley et al., 2000). Antigen detection for immunohistochemistry (IHC) was performed using a VECTASTAIN kit and ABC (Vector Laboratories, Burlingame, CA, USA). Images were acquired on a Nikon 80i microscope equipped with a Nikon DS-Fi1 color camera using the 10×/0.45 objective and Nikon Elements software. Some images were processed minimally in Adobe Photoshop only by histogram stretching and gamma adjustment. At least four random fields were manually counted for cleaved caspase-3 experiments. Number of positive cells was averaged for the four fields.

TUNEL staining was performed using the FragEL DNA fragmentation detection kit (Calbiochem, Darmstadt, Germany) and quantitated as above. SAβGal assay was performed essentially as described by Dimri et al. (1995) for in vitro and in vivo experiments. Tumor segments ~1 mm thick were fixed in 2% formaldehyde, 0.2% glutaraldehyde in PBS, stained for SAβGal, cut to 6 μm sections, and counterstained with Nuclear Fast Red (Vector Laboratories). These results were verified by staining of frozen sections in parallel.

Western Blotting

Frozen pulverized tumors were lysed and separated by SDS-PAGE as previously described by Pant et al. (2011). Antibodies and dilutions were p21 (for mouse p21 detection), 1:1,000, #556431 (BD PharMingen, San Jose, CA, USA); Vinculin, 1:1,000, #V-9131 (Sigma-Aldrich); p21 (for human p21 detection), 1:200, SC6246 (Santa Cruz Biotechnology, Santa Cruz, CA, USA); and mouse monoclonal p53, 1:200, OP09 (EMD Biosciences, Darmstadt, Germany).

Statistical Analysis

Two-tailed Student's t tests and ANOVA using Newman-Keuls posttest were performed using GraphPad Prism software (La Jolla, CA, USA).

Anaphase Bridges and Mitotic Activity

H&E MMTV-*Wnt1* tumor sections were scanned on a microscope at 400×, and cells in anaphase were photographed. Two different observers identified the presence or absence of bridges. For mitotic figures, ten random, 400×, high-powered fields for each tumor were selected, and mitotic figures were identified and counted by two different observers.

Flow Cytometry

Tumors were harvested and processed as for transplants (above). After filtering, cells were washed in PBS, then fixed in 70% ethanol for at least 24 hr at −20°C. Propidium iodide staining was performed as previously described by Jackson and Pereira-Smith (2006).

Transplants

Primary MMTV-*Wnt1* tumors were removed from euthanized mice, minced thoroughly with a scalpel blade, and then trypsinized for 10 min at 37°C. Trypsin was inactivated with DMEM plus 10% fetal calf serum, followed by passage through a 40 μM filter. After PBS washing, cells were resuspended in Matrigel/PBS (BD Biosciences) at a concentration of 4 × 10^6/50 μl. The 50 μl solution was injected into each abdominal mammary fat pad of recipient C57Bl6 mice using a 30G needle. Tumors were detectable at ~2 weeks, typically.

SUPPLEMENTAL INFORMATION

Supplemental Information includes six figures and Supplemental Experimental Procedures and can be found with this article online at doi:10.1016/j.ccr.2012.04.027.

ACKNOWLEDGMENTS

The authors wish to thank MDACC Animal Support Facility-Smithville, the DNA Analysis Facility, the Flow Cytometry & Imaging Core Facility, and the

(D–G) Phospho-Stat3 and Ki67 staining in treated, senescent tumors. Serial sections from formalin-fixed paraffin-embedded tumors from Figure 3A were stained for Ki67 (upper panels) or phosphoTyr705-Stat3 (antibody clone D3A7) (lower panels). (D–F) Representative examples of positive/negative or negative/positive phospho-Stat3 (antibody clone D3A7) and Ki67 from treated tumors. (F) Inverse staining of adjacent areas within the same tumor sections, and an area of double positivity marked by red dashed line. (G) Similar staining results with a second polyclonal phosphoTyr705-Stat3 antibody, with more intense phospho-Stat3-positive/Ki67-negative areas (indicated by black arrows) and less intense phospho-Stat3 staining/Ki67-positive areas (indicated by red arrows). Scale bar, 50 μM. (H) Tumor cells isolated from an MMTV-*Wnt1* mammary tumor and cultured were plated at 8,000 cells per well in a 24-well plate overnight, then media were changed to serum-free media (SFM), or 100 ng/ml cytokine. EGF and insulin, known mitogens in breast cancer, were at 20 ng/ml and 10 μg/ml, respectively. Cell number was determined at day 4 by MTT assay. Error bars are ± SEM. For comparison of SFM to Eotaxin, *$p < 0.05$ by Student's t test. For comparison of SFM, Cxcl5, and Rantes, $p < 0.005$ by ANOVA and Newman-Keuls.
See also Figure S5.

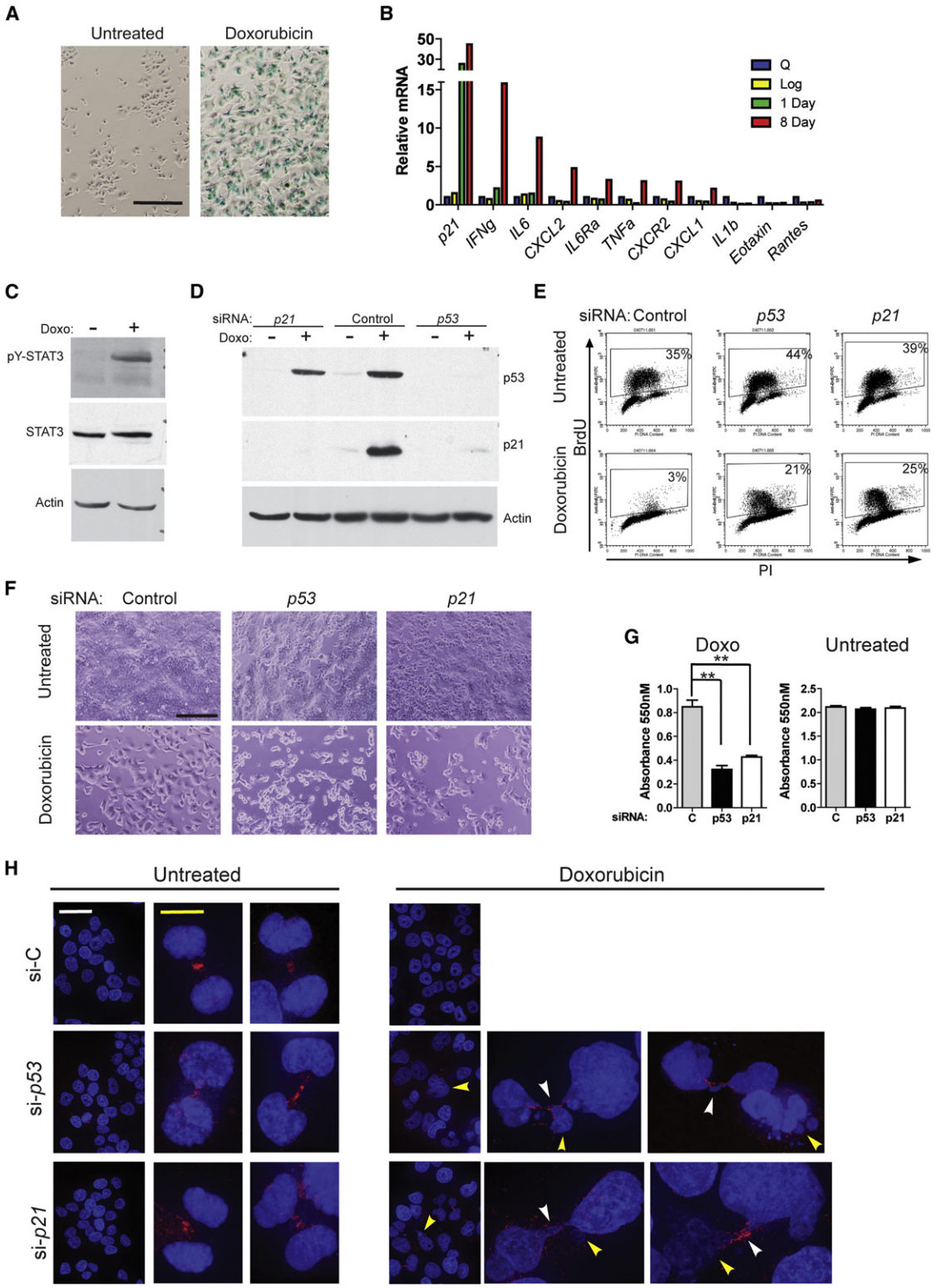

Figure 7. *p53* or *p21* Knockdown Improves Doxorubicin Response in *p53* Wild-type MCF-7 Breast Cancer Cells

(A) MCF-7 human breast cancer cells untreated or treated with 200 nM doxorubicin for 24 hr and harvested 8 days later were fixed and stained for SAβGal. Scale bar, 500 μM.

(B) mRNA levels for cytokines indicated in the figure were determined for MCF-7 cells that were serum starved for 72 hr (Q), growing in log phase (Log), or treated with doxorubicin as in (A) and harvested 1 or 8 days later.

Department of Veterinary Medicine and Surgery and the Histology Core Research Lab, each supported by NCI Grant CA16672. We also acknowledge Courtney Vallien for histological sectioning, Henry P. Adams for technical help with microscopy, and Archana Sidalaghatta Nagaraja for assistance with mouse necropsy and RNA preparation. J.G.J. was funded as an Odyssey Scholar by the Theodore N. Law Endowment for Scientific Achievement, a Dodie P. Hawn Fellowship in Genetics, and by NIH Grant U01DE019765-01. Q.L. and V.P. are supported by NIH Grant CA47296. G.L. is supported by NIH Grants CA34936 and CA82577.

J.G.J. conceived, designed, and performed all the experiments except where noted, and wrote the manuscript. V.P. and J.G.J. performed protein expression analysis. J.G.J., Q.L., and V.P. performed mRNA analysis. J.G.J., L.L.C., Q.L., D.G., and A.Q.-C. performed immunohistochemical analyses. T.M. performed the Bio-Plex cytokine array. J.G.J., D.G., and A.Q.-C. performed quantitative analysis of mitosis. Y.L. developed cell lines. J.G.J. and O.T. performed senescence associated β-galactosidase studies. P.Y. and J.G.J. determined loss of heterozygosity in tumors. A.K.E-N. performed pathological analysis. A.Q.-C. edited the manuscript. G.L. was the principal investigator for the study.

Received: October 1, 2011
Revised: March 2, 2012
Accepted: April 14, 2012
Published: June 11, 2012

REFERENCES

Aas, T., Børresen, A.L., Geisler, S., Smith-Sørensen, B., Johnsen, H., Varhaug, J.E., Akslen, L.A., and Lønning, P.E. (1996). Specific P53 mutations are associated with de novo resistance to doxorubicin in breast cancer patients. Nat. Med. *2*, 811–814.

Acosta, J.C., O'Loghlen, A., Banito, A., Guijarro, M.V., Augert, A., Raguz, S., Fumagalli, M., Da Costa, M., Brown, C., Popov, N., et al. (2008). Chemokine signaling via the CXCR2 receptor reinforces senescence. Cell *133*, 1006–1018.

Bearss, D.J., Subler, M.A., Hundley, J.E., Troyer, D.A., Salinas, R.A., and Windle, J.J. (2000). Genetic determinants of response to chemotherapy in transgenic mouse mammary and salivary tumors. Oncogene *19*, 1114–1122.

Begley, L.A., Kasina, S., Mehra, R., Adsule, S., Admon, A.J., Lonigro, R.J., Chinnaiyan, A.M., and Macoska, J.A. (2008). CXCL5 promotes prostate cancer progression. Neoplasia *10*, 244–254.

Berns, E.M., Foekens, J.A., Vossen, R., Look, M.P., Devilee, P., Henzen-Logmans, S.C., van Staveren, I.L., van Putten, W.L., Inganäs, M., Meijer-van Gelder, M.E., et al. (2000). Complete sequencing of TP53 predicts poor response to systemic therapy of advanced breast cancer. Cancer Res. *60*, 2155–2162.

Bertheau, P., Plassa, F., Espié, M., Turpin, E., de Roquancourt, A., Marty, M., Lerebours, F., Beuzard, Y., Janin, A., and de Thé, H. (2002). Effect of mutated TP53 on response of advanced breast cancers to high-dose chemotherapy. Lancet *360*, 852–854.

Bertheau, P., Turpin, E., Rickman, D.S., Espié, M., de Reyniès, A., Feugeas, J.P., Plassa, L.F., Soliman, H., Varna, M., de Roquancourt, A., et al. (2007). Exquisite sensitivity of TP53 mutant and basal breast cancers to a dose-dense epirubicin-cyclophosphamide regimen. PLoS Med. *4*, e90.

Bertheau, P., Espié, M., Turpin, E., Lehmann, J., Plassa, L.F., Varna, M., Janin, A., and de Thé, H. (2008). TP53 status and response to chemotherapy in breast cancer. Pathobiology *75*, 132–139.

Bonnefoi, H., Piccart, M., Bogaerts, J., Mauriac, L., Fumoleau, P., Brain, E., Petit, T., Rouanet, P., Jassem, J., Blot, E., et al; EORTC 10994/BIG 1-00 Study Investigators. (2011). TP53 status for prediction of sensitivity to taxane versus non-taxane neoadjuvant chemotherapy in breast cancer (EORTC 10994/BIG 1-00): a randomised phase 3 trial. Lancet Oncol. *12*, 527–539.

Brown, J.M., and Attardi, L.D. (2005). The role of apoptosis in cancer development and treatment response. Nat. Rev. Cancer *5*, 231–237.

Brown, J.P., Wei, W., and Sedivy, J.M. (1997). Bypass of senescence after disruption of p21CIP1/WAF1 gene in normal diploid human fibroblasts. Science *277*, 831–834.

Brugarolas, J., Chandrasekaran, C., Gordon, J.I., Beach, D., Jacks, T., and Hannon, G.J. (1995). Radiation-induced cell cycle arrest compromised by p21 deficiency. Nature *377*, 552–557.

Bunz, F., Dutriaux, A., Lengauer, C., Waldman, T., Zhou, S., Brown, J.P., Sedivy, J.M., Kinzler, K.W., and Vogelstein, B. (1998). Requirement for p53 and p21 to sustain G2 arrest after DNA damage. Science *282*, 1497–1501.

Bunz, F., Hwang, P.M., Torrance, C., Waldman, T., Zhang, Y., Dillehay, L., Williams, J., Lengauer, C., Kinzler, K.W., and Vogelstein, B. (1999). Disruption of p53 in human cancer cells alters the responses to therapeutic agents. J. Clin. Invest. *104*, 263–269.

Carey, L.A., Dees, E.C., Sawyer, L., Gatti, L., Moore, D.T., Collichio, F., Ollila, D.W., Sartor, C.I., Graham, M.L., and Perou, C.M. (2007). The triple negative paradox: primary tumor chemosensitivity of breast cancer subtypes. Clin. Cancer Res. *13*, 2329–2334.

Chang, B.D., Xuan, Y., Broude, E.V., Zhu, H., Schott, B., Fang, J., and Roninson, I.B. (1999). Role of p53 and p21waf1/cip1 in senescence-like terminal proliferation arrest induced in human tumor cells by chemotherapeutic drugs. Oncogene *18*, 4808–4818.

Clarke, A.R., Purdie, C.A., Harrison, D.J., Morris, R.G., Bird, C.C., Hooper, M.L., and Wyllie, A.H. (1993). Thymocyte apoptosis induced by p53-dependent and independent pathways. Nature *362*, 849–852.

Clevenger, C.V. (2004). Roles and regulation of stat family transcription factors in human breast cancer. Am. J. Pathol. *165*, 1449–1460.

Collado, M., Gil, J., Efeyan, A., Guerra, C., Schuhmacher, A.J., Barradas, M., Benguría, A., Zaballos, A., Flores, J.M., Barbacid, M., et al. (2005). Tumour biology: senescence in premalignant tumours. Nature *436*, 642.

Coppé, J.P., Patil, C.K., Rodier, F., Sun, Y., Muñoz, D.P., Goldstein, J., Nelson, P.S., Desprez, P.Y., and Campisi, J. (2008). Senescence-associated secretory phenotypes reveal cell-nonautonomous functions of oncogenic RAS and the p53 tumor suppressor. PLoS Biol. *6*, 2853–2868.

Deng, C., Zhang, P., Harper, J.W., Elledge, S.J., and Leder, P. (1995). Mice lacking p21CIP1/WAF1 undergo normal development, but are defective in G1 checkpoint control. Cell *82*, 675–684.

Dhawan, P., and Richmond, A. (2002). Role of CXCL1 in tumorigenesis of melanoma. J. Leukoc. Biol. *72*, 9–18.

Dimri, G.P., Lee, X., Basile, G., Acosta, M., Scott, G., Roskelley, C., Medrano, E.E., Linskens, M., Rubelj, I., Pereira-Smith, O., et al. (1995). A biomarker that identifies senescent human cells in culture and in aging skin in vivo. Proc. Natl. Acad. Sci. USA *92*, 9363–9367.

(C) MCF-7 cells untreated or 8 days following treatment as in (A) were harvested 48 hr after a media change, and western blots were performed with indicated antibodies.
(D–F) MCF-7 cells were transfected with nontargeting siRNA (Control) or siRNA targeting *p53* or *p21*. After 24 hr, cells were treated with doxorubicin for 24 hr, or untreated as indicated. (D) Cells were harvested 24 hr after treatment for western blot with *p53*, *p21*, or actin antibodies. (E) Cells were pulsed for 1 hr with BrdU 24 hr after doxorubicin treatment, fixed, stained with anti-BrdU FITC, and sorted by flow cytometry. Percent BrdU-positive cells are indicated in the figure. (F) Four days following treatment and media change, cells were photographed using bright-field microscopy (scale bar, 500 μM).
(G) Cell number was determined by MTT assay 9 days following treatment. Error bars are ± SEM. $^{**}p < 0.005$ by ANOVA and Newman-Keuls posttest.
(H) MCF-7 cells were untreated or treated with 200 nM doxorubicin for 24 hr, then fixed and stained for α-tubulin and DAPI 72 hr later. Scale bars, 40 μM (white) and 10 μM (yellow). Yellow arrows indicate micronuclei and white arrows anaphase bridges.
See also Figure S6.

Donehower, L.A., Godley, L.A., Aldaz, C.M., Pyle, R., Shi, Y.P., Pinkel, D., Gray, J., Bradley, A., Medina, D., and Varmus, H.E. (1995). Deficiency of p53 accelerates mammary tumorigenesis in Wnt-1 transgenic mice and promotes chromosomal instability. Genes Dev. *9*, 882–895.

Jacks, T., Remington, L., Williams, B.O., Schmitt, E.M., Halachmi, S., Bronson, R.T., and Weinberg, R.A. (1994). Tumor spectrum analysis in p53-mutant mice. Curr. Biol. *4*, 1–7.

Jackson, J.G., and Pereira-Smith, O.M. (2006). Primary and compensatory roles for RB family members at cell cycle gene promoters that are deacetylated and downregulated in doxorubicin-induced senescence of breast cancer cells. Mol. Cell. Biol. *26*, 2501–2510.

Jackson, J.G., Post, S.M., and Lozano, G. (2011). Regulation of tissue- and stimulus-specific cell fate decisions by p53 in vivo. J. Pathol. *223*, 127–136.

Karnoub, A.E., and Weinberg, R.A. (2006–2007). Chemokine networks and breast cancer metastasis. Breast Dis. *26*, 75–85.

Komarova, E.A., Kondratov, R.V., Wang, K., Christov, K., Golovkina, T.V., Goldblum, J.R., and Gudkov, A.V. (2004). Dual effect of p53 on radiation sensitivity in vivo: p53 promotes hematopoietic injury, but protects from gastrointestinal syndrome in mice. Oncogene *23*, 3265–3271.

Kröger, N., Milde-Langosch, K., Riethdorf, S., Schmoor, C., Schumacher, M., Zander, A.R., and Löning, T. (2006). Prognostic and predictive effects of immunohistochemical factors in high-risk primary breast cancer patients. Clin. Cancer Res. *12*, 159–168.

Krtolica, A., Parrinello, S., Lockett, S., Desprez, P.Y., and Campisi, J. (2001). Senescent fibroblasts promote epithelial cell growth and tumorigenesis: a link between cancer and aging. Proc. Natl. Acad. Sci. USA *98*, 12072–12077.

Kuilman, T., Michaloglou, C., Vredeveld, L.C., Douma, S., van Doorn, R., Desmet, C.J., Aarden, L.A., Mooi, W.J., and Peeper, D.S. (2008). Oncogene-induced senescence relayed by an interleukin-dependent inflammatory network. Cell *133*, 1019–1031.

Lang, G.A., Iwakuma, T., Suh, Y.A., Liu, G., Rao, V.A., Parant, J.M., Valentin-Vega, Y.A., Terzian, T., Caldwell, L.C., Strong, L.C., et al. (2004). Gain of function of a p53 hot spot mutation in a mouse model of Li-Fraumeni syndrome. Cell *119*, 861–872.

Lehmann-Che, J., André, F., Desmedt, C., Mazouni, C., Giacchetti, S., Turpin, E., Espié, M., Plassa, L.F., Marty, M., Bertheau, P., et al. (2010). Cyclophosphamide dose intensification may circumvent anthracycline resistance of p53 mutant breast cancers. Oncologist *15*, 246–252.

Liu, G., Parant, J.M., Lang, G., Chau, P., Chavez-Reyes, A., El-Naggar, A.K., Multani, A., Chang, S., and Lozano, G. (2004). Chromosome stability, in the absence of apoptosis, is critical for suppression of tumorigenesis in Trp53 mutant mice. Nat. Genet. *36*, 63–68.

Lowe, S.W., Ruley, H.E., Jacks, T., and Housman, D.E. (1993a). p53-dependent apoptosis modulates the cytotoxicity of anticancer agents. Cell *74*, 957–967.

Lowe, S.W., Schmitt, E.M., Smith, S.W., Osborne, B.A., and Jacks, T. (1993b). p53 is required for radiation-induced apoptosis in mouse thymocytes. Nature *362*, 847–849.

Lowe, S.W., Bodis, S., McClatchey, A., Remington, L., Ruley, H.E., Fisher, D.E., Housman, D.E., and Jacks, T. (1994). p53 status and the efficacy of cancer therapy in vivo. Science *266*, 807–810.

Makris, A., Powles, T.J., Dowsett, M., and Allred, C. (1995). p53 protein overexpression and chemosensitivity in breast cancer. Lancet *345*, 1181–1182.

Mathieu, M.C., Koscielny, S., Le Bihan, M.L., Spielmann, M., and Arriagada, R.; Institut Gustave-Roussy Breast Cancer Group. (1995). p53 protein overexpression and chemosensitivity in breast cancer. Lancet *345*, 1182.

Mazars, R., Spinardi, L., BenCheikh, M., Simony-Lafontaine, J., Jeanteur, P., and Theillet, C. (1992). p53 mutations occur in aggressive breast cancer. Cancer Res. *52*, 3918–3923.

McGinley, J.N., Knott, K.K., and Thompson, H.J. (2000). Effect of fixation and epitope retrieval on BrdU indices in mammary carcinomas. J. Histochem. Cytochem. *48*, 355–362.

Novakova, Z., Hubackova, S., Kosar, M., Janderova-Rossmeislova, L., Dobrovolna, J., Vasicova, P., Vancurova, M., Horejsi, Z., Hozak, P., Bartek, J., and Hodny, Z. (2010). Cytokine expression and signaling in drug-induced cellular senescence. Oncogene *29*, 273–284.

Pant, V., Xiong, S., Iwakuma, T., Quintás-Cardama, A., and Lozano, G. (2011). Heterodimerization of Mdm2 and Mdm4 is critical for regulating p53 activity during embryogenesis but dispensable for p53 and Mdm2 stability. Proc. Natl. Acad. Sci. USA *108*, 11995–12000.

Pirianov, G., and Colston, K.W. (2001). Interactions of vitamin D analogue CB1093, TNFalpha and ceramide on breast cancer cell apoptosis. Mol. Cell. Endocrinol. *172*, 69–78.

Post, S.M., Quintás-Cardama, A., Terzian, T., Smith, C., Eischen, C.M., and Lozano, G. (2010). p53-dependent senescence delays Emu-myc-induced B-cell lymphomagenesis. Oncogene *29*, 1260–1269.

Rahko, E., Blanco, G., Soini, Y., Bloigu, R., and Jukkola, A. (2003). A mutant TP53 gene status is associated with a poor prognosis and anthracycline-resistance in breast cancer patients. Eur. J. Cancer *39*, 447–453.

Riley, T., Sontag, E., Chen, P., and Levine, A. (2008). Transcriptional control of human p53-regulated genes. Nat. Rev. Mol. Cell Biol. *9*, 402–412.

Sah, V.P., Attardi, L.D., Mulligan, G.J., Williams, B.O., Bronson, R.T., and Jacks, T. (1995). A subset of p53-deficient embryos exhibit exencephaly. Nat. Genet. *10*, 175–180.

Soussi, T., and Lozano, G. (2005). p53 mutation heterogeneity in cancer. Biochem. Biophys. Res. Commun. *331*, 834–842.

Straver, M.E., Glas, A.M., Hannemann, J., Wesseling, J., van de Vijver, M.J., Rutgers, E.J., Vrancken Peeters, M.J., van Tinteren, H., Van't Veer, L.J., and Rodenhuis, S. (2010). The 70-gene signature as a response predictor for neoadjuvant chemotherapy in breast cancer. Breast Cancer Res. Treat. *119*, 551–558.

Takamori, H., Oades, Z.G., Hoch, O.C., Burger, M., and Schraufstatter, I.U. (2000). Autocrine growth effect of IL-8 and GROalpha on a human pancreatic cancer cell line, Capan-1. Pancreas *21*, 52–56.

te Poele, R.H., Okorokov, A.L., Jardine, L., Cummings, J., and Joel, S.P. (2002). DNA damage is able to induce senescence in tumor cells in vitro and in vivo. Cancer Res. *62*, 1876–1883.

Tsukamoto, A.S., Grosschedl, R., Guzman, R.C., Parslow, T., and Varmus, H.E. (1988). Expression of the int-1 gene in transgenic mice is associated with mammary gland hyperplasia and adenocarcinomas in male and female mice. Cell *55*, 619–625.

Varna, M., Lehmann-Che, J., Turpin, E., Marangoni, E., El-Bouchtaoui, M., Jeanne, M., Grigoriu, C., Ratajczak, P., Leboeuf, C., Plassa, L.F., et al. (2009). p53 dependent cell-cycle arrest triggered by chemotherapy in xenografted breast tumors. Int. J. Cancer *124*, 991–997.

Wajapeyee, N., Serra, R.W., Zhu, X., Mahalingam, M., and Green, M.R. (2008). Oncogenic BRAF induces senescence and apoptosis through pathways mediated by the secreted protein IGFBP7. Cell *132*, 363–374.

Waldman, T., Kinzler, K.W., and Vogelstein, B. (1995). p21 is necessary for the p53-mediated G1 arrest in human cancer cells. Cancer Res. *55*, 5187–5190.

Waldman, T., Zhang, Y., Dillehay, L., Yu, J., Kinzler, K., Vogelstein, B., and Williams, J. (1997). Cell-cycle arrest versus cell death in cancer therapy. Nat. Med. *3*, 1034–1036.

Willis, A., Jung, E.J., Wakefield, T., and Chen, X. (2004). Mutant p53 exerts a dominant negative effect by preventing wild-type p53 from binding to the promoter of its target genes. Oncogene *23*, 2330–2338.

Yang, X., Lu, P., Fujii, C., Nakamoto, Y., Gao, J.L., Kaneko, S., Murphy, P.M., and Mukaida, N. (2006). Essential contribution of a chemokine, CCL3, and its receptor, CCR1, to hepatocellular carcinoma progression. Int. J. Cancer *118*, 1869–1876.

Cancer Cell
Article

A TARBP2-Dependent miRNA Expression Profile Underlies Cancer Stem Cell Properties and Provides Candidate Therapeutic Reagents in Ewing Sarcoma

Claudio De Vito,[1,3] Nicolo Riggi,[1,3] Sandrine Cornaz,[1] Mario-Luca Suvà,[1] Karine Baumer,[1] Paolo Provero,[2] and Ivan Stamenkovic[1,*]
[1]Institute of Pathology, Centre Hospitalier Universitaire Vaudois, Faculty of Biology and Medicine, University of Lausanne, Lausanne, Switzerland
[2]Department of Genetics, Biology and Biochemistry, University of Torino, Torino, Italy
[3]These authors contributed equally to the work
*Correspondence: ivan.stamenkovic@chuv.ch
DOI 10.1016/j.ccr.2012.04.023

SUMMARY

We have recently demonstrated that human pediatric mesenchymal stem cells can be reprogrammed toward a Ewing sarcoma family tumor (ESFT) cancer stem cell (CSC) phenotype by mechanisms that implicate microRNAs (miRNAs). Here, we show that the miRNA profile of ESFT CSCs is shared by embryonic stem cells and CSCs from divergent tumor types. We also provide evidence that the miRNA profile of ESFT CSCs is the result of reversible disruption of TARBP2-dependent miRNA maturation. Restoration of TARBP2 activity and systemic delivery of synthetic forms of either of two of its targets, miRNA-143 or miRNA-145, inhibited ESFT CSC clonogenicity and tumor growth in vivo. Our observations suggest that CSC self-renewal and tumor maintenance may depend on deregulation of TARBP2-dependent miRNA expression.

INTRODUCTION

Cancer development is a multistep process that relies primarily on alterations in the form of mutation, deletion, or translocation of genes that control cell growth, proliferation, and survival. Mounting evidence suggests that, despite originating from a single transformed cell, a tumor may adopt a hierarchical cellular organization, the apex of which is occupied by poorly differentiated cells that acquire or retain at least a subset of stem cell properties, including the capacity for self-renewal and differentiation (Clarke et al., 2006; Clevers, 2011; Frank et al., 2010; Visvader, 2011). These cells, termed cancer stem cells (CSCs), have the ability to generate proliferating cell pools that repopulate tumors and to differentiate into nontumorigenic progeny that contributes to the phenotypic heterogeneity characteristic of most tumor types. CSCs have therefore been advocated to constitute the sustaining force of a tumor. This notion has led to the view that CSC-directed therapeutic approaches may provide an attractive alternative in malignancies that are resistant to conventional chemotherapy aimed at indiscriminate elimination of the tumor bulk (Frank et al., 2010).

Exactly how CSCs emerge remains unclear but possible mechanisms include transformation of primary stem cells or acquisition of stem cell properties by more differentiated cells as a result of transformation-associated genetic reprogramming (Liu et al., 2009; Marión et al., 2009). Subsequent maintenance of stem cell features may be ensured, in part, by the genetic alterations responsible for transformation itself and, in part, by posttranscriptional events, including regulation of gene expression by microRNAs (miRNAs).

miRNAs are noncoding transcripts capable of recognizing complementary sequences within the 3′ untranslated regions, introns, and even exons of a wide range of genes (Bartel, 2009). Human tumors display broad miRNA downregulation that appears to be responsible, at least in part, for their malignancy and stems from defects in their production, intracellular

Significance

Mechanisms that generate cancer stem cells (CSCs), which are believed to constitute the driving force of many malignancies, are poorly understood. We show that Ewing sarcoma family tumor (ESFT) CSCs emerge as a result of a defect in microRNA (miRNA) maturation stemming from reversible repression of the gene encoding TARBP2, a protein implicated in stabilizing the miRNA processing machinery. The resulting miRNA expression repertoire regulates networks of genes whose expression changes underlie ESFT pathogenesis. Reconstitution of TARBP2 function or expression of its target miRNAs blunts ESFT CSC tumor-forming capacity and offers an attractive therapeutic option for one of the most aggressive pediatric malignancies.

transport, and/or maturation (Kumar et al., 2007; Melo and Esteller, 2011; Ventura and Jacks, 2009). miRNA biogenesis is a multistep process initiated by RNA polymerase II-mediated transcription to generate a primary miRNA (pri-miRNA) (Newman and Hammond, 2010; Winter et al., 2009). Pri-miRNAs are processed by the multiprotein microprocessor complex that includes Drosha, an RNaseIII enzyme, and DGCR8, a double-stranded RNA-binding domain protein, to produce a ~70 nt precursor miRNAs (pre-miRNAs). Pre-miRNAs are exported from the nucleus to the cytoplasm by Exportin-5 by a Ran-GTP-dependent mechanism and are further processed by the multiprotein Dicer complex to generate mature 21–23 nt oligomers. The two miRNA strands are then separated, and one is loaded onto the RNA-induced silencing complex (RISC) by binding to an Argonaute (Ago) protein, whereas the carrier strand is degraded (Newman and Hammond, 2010; Winter et al., 2009). The miRNA guides RISC to its complementary sequences within target transcripts to silence their expression by either facilitating corresponding mRNA degradation or blocking its translation. Because complementary sequences to any given miRNA are found in numerous genes, a restricted number of miRNAs can regulate expression of large gene repertoires implicated in the control of key cell functions. Increasing evidence indicates miRNA involvement in stem cell generation, maintenance, and differentiation, as well as in tumor initiation and progression, consistent with the possibility that miRNAs may play a key role in CSC establishment. As active participants in the orchestration of tumor development, miRNAs may also provide potentially attractive therapeutic targets and/or reagents in cancer.

Work from our own laboratory has shown that miRNAs are implicated in the emergence of CSCs in Ewing sarcoma family tumors (ESFT), the second most common bone malignancy in children and young adults (Riggi et al., 2010). ESFTs are characterized by unique chromosomal translocations that give rise to fusion genes composed of EWS and one of several ets family members of transcription factors (Riggi et al., 2007). The most common fusion gene, *EWS-FLI1*, arises as a result of the chromosomal translocation t(11;22)(q24;q12) and is expressed in 85%–90% of ESFTs. The EWS-FLI-1 fusion protein is believed to provide the key oncogenic event in ESFT by inducing and repressing target genes that lead to transformation of permissive primary cells. Mesenchymal stem cells (MSCs) have been shown to provide permissiveness for EWS-FLI-1 expression and oncogenicity (Riggi et al., 2005, 2008) and are currently considered to be the most likely cell of origin of ESFT. Human pediatric MSCs (hpMSCs) transduced with EWS-FLI-1 (hpMSC$^{EWS\text{-}FLI\text{-}1}$) adopt a transcriptome that resembles that of ESFT more closely than any other primary or immortalized cell type tested (Riggi et al., 2010). Remarkably, expression of EWS-FLI-1 in hpMSCs cultured in serum-free conditions generates a subpopulation of cells that express the CD133 marker characteristic of CSCs in a variety of malignancies and in ESFT in particular (Suvà et al., 2009). These cells constitute no more than 5%–8% of the bulk hpMSC$^{EWS\text{-}FLI\text{-}1}$ population and display upregulation of the embryonic stem cell-associated genes *OCT4* and *NANOG* (Suvà et al., 2009) and repression of miRNA-145, a master regulator of ESC differentiation that acts by suppressing *OCT4*, *KLF4*, and *SOX2* expression (Xu et al., 2009). On the basis of these observations, we assessed miRNA implication in ESFT CSC development using reprogrammed hpMSC$^{EWS\text{-}FLI\text{-}1}$ cells, ESFT cell lines, and primary CSCs and addressed the mechanisms that underlie miRNA deregulation in CSCs.

RESULTS

The ESFT CSC Subpopulation Displays Repression of a Broad Range of miRNAs that Is Shared by the CD133$^+$ Fraction of hpMSC$^{EWS\text{-}FLI\text{-}1}$, Human Embryonic Stem Cells, Induced Pluripotent Stem Cells, and CSC from Diverse Carcinomas

To identify miRNAs that may be relevant to ESFT CSC generation and maintenance, we performed miRNA microarray expression profiling of the CD133$^+$ and CD133$^-$ subpopulations derived from primary ESFT, hpMSC$^{EWS\text{-}FLI\text{-}1}$, and the ESFT STA-ET-8.2 cell line. A total of four primary ESFT tumors were used, two of which (ESFT1 and 2) have been described previously (Suvà et al., 2009), whereas two others (ESFT3 and 4) were obtained more recently (Table S1 available online). All tumors displayed a poorly differentiated small round cell phenotype and harbored a subpopulation of CD133$^+$ cells ranging between 6.5% and 15.2%. Tumors 1 and 2 were used for initial miRNA profiling and qRT-PCR validation of miRNA expression, whereas tumors 3 and 4, whose CD133$^+$ subpopulations displayed features comparable to those of tumors 1 and 2 in terms of miRNA expression profiles, were used for all subsequent functional experiments. ESFT CD133$^+$ (corresponding to CSC) and CD133$^-$ cells were isolated from primary tumors, whereas CD133$^+$ and CD133$^-$ hpMSC$^{EWS\text{-}FLI\text{-}1}$ were generated by retrovirally mediated introduction of EWS-FLI-1 into hpMSCs grown in serum-free stem cell medium, as previously reported (Riggi et al., 2010). Expression profile analysis revealed broad miRNA repression in CD133$^+$ hpMSC$^{EWS\text{-}FLI\text{-}1}$ and ESFT cells, and cluster analysis showed that CD133$^+$ and CD133$^-$ cells derived from different primary ESFT cluster together, respectively (Figure 1A). The total number of miRNAs detected in ESFT samples 1 and 2 was 205 and 182, respectively. In CD133$^+$ cells of sample 1, 122 miRNAs (60%) were downregulated, whereas 29 (14%) were upregulated. In sample two, the corresponding numbers for CD133$^+$ cells were 102 (56%) and 4 (2%). Not surprisingly, a highly significant number of downregulated miRNAs was shared by CD133$^+$ ESFT and hpMSC$^{EWS\text{-}FLI1}$ cells (Figure 1B). miRNA repertoire distinction between CD133$^+$ and CD133$^-$ hpMSC$^{EWS\text{-}FLI\text{-}1}$ was found to resemble that between their respective primary ESFT CD133$^+$ and CD133$^-$ counterparts, as shown by the highly significant overlap between the lists of differentially expressed miRNAs (Figure 1B). Real-time PCR (qRT-PCR) assessment of the miRNA profile of CD133$^+$ and CD133$^-$ cell fractions derived from ESFT 1 and 2 and three distinct hpMSC$^{EWS\text{-}FLI\text{-}1}$ populations validated the microarray results, consistent with the notion that CD133$^+$ hpMSC$^{EWS\text{-}FLI\text{-}1}$ bear molecular resemblance to ESFT CSCs.

The above analysis was repeated using the ESFT cell line STA-ET-8.2, which has recently been suggested to mirror the CSC model (Jiang et al., 2010). However, microarray profiling of STA-ET-8.2-derived CD133$^+$ and CD133$^-$ subpopulations, as well as the corresponding qRT-PCR data validation, failed to show any difference in their miRNA repertoire, and no similarity

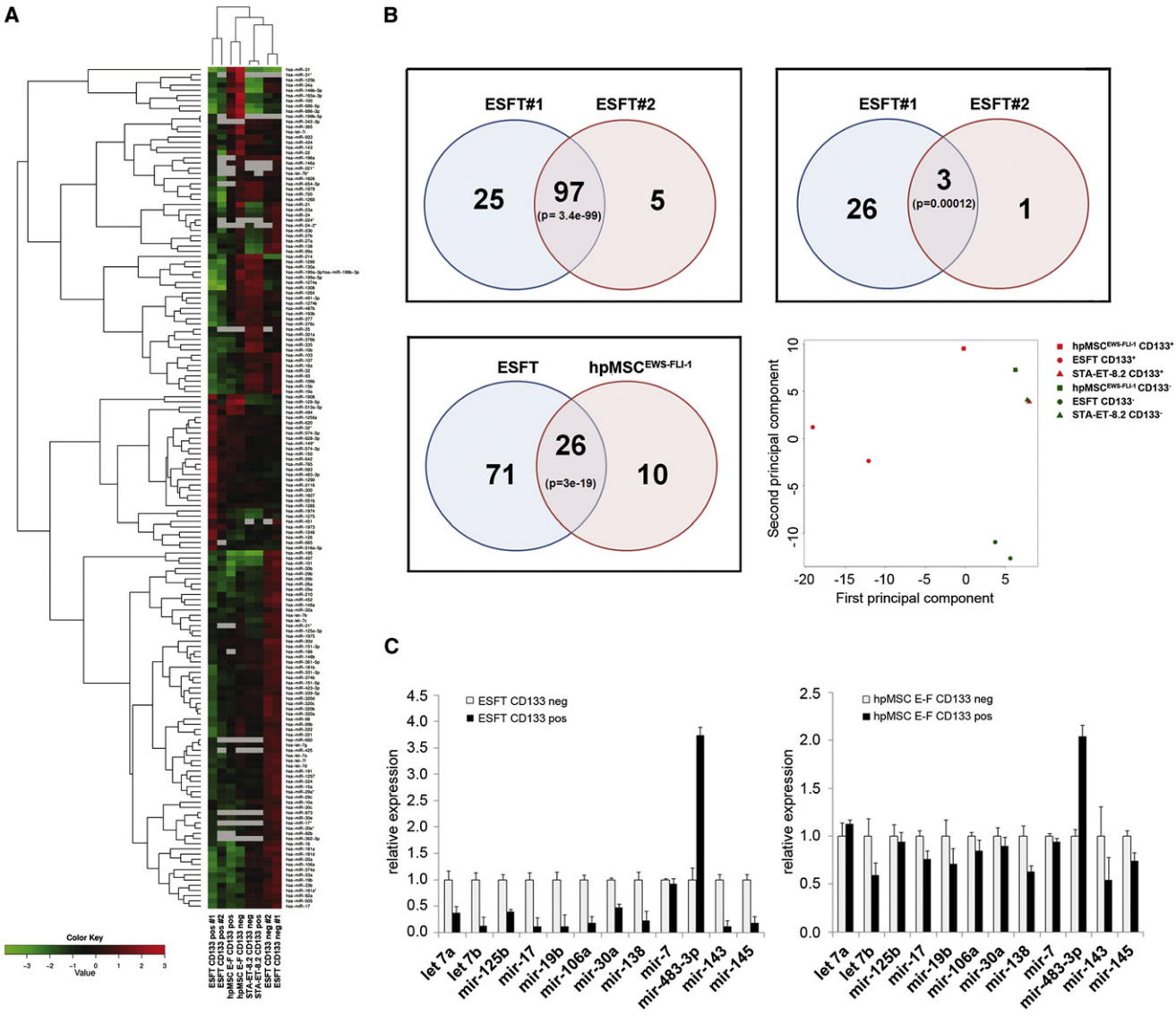

Figure 1. Mature miRNA Expression in ESFT

(A) Clustering of CD133$^+$ and CD133$^-$ hpMSC$^{EWS\text{-}FLI1}$, primary ESFT cells, and STA-ET-8.2 cells.

(B) Venn diagrams indicating shared repressed (top left) and induced (top right) miRNAs between primary CD133$^+$ cells from different ESFT samples, and shared repressed miRNAs between primary CD133$^+$ ESFT and hpMSC$^{EWS\text{-}FLI\text{-}1}$ cells (lower left). Principle of component analysis of the eight samples used is shown (lower right).

(C) Real-time PCR analysis of the expression of selected mature miRNAs in CD133$^+$ and CD133$^-$ primary ESFT cells (left) and hpMSC$^{EWS\text{-}FLI1}$ (right). Real-time PCR experiments were normalized to SNORD49a and were done in triplicate. Error bars represent the SD of three independent determinations.

See also Figure S1 and Tables S1, S2, S3, S4, and S5.

was observed with either primary ESFT CSC or hpMSC$^{EWS\text{-}FLI\text{-}1}$ CD133$^+$ cells (Figure 1A and Figure S1A). Established cell lines may therefore not be representative of CSCs, having adapted to in vitro culture conditions. Comparison of CD133$^+$ CSC and hpMSC$^{EWS\text{-}FLI\text{-}1}$ miRNA signatures to recently published miRNA expression profiles of normal human embryonic stem cells (hESCs), induced pluripotent stem cells (iPSCs), and fibroblasts (Wilson et al., 2009) showed that both CD133$^+$ populations share a significant portion of their miRNA repertoire with hESCs and iPSCs but not with fibroblasts (Table S2). Moreover, comparative analysis of ESFT CSCs and currently publicly available solid tumor miRNA CSC profiles, including those of hepatocellular (Ma et al., 2010b) (Table S3), prostate (Liu et al., 2011) (Table S4), and breast (Iliopoulos et al., 2011) (Table S5) carcinomas, revealed significant similarity. Thus, there appears to be marked molecular resemblance between ESFT CSCs, hESC/iPSCs, and CSCs from diverse tumor types, suggesting that the intrinsic stemness shared by these cells may rely on a common miRNA expression profile that overrides the differences in their ontogeny.

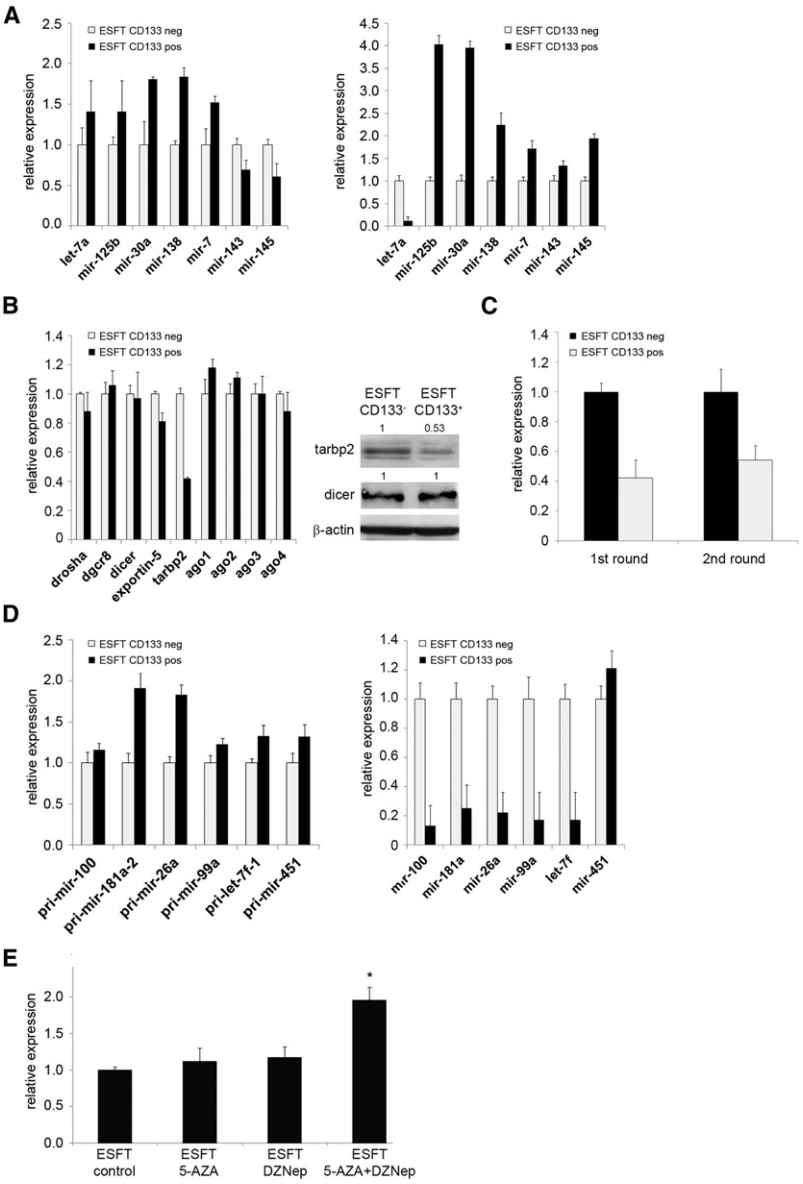

Figure 2. Tarbp2 Is Repressed in ESFT CSC

(A) Real-time PCR analysis of primary (pri-) miRNA expression (left) and primary and precursor (pre-) miRNA expression (right) in primary CD133$^+$ and CD133$^-$ ESFT cells.

(B) Left: Real-time PCR analysis of the expression of key components of the miRNA maturation machinery in primary CD133$^+$ and CD133$^-$ ESFT cells. Right: Western blot analysis of Tarbp2 and Dicer expression in primary ESFT CD133$^-$ and CD133$^+$ cells.

(C) Real-time PCR analysis of *TARBP2* expression in CD133$^+$ and CD133$^-$ ESFT cells after the first round of sorting from tumor samples and after ESFT sphere formation (second round of sorting).

(D) Real-time PCR analysis in primary CD133$^+$ and CD133$^-$ ESFT cells of the expression of primary (left) and mature (right) miRNAs that are regulated by Tarbp2 in both ESFT CSCs and colon cancer cells. Expression of the Tarbp2-independent miRNA-451 is included as an internal control.

(E) Real-time PCR analysis of *TARBP2* expression after 5 days of treatment with 5-AzaC (20 μM) and/or DZNep (10 μM). Real-time PCR experiments were normalized to 18S for mRNA or SNORD49a for miRNAs and were done in triplicate. Error bars represent the SD of three independent determinations. *p<0.05.

See also Figure S2.

ESFT CSCs Display Decreased TARBP2 Expression

Studies on Dicer KO mice showed that global reduction in miRNA processing and expression augments the tumorigenic potential of transformed cells (Kumar et al., 2007). Subsequent work suggested that defective miRNA biogenesis, resulting in a reduction in the amounts of their mature 21–23 nt form, is responsible for the repressed miRNA signature observed in cancer cells (Kumar et al., 2009). We hypothesized that the miRNA expression profile of CSC may reflect intrinsic deregulation of miRNA maturation, which could explain, at least in part, their phenotype and tumorigenic potential.

Expression of a panel of relevant pri-miRNAs, whose corresponding mature form was found to be repressed (Figure 1C), was assessed by qRT-PCR in CD133$^+$ and CD133$^-$ hpMSC$^{EWS\text{-}FLI\text{-}1}$, as well as in freshly isolated primary cells from ESFT 3 and 4. With the exception of the miRNA 143-145 cluster, which is known to be transcriptionally repressed by Oct-4, (Xu et al., 2009) no decrease in the tested pri-miRNA transcripts was observed in either of the CD133$^+$ populations (Figure 2A, left, and Figure S2A, left), indicating that, for most of the repressed mature miRNAs, the initial transcription step is not affected. Expression of combined pri- and pre-forms of each of a selected panel of miRNAs was assessed according to recently described methods (Shan et al., 2008) to exclude a possible blockade in the pri- to pre-miRNA maturation step. With the exception of let-7a, combined pri- and pre-miRNA levels were found to be increased in CD133$^+$ compared to CD133$^-$ cells (Figure 2A, right, and Figure S2A, right) for all species tested, consistent with pre-miRNA accumulation and a late miRNA maturation defect in CSCs. The strong decrease in combined let-7a pri- and pre-miRNA may be attributed to elevated expression of Lin28B in ESFT CSCs (De Vito et al., 2011), reported to act primarily on pre-let-7a (Piskounova et al., 2011).

Because CD133$^-$ cells are derived from their CD133$^+$ counterparts (Suvà et al., 2009), we reasoned that any miRNA maturation defect responsible for CSC development should be reversible. A putative underlying mechanism may therefore include altered transcriptional regulation of molecules implicated in miRNA biogenesis. Accordingly, we assessed the expression of *DROSHA, DGCR8, DICER, TARBP2, AGO1-4*, and *EXPORTIN5* by qRT-PCR in primary ESFT cells and hpMSC$^{EWS\text{-}FLI\text{-}1}$. Interestingly, the *TARBP2* transcript (Figure 2B, left), as well as the corresponding protein (Figure 2B, right), were significantly repressed in CD133$^+$ ESFT cells. The *TARBP2* transcript was also repressed in hpMSC$^{EWS\text{-}FLI\text{-}1}$ (Figure S2B), albeit less markedly

Table 1. Downregulated miRNAs Common to CD133$^+$ ESFT Cells and CD133$^+$ hpMSC$^{EWS-FLI-1}$ that Are Modulated in Colon Cancer-Bearing Mutated *TARBP2*

ESFT CD133 pos #1	ESFT CD133 pos #2	hpMSC$^{EWS-FLI-1}$ CD133 pos
hsa-miR-181a	hsa-miR-26a	hsa-miR-26a
hsa-miR-99a	hsa-miR-99a	hsa-miR-125b
hsa-let-7f	hsa-miR-181a	hsa-miR-100
hsa-miR-26a	hsa-miR-125b	Hsa-let-7f
hsa-miR-125b	hsa-let-7f	
hsa-miR-196a	hsa-miR-10a	
hsa-miR-100	hsa-miR-100	
p = 0.0063	p = 0.0022	p = 0.024

so than in primary CD133$^+$ ESFT cells, whereas no difference in *TARBP2* expression was observed between STA-ET-8.2-derived CD133$^+$ and CD133$^-$ fractions (data not shown). Among the other genes implicated in miRNA biogenesis tested, only *XPO5* was observed to be modestly repressed in CD133$^+$ ESFT cells, prompting us to focus on *TARBP2*.

ESFT CSCs Display a TARBP2 Expression-Dependent Defect in miRNA Maturation

The *TARBP2* gene encodes an integral component of a Dicer1-containing complex whose mutation has recently been reported to participate in the pathogenesis of sporadic and hereditary colon carcinomas with microsatellite instability (Melo et al., 2009). The observed frameshift mutations cause a decrease in Tarbp2 protein expression, which leads to a broad defect in miRNA maturation, possibly as a result of Dicer1 protein destabilization (Melo et al., 2009). To exclude the possibility that *TARBP2* downregulation in our CSC model might be due to mutation, primary ESFT *TARBP2* cDNA was sequenced and found to be wild-type (data not shown). Interestingly, Dicer1 expression was unaltered at the protein level in primary ESFT CD133$^+$ fractions (Figure 2B left), suggesting that the reduced Tarbp2 levels may suffice to maintain Dicer protein stability but not to ensure full Dicer complex function.

As previously observed (Suvà et al., 2009), only CD133$^+$ ESFT cells were able to generate spheres, which contain both CD133$^+$ and CD133$^-$ cell fractions. Similar to freshly isolated CD133$^+$ cells, sphere-derived CD133$^+$ cells displayed decreased *TARBP2* expression compared to their CD133$^-$ derivatives, highlighting the reversibility of *TARBP2* repression in CSC (Figure 2C).

The ESFT CSC miRNA signature revealed significant overlap with that observed upon *TARBP2* mutation in colon cancer cell lines (Melo et al., 2009) (Table 1), suggesting that the partial *TARBP2* repression identified in ESFT CSCs may underlie their defective miRNA maturation. qRT-PCR assessment of a panel of pri- and mature miRNAs, including miRNAs 100, 181a, 26a, 99a, and let-7f, reported to be part of the *TARBP2* miRNA profile in colon cancer cells, validated the molecular similarity suggested by array analysis, further supporting a putative implication of Tarbp2 in the generation of the ESFT CSC miRNA profile (Figure 2D). To verify that repression of miRNAs in ESFT CSCs results, at least in part, from a Tarbp2/Dicer-dependent maturation blockade, we measured by qRT-PCR the expression of miRNA-451, which has been shown to be processed in a Dicer-independent manner (Yang et al., 2010). No difference in miRNA-451 expression was observed between ESFT CD133$^+$ and CD133$^-$ cells (Figure 2D).

Given the reversibility of *TARBP2* repression in CD133$^+$ ESFT cells and preclusion of detailed promoter methylation analysis by the paucity of CD133$^+$ cells, we addressed possible epigenetic mechanisms that may underlie the observed *TARBP2* repression using a pharmacological approach. CD133$^+$ ESFT cells were subjected to treatment with 20 μM 5-Aza-2-deoxycytidine (5-AzaC), to block CpG island methylation in the *TARBP2* promoter, and with 10 μM of the S-adenosyl homocysteine hydrolase inhibitor 3-Deazaneplanocin A (DZNep), to block histone H3K27 and H3K9 methylation (Tan et al., 2007). The two reagents were applied alone or in combination for 5 days, and corresponding changes in *TARBP2* expression were assessed by qRT-PCR. Although neither reagent alone altered expression significantly, the combination of both resulted in a 2-fold increase in expression, de facto restoring expression to the level observed in CD133$^-$ cells (Figure 2E).

Interestingly, several miRNAs that are downregulated in ESFT CSCs are also repressed in relapsing tumors (Nakatani et al., 2012), including miRNA-34a, 224, 376a, and 26a (Figure S2).

TARBP2-Depleted ESFT Cell Lines Mimic ESFT CSC Behavior

To address its role in generating the miRNA expression profile observed in ESFT CSCs, as well as its involvement in their tumorigenic potential, *TARBP2* was depleted in three different ESFT cell lines using an shRNA approach. A 52%–60% reduction in *TARBP2* mRNA and protein expression, as assessed by qRT-PCR (Figure 3A, left) and western blot (Figure 3A, right) analysis, respectively, was obtained that corresponds to the difference in Tarbp2 expression levels observed between freshly isolated CD133$^+$ and CD133$^-$ ESFT cells. Similar to primary ESFT, Dicer protein expression was unaltered upon Tarbp2 depletion (Figure 3A). miRNA expression analysis of control vector-infected and sh*TARBP2*-expressing cells revealed that *TARBP2*-depleted cells acquire a miRNA profile that is remarkably similar to that of CD133$^+$ hpMSC$^{EWS-FLI-1}$ and ESFT CSCs (Figure 3B). Consistent with this observation, qRT-PCR analysis confirmed that expression of a panel of mature miRNAs regulated by Tarbp2 in both ESFT CSCs and colon cancer cells was repressed in *TARBP2*-depleted ESFT cell lines, without decreasing transcription of their corresponding pri-miRNA forms (Figure 3C, Figure S3A, and data not shown). miRNAs that were upregulated in CD133$^+$ cells were also upregulated in sh*TARBP2*-expressing cells, suggesting that the same or related internal regulatory pathways are modified in ESFT CSCs and ESFT cell lines upon *TARBP2* depletion.

Because *TARBP2*-depleted ESFT cell lines display a miRNA expression profile reminiscent of that of ESFT CSCs, we assessed the effect of *TARBP2* depletion on ESFT cell line proliferation and tumorigenicity. Although there was no significant difference in ESFT cell proliferation in vitro (Figure S3B), subcutaneous injection of control vector- and sh*TARBP2*-infected A673, TC252, and STA-ET-8.2 cells into six NOD-SCID mice each revealed accelerated tumor emergence from *TARBP2*-depleted cells (Figure 3D). The decreased *TARBP2* expression

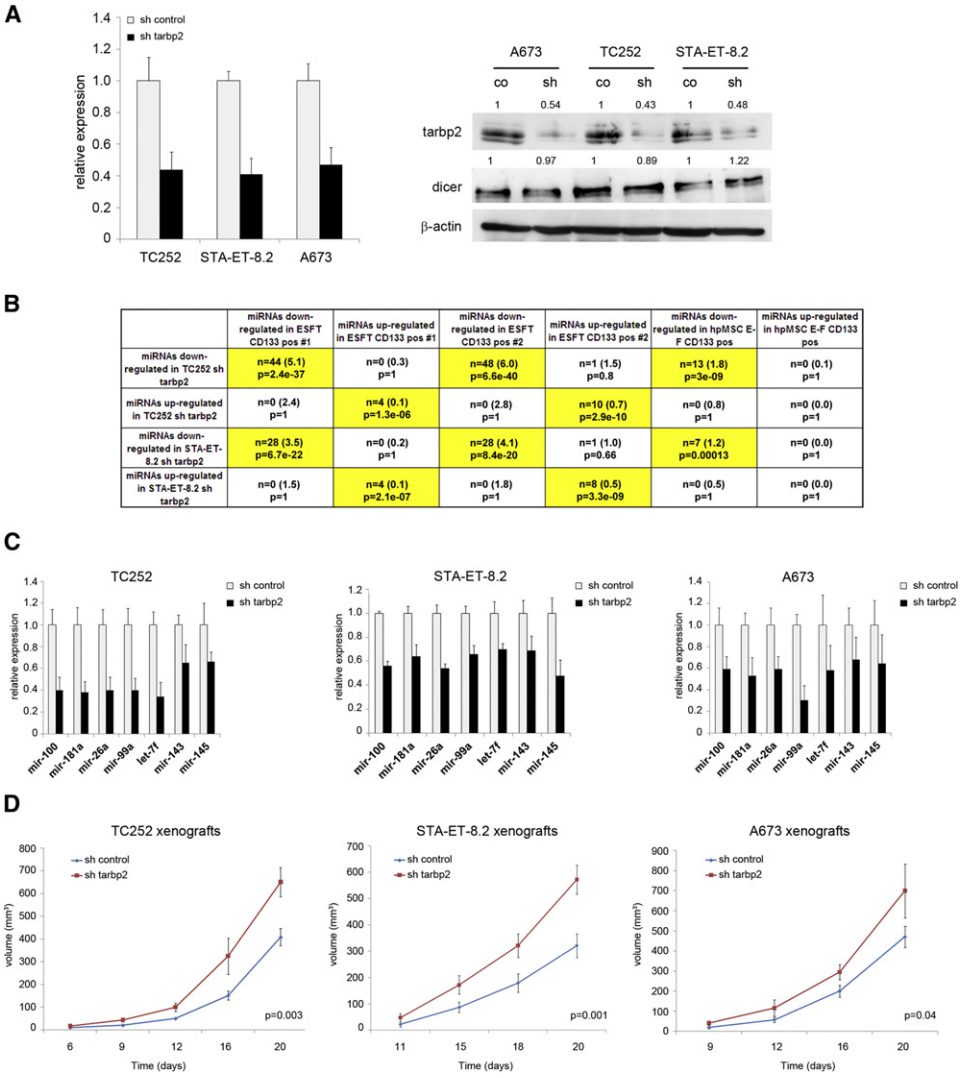

	miRNAs down-regulated in ESFT CD133 pos #1	miRNAs up-regulated in ESFT CD133 pos #1	miRNAs down-regulated in ESFT CD133 pos #2	miRNAs up-regulated in ESFT CD133 pos #2	miRNAs down-regulated in hpMSC E-F CD133 pos	miRNAs up-regulated in hpMSC E-F CD133 pos
miRNAs down-regulated in TC252 sh tarbp2	n=44 (5.1) p=2.4e-37	n=0 (0.3) p=1	n=48 (6.0) p=6.6e-40	n=1 (1.5) p=0.8	n=13 (1.8) p=3e-09	n=0 (0.1) p=1
miRNAs up-regulated in TC252 sh tarbp2	n=0 (2.4) p=1	n=4 (0.1) p=1.3e-06	n=0 (2.8) p=1	n=10 (0.7) p=2.9e-10	n=0 (0.8) p=1	n=0 (0.0) p=1
miRNAs down-regulated in STA-ET-8.2 sh tarbp2	n=28 (3.5) p=6.7e-22	n=0 (0.2) p=1	n=28 (4.1) p=8.4e-20	n=1 (1.0) p=0.66	n=7 (1.2) p=0.00013	n=0 (0.0) p=1
miRNAs up-regulated in STA-ET-8.2 sh tarbp2	n=0 (1.5) p=1	n=4 (0.1) p=2.1e-07	n=0 (1.8) p=1	n=8 (0.5) p=3.3e-09	n=0 (0.5) p=1	n=0 (0.0) p=1

Figure 3. Depletion of Tarbp2 in ESFT Cells Leads to an ESFT CSC miRNA Profile and Increases Tumorigenicity

(A) Real-time PCR (left) and western blot (right) analysis of *TARBP2* depletion in A673, TC252, and STA-ET-8.2 ESFT cell lines.

(B) Comparison of miRNA profiles between ESFT cell lines depleted of TARBP2, CD133^{+} ESFT cells, and CD133^{+} hpMSC$^{EWS\text{-}FLI1}$. N indicates the number of shared miRNAs by each cell population pair. The number of expected shared miRNAs is shown in brackets, and the p value is indicated. Statistically significant similarities are highlighted in yellow.

(C) Real-time PCR comparison of mature miRNA expression in *TARBP2*-depleted and control shRNA-treated ESFT cell lines.

(D) Growth curve of TC252 STA-ET-8.2 and A673 tumors depleted or not of *TARBP2*. Real-time PCR experiments were normalized to 18S for mRNA or SNORD49a for miRNAs and were done in triplicate. Error bars represent the SD of three independent determinations. Student's t test was used for statistical analysis.

See also Figure S3.

observed in ESFT CSCs may therefore be implicated in their tumorigenic potential.

To compare the effect of depleting *DICER* to that of depleting *TARBP2* on ESFT tumorigenicity, *DICER*-specific shRNA was stably expressed in the ESFT cell lines A673 and TC71 and resulted in a 42%–43% depletion of Dicer protein (Figure S3C). Neither cell viability nor proliferation (Figure S3D) was affected. However, xenografts of the cells in immunocompromised mice displayed a significant increase in tumorigenicity (Figure S3E) and downregulation of a panel of Tarbp2/Dicer-dependent miRNAs (Figure S3F).

Enoxacin Inhibits Tumor Development from ESFT Cell Lines

To address the potential effectiveness of restoring miRNA expression in inhibiting tumor growth, we explored methods of augmenting Tarbp2 function that may be applicable to therapy. The possibility to specifically enhance Tarbp2 activity, without affecting its expression level, has been recently demonstrated using enoxacin, an antibacterial agent of the fluoroquinolone family (Melo et al., 2011; Shan et al., 2008). We therefore assessed the effect of enoxacin on ESFT cell line miRNA expression in vitro and tumorigenesis in vivo. ESFT cell lines TC252,

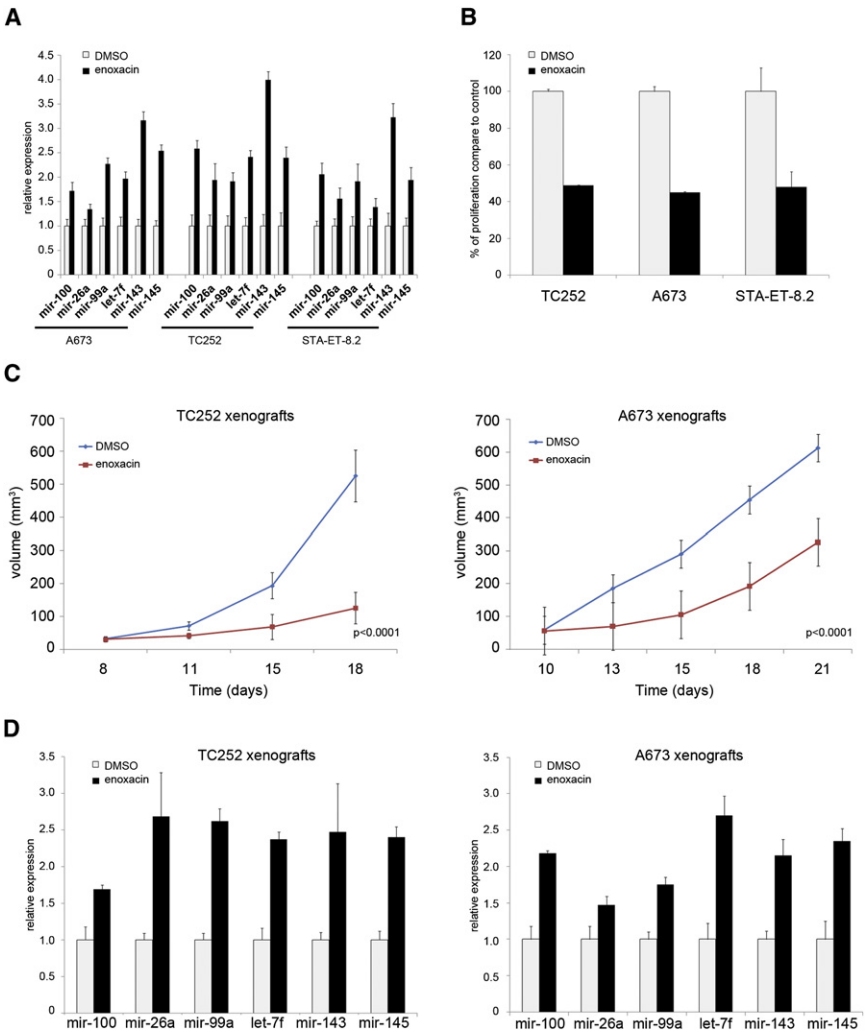

Figure 4. Enoxacin Blocks ESFT Cell Line Growth In Vivo

(A) Real-time PCR analysis of expression of a panel of mature Tarbp2-dependent miRNAs upon DMSO or 40 μg/ml enoxacin treatment of A673, TC252, and STA-ET-8.2 cells.

(B) MTT assay in DMSO- or enoxacin-treated (40 μg/ml) ESFT cells for 72 hr.

(C) Growth curves of established TC252 and A673 tumors in mice receiving daily i.p. enoxacin (10 mg/kg) or DMSO injections.

(D) Real-time PCR analysis of mature miRNA expression in DMSO- or enoxacin-treated tumors at autopsy. Real-time PCR experiments were normalized to SNORD49a and were done in triplicate. Error bars represent the SD of three independent determinations. Student's t test was used for statistical analysis.

See also Figure S4.

STA-ET-8.2, and A673 treated for 72 hr with enoxacin (40 μg/ml) showed an increase in Tarbp2-dependent miRNA expression (Figure 4A), without alteration of Tarbp2 expression itself (Figure S4). They also displayed significant reduction in their in vitro proliferation, as assessed by MTT assays (Figure 4B).

TC252 and A673 cells were injected subcutaneously into 12 NOD-SCID mice, and daily intraperitoneal treatment with enoxacin (n = 6) or solvent (DMSO, n = 6) was initiated at a dose of 10 mg/kg for a total of 10 days, once tumor volume reached 60 mm^3. Tumor growth was significantly inhibited in enoxacin-treated compared to DMSO-treated animals (Figure 4C). As expected, upregulation of Tarbp2-dependent miRNAs in enoxacin-treated tumors was observed (Figure 4D), consistent with the notion that enoxacin enhances endogenous Tarbp2 activity, which leads to increased miRNA maturation and inhibition of ESFT tumor growth.

Reconstitution of TARBP2 Expression and Function in ESFT CSC Impairs Their Self-Renewal In Vitro and Tumorigenic Potential In Vivo

We next addressed the effect of enoxacin on primary ESFT spheres. ESFT CSCs cultured as spheres in serum free conditions were treated with enoxacin (40 μg/ml) or solvent (DMSO) for 3 days, following which their clonogenic capacity, miRNA expression profile, and stem cell protein expression levels were assessed. Clonogenic assays revealed a 50% reduction in sphere formation by enoxacin-treated CSCs (Figure 5A). Enoxacin-treated spheres also displayed increased expression of a panel of Tarbp2/Dicer-dependent miRNAs (Figure 5B) and decreased expression of Oct-4, Nanog, and Sox-2 proteins (Figure 5C). To validate the notion that the effect of enoxacin was due to enhancement of Tarbp2 activity, we assessed the effect of *TARBP2* overexpression on ESFT spheres. Lentivirus-mediated introduction of *TARBP2* into primary ESFT spheres resulted in a marked decrease in their clonogenicity (Figure 5D) and a concomitant increase in the expression of a panel of Tarbp2-dependent miRNAs, including miRNAs 100, 181a, 26a, 99a, Let-7f, 143, and 145 (Figure 5E). Partial repression of Oct-4, Nanog, and Sox-2 (Figure 5F), comparable to that observed upon enoxacin treatment, was also noted. These observations indicate that enoxacin mimics the effect of exogenous *TARBP2* introduction and that enhanced Tarbp2 activity impairs ESFT CSC self-renewal.

To address the effect of restoring Tarbp2 activity on primary tumor growth and CSC population maintenance, 200,000 ESFT cells freshly isolated from ESFT 3, of which 15% were $CD133^+$, were injected beneath the renal capsule of 12 immunocompromised mice each. After 3 weeks of growth, six of the mice were treated with vehicle (DMSO) only, whereas the remaining six received daily injections of enoxacin at 10 mg/kg for 10 days. The mice were then sacrificed and tumors examined for size, morphology, and $CD133^+$ cell content. Although tumor size was comparable in control and enoxacin-treated animals (Figure 5G, left), control tumors were firm with little or no necrosis, whereas tumors from enoxacin-treated animals were

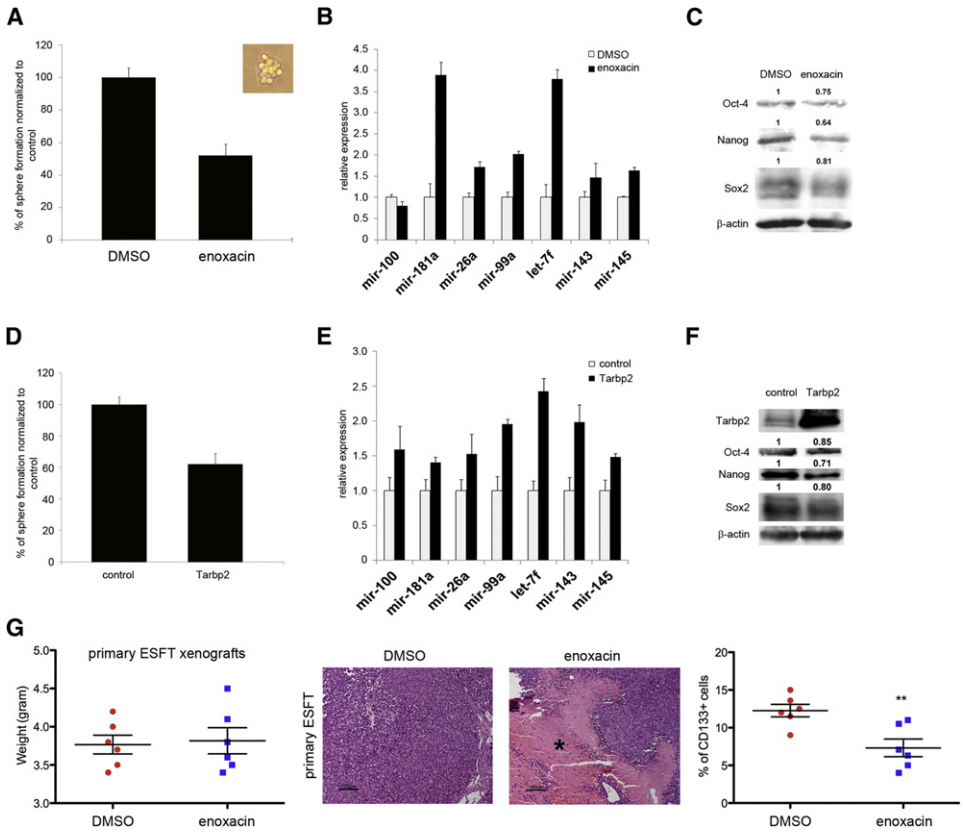

Figure 5. Enoxacin Treatment Inhibits ESFT CSC Self-Renewal In Vitro and Depletes CSC Populations In Vivo

(A) Clonogenic assay of DMSO- or enoxacin-treated primary ESFTs as assessed by sphere formation from single cell cultures. Sphere formation (inset) was scored after 30 days; 40 μg/ml of enoxacin was added to the cultures every 5 days.

(B) Real-time PCR analysis of expression of a panel of mature miRNAs in primary ESFT spheres treated with DMSO or enoxacin (40 μg/ml) for 5 days.

(C) Western blot analysis of Oct-4, Nanog, and Sox-2 proteins in primary ESFT spheres treated with DMSO or enoxacin (40 μg/ml) for 5 days.

(D) Clonogenic assay of primary ESFT cells overexpressing exogenous TARBP2, as assessed by sphere formation from single cell cultures. Sphere formation was scored after 30 days.

(E) Real-time PCR analysis of expression of a panel of mature miRNAs in primary control ESFT cells and ESFT cells overexpressing exogenous TARBP2.

(F) Western blot analysis of the expression of Tarbp2 and Oct-4, Nanog, and Sox-2 proteins in primary ESFT spheres infected with *TARBP2* cDNA-containing lentivirus.

(G) Left panel: weight of primary ESFT xenografts grown under the renal capsule for 3 weeks prior to daily i.p. injections of enoxacin (10 mg/kg) for 10 days. Middle panel: histology of DMSO- and enoxacin-treated tumors. The asterisk indicates necrosis. Scale bar = 100 μm. Right panel: fraction of viable cells from DMSO- and enoxacin-treated tumors expressing CD133. Real-time PCR experiments were normalized to SNORD49a and were done in triplicate. Error bars represent the SD of three independent determinations. $^{**}p < 0.005$.

soft and hemorrhagic with extensive necrosis (Figure 5G, middle). Importantly, the $CD133^+$ cell subpopulation was reduced from 15% to 7% (Figure 5G, right).

miRNA-143 and miRNA-145 Control ESFT CSC Self-Renewal and Tumorigenicity

ESFT spheres cultured in the presence of serum for 1 week become adherent, acquire an elongated MSC-like phenotype, and lose their tumorigenic potential (Figure 6A). We therefore compared the miRNA expression profile of spheres and their adherent cell counterparts from two different ESFTs (Figure 6B). Similar to ESFT $CD133^+$ and $CD133^-$ cells, PCA analysis showed that spheres and adherent cells from the two populations cluster together, respectively (Figure S5). Compared to their adherent counterparts, ESFT spheres displayed upregulation of the known oncogenic 17-92a miRNA cluster (Figure 6B and C), whereas the *TARBP2*-dependent miR-143/miR-145 cluster (Melo et al., 2011) was among their most strongly repressed miRNAs (Figure 6B and C). miRNA expression profile differences between spheres and adherent cells were not identical to those observed between primary $CD133^+$ and $CD133^-$ ESFT cells, because spheres are composed of both $CD133^+$ and $CD133^-$ cells. Moreover, comparison of spheres and adherent cells highlights serum-induced differences in differentiation and tumorigenicity, whereas comparison between $CD133^+$ and $CD133^-$ cells underscores differences in stemness. miRNAs that show similar expression differences in the two comparisons are therefore likely to be relevant to CSC constitution and maintenance.

Having previously shown that miRNA-145 plays an important role in the generation of ESFT CSCs and in ESFT tumorigenicity (Riggi et al., 2010), we addressed the function of the miRNA

143-145 cluster in ESFT CSC self-renewal. By introducing the cluster into primary ESFT spheres using a lentiviral system, we obtained a 260- and 220-fold expression of miRNA-143 and miRNA-145, respectively (Figure 6D). Clonogenic assays showed that both miRNA-143- and miRNA-145-overexpressing-ESFT spheres have lower self-renewal capacity (Figure 6E) that correlates with suppression of *OCT4* and *NANOG* but not *SOX2* transcripts (Figure 6F). Although *SOX2* is a target of miRNA-145, its response to changes in miRNA-145 expression may occur at the transcriptional or translational level and may vary according to cell type (Xu et al., 2009). Downregulation of the miRNA 143-145 cluster therefore appears to play an important role in ESFT CSC self-renewal.

Because both miRNA-143 and miRNA-145 impair in vitro ESFT CSC self-renewal, we assessed whether, similar to miRNA-145, miRNA-143 could inhibit ESFT tumorigenicity. The introduction of miRNA-143 into ESFT cell lines A673 and TC252 resulted in a 150- to 200-fold increase in its expression, respectively (Figure 7A). Although proliferation was only minimally affected (Figure 7B), subcutaneous injection of control vector-infected or miRNA-143-overexpressing ESFT cells into six NOD-SCID mice each revealed that miRNA-143 overexpression significantly reduced ESFT tumor growth in vivo (Figure 7C). Because exogenous miRNA administration has been shown to effectively control tumor growth in experimental models (Ma et al., 2010a; Wiggins et al., 2010), we asked whether systemic injection of synthetic miRNAs can block or reverse growth of established tumors. Similar to in vivo treatment using enoxacin, miRNA-based treatment was initiated once the tumor reached a volume of 60 mm^3. Tail vein injection of 30 μg of synthetic miRNA-143 or miRNA-145 was administrated on days 11, 14, and 18. Mice treated with either miRNA-143 or miRNA-145 showed significant reduction of tumor volume compared to control-treated animals (Figure 7D). To verify that synthetic miRNAs had reached the tumors, total RNA was extracted from the tumors, and expression of miRNA-143 and miRNA-145 were assessed by qRT-PCR (Figure 7E), along with the expression level of the known miRNA-145 target genes *OCT4* and *KLF4* (Figure 7F). A 2-fold increase in miRNA-143 and miRNA-145 expression, along with a significant decrease in of *OCT4* and *KLF4* expression levels, were found in the treated tumors.

DISCUSSION

A Common miRNA Signature and Functionally Related miRNAs May Underlie and Sustain the CSC Phenotype

Although broad miRNA repression is a well-established feature of malignant cells, there has been little evidence of shared miRNA profiles among different cancer types. The present study demonstrates that the miRNA profile of $CD133^+$ ESFT CSC and $hpMSC^{EWS\text{-}FLI\text{-}1}$ populations is at least partially shared by hESCs and iPSCs, but not by terminally differentiated fibroblasts, consistent with the notion that their stem cell properties reflect a common intrinsic molecular profile. Greater similarity was observed between miRNA expression profiles of ESFT CSCs and hepatocellular, breast, and prostate carcinoma CSCs than between those of $CD133^+$ $hpMSC^{EWS\text{-}FLI1}$ and the different carcinomas. This may reflect the distinction between cells of origin of a tumor that incur the initial transforming events to become tumor initiating cells (TICs) and CSCs that represent the self-renewing and tumor-sustaining population in the established tumor (Visvader, 2011). The observed miRNA expression profile similarity between $CD133^+$ $hpMSC^{EWS\text{-}FLI\text{-}1}$ and ESFT CSCs suggests that $CD133^+$ $hpMSC^{EWS\text{-}FLI\text{-}1}$ may represent early stages of ESFT TIC generation that retain traces of the miRNA expression profile of the cell of origin. These traces may be diluted in established CSCs, whose miRNA profile more strongly reflects their transformed stem-cell-like properties.

Our observations indicate that miRNA expression signatures shared by CSCs from highly divergent tumor types not only resemble those of ESCs and iPSCs but may underlie and help sustain their phenotype and functional properties. Several studies have shown that an ESC-like transcriptional signature is associated with the most aggressive and undifferentiated form of cancers of diverse origin, suggesting the existence of a shared core pluripotency gene network. This putative network is composed of the target gene repertoire of a limited group of stem cell-related transcription factors, namely the Core, Polycomb, and c-Myc modules (Ben-Porath et al., 2008; Kim et al., 2010; Wong et al., 2008).

The core module is composed of target genes regulated by, among others, Oct-4, Nanog, Klf-4, Sox-2, and Lin-28; whereas the PRC module comprises Suz12, Ezh1/2, and Eed; and the c-Myc module includes Max and Rex1 (Wong et al., 2008). Each of these genes or group of genes is silenced by miRNAs found to be repressed in ESFT CSC. Thus, miRNA-145 represses *OCT4*, *KLF4*, and *SOX2* (Xu et al., 2009); let-7a silences *MYC* and *LIN28* (Kim et al., 2009) and is itself silenced by *LIN28* (Viswanathan et al., 2008); miRNA-26a controls *MYC* and *EZH2* (Sander et al., 2008); and miRNA-101 represses *EZH2* (Varambally et al., 2008). Furthermore, miRNA-145 is repressed in breast (Iorio et al., 2005) and colorectal cancer (Schepeler et al., 2008), miRNA-26a expression is reduced in hepatocellular carcinoma (Chen et al., 2011), let-7 repression is associated with lung cancer development (Trang et al., 2010), whereas miRNA-101 is downregulated in prostate (Varambally et al., 2008), liver (Su et al., 2009), and bladder cancer (Friedman et al., 2009). A plausible scenario may therefore be that deregulation of a restricted set of ESC-related miRNAs may govern expression of different transcription modules, which help generate and sustain the CSC population. The miRNA signatures, however, need not be identical. Because expression of numerous transcripts can be regulated by different miRNAs, it is conceivable that CSC derived from diverse tumor types, and therefore generated by distinct oncogenic events, may exploit different miRNAs to modulate expression of an identical set of transcription factors that are required for their survival. For example, ESFT- and breast cancer-derived CSC appear to share the same let-7a-mediated regulation of c-*myc* (Yu et al., 2007), whereas for the Polycomb group proteins, they use miRNA-26a/101 (Sander et al., 2008; Varambally et al., 2008) and miRNA-200 (Shimono et al., 2009), respectively.

Reversible Deregulation of TARBP2 Expression Determines CSC miRNA Profiles and Tumor Growth

Mutations in *TARBP2* have been identified in colon cancer associated with microsatellite instability (Melo et al., 2009). The resulting decrease in Trbp expression is associated with Dicer1

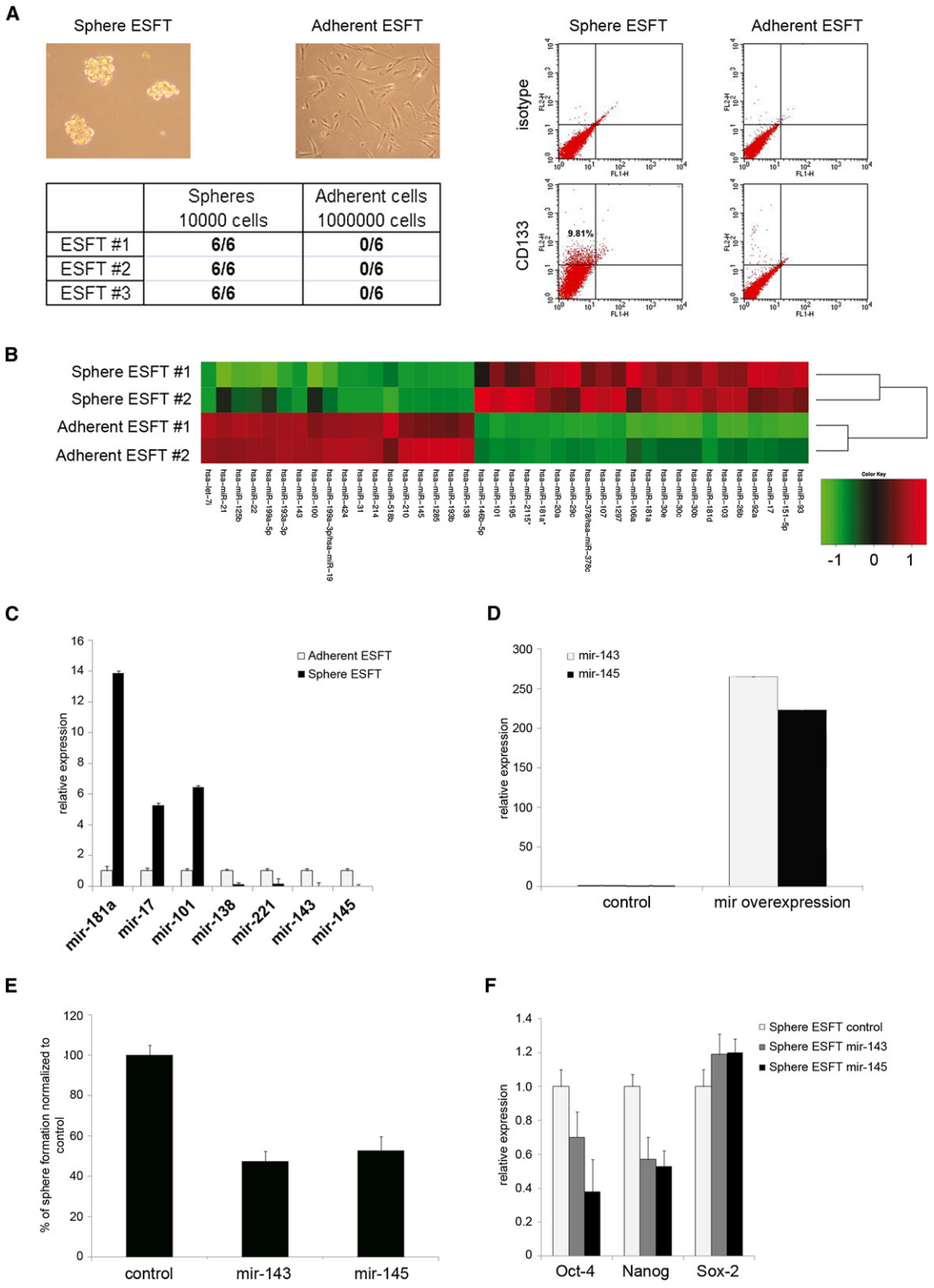

Figure 6. miRNA-143 and miRNA-145 Are Repressed in ESFT Spheres

(A) Upper left panel: ESFT sphere and adherent cell cultures are shown. Lower left panel: Tumor development following subcapsular kidney injection of primary ESFT spheres and adherent cells. The number of cells injected and the number of mice that developed tumors are indicated. Cells from three independent primary ESFTs were used. Right panel: Flow cytometry analysis of CD133 expression in ESFT spheres and adherent cell cultures.

(B) Clustering of primary ESFT spheres and adherent ESFT cells.

(C) Real-time PCR comparison of the expression of a panel of mature miRNAs in primary ESFT spheres and adherent ESFT cells.

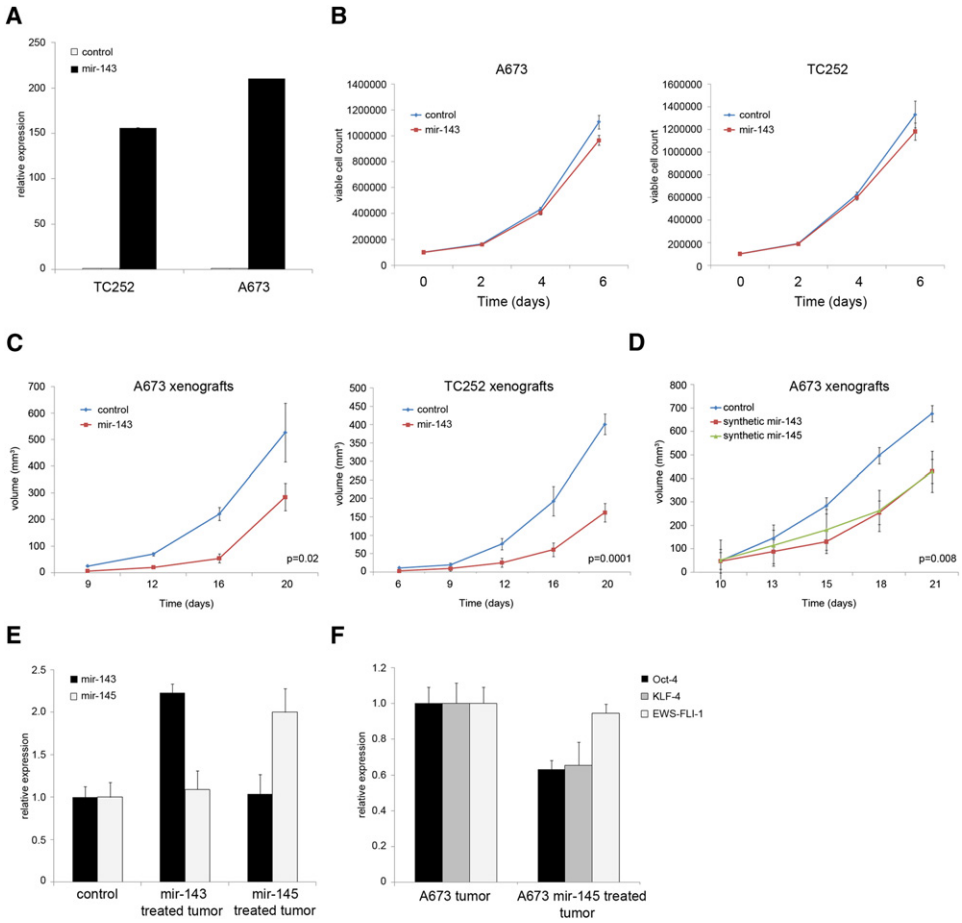

Figure 7. Synthetic miRNA-143 and miRNA-145 Inhibit ESFT Tumor Growth

(A) miRNA-143 overexpression in TC252 and A673 ESFT cells following retroviral introduction.

(B) Curve growth of control and miR-143 overexpressing A673 and TC252 cells.

(C) Tumor growth curves in six mice each from miRNA-143 and empty vector-infected A673 and TC252 cells.

(D) Growth curves of established A673 tumors in mice treated by tail vein injection of 30 μg of synthetic miRNA-143 or miRNA-145. miRNA-143 or miRNA145 was administered on days 11, 14, and 17 following subcutaneous A673 cell injection. Mice were sacrificed on day 20, and tumor size was assessed.

(E) Real-time PCR analysis of miRNA-143 and miRNA-145 expression in A673 tumors from miRNA-treated or control mice.

(F) Real-time PCR analysis of *OCT4* and *KLF4* expression in tumors from miRNA-145 treated or control mice. Real-time PCR experiments were normalized to SNORD49a for miRNA or 18S for mRNA and were done in triplicate. Error bars represent the SD of three independent determinations. Student's t test was used for statistical analysis.

protein instability or Dicer complex dysfunction that leads to defective miRNA processing (Chendrimada et al., 2005). Interestingly, the degree of reduction in Trbp expression observed in colon cancer cells corresponds to the 50% lower expression in CD133$^+$ ESFT CSCs compared to CD133$^-$ cells seen here. The notion that partial *TARBP2* repression may underlie the miRNA expression profile in ESFT CSCs is supported by the observation that shRNA-mediated depletion, by roughly 50%, of *TARBP2* in ESFT cell lines results in a miRNA expression profile that is highly reminiscent of that of ESFT CSCs, along with an increase in their tumorigenic potential. Furthermore, both introduction of exogenous *TARBP2* and enhancement of endogenous Tarbp2 activity by enoxacin resulted in reexpression of the broad panel of repressed miRNAs in ESFT CSCs, in addition to decreased clonogenicity. After 10 days of enoxacin treatment, CSC-derived tumors displayed massive necrosis, hemorrhage, and, most importantly, a roughly 50% decrease in the CD133$^+$ cell population. The extent of the necrosis observed is consistent with the notion that, in addition to promoting CSC differentiation, reconstitution of Tarbp2 activity

(D) Expression of miRNA-143 and miRNA-145 following lentiviral vector-mediated introduction into primary ESFT cells.

(E) Clonogenic assay showing reduced self-renewal of miRNA-143- and miRNA-145-overexpressing-ESFT cells.

(F) Real-time PCR analysis of *OCT4*, *NANOG*, and *SOX2* in empty vector-infected and miRNA-143 or miRNA-145 overexpressing primary ESFT spheres. Real-time PCR experiments were normalized to 18S for mRNA or SNORD49a for miRNAs and were done in triplicate. Error bars represent the SD of three independent determinations.

See also Figure S5.

drives a substantial proportion of the cells that constitute the tumor bulk toward death. One among several possible mechanisms may be downregulation of EWS-FLI-1 expression by miRNA-145 (Riggi et al., 2010), which could reduce the oncogenic driving force in both CSC and non-CSC populations, resulting in impairment of their growth and survival. Consistent with this view, the effect of enoxacin on cell line-derived tumors, which may at least partially mimic the tumor bulk, was to inhibit their growth.

Our observations suggest that partial inhibition of Tarbp2 function may constitute a key component of the mechanism that underlies defective miRNA maturation required for the emergence and maintenance of the CSC phenotype. Interestingly, the observed repression of *TARBP2* was not accompanied by Dicer protein instability, as assessed by western blot analysis, suggesting that partial *TARBP2* repression may deregulate the function of the Dicer complex without augmenting Dicer degradation itself. Alternatively, there may be a Tarbp2 repression range within which effects on miRNA expression are Tarbp2 specific. As expected, Dicer depletion by shRNA resulted in augmented tumorigenicity of ESFT cell lines, similar to the effect of Tarbp2 depletion, underscoring the importance of miRNA biogenesis in determining the tumorigenic potential of ESFT independently of the mechanisms that underlie initial transformation.

Robust upregulation of repressed Tarbp2-dependent miRNAs upon exposure of CSCs to serum indicates that the mechanisms underlying the defect in *TARBP2* expression are reversible. Consistent with this notion, we found that *TARBP2* expression could be restored by treating $CD133^+$ ESFT cells with a combination of 5-AzaC and DZNep, which suggests that *TARBP2* repression in these cells is likely due to a combination of DNA and histone methylation. Modulation of miRNA maturation as a means of altering expression of a broad panel of genes that orchestrate the full spectrum of CSC properties may provide tumor cells with a relatively simple way to acquire or lose the CSC phenotype. Epigenetic regulation of *TARBP2* expression may therefore constitute an important molecular switch that allows tumor cells to gain or relinquish CSC status in response to intrinsic or microenvironmental signals. Such regulation could maintain CSC as dynamic rather than fixed populations and account for their temporal and intertumor type size variability.

The similarities we have uncovered between miRNAs that are repressed in CSCs and in relapsing ESFT patients are consistent with the notion that CSCs constitute the population that is resistant to current chemotherapeutic agents and whose survival upon treatment is likely to be responsible for tumor relapse. The recent identification of miRNA-34a, the most robust event-free predictor miRNA in ESFT (Nakatani et al., 2012), as a p53 downstream target whose repression enhances somatic cell reprogramming and iPSC generation (Choi et al., 2011) further supports a potentially important mechanistic link between Tarbp2-dependent miRNA expression, CSC maintenance, and resistance to therapy in human tumors.

Targeting of Selected miRNAs Provides a Means to Control ESFT Growth

The miRNA 143-145 cluster has been observed to display tumor suppressor properties and to be downregulated in a broad range of tumor types (Tong and Nemunaitis, 2008). Moreover, we have previously shown the involvement of miRNA-145 in the generation of a $CD133^+$ subpopulation of $hpMSC^{EWS\text{-}FLI\text{-}1}$ that display CSC features (Riggi et al., 2010). Here, we demonstrate that both miRNA-145 and miRNA-143 are strongly repressed in ESFT CSCs and that their reexpression impairs self-renewal. miRNA-145 induction upon ESFT sphere exposure to serum may result in *OCT4* and *SOX2* repression, thereby inducing CSC differentiation and leading to loss of their tumor-initiating and -sustaining properties. In addition, miRNA-145 can repress EWS-FLI-1 expression (Riggi et al., 2010), neutralizing ESFT CSCs by at least two mechanisms: induction of differentiation on the one hand and silencing of the key oncogene on the other.

Taken together, our observations provide a plausible scenario for the emergence of CSCs in ESFTs. Expression of EWS-FLI-1 in appropriate primary host cells suppresses the miRNA 143-145 cluster, leading to genetic reprogramming that induces expression of *OCT4*, *NANOG*, and *SOX2*. The resulting network of induced target genes may modify the epigenetic landscape of EWS-FLI-1-expressing cells, leading to partial *TARBP2* suppression, which results in defective maturation of a host of miRNAs and the acquisition of the full-blown CSC phenotype. Depending on microenvironmental conditions, these cells may reexpress *TARBP2* and lose their tumorigenic potential, whereas others that are nontumorigenic may undergo partial *TARBP2* depletion and acquire or regain CSC features. Given the power of miRNA-driven gene expression to override the oncogenic effect of genetic mutations, restoration of relevant miRNA expression by systemic administration of synthetic miRNAs or correction of the underlying transient maturation defect may provide a potential means to control malignant growth. Effective therapy for any malignancy that harbors CSCs should simultaneously target the CSC population, to hamper tumor progression, as well as the bulk of the tumor to avoid the possibility that differentiated cells become reprogrammed toward the CSC phenotype. Increasing Tarbp2 activity by enoxacin may force ESFT CSCs to differentiate, while abrogating the opportunity for differentiated tumor cells to modulate their miRNA repertoire and to revert their phenotype to that of CSCs.

EXPERIMENTAL PROCEDURES

Cell Culture, Retroviral and Lentiviral Infection, and Tarbp2 Construct

Human pediatric mesenchymal stem cells (hpMSCs) were isolated and cultured as previously described (Riggi et al., 2010). A673 (ATCC), TC252 (kindly provided by Dr. T. Triche), STA-ET-8.2 (kindly provided by Dr. H. Kovar), and TC71 (kindly provided by Dr. E. De Alava) ESFT cells lines were cultured in RPMI (GIBCO) supplemented with 10% FCS (GIBCO). HpMSC, A673, TC252, STA-ET-8.2, and TC71 cells were infected as previously described (Riggi et al., 2010). MiR-143 vector was kindly provided by Dr. R. Agami. For stable knock-down of Tarbp2 (V3LHS_300582), pGIPZ lentiviral system from Open Biosystems was used. For stable knock-down of Dicer pSicoR sh dicer#1 (Addgene plasmid 14763) was used. Primary ESFT samples were obtained at surgery with approval of the ethics committee of the Canton de Vaud. All human samples were deidentified prior to analysis and were exempt from informed consent in accordance with the law of the Canton de Vaud. Spheres were cultured in IMDM (GIBCO), supplemented with 20% KO serum (GIBCO), 10 μg/ml LIF (Millipore), 10 ng/ml recombinant human epidermal growth factor (Invitrogen), and 10 ng/ml recombinant human basic fibroblast growth factor (Invitrogen). Single ESFT cell suspensions were infected using lentivirus-expressing miRNA control and mir-143-RFP (Biosettia) or miRNA-control

and mir-145-GFP (System Biosciences). *TARBP2* was amplified from cDNA of A673 cells and cloned into pLiV lentiviral vector.

RNA Isolation and Real-Time PCR

Total RNA was isolated using Trifast (Peqlab) according to the manufacturer's recommendations. Real-time PCR was performed as previously described (Riggi et al., 2010). TaqMan probes included 18S, *OCT4*, *NANOG*, *DROSHA*, *DICER*, pri-mir-138-1, and pri-mir-17 (Applied Biosystems). Primer sequences for SYBR Green gene expression quantification are listed in Supplemental Experimental Procedures. For microRNA quantification, 30 ng of total RNA was amplified using miRCURY LNA Universal RT microRNA PCR kit (Exiqon, DK) according to the manufacturer's recommendations. LNA PCR primers from Exiqon were used for RT-PCR amplification, and snord49a provided the endogenous control.

MicroRNA Array Profiling

Total RNA quality was verified by an Agilent 2100 Bioanalyzer profile. Total sample and reference RNA was labeled with Hy3 and Hy5 fluorescent label, respectively, using the miRCURY LNA Array power labeling kit (Exiqon, Denmark) according to the manufacturer's recommendations. Hy3-labeled samples and a Hy5-labeled reference RNA sample were mixed pairwise and hybridized to the miRCURY LNA array version sixth generation (Exiqon, Denmark), which contains capture probes targeting all miRNAs for human, mouse, or rat registered in the miRBASE version 16.0 at the Sanger Institute. Hybridization was performed according to the miRCURY LNA array manual using a Tecan HS4800 hybridization station (Tecan, Austria). The miRCURY LNA array microarray slides were scanned using the Agilent G2565BA Microarray Scanner System (Agilent Technologies, Inc., USA) and image analysis was performed using the ImaGene 9.0 software (BioDiscovery, Inc., USA). The quantified signals were background corrected and normalized using the global Lowess (LOcally WEighted Scatterplot Smoothing) regression algorithm.

Analysis of Microarray Data

Normalization of the microarray data was performed with the global Lowess regression algorithm. MicroRNAs showing expression fold-change greater than 2 (1.5 for the TARBP2-silenced cell lines) were considered differentially expressed. Clustering analysis was performed using average-linkage hierarchical clustering based on Pearson correlation coefficient. The statistical significance of the overlap between our microRNA lists and published ones was established in all cases using a one-sided exact Fisher test and Bonferroni correction for multiple testing.

Western Blots and Chemical Compounds

Western blots were performed according to standard procedures. Antibodies used for the study were anti-Tarbp2 (Abnova), anti-Dicer (Santa Cruz), anti-OCT-4 (Santa Cruz), anti-Nanog (R&D), anti-Sox2 (Chemicon Millipore), and anti-β-actin (Sigma). Quantification of bands was performed using imageJ Software. ESFT spheres were treated with 5-AzaC 20 μM (Sigma) and/or 3-Deazaneplanocin A (DZnep) 10 μM for 5 days.

Tumorigenicity Assays

Six NOD/SCID IL2 receptor common γ-chain knockout mice were anesthetized, and sphere-derived or adherent ESFT cells were injected beneath the renal capsule. All mice were sacrificed 3 months later, and the kidneys were removed at autopsy for histological analysis.

For assessment of the tumorigenic potential of TARBP2 depletion and miRNA-143-overexpression ESFT cells, NOD-SCID mice were anesthetized, and 1×10^6, 2×10^6, or 3×10^6 A673, TC252, or STA-ET-8.2 cells, respectively, were injected subcutaneously into six mice each. For assessment of the tumorigenic potential of Dicer depletion, NOD-SCID mice were anesthetized, and 1×10^6 or 4×10^6 A673 or TC71 cells, respectively, were injected subcutaneously into six mice each. The animals were sacrificed 4 weeks after injection. All tumors were removed at autopsy and sectioned for histological analysis. For in vivo treatment assays, 30 μg of miScript microRNA mimic (QIAGEN) were formulated with MaxSuppressor in vivo RNALancerII (BIOO Scientific, Inc), according to the manufacturer's recommendations. miRNAs were administrated intravenously by tail vein injection on days 11, 14, and 18. Tumor volume was measured as previously described (Esquela-Kerscher et al., 2008). Experimental protocols involving mice were approved by the Etat de Vaud, Service Vétérinaire, authorization number VD1942.1.

Cell Growth, Magnetic Cell Sorting, and FACS Analysis

ESFT cell lines were plated in triplicate wells and total cell counts and cell viability determined using trypan blue. The MTT assay was performed according to standard procedures. Magnetic cell sorting and FACS analysis were performed as previously described (Suvà et al., 2009).

Clonogenic Assays

Empty vector-infected, miRNA-143-RFP- or miRNA-145-GFP-expressing ESFT cells were plated as single cells in four 96-well plates and were cultured for 30 days in IMDM, 20% KO serum, LIF, EGF, and FGF. Sphere formation was scored 30 days later.

ACCESSION NUMBER

The Gene Expression Omnibus accession number for the miRNA expression profiles reported in this article is GSE31146.

SUPPLEMENTAL INFORMATION

Supplemental Information includes five figures, five tables, and Supplemental Experimental Procedures and can be found with this article online at doi:10.1016/j.ccr.2012.04.023.

ACKNOWLEDGMENTS

We thank Dr. T. Jacks for providing the pSicoR sh Dicer construct and Esther Rheinbay for graphic design. This work was supported by Swiss National Science Foundation (Grant 310030_130350), Oncosuisse (Grant 02158), the NCCR Molecular Oncology (to I.S.), and the Swiss Institute for Experimental Cancer Research Foundation (to I.S.). N.R. was supported by the Nuovo-Soldati Foundation and the Fonds Suisse Bourse Medecine et Biologie (Grant PASMP_134375/1). S.C. was supported by the FNS (MD-PhD Grant 323630-133894). P.P. was supported by the Italian Association for Cancer Research (Grant IG9408).

Received: June 30, 2011
Revised: January 12, 2012
Accepted: April 9, 2012
Published: June 11, 2012

REFERENCES

Bartel, D.P. (2009). MicroRNAs: target recognition and regulatory functions. Cell *136*, 215–233.

Ben-Porath, I., Thomson, M.W., Carey, V.J., Ge, R., Bell, G.W., Regev, A., and Weinberg, R.A. (2008). An embryonic stem cell-like gene expression signature in poorly differentiated aggressive human tumors. Nat. Genet. *40*, 499–507.

Chen, L., Zheng, J., Zhang, Y., Yang, L., Wang, J., Ni, J., Cui, D., Yu, C., and Cai, Z. (2011). Tumor-specific expression of microRNA-26a suppresses human hepatocellular carcinoma growth via cyclin-dependent and -independent pathways. Mol. Ther. *19*, 1521–1528.

Chendrimada, T.P., Gregory, R.I., Kumaraswamy, E., Norman, J., Cooch, N., Nishikura, K., and Shiekhattar, R. (2005). TRBP recruits the Dicer complex to Ago2 for microRNA processing and gene silencing. Nature *436*, 740–744.

Choi, Y.J., Lin, C.P., Ho, J.J., He, X., Okada, N., Bu, P., Zhong, Y., Kim, S.Y., Bennett, M.J., Chen, C., et al. (2011). miR-34 miRNAs provide a barrier for somatic cell reprogramming. Nat. Cell Biol. *13*, 1353–1360.

Clarke, M.F., Dick, J.E., Dirks, P.B., Eaves, C.J., Jamieson, C.H., Jones, D.L., Visvader, J., Weissman, I.L., and Wahl, G.M. (2006). Cancer stem cells—perspectives on current status and future directions: AACR Workshop on cancer stem cells. Cancer Res. *66*, 9339–9344.

Clevers, H. (2011). The cancer stem cell: premises, promises and challenges. Nat. Med. *17*, 313–319.

De Vito, C., Riggi, N., Suvà, M.L., Janiszewska, M., Horlbeck, J., Baumer, K., Provero, P., and Stamenkovic, I. (2011). Let-7a is a direct EWS-FLI-1 target implicated in Ewing's sarcoma development. PLoS ONE *6*, e23592.

Esquela-Kerscher, A., Trang, P., Wiggins, J.F., Patrawala, L., Cheng, A., Ford, L., Weidhaas, J.B., Brown, D., Bader, A.G., and Slack, F.J. (2008). The let-7 microRNA reduces tumor growth in mouse models of lung cancer. Cell Cycle *7*, 759–764.

Frank, N.Y., Schatton, T., and Frank, M.H. (2010). The therapeutic promise of the cancer stem cell concept. J. Clin. Invest. *120*, 41–50.

Friedman, J.M., Liang, G., Liu, C.C., Wolff, E.M., Tsai, Y.C., Ye, W., Zhou, X., and Jones, P.A. (2009). The putative tumor suppressor microRNA-101 modulates the cancer epigenome by repressing the polycomb group protein EZH2. Cancer Res. *69*, 2623–2629.

Iliopoulos, D., Hirsch, H.A., Wang, G., and Struhl, K. (2011). Inducible formation of breast cancer stem cells and their dynamic equilibrium with non-stem cancer cells via IL6 secretion. Proc. Natl. Acad. Sci. USA *108*, 1397–1402.

Iorio, M.V., Ferracin, M., Liu, C.G., Veronese, A., Spizzo, R., Sabbioni, S., Magri, E., Pedriali, M., Fabbri, M., Campiglio, M., et al. (2005). MicroRNA gene expression deregulation in human breast cancer. Cancer Res. *65*, 7065–7070.

Jiang, X., Gwye, Y., Russell, D., Cao, C., Douglas, D., Hung, L., Kovar, H., Triche, T.J., and Lawlor, E.R. (2010). CD133 expression in chemo-resistant Ewing sarcoma cells. BMC Cancer *10*, 116.

Kim, H.H., Kuwano, Y., Srikantan, S., Lee, E.K., Martindale, J.L., and Gorospe, M. (2009). HuR recruits let-7/RISC to repress c-Myc expression. Genes Dev. *23*, 1743–1748.

Kim, J., Woo, A.J., Chu, J., Snow, J.W., Fujiwara, Y., Kim, C.G., Cantor, A.B., and Orkin, S.H. (2010). A Myc network accounts for similarities between embryonic stem and cancer cell transcription programs. Cell *143*, 313–324.

Kumar, M.S., Lu, J., Mercer, K.L., Golub, T.R., and Jacks, T. (2007). Impaired microRNA processing enhances cellular transformation and tumorigenesis. Nat. Genet. *39*, 673–677.

Kumar, M.S., Pester, R.E., Chen, C.Y., Lane, K., Chin, C., Lu, J., Kirsch, D.G., Golub, T.R., and Jacks, T. (2009). Dicer1 functions as a haploinsufficient tumor suppressor. Genes Dev. *23*, 2700–2704.

Liu, C., Kelnar, K., Liu, B., Chen, X., Calhoun-Davis, T., Li, H., Patrawala, L., Yan, H., Jeter, C., Honorio, S., et al. (2011). The microRNA miR-34a inhibits prostate cancer stem cells and metastasis by directly repressing CD44. Nat. Med. *17*, 211–215.

Liu, Y., Clem, B., Zuba-Surma, E.K., El-Naggar, S., Telang, S., Jenson, A.B., Wang, Y., Shao, H., Ratajczak, M.Z., Chesney, J., and Dean, D.C. (2009). Mouse fibroblasts lacking RB1 function form spheres and undergo reprogramming to a cancer stem cell phenotype. Cell Stem Cell *4*, 336–347.

Ma, L., Reinhardt, F., Pan, E., Soutschek, J., Bhat, B., Marcusson, E.G., Teruya-Feldstein, J., Bell, G.W., and Weinberg, R.A. (2010a). Therapeutic silencing of miR-10b inhibits metastasis in a mouse mammary tumor model. Nat. Biotechnol. *28*, 341–347.

Ma, S., Tang, K.H., Chan, Y.P., Lee, T.K., Kwan, P.S., Castilho, A., Ng, I., Man, K., Wong, N., To, K.F., et al. (2010b). miR-130b Promotes CD133(+) liver tumor-initiating cell growth and self-renewal via tumor protein 53-induced nuclear protein 1. Cell Stem Cell *7*, 694–707.

Marión, R.M., Strati, K., Li, H., Murga, M., Blanco, R., Ortega, S., Fernandez-Capetillo, O., Serrano, M., and Blasco, M.A. (2009). A p53-mediated DNA damage response limits reprogramming to ensure iPS cell genomic integrity. Nature *460*, 1149–1153.

Melo, S.A., and Esteller, M. (2011). Dysregulation of microRNAs in cancer: playing with fire. FEBS Lett. *585*, 2087–2099.

Melo, S.A., Ropero, S., Moutinho, C., Aaltonen, L.A., Yamamoto, H., Calin, G.A., Rossi, S., Fernandez, A.F., Carneiro, F., Oliveira, C., et al. (2009). A TARBP2 mutation in human cancer impairs microRNA processing and DICER1 function. Nat. Genet. *41*, 365–370.

Melo, S.A., Villanueva, A., Moutinho, C., Davalos, V., Spizzo, R., Ivan, C., Rossi, S., Setien, F., Casanovas, O., Simo-Riudalbas, L., et al. (2011). Small molecule enoxacin is a cancer-specific growth inhibitor that acts by enhancing TAR RNA-binding protein 2-mediated microRNA processing. Proc. Natl. Acad. Sci. USA *108*, 4394–4399.

Nakatani, F., Ferracin, M., Manara, M.C., Ventura, S., Del Monaco, V., Ferrari, S., Alberghini, M., Grilli, A., Knuutila, S., Schaefer, K.L., et al. (2012). miR-34a predicts survival of Ewing's sarcoma patients and directly influences cell chemosensitivity and malignancy. J. Pathol. *226*, 796–805.

Newman, M.A., and Hammond, S.M. (2010). Emerging paradigms of regulated microRNA processing. Genes Dev. *24*, 1086–1092.

Piskounova, E., Polytarchou, C., Thornton, J.E., LaPierre, R.J., Pothoulakis, C., Hagan, J.P., Iliopoulos, D., and Gregory, R.I. (2011). Lin28A and Lin28B inhibit let-7 microRNA biogenesis by distinct mechanisms. Cell *147*, 1066–1079.

Riggi, N., Cironi, L., Provero, P., Suvà, M.L., Kaloulis, K., Garcia-Echeverria, C., Hoffmann, F., Trumpp, A., and Stamenkovic, I. (2005). Development of Ewing's sarcoma from primary bone marrow-derived mesenchymal progenitor cells. Cancer Res. *65*, 11459–11468.

Riggi, N., Cironi, L., Suvà, M.L., and Stamenkovic, I. (2007). Sarcomas: genetics, signalling, and cellular origins. Part 1: The fellowship of TET. J. Pathol. *213*, 4–20.

Riggi, N., Suvà, M.L., Suvà, D., Cironi, L., Provero, P., Tercier, S., Joseph, J.M., Stehle, J.C., Baumer, K., Kindler, V., and Stamenkovic, I. (2008). EWS-FLI-1 expression triggers a Ewing's sarcoma initiation program in primary human mesenchymal stem cells. Cancer Res. *68*, 2176–2185.

Riggi, N., Suvà, M.L., De Vito, C., Provero, P., Stehle, J.C., Baumer, K., Cironi, L., Janiszewska, M., Petricevic, T., Suvà, D., et al. (2010). EWS-FLI-1 modulates miRNA145 and SOX2 expression to initiate mesenchymal stem cell reprogramming toward Ewing sarcoma cancer stem cells. Genes Dev. *24*, 916–932.

Sander, S., Bullinger, L., Klapproth, K., Fiedler, K., Kestler, H.A., Barth, T.F., Möller, P., Stilgenbauer, S., Pollack, J.R., and Wirth, T. (2008). MYC stimulates EZH2 expression by repression of its negative regulator miR-26a. Blood *112*, 4202–4212.

Schepeler, T., Reinert, J.T., Ostenfeld, M.S., Christensen, L.L., Silahtaroglu, A.N., Dyrskjøt, L., Wiuf, C., Sørensen, F.J., Kruhøffer, M., Laurberg, S., et al. (2008). Diagnostic and prognostic microRNAs in stage II colon cancer. Cancer Res. *68*, 6416–6424.

Shan, G., Li, Y., Zhang, J., Li, W., Szulwach, K.E., Duan, R., Faghihi, M.A., Khalil, A.M., Lu, L., Paroo, Z., et al. (2008). A small molecule enhances RNA interference and promotes microRNA processing. Nat. Biotechnol. *26*, 933–940.

Shimono, Y., Zabala, M., Cho, R.W., Lobo, N., Dalerba, P., Qian, D., Diehn, M., Liu, H., Panula, S.P., Chiao, E., et al. (2009). Downregulation of miRNA-200c links breast cancer stem cells with normal stem cells. Cell *138*, 592–603.

Su, H., Yang, J.R., Xu, T., Huang, J., Xu, L., Yuan, Y., and Zhuang, S.M. (2009). MicroRNA-101, down-regulated in hepatocellular carcinoma, promotes apoptosis and suppresses tumorigenicity. Cancer Res. *69*, 1135–1142.

Suvà, M.L., Riggi, N., Stehle, J.C., Baumer, K., Tercier, S., Joseph, J.M., Suvà, D., Clément, V., Provero, P., Cironi, L., et al. (2009). Identification of cancer stem cells in Ewing's sarcoma. Cancer Res. *69*, 1776–1781.

Tan, J., Yang, X., Zhuang, L., Jiang, X., Chen, W., Lee, P.L., Karuturi, R.K., Tan, P.B., Liu, E.T., and Yu, Q. (2007). Pharmacologic disruption of Polycomb-repressive complex 2-mediated gene repression selectively induces apoptosis in cancer cells. Genes Dev. *21*, 1050–1063.

Tong, A.W., and Nemunaitis, J. (2008). Modulation of miRNA activity in human cancer: a new paradigm for cancer gene therapy? Cancer Gene Ther. *15*, 341–355.

Trang, P., Medina, P.P., Wiggins, J.F., Ruffino, L., Kelnar, K., Omotola, M., Homer, R., Brown, D., Bader, A.G., Weidhaas, J.B., and Slack, F.J. (2010). Regression of murine lung tumors by the let-7 microRNA. Oncogene *29*, 1580–1587.

Varambally, S., Cao, Q., Mani, R.S., Shankar, S., Wang, X., Ateeq, B., Laxman, B., Cao, X., Jing, X., Ramnarayanan, K., et al. (2008). Genomic loss of microRNA-101 leads to overexpression of histone methyltransferase EZH2 in cancer. Science *322*, 1695–1699.

Ventura, A., and Jacks, T. (2009). MicroRNAs and cancer: short RNAs go a long way. Cell *136*, 586–591.

Visvader, J.E. (2011). Cells of origin in cancer. Nature *469*, 314–322.

Viswanathan, S.R., Daley, G.Q., and Gregory, R.I. (2008). Selective blockade of microRNA processing by Lin28. Science *320*, 97–100.

Wiggins, J.F., Ruffino, L., Kelnar, K., Omotola, M., Patrawala, L., Brown, D., and Bader, A.G. (2010). Development of a lung cancer therapeutic based on the tumor suppressor microRNA-34. Cancer Res. *70*, 5923–5930.

Wilson, K.D., Venkatasubrahmanyam, S., Jia, F., Sun, N., Butte, A.J., and Wu, J.C. (2009). MicroRNA profiling of human-induced pluripotent stem cells. Stem Cells Dev. *18*, 749–758.

Winter, J., Jung, S., Keller, S., Gregory, R.I., and Diederichs, S. (2009). Many roads to maturity: microRNA biogenesis pathways and their regulation. Nat. Cell Biol. *11*, 228–234.

Wong, D.J., Liu, H., Ridky, T.W., Cassarino, D., Segal, E., and Chang, H.Y. (2008). Module map of stem cell genes guides creation of epithelial cancer stem cells. Cell Stem Cell *2*, 333–344.

Xu, N., Papagiannakopoulos, T., Pan, G., Thomson, J.A., and Kosik, K.S. (2009). MicroRNA-145 regulates OCT4, SOX2, and KLF4 and represses pluripotency in human embryonic stem cells. Cell *137*, 647–658.

Yang, J.S., Maurin, T., Robine, N., Rasmussen, K.D., Jeffrey, K.L., Chandwani, R., Papapetrou, E.P., Sadelain, M., O'Carroll, D., and Lai, E.C. (2010). Conserved vertebrate mir-451 provides a platform for Dicer-independent, Ago2-mediated microRNA biogenesis. Proc. Natl. Acad. Sci. USA *107*, 15163–15168.

Yu, F., Yao, H., Zhu, P., Zhang, X., Pan, Q., Gong, C., Huang, Y., Hu, X., Su, F., Lieberman, J., and Song, E. (2007). let-7 regulates self renewal and tumorigenicity of breast cancer cells. Cell *131*, 1109–1123.

Cancer Cell
Article

Tumor-Derived Granulocyte-Macrophage Colony-Stimulating Factor Regulates Myeloid Inflammation and T Cell Immunity in Pancreatic Cancer

Lauren J. Bayne,[1] Gregory L. Beatty,[1,3] Nirag Jhala,[5] Carolyn E. Clark,[1] Andrew D. Rhim,[1,4] Ben Z. Stanger,[1,2,4] and Robert H. Vonderheide[1,2,3,*]
[1]Abramson Family Cancer Research Institute
[2]Abramson Cancer Center
[3]Division of Hematology-Oncology
[4]Division of Gastroenterology, Department of Medicine
[5]Department of Pathology and Laboratory Medicine
University of Pennsylvania School of Medicine, Philadelphia, PA 19104, USA
*Correspondence: rhv@exchange.upenn.edu
DOI 10.1016/j.ccr.2012.04.025

SUMMARY

Cancer-associated inflammation is thought to be a barrier to immune surveillance, particularly in pancreatic ductal adenocarcinoma (PDA). Gr-1$^+$ CD11b$^+$ cells are a key feature of cancer inflammation in PDA, but remain poorly understood. Using a genetically engineered mouse model of PDA, we show that tumor-derived granulocyte-macrophage colony-stimulating factor (GM-CSF) is necessary and sufficient to drive the development of Gr-1$^+$ CD11b$^+$ cells that suppressed antigen-specific T cells. In vivo, abrogation of tumor-derived GM-CSF inhibited the recruitment of Gr-1$^+$ CD11b$^+$ cells to the tumor microenvironment and blocked tumor development—a finding that was dependent on CD8$^+$ T cells. In humans, PDA tumor cells prominently expressed GM-CSF in vivo. Thus, tumor-derived GM-CSF is an important regulator of inflammation and immune suppression within the tumor microenvironment.

INTRODUCTION

Host inflammatory responses often accompany and even promote tumor development. Although the prevailing theory of immunosurveillance holds that the adaptive arm of the immune system can mount productive anti-tumor responses that eliminate malignant cells (Schreiber et al., 2011), the developing tumor will often co-opt the host immune system for its own tumor-promoting purposes. This phenomenon is particularly notable in the development of pancreatic ductal adenocarcinoma (PDA), a highly lethal malignancy associated with a striking desmoplastic reaction and a marked infiltration of leukocytes into the stromal compartment (Clark et al., 2007). Leukocytes infiltrating PDA lesions are predominantly derived from the innate immune system and coordinate a network of local immune suppression (Clark et al., 2007, 2009). Nevertheless, these immunosuppressive cells exhibit dynamic motility and function, such that a detailed understanding of inflammatory cellular mechanisms in this disease has revealed therapeutic targets that can be translated to clinical success in patients (Beatty et al., 2011).

Although multiple mechanisms are thought to contribute to immune suppression in tumor-bearing hosts, tumor-associated changes in myelopoiesis that result in an abnormal accumulation of immature myeloid cells in the tumor are thought to play a critical immunosuppressive role (Gabrilovich and Nagaraj, 2009; Ostrand-Rosenberg and Sinha, 2009; Peranzoni et al., 2010). In mice, these immature myeloid cells, often called myeloid-derived suppressor cells (MDSC), co-express the markers Gr-1 and CD11b and represent a heterogeneous population of cells

Significance

PDA carries a dire prognosis for which novel therapeutic strategies are urgently needed. An inflammatory desmoplastic stromal reaction is characteristic of PDA and likely contributes to disease progression. Here, using a spontaneous murine model of PDA, we demonstrate that tumor-derived GM-CSF drives the accumulation of Gr-1$^+$ CD11b$^+$ myeloid cells as part of the cancer-associated inflammatory reaction, which in turn suppresses antitumor T cell immunity. In humans, PDA tumor cells prominently expressed GM-CSF in vivo. Our findings suggest a therapeutic potential for disrupting the crosstalk between tumor cells and the immune system by targeting Gr-1$^+$ CD11b$^+$ cells or the cytokines that regulate their differentiation.

comprised of precursors to macrophages, dendritic cells, and granulocytes at earlier stages of differentiation (Gabrilovich and Nagaraj, 2009; Ostrand-Rosenberg and Sinha, 2009; Peranzoni et al., 2010). Normal mouse bone marrow contains 20%–30% of Gr-1$^+$ CD11b$^+$ cells, although these cells only comprise 2%–4% of spleen cells and are virtually absent from the lymph nodes (Gabrilovich and Nagaraj, 2009). Numerous studies have reported the expansion of Gr-1$^+$ CD11b$^+$ cells in a variety of implantable tumor models and have demonstrated the ability of these myeloid cells to impair T cell responses in vitro (Bronte et al., 2003; Kusmartsev et al., 2004; Sinha et al., 2005). In genetically defined mouse models of cancer—which more closely recapitulate the tumor microenvironments observed in patients with the same disease—the role of these cells remains controversial particularly with regard to the in vivo relevance of the T cell suppressive qualities that are typically demonstrated in vitro (Andreu et al., 2010; Clark et al., 2007; Melani et al., 2003; Stairs et al., 2011). Moreover, the soluble factors that drive the accumulation of Gr-1$^+$ CD11b$^+$ cells in genetically defined models of cancer, particularly in PDA, remain largely unknown.

To understand the role of Gr-1$^+$ CD11b$^+$ cells in PDA, we focused on the KPC mouse model of spontaneous PDA in which expression of oncogenic *Kras*^{G12D} and mutant *p53*^{R172H} is targeted to the pancreas by Cre recombinase under the control of the pancreatic specific promoter *Pdx-1* (Hingorani et al., 2005). This model is fully penetrant with regard to tumor formation, and KPC mice develop primary PDA lesions that faithfully recapitulate the salient clinical, histopathological, and molecular features of the human disease, including progression from preinvasive pancreatic intraepithelial neoplasia (PanIN) to invasive cancer to metastatic disease (Hingorani et al., 2005). Using the KPC model, we evaluate a mechanism of tumor-induced immune modulation that is critical to maintaining the local immune suppressive network characteristic of PDA.

RESULTS

The dense desmoplasia and leukocytic infiltration classically observed in the tumor stroma of patients with PDA is reproduced with high fidelity in the KPC murine model of the disease (Beatty et al., 2011; Clark et al., 2009; Hingorani et al., 2005). In tumor-bearing KPC mice, we found that Gr-1$^+$ CD11b$^+$ cells prominently accumulated in both the tumor and the spleen compared to normal controls, comprising 20%–30% of all leukocytes in these tissues (Figure 1A). By immunohistochemistry, Gr-1$^+$ CD11b$^+$ cells were evident in close proximity to tumor cells (Figure 1B). Gr-1$^+$ CD11b$^+$ cells were also prominently associated with metastatic lesions in this model, but were not found in other tissues that lacked metastases (Figure 1C). Sorted Gr-1$^+$ CD11b$^+$ leukocytes from the spleen or tumor of KPC mice comprised a heterogeneous population of myeloid cells including myelocytes, metamyelocytes, band and segmented neutrophils, and monocytoid cells (Figure 1D), consistent with previous observations of cancer-associated Gr-1$^+$ CD11b$^+$ cells (Andreu et al., 2010; Bronte et al., 2000; Stairs et al., 2011).

Various terms have been used in the literature to describe Gr-1$^+$ CD11b$^+$ cells, including immature myeloid cells (Kusmartsev and Gabrilovich, 2006) or myeloid derived suppressor cells (MDSC) (Gabrilovich et al., 2007). Because the latter term suggests that Gr-1$^+$ CD11b$^+$ cells act to suppress T cell activation, we sought to understand the potential immunosuppressive function of Gr-1$^+$ CD11b$^+$ cells in the KPC model. We therefore evaluated the capacity of highly enriched or sorted Gr-1$^+$ CD11b$^+$ cells from tumor-bearing mice to suppress in vitro proliferation of ovalbumin-specific CD8$^+$ T cells from OT-1 transgenic mice in response to cognate peptide antigen. We found that Gr-1$^+$ CD11b$^+$ cells isolated from either the spleen or pancreas of tumor-bearing KPC mice potently suppressed proliferation (Figure 2A; Figure S1 available online) as well as interferon-gamma (IFN-γ) production by OT-1 cells (Figure 2B). Gr-1$^+$ CD11b$^+$ cells from tumor-bearing KPC mice also suppressed the proliferation of splenic T cells from normal mice stimulated polyclonally with anti-CD3 plus anti-CD28 antibodies (Figure S1). Moreover, Gr-1$^+$ CD11b$^+$ cells exhibited high levels of arginase activity (Figure 2C) and produced high levels of nitrite upon culture (Figure 2D), suggesting expression of inducible nitric oxide synthase (iNOS); both arginase and iNOS have been previously linked to immunosuppression by Gr-1$^+$ CD11b$^+$ cells in tumor-bearing mice (Bronte and Zanovello, 2005; Ma et al., 2011). We found that inhibition of iNOS and, to a lesser extent, arginase abrogated the capacity of Gr-1$^+$ CD11b$^+$ cells to suppress T cell proliferation (Figure 2E). This set of properties of Gr-1$^+$ CD11b$^+$ cells in KPC mice is consistent with described properties of MDSC (Gabrilovich et al., 2007).

We then examined the potential origin of Gr-1$^+$ CD11b$^+$ cells. We noted that unlike normal controls, tumor-bearing KPC mice developed splenomegaly as a result of extramedullary hematopoiesis (Figures 3A and 3B) and concomitant to accumulation of Gr-1$^+$ CD11b$^+$ cells in the spleen (Figure 1A). Splenocytes from tumor-bearing KPC mice exhibited a distinct c-kit$^+$ population, higher in percentage than found in splenocytes from normal mice and similar to the percentage of c-kit$^+$ precursors found in bone marrow (Figure 3B). Given the link between the tumor microenvironment and accumulation of functional Gr-1$^+$ CD11b$^+$ cells in the KPC model, we hypothesized that a tumor-derived factor might drive the generation of Gr-1$^+$ CD11b$^+$ cells from c-kit$^+$ cells in the spleen. We therefore isolated c-kit$^+$ Gr-1$^-$ CD11b$^-$ lineage$^-$ cells from the spleens of tumor-bearing KPC mice and incubated them with conditioned media obtained from cultured PDA tumor cells that had been previously isolated. Conditioned media from tumor cells, but not control media, triggered proliferation of c-kit$^+$ splenocytes, as evidenced by carboxyfluorescein diacetate succinimidyl ester (CFSE) dilution (Figure 3C) or bromodeoxyuridine (BrdU) incorporation (Figure S2). In contrast, Gr-1$^+$ CD11b$^+$ splenocytes isolated from the same mice did not proliferate in response to tumor cell conditioned media (Figure 3C). Importantly, after 5 days of co-culture, c-kit$^+$ cells expressed high levels of Gr-1 and CD11b (Figure 3C), exhibited arginase and iNOS activity (Figure 3D), and potently suppressed T cell proliferation in the OT-1 T cell suppression assay (Figure 3E).

To identify tumor-derived soluble factors contributing to the generation of Gr-1$^+$ CD11b$^+$ cells from c-kit$^+$ precursors, we measured a set of secreted proteins in conditioned media from a panel of PDA tumor cell lines and compared the results to those for conditioned media from benign pancreatic ductal cells from normal control mice. Conditioned media from every PDA line supported proliferation of c-kit+ cells into Gr-1$^+$ CD11b$^+$ cells

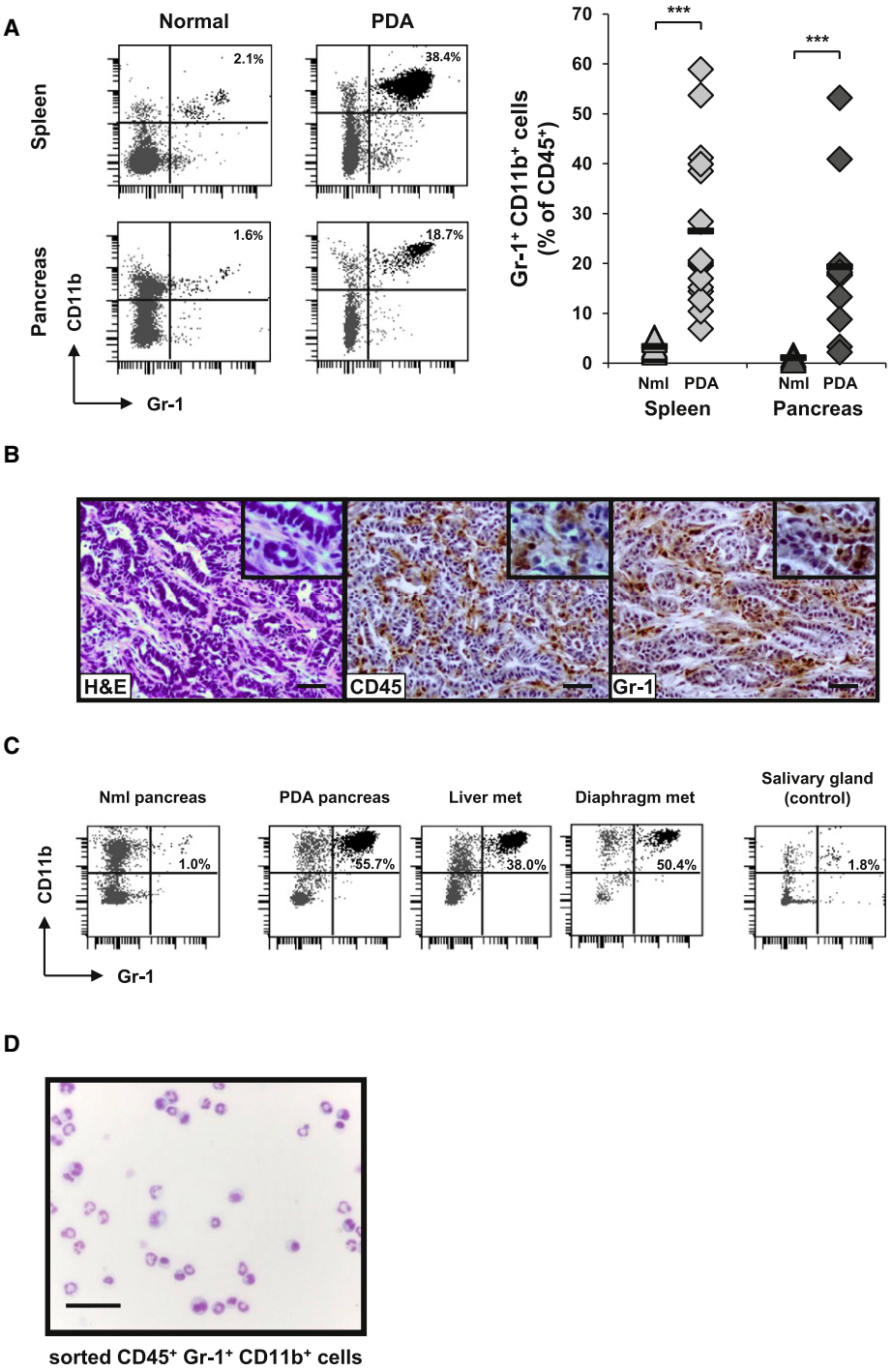

Figure 1. Gr-1$^+$ CD11b$^+$ Cells Accumulate in the Spleen and Tumor of PDA-Bearing KPC Mice

(A) Gr-1$^+$ CD11b$^+$ cells from the spleen and pancreas of tumor-bearing KPC mice versus normal control mice were evaluated by flow cytometry. Representative flow plots for one mouse in each category (left) and summary data (right) are shown. Cells were gated for CD45 expression and then analyzed. Numbers in top right corner of the plots represent the percentage of Gr-1$^+$ CD11b$^+$ cells among total CD45$^+$ cells. For summary data, each symbol represents an individual mouse: spleen (light gray), pancreas (dark gray), normal mice (triangles) and PDA mice (diamonds). Black horizontal bars represent the mean for each group (n = 10 for normal spleen, n = 15 for PDA spleen, n = 3 for normal pancreas, and n = 13 for PDA pancreas). Nml, normal. ***$p < 0.001$ for the comparisons shown.

(B) H&E stain (left) and immunohistochemistry for CD45 (middle) or Gr-1 (right) on a representative PDA lesion. Scale bars, 50 μM. Higher magnification images are shown in the top right corner of each panel.

(C) Metastatic lesions on the liver and diaphragm of a representative KPC mouse were evaluated by flow cytometry for Gr-1$^+$ CD11b$^+$ cells (after gating for CD45 expression), compared to salivary gland cells as a control.

(D) Diff-Quick stain of cytospin preparation of sorted CD45$^+$ Gr-1$^+$ CD11b$^+$ cells from the spleen of a tumor-bearing KPC mouse. Scale bar, 20 μM.

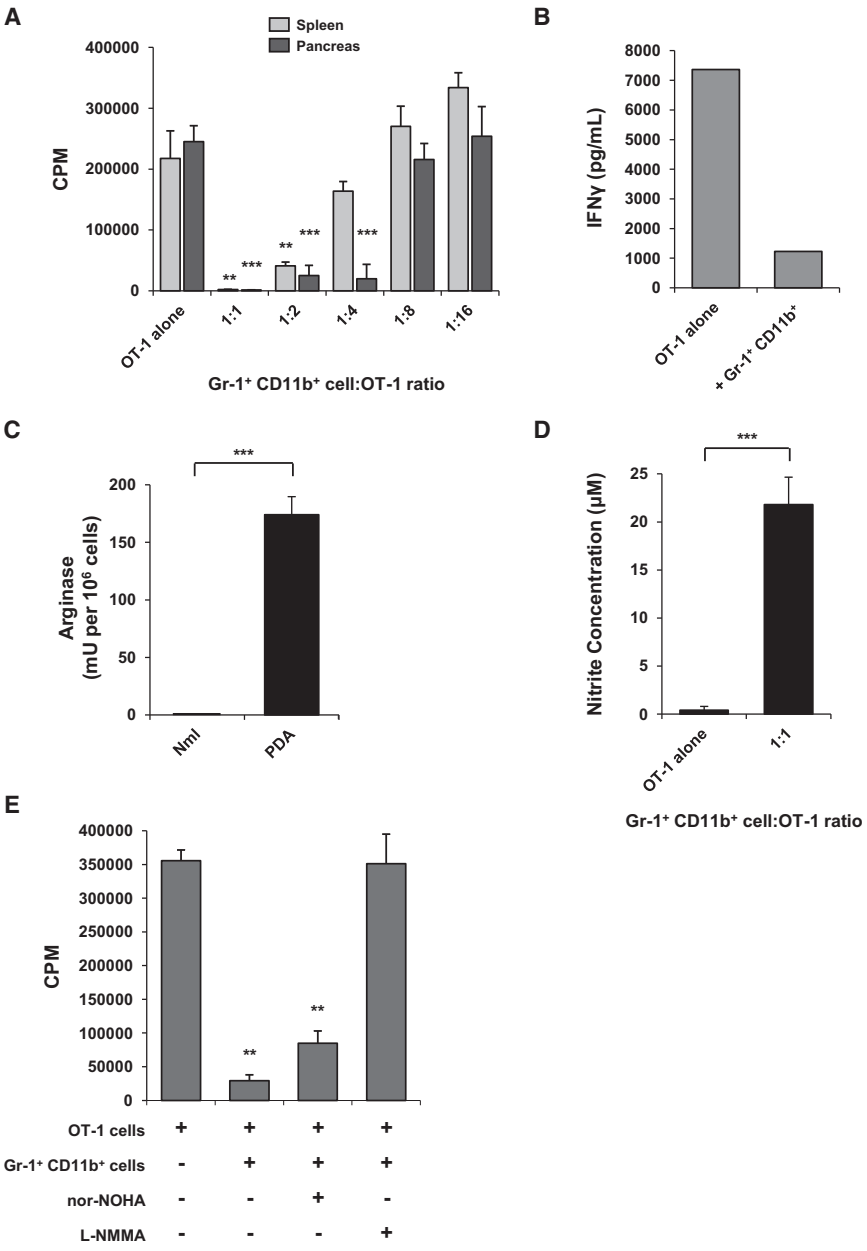

Figure 2. Gr-1$^+$ CD11b$^+$ Cells Isolated from Tumor-Bearing KPC Mice Suppress Antigen-Specific T Cell Responses In Vitro

(A) Gr-1$^+$ CD11b$^+$ cells isolated from either the spleen (light gray bars) or pancreas (dark gray bars) of tumor-bearing KPC mice were cocultured with peptide-stimulated OT-1 splenocytes and proliferation was evaluated by ^{3}[H]-thymidine incorporation. Assay was performed in triplicate; data are mean ± SD, representative of 5–10 independent experiments. **p < 0.01, ***p < 0.001, compared to OT-1 alone.

(B) IFN-γ in supernatant from co-culture of Gr-1$^+$ CD11b$^+$ cells with OT-1 splenocytes (1:1 ratio) was measured by cytokine bead array. Data are representative of two independent experiments.

(C) Arginase activity was evaluated in the Gr-1$^+$ fraction of normal spleens and tumor-bearing KPC spleens. Assay was performed in triplicate; data are mean ± SD, representative of two independent experiments. *** indicates p < 0.001.

(D) Nitrite concentration in supernatant from coculture of Gr-1$^+$ CD11b$^+$ cells with OT-1 splenocytes (1:1 ratio) was measured by the Griess reaction as an indicator of iNOS activity. Data are mean ± SD, representative of 3 independent experiments. *** indicates p < 0.001.

(E) Small molecule inhibition of iNOS relieves antigen-specific suppression of T cell proliferation mediated by Gr-1$^+$ CD11b$^+$ cells. Proliferation assay was performed in triplicate at 1:1 ratio of Gr-1$^+$ CD11b$^+$ cells to OT-1 cells; data are mean ± SD nor-NOHA (arginase inhibitor), N$^{\omega}$-hydroxy-nor-L-arginine; L-NMMA (iNOS inhibitor), N^G-monomethyl-L-arginine. **p < 0.01, compared to OT-1 alone.

See also Figure S1.

whereas media from none of the normal pancreatic ductal cells supported c-kit$^+$ cell proliferation (Figure 4A). Among 11 proteins examined, only granulocyte-macrophage colony-stimulating factor (GM-CSF) was expressed at high levels by every PDA line but not by any of the normal pancreatic ductal lines (Figure 4A), suggesting that tumor-derived GM-CSF might be linked to Gr-1$^+$ CD11b$^+$ cell generation. We therefore tested recombinant GM-CSF in our in vitro assays and found that GM-CSF drove proliferation and differentiation of c-kit$^+$ Gr-1$^-$ CD11b$^-$ splenocytes isolated from tumor-bearing mice into functional MDSC (Figure 4B). Proliferation and differentiation of c-kit$^+$ Gr-1$^-$ CD11b$^-$ splenocytes was not observed with recombinant vascular endothelial cell growth factor (VEGF) or stem cell factor (SCF, also known as c-kit ligand) and only minimally with interleukin-6 (IL-6) (Figure S3). Intermediate proliferation was observed with only high concentrations of recombinant macrophage colony-stimulating factor (M-CSF). In each case, neutralization of GM-CSF in tumor cell conditioned media by the addition of anti-GM-CSF mAb completely abrogated generation of Gr-1$^+$ CD11b$^+$ cells from c-kit$^+$ precursors (Figure 4C and Figure S3). Neutralizing antibodies to other cytokines such as anti-SCF, anti-IL-6, or anti-interleukin-1β (IL-1β) had no effect (Figure S3), suggesting that GM-CSF is both necessary and sufficient for in vitro generation of functional, immunosuppressive Gr-1$^+$ CD11b$^+$ cells.

To understand the relevance of tumor-derived GM-CSF in vivo, first we isolated fresh pancreatic tissue from tumor-bearing KPC mice versus normal controls and measured GM-CSF concentrations in tissue supernatant. Higher amounts of GM-CSF (>1 log) per gram of tissue were detected in pancreata from tumor-bearing KPC mice relative to pancreata from normal mice (Figure 5A). (Chemokines KC and CCL2 were also elevated in tumor tissue, consistent with the cell line cytokine data.) To determine which cells produce GM-CSF within tumors from genetically

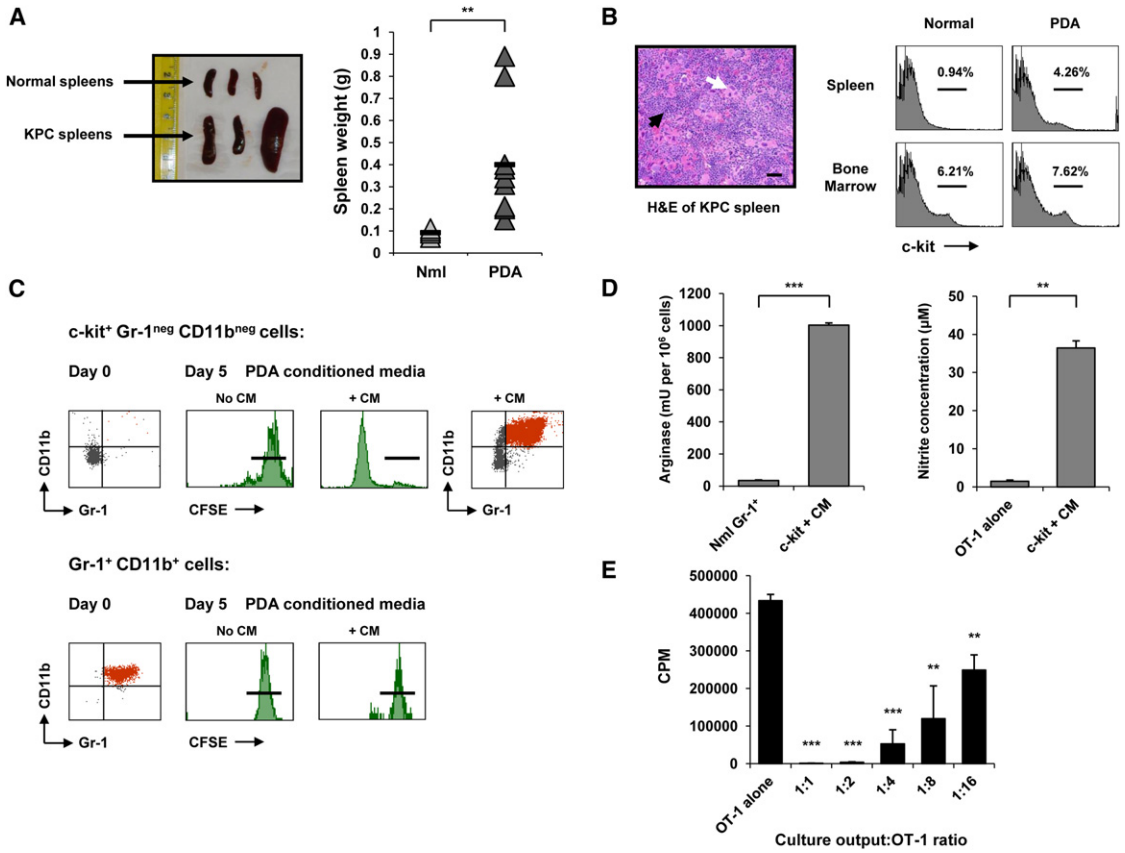

Figure 3. c-kit$^+$ Lineage$^-$ Splenocytes Are Highly Proliferative Precursors of Gr-1$^+$ CD11b$^+$ Cells and Are Driven to Proliferate via Tumor-Derived Factors

(A) Tumor-bearing KPC mice exhibit splenomegaly as indicated by spleen size of normal mice and tumor-bearing KPC mice (left) and spleen weight of normal and KPC mice (right). Black horizontal bars represent the mean for each group (n = 5 for normal mice, n = 12 for KPC mice). Nml, normal. **p < 0.01.

(B) H&E of tumor-bearing KPC spleen (left) reveals marked disruption of normal splenic architecture and classic findings of extramedullary hematopoiesis. Note the abundance of megakaryocytes (white arrow) and areas of erythropoiesis (black arrow). Scale bars, 50 μM. Spleen and bone marrow from normal and tumor-bearing KPC mice (right) were evaluated by flow cytometry for c-kit$^+$ cells.

(C) c-kit$^+$ Gr-1$^-$ CD11b$^-$ cells (top) and Gr-1$^+$ CD11b$^+$ cells (bottom) from the spleens of tumor-bearing KPC mice were labeled with CFSE and cultured in the presence of either unconditioned control media (No CM) or PDA conditioned culture media from KPC tumor lines (+ CM). Gr-1$^+$ CD11b$^+$ phenotype is shown at baseline post-isolation (left). Flow cytometric analysis of CFSE dilution on day 5 (middle) demonstrates that Gr-1$^-$ CD11b$^-$ c-kit$^+$ cells proliferate in response to tumor conditioned media, but not control media, whereas freshly isolated Gr-1$^+$ CD11b$^+$ MDSC do not proliferate in either condition. Black horizontal bars indicate undiluted CFSE intensity on day 5. The day 5 output of the proliferative Gr-1$^-$ CD11b$^-$ c-kit$^+$ culture was evaluated by flow cytometry for surface expression of Gr-1 and CD11b (far right). Data are representative of 5–10 independent experiments.

(D) The Gr-1$^+$ CD11b$^+$ cells generated from c-kit$^+$ cells after 5 days with CM were evaluated for arginase (left) and iNOS (right) activity. Data are mean ± SD from one of two independent experiments; **p < 0.01, ***p < 0.001.

(E) Suppressive capacity of the Gr-1$^+$ CD11b$^+$ cells generated from c-kit$^+$ cells after 5 days with CM was assessed in the OT-1 T cell suppression assay, performed in triplicate. Data are mean ± SD. **p < 0.01, ***p < 0.001, compared to OT-1 alone.

See also Figure S2.

engineered mice, we utilized a lineage marking approach (Figure 5B). A conditional *Rosa26-Lox-STOP-Lox-YFP* (*RosaYFP*) allele was bred onto the *Kras^{G12D}; p53$^{fl/+}$; Pdx-1-Cre* background to permanently label the pancreatic epithelial compartment during embryonic development. This approach led to sensitive (>95% of all pancreatic epithelial cells) and specific labeling of pancreas epithelial-derived cells, with no stromal cells labeled (Rhim et al., 2012). Tumors from these mice and normal pancreata from lineage labeled wild-type mice (*Pdx-1-Cre; RosaYFP*) were harvested, dissociated, and single cells were directly sorted based on YFP fluorescence. Subsequent transcriptional analysis revealed that YFP$^+$ cells from tumor-bearing mice expressed high levels of GM-CSF mRNA compared to YFP$^-$ cells from the same mice (Figure 5B). GM-CSF mRNA was undetectable in either YFP$^+$ or YFP$^-$ cells from control mice. To investigate GM-CSF expression by human tumors in vivo, we performed immunohistochemistry for GM-CSF on 20 PDA tumor samples obtained from patients who had undergone surgical resection of a primary PDA tumor. In 19 of these cases, tumor cells prominently expressed GM-CSF (>50% of tumor cells positive) (Figure 5C). For the positive samples, the percentage of tumor cells that expressed GM-CSF was 84.2% ± 13.8% (mean ± SD). Tumor cells that lacked GM-CSF expression were observed scattered throughout the tumor

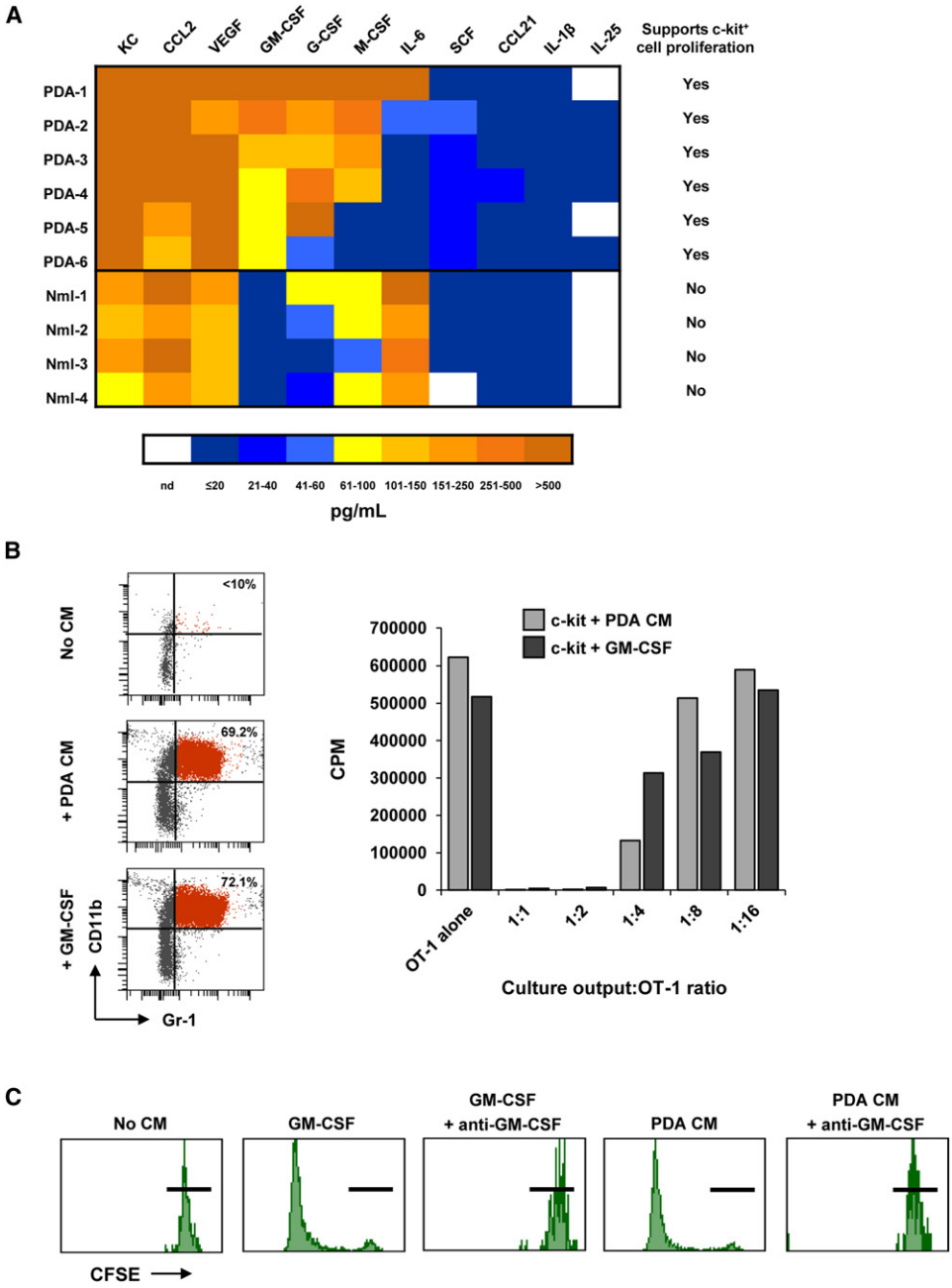

Figure 4. Tumor-Derived GM-CSF Induces Proliferation and Differentiation of c-kit$^+$ Lineage$^-$ Precursors into Functional MDSC

(A) Cytokines produced by primary PDA lines derived from KPC tumors and normal pancreatic ductal cell lines are compared in a heat map. Color scale and corresponding cytokine values (pg/ml) are shown below. Last column indicates whether conditioned media from that cell line was found to drive proliferation of c-kit$^+$ lineage$^-$ cells in a CFSE proliferation assay. Nml, normal; nd, not determined.

(B) Recombinant GM-CSF is sufficient to induce proliferation and differentiation of c-kit$^+$ lineage$^-$ cells into MDSC. Day 5 FACS analysis (left) was performed to evaluate Gr-1 and CD11b expression on c-kit$^+$ lineage$^-$ splenocytes cultured with control media (No CM), CM from PDA lines (+ PDA CM), or recombinant GM-CSF (200 pg/ml). Suppressive capacity of culture outputs (right) was evaluated in the OT-1 T cell suppression assay. Data are representative of at least three independent experiments.

(C) CFSE dilution of c-kit$^+$ lineage$^-$ cultures is shown for day 5. Neutralization of GM-CSF by anti-GM-CSF mAb (100 μg/ml) in PDA-1 conditioned media blocks proliferation of c-kit$^+$ lineage$^-$ cells. Black horizontal bars indicate undiluted CFSE intensity on day 5. Data are representative of independent experiments using conditioned media from 3 different PDA cell lines. As a control, the neutralizing capability of this anti-GM-CSF mAb was shown by its effect on recombinant GM-CSF in this assay.

See also Figure S3.

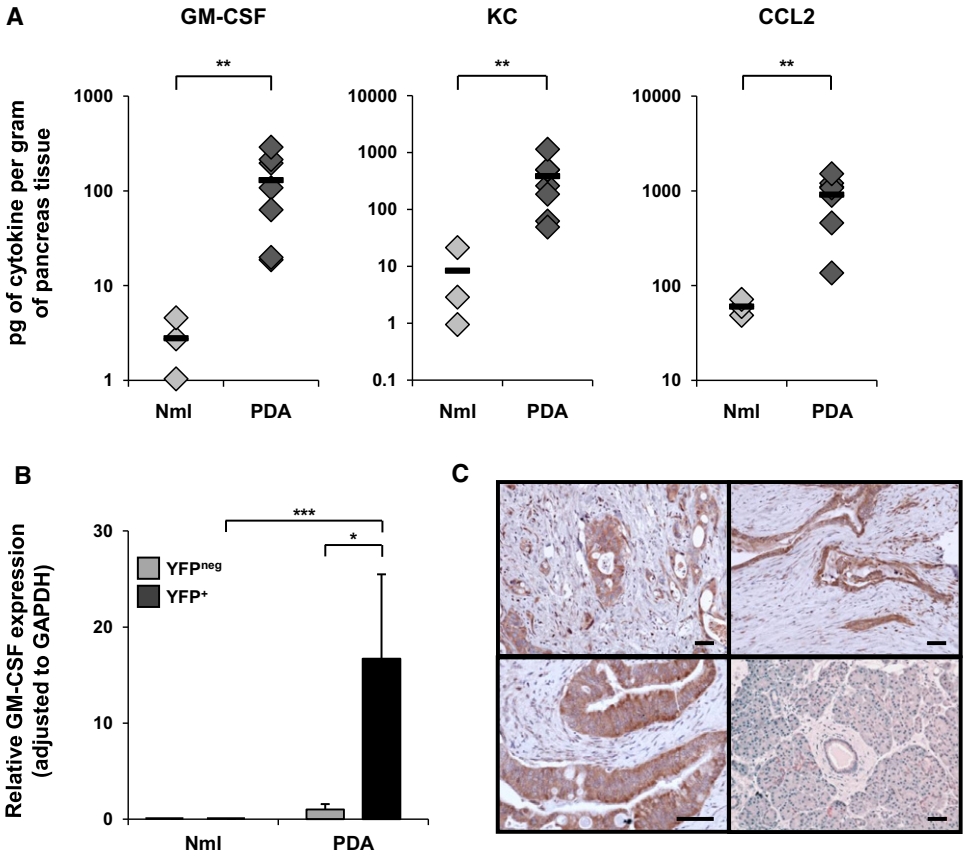

Figure 5. PDA Cells Produce GM-CSF and Other Factors In Vivo in KPC Mice

(A) Cytokines in fresh PDA supernatant (directly ex vivo) versus normal pancreas supernatant were compared by cytokine bead array. y-Axes are on log scales; each symbol represents an individual mouse: normal mice (light gray diamonds) and PDA mice (dark gray diamonds). Black horizontal bars represent the mean for each group (n = 3 for normal mice, n = 7 for PDA mice). **p < 0.01.

(B) Transcriptional analysis was used to evaluate GM-CSF mRNA expression of YFP$^+$ (epithelial) cells versus YFP$^-$ (stromal) cells sorted from tumors of *Kras^{G12D}*; *p53$^{fl/+}$*; *Pdx-1-Cre*; *RosaYFP* mice (n = 3) or normal pancreata from lineage labeled wild-type mice (*Pdx-1-Cre*; *RosaYFP*) (n = 3). Data are mean ± SD. *p < 0.05, ***p < 0.001.

(C) Immunohistochemistry for GM-CSF was performed on surgical pancreas samples from 20 patients with PDA. PDA tumors from three representative patients are shown (upper left, upper right, lower left), and adjacent pancreatic tissue without invasive tumor is shown for one patient (lower right). The lower left panel is shown at higher power magnification. Scale bars, 50 μM.

without any association to tumor grade and were only occasionally found as clusters of cells.

We then studied the role of GM-CSF on tumor growth and inflammation in vivo. PDA tumor cells that secreted GM-CSF (cell line PDA-1) were injected subcutaneously in a matrigel plug containing neutralizing anti-GM-CSF mAb (versus purified rat IgG2a as a control) into the flanks of normal control mice. This matrigel subcutaneous assay was developed to allow for GM-CSF neutralization within the local tumor microenvironment given that systemic administration of anti-GM-CSF antibody was unable to achieve sufficient concentrations within the tumor microenvironment to neutralize GM-CSF effectively (data not shown). Six days after implantation, PDA-1 cells injected with IgG2a established tumors, but PDA-1 cells injected with anti-GM-CSF failed to grow and the injected plugs, upon resection, weighed statistically significantly less (Figure 6A). Histologically, PDA-1 cells injected with anti-GM-CSF mAb appeared necrotic after 6 days compared to viable tumor cell nests in the control (Figure 6A). Moreover, the infiltration of CD45$^+$ Gr-1$^+$ CD11b$^+$ cells observed in control tumors was reduced in tumor cells implanted with anti-GM-CSF mAb (Figures 6B and 6C). Weight, histology, and leukocyte infiltration on day 6 was the same for PDA-1 cells injected with anti-GM-CSF mAb as for lethally irradiated (10 Gy) PDA-1 cells injected with anti-GM-CSF mAb (Figures 6A and 6C).

To determine whether the GM-CSF that was required for tumor formation in this assay was tumor-derived, we knocked down GM-CSF expression in PDA-1 cells using short-hairpin RNA (shRNA) technology. Compared to vector only (mock PDA-1 cells), shGM-CSF PDA-1 cells expressed > 90% less GM-CSF, whereas expression of other cytokines such as VEGF and KC was not affected (Figure S5). shGM-CSF PDA-1 cells or mock PDA-1 cells were then implanted subcutaneously in matrigel into the flanks of normal control mice and observed for 6 days. Similar to the experiments with anti-GM-CSF, mock PDA-1 cells established tumors in vivo, but

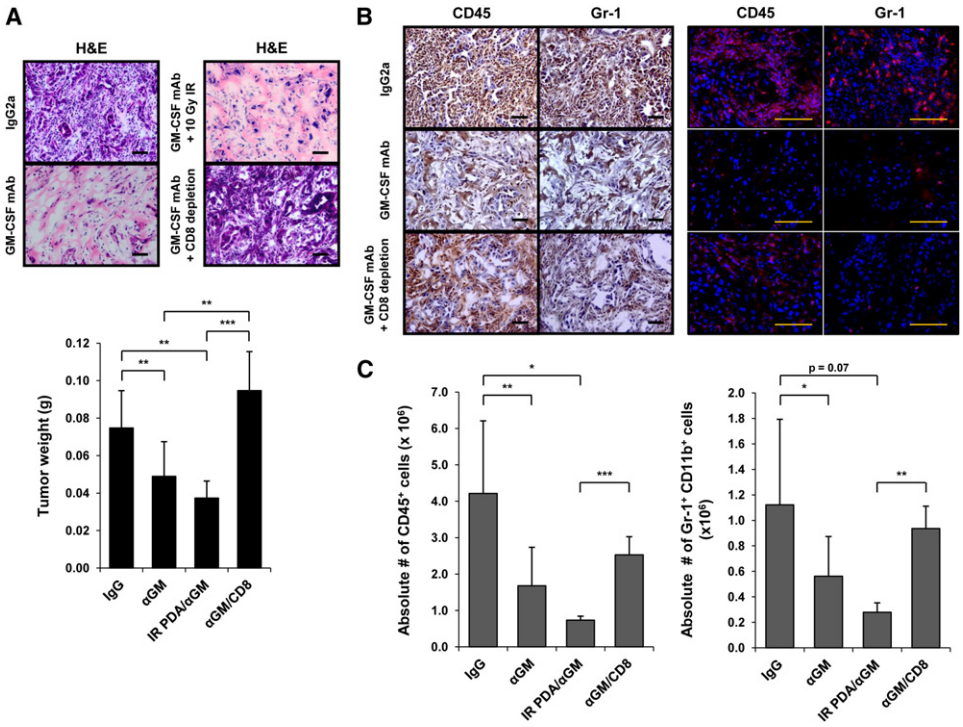

Figure 6. GM-CSF Neutralization with Anti-GM-CSF Antibody Limits Tumor Growth and Recruitment of Gr-1$^+$ CD11b$^+$ Cells In Vivo

(A) Normal control mice (6–14 weeks) were implanted subcutaneously with the GM-CSF-producing cell line PDA-1 in matrigel with either a neutralizing anti-GM-CSF mAb (αGM) or isotype control antibody, with or without tumor cell irradiation (IR), and with or without intraperitoneal administration of a depleting CD8 mAb. On day 6, tumor growth was evaluated by H&E (top; images of one representative mouse per group are shown) and tumor weight (bottom; data are mean ± SD). n = 3–11 mice per group. Scale bars, 50 μM. $^{**}p < 0.01$, $^{***}p < 0.001$.

(B) The immune infiltrate was evaluated by immunohistochemistry (left) and immunofluorescence (right) for CD45 and Gr-1. Images of one representative mouse per group are shown (3–11 mice per group). Scale bars, 50 μM.

(C) Absolute numbers of CD45$^+$ cells (left) and Gr-1$^+$ CD11b$^+$ cells (right) were quantified by flow cytometry. Data are mean ± SD. $^*p < 0.05$, $^{**}p < 0.01$, $^{***}p < 0.001$. See also Figure S4.

shGM-CSF PDA-1 cells failed to grow and the resected plugs weighed significantly less (Figure 7A). Histologically, shGM-CSF PDA-1 cells appeared necrotic after 6 days compared to viable tumor cell nests in the control (Figure 7A). There was a significant reduction in the inflammatory infiltrate in experiments with shGM-CSF PDA-1 cells, including fewer Gr-1$^+$ CD11b$^+$ cells (Figures 7B and 7C). Weight, histology, and leukocyte infiltration on day 6 was the same for shGM-CSF PDA-1 cells as these parameters were for lethally irradiated (10 Gy) shGM-CSF PDA-1 cells (Figures 7A and 7C).

We also examined the effect of GM-CSF blockade and knockdown on Gr-1$^-$ CD11b$^+$ monocytes/macrophages in the implanted tumor model. In each experimental system (i.e., anti-GM-CSF antibody or shGM-CSF), we observed a statistically significant decrease in tumor infiltrating Gr-1$^-$ CD11b$^+$ cells compared to control tumors (Figure S4). Importantly, a major subset of Gr-1$^+$ CD11b$^+$ cells were found to express high levels of Ly6C, and among this population, > 90% expressed the macrophage marker F4/80 (data not shown), underscoring a potential biological continuum of monocytes, macrophages, and immature myeloid cells. We were unable to identify an adequate method of depleting macrophages without impacting Gr-1$^+$ CD11b$^+$ cells in our mice. For example, we found that administration of clodronate encapsulated liposomes (CEL) depleted Gr-1$^-$ CD11b$^+$ F4/80$^+$ macrophages as well as Ly6C^{high} Gr-1$^+$ CD11b$^+$ cells (data not shown). We therefore repeated our tumor implantation experiments with anti-Gr-1 antibody versus isotype control and found that administration of anti-Gr-1 antibody depletes Gr-1$^+$ CD11b$^+$ myeloid cells but not Gr-1$^-$ CD11b$^+$ macrophages (Figure S4). Importantly, coinjection of anti-Gr-1 antibody with PDA-1 cells recapitulated our findings with anti-GM-CSF such that tumor implants failed to grow (Figure S4). Thus, depletion of Gr-1$^+$ CD11b$^+$ cells alone is sufficient for impaired tumor growth in this model.

We hypothesized that GM-CSF produced by tumor cells may drive the generation of Gr-1$^+$ CD11b$^+$ cells, which suppress anti-tumor T cell immunity. We therefore examined whether tumor rejection observed in the setting of GM-CSF neutralization or genetic knockdown was mediated by CD8$^+$ T cells. We repeated the 6 day implantation experiments in the setting of in vivo CD8 depletion (Figure S4). Strikingly, CD8 depletion restored tumor growth for both PDA-1 cells implanted with anti-GM-CSF and shGM-CSF PDA-1 cells (Figures 6A and 7A), linking tumor-derived GM-CSF to Gr-1$^+$ CD11b$^+$ cell accumulation and CD8$^+$ T cell suppression. To confirm this, we used a genetic approach and repeated experiments in *Rag2*$^{-/-}$ mice. We found that shGM-CSF PDA-1 tumor cells grew vigorously in *Rag2*$^{-/-}$ mice, even though they failed to grow in T cell replete

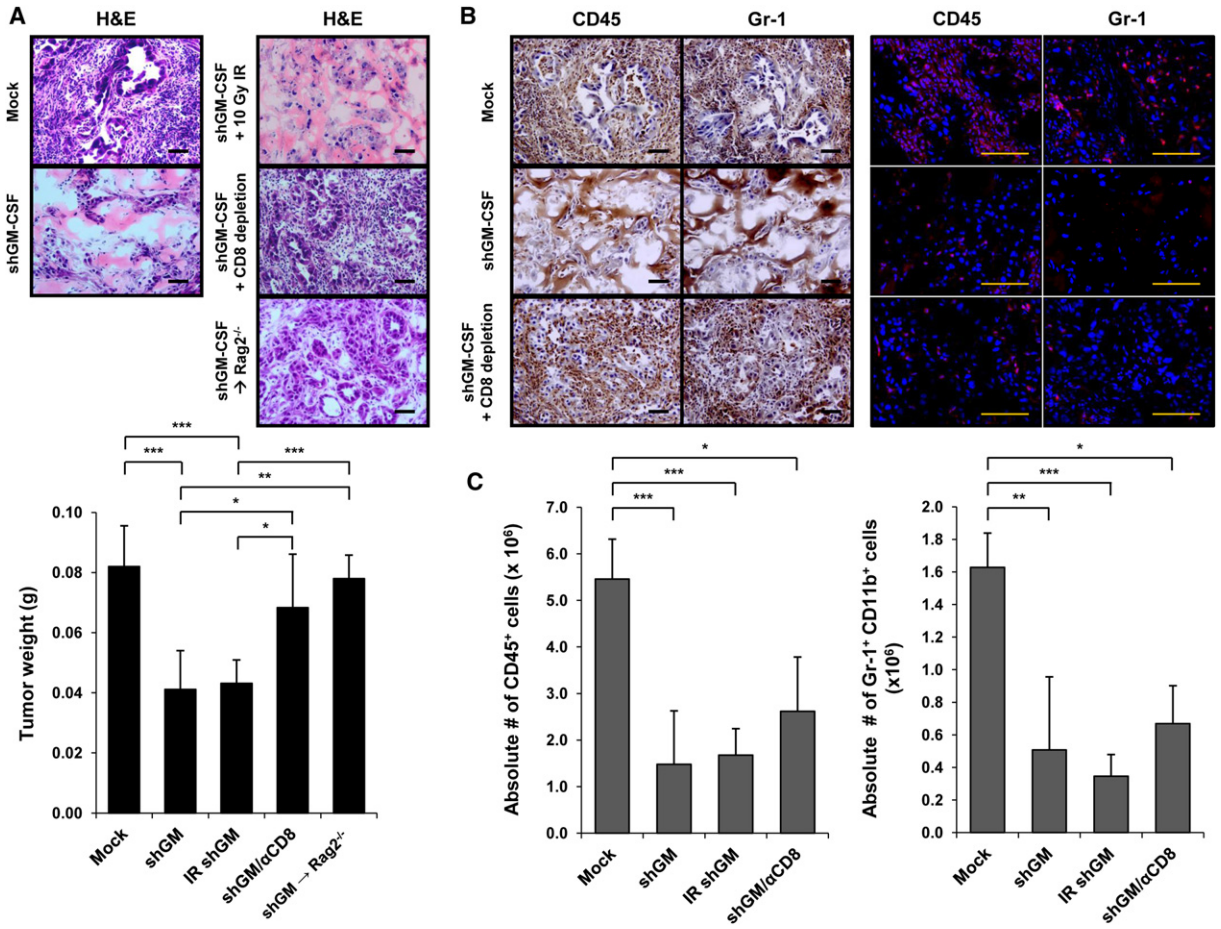

Figure 7. Genetic Knockdown of GM-CSF Demonstrates that Tumor-Derived GM-CSF Regulates Tumor Growth and Recruitment of Gr-1$^+$ CD11b$^+$ Cells In Vivo

(A) Normal control mice or *Rag2*$^{-/-}$ mice (6–14 weeks) were implanted subcutaneously with either shGM-CSF PDA-1 cells (shGM) or vector only PDA-1 cells (Mock) in matrigel with or without tumor cell irradiation (IR), and with or without intraperitoneal administration of a depleting CD8 mAb. On day 6, tumor growth was evaluated by H&E (top; images of one representative mouse per group are shown) and tumor weight (bottom; data are mean ± SD). n = 3 to 7 mice per group. Scale bars, 50 μM. *p < 0.05, **p < 0.01, ***p < 0.001.

(B) The immune infiltrate was evaluated by immunohistochemistry (left) and immunofluorescence (right) for CD45 and Gr-1. Images of one representative mouse per group are shown (3–7 mice per group). Scale bars, 50 μM.

(C) Absolute numbers of CD45$^+$ cells (left) and Gr-1$^+$ CD11b$^+$ cells (right) were quantified by flow cytometry. Data are mean ± SD. *p < 0.05, **p < 0.01, ***p < 0.001. See also Figure S5.

mice (Figure 7A). In addition, we found that CD8$^+$ T cells infiltrated tumors more vigorously after GM-CSF knockdown. This finding was demonstrated by immunofluorescence for CD8 expression and quantified by flow cytometry (Figure S5). To understand if CD8$^+$ T cells from GM-CSF knockdown tumors exhibited effector functions, we evaluated tumor-infiltrating CD8$^+$ T cells for their capacity to secrete IFN-γ and mobilize CD107a, the latter serving as a biomarker of lytic function (Betts et al., 2003). We found that compared to CD8$^+$ T cells from mock PDA-1 tumors, CD8$^+$ T cells from shGM-CSF PDA-1 tumors exhibited a higher percentage of IFN-γ$^+$ CD107a$^+$ cells (Figure S5). Importantly, CD8 depletion did not rescue infiltration of Gr-1$^+$ CD11b$^+$ cells into shGM-CSF PDA-1 tumors, suggesting that PDA-1 tumor cells can grow in the setting of minimal Gr-1$^+$ CD11b$^+$ cells, provided CD8$^+$ T cells are absent (Figure 7).

DISCUSSION

It has become widely appreciated that tumor-associated inflammation is an enabling characteristic of cancer and contributes to tumor escape from immune destruction (Hanahan and Weinberg, 2011). Here, focusing on PDA in mice as a model of the human disease, we demonstrate that tumor cell-derived GM-CSF can orchestrate an immunosuppressive crosstalk between Gr-1$^+$ CD11b$^+$ immature myeloid cells and CD8$^+$ T cells. Overall, our data support a model in which myeloid inflammatory cells negatively regulate CD8$^+$ T cells via tumor-derived GM-CSF (Figure 8).

Although GM-CSF clearly regulates hematopoiesis as a growth factor, its role as an immunomodulatory cytokine has become increasingly appreciated. Depending on the setting, these effects can either promote or suppress cellular immune

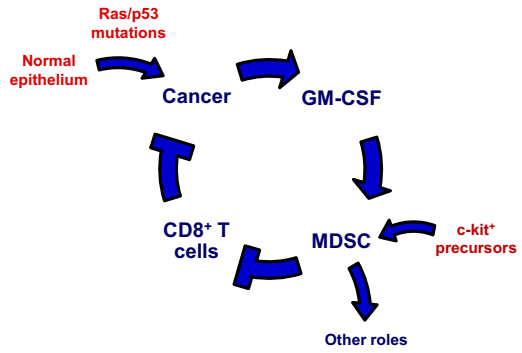

Figure 8. Working Model Links Tumor-Derived GM-CSF, MDSC Generation, and CD8$^+$ T Cell Suppression in PDA

responses. In studies of implantable tumor models, GM-CSF has been linked to the generation of Gr-1$^+$ CD11b$^+$ cells with immunosuppressive features (Bronte et al., 1999; Dolcetti et al., 2010; Morales et al., 2010; Serafini et al., 2004). For example, GM-CSF-transduced melanoma cells induce the systemic expansion of Gr-1$^+$ CD11b$^+$ cells and inhibit memory CD8$^+$ T cells (Bronte et al., 1999). Knockdown of GM-CSF in tumor cell lines has been shown to alter the subset distribution of Gr-1$^+$ CD11b$^+$ myeloid cells following implantation in mice, primarily reducing the Gr-1^{low} and Gr-1^{int} populations which are the most suppressive in these models (Dolcetti et al., 2010). Here, we show that GM-CSF is produced in vivo in a spontaneous tumor that is characterized by prominent infiltration of suppressive Gr-1$^+$ CD11b$^+$ cells. We also demonstrate that human pancreatic tumors cells express GM-CSF in vivo; therefore, these findings are significantly relevant to understanding the human disease.

GM-CSF may not be critical for the development of Gr-1$^+$ CD11b$^+$ cells in every tumor model or histology. In mice with combined loss of IFN-γ, IL-3, and GM-CSF, lung carcinomas develop at a high frequency and exhibit an infiltrate of Gr-1$^+$ CD11b$^+$ leukocytes (Dougan et al., 2011). Moreover, cytokines and growth factors other than GM-CSF have been implicated in the pathophysiology of Gr-1$^+$ CD11b$^+$ leukocytes in other mouse models—including IL-1β, IL-6, and VEGF (Melani et al., 2003)—but none of these factors explains the effects we observed regarding the generation of suppressive Gr-1$^+$ CD11b$^+$ cells in the PDA model. For example, the pro-inflammatory cytokine IL-1β has been implicated in MDSC pathophysiology such that fibrosarcoma or 4T1 mammary carcinoma cell lines engineered to secrete IL-1β grow more rapidly than control tumors upon implantation due to enhanced accumulation of Gr-1$^+$ CD11b$^+$ and concomitant T cell suppression (Bunt et al., 2006; Song et al., 2005). Mice lacking the IL-1 receptor exhibit delayed accumulation of MDSC and slower progression of implanted 4T1 mammary tumors and interestingly, these effects are partially restored by exogenous administration of IL-6, indicating that IL-6 may contribute independently to MDSC expansion (Bunt et al., 2007). Stomach-specific expression of human IL-1β in transgenic mice leads to spontaneous gastric inflammation, invasive cancer, and mobilization of MDSC (Tu et al., 2008). In the KPC model of PDA, however, we observed accumulation of Gr-1$^+$ CD11b$^+$ cells in the spleen and tumor despite the observations that (1) PDA tumor cells did not secrete IL-1β, and (2) the addition of neutralizing anti-IL-1β antibody to PDA-conditioned media failed to attenuate the proliferation and induction of MDSC from precursor cells. Although recombinant IL-6 did trigger low level proliferation of c-kit$^+$ splenocytes, PDA tumors cells (with one exception) did not produce IL-6 and the addition of neutralizing anti-IL-6 antibody to PDA-conditioned media had no effect in these assays. More likely in PDA, tumor-associated macrophages release IL-6 that directly affects the epithelium and promotes PanIN progression and PDA development in vivo (Beatty et al., 2011; Lesina et al., 2011). Indeed, our data are consistent with those of previous studies demonstrating IL-6 production primarily by stromal cells, not the tumor, in mouse models (Lesina et al., 2011) as well as human PDA (Bellone et al., 2006; Lesina et al., 2011). In mice, IL-6 production can be induced in PDA tumor cells, or in pancreas epithelium harboring mutant Kras, but only after an acute inflammatory insult (Fukuda et al., 2011). IL-6 production has been reported in some, but not all, human PDA cell lines (e.g., Bellone et al., 2006). In addition, IL-6 expression in tumors may be silenced by DNA methylation (Dandrea et al., 2009). For IL-1β, variable expression by human PDA cell lines has been described (Bellone et al., 2006), and in mice, IL-1β can be induced in pancreas epithelium harboring mutant Kras, but only after an acute inflammatory insult (Fukuda et al., 2011). Overexpression of IL-1β in the mouse pancreas results in pancreatitis but interestingly, not PanIN or PDA (Marrache et al., 2008).

To understand whether GM-CSF production is an early event in oncogenesis, we generated PanIN epithelial cell lines from PanIN-only-bearing KPC mice and found low level production of GM-CSF. Supernatant from PanIN lines supported the proliferation of c-kit+ splenocytes into Gr-1+ CD11b+ cells, but not to the extent of supernatant from PDA lines (data not shown). This proliferation, however, could be fully blocked by anti-GM-CSF antibody. A caveat from our studies is that we cannot determine the grade of the PanIN lesions from which the lines were derived. Importantly, our results are consistent with data described by Pylayeva-Gupta et al. (Pylayeva-Gupta et al., 2012).

VEGF and granulocyte colony-stimulating factor (G-CSF) have also been implicated in MDSC development (Gabrilovich et al., 1998; Huang et al., 2007; Roland et al., 2009; Dolcetti et al., 2010). In our model of PDA, however, recombinant VEGF had little or no effect on the generation of Gr-1$^+$ CD11b$^+$ myeloid cells from precursor cells isolated from PDA-bearing KPC mice even though our PDA lines produce high levels of VEGF. Furthermore, normal pancreatic ductal cells also secreted VEGF (albeit somewhat less so than PDA cells) yet Gr-1$^+$ CD11b$^+$ cells did not accumulate around normal ducts in vivo and conditioned media from normal ductal cells failed to support proliferation of c-kit$^+$ splenocytes into MDSC. We found that most PDA lines produced G-CSF; however, supernatant from a G-CSF negative line supported proliferation of c-kit$^+$ splenocytes. Some of the normal ductal cell lines also produced G-CSF yet supernatant from these normal lines did not support c-kit$^+$ cell expansion.

Recent studies have also linked the chemokine CCL21 to the appearance of MDSC in the B16-F10 implantable model of melanoma (Shields et al., 2010), and other investigators have uncovered that IL-25 elicits a multipotent progenitor cell population in mucosal tissue that can differentiate into cells of various myeloid lineages (Saenz et al., 2010), but neither CCL21 nor IL-25 is

produced by PDA in our model. Because all PDA lines produce high levels of CCL2 and KC, we also evaluated these factors in our in vitro assays, but neither supported the proliferation of precursors into MDSC, and moreover, these factors were produced by normal pancreatic epithelial cells. Rather, GM-CSF was the only factor that met all the criteria of a tumor-associated driving factor for MDSC generation in our experimental system (i.e., secreted by PDA, not secreted by normal pancreatic epithelial cells, and contributed necessarily to the generation of suppressive MDSC from c-kit$^+$ splenocytes).

Disruption of CD8 immunity by elements of the tumor microenvironment is thought to be a major mechanism of tumor immune escape (Schreiber et al., 2011). Our data demonstrate the critical role Gr-1$^+$ CD11b$^+$ cells play in suppressing T cell immune responses in vitro and in vivo in PDA. In particular, abrogation of tumor-derived GM-CSF reduced Gr-1$^+$ CD11b$^+$ cell infiltration and implanted tumors failed to grow; however, CD8$^+$ T cell depletion fully rescued tumor growth, even though Gr-1$^+$ CD11b$^+$ cell infiltration was not completely restored. These data suggest that Gr-1$^+$ CD11b$^+$ cells can play a primary immune suppressive role. Other potential roles of Gr-1$^+$ CD11b$^+$ cells in regulating tumor growth (Yang et al., 2004, 2008, 2011) appear therefore to be secondary or noncontributory to tumor growth, at least in this assay. This may explain our previous observation that in genetically engineered murine models of PDA, the infiltration of CD8+ T cells and Gr-1+ CD11b+ cells is mutually exclusive (Clark et al., 2007).

In summary, we propose that the secretion of GM-CSF by transformed pancreatic epithelial cells is critically involved in the regulation of inflammation associated with PDA. A major component of this inflammation is the generation of Gr-1$^+$ CD11b$^+$ immature myeloid cells from c-kit$^+$ lineage$^-$ precursor cells. We show that these myeloid cells can suppress antitumor T cell immunity as a primary function and suggest that MDSC contribute to the failure of T cell immunosurveillance in PDA-bearing hosts. In patients, nearly every tumor studied had high GM-CSF expression so that it was not practical to correlate levels of tumor GM-CSF with Kras mutational status. Our findings carry important implications for the design of novel therapies for patients with PDA and highlight the potential for disrupting the crosstalk of tumor cells with the immune system by targeting Gr-1$^+$ CD11b$^+$ cells or the cytokines that regulate their differentiation.

EXPERIMENTAL PROCEDURES

Mice

All animal protocols were reviewed and approved by the Institutional Animal Care and Use Committee of the University of Pennsylvania. *Kras*$^{LSL\text{-}G12D/+}$, *Trp53*$^{LSL\text{-}R172H/+}$, *Pdx1-Cre* (KPC) mice have been previously described (Hingorani et al., 2005). Normal healthy *Trp53*$^{LSL\text{-}R172H/+}$, *Pdx1-Cre* mice or *Pdx1-Cre* mice were used as controls or hosts for implantable tumor studies. *Rag2*$^{-/-}$ mice were used as hosts in some implantable tumor studies. *Kras*^{G12D}; *p53*$^{fl/+}$; *Pdx1-Cre; Rosa*^{YFP} and *Pdx1-Cre*; *Rosa*^{YFP} mice (Rhim et al., 2012) were used for lineage tracing studies.

Collection of Tissue Samples from Mice

The entire pancreas containing tumor, peripancreatic lymph nodes, and normal pancreas tissue was washed in PBS, minced into small fragments, and incubated in collagenase solution (1 mg/ml collagenase V in RPMI-1640) at 37°C for 45 min. Dissociated cells were passed through a 70 μM cell strainer and washed three times in RPMI-1640 supplemented with 10% FCS and 0.05 mM 2-mercaptoethanol, gentamicin and L-glutamine (complete media). Spleens were homogenized and passed through a 70 μM cell strainer to achieve single cell suspensions. Red blood cells were lysed using ACK Lysis Buffer (Cambrex/BioWhittaker).

Antibodies

The following monoclonal antibodies were used in flow cytometry: anti-CD45 (30-F11; PE, PE-Cy7, APC), anti-Gr-1 (RB6-8C5; APC-Cy7), anti-CD11b (M1/70; PE, PerCP-Cy5.5), anti-CD3 (145-2C11; FITC), anti-CD8 (Ly-2; PE-Cy7, APC-Cy7), anti-CD4 (RM4-5; PerCP-Cy5.5), anti-CD19 (1D3; PerCP-Cy5.5), CD107a (1D4B; FITC), IFN-γ (XMG1.2; PE) (all from BD Biosciences), and anti-CD11c (eBioscience; N418; PerCP-Cy5.5). The viability marker 7-amino-actinomycin D (7-AAD) was from BD Biosciences. For in vivo studies, endotoxin-free antibodies were used: anti-GM-CSF (Biolegend; MP1-22E9), anti-CD8 (BioXcell; 2.43), anti-Gr-1 (BioXcell; RB6-8C5), isotype control rat IgG2a (BioXcell; 2A3), and isotype control rat IgG2b (BioXcell; LTF-2).

Flow Cytometry

Single cell suspensions were stained with fluorochrome-labeled antibodies at 4°C for 15 min in PBS/1% FCS. Cells were analyzed on a FACSCanto flow cytometer (BD Biosciences) using BD FACSDiva software (BD Biosciences Immunocytochemistry).

Cytology of Gr-1$^+$ CD11b$^+$ Cells

CD45$^+$ Gr-1$^+$ CD11b$^+$ cells were sorted (>98%) from spleens and pancreata of tumor-bearing KPC mice using a BD FACSAria flow cytometer. Cytospin preparations were stained with Diff-Quick modified Giemsa reagent (Polysciences).

Isolation of Gr-1$^+$ CD11b$^+$ Cells and Functional T Cell Suppression Assay

Gr-1$^+$ CD11b$^+$ cells were isolated from the spleen and pancreas of KPC mice by cell sorting or by high-gradient magnetic cell separation (MACS; Miltenyi Biotec, Bergisch-Gladbach, Germany). For magnetic separation, single cell suspensions were incubated with Gr-1 biotinylated mAb (RB6-8C5) followed by anti-biotin mAb coupled to magnetic beads (Miltenyi Biotec) and sorted using MS MACS columns and the MidiMACS system (Miltenyi Biotec) (>90% Gr-1$^+$ CD11b$^+$ cells by flow cytometry). Antigen-specific and polyclonal suppression of CD8$^+$ T cells was evaluated in a co-culture assay in which splenocytes from either OT-1 transgenic mice (antigen-specific assay) or normal mice (polyclonal assay) were seeded in triplicates in 96-well round bottom plates (8 × 10^5/well). Splenocytes were cultured in the presence of increasing ratios of Gr-1$^+$ CD11b$^+$ cells and stimulated with either cognate antigen, OVA-derived peptide SIINFEKL (1 μg/ml; New England Peptide) (antigen-specific assay), or anti-CD3 (0.5 μg/ml; BD Biosciences; 145-2C11) and anti-CD28 (1 μg/ml; BD Biosciences; 37.51) (polyclonal assay). On day 3 of the co-culture, cells were pulsed with ^{3}[H]-thymidine (1 μCi per well; Amersham Biosciences) and 18 hr later ^{3}[H]-thymidine incorporation was assessed. In some experiments, the OT-1 splenocytes were labeled with CFSE. OT-1 CD8$^+$ T cells were evaluated on day 3 by flow cytometry for CFSE dilution.

CFSE Labeling of Mouse Cells

Cells were resuspended at 10-20x10^6 per mL in a minimum volume of 500 μl PBS and incubated with CFSE (0.5 μM) at RT for 8 min with constant swirling. The reaction was then quenched with media containing 10% FCS.

Arginase Production

Gr-1$^+$ CD11b$^+$ cells (10^6) were isolated, resuspended in 50 μl lysis buffer (0.1% Triton X-100 with 100 μg/ml Pepstatin A, Aprotinin, and Antipain), and shaken for 30 min at 37°C. Following lysis, 50 μl of 50 mM Tris-HCl / 10 mM $MnCl_2$ was added and the mixture was heated for 10 min at 56°C. The lysate was incubated with 100 μl of 0.5 M L-arginine for 120 min at 37°C. The reaction was stopped with 800 μl of H_2SO_4 (96%) / H_3PO_4 (85%) / H_20 (1:3:7 by volume). Subsequently, 40 μl of 9% (by weight) α-isonitrosopropiophenone (ISPF) in 100% ethanol was added, followed by heating at 95°C for 30 min. After 10 min in the dark, urea concentration was measured at 540 nm and compared to a standard curve generated by serial dilution of 750 μg/ml urea. Arginase activity (units) was determined by the amount of urea (μg) formed per minute.

Nitric Oxide Production

Nitric oxide production by Gr-1$^+$ CD11b$^+$ cells was evaluated in culture supernatant from the OT-1 T cell suppression assay using the Griess Reagent System (Promega). Equal volumes of supernatant (40 μl) and 1% sulfanilamide in 5% phosphoric acid were incubated at RT for 10 min, followed by addition of 0.1% N-1-naphthylethylenediamine dihydrochloride in water. After 10 min at RT, absorbance at 550 nm was measured. Nitrite concentrations were determined by comparing absorbance values to a standard curve generated by serial dilution of 0.1 mM sodium nitrite.

BrdU Labeling and Analysis

c-kit$^+$ lineage$^-$ cells on day 4 of culture were labeled with BrdU (BD Biosciences; 10 μM) for 2 hr at 37°C and prepared for flow cytometric analysis according to the FITC BrdU Flow Kit (BD Biosciences).

Cell Lines

PDA cell lines from KPC mice were derived by from single cell suspensions of PDA tissue. Dissociated cells were plated in a 6-well dish with serum free DMEM. After 2 weeks, media was changed to DMEM + 10% FCS. After 3–6 passages, cells were used in experiments. Cell lines established from PDA tumors of KPC mice with confirmed genotypes were injected into normal mice to confirm tumorigenicity. At necropsy, transplanted tumors were inspected pathologically by H&E staining and invasive carcinoma was confirmed.

Fresh Tumor Supernatant Collection

Tumors were excised, washed in PBS, weighed, and minced into small fragments with sterile scissors. Tissue supernatant was harvested by adding 400 μl complete media and compressing tumor fragments with the plunger of a 3 ml syringe. The tumor tissue solution was centrifuged at 13,000 rpm × 10 min, and the supernatant carefully collected.

Cytokine Analysis

Cytometric bead array (BD Biosciences) and ELISA (R&D systems) were used to quantify cytokines in supernatant from PDA lines and wild-type pancreatic ductal cell lines cultured in DMEM + 10% FCS and in supernatant harvested from freshly isolated KPC tumors. For both methods, quantification of cytokines was determined by reference to recombinant murine standards.

Pancreas Cell Sorting and Transcriptional Analysis

Single pancreas cells from tumor-bearing *Kras*^{G12D}; *p53*$^{fl/+}$; *Pdx1-Cre; Rosa*^{YFP} mice and non-tumor-bearing *Pdx1-Cre*; *Rosa*^{YFP} control mice were sorted based on YFP fluorescence into tubes with chilled RLT buffer (QIAGEN). The sorted YFP$^+$ and YFP$^-$ populations are referred to as pancreatic epithelial and stromal compartments, respectively. RNA was extracted from samples using the RNEasy kit (QIAGEN). First strand cDNA was synthesized using SuperScript III (Invitrogen). qPCR was performed using Taqman probes for GAPDH and GM-CSF (Applied Biosystems). Relative expression was determined after adjusting for GAPDH.

shRNA Knockdown of GM-CSF in PDA-1 Cells

GIPZ lentiviral shRNAmir targeting GM-CSF (Clone ID: V2LMM_64126) and GIPZ nonsilencing control viral particles (Catalog # RHS4348) were purchased from OpenBiosystems. PDA-1 cells were infected with high-titer concentrated lentiviral suspensions and selected with 10 μg/ml Puromycin. GFP-positive single cells were sorted using a MoFlo cell sorter and clonal PDA-1 cell lines were derived. In vitro growth kinetics for shGM-CSF PDA-1 cells or mock PDA-1 cells did not differ from the parental PDA-1 cell line.

Short-Term PDA Implantation Studies

PDA-1 tumor cells (10^6) were injected subcutaneously with anti-GM-CSF mAb (BioLegend; 250 μg) or purified rat IgG2a (BioXcell; 250 μg) imbedded as plugs with matrigel matrix (Collaborative Biomedical Products) into the flanks of normal control mice for 6 days. For GM-CSF knockdown studies, mock PDA-1 cells (10^6) or shGM-CSF PDA-1 cells (10^6) were injected subcutaneously with matrigel matrix for 6 days. In some experiments, tumor cells were lethally gamma-irradiated (10 Gy) prior to implantation. For depletion of CD8$^+$ T cells or Gr-1$^+$ cells, anti-CD8 mAb (BioXcell; 200 μg), anti-Gr-1 mAb (BioXcell; 500 μg), or as a control purified isotype control rat IgG2b (BioXcell; 200 μg) was injected intraperitoneally on days −1, 0, 1, and 3 with respect to tumor cell inoculation.

Immunohistochemistry and Histopathology

Immunohistochemistry and histopathology were performed on frozen tissue sections. Sections were fixed in 3% formaldehyde for analysis of CD45 (BD Biosciences; 3-F11; 1:50) and Gr-1 (BioXCell; RB6-8C5; 15 μg/ml). Endogenous peroxidases were quenched in 0.3% H_2O_2 in water for 10 min. Sections were blocked with 10% goat serum in PBS + 0.1% Tween-20 for 30 min followed by labeling with primary antibody overnight at 4°C. Sections were washed and incubated with goat anti-rat biotinylated secondary antibody (BD Biosciences; 1:200) for 1 hr at RT. Remaining steps were performed using Vectastain ABC kits (Vector Labs). Slides were counterstained with hematoxylin.

Human surgical material was obtained after informed consent using an Institutional Review Board approved protocol. Formalin-fixed paraffin-embedded tissues were sectioned for immunohistochemistry. After rehydration, sections were incubated in 1% hydrogen peroxide/methanol then with 10 mM sodium citrate/0.05% Tween-20 (pH 6.0) in a microwave oven for antigen retrieval. Sections were then blocked with 10% serum/1% BSA/0.5% Tween-20 for 1 hr at RT, then incubated with rabbit anti-GM-CSF (Novus Biologicals) overnight at 4°C. Secondary antibody was biotinylated goat anti-rabbit IgG (Vector Laboratories).

Immunofluorescence

Immunofluorescence was performed on frozen tissue sections. Section were fixed in 3% formaldehyde for analysis of CD45 (BD Biosciences; 3-F11; 1:50) or −20°C methanol for analysis of Gr-1 (BioXCell; RB6-8C5; 15 μg/ml) and CD8 (BioXCell; 2.43; 15 μg/ml). Sections were blocked with 10% goat serum in PBS + 0.1% Tween-20 for 30 min followed by labeling with primary antibody overnight at 4°C. Sections were washed and incubated with Alexa Fluor 568 goat anti-rat secondary antibody (Invitrogen; 1:500) along with DAPI (Invitrogen; 1:1000) for 1 hr at RT protected from the light. Sections were mounted with Aqua-Poly/Mount (Polysciences).

CD8+ T Cell IFN-γ/CD107a Analysis

Single cell suspensions of matrigel tumor plugs were mixed with anti-CD107a FITC (1:100) and plated in a 96-well round bottom plate with GolgiStop protein transport inhibitor (containing monensin) (BD Biosciences) and complete media or media containing anti-CD3 (0.5 μg/ml) and anti-CD28 (1 μg/ml) as a positive control. Cells were incubated at 37°C for 5 hr, then were washed and stained for surface molecules. Cells were fixed and permeabilized (eBiosciences) followed by intracellular cytokine staining with anti-IFN-γ PE (1:50; BD Biosciences) prepared in permeabilization buffer for 20 min at 4°C. Cells were washed and analyzed on a FACSCanto flow cytometer (BD Biosciences) for IFN-γ and CD107a expression on CD45$^+$ CD8$^+$ CD11b$^-$ CD11c$^-$ CD4$^-$ CD19$^-$ cells.

Statistical Analyses

All statistical analyses were determined by Student's t test using GraphPad Prism software.

SUPPLEMENTAL INFORMATION

Supplemental Information includes five figures and can be found with this article online at doi:10.1016/j.ccr.2012.04.025.

ACKNOWLEDGMENTS

We thank Carmine Carpenito, Qian-Chun Yu, Hong Wei, Nicole Aiello, and Emily Mirek for important discussions. This work was supported by the Abramson Family Cancer Research Institute (R.H.V. and B.Z.S.) and by grants from the Cancer Research Institute (to L.J.B.), the National Institutes of Health (Grants K12 CA076931 to G.L.B. and K08 088945 to A.D.R.), the Gabrielle's Angel Foundation for Cancer Research (to G.L.B.), the American Gastroenterological Association (to A.D.R.), and the Pennsylvania Department of Health

(to R.H.V. and B.Z.S) The Pennsylvania Department of Health specifically disclaims responsibility for any analyses, interpretations, or conclusions.

Received: July 13, 2011
Revised: February 4, 2012
Accepted: April 9, 2012
Published: June 11, 2012

REFERENCES

Andreu, P., Johansson, M., Affara, N.I., Pucci, F., Tan, T., Junankar, S., Korets, L., Lam, J., Tawfik, D., DeNardo, D.G., et al. (2010). FcRgamma activation regulates inflammation-associated squamous carcinogenesis. Cancer Cell *17*, 121–134.

Beatty, G.L., Chiorean, E.G., Fishman, M.P., Saboury, B., Teitelbaum, U.R., Sun, W., Huhn, R.D., Song, W., Li, D., Sharp, L.L., et al. (2011). CD40 agonists alter tumor stroma and show efficacy against pancreatic carcinoma in mice and humans. Science *331*, 1612–1616.

Bellone, G., Carbone, A., Smirne, C., Scirelli, T., Buffolino, A., Novarino, A., Stacchini, A., Bertetto, O., Palestro, G., Sorio, C., et al. (2006). Cooperative induction of a tolerogenic dendritic cell phenotype by cytokines secreted by pancreatic carcinoma cells. J. Immunol. *177*, 3448–3460.

Betts, M.R., Brenchley, J.M., Price, D.A., De Rosa, S.C., Douek, D.C., Roederer, M., and Koup, R.A. (2003). Sensitive and viable identification of antigen-specific CD8+ T cells by a flow cytometric assay for degranulation. J. Immunol. Methods *281*, 65–78.

Bronte, V., and Zanovello, P. (2005). Regulation of immune responses by L-arginine metabolism. Nat. Rev. Immunol. *5*, 641–654.

Bronte, V., Chappell, D.B., Apolloni, E., Cabrelle, A., Wang, M., Hwu, P., and Restifo, N.P. (1999). Unopposed production of granulocyte-macrophage colony-stimulating factor by tumors inhibits CD8+ T cell responses by dysregulating antigen-presenting cell maturation. J. Immunol. *162*, 5728–5737.

Bronte, V., Apolloni, E., Cabrelle, A., Ronca, R., Serafini, P., Zamboni, P., Restifo, N.P., and Zanovello, P. (2000). Identification of a CD11b(+)/Gr-1(+)/CD31(+) myeloid progenitor capable of activating or suppressing CD8(+) T cells. Blood *96*, 3838–3846.

Bronte, V., Serafini, P., De Santo, C., Marigo, I., Tosello, V., Mazzoni, A., Segal, D.M., Staib, C., Lowel, M., Sutter, G., et al. (2003). IL-4-induced arginase 1 suppresses alloreactive T cells in tumor-bearing mice. J. Immunol. *170*, 270–278.

Bunt, S.K., Sinha, P., Clements, V.K., Leips, J., and Ostrand-Rosenberg, S. (2006). Inflammation induces myeloid-derived suppressor cells that facilitate tumor progression. J. Immunol. *176*, 284–290.

Bunt, S.K., Yang, L., Sinha, P., Clements, V.K., Leips, J., and Ostrand-Rosenberg, S. (2007). Reduced inflammation in the tumor microenvironment delays the accumulation of myeloid-derived suppressor cells and limits tumor progression. Cancer Res. *67*, 10019–10026.

Clark, C.E., Hingorani, S.R., Mick, R., Combs, C., Tuveson, D.A., and Vonderheide, R.H. (2007). Dynamics of the immune reaction to pancreatic cancer from inception to invasion. Cancer Res. *67*, 9518–9527.

Clark, C.E., Beatty, G.L., and Vonderheide, R.H. (2009). Immunosurveillance of pancreatic adenocarcinoma: insights from genetically engineered mouse models of cancer. Cancer Lett. *279*, 1–7.

Dandrea, M., Donadelli, M., Costanzo, C., Scarpa, A., and Palmieri, M. (2009). MeCP2/H3meK9 are involved in IL-6 gene silencing in pancreatic adenocarcinoma cell lines. Nucleic Acids Res. *37*, 6681–6690.

Dolcetti, L., Peranzoni, E., Ugel, S., Marigo, I., Fernandez Gomez, A., Mesa, C., Geilich, M., Winkels, G., Traggiai, E., Casati, A., et al. (2010). Hierarchy of immunosuppressive strength among myeloid-derived suppressor cell subsets is determined by GM-CSF. Eur. J. Immunol. *40*, 22–35.

Dougan, M., Li, D., Neuberg, D., Mihm, M., Googe, P., Wong, K.K., and Dranoff, G. (2011). A dual role for the immune response in a mouse model of inflammation-associated lung cancer. J. Clin. Invest. *121*, 2436–2446.

Fukuda, A., Wang, S.C., Morris, J.P., 4th, Folias, A.E., Liou, A., Kim, G.E., Akira, S., Boucher, K.M., Firpo, M.A., Mulvihill, S.J., and Hebrok, M. (2011). Stat3 and MMP7 contribute to pancreatic ductal adenocarcinoma initiation and progression. Cancer Cell *19*, 441–455.

Gabrilovich, D.I., and Nagaraj, S. (2009). Myeloid-derived suppressor cells as regulators of the immune system. Nat. Rev. Immunol. *9*, 162–174.

Gabrilovich, D., Ishida, T., Oyama, T., Ran, S., Kravtsov, V., Nadaf, S., and Carbone, D.P. (1998). Vascular endothelial growth factor inhibits the development of dendritic cells and dramatically affects the differentiation of multiple hematopoietic lineages in vivo. Blood *92*, 4150–4166.

Gabrilovich, D.I., Bronte, V., Chen, S.H., Colombo, M.P., Ochoa, A., Ostrand-Rosenberg, S., and Schreiber, H. (2007). The terminology issue for myeloid-derived suppressor cells. Cancer Res. *67*, 425, author reply 426.

Hanahan, D., and Weinberg, R.A. (2011). Hallmarks of cancer: the next generation. Cell *144*, 646–674.

Hingorani, S.R., Wang, L., Multani, A.S., Combs, C., Deramaudt, T.B., Hruban, R.H., Rustgi, A.K., Chang, S., and Tuveson, D.A. (2005). Trp53R172H and KrasG12D cooperate to promote chromosomal instability and widely metastatic pancreatic ductal adenocarcinoma in mice. Cancer Cell *7*, 469–483.

Huang, Y., Chen, X., Dikov, M.M., Novitskiy, S.V., Mosse, C.A., Yang, L., and Carbone, D.P. (2007). Distinct roles of VEGFR-1 and VEGFR-2 in the aberrant hematopoiesis associated with elevated levels of VEGF. Blood *110*, 624–631.

Kusmartsev, S., and Gabrilovich, D.I. (2006). Role of immature myeloid cells in mechanisms of immune evasion in cancer. Cancer Immunol. Immunother. *55*, 237–245.

Kusmartsev, S., Nefedova, Y., Yoder, D., and Gabrilovich, D.I. (2004). Antigen-specific inhibition of CD8+ T cell response by immature myeloid cells in cancer is mediated by reactive oxygen species. J. Immunol. *172*, 989–999.

Lesina, M., Kurkowski, M.U., Ludes, K., Rose-John, S., Treiber, M., Klöppel, G., Yoshimura, A., Reindl, W., Sipos, B., Akira, S., et al. (2011). Stat3/Socs3 activation by IL-6 transsignaling promotes progression of pancreatic intraepithelial neoplasia and development of pancreatic cancer. Cancer Cell *19*, 456–469.

Ma, G., Pan, P.Y., Eisenstein, S., Divino, C.M., Lowell, C.A., Takai, T., and Chen, S.H. (2011). Paired immunoglobin-like receptor-B regulates the suppressive function and fate of myeloid-derived suppressor cells. Immunity *34*, 385–395.

Marrache, F., Tu, S.P., Bhagat, G., Pendyala, S., Osterreicher, C.H., Gordon, S., Ramanathan, V., Penz-Osterreicher, M., Betz, K.S., Song, Z., and Wang, T.C. (2008). Overexpression of interleukin-1beta in the murine pancreas results in chronic pancreatitis. Gastroenterology *135*, 1277–1287.

Melani, C., Chiodoni, C., Forni, G., and Colombo, M.P. (2003). Myeloid cell expansion elicited by the progression of spontaneous mammary carcinomas in c-erbB-2 transgenic BALB/c mice suppresses immune reactivity. Blood *102*, 2138–2145.

Morales, J.K., Kmieciak, M., Knutson, K.L., Bear, H.D., and Manjili, M.H. (2010). GM-CSF is one of the main breast tumor-derived soluble factors involved in the differentiation of CD11b-Gr1- bone marrow progenitor cells into myeloid-derived suppressor cells. Breast Cancer Res. Treat. *123*, 39–49.

Ostrand-Rosenberg, S., and Sinha, P. (2009). Myeloid-derived suppressor cells: linking inflammation and cancer. J. Immunol. *182*, 4499–4506.

Peranzoni, E., Zilio, S., Marigo, I., Dolcetti, L., Zanovello, P., Mandruzzato, S., and Bronte, V. (2010). Myeloid-derived suppressor cell heterogeneity and subset definition. Curr. Opin. Immunol. *22*, 238–244.

Pylayeva-Gupta, Y., Lee, K.E., Hajdu, C.H., Miller, G., and Bar-Sagi, D. (2012). Oncogenic KRas-induced GM-CSF production supports the development of pancreatic neoplasia. Cancer Cell, in press.

Rhim, A.D., Mirek, E.T., Aiello, N.M., Maitra, A., Bailey, J.M., McAllister, F., Reichert, M., Beatty, G.L., Rustgi, A.K., Vonderheide, R.H., et al. (2012). EMT and dissemination precede pancreatic tumor formation. Cell *148*, 349–361.

Roland, C.L., Lynn, K.D., Toombs, J.E., Dineen, S.P., Udugamasooriya, D.G., and Brekken, R.A. (2009). Cytokine levels correlate with immune cell infiltration after anti-VEGF therapy in preclinical mouse models of breast cancer. PLoS ONE *4*, e7669.

Saenz, S.A., Siracusa, M.C., Perrigoue, J.G., Spencer, S.P., Urban, J.F., Jr., Tocker, J.E., Budelsky, A.L., Kleinschek, M.A., Kastelein, R.A., Kambayashi, T., et al. (2010). IL25 elicits a multipotent progenitor cell population that promotes T(H)2 cytokine responses. Nature *464*, 1362–1366.

Schreiber, R.D., Old, L.J., and Smyth, M.J. (2011). Cancer immunoediting: integrating immunity's roles in cancer suppression and promotion. Science *331*, 1565–1570.

Serafini, P., Carbley, R., Noonan, K.A., Tan, G., Bronte, V., and Borrello, I. (2004). High-dose granulocyte-macrophage colony-stimulating factor-producing vaccines impair the immune response through the recruitment of myeloid suppressor cells. Cancer Res. *64*, 6337–6343.

Shields, J.D., Kourtis, I.C., Tomei, A.A., Roberts, J.M., and Swartz, M.A. (2010). Induction of lymphoidlike stroma and immune escape by tumors that express the chemokine CCL21. Science *328*, 749–752.

Sinha, P., Clements, V.K., and Ostrand-Rosenberg, S. (2005). Reduction of myeloid-derived suppressor cells and induction of M1 macrophages facilitate the rejection of established metastatic disease. J. Immunol. *174*, 636–645.

Song, X., Krelin, Y., Dvorkin, T., Bjorkdahl, O., Segal, S., Dinarello, C.A., Voronov, E., and Apte, R.N. (2005). CD11b+/Gr-1+ immature myeloid cells mediate suppression of T cells in mice bearing tumors of IL-1beta-secreting cells. J. Immunol. *175*, 8200–8208.

Stairs, D.B., Bayne, L.J., Rhoades, B., Vega, M.E., Waldron, T.J., Kalabis, J., Klein-Szanto, A., Lee, J.S., Katz, J.P., Diehl, J.A., et al. (2011). Deletion of p120-catenin results in a tumor microenvironment with inflammation and cancer that establishes it as a tumor suppressor gene. Cancer Cell *19*, 470–483.

Tu, S., Bhagat, G., Cui, G., Takaishi, S., Kurt-Jones, E.A., Rickman, B., Betz, K.S., Penz-Oesterreicher, M., Bjorkdahl, O., Fox, J.G., and Wang, T.C. (2008). Overexpression of interleukin-1beta induces gastric inflammation and cancer and mobilizes myeloid-derived suppressor cells in mice. Cancer Cell *14*, 408–419.

Yang, L., DeBusk, L.M., Fukuda, K., Fingleton, B., Green-Jarvis, B., Shyr, Y., Matrisian, L.M., Carbone, D.P., and Lin, P.C. (2004). Expansion of myeloid immune suppressor Gr+CD11b+ cells in tumor-bearing host directly promotes tumor angiogenesis. Cancer Cell *6*, 409–421.

Yang, L., Huang, J., Ren, X., Gorska, A.E., Chytil, A., Aakre, M., Carbone, D.P., Matrisian, L.M., Richmond, A., Lin, P.C., and Moses, H.L. (2008). Abrogation of TGF beta signaling in mammary carcinomas recruits Gr-1+CD11b+ myeloid cells that promote metastasis. Cancer Cell *13*, 23–35.

Yang, X.D., Ai, W., Asfaha, S., Bhagat, G., Friedman, R.A., Jin, G., Park, H., Shykind, B., Diacovo, T.G., Falus, A., and Wang, T.C. (2011). Histamine deficiency promotes inflammation-associated carcinogenesis through reduced myeloid maturation and accumulation of CD11b+Ly6G+ immature myeloid cells. Nat. Med. *17*, 87–95.

Cancer Cell
Article

Oncogenic Kras-Induced GM-CSF Production Promotes the Development of Pancreatic Neoplasia

Yuliya Pylayeva-Gupta,[1] Kyoung Eun Lee,[1,4] Cristina H. Hajdu,[2] George Miller,[3] and Dafna Bar-Sagi[1,*]
[1]Department of Biochemistry and Molecular Pharmacology
[2]Department of Pathology
[3]Departments of Surgery and Cell Biology
New York University School of Medicine, New York, NY 10016, USA
[4]Present address: Abramson Family Cancer Research Institute, Howard Hughes Medical Institute, Perelman School of Medicine, University of Pennsylvania, Philadelphia, PA 19104, USA
*Correspondence: dafna.bar-sagi@med.nyu.edu
DOI 10.1016/j.ccr.2012.04.024

SUMMARY

Stromal responses elicited by early stage neoplastic lesions can promote tumor growth. However, the molecular mechanisms that underlie the early recruitment of stromal cells to sites of neoplasia remain poorly understood. Here, we demonstrate an oncogenic $Kras^{G12D}$-dependent upregulation of GM-CSF in mouse pancreatic ductal epithelial cells (PDECs). An enhanced GM-CSF production is also observed in human PanIN lesions. $Kras^{G12D}$-dependent production of GM-CSF in vivo is required for the recruitment of $Gr1^+CD11b^+$ myeloid cells. The suppression of GM-CSF production inhibits the in vivo growth of $Kras^{G12D}$-PDECs, and, consistent with the role of GM-CSF in $Gr1^+CD11b^+$ mobilization, this effect is mediated by $CD8^+$ T cells. These results identify a pathway that links oncogenic activation to the evasion of antitumor immunity.

INTRODUCTION

Pancreatic ductal adenocarcinoma (PDA) is a highly aggressive malignancy with a dismal long-term prognosis. Indeed, the disease exhibits a median survival of less than 6 months and a 5-year survival rate of 3%–5% (Kern et al., 2011; Maitra and Hruban, 2008). PDA evolves through a series of histopathological changes, referred to as pancreatic intraepithelial neoplasia (PanIN), accompanied by a recurrent pattern of genetic lesions, the earliest and most ubiquitous of which is oncogenic activation of Kras (Hong et al., 2011; Maitra and Hruban, 2008; Shi et al., 2008). The essential role of oncogenic Kras in the pathogenesis of PDA is indicated by several genetically engineered mouse models, wherein the conditional expression of the mutated allele of *Kras* in the pancreas is necessary and/or sufficient to drive disease progression from the early preinvasive to a malignant stage (Hingorani et al., 2003; Seidler et al., 2008). Though the mechanisms by which oncogenic Kras contributes to the genesis and progression of PDA have not been fully elucidated, the proliferative and survival advantages conferred on epithelial cells by the expression of endogenous oncogenic Kras have been clearly implicated (Pylayeva-Gupta et al., 2011).

In addition to the well-documented molecular and histological alterations exhibited by the tumor cells themselves, as well as by their preneoplastic precursors, a hallmark of PDA is an extensive stromal remodeling, the most prominent features of which are the recruitment of inflammatory and mesenchymal cells as well as fibrotic replacement of the pancreatic parenchyma (Chu et al., 2007; Kleeff et al., 2007; Maitra and Hruban, 2008). Strikingly, histological assessment of pancreata of human patients afflicted with PDA or mice engineered to express oncogenic Kras in the epithelial compartment of the pancreas reveals that even early stages of PanIN development are associated with a stromal reaction, which is characterized by a robust desmoplastic response and recruitment of immune cells (Chu et al.,

Significance

Pancreatic ductal adenocarcinoma (PDA) is a highly aggressive malignancy currently ranked as the fourth-leading cause of cancer-related deaths in the United States. PDA development is accompanied by pronounced changes in stromal responses and immune surveillance programs. However, the mechanisms that contribute to these changes have not been clearly defined. In this study, we demonstrate that mutational activation of Kras in pancreatic ductal cells triggers the production of GM-CSF, which, in turn, promotes the expansion of immunosuppressive $Gr1^+CD11b^+$ myeloid cells, leading to the evasion of $CD8^+$ T cell-driven antitumor immunity. Our findings implicate oncogenic Kras in restraining the antitumor immune response and provide insights into critical barriers for designing effective immunotherapeutic strategies against pancreatic cancer.

2007; Clark et al., 2007). However, the precise role played by the PanIN-associated stroma in PDA development has not been established. On the basis of the composition of the immune infiltrates surrounding the PanINs, it has been proposed that the stromal constituents around PanINs form an inflammatory and immune suppressive environment, thereby allowing the precursor lesions to escape immune surveillance (Clark et al., 2009). Consistent with this idea, studies in both humans and mice have demonstrated a dampened adaptive immune response accompanying the formation of oncogenic Ras-driven cancers (Clark et al., 2009; DuPage et al., 2011; Fossum et al., 1995; Gjertsen and Gaudernack, 1998; Kubuschok et al., 2006; Qin et al., 1995; Weijzen et al., 1999). Moreover, there is growing evidence that targeting the tumor immune microenvironment may provide an effective therapeutic strategy (Quezada et al., 2011).

To explore the functional interactions between PanINs and their microenvironment, we sought to identify the mechanisms by which precursor lesions harboring oncogenic Kras instigate a stromal response.

RESULTS

To investigate the role of oncogenic Kras in modulating the host immune response during PanIN evolution, we established an orthotopic allograft system in which primary ductal epithelial cells (PDECs) isolated from *LSL-$Kras^{G12D}$* knock-in mice were injected into the pancreata of syngeneic C57Bl/6 mice. The expression of the *$Kras^{G12D}$* allele in these cells was induced prior to implantation by Cre-mediated recombination, as previously described (Lee and Bar-Sagi, 2010); for the purpose of their in situ identification, the cells were engineered to express green fluorescent protein (GFP). Unless otherwise specified, these cells are referred to throughout the article as *GFP-$Kras^{G12D}$*-PDECs. To minimize the possibility of a genetic drift, PDECs were propagated in culture only for a limited number of passages (<16). As illustrated in Figure 1A, implanted *GFP-$Kras^{G12D}$*-PDECs formed ductal structures of heterogeneous size and architecture mostly resembling early PanIN lesions and reactive ducts. Notably, the grafts were characterized by a pronounced localized desmoplasia (Trichrome staining, Figure 1A) and the overt presence of $CD45^+$ immune cells (Figure 1B). The same results were obtained using five independent PDEC isolates, indicating that *GFP-$Kras^{G12D}$*-PDEC implants possess an intrinsic capacity to invoke a robust stromal response. Sham injections had no apparent effect on the pancreatic parenchyma (data not shown), ruling out the contribution of injury-induced inflammation to the observed immune response. GFP-labeled wild-type PDECs (*GFP*-WT-PDECs) failed to engraft (Figure S1A available online) consistent with their previously reported survival disadvantage relative to *$Kras^{G12D}$*-PDEC (Lee and Bar-Sagi, 2010).

To ascertain whether the immunologic reaction evoked by *$Kras^{G12D}$*-PDECs in the orthogenic system is physiologically relevant, we compared by flow cytometry analysis the overall abundance and subtype distribution of immune cells in pancreata containing *GFP-$Kras^{G12D}$*-PDEC grafts and pancreata from *p48-Cre;LSL-$Kras^{G12D}$* mice (Hingorani et al., 2003). At 8 weeks after implantation, the abundance of $CD45^+$ cells in *GFP-$Kras^{G12D}$*-PDEC pancreata was similar to that observed in pancreata from 12-week-old *p48-Cre;LSL-$Kras^{G12D}$* mice (Figure S1B), which, at this stage, typically display early PanIN lesions that are scattered throughout the organ (Hingorani et al., 2003). By and large, the distribution of the major immune cell subtypes was similar in both models (Figure 1C). In addition, both models displayed an increased intrapancreatic as well as splenic accumulation of $Gr1^+CD11b^+$ myeloid cells and $CD4^+Foxp3^+CD25^+$ regulatory T cells (Tregs), compared with normal pancreas and spleen (Figure 1D and Figures S1C and S1D) and in agreement with the reported increase in the abundance of these putative immunosuppressive cell populations during early pancreatic neoplasia (Clark et al., 2007). Together, these observations credential the use of *$Kras^{G12D}$*-PDECs to elucidate the interaction of the neoplastic epithelium with the host immune system and suggest that oncogenic activation of Kras may be sufficient to instigate immune responses that contribute to disease progression.

To further test this idea, we sought to identify mechanisms by which the expression of oncogenic Kras in PDECs could modulate an immune reaction. Given the documented effect of oncogenic forms of Ras on the expression of immune mediators (Ancrile et al., 2008; Coppé et al., 2008), we began by analyzing the supernatants of wild-type and *GFP-$Kras^{G12D}$*-PDECs for cytokine production using the Milliplex cytokine bead panel (Figure 2A and Figure S2A). Of the 32 cytokines represented in this panel, GM-CSF was most robustly upregulated in *GFP-$Kras^{G12D}$*-PDECs (Figure 2A and Figure S2A). The increase in GM-CSF protein levels was corroborated by an increase in the levels of *GM-CSF* transcripts, suggesting a role for $Kras^{G12D}$ in the transcriptional upregulation of *GM-CSF* (Figure 2A). Pharmacological inhibition of either PI-3K or MAPK pathways resulted in abrogation of *GM-CSF* expression in *GFP-$Kras^{G12D}$*-PDECs, indicating that the regulation of GM-CSF expression by oncogenic Kras is mediated by multiple effector pathways (Figure 2B and Figure S2B).

To examine whether increased GM-CSF expression is also a feature of pancreatic neoplasia in vivo, we first used ELISA analysis of tissue supernatants to measure the production of GM-CSF in *GFP-$Kras^{G12D}$*-PDEC and *p48-Cre;LSL-$Kras^{G12D}$* pancreata in comparison to that from normal pancreatic tissues. In both model systems, GM-CSF levels were found to be significantly upregulated (Figure 2C). Next, we evaluated the production of GM-CSF in human PDA by immunohistochemical staining of tissue sections. At least 75% of all PanINs within a section had to exhibit 50% or more GM-CSF-stained cells per lesion to be considered positive. Using this criterion, 14 of the 16 PDA patient samples were positive for GM-CSF staining of PanIN lesions (Figure 2D). Invasive PDA lesions were also positive for GM-CSF expression, indicating that GM-CSF upregulation persists through disease progression (Figure 2D). Of note, compared to PDA-associated PanIN lesions, pancreatic lesions from four non-PDA cases (chronic pancreatitis, pancreatic dermoid cyst, pancreatic endocrine neoplasm, and serous cystadenoma) had no detectable GM-CSF expression (Figure S2C and data not shown). Because these diseases typically are not associated with mutations in the *Kras* allele, the absence of GM-CSF expression is consistent with a role for oncogenic Kras signaling in GM-CSF

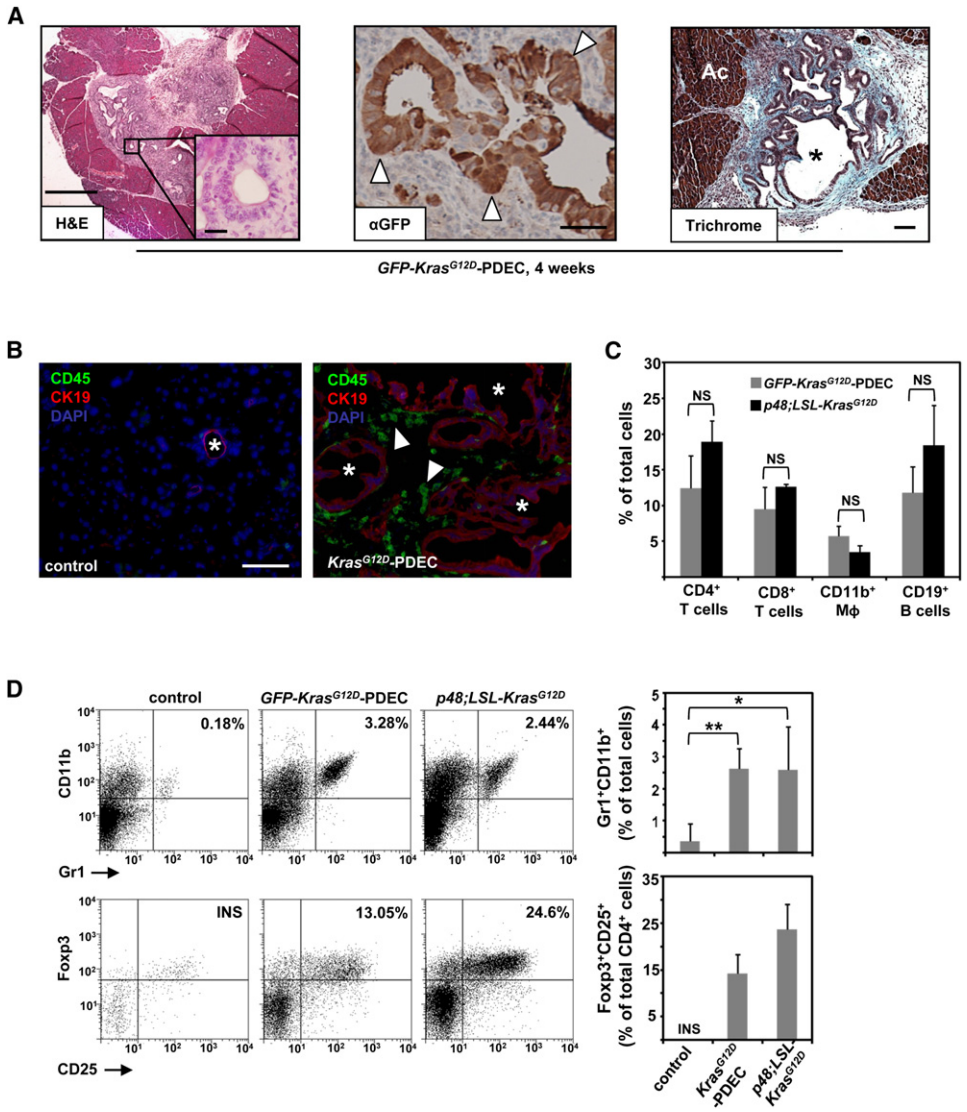

Figure 1. Orthotopic Implantation of *Kras^{G12D}*-PDECs Generates a Robust Immune Response

(A) Sections from orthotopic pancreatic grafts formed by *GFP-Kras^{G12D}*-PDECs at 4 weeks after implantation were stained with hematoxylin and eosin (H&E; scale bar, 500 μm; inset scale bar, 25 μm), anti-GFP antibody (scale bar, 50 μm), and Trichrome blue (scale bar, 100 μm). White arrowheads indicate GFP-positive neoplastic pancreatic ducts; black asterisk indicates neoplastic ducts; Ac stands for acinar compartment.

(B) Immunofluorescence staining for CD45 and CK19 in pancreata of normal sham-injected control and orthotopic *GFP-Kras^{G12D}*-PDEC animals (4 weeks after implantation). CK19 was used to identify ductal epithelia, CD45 was used to identify immune cells, and nuclei were counterstained with DAPI. White asterisk indicates pancreatic ductal structures (left panel) and grafted ductal structures (right panel); white arrowheads indicate CD45$^+$ cells. Scale bar, 100 μm.

(C) Percentage of immune cell types in pancreata was determined by flow cytometry of pancreatic tissue and quantified. After gating on the CD45$^+$ population, cells were analyzed for the presence of respective lineage markers (percentage of each immune cell subtype out of total number of live cells sorted from the pancreas is shown). Error bars indicate SD (n = 3–8 mice per group).

(D) Flow cytometry analysis of pancreatic tissue for the presence of Gr1$^+$CD11b$^+$ myeloid and Foxp3$^+$CD25$^+$ Tregs. After gating on the CD45$^+$ population (top), cells were analyzed for the presence of Gr1$^+$CD11b$^+$ subpopulation. The graph shows the percentage of Gr1$^+$CD11b$^+$ cells out of the total number of live cells sorted from the pancreas. After gating on CD45$^+$CD3$^+$ T cells (bottom), cells were gated on CD4$^+$ to examine intracellular Foxp3 versus surface CD25 staining. The graph shows the percentage of Tregs out of the total number of CD4$^+$ T cells. Representative flow cytometry plots are shown. Error bars indicate SD; INS, insufficient number of cells for analysis (n = 4–8 mice per group).

*$p < 0.05$; **$p < 0.01$; NS, not significant. See also Figure S1.

upregulation. Together, these results suggest that heightened tumor cell-derived GM-CSF levels represent an early Kras^{G12D}-dependent facet of pancreatic neoplasia that is sustained over the course of malignant transformation.

GM-CSF plays a versatile role in the development of immunological responses and has been implicated in the regulation of proliferation and maturation of multiple immune cell lineages, including monocyte, granulocyte, dendritic cells, and putative

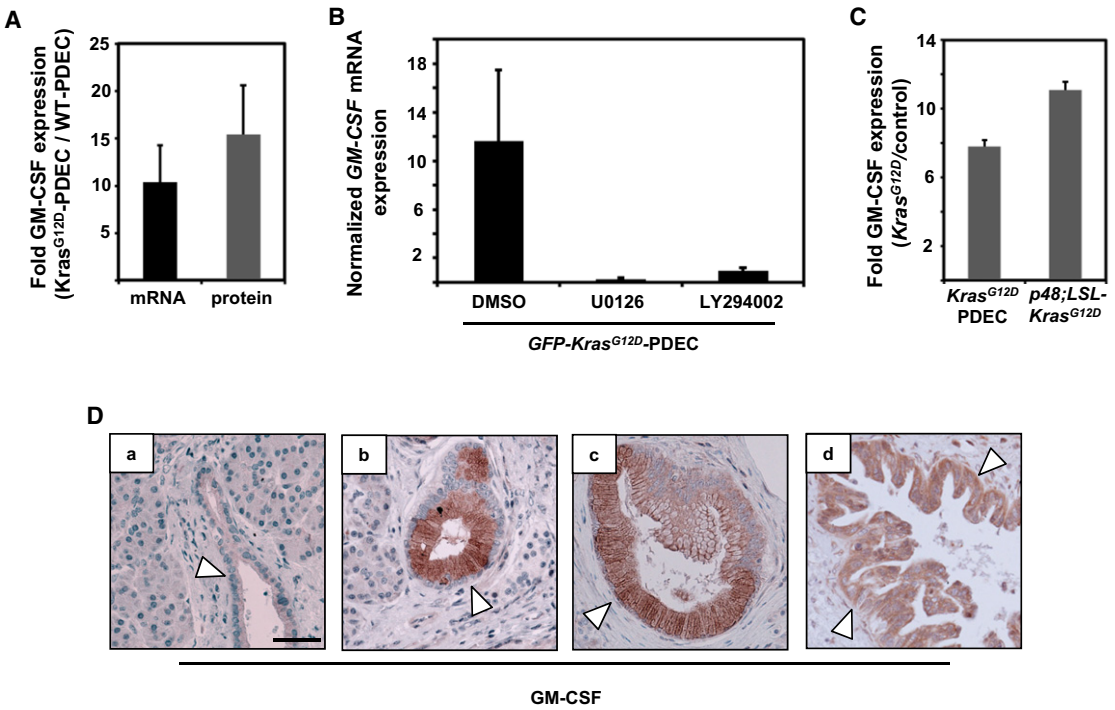

Figure 2. GM-CSF Is Upregulated in *Kras^{G12D}*-PDECs as Well as PanIN-Harboring Mouse and Human Pancreata

(A) Levels of *GM-CSF* mRNA (black bar) and protein (gray bar) in *GFP-Kras^{G12D}*-PDEC were assessed by quantitative RT-PCR and ELISA, respectively. Data are presented as an average fold induction over values from isogenic *GFP*-WT-PDECs. Error bars indicate SD (n = 3).

(B) Normalized expression of *GM-CSF* mRNA in *GFP-Kras^{G12D}*-PDECs (black bars) after 24 hr of treatment with DMSO, MAPK inhibitor U0126 (2 μM), or PI3K inhibitor LY294002 (10 μM) was analyzed by quantitative RT-PCR. Error bars indicate SD (n = 3).

(C) Levels of GM-CSF protein in pancreata grafted with *GFP-Kras^{G12D}*-PDECs or pancreata from *p48;LSL-Kras^{G12D}* mice. Data are presented as an average fold induction over values from normal pancreatic tissue. Error bars indicate SD (n = 3).

(D) Immunohistochemical staining for GM-CSF protein in representative samples of human pancreatic cancer containing PanIN lesions (a, normal duct from adjacent nonmalignant tissue; b and c, PanIN lesions; d, invasive PDA). White arrowheads indicate pancreatic duct (a), PanIN (b and c), and PDA (d). Scale bar, 50 μm.

See also Figure S2.

immunosuppressive Gr1$^+$CD11b$^+$ myeloid cells (Barreda et al., 2004). Because Gr1$^+$CD11b$^+$ cell accumulation is consistently observed in *GFP-Kras^{G12D}*-PDEC and *p48-Cre;LSL-Kras^{G12D}* pancreata (Figure 1D), we sought to determine whether the GM-CSF produced by *GFP-Kras^{G12D}*-PDEC can induce the differentiation of progenitor Gr1$^-$CD11b$^-$ cells to Gr1$^+$CD11b$^+$. As illustrated in Figure 3A, the coculturing of bone marrow-derived Lin^{neg}CD34$^+$ hematopoietic progenitor cells (HPCs) with *GFP-Kras^{G12D}*-PDECs that were seeded on Transwell inserts, induced an accumulation of Gr1$^+$CD11b$^+$ cells. Recombinant GM-CSF alone was used as a positive control (Figure 3A). The addition of neutralizing anti-GM-CSF monoclonal antibody MP1-22E9 (α-GM) (Schön et al., 2000) significantly attenuated the expansion of Gr1$^+$CD11b$^+$ cells, indicating that their generation is largely dependent on *GFP-Kras^{G12D}*-PDEC-derived GM-CSF (Figure 3A). To establish whether these Gr1$^+$CD11b$^+$ cells display suppressive activity, the coculture-derived, sorted, double-positive population was incubated with splenic T cells, and the CD3/CD28-induced proliferation of CD3$^+$ T cells was assessed by BrdU incorporation. Proliferation of CD3$^+$ cells was inhibited in the presence of Gr1$^+$CD11b$^+$ cells, indicating that GM-CSF produced by *Kras^{G12D}*-PDEC can drive the generation of differentiated Gr1$^+$CD11b$^+$ myeloid cells with immunosuppressive potential (Figure 3B). Significantly, Gr1$^+$CD11b$^+$ double-positive cells but not Gr1$^-$CD11b$^+$ single-positive cells isolated from *GFP-Kras^{G12D}*-PDEC grafted pancreata suppressed proliferation of splenic T cells (Figure 3C), indicating that the accumulation of Gr1$^+$CD11b$^+$ cells at the sites of pancreatic neoplasia could contribute to the induction of a tolerogenic immune state. Because we have observed that the numbers of Gr1$^+$CD11b$^+$ cells were augmented in the spleens of orthotopically injected animals, we sought to determine whether there was a systemic increase in the levels of GM-CSF following engraftment of *GFP-Kras^{G12D}*-PDECs. We found that the levels of circulating GM-CSF in mice with *GFP-Kras^{G12D}*-PDEC lesions were significantly elevated as compared to control animals (Figure 3D), suggesting that, in addition to its localized intrapancreatic effect, GM-CSF production by *Kras^{G12D}*-PDECs may affect hematopoietic processes in secondary lymphoid organs.

To establish whether the upregulation of GM-CSF in *Kras^{G12D}*-PDECs is responsible for the accumulation of Gr1$^+$CD11b$^+$ in vivo, we utilized short hairpin RNAi to stably knock down GM-CSF expression in *GFP-Kras^{G12D}*-PDECs. A significant

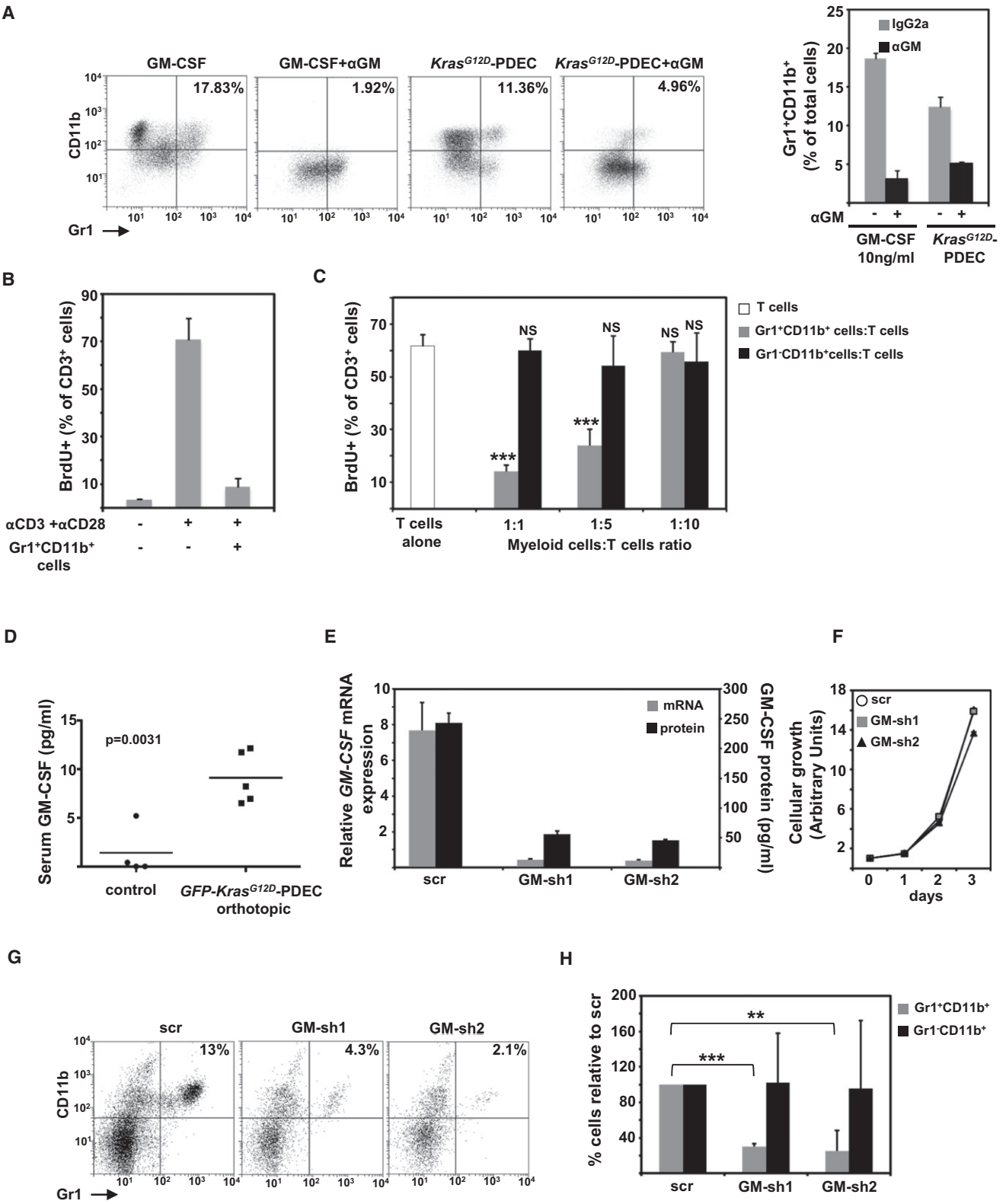

Figure 3. Kras^{G12D}-PDECs Promote Accumulation of Immunosuppressive Gr1$^+$CD11b$^+$ Cells in a GM-CSF-Dependent Manner

(A) Flow cytometry analysis of Lin^{neg}CD34$^+$ hematopoietic progenitor cells for the surface markers CD11b and Gr1 following coculture with GM-CSF or *GFP-Kras^{G12D}*-PDECs with or without α-GM-CSF antibody (α-GM). Representative flow cytometry plots and a graph indicating percentage of the Gr1$^+$CD11b$^+$ cells out of the total number of live cells are shown. Error bars indicate SD (n = 3).

reduction of GM-CSF at the level of both mRNA and protein was achieved using two independent hairpin sequences (Figure 3E). GM-CSF knock-down did not produce an adverse effect on the growth of *GFP-Kras^{G12D}*-PDEC in culture (Figure 3F), consistent with our findings that these cells do not express the GM-CSF receptor beta chain CD131 (data not shown). We next analyzed the composition of leukocytic infiltrates in pancreata grafted with *GFP-Kras^{G12D}*-PDECs expressing scrambled (scr-*GFP-Kras^{G12D}*-PDEC) or GM-CSF shRNAs (GM-sh1- and GM-sh2-*GFP-Kras^{G12D}*-PDEC). Among all CD45$^+$ cells found in the pancreas, GM-CSF knock-down led to a specific reduction in the abundance of Gr1$^+$CD11b$^+$ cells but not Gr1$^-$CD11b$^+$ cells (Figures 3G and 3H), indicating that the production of GM-CSF by ductal cells harboring the *Kras^{G12D}* allele is necessary to promote local accumulation of immune cells of the Gr1$^+$CD11b$^+$ lineage.

Because Gr1$^+$CD11b$^+$ myeloid cells have been implicated in tumor-induced immune tolerance (Gabrilovich and Nagaraj, 2009), we reasoned that the *Kras^{G12D}*-PDEC-mediated production of GM-CSF and the resulting accumulation of Gr1$^+$CD11b$^+$ cells could be critical for the establishment of an immunosuppressive environment that is growth permissive. To investigate this possibility, we have characterized the engraftment of *GFP-Kras^{G12D}*-PDEC in relation to GM-CSF production. As illustrated in Figure 4A, the implantation frequency of GM-sh-*GFP-Kras^{G12D}*-PDECs was significantly reduced as compared to scr-*GFP-Kras^{G12D}*-PDECs, and the average size of the knock-down lesions was significantly decreased. To gain insight into the process underlying compromised engraftment of GM-sh-*GFP-Kras^{G12D}*-PDECs, we analyzed the fate of the grafts at different time points after implantation by immunohistochemical staining against GFP. At 1 week after implantation, grafts generated from scr- and GM-sh-*GFP-Kras^{G12D}*-PDECs were essentially indistinguishable with respect to size, histological appearance, and cell number (Figure 4B and Figure S3). Thus, it appears that GM-CSF deficiency has no adverse effect on the initial growth and survival capabilities of *Kras^{G12D}*-PDEC in vivo. However, at 2 weeks after implantation, although scr-*GFP-Kras^{G12D}*-PDEC grafts displayed a sizable expansion and the characteristic elaboration of ductal structures, graft areas in pancreata that were implanted with GM-sh-*GFP-Kras^{G12D}*-PDECs were virtually devoid of GFP-positive cells (Figure 4B and Figure S3). These observations are consistent with the postulate that the production of GM-CSF enables *Kras^{G12D}*-PDEC to engage host-dependent responses that favor their maintenance and expansion.

Recent studies have indicated that Gr1$^+$CD11b$^+$ cells may contribute to tumor immune evasion by restraining the activity of CD8$^+$ T cells (Gabrilovich and Nagaraj, 2009; Marigo et al., 2008). To examine the relevance of this mechanism to the engraftment potential of *Kras^{G12D}*-PDECs, the accumulation of CD8$^+$ T cells was analyzed by immunohistochemistry. The pancreatic parenchyma associated with grafts from scr-*GFP-Kras^{G12D}*-PDECs was devoid of CD8$^+$ T cells both at 1 and 2 weeks after implantation (Figure 5A and Figure S4A). In contrast, a pronounced accumulation of CD8$^+$ T cells in the parenchyma of GM-sh-*GFP-Kras^{G12D}*-PDEC grafts was detected at 2 weeks after implantation (Figure 5A). A similar pattern of CD8$^+$ cell accumulation was observed when control or GM-sh-*Kras^{G12D}*-PDEC lacking GFP expression were injected into the pancreas, indicating that the CD8$^+$ T cell response was not instigated by ectopically expressed GFP, but was elicited by the transformed epithelium (Figure S4B). Significantly no infiltration of CD8$^+$ cells was observed at 1 week after implantation in GM-sh-*GFP-Kras^{G12D}*-PDEC grafts (Figure S4A), consistent with the time requirement associated with the priming of the adaptive immune responses. Of note, at later time points after implantation (~4 weeks), some of the CD8$^+$ T cells were found in clusters that contain B cells, likely signifying the formation of secondary lymphoid tissue, which is indicative of a persisting immune response (Carragher et al., 2008) (Figure 5B).

Coincident with the accumulation of CD8$^+$ T cells, we have observed an increase in the frequency of apoptosis within the GM-CSF knock-down grafts only at 2 weeks after implantation (Figure 5A and Figure S4A). These results suggest that, in the absence of GM-CSF, the cytotoxic activity of CD8$^+$ T cells at the site of engraftment may be responsible for the clearance of implanted *GFP-Kras^{G12D}*-PDECs. A prediction borne by this interpretation is that the growth defect of GM-sh *Kras^{G12D}*-PDECs would be rescued by CD8$^+$ T cell depletion. To test this prediction, we performed orthotopic implantations in animals depleted of CD8$^+$ T cells by intraperitoneal administration of anti-CD8 antibody over a period of 2 weeks. This regiment resulted in >90% depletion of CD3$^+$CD8$^+$ T cells (Figure S5). At 2 weeks after implantation, no GM-sh-*GFP-Kras^{G12D}*-PDECs were detected in pancreata animals injected with control

(B) Quantification of BrdU$^+$CD3$^+$ T cells treated as indicated. T cells and Gr1$^+$CD11b$^+$ cells were cocultured at a 1:1 ratio. Error bars indicate SD (n = 3).
(C) Representative quantification of BrdU$^+$CD3$^+$ T cells cocultured with either Gr1$^-$CD11b$^+$ or Gr1$^+$CD11b$^+$ cells isolated from mouse pancreata 8 weeks after injection with *GFP-Kras^{G12D}*-PDECs. For proliferation assays, myeloid cells and T cells were cultured at ratios of 1:1, 1:5, or 1:10 respectively. T cells incubated in αCD3-coated wells and in the presence of αCD28 serve as control. Error bars indicate SD (n = 3).
(D) Expression of mouse GM-CSF in the sera of either uninjected mice (control, n = 4) or mice with *GFP-Kras^{G12D}*-PDEC grafts 8 weeks after implantation (n = 5) was measured using ELISA. Each symbol represents a mouse, and mean values for each group are represented by black lines.
(E) Relative expression of *GM-CSF* mRNA (gray bars, left axis) and protein (black bars, right axis) in *GFP-Kras^{G12D}*-PDECs 4 days after infection with lentiviruses containing either scrambled shRNA (scr) or GM-CSF shRNAs (GM-sh1, GM-sh2) was assessed by quantitative RT-PCR and ELISA. Error bars indicate SD (n = 3).
(F) Growth analysis of scr (circles), GM-sh1 (squares), and GM-sh2 *GFP-Kras^{G12D}*-PDEC (triangles) was assessed by MTT assay. Error bars indicate SD (n = 3).
(G) Representative flow cytometry plots of pancreatic immune cells for the surface expression of Gr1 and CD11b markers at 4 weeks after implantation of scr-, GM-sh1-, and GM-sh2 *GFP-Kras^{G12D}*-PDEC. After gating on the CD45$^+$ population, cells were analyzed for the presence of CD11b$^+$ and Gr1$^+$ populations.
(H) Quantification of relative abundance of Gr1$^+$CD11b$^+$ and Gr1$^-$CD11b$^+$ cell populations is presented as a percentage change in CD45$^+$ single-positive Gr1$^-$CD11b$^+$ cells (black bars) and double-positive Gr1$^+$CD11b$^+$ population (gray bars) relative to scr *GFP-Kras^{G12D}*-PDECs. Error bars indicate SD (n = 6 mice per group).
**$p < 0.01$; ***$p < 0.001$; NS, not significant.

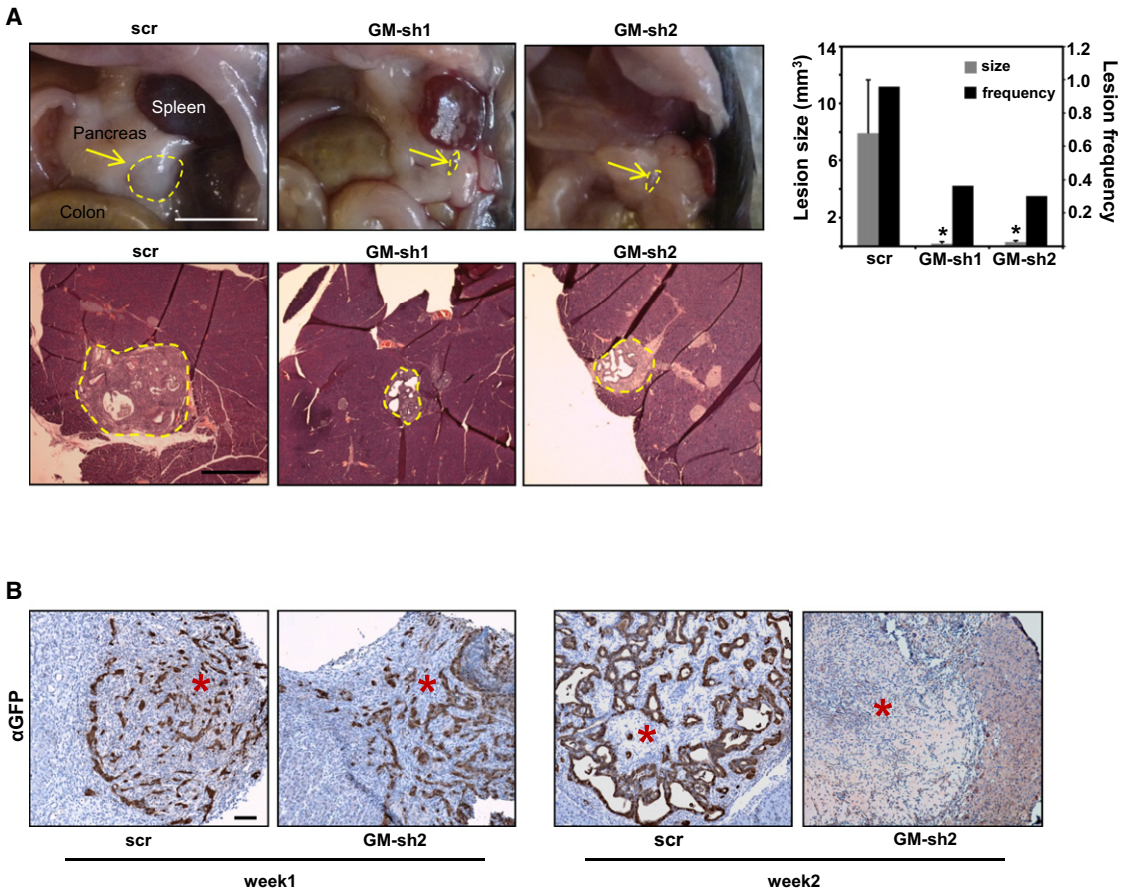

Figure 4. Functional Consequence of Ablating GM-CSF on Growth of *Kras^{G12D}*-PDECs In Vivo

(A) Gross anatomical view of scr- and GM-sh *GFP-Kras^{G12D}*-PDEC grafts (top, dotted outlines and arrows) at 8 weeks after implantation. Scale bar, 5 mm. Quantification of the graft size at 8 weeks after implantation (gray bars, left axis) and percentage of overall lesion frequency (black bars, right axis) is indicated in the graph. Error bars indicate SD (n = 3). Sections from pancreata containing scr- and GM-sh *GFP-Kras^{G12D}*-PDEC orthotopic grafts at 4 weeks after implantation were stained with H&E (bottom, lesions are delineated by dotted outlines). Scale bar, 500 μm.

(B) Immunohistochemical staining for GFP on sections of scr- and GM-sh *GFP-Kras^{G12D}*-PDEC orthotopic grafts at 1 and 2 weeks after implantation. Red asterisks indicate engrafted area. Scale bar, 100 μm.

*$p < 0.05$. See also Figure S3.

antibody (Figure 6), and the implanted area displayed many apoptotic cells (data not shown). In contrast, the injection of anti-CD8 antibody was sufficient to permit the establishment of GM-sh-*GFP-Kras^{G12D}*-PDEC grafts that were indistinguishable in size and overall appearance from scr-*GFP-Kras^{G12D}*-PDEC grafts (Figure 6), indicating that CD8$^+$ T cells are the primary immune cell type responsible for mounting and executing the immune response against *Kras^{G12D}*-PDEC.

DISCUSSION

The critical role of host immunity in regulating tumorigenesis is undisputed (Grivennikov et al., 2010). Furthermore, it is becoming increasingly evident that immune cells in the tumor microenvironment fail to mount an effective antitumor immune response (Ruffell et al., 2010). However, the underlying mechanisms that allow tumors to escape immune surveillance have not been fully characterized. In the present study, we implicate oncogenic Kras in restraining the antitumor immune response through the production of GM-CSF and the subsequent suppression of T cell immunity. This immune evasion strategy may contribute to immunotherapeutic resistance in oncogenic Kras-driven cancers.

The progression of pancreatic neoplasia is accompanied by cellular and molecular alterations in both the parenchymal and stromal compartments of the pancreas (Kleeff et al., 2007). The parenchymal component gives rise to PanINs, and the contribution of oncogenic Kras to this transition has been amply documented using genetically engineered mouse models (Hingorani et al., 2003, 2005). In contrast, little is known about the stroma-modulating capabilities of oncogenic Kras during the early stages of pancreatic cancer. The demonstration that GM-CSF production in response to activation of Kras modulates the immune reaction to pancreatic precursor lesions thus provides insights into how this oncogenic event could lead to the reprogramming of the microenvironment from the very beginning of the disease. The recent demonstration of the role of pancreas-specific oncogenic activation of Kras in generating

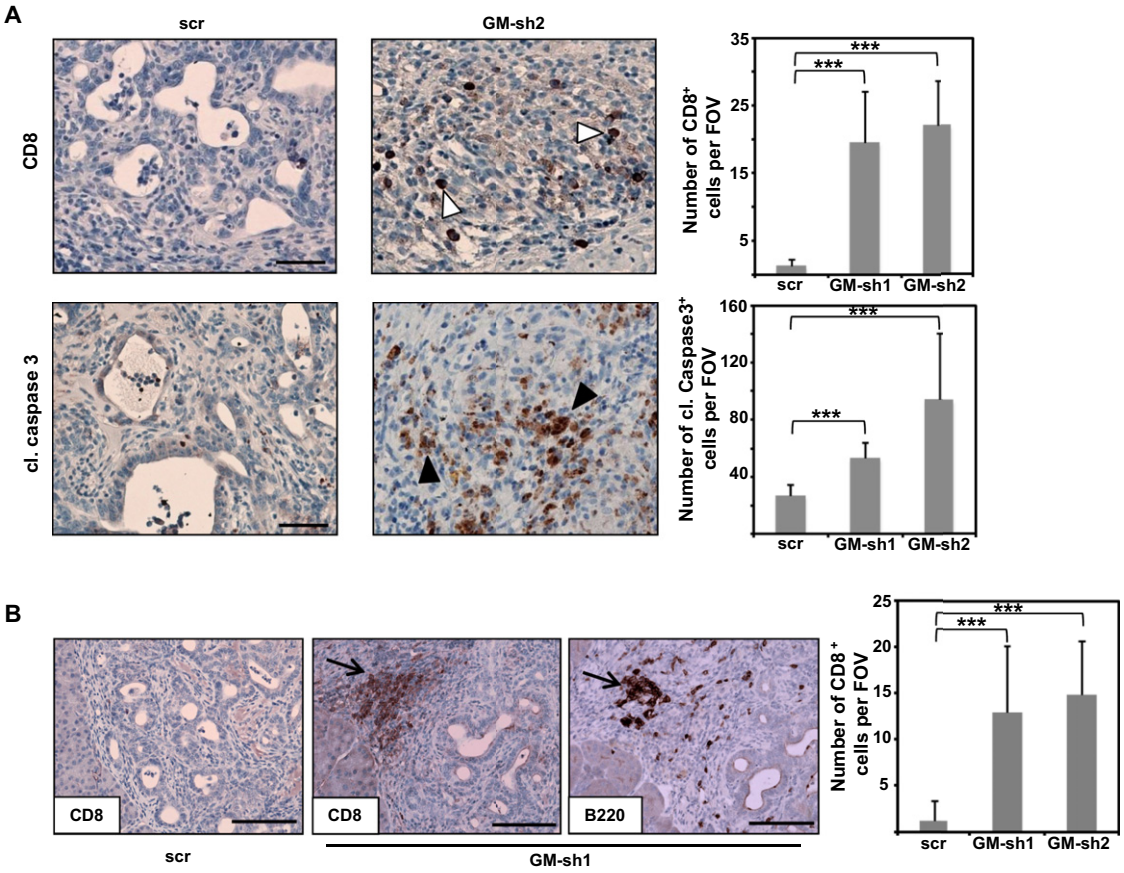

Figure 5. Engraftment of GM-CSF Knock-Down *Kras^{G12D}*-PDEC Is Accompanied by an Increase in Infiltrating CD8$^+$ T Cells

(A) Immunohistochemical staining and quantification of CD8 and cleaved caspase 3 staining on sections of scr- and GM-sh *GFP-Kras^{G12D}*-PDEC orthotopic grafts at 2 weeks after implantation. CD8$^+$ or cleaved caspase3-positive cells within the boundaries of orthotopic grafts were counted per field of view (FOV) at 20× magnification. White arrowheads indicate CD8$^+$ cells; black arrowheads indicate caspase-3-positive cells. Scale bars, 50 μm. Error bars indicate SD (n = 4 mice per group, 4 FOV per mouse).

(B) Immunohistochemical staining for CD8 and B220 on consecutive sections of scr- and GM-sh *GFP-Kras^{G12D}*-PDEC orthotopic grafts at 4 weeks after implantation. Numbers of CD8$^+$ cells were counted per FOV at 20× magnification and are shown in the graph. Arrows indicate coaggregation of CD8$^+$ cells and B220$^+$ cells. Scale bar, 100 μm. Error bars indicate SD (n = 3 mice per group, 5 FOV per mouse).

***p < 0.001. See also Figure S4.

a protumorigenic inflammatory microenvironment (Fukuda et al., 2011; Lesina et al., 2011) further underscores the crucial contribution of non-cell-autonomous mechanisms to pancreatic tumor initiation and progression.

The identification of GM-CSF as a transcriptional target of oncogenic Kras in PDECs is consistent with the existence of Ras-regulated transcription factor-binding sites, such as AP-1 and ETS, in the *GM-CSF* promoter region (Osborne et al., 1995). The pathophysiological relevance of the activation of this transcriptional program is indicated by the increased levels of GM-CSF we have observed in human PanIN lesions. It is possible that a similar Kras-mediated mechanism of GM-CSF upregulation is responsible for the enhanced serum levels of GM-CSF detected in patients with pancreatic cancer (Mroczko et al., 2005). Our initial analysis suggests that the upregulation of GM-CSF in response to oncogenic Kras is mediated by the concerted action of multiple effector pathways, including Erk and PI-3K (Figure 2B). Because these pathways are frequently activated in various malignancies, the induction of GM-CSF might not be restricted to oncogenic Kras-driven cancers and/or the pancreas. This idea is supported by studies demonstrating the overexpression of GM-CSF in several human cancer lines, including those of breast, bladder, and melanoma origin (Bronte et al., 1999; Dolcetti et al., 2010; Steube et al., 1998). Thus, the functional significance of GM-CSF upregulation might have broader implications.

Under normal physiological conditions, GM-CSF serves as a bona fide growth factor for hematopoietic cells, promoting the proliferation and maturation of multiple myeloid cell lineages in a concentration-dependent manner (Barreda et al., 2004). In neoplastic settings, GM-CSF has been shown to be endowed with the potential to exert both pro- and antitumorigenic effects by suppressing or enhancing tumor immunity, respectively (Hamilton, 2008). Our findings demonstrate that, in pancreatic ductal cells harboring oncogenic Kras, GM-CSF production is linked to the expansion of Gr1$^+$CD11b$^+$ myeloid cells. A similar consequential relationship between GM-CSF generation and Gr1$^+$CD11b$^+$ cell expansion has been documented in other

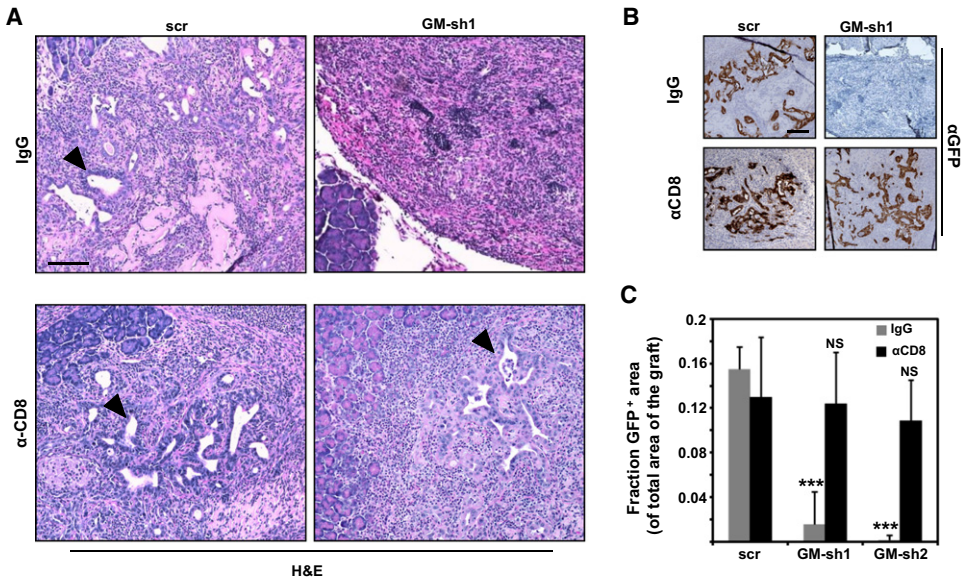

Figure 6. CD8$^+$ T Cells Are Instrumental in the Clearance of GM-CSF Knock-Down *Kras^{G12D}*-PDECs

(A) Orthotopic grafts formed by scr- or GM-sh *GFP-Kras^{G12D}*-PDECs implanted into either mock-depleted (IgG) or CD8-depleted animals were analyzed at 2 weeks after implantation by H&E. Black arrowheads indicate pancreatic ductal structures. Scale bar, 100 μm.

(B) The extent of colonization of the grafted areas by scr- or GM-sh *GFP-Kras^{G12D}*-PDECs in mock-depleted (IgG) or CD8-depleted animals at 2 weeks after implantation was analyzed by immunohistochemistry for GFP. Scale bar, 100 μm.

(C) Graph depicts quantification of the data from (B) and indicates the fraction of GFP$^+$ area per total area of the graft. Error bars indicate SD (n = 4 mice per group, 5 FOV per mouse).

***p < 0.001; NS, not significant. See also Figure S5.

tumor models (Dolcetti et al., 2010; Marigo et al., 2010; Morales et al., 2010). However, in the mouse, Gr1$^+$CD11b$^+$ double-positive cells represent a heterogeneous population composed of myeloid derived suppressor cells, monocytes, and immature myeloid cells (Ostrand-Rosenberg and Sinha, 2009). Several lines of evidence suggest that the Gr1$^+$CD11b$^+$ cells that accumulate in response to GM-CSF production by pancreatic precursor lesions are immunosuppressive in nature. First, when isolated from pancreata grafted with *GFP-Kras^{G12D}*-PDECs, the Gr1$^+$CD11b$^+$ cells displayed a suppressive effect in a T cell proliferation assay. Second, the reduction in the abundance of Gr1$^+$CD11b$^+$ cells following the suppression of GM-CSF expression in vivo was accompanied by the infiltration of CD8$^+$ T cells. Third, the immune response-mediated elimination of orthotopic *GFP-Kras^{G12D}*-PDEC lesions observed under these conditions could be fully rescued by CD8$^+$ T cell depletion, indicating a principal role for Gr1$^+$CD11b$^+$ cells in disrupting T cell immune surveillance during the early stages of pancreatic neoplasia. The potential relevance of this immune modulatory mechanism to more advanced stages of pancreatic cancer is suggested by the reciprocal relationship between CD8$^+$ T and Gr1$^+$CD11b$^+$ cell infiltrates observed in pancreatic tumors from the *p48-Cre;LSL-Kras^{G12D}* mice (Clark et al., 2007).

GM-CSF is not unique in its ability to promote the expansion and tumor mobilization of Gr1$^+$CD11b$^+$ immunosuppressive cells. For example, IL1-β, IL-6, and VEGF have been shown to induce the accumulation of Gr1$^+$CD11b$^+$ myeloid cells and the concomitant suppression of T cell immune response in a variety of mouse tumor models (Bunt et al., 2007; Melani et al., 2003; Pilon-Thomas et al., 2011; Tu et al., 2008). Significantly, IL1-β, IL-6, and VEGF are targets of oncogenic Ras signaling, and their production by cancer cells harboring oncogenic Ras has been implicated in various protumorigenic processes, such as inflammation, angiogenesis, and metastasis (Ancrile et al., 2008; Coppé et al., 2008; Kranenburg et al., 2004). Because the expression of IL1-β, IL-6, and VEGF in *GFP-Kras^{G12D}*-PDECs is not elevated relative to the levels measured in wild-type PDECs (Figure S2A) and the suppression of GM-CSF production is accompanied by a decrease in Gr1$^+$CD11b$^+$ cells, we conclude that the production of GM-CSF by the precursor lesions formed by these cells is necessary and sufficient to induce the observed increase in Gr1$^+$CD11b$^+$ cells and the impaired response of CD8$^+$ T cells. The molecular mechanisms responsible for the selective upregulation of GM-CSF observed in *Kras^{G12D}*-PDECs remain to be defined. Differences in genetic profile, cellular background, and levels of Ras expression between the experimental system described in this study and those used in other reports could be important contributors. Moreover, our findings do not rule out the possibility that IL1-β, IL-6, and VEGF as well as potentially other secreted factors can participate in establishing an immunosuppressive environment in oncogenic Ras-driven cancers. The existence of such redundancy in the mechanism by which oncogenic Ras can invoke tumor-induced tolerance may serve to secure the sustenance of this mechanism at various stages of tumor development.

Our studies reinforce the role of intrinsic immune surveillance in restraining tumor initiation and support the idea that the

evolution of pancreatic neoplasia is critically dependent on the subversion of T cell responses against antigens that are expressed by pancreatic tumor cells. Although the specific antigen recognized by the CD8$^+$ cells in our experimental system remains to be identified, it is of relevance to note that a T cell response against oncogenic Ras has been documented in a significant proportion of patients with PDA (Gedde-Dahl et al., 1994; Kubuschok et al., 2006; Linard et al., 2002; Weijzen et al., 1999). Given the ubiquitous occurrence of oncogenic Kras mutations in pancreatic adenocarcinomas, the disruption of mechanisms that induce T cell tolerance might offer a broadly applicable strategy for the targeting of immune escape in pancreatic cancer.

EXPERIMENTAL PROCEDURES

Animal Models

The *LSL-Kras^{G12D}* and *p48-Cre* strains have been described previously (Jackson et al., 2001; Kawaguchi et al., 2002). C57BL/6 mice were obtained from The Charles River Laboratories. For orthotopic implantation of PDECs, mice were anesthetized using a ketamine/xylazine cocktail, and a small (7 mm) left abdominal side incision was made. PDECs (1 × 10^6 cells/mouse) were suspended in Matrigel (Becton Dickinson) diluted 1:1 with cold PBS (total volume of 50 μl) and were injected into the tail region of the pancreas using a 26-gauge needle. A successful injection was verified by the appearance of a fluid bubble without intraperitoneal leakage. The abdominal wall was closed with absorbable Vicryl *RAPIDE* sutures (Ethicon), and the skin was closed with wound clips (Roboz). Mice were sacrificed at the indicated time points, and grafts were measured and processed for histology or flow cytometry. All animal care and procedures were approved by the Institutional Animal Care and Use Committee at NYU School of Medicine.

Isolation, Culture, and Infection of PDECs

Isolation, culture, and adenoviral infection of PDECs were performed as previously described (Agbunag et al., 2006; Lee and Bar-Sagi, 2010). Lentiviral vectors containing shRNAs directed against the *GM-CSF* gene (GM-sh1 and GM-sh2; clone ID TRCN0000054618 and TRCN0000054620) and control scrambled shRNA (scr) were obtained from Open Biosystems (pLKO.1, TRC Consortium). Lentiviral vector encoding GFP (pLVTHM-GFP) was a kind gift from Dr. F. Giancotti. To generate lentiviral particles, HEK293T cells were cotransfected with the vector, the packaging construct (pHR-CMV-dR8.2), and the envelope plasmid (pCMV-VSVG). Viral stocks were collected for 2 days, filtered through a 0.45 μm filter, and concentrated using 100MWCO Amicon Ultra centrifugal filters (Millipore). A multiplicity of infection of 15 was used for lentiviral infection of WT- or *Kras^{G12D}*-PDECs in the presence of 10 μg/ml Polybrene (Chemicon).

Immunoblot Analysis

Cells were lysed in 1% Triton-X buffer (50 mM HEPES [pH 7.4], 1% Triton X-100, 150 mM NaCl, 10% glycerol, 1 mM EGTA, 1 mM EDTA, 25 mM NaF, 1 mM Na vanadate, 1 mM phenylmethanesulfonyl fluoride [PMSF] and protease inhibitors). The following primary antibodies were used: mouse anti-HA (12CA5), mouse anti-vinculin (Sigma-Aldrich), rabbit anti-phospho-ERK (Cell Signaling), mouse anti-ERK (Cell Signaling), rabbit anti-phospho-AKT (S473, Cell Signaling), and rabbit anti-AKT (Cell Signaling). After incubation with either the secondary IRDye Alexa Fluor 680 goat anti-mouse antibody or 800 goat anti-rabbit antibody (Molecular Probes), the membranes were visualized with the Odyssey Infrared Imaging System (Li-Cor).

Quantitative RT-PCR

Extraction and reverse transcription of total RNA from PDECs was performed using RNeasy mini kit (QIAGEN) and QuantiTect reverse transcription kit (QIAGEN), respectively. SYBR Green PCR Master Mix (USB) was used for amplification, and the samples were run on the Stratagene Mx 3005P. Expression levels were normalized by GAPDH.

Human Pancreas Specimens

The use of human tissue was reviewed and approved by the Institutional Review Board of NYU School of Medicine, and samples (provided by the Tissue Acquisition and Biorepository Service) were obtained after informed consent. Sections (5 μm) were cut from formalin-fixed paraffin-embedded samples for the purpose of immunohistochemistry. A total of 16 pancreatic adenocarcinoma, one chronic pancreatitis, one benign pancreatic cyst, one serous cystadenoma, and one intraductal papillary mucinous neoplasm samples were analyzed.

Histology and Immunohistochemistry

Mouse pancreata were fixed overnight in 10% formalin (Fisher) and were processed for paraffin embedding. For histology, deparaffinized sections (6 μm) were stained with Harris hematoxylin and eosin (both from Sigma-Aldrich) followed by an alcohol dehydration series and mounting (Permount, Fisher). Trichrome staining was performed at NYU School of Medicine Histopathology Core Facility. For immunohistochemistry, deparaffinized sections (6 μm) were rehydrated and quenched in 1% hydrogen peroxide/methanol for 15 min, and antigen retrieval was performed in 10 mM sodium citrate and 0.05% Tween-20 (pH 6.0) for 15 min in a microwave oven. Blocking was done in 10% serum, 1% BSA, and 0.5% Tween-20 for 1 hr at room temperature, followed by incubation with the primary antibodies diluted in 2% BSA overnight at 4°C. The following primary antibodies were used: rabbit anti-GFP (Cell Signaling), rabbit anti-GM-CSF (Novus Biologicals), rat anti-CD8 (53-6.7, BD Biosciences), rabbit anti-cleaved caspase-3 (Cell Signaling), and rat anti-B220 (BD Biosciences). After incubating with secondary biotinylated antibodies and ABC solution (both from Vector Laboratories), sections were developed with 3,3′-diaminobenzidine tetrahydrochloride (Sigma-Aldrich). After counterstaining with Harris hematoxylin (Sigma), slides were subjected to an alcohol dehydration series and mounted with Permount (Fisher). Slides were examined on a Nikon Eclipse 80i microscope.

Immunofluorescence

Mouse pancreata were embedded in OCT compound (Tissue-Tek) by snap freezing OCT-covered tissues in liquid nitrogen, and 8 μm sections were cut on a Leica microtome. After fixing the sections in 4% paraformaldehyde for 10 min on ice and permeabilizing with 0.25% Triton X-100 for 10 min on ice, sections were blocked with 10% serum, 2% BSA, and 0.1% Tween-20 for 1 hr at room temperature. Incubation with primary antibodies diluted in 2% BSA and 0.5% Tween-20 was performed overnight at 4°C. The following antibodies were used: rat anti-CD45 (BD Biosciences) and rat anti-CK19 (Troma III, developed by R. Kemler, made available by Developmental Studies Hybridoma Bank under the auspices of the NICHD). After incubating with Alexa Fluor-labeled secondary antibodies (Invitrogen) diluted in 1% BSA for 1 hr at room temperature, sections were stained with DAPI and mounted using polyvinyl alcohol mounting media with DABCO (Fluka). Slides were examined on a Zeiss Axiovert 200M microscope.

Flow Cytometry

Cellular suspensions from the tissues were prepared as follows: spleens were mechanically disrupted, suspended in 1% FBS and PBS, passed through a 70 μm strainer, and treated with RBC lysis buffer (eBioscience). Pancreata were minced using sterile razor blades and were incubated in 1.25 mg/ml collagenase type IV and 0.1% soybean trypsin inhibitor (Sigma-Aldrich) in RPMI for 15 min at 37°C. Cells were suspended in 1% FBS and PBS, were passed through a 70 μm strainer, and were treated with RBC lysis buffer. Single-cell suspensions from spleens and pancreata were blocked with anti-CD16/CD32 antibody (Fc Block, BD Biosciences) for 5 min on ice and were labeled with the following antibodies: anti-CD45.2 (104), anti-CD3ε (500A2), anti-CD4 (RM4-5), anti-CD8α (53-6.7), anti-CD45R/B220 (RA3-6B2), anti-CD19 (1D3), anti-CD11b (M1/70), anti-Gr1 (RB6-8C5), and anti-CD25 (PC61.5) (all from BD Biosciences). Staining for intracellular Foxp3 was performed using Mouse Regulatory T Cell Staining Kit (FJK-16, eBioscience). Dead cells were excluded by staining with propidium iodine (Sigma-Aldrich). Flow cytometry was performed on FACScan (BD Biosciences) at NYU School of Medicine Flow Cytometry Core Facility, and data were analyzed using FlowJo software.

Supernatant Collection and Cytokine Analysis

For cytokine analysis of PDEC cultures, cells were cultured in complete medium at a concentration of 1 × 10^6 cells/ml for 24 hr before supernatant harvest. For cytokine analysis of mouse pancreata, the tissues were harvested, weighed, minced with a sterile razor blade, and incubated in 500 μl of complete media for 24 hr before supernatant collection. Analysis of the cytokines was done with Milliplex Map Immunoassay (Millipore) and the Luminex 200 system (Luminex) according to the manufacturer's instructions. Where indicated, mouse GM-CSF protein levels were determined by Mouse GM-CSF Quantikine ELISA Kit (mean MDD = 1.8 pg/ml; R&D Systems). For analysis of GM-CSF levels in mouse sera, blood samples were collected retro-orbitally, and the samples were processed according to the manufacturer of the ELISA kit.

Culture of Sorted HPCs

Bone marrow cells were isolated from C57Bl/6 mice, and HPCs were sorted using Mouse Hematopoietic Stem and Progenitor Cell Isolation Kit (BD Biosciences), according to the manufacturer's instructions. Isolated HPCs were cultured in 6-well plates (1 × 10^5 cells/well) for a total of 6 days. On day 0, either GM-CSF (10 ng/ml, Monoclonal Antibody Core Facility at Memorial Sloan-Kettering Cancer Center) or a 24 mm Transwell insert with a 0.4 μm pore size (Corning Life Sciences) containing *Kras^{G12D}*-PDEC (2 × 10^5 cells/insert) were added to the HPCs. On day 3, fresh cytokine or inserts with cells were added. Where indicated, HPC cultures were supplemented with either control IgG2a antibody (1 μg/ml, eBioscience) or anti-GM-CSF antibody (1 μg/ml MP1-22E9, eBioscience). For T cell proliferation assays, Gr1$^+$CD11b$^+$ cells were sorted on day 6 of culture. Cellular purity was greater than 90%.

Proliferation and Viability Assays

For in vitro T cell proliferation assays, splenic T cells suspended in complete RPMI medium were added to 96-well plates precoated with anti-CD3 antibody (BD Biosciences) at a density of 5 × 10^4 cells/well. Anti-CD28 antibody (37.51, eBioscience) was added to T cells at a concentration of 1 μg/ml. Autologous Gr1$^+$CD11b$^+$ cells derived from coculture of *Kras^{G12D}*-PDEC and HPC were irradiated and added in triplicates directly to T cells (5 × 10^4 Gr1$^+$CD11b$^+$ cells/well) 24 hr before adding BrdU reagent. Pancreas-associated myeloid Gr1$^-$CD11b$^+$ or Gr1$^+$CD11b$^+$ cells were sorted from *Kras^{G12D}*-PDEC-grafted pancreata at 8 weeks after implantation and were added in triplicates and at indicated ratios directly to T cells 24 hr before adding BrdU reagent (Sigma-Aldrich). T cells were labeled by adding BrdU to the culture medium at a final concentration of 10 μM for 48 hr. Staining for BrdU was achieved using APC BrdU Flow Kit (BD Biosciences). The percentage of BrdU-positive T cells was determined by FACS analysis of CD3$^+$BrdU$^+$ cells.

For *Kras^{G12D}*-PDEC growth assays, cells were seeded at a density of 2,000 cells/well in a 96-well plate. At indicated time points, cell culture medium was aspirated, the wells were washed with RPMI (without phenol red, BioWhittaker), and 0.5 mg/ml 3-[4,5-dimethylthiazol-2-yl]-2,5-diphenyl tetrazolium bromide (MTT; Sigma-Aldrich) was added for 2 hr at 37°C. The reagent was aspirated, and 100 μl of DMSO was added to each well for 20 min at room temperature. Plates were read at an absorbance of 570 nm using a VERSAmax microplate reader (Molecular Devices). For the day 0 time point, cells were treated with MTT reagent 2 hr after plating.

CD8 Depletion

Mice were depleted of CD8$^+$ T cells via intraperitoneal injection of control rat IgG antibody (eBioscience) or anti-CD8a antibody at a concentration of 0.2 mg/mouse (53-6.72, Monoclonal Antibody Core Facility at Memorial Sloan-Kettering Cancer Center). Injections were administered every day for 3 days prior to orthotopic injection, and twice a week thereafter until the experimental endpoint. The efficiency of CD8$^+$ T cell depletion was assessed by FACS of splenic tissues using anti-CD3 and anti-CD8 antibodies.

Statistical Analyses

Data are presented as means ± standard deviations (SD). Quantification of GFP positivity was performed using ImageJ analysis. Data were analyzed by the Microsoft Excel or GraphPad Prism built-in t test (unpaired, two-tailed), and results were considered significant at $p < 0.05$.

SUPPLEMENTAL INFORMATION

Supplemental Information includes five figures and can be found with this article online at doi:10.1016/j.ccr.2012.04.024.

ACKNOWLEDGMENTS

We thank L.J. Taylor and R. Soydaner-Azeloglu for discussions and help with manuscript preparation, J.S. Handler and E. Bekes for technical assistance, and the members of the Bar-Sagi laboratory for comments. The FACS, Histopathology Cores, and Tissue Acquisition and Biorepository Service of NYU School of Medicine are partially supported by the National Institutes of Health (Grant 5 P30CA016087-31). This work was supported by the National Institutes of Health (Grant CA055360) and AACR-PanCAN (Grant 08-60-25-BARS) (both to D.B.-S.) and by The Irvington Institute Postdoctoral Fellowship Program of the Cancer Research Institute (support to Y.P.-G.).

Received: July 13, 2011
Revised: February 5, 2012
Accepted: April 9, 2012
Published: June 11, 2012

REFERENCES

Agbunag, C., Lee, K.E., Buontempo, S., and Bar-Sagi, D. (2006). Pancreatic duct epithelial cell isolation and cultivation in two-dimensional and three-dimensional culture systems. Methods Enzymol. *407*, 703–710.

Ancrile, B.B., O'Hayer, K.M., and Counter, C.M. (2008). Oncogenic ras-induced expression of cytokines: a new target of anti-cancer therapeutics. Mol. Interv. *8*, 22–27.

Barreda, D.R., Hanington, P.C., and Belosevic, M. (2004). Regulation of myeloid development and function by colony stimulating factors. Dev. Comp. Immunol. *28*, 509–554.

Bronte, V., Chappell, D.B., Apolloni, E., Cabrelle, A., Wang, M., Hwu, P., and Restifo, N.P. (1999). Unopposed production of granulocyte-macrophage colony-stimulating factor by tumors inhibits CD8+ T cell responses by dysregulating antigen-presenting cell maturation. J. Immunol. *162*, 5728–5737.

Bunt, S.K., Yang, L., Sinha, P., Clements, V.K., Leips, J., and Ostrand-Rosenberg, S. (2007). Reduced inflammation in the tumor microenvironment delays the accumulation of myeloid-derived suppressor cells and limits tumor progression. Cancer Res. *67*, 10019–10026.

Carragher, D.M., Rangel-Moreno, J., and Randall, T.D. (2008). Ectopic lymphoid tissues and local immunity. Semin. Immunol. *20*, 26–42.

Chu, G.C., Kimmelman, A.C., Hezel, A.F., and DePinho, R.A. (2007). Stromal biology of pancreatic cancer. J. Cell. Biochem. *101*, 887–907.

Clark, C.E., Hingorani, S.R., Mick, R., Combs, C., Tuveson, D.A., and Vonderheide, R.H. (2007). Dynamics of the immune reaction to pancreatic cancer from inception to invasion. Cancer Res. *67*, 9518–9527.

Clark, C.E., Beatty, G.L., and Vonderheide, R.H. (2009). Immunosurveillance of pancreatic adenocarcinoma: insights from genetically engineered mouse models of cancer. Cancer Lett. *279*, 1–7.

Coppé, J.P., Patil, C.K., Rodier, F., Sun, Y., Muñoz, D.P., Goldstein, J., Nelson, P.S., Desprez, P.Y., and Campisi, J. (2008). Senescence-associated secretory phenotypes reveal cell-nonautonomous functions of oncogenic RAS and the p53 tumor suppressor. PLoS Biol. *6*, 2853–2868.

Dolcetti, L., Peranzoni, E., Ugel, S., Marigo, I., Fernandez Gomez, A., Mesa, C., Geilich, M., Winkels, G., Traggiai, E., Casati, A., et al. (2010). Hierarchy of immunosuppressive strength among myeloid-derived suppressor cell subsets is determined by GM-CSF. Eur. J. Immunol. *40*, 22–35.

DuPage, M., Cheung, A.F., Mazumdar, C., Winslow, M.M., Bronson, R., Schmidt, L.M., Crowley, D., Chen, J., and Jacks, T. (2011). Endogenous T cell responses to antigens expressed in lung adenocarcinomas delay malignant tumor progression. Cancer Cell *19*, 72–85.

Fossum, B., Olsen, A.C., Thorsby, E., and Gaudernack, G. (1995). CD8+ T cells from a patient with colon carcinoma, specific for a mutant p21-Ras-derived

peptide (Gly13→Asp), are cytotoxic towards a carcinoma cell line harbouring the same mutation. Cancer Immunol. Immunother. *40*, 165–172.

Fukuda, A., Wang, S.C., Morris, J.P., 4th, Folias, A.E., Liou, A., Kim, G.E., Akira, S., Boucher, K.M., Firpo, M.A., Mulvihill, S.J., and Hebrok, M. (2011). Stat3 and MMP7 contribute to pancreatic ductal adenocarcinoma initiation and progression. Cancer Cell *19*, 441–455.

Gabrilovich, D.I., and Nagaraj, S. (2009). Myeloid-derived suppressor cells as regulators of the immune system. Nat. Rev. Immunol. *9*, 162–174.

Gedde-Dahl, T., 3rd, Spurkland, A., Fossum, B., Wittinghofer, A., Thorsby, E., and Gaudernack, G. (1994). T cell epitopes encompassing the mutational hot spot position 61 of p21 ras: promiscuity in ras peptide binding to HLA. Eur. J. Immunol. *24*, 410–414.

Gjertsen, M.K., and Gaudernack, G. (1998). Mutated Ras peptides as vaccines in immunotherapy of cancer. Vox Sang. *74* (*Suppl 2*), 489–495.

Grivennikov, S.I., Greten, F.R., and Karin, M. (2010). Immunity, inflammation, and cancer. Cell *140*, 883–899.

Hamilton, J.A. (2008). Colony-stimulating factors in inflammation and autoimmunity. Nat. Rev. Immunol. *8*, 533–544.

Hingorani, S.R., Petricoin, E.F., Maitra, A., Rajapakse, V., King, C., Jacobetz, M.A., Ross, S., Conrads, T.P., Veenstra, T.D., Hitt, B.A., et al. (2003). Preinvasive and invasive ductal pancreatic cancer and its early detection in the mouse. Cancer Cell *4*, 437–450.

Hingorani, S.R., Wang, L., Multani, A.S., Combs, C., Deramaudt, T.B., Hruban, R.H., Rustgi, A.K., Chang, S., and Tuveson, D.A. (2005). Trp53R172H and KrasG12D cooperate to promote chromosomal instability and widely metastatic pancreatic ductal adenocarcinoma in mice. Cancer Cell *7*, 469–483.

Hong, S.M., Park, J.Y., Hruban, R.H., and Goggins, M. (2011). Molecular signatures of pancreatic cancer. Arch. Pathol. Lab. Med. *135*, 716–727.

Jackson, E.L., Willis, N., Mercer, K., Bronson, R.T., Crowley, D., Montoya, R., Jacks, T., and Tuveson, D.A. (2001). Analysis of lung tumor initiation and progression using conditional expression of oncogenic K-ras. Genes Dev. *15*, 3243–3248.

Kawaguchi, Y., Cooper, B., Gannon, M., Ray, M., MacDonald, R.J., and Wright, C.V. (2002). The role of the transcriptional regulator Ptf1a in converting intestinal to pancreatic progenitors. Nat. Genet. *32*, 128–134.

Kern, S.E., Shi, C., and Hruban, R.H. (2011). The complexity of pancreatic ductal cancers and multidimensional strategies for therapeutic targeting. J. Pathol. *223*, 295–306.

Kleeff, J., Beckhove, P., Esposito, I., Herzig, S., Huber, P.E., Lohr, J.M., and Friess, H. (2007). Pancreatic cancer microenvironment. Int. J. Cancer *121*, 699–705.

Kranenburg, O., Gebbink, M.F., and Voest, E.E. (2004). Stimulation of angiogenesis by Ras proteins. Biochim. Biophys. Acta *1654*, 23–37.

Kubuschok, B., Neumann, F., Breit, R., Sester, M., Schormann, C., Wagner, C., Sester, U., Hartmann, F., Wagner, M., Remberger, K., et al. (2006). Naturally occurring T-cell response against mutated p21 ras oncoprotein in pancreatic cancer. Clin. Cancer Res. *12*, 1365–1372.

Lee, K.E., and Bar-Sagi, D. (2010). Oncogenic KRas suppresses inflammation-associated senescence of pancreatic ductal cells. Cancer Cell *18*, 448–458.

Lesina, M., Kurkowski, M.U., Ludes, K., Rose-John, S., Treiber, M., Klöppel, G., Yoshimura, A., Reindl, W., Sipos, B., Akira, S., et al. (2011). Stat3/Socs3 activation by IL-6 transsignaling promotes progression of pancreatic intraepithelial neoplasia and development of pancreatic cancer. Cancer Cell *19*, 456–469.

Linard, B., Bézieau, S., Benlalam, H., Labarrière, N., Guilloux, Y., Diez, E., and Jotereau, F. (2002). A ras-mutated peptide targeted by CTL infiltrating a human melanoma lesion. J. Immunol. *168*, 4802–4808.

Maitra, A., and Hruban, R.H. (2008). Pancreatic cancer. Annu. Rev. Pathol. *3*, 157–188.

Marigo, I., Dolcetti, L., Serafini, P., Zanovello, P., and Bronte, V. (2008). Tumor-induced tolerance and immune suppression by myeloid derived suppressor cells. Immunol. Rev. *222*, 162–179.

Marigo, I., Bosio, E., Solito, S., Mesa, C., Fernandez, A., Dolcetti, L., Ugel, S., Sonda, N., Bicciato, S., Falisi, E., et al. (2010). Tumor-induced tolerance and immune suppression depend on the C/EBPbeta transcription factor. Immunity *32*, 790–802.

Melani, C., Chiodoni, C., Forni, G., and Colombo, M.P. (2003). Myeloid cell expansion elicited by the progression of spontaneous mammary carcinomas in c-erbB-2 transgenic BALB/c mice suppresses immune reactivity. Blood *102*, 2138–2145.

Morales, J.K., Kmieciak, M., Knutson, K.L., Bear, H.D., and Manjili, M.H. (2010). GM-CSF is one of the main breast tumor-derived soluble factors involved in the differentiation of CD11b-Gr1- bone marrow progenitor cells into myeloid-derived suppressor cells. Breast Cancer Res. Treat. *123*, 39–49.

Mroczko, B., Szmitkowski, M., Wereszczyńska-Siemiatkowska, U., and Jurkowska, G. (2005). Hematopoietic cytokines in the sera of patients with pancreatic cancer. Clin. Chem. Lab. Med. *43*, 146–150.

Osborne, C.S., Vadas, M.A., and Cockerill, P.N. (1995). Transcriptional regulation of mouse granulocyte-macrophage colony-stimulating factor/IL-3 locus. J. Immunol. *155*, 226–235.

Ostrand-Rosenberg, S., and Sinha, P. (2009). Myeloid-derived suppressor cells: linking inflammation and cancer. J. Immunol. *182*, 4499–4506.

Pilon-Thomas, S., Nelson, N., Vohra, N., Jerald, M., Pendleton, L., Szekeres, K., and Ghansah, T. (2011). Murine pancreatic adenocarcinoma dampens SHIP-1 expression and alters MDSC homeostasis and function. PLoS ONE *6*, e27729.

Pylayeva-Gupta, Y., Grabocka, E., and Bar-Sagi, D. (2011). RAS oncogenes: weaving a tumorigenic web. Nat. Rev. Cancer *11*, 761–774.

Qin, H., Chen, W., Takahashi, M., Disis, M.L., Byrd, D.R., McCahill, L., Bertram, K.A., Fenton, R.G., Peace, D.J., and Cheever, M.A. (1995). CD4+ T-cell immunity to mutated ras protein in pancreatic and colon cancer patients. Cancer Res. *55*, 2984–2987.

Quezada, S.A., Peggs, K.S., Simpson, T.R., and Allison, J.P. (2011). Shifting the equilibrium in cancer immunoediting: from tumor tolerance to eradication. Immunol. Rev. *241*, 104–118.

Ruffell, B., DeNardo, D.G., Affara, N.I., and Coussens, L.M. (2010). Lymphocytes in cancer development: polarization towards pro-tumor immunity. Cytokine Growth Factor Rev. *21*, 3–10.

Schön, M., Denzer, D., Kubitza, R.C., Ruzicka, T., and Schön, M.P. (2000). Critical role of neutrophils for the generation of psoriasiform skin lesions in flaky skin mice. J. Invest. Dermatol. *114*, 976–983.

Seidler, B., Schmidt, A., Mayr, U., Nakhai, H., Schmid, R.M., Schneider, G., and Saur, D. (2008). A Cre-loxP-based mouse model for conditional somatic gene expression and knockdown in vivo by using avian retroviral vectors. Proc. Natl. Acad. Sci. USA *105*, 10137–10142.

Shi, C., Fukushima, N., Abe, T., Bian, Y., Hua, L., Wendelburg, B.J., Yeo, C.J., Hruban, R.H., Goggins, M.G., and Eshleman, J.R. (2008). Sensitive and quantitative detection of KRAS2 gene mutations in pancreatic duct juice differentiates patients with pancreatic cancer from chronic pancreatitis, potential for early detection. Cancer Biol. Ther. *7*, 353–360.

Steube, K.G., Meyer, C., and Drexler, H.G. (1998). Secretion of functional hematopoietic growth factors by human carcinoma cell lines. Int. J. Cancer *78*, 120–124.

Tu, S., Bhagat, G., Cui, G., Takaishi, S., Kurt-Jones, E.A., Rickman, B., Betz, K.S., Penz-Oesterreicher, M., Bjorkdahl, O., Fox, J.G., and Wang, T.C. (2008). Overexpression of interleukin-1beta induces gastric inflammation and cancer and mobilizes myeloid-derived suppressor cells in mice. Cancer Cell *14*, 408–419.

Weijzen, S., Velders, M.P., and Kast, W.M. (1999). Modulation of the immune response and tumor growth by activated Ras. Leukemia *13*, 502–513.

Cancer Cell
Report

Proliferation and Tumorigenesis of a Murine Sarcoma Cell Line in the Absence of DICER1

Arvind Ravi,[1,3,5] Allan M. Gurtan,[4,5] Madhu S. Kumar,[1,6] Arjun Bhutkar,[4] Christine Chin,[1] Victoria Lu,[1] Jacqueline A. Lees,[1,4] Tyler Jacks,[1,2,4] and Phillip A. Sharp[1,4,*]
[1]Department of Biology
[2]Howard Hughes Medical Institute, Department of Biology
Massachusetts Institute of Technology, Cambridge, MA 02139, USA
[3]Harvard-MIT Health Sciences and Technology Program, Cambridge, MA 02139, USA
[4]David H. Koch Institute for Integrative Cancer Research, Cambridge, MA 02139, USA
[5]These authors contributed equally to this work
[6]Present address: Cancer Research UK London Research Institute, 44 Lincoln's Inn Fields, London WC2A 3PX, UK
*Correspondence: sharppa@mit.edu
DOI 10.1016/j.ccr.2012.04.037

SUMMARY

MicroRNAs are a class of short ~22 nucleotide RNAs predicted to regulate nearly half of all protein coding genes, including many involved in basal cellular processes and organismal development. Although a global reduction in miRNAs is commonly observed in various human tumors, complete loss has not been documented, suggesting an essential function for miRNAs in tumorigenesis. Here we present the finding that transformed or immortalized *Dicer1* null somatic cells can be isolated readily in vitro, maintain the characteristics of DICER1-expressing controls and remain stably proliferative. Furthermore, *Dicer1* null cells from a sarcoma cell line, though depleted of miRNAs, are competent for tumor formation. Hence, miRNA levels in cancer may be maintained in vivo by a complex stabilizing selection in the intratumoral environment.

INTRODUCTION

MicroRNAs (miRNAs) are short ~22 nucleotide RNAs that comprise an essential class of regulators predicted to repress over half of all genes posttranscriptionally (Bartel, 2009; Friedman et al., 2009). Consistent with computational predictions of widespread targeting, they have been implicated experimentally in a variety of fundamental cellular processes such as cell cycle (Wang et al., 2008), apoptosis (Chivukula and Mendell, 2008), and differentiation (Herranz and Cohen, 2010; Stefani and Slack, 2008). Given these broad roles, the relationship between miRNAs and cancer is understandably complex. At the level of individual miRNAs, either gains or losses may promote tumor formation. However, analysis of global miRNA levels in tumors suggests a surprisingly unidirectional relationship, with multiple human tumors showing decreased miRNA content (Gaur et al., 2007; Lu et al., 2005). In some cases, this downregulation may be directly achieved by decreased expression of DICER1 and DROSHA, key processing enzymes of miRNA production (Lin et al., 2010; Martello et al., 2010; Torres et al., 2011) or mutations in their binding partners (Melo et al., 2009).

Despite these trends toward decreased miRNA expression, a number of observations suggest that miRNAs may in fact be important for a variety of tumor types. For instance, although heterozygous somatic mutations in *DICER1* can be found in tumor genotyping atlases, homozygous loss has not been reported in these databases (Kumar et al., 2009). Similarly, in rare cases of heterozygous germline *DICER1* mutations,

Significance

The nearly global decrease in miRNAs observed across a range of human tumors suggests that restoration of miRNA levels may have a valuable therapeutic role. Here we report that some tumor cells devoid of miRNA activity are viable and form tumors under certain conditions. However, the failure to detect human tumors with complete loss suggests that the opposite approach, namely a further decrease in these levels, may surprisingly also be beneficial. We explore this alternative in a well-characterized sarcoma model, demonstrating that miRNA depletion can indeed inhibit tumor growth rates through reduced proliferation and increased cell death. These findings suggest that the targeted inhibition of miRNA pathway elements, particularly DICER1, may be a potential therapy for the treatment of cancer.

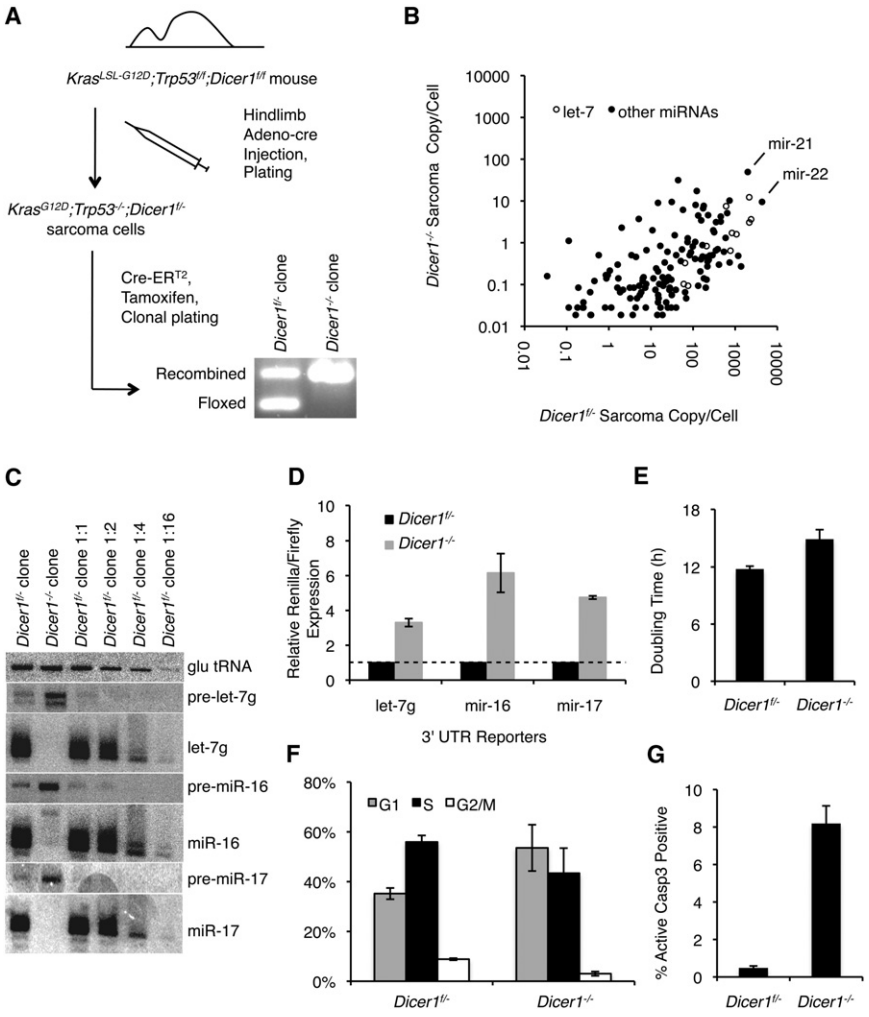

Figure 1. Characterization of *Kras*^{G12D};*Trp53*$^{-/-}$;*Dicer1*$^{-/-}$ Sarcoma Cells

(A) Derivation scheme for *Dicer1*$^{-/-}$ sarcoma cells. Hindlimb injection of Adeno-Cre generates *Kras*^{G12D}; *Trp53*$^{-/-}$;*Dicer1*$^{f/-}$ tumors. Clones isolated following Cre-ER integration and tamoxifen treatment were genotyped by PCR to identify *Dicer1*$^{-/-}$ clones.

(B) miRNA expression (copies per cell). Per cell calculations are based on relative representation of each miRNA in *Dicer1*$^{f/-}$ and *Dicer1*$^{-/-}$ small RNA-seq libraries, normalized to quantitative northern blot of miR-22 in *Dicer1*$^{f/-}$ cells (shown in Figure S1C). miR-21, miR-22, and let-7 family members are indicated.

(C) Northern analysis for precursor and mature miRNAs. Glutamine tRNA was used to control for loading, and a dilution series of *Dicer1*$^{f/-}$ RNA (1:1 to 1:16) is provided for quantitation.

(D) Luciferase reporter assays for abundant miRNAs. The Renilla luciferase reporter contains six bulged sites for the let-7 family, and two perfect sites for miR-16 and miR-17. Targeted Renilla luciferase reporters were normalized to non-targeted firefly luciferase reporters. Renilla/firefly luciferase expression was normalized to expression in the *Dicer1*$^{f/-}$ sarcoma cell line.

(E) Proliferation assay.

(F) Cell cycle distribution determined by BrdU labeling.

(G) Apoptosis determined by caspase-3 cleavage assay.

All error bars represent the SEM (D–G). See also Figure S1 and Table S1.

the pleuropulmonary blastomas to which patients are predisposed retain an intact *DICER1* allele in tumor tissue (Hill et al., 2009). Somatic point mutations in *DICER1* associated with nonepithelial ovarian cancers are hypomorphic, likely resulting in expression of a full-length protein but in loss of some specific miRNAs and retention of others, further suggesting a requirement for *DICER1* and miRNA expression in tumors (Heravi-Moussavi et al., 2012). Mouse models of *Dicer1* loss in cancer also suggest an advantage of retaining miRNA regulation. In a mouse model of *Dicer1* deletion in the liver, tumors emerge several months after deletion following a period of hepatic repopulation by *Dicer1*-intact "escapers" (Sekine et al., 2009). In *Dicer1*-conditional mouse models of either soft tissue sarcoma or lung adenocarcinoma, haploinsufficiency of *Dicer1* promotes tumor development but homozygous loss of *Dicer1* is not observed (Kumar et al., 2009). Similarly, in both an *Eμ-myc* lymphoma model and a retinoblastoma model, viable tumors could not be identified following homozygous *Dicer1* deletion (Arrate et al., 2010; Lambertz et al., 2010). These studies suggest that complete *Dicer1* loss and the subsequent misregulation of gene expression are highly deleterious to tumor development.

To better understand how cancer cells respond to loss of miRNA expression, we characterized the effects of homozygous deletion of *Dicer1*-conditional alleles on the tumorigenicity of an established line of murine sarcoma cells and on the cellular phenotype of immortalized murine mesenchymal stem cells (MSCs).

RESULTS

Dicer1 Null Cells Derived from a Mouse Sarcoma Proliferate Indefinitely In Vitro

Previously, we generated *Dicer1*-heterozygous tumors by injection of Adeno-Cre virus into the hindlimbs of *Kras*$^{LSL-G12D}$;*Trp53*$^{f/f}$;*Dicer1*$^{f/f}$ mice. The resultant tumors always retained at least one conditional *Dicer1* allele (Kumar et al., 2009). From these *Kras*^{G12D};*Trp53*$^{-/-}$;*Dicer1*$^{f/-}$ tumors, we established sarcoma cell lines and deleted the remaining allele of *Dicer1* by transducing the cells with a retroviral construct encoding MSCV.CreER^{T2}.puro and then activating recombination in vitro with tamoxifen treatment (Figure 1A). A genotyping time course indicated efficient homozygous recombination (Figure S1A available online). After multiple passages, however, genotyping PCR indicated the outgrowth of heterozygous cells, consistent with previous findings in both this sarcoma model and an *Eμ-myc*/*Dicer1* lymphoma model (Arrate et al., 2010; Kumar et al., 2009).

To prevent the preferential outgrowth of DICER1-expressing cells, we isolated monoclonal populations by plating low-density cultures immediately after a 24 hr treatment with tamoxifen. The resulting clones appeared at comparable frequencies in tamoxifen-treated and control cultures, and were also morphologically similar to the parental cell lines. Genotyping PCR indicated that the majority of isolated clones had deleted the second allele of *Dicer1* (Figure 1A). We also confirmed recombination of the conditional *Dicer1* allele at the protein level by western blot against DICER1 (Figure S1B). Once a *Kras*^{G12D}*;Trp53*$^{-/-}$*;Dicer1*$^{-/-}$ clonal line was established, we did not observe outgrowth of *Kras*^{G12D}*;Trp53*$^{-/-}$*;Dicer1*$^{f/-}$ cells, even after several months of continual passage. Hereafter, we will refer to the monoclonal homozygous *Kras*^{G12D}*;Trp53*$^{-/-}$*;Dicer1*$^{-/-}$ line as *Dicer1*$^{-/-}$ cells and the parental heterozygous *Kras*^{G12D}*;Trp53*$^{-/-}$*;Dicer1*$^{f/-}$ cell line as *Dicer1*$^{f/-}$ cells. These results suggest that sarcoma cells survive after homozygous *Dicer1* deletion but have a growth disadvantage relative to cells retaining *Dicer1* expression. To prevent outgrowth of *Dicer1*$^{f/-}$ sarcoma cells, all subsequent experiments were carried out with monoclonal *Dicer1*$^{-/-}$ sarcoma cell lines.

To determine whether *Dicer1*$^{-/-}$ clones lacked miRNAs, we carried out massively parallel sequencing of small RNAs (small RNA-seq), ~15–50 nucleotides in length, from *Dicer1*$^{f/-}$ and *Dicer1*$^{-/-}$ sarcoma cells. Both libraries contained comparable sequencing depths at 9.3 and 9.6 million reads, respectively. However, due to miRNA loss, sequence complexity was greater in *Dicer1*$^{-/-}$ cells, which contained 830,000 unique sequences, relative to 190,000 unique sequences in *Dicer1*$^{f/-}$ cells. Of all reads mapping to the genome with 0 or 1 mismatch, 58% correspond to mature miRNAs in *Dicer1*$^{f/-}$ cells in comparison to 0.8% in *Dicer1*$^{-/-}$ cells. Approximately 48% of mature miRNAs detected in *Dicer1*$^{f/-}$ cells became undetectable in *Dicer1*$^{-/-}$ cells, whereas the remainder of miRNAs underwent a median decrease of 111-fold, confirming the global loss of mature miRNAs with homozygous *Dicer1* loss. By quantitative northern blot, miR-22 was present at ~4,000 copies per cell in *Dicer1*$^{f/-}$ sarcoma cells (Figure S1C). Based on the ratio of miRNA reads in the *Dicer1*$^{f/-}$ to *Dicer1*$^{-/-}$ small RNA-seq libraries normalized to the copy number of miR-22 in *Dicer1*$^{f/-}$ sarcoma cells, miR-22 is present at fewer than 10 copies per *Dicer1*$^{-/-}$ sarcoma cell. Similarly, based on normalization to miR-22, other abundant miRNAs such as individual let-7 family members are also expressed at fewer than ten copies per cell in *Dicer1*$^{-/-}$ cells, as compared to several thousand in *Dicer1*$^{f/-}$ cells (Figure 1B). miR-451, a DICER1-independent miRNA processed by Ago2 and expressed abundantly in red blood cells, is not detectable in *Dicer1*$^{f/-}$ sarcoma cells and is present at extremely low levels (0.4 copies/cell) in *Dicer1*$^{-/-}$ sarcoma cells (Cheloufi et al., 2010; Cifuentes et al., 2010). These results indicate near-complete loss of miRNAs upon *Dicer1* deletion.

In *Dicer1*$^{f/-}$ cells, the five most abundant miRNAs were miR-22 (13%), let-7f (7%), let-7a (7%), let-7c (7%), and miR-21 (6%) (Table S1). Collapsing miRNAs by seeds, the dominant heptamer seed sequence corresponds to let-7, accounting for 31.6% of all miRNA reads. Let-7 dominance has been observed in other somatic tissues, such as embryonic fibroblasts and neural precursors (Marson et al., 2008). In addition, we observed miRNAs associated with tissue-specific expression and function, such as kidney-specific miR-196a and -196b (1.2% combined) (Landgraf et al., 2007) and miR-96 (2.2%), implicated in progressive hearing loss (Lewis et al., 2009), suggesting broader regulatory roles for these short RNAs. Reads from the miR-290-295 cluster, specific to embryonic stem cells, were negligible in number, distinguishing these cells as somatic. In total, our results establish let-7 as the dominant seed in *Dicer1*$^{f/-}$ sarcoma cells and confirm the loss of mature miRNAs following *Dicer1* deletion.

As a confirmation of these sequencing results, we performed northern analysis for let-7g, miR-16, and miR-17, all detected abundantly in our *Dicer1*$^{f/-}$ sequencing library. In contrast to *Dicer1*$^{f/-}$ cells, *Dicer1*$^{-/-}$ cells showed an absence of mature miRNAs and concomitant accumulation of precursors (Figure 1C). Luciferase reporters containing six bulged sites for let-7g or one perfect site for either miR-16 or miR-17 were also derepressed 3- to 6-fold, consistent with functional loss (Figure 1D). To evaluate proliferative differences, we measured doubling times for each genotype (Figure 1E). *Dicer1*$^{-/-}$ cells divided more slowly (~15 hr) than the *Dicer1*$^{f/-}$ controls (~12 hr), but without obvious senescence or onset of crisis. *Dicer1*$^{-/-}$ sarcoma cells exhibited a delay in G1 phase relative to *Dicer1*$^{f/-}$ sarcoma cells (Figure 1F). Additionally, the *Dicer1*$^{-/-}$ sarcoma cells exhibited elevated levels of apoptosis (Figure 1G).

Dicer1$^{-/-}$ Sarcoma Cells Retain Tumorigenicity In Vivo

Our findings indicate that genetic ablation of *Dicer1* is tolerated in mouse sarcoma cells in vitro. However, in vivo mouse models and human patient data suggest that homozygous deletion of *Dicer1* is not tolerated in tumors. To test whether proliferative defects in homozygous *Dicer1*-deleted tumors, and subsequent loss through competition in vivo by DICER1-expressing cells, account for these differences, we carried out tumor formation assays. Upon subcutaneous injection of 1×10^6 cells into the flanks of immune-compromised mice, *Dicer1*$^{-/-}$ cells were indeed tumorigenic, forming tumors at 7/18 sites within 24 days, as compared to 4/8 sites by day 14 for the original *Dicer1*$^{f/-}$ strain. To better evaluate the difference in tumor formation kinetics, we repeated this injection experiment with 2.5×10^4 cells. At this lower cell number, *Dicer1*$^{-/-}$ sarcoma cells began to develop tumors in ~45 days, as compared to 22 days for the parental *Dicer1*$^{f/-}$ sarcoma cell line (Figure 2A). Pathologic analysis of either *Dicer1*$^{-/-}$ or *Dicer1*$^{f/-}$ tumors identified both as high grade sarcomas with pleomorphic nuclei and abnormal mitoses, consistent with previous reports of KRAS-driven sarcoma models (Figure 2B) (Kirsch et al., 2007; Kumar et al., 2007). Sample genotypes could not be readily distinguished in a blinded analysis.

We also performed syngeneic injections into immunocompetent C57Bl6/SV129 F1 mice. As before, the rate was slower than the parental *Dicer1*$^{f/-}$ line, with the first tumors appearing 7 days after injection of the *Dicer1*$^{f/-}$ cells and 21 days after injection of the *Dicer1*$^{-/-}$ cells (Figure S2). Thus, the absence of DICER1 impairs but does not preclude tumor formation, even in an immunocompetent background.

Although the sarcoma cells at the time of the injection were *Dicer1*$^{-/-}$, it is possible that in vivo selection resulted in outgrowth of contaminating *Dicer1*$^{f/-}$ cells. Therefore, we

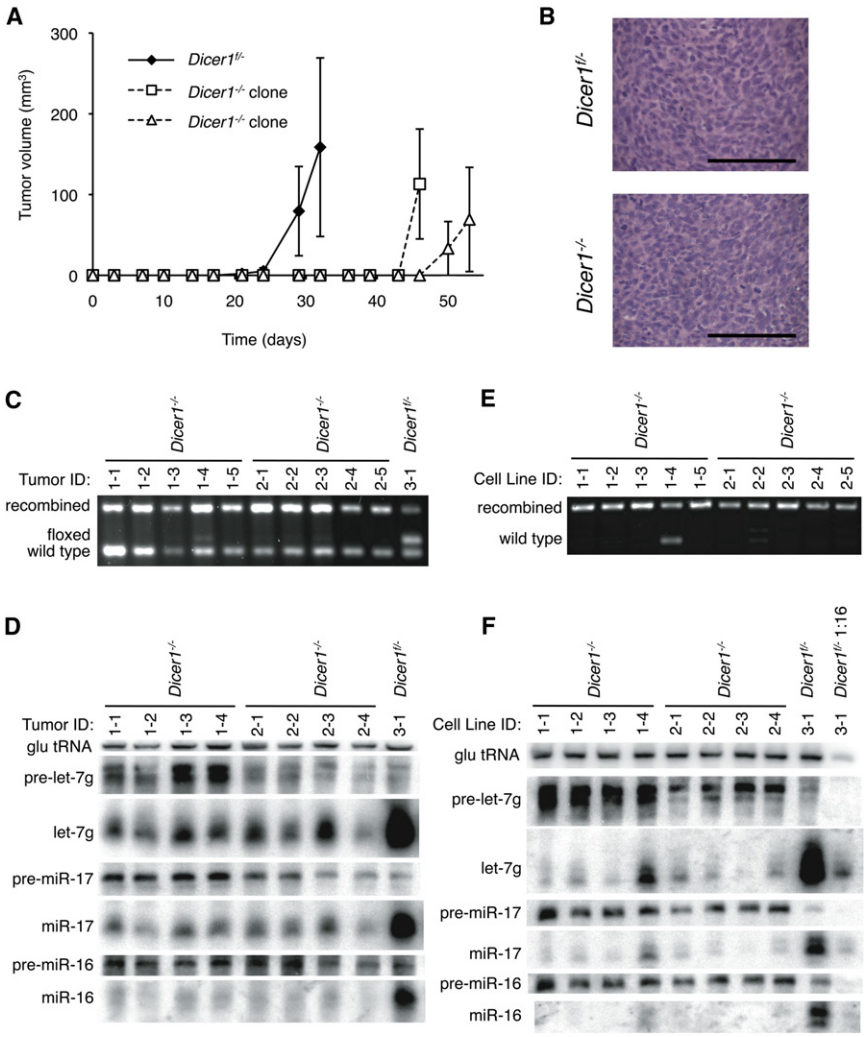

Figure 2. Tumorigenesis of *Kras*^{G12D}; *Trp53*$^{-/-}$;*Dicer1*$^{-/-}$ Sarcoma Cells in Transplant Assays

(A) Injection of 2.5 × 10^4 *Dicer1*$^{f/-}$ and *Dicer1*$^{-/-}$ sarcoma cells into the flanks of nude mice. Error bars represent the SEM.

(B) Hematoxylin and eosin section of *Dicer1*$^{f/-}$ and *Dicer1*$^{-/-}$ tumors. In (C–F) each lane represents an independent tumor derived from one injection of the indicated *Dicer1*$^{-/-}$ sarcoma cell line. Scale bar represents 100 μm.

(C) PCR genotyping of *Dicer1*$^{-/-}$ tumors. Recombined and floxed bands are derived from the injected tumor cells, whereas wild-type bands derive from host tissue.

(D) Northern analysis of tumor tissue derived from sarcoma injections.

(E and F) PCR (E) and northern (F) analysis following one round of in vitro passage of secondary tumors. In (C–F), each sample ID contains a prefix identifying the injected sarcoma cell clone followed by a suffix identifying the tumor replicate (e.g., sample 1-3 corresponds to clone 1 and tumor replicate 3).

See also Figure S2.

genotyped DNA prepared from primary tumor tissue and confirmed a significant recombined band corresponding to the injected *Dicer1*$^{-/-}$ cells with an accompanying background wild-type band contributed by contaminating host tissue (Figure 2C). Northern analysis of primary tumors revealed accumulation of precursors as well as significant but incomplete depletion of mature miRNAs (Figure 2D).

To test if the residual miRNAs were a result of contaminating wild-type tissue, we generated cell lines from these tumors. PCR genotyping confirmed a depletion of the wild-type tissue during this process (Figure 2E). By northern blotting, the level of mature miRNAs was lower than the detection limit of the blot, and this was again accompanied by enrichment in the pre-miRNA (Figure 2F). The residual mature miRNA observed is likely due to host tissue contamination, as evidenced by the greatest miRNA signal in the tumor sample showing the greatest wild-type contaminant band by PCR (Figures 2E and 2F). Thus, injected *Dicer1*$^{-/-}$ cells survived and proliferated in vivo without recovery of miRNA processing. The earlier in vitro results extend to an in vivo setting, with sarcoma cells retaining the capacity to form phenotypically similar tumors, albeit more slowly, in the absence of DICER1 and miRNAs.

Mesenchymal Stem Cells Were Generated as an Alternative Model of Somatic *Dicer1* Deletion

The viability of *Dicer1* null sarcoma cells, which lack TRP53 and express oncogenic KRAS, may be a function of the strong oncogenic background required for rapid in vivo growth or may require additional genetic alterations that occur during tumor formation. Therefore, we tested whether *Dicer1* loss could be tolerated in a defined immortalized cell model. Because sarcomas are thought to be mesenchymal in origin (Clark et al., 2005), we turned to mesenchymal stem cells (MSCs), a multipotent population of cells that can differentiate into osteoblasts, chondrocytes, adipocytes, or myocytes (Pittenger et al., 1999).

From a 1-year-old adult *Dicer1*$^{f/f}$ mouse, we prepared a primary culture of MSCs that was then immortalized with a retroviral vector encoding SV40 large T-antigen (Figure 3A). Individual clones were isolated and analyzed by flow cytometry to confirm the expression of CD49e and CD106 (Figure 3B, left panels), surface markers associated with MSCs (Pittenger, 2008), and the absence of CD31, specific to endothelial cells, and CD45, a marker of hematopoietic stem cells (data not shown).

To delete *Dicer1*, we carried out Adeno-Cre-GFP infection and sorted the infected cells by GFP. This protocol enriched for *Dicer1*$^{-/-}$ cells, as seen by the predominance of the deletion-specific PCR product 6 days after sorting (Figure S3A). This signal was accompanied by loss of DICER1 protein (Figure S3B), as well as a decrease in mature miRNA levels by qPCR (Figure S3C) and northern blot at day 7 (Figure S3D). However, as observed for the sarcoma cells, additional passage

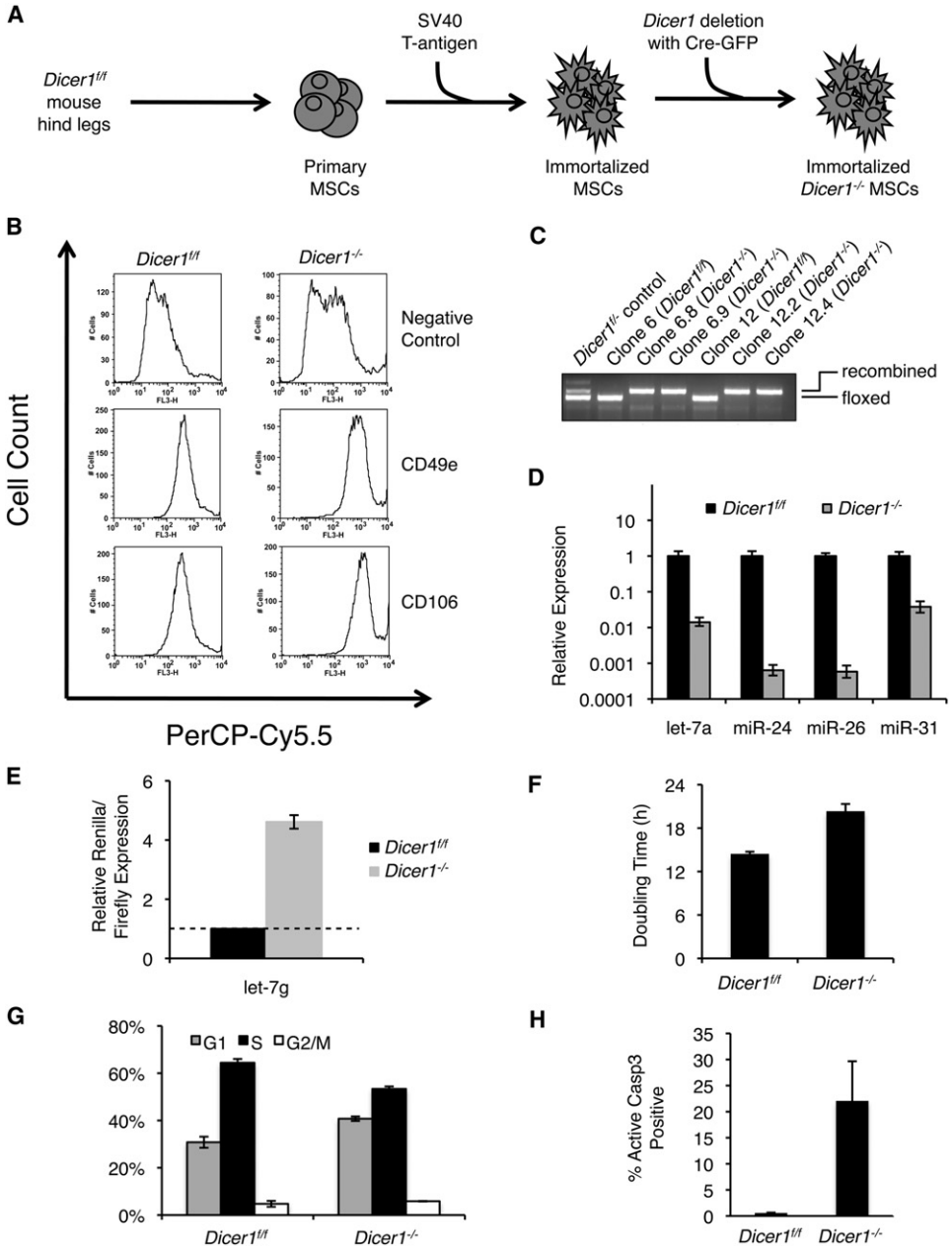

Figure 3. Derivation and Characterization of *Dicer1*$^{-/-}$ Mesenchymal Stem Cells

(A) Schematic of MSC preparation. Primary MSC cultures were prepared from the tibia, femur, and pelvic bones of a 1-year-old *Dicer1*$^{f/f}$ mouse. The primary cells were then infected with retrovirus encoding SV40 large T-antigen. Monoclonal cultures were then isolated, infected with Adeno-Cre-GFP, sorted by FACS for GFP-positive cells, and plated at low density to isolate *Dicer1*-recombined clones.

(B) Cell surface marker expression in *Dicer1*$^{f/f}$ (left) and *Dicer1*$^{-/-}$ (right) MSCs. Cells were analyzed by flow cytometry with antibodies against CD49e and CD106.

(C) PCR genotyping of clonally isolated *Dicer1*$^{f/f}$ or *Dicer1*$^{-/-}$ MSCs. Clones 6.8 and 6.9 (lanes 3, 4) were derived from parental clone 6 (lane 2), and clones 12.2 and 12.4 (lanes 6, 7) were derived from parental clone 12 (lane 5). PCR genotyping of a *Dicer1*$^{f/-}$ sarcoma cell line was used as a heterozygous control (lane 1).

(D) Expression of miRNAs in *Dicer1*$^{f/f}$ and *Dicer1*$^{-/-}$ MSCs. Total RNA was analyzed with a QIAGEN miScript qPCR assay for let-7a, miR-24, -26, and -31. A representative qPCR experiment is shown. Error bars represent standard deviation.

(E) Luciferase reporter assay for let-7g. The reporter contains six bulged sites. Targeted Renilla luciferase reporters were normalized to nontargeted firefly luciferase reporters. Renilla/firefly luciferase expression was normalized to expression in the *Dicer1*$^{f/f}$ MSC line.

(F) Proliferation assay.

(G) Cell cycle distribution determined by BrdU labeling.

(H) Apoptosis determined by caspase-3 cleavage assay.

Error bars represent SEM (E–H). See also Figure S3.

led to a decrease in the deletion-specific PCR band (Figure S3A), suggesting outgrowth of DICER1-expressing cells.

To prevent competition by cells retaining *Dicer1*, we repeated the strategy used for the sarcoma cell lines and isolated clones. MSCs were infected with Adeno-Cre-GFP, sorted for GFP 2 days later, then plated at low-density after an additional 10 days. Clones were then isolated, expanded, and PCR genotyped to confirm recombination (Figure 3C). Of these clones, a majority (55%) had undergone homozygous deletion of *Dicer1*, indicating that immortalized MSCs can readily tolerate loss of *Dicer1*. *Dicer1*$^{-/-}$ clones were stably proliferative and remained *Dicer1* null after multiple passages (>3 months) as determined by PCR genotyping (data not shown). All subsequent experiments were carried out with a monoclonal *Dicer1*$^{-/-}$ MSC line. Following loss of *Dicer1*, we observed an ~100-fold reduction of miRNA expression by qPCR analysis of abundant miRNAs (let-7a, miR-24, -26, and -31) (Figure 3D). We also observed ~5-fold derepression of a let-7g luciferase reporter in *Dicer1*$^{-/-}$ cells (Figure 3E). *Dicer1*$^{-/-}$ MSCs exhibited a proliferative lag, with a doubling time of ~20 hr relative to ~14 hr for *Dicer1*$^{f/f}$ cells (Figure 3F). *Dicer1*$^{-/-}$ MSCs also exhibited a G1 delay in cell cycle (Figure 3G) and elevated levels of basal apoptosis (Figure 3H). Notably, *Dicer1*$^{-/-}$ MSCs remained positive for CD49e and CD106 (Figure 3B, right panels) and negative for CD31 and CD45 (data not shown), suggesting a retention of cell identity in the absence of miRNAs.

DISCUSSION

We have carried out homozygous *Dicer1* deletion in a *Dicer1*-conditional KRAS-activated, *Trp53* null sarcoma cell line and observed resultant loss of miRNA expression by small RNA sequencing. Relative to *Dicer1*$^{f/-}$ sarcoma cells, these miRNA-depleted cells proliferate more slowly, exhibit a cell cycle delay in G1 phase, and have a higher level of basal apoptosis. Additionally, we have generated a second in vitro model of homozygous *Dicer1*-deletion in murine mesenchymal stem cells, related in cell type to sarcomas, established from an adult *Dicer1*$^{f/f}$ mouse and immortalized in vitro. Similar to the sarcoma model, MSCs that had undergone homozygous *Dicer1* deletion were readily isolatable but exhibited a reduction in proliferation, a delay in G1, and an increase in basal apoptosis.

Strikingly, *Dicer1*$^{-/-}$ sarcoma cells retain the ability, upon transplant, to form tumors in both immunocompromised and immunocompetent recipient mice, albeit at slower rates relative to *Dicer1*$^{f/-}$ sarcoma cells. We present three compelling lines of evidence excluding the possibility that these tumors arose from contaminating *Dicer1*$^{f/-}$ cells:

(1) Clonal *Dicer1*$^{-/-}$ sarcoma cells were used for the tumor injection studies to preclude the possibility of *Dicer1*$^{f/-}$ outgrowth.
(2) Tumors derived from *Dicer1*$^{-/-}$ injections exhibit strong PCR genotyping bands for (1) recombined *Dicer1*, and (2) wild-type *Dicer1*, derived from host wild-type tissue associated with the tumors. In contrast, the control tumor derived from *Dicer1*$^{f/-}$ cells exhibits a third PCR band, representing unrecombined floxed *Dicer1*. This stark difference in genotype demonstrates that the tumors that arose from *Dicer1*$^{-/-}$ injections are composed predominantly of *Dicer1*$^{-/-}$ cells.
(3) In vitro passage of cells derived from *Dicer1*$^{-/-}$ tumors resulted in depletion of wild-type primary host tissue and outgrowth of *Dicer1*$^{-/-}$ cells, as determined by PCR genotyping, and concomitant depletion in miRNA signal by northern blot. Furthermore, in most tumor samples, miRNAs were present at levels less than one-sixteenth of the *Dicer1*$^{f/-}$ control, likely an overestimate given the low level of contaminating host-derived cells.

Our results stand in stark contrast to many published reports. The failure to observe *Dicer1* null tumors from *Dicer1*-conditional in vivo mouse models of cancer have been interpreted to suggest that DICER1 and miRNAs are essential for tumor formation and, furthermore, may be required for tumor cell survival. Contrary to these observations, our results indicate that miRNAs are not essential for in vitro survival or proliferation. In vivo, *Dicer1* null sarcoma cells, though depleted of miRNAs, are competent for tumor development. Furthermore, our observation of tumor growth in an immunocompetent background demonstrates that miRNAs are not essential for escape from immune surveillance. In addition, the histological resemblance of *Dicer1*$^{-/-}$ sarcomas to *Dicer1*$^{f/-}$ sarcomas, as well as the retention of cell type-specific cell surface markers in *Dicer1*$^{-/-}$ MSCs, suggest that cellular identity is largely retained despite loss of miRNAs. Given the high frequency with which *Dicer1* null cells can be isolated in both the sarcoma and MSC models, secondary mutational or other low frequency events beyond the initial immortalization are likely not necessary to tolerate DICER1 loss.

Based on the outgrowth of DICER1-expressing cells in vitro relative to *Dicer1*$^{-/-}$ cells, and the proliferative delay observed in monoclonal *Dicer1*$^{-/-}$ cells, we conclude that the absence of *Dicer1* null cells in previously characterized mouse models of cancer is due in part to the preferential outgrowth, in vivo, of cells expressing DICER1. Notably, tumor genotyping analyses in published studies have typically been carried out in whole tumor samples and, as such, do not exclude the possibility that *Dicer1* null cells comprise a subpopulation of the samples.

Furthermore, factors additional to proliferative capacity may contribute to the preferential outgrowth of DICER1-expressing cells in vivo. The viability of *Dicer1* null transformed cells in our study indicates that total miRNA loss itself, and resultant genetic misregulation, is not intrinsically catastrophic, but rather triggers secondary signals that initiate changes in proliferation or cell death. Numerous studies have reported that miRNAs mediate stress responses (Hermeking, 2007; Leung and Sharp, 2010; Leung et al., 2011a) and loss of DICER1 in embryonic stem cells results in increased sensitivity to stress (Zheng et al., 2011). Similarly, we have observed that sarcoma cells and MSCs that lack DICER1 exhibit increased apoptosis. Given the intrinsically stressful nature of the in vivo tumor environment, the retention of a miRNA-mediated stress response may provide an additional growth advantage to tumor cells that retain at least one copy of *Dicer1*.

Notably, inactivation of TRP53 is a common feature in both the sarcoma and MSC models presented here and may facilitate or

be required for viability in the absence of DICER1. This possibility is consistent with the observation that TRP53 loss allows primary MEFs to bypass an immediate senescence phenotype induced by DICER1 loss (Mudhasani et al., 2008). However, TRP53 loss alone only prolongs proliferative capacity of *Dicer1*$^{-/-}$ MEFs for a few additional passages (S.N. Jones, personal communication), suggesting that other events, such as activation of oncogenes or inactivation of additional tumor suppressor genes, are required.

In addition to expanding our understanding of DICER1 in tumorigenesis, the cell lines reported here may complement existing models such as the hypomorphic *DICER1* HCT116 line, a human colorectal cancer line containing homozygous deletion of exon 5 in the *DICER1* gene (Cummins et al., 2006). The availability of *Dicer1*$^{-/-}$ cancer cells will permit further characterization of somatic miRNA families through miRNA transfection and "add-back" cell culture experiments. Finally, the observations that DICER1 loss leads to a negative selective pressure in vitro and in vivo suggests that DICER1 activity could be a therapeutic target.

EXPERIMENTAL PROCEDURES

Animal Work

All animal studies were performed with protocols approved by the NIH and the Massachusetts Institute of Technology Committee for Animal Care, and were consistent with the Guide for Care and Use of Laboratory Animals, National Research Council, 1996 (Institutional Animal Welfare Assurance No. A-3125-01).

Cell Culture

Sarcoma cells were generated from hindlimb injection of Adeno-Cre into *Kras*$^{LSL\text{-}G12D}$;*Trp53*$^{f/f}$;*Dicer1*$^{f/f}$ mice as described previously (Kirsch et al., 2007). Sarcoma cells infected with MSCV.CreER^{T2}.puro were treated with 250 nM 4-hydroxy tamoxifen for 24 hr to recombine the floxed *Dicer1* allele and plated at clonal density. Primary MSC cultures were prepared from an adult *Dicer1*$^{f/f}$ mouse using a previously described protocol (Mukherjee et al., 2008), immortalized with SV40 large T-antigen, and infected with Adeno-Cre-GFP to recombine the floxed alleles. Cells were genotyped as described previously (Calabrese et al., 2007).

Histology

Tumor-bearing animals were sacrificed with CO_2 asphyxiation. Tumors were isolated, fixed in 4% paraformaldehyde, transferred to 70% ethanol, and embedded in paraffin. Tumors were then sectioned and stained with hematoxylin and eosin.

Tumor Injection

A total of 2.5 × 10^4, 10^5, or 10^6 *Kras*^{G12D};*Trp53*$^{-/-}$ sarcoma cells of *Dicer1*$^{f/-}$ or *Dicer1*$^{-/-}$ genotype were suspended in PBS and subcutaneously injected into the flanks of *Rag2*$^{-/-}$ or C57Bl6/SV129 F1 mice. Tumors were measured over time by calipers and volumes were assessed as described previously (Sage et al., 2000). DNA, RNA, and histological sections were prepared from tumors. Some tumors were trypsinized and replated for the development of secondary cell lines as described above.

Small RNA Northerns and Cloning

Small RNA northern blots were performed using 20 μg total RNA on a 15% denaturing polyacrylamide gel. Following semi-dry transfer to a Hybond-N+ membrane, a DNA oligo probe for glutamine tRNA or LNA probes for let-7, mir-16, and mir-17 were used for visualization. Small RNA sequencing from sarcoma lines was carried out as described previously (Leung et al., 2011b). The sequencing data are available under Gene Expression Omnibus accession GSE34825.

SUPPLEMENTAL INFORMATION

Supplemental Information includes three figures, one table, and Supplemental Experimental Procedures and can be found with this article online at doi:10.1016/j.ccr.2012.04.037.

ACKNOWLEDGMENTS

We thank members of the Sharp, Jacks, and Lees Labs for many helpful discussions. We are also specifically grateful to Margaret Ebert, Amy Seila, and Eliezer Calo for their generous contribution of reagents. We thank Allison Landman for providing assistance with mesenchymal stem cell isolation and cultures. We thank Roderick Bronson for analysis of histology slides. Massively parallel Illumina sequencing was carried out by the Biopolymers & Proteomics Core Facility in the Swanson Biotechnology Center at the David H. Koch Institute for Integrative Cancer Research at M.I.T. Bioinformatic analysis was carried out in the Bioinformatics & Computing division of the Swanson Biotechnology Center. This work was supported by a Fannie and John Hertz Foundation Fellowship (A.R.), a Leukemia and Lymphoma Society grant 5198-09 (A.M.G.), an NIH grant RO1-CA133404 (P.A.S.), an NCI grant PO1-CA42063 (P.A.S., T.J., J.A.L.), and partially by the NCI Cancer Center Support (core) grant P30-CA14051.

A.R., A.M.G., and M.S.K. designed and performed the experiments. A.B. performed the informatics for the sequencing data. C.C. and V.L. performed experiments. A.R., A.M.G., and P.A.S. wrote the paper. J.A.L., T.J., and P.A.S. provided supervision and assisted with manuscript preparation. All authors reviewed and approved the manuscript.

Received: December 25, 2011
Revised: March 7, 2012
Accepted: April 24, 2012
Published: June 11, 2012

REFERENCES

Arrate, M.P., Vincent, T., Odvody, J., Kar, R., Jones, S.N., and Eischen, C.M. (2010). MicroRNA biogenesis is required for Myc-induced B-cell lymphoma development and survival. Cancer Res. *70*, 6083–6092.

Bartel, D.P. (2009). MicroRNAs: target recognition and regulatory functions. Cell *136*, 215–233.

Calabrese, J.M., Seila, A.C., Yeo, G.W., and Sharp, P.A. (2007). RNA sequence analysis defines Dicer's role in mouse embryonic stem cells. Proc. Natl. Acad. Sci. USA *104*, 18097–18102.

Cheloufi, S., Dos Santos, C.O., Chong, M.M., and Hannon, G.J. (2010). A dicer-independent miRNA biogenesis pathway that requires Ago catalysis. Nature *465*, 584–589.

Chivukula, R.R., and Mendell, J.T. (2008). Circular reasoning: microRNAs and cell-cycle control. Trends Biochem. Sci. *33*, 474–481.

Cifuentes, D., Xue, H., Taylor, D.W., Patnode, H., Mishima, Y., Cheloufi, S., Ma, E., Mane, S., Hannon, G.J., Lawson, N.D., et al. (2010). A novel miRNA processing pathway independent of Dicer requires Argonaute2 catalytic activity. Science *328*, 1694–1698.

Clark, M.A., Fisher, C., Judson, I., and Thomas, J.M. (2005). Soft-tissue sarcomas in adults. N. Engl. J. Med. *353*, 701–711.

Cummins, J.M., He, Y., Leary, R.J., Pagliarini, R., Diaz, L.A., Jr., Sjoblom, T., Barad, O., Bentwich, Z., Szafranska, A.E., Labourier, E., et al. (2006). The colorectal microRNAome. Proc. Natl. Acad. Sci. USA *103*, 3687–3692.

Friedman, R.C., Farh, K.K., Burge, C.B., and Bartel, D.P. (2009). Most mammalian mRNAs are conserved targets of microRNAs. Genome Res. *19*, 92–105.

Gaur, A., Jewell, D.A., Liang, Y., Ridzon, D., Moore, J.H., Chen, C., Ambros, V.R., and Israel, M.A. (2007). Characterization of microRNA expression levels and their biological correlates in human cancer cell lines. Cancer Res. *67*, 2456–2468.

Heravi-Moussavi, A., Anglesio, M.S., Cheng, S.W., Senz, J., Yang, W., Prentice, L., Fejes, A.P., Chow, C., Tone, A., Kalloger, S.E., et al. (2012).

Recurrent somatic DICER1 mutations in nonepithelial ovarian cancers. N. Engl. J. Med. *366*, 234–242.

Hermeking, H. (2007). p53 enters the microRNA world. Cancer Cell *12*, 414–418.

Herranz, H., and Cohen, S.M. (2010). MicroRNAs and gene regulatory networks: managing the impact of noise in biological systems. Genes Dev. *24*, 1339–1344.

Hill, D.A., Ivanovich, J., Priest, J.R., Gurnett, C.A., Dehner, L.P., Desruisseau, D., Jarzembowski, J.A., Wikenheiser-Brokamp, K.A., Suarez, B.K., Whelan, A.J., et al. (2009). DICER1 mutations in familial pleuropulmonary blastoma. Science *325*, 965.

Kirsch, D.G., Dinulescu, D.M., Miller, J.B., Grimm, J., Santiago, P.M., Young, N.P., Nielsen, G.P., Quade, B.J., Chaber, C.J., Schultz, C.P., et al. (2007). A spatially and temporally restricted mouse model of soft tissue sarcoma. Nat. Med. *13*, 992–997.

Kumar, M.S., Lu, J., Mercer, K.L., Golub, T.R., and Jacks, T. (2007). Impaired microRNA processing enhances cellular transformation and tumorigenesis. Nat. Genet. *39*, 673–677.

Kumar, M.S., Pester, R.E., Chen, C.Y., Lane, K., Chin, C., Lu, J., Kirsch, D.G., Golub, T.R., and Jacks, T. (2009). Dicer1 functions as a haploinsufficient tumor suppressor. Genes Dev. *23*, 2700–2704.

Lambertz, I., Nittner, D., Mestdagh, P., Denecker, G., Vandesompele, J., Dyer, M.A., and Marine, J.C. (2010). Monoallelic but not Biallelic loss of Dicer1 promotes tumorigenesis in vivo. Cell Death Differ. *17*, 633–641.

Landgraf, P., Rusu, M., Sheridan, R., Sewer, A., Iovino, N., Aravin, A., Pfeffer, S., Rice, A., Kamphorst, A.O., Landthaler, M., et al. (2007). A mammalian microRNA expression atlas based on small RNA library sequencing. Cell *129*, 1401–1414.

Leung, A.K., and Sharp, P.A. (2010). MicroRNA functions in stress responses. Mol. Cell *40*, 205–215.

Leung, A.K., Vyas, S., Rood, J.E., Bhutkar, A., Sharp, P.A., and Chang, P. (2011a). Poly(ADP-ribose) regulates stress responses and microRNA activity in the cytoplasm. Mol. Cell *42*, 489–499.

Leung, A.K., Young, A.G., Bhutkar, A., Zheng, G.X., Bosson, A.D., Nielsen, C.B., and Sharp, P.A. (2011b). Genome-wide identification of Ago2 binding sites from mouse embryonic stem cells with and without mature microRNAs. Nat. Struct. Mol. Biol. *18*, 237–244.

Lewis, M.A., Quint, E., Glazier, A.M., Fuchs, H., De Angelis, M.H., Langford, C., van Dongen, S., Abreu-Goodger, C., Piipari, M., Redshaw, N., et al. (2009). An ENU-induced mutation of miR-96 associated with progressive hearing loss in mice. Nat. Genet. *41*, 614–618.

Lin, R.J., Lin, Y.C., Chen, J., Kuo, H.H., Chen, Y.Y., Diccianni, M.B., London, W.B., Chang, C.H., and Yu, A.L. (2010). microRNA signature and expression of Dicer and Drosha can predict prognosis and delineate risk groups in neuroblastoma. Cancer Res. *70*, 7841–7850.

Lu, J., Getz, G., Miska, E.A., Alvarez-Saavedra, E., Lamb, J., Peck, D., Sweet-Cordero, A., Ebert, B.L., Mak, R.H., Ferrando, A.A., et al. (2005). MicroRNA expression profiles classify human cancers. Nature *435*, 834–838.

Marson, A., Levine, S.S., Cole, M.F., Frampton, G.M., Brambrink, T., Johnstone, S., Guenther, M.G., Johnston, W.K., Wernig, M., Newman, J., et al. (2008). Connecting microRNA genes to the core transcriptional regulatory circuitry of embryonic stem cells. Cell *134*, 521–533.

Martello, G., Rosato, A., Ferrari, F., Manfrin, A., Cordenonsi, M., Dupont, S., Enzo, E., Guzzardo, V., Rondina, M., Spruce, T., et al. (2010). A MicroRNA targeting dicer for metastasis control. Cell *141*, 1195–1207.

Melo, S.A., Ropero, S., Moutinho, C., Aaltonen, L.A., Yamamoto, H., Calin, G.A., Rossi, S., Fernandez, A.F., Carneiro, F., Oliveira, C., et al. (2009). A TARBP2 mutation in human cancer impairs microRNA processing and DICER1 function. Nat. Genet. *41*, 365–370.

Mudhasani, R., Zhu, Z., Hutvagner, G., Eischen, C.M., Lyle, S., Hall, L.L., Lawrence, J.B., Imbalzano, A.N., and Jones, S.N. (2008). Loss of miRNA biogenesis induces p19Arf-p53 signaling and senescence in primary cells. J. Cell Biol. *181*, 1055–1063.

Mukherjee, S., Raje, N., Schoonmaker, J.A., Liu, J.C., Hideshima, T., Wein, M.N., Jones, D.C., Vallet, S., Bouxsein, M.L., Pozzi, S., et al. (2008). Pharmacologic targeting of a stem/progenitor population in vivo is associated with enhanced bone regeneration in mice. J. Clin. Invest. *118*, 491–504.

Pittenger, M.F. (2008). Mesenchymal stem cells from adult bone marrow. Methods Mol. Biol. *449*, 27–44.

Pittenger, M.F., Mackay, A.M., Beck, S.C., Jaiswal, R.K., Douglas, R., Mosca, J.D., Moorman, M.A., Simonetti, D.W., Craig, S., and Marshak, D.R. (1999). Multilineage potential of adult human mesenchymal stem cells. Science *284*, 143–147.

Sage, J., Mulligan, G.J., Attardi, L.D., Miller, A., Chen, S., Williams, B., Theodorou, E., and Jacks, T. (2000). Targeted disruption of the three Rb-related genes leads to loss of G(1) control and immortalization. Genes Dev. *14*, 3037–3050.

Sekine, S., Ogawa, R., Ito, R., Hiraoka, N., McManus, M.T., Kanai, Y., and Hebrok, M. (2009). Disruption of Dicer1 induces dysregulated fetal gene expression and promotes hepatocarcinogenesis. Gastroenterology *136*, 2304–2315.

Stefani, G., and Slack, F.J. (2008). Small non-coding RNAs in animal development. Nat. Rev. Mol. Cell Biol. *9*, 219–230.

Torres, A., Torres, K., Paszkowski, T., Jodłowska-Jędrych, B., Radomański, T., Książek, A., and Maciejewski, R. (2011). Major regulators of microRNAs biogenesis Dicer and Drosha are down-regulated in endometrial cancer. Tumour Biol. *32*, 769–776.

Wang, Y., Baskerville, S., Shenoy, A., Babiarz, J.E., Baehner, L., and Blelloch, R. (2008). Embryonic stem cell-specific microRNAs regulate the G1-S transition and promote rapid proliferation. Nat. Genet. *40*, 1478–1483.

Zheng, G.X., Ravi, A., Calabrese, J.M., Medeiros, L.A., Kirak, O., Dennis, L.M., Jaenisch, R., Burge, C.B., and Sharp, P.A. (2011). A latent pro-survival function for the mir-290-295 cluster in mouse embryonic stem cells. PLoS Genet. *7*, e1002054.

Cancer Cell
Erratum

The Histone Demethylase KDM1A Sustains the Oncogenic Potential of MLL-AF9 Leukemia Stem Cells

William J. Harris,[1] Xu Huang,[1] James T. Lynch,[1] James R. Hitchin,[2] Yaoyong Li,[3] Filippo Ciceri,[1] Julian G. Blaser,[1] Brigit F. Greystoke,[1] Allan M. Jordan,[2] Donald J. Ogilvie,[2] and Tim C.P. Somervaille[1,*]
[1]Cancer Research UK Leukaemia Biology Laboratory
[2]Cancer Research UK Drug Discovery Unit
[3]Cancer Research UK Applied Computational Biology and Bioinformatics Group
Paterson Institute for Cancer Research, University of Manchester, Manchester, M20 4BX, United Kingdom
*Correspondence: tsomervaille@picr.man.ac.uk
DOI 10.1016/j.ccr.2012.05.035

(Cancer Cell *21*, 473–487; April 17, 2012)

Following the publication of this paper, the authors discovered that the list of genes shown in Table S5 as ''KIM MYC CORE MODULE HUMAN ORTHOLOGS'' was in fact the set of murine genes prior to conversion to their human orthologs. This error does not affect the conclusions, but the authors apologize for the mistake. The online Table S5 has been corrected.